NUCLEI
Experiment

Independent Yields of Kr and Xe Fragments in the Photofission of ^{237}Np and ^{243}Am Odd Nuclei

Yu. P. Gangrsky*, V. I. Zhemenik, G. V. Mishinsky, and Yu. E. Penionzhkevich

Joint Institute for Nuclear Research, Dubna, Moscow oblast, 141980 Russia
Received August 5, 2004

Abstract—Results are presented that were obtained by measuring the independent yields of Kr ($A = 89-93$) and Xe ($A = 135-142$) appearing as fragments in the photofission of ^{237}Np and ^{243}Am odd nuclei. The respective experiments were performed in a beam of bremsstrahlung photons from electrons accelerated to an energy of 25 MeV at the microtron of the Laboratory of Nuclear Reactions at the Joint Institute for Nuclear Research (JINR, Dubna). Use was made of the procedure involving the transportation of fragments emitted from the target by a gas flow along a capillary and the condensation of inert gases in a cryostat at liquid-nitrogen temperature. The identification of Kr and Xe appearing as fragments was performed by the gamma spectra of their daughter products. The mass-number distributions of the independent yields of Kr and Xe isotopes were obtained, along with those for the complementary fragments (Y and La in the fission of ^{237}Np and Nb and Pr in the fission of ^{243}Am). © *2005 Pleiades Publishing, Inc.*

INTRODUCTION

Measurement of fragment yields and of their dependences on various features of fissile nuclei and fragments formed (nucleonic composition, excitation energy, angular momentum) is one of the lines of investigation into the mechanism of the nuclear-fission process. Measurement of the yields of primary fragments (independent yields)—that is, those fragments that were formed upon the scission of a fissile nucleus and neutron emission, but which have not yet undergone beta decay—is of particular interest. Such measurements furnish important information about the formation of the nucleonic composition of fragments in the process of their transition from the saddle to the scission point.

However, data on this process are obviously insufficient and refer predominantly to the neutron-induced fission of U and Pu nuclei and to the spontaneous fission of ^{252}Cf [1, 2]. It is of interest to extend the range of such investigations by including in them fission reactions caused by other bombarding particles—for example, photons. Special features of photofission reactions (a fixed angular momentum that is introduced in a fissile nucleus by a photon and the absence of Coulomb energy and binding energy) make it possible to obtain new information about the effect of external conditions on the formation of the nucleonic composition of fragments.

The present study is devoted to measuring the independent yields of fragments—isotopes of Kr and

Xe inert gases—originating from the photofission of ^{237}Np and ^{243}Am odd nuclei and is a continuation of similar experiments performed with ^{232}Th, ^{238}U, and ^{244}Pu even−even nuclei and reported in [3, 4]. An analysis of the measured fragment-mass-number dependences of the yields with allowance for known similar data on even nuclei would make it possible to explore the effect of an odd particle in a fissile nucleus on the formation of fragments. There are virtually no data on the independent yields of fragments in the photofission of nuclei featuring an odd number of protons or neutrons (we can only indicate the study reported in [5]). Moreover, the use of known data on the number of prompt fission neutrons would make it possible to deduce additional information about the yields of the complementary fragments as well—Nb and Pr in the photofission of ^{243}Am and Y and La in the fission of ^{237}Np.

EXPERIMENTAL PROCEDURE

In the present experiments, we employed the same procedure as in the studies of our group that were devoted to the photofission of even−even nuclei and which were reported in [3, 4]. Within this procedure, one implements an efficient separation of Kr and Xe isotopes from other fission fragments by using the fact that the chemical properties of the former are strongly different from the chemical properties of the latter. Krypton and xenon nuclei originating as fission fragments from a target irradiated with bremsstrahlung

*e-mail: `gangr@jinr.ru`

Table 1. Independent yields of Kr and Xe fragments

Frag- ment	^{237}Np (γ, f)		^{243}Am (γ, f)	
	Y_{rel}, %	Y_{abs}, fiss.$^{-1}$	Y_{rel}, %	Y_{abs}, fiss.$^{-1}$
^{89}Kr	65(8)	0.0019(2)	81(3)	0.019(2)
^{91}Kr	100	0.025(3)*	100	0.023(2)*
^{92}Kr	44(7)	0.011(1)	42(2)	0.0095(9)
^{93}Kr	18(4)	0.0045(5)		
^{135}Xe	61(3)	0.023(3)	42(5)	0.015(2)
^{137}Xe	100	0.038(4)*	100	0.035(4)*
^{138}Xe	80(10)	0.030(3)	76(8)	0.027(3)
^{139}Xe	31(4)	0.012(1)	35(3)	0.012(1)
^{140}Xe	8.0(9)	0.0030(3)	9.8(6)	0.0034(3)
^{141}Xe	3.0(3)	0.0011(1)	6.0(6)	0.0021(2)
^{142}Xe	2.0(3)	0.00076(8)	3.4(7)	0.0012(1)

* Estimated yield values.

photons were moderated in a gas and were transported by its flow along a Teflon capillary to a cryostat, where they were condensed on the walls of a 1-m-long copper pipe coiled into a spiral and placed in a Dewar flask that was filled with liquid nitrogen. All other fragments stopped in the gas were blocked by a filter at the inlet of the capillary. Thus, only Kr and Xe isotopes, whose half-lives were longer than 0.2 s (the time of fragment transportation along the capillary was about 0.5 s), and the products of their beta decay reached the copper pipe. For the carrier gas, we employed pure helium at a pressure of 2.5 atm in the chamber. This gas was characterized by the highest velocity of fragment transportation and was not activated by neutrons or bremsstrahlung from the microtron used.

In identifying Kr and Xe isotopes and in determining their yields, we relied on the spectra of gamma radiation that they emitted (for data on these spectra, see [6]). The identification of short-lived Kr and Xe isotopes (in the case of half-lives shorter than 1 min) was based on the gamma spectra of their daughter products (Rb and Sr for Kr and Ba and La for Xe). These daughter products, which were formed directly in the scission of a fissile nucleus, were blocked by the filter at the inlet of the capillary. Therefore, they did not contribute to the measured yields of Kr and Xe fragments. Also, the filter blocked Se, Br, Te, and I fragments, whose beta decay could produce Kr and Xe isotopes being studied. Thus, one can see that, in order to measure gamma spectra, we separated only those Kr and Xe fragments that emerged immediately

after the scission of a fissile nucleus and neutron emission, but which did not have time to undergo beta decay. The measurements were performed in a room that was protected from microtron radiation—that is, under conditions of a low gamma-ray and neutron background.

For targets subjected to irradiation, we used 50-μg/cm^2-thick layers made from Np and Am oxides and deposited onto an aluminum substrate 20 μm thick. At these layer and substrate thicknesses, half of the fragments formed in a target were emitted from it and were moderated in the gas.

In order to measure the gamma spectra in question, we employed an HpGe detector of volume 100 cm^3 and resolution 2.1 keV for the 1332-keV gamma line of ^{60}Co. The resulting spectra were saved in the memory of a PC for a subsequent analysis with the aid of the AKTIV code [7]. The yields of identified Kr and Xe fragments were determined from the areas of their gamma lines (or the gamma lines of their daughter products) in the spectra with allowance for the detection efficiency, the intensity per decay event, the irradiation time, the time of transportation along the capillary, and the time of the measurements.

The experiments were performed at an accelerated-electron energy of 25 MeV, the corresponding average excitation energy of a fissile nucleus being 13 MeV (it was determined from the shape of the bremsstrahlung spectrum [8] and the excitation function for the photofission of ^{237}Np and ^{243}Am nuclei under the assumption that this function is similar to the well-known dependence that was determined in [9] for ^{238}U).

RESULTS OF THE MEASUREMENTS

By analyzing the measured gamma spectra, we were able to identify four krypton isotopes and seven xenon isotopes. The ratios of the independent yields of these isotopes to the yields of ^{91}Kr and ^{137}Xe, respectively, are given in Table 1. In order to determine these yields per fission event, we measured the cumulative yields of fragments characterized by the mass numbers of $A = 91$ and $A = 137$ and estimated the fractions of Kr and Xe (fractional yields) in these isobars. The cumulative yields were obtained from the intensities of the gamma lines of the ^{91}Sr and ^{137}Cs isotopes, which are at the end of the beta-decay chains for these A values. The results proved to be 4.2(2)% and 6.3(3)% of the number of fission events. The fractional yields of ^{91}Kr and ^{137}Xe fragments were estimated by using the systematics of yields in the neutron-induced fission of U and Pu nuclei [1] and were found to be 0.60(6) for ^{237}Np and 0.55(6)

for ^{243}Am. These values make it possible to determine the independent yields per fission event for ^{91}Kr and ^{137}Xe and, from them, for all other Kr and Xe fragments. The yield values obtained in this way are also given in Table 1, while their dependences on the fragment mass number are displayed in the figure.

These dependences (isotope distributions of fragments) are usually approximated by the Gaussian distribution

$$Y(A) = K \exp\left[-\frac{(A - \bar{A})^2}{2\sigma^2}\right], \qquad (1)$$

where $\bar{A}$ and σ are, respectively, the mean mass number and the variance of the distribution, while K is a normalization factor. From the figure, it can be seen that, in just the same way as in the photofission of even−even nuclei, the measured distributions are well described by expression (1). However, an excess of the measured yield values above their calculated counterparts is observed for neutron-rich xenon fragments (^{141}Xe and ^{142}Xe). This may be associated with the nuclear structure of these fragments.

The fitted values of the parameters of isotope distributions are given in Table 2. A comparison with the known distributions for even−even nuclei shows that, both for ^{237}Np and for ^{243}Am, the values of $\bar{A}$ are well below those for ^{232}Th, ^{238}U, and ^{244}Pu [3], but that they are close to the value of $\bar{A}$ for ^{235}U fission induced by thermal neutrons [2]. This relationship between the $\bar{A}$ values reflects their dependence on the neutron excess in a fissile nucleus. The ratio N/A is 1.587 for ^{238}U (similar values were found previously for ^{232}Th and ^{244}Pu), 1.549 for ^{237}Np, and 1.558 for ^{243}Am. The values of σ for ^{237}Np and ^{243}Am correspond to the systematics of variances of isotope distributions in the neutron-induced fission and photofission of nuclei.

From the results obtained here for the isotope distributions of Kr and Xe, one can derive the analogous distributions for the complementary fragments. For Kr fragments, these are La isotopes in ^{237}Np fission and Pr isotopes in ^{243}Am fission. For Xe fragments, these are, respectively, Y and Nb isotopes. For fragments characterized by identical independent yields, we have

$$A_l + A_h + \nu = A_0, \qquad (2)$$

where A_l, A_h, and A_0 are the mass numbers of, respectively, a light fragment, a heavy fragment, and the fissile nucleus being considered, while ν is the total number of neutrons emitted from the two fragments.

By employing the known numbers of neutrons emitted in the neutron-induced fission of nuclei in the reactions ^{236}Np(n, f) and ^{242}Am(n, f) [10, 11] and taking into account corrections for the excitation
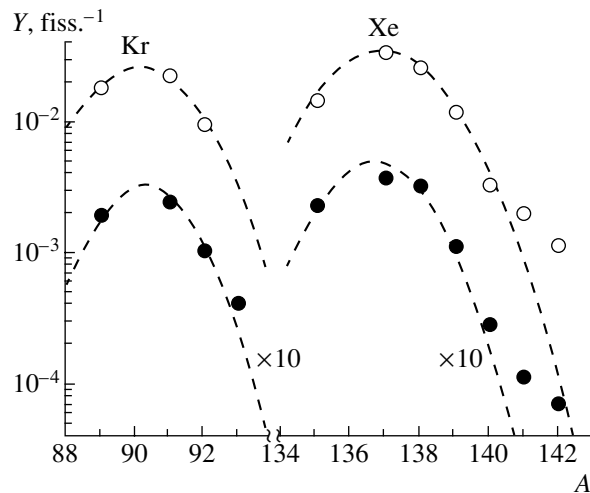
Mass-number (isotope) distributions of the independent yields of Kr and Xe fragments in the reactions (closed circles) ^{237}Np(γ, f) and (open circles) ^{243}Am(γ, f). The points represent experimental data, while the dashed curves correspond to the calculation by formula (1) whose parameters are set to the values in Table 2.

energies of the ^{237}Np and ^{243}Am nuclei undergoing fission, one can evaluate ν. The result is $\nu = 4$ for ^{237}Np and $\nu = 46$ for ^{243}Am. These values of ν make it possible to determine the mean mass numbers $\bar{A}$ of Y, Nb, La, and Pr fragments. The results are given in Table 2.

The data obtained in the present study for the photofission of ^{237}Np and ^{243}Am nuclei supplement the systematics of independent yields of fission fragments. They give sufficient grounds to conclude that an odd particle in a fissile nucleus does not change significantly the isotope distribution of fragments in relation to what was observed for even−even nuclei and that the distributions themselves are close to those that were obtained in the fast-neutron-induced fission of the corresponding nuclei.

Table 2. Parameters of the isotope distributions of photofission fragments

Element	^{237}Np(γ, f)		^{243}Am(γ, f)	
	$\bar{A}$	σ	$\bar{A}$	σ
Kr	903(2)	1.2(1)	90.1(3)	1.4(2)
Y	96.3(3)	1.3(1)		
Nb			101.5(2)	1.5(1)
Xe	136.7(2)	1.3(1)	136.9(1)	1.5(1)
La	142.7(3)	1.3(1)		
Pr			148.3(5)	1.4(2)

REFERENCES

1. A. C. Wahl, At. Data Nucl. Data Tables **39**, 1 (1988).
2. T. R. England and B. E. Rides, Preprint No. La-Ur-94-3106, LANL (Los Alamos National Laboratory, Los Alamos, 1994).
3. Yu. P. Gangrsky, V. I. Zhemenik, N. Yu. Maslova, *et al.*, Yad. Fiz. **66**, 1251 (2003) [Phys. At. Nucl. **66**, 1211 (2003)].
4. Yu. P. Gangrsky, V. I. Zhemenik, S. G. Zemlyanoĭ, *et al.*, Izv. Akad. Nauk, Ser. Fiz. **67**, 1475 (2003).
5. D. De Frenne, H. Thierens, B. Proot, *et al.*, Phys. Rev. C **26**, 1356 (1982).
6. E. Broune and R. B. Firenstone, *Table of Radioactive Isotopes* (Wiley, New York, 1986).
7. V. E. Zlokazov, Comput. Phys. Commun. **28**, 27 (1982).
8. Ph. G. Kondev, A. P. Tonchev, Kh. G. Khristov, and V. E. Zhuchko, Nucl. Instrum. Methods Phys. Res. B **71**, 126 (1992).
9. J. T. Caldwell, E. L. Dowly, B. L. Berman, *et al.*, Phys. Rev. C **21**, 1215 (1980).
10. F. Manero and V. A. Konshin, At. Energy Rev. **10**, 657 (1972).
11. Yu. P. Gangrsky, B. Dalkhsuren, and B. N. Markov, *Nuclear-Fission Fragments* (Énergoatomizdat, Moscow, 1986) [in Russian].

Translated by A. Isaakyan

======================================
NUCLEI
Theory
======================================

Subthreshold Photofission of Even−Even Nuclei

S. G. Kadmensky[*] and L. V. Rodionova

Voronezh State University, Universitetskaya pl. 1, Voronezh, 394693 Russia

Received February 14, 2005

Abstract—Within quantum-mechanical fission theory, the angular distributions of fragments originating from the subthreshold photofission of the even−even nuclei ^{232}Th, ^{234}U, ^{236}U, ^{238}U, ^{238}Pu, ^{240}Pu, and ^{242}Pu are analyzed for photon energies below 7 MeV. Special features of various fission channels are assessed under the assumption that the fission barrier has a two-humped shape. It is shown that the maximum value of the relative orbital angular momentum L_m of fission fragments can be found upon taking into account deviations from the predictions of A. Bohr's formula for the angular distributions of fission fragments. The result is $L_m \approx 30$. The existence of an "isomeric shelf" for the angular distributions of fragments from ^{236}U and ^{238}U photofission in the low-energy region is confirmed. ⓒ *2005 Pleiades Publishing, Inc.*

1. INTRODUCTION

The discovery [1] of a sizable anisotropy in the angular distributions of fragments originating from the subthreshold photofission of ^{232}Th and ^{238}U nuclei served as a basis for introducing the concept of A. Bohr's transition fission states [2, 3] (fission channels) that are formed at the saddle points of the deformation potential and which are associated with "cold" intrinsic states of a fissile nucleus. The analysis of the angular distributions of photofission fragments that was performed in the review article of Ostapenko *et al.* [4] on the basis of a vast body of experimental information and under the assumption [5] that the deformation potential of a fissile nucleus has a two-humped shape confirmed that transition fission states associated both with the inner and with the outer fission barrier play a decisive role in the formation of these distributions.

For the angular distributions of fragments from ^{236}U and ^{238}U photofission in the low-energy region, an interesting phenomenon was discovered in [6, 7] that was associated with the emergence of an "isomeric shelf," which was determined by the radiative population of shape-isomer states [8] in the second well of the deformation potential of a fissile nucleus.

We note that the results obtained previously from an analysis of angular distributions of photofission fragments—for example, in [4]—were based on the use of A. Bohr's [2, 3] formula for the angular distributions of fragments originating from the fission channel where an axisymmetric fissile nucleus has a spin J whose projection onto the symmetry axis of this nucleus is K. This formula is a realization

of the qualitative physical assumption that fission fragments are emitted along or against the direction of the fissile-nucleus-symmetry axis. Within the quantum-mechanical theory of binary nuclear fission [9], it is shown that this assumption is at odds with the quantum-mechanical uncertainty relation between the orbital angular momentum and the particle emission angle. Therefore, A. Bohr's formula can only be valid approximately under the condition that, in the asymptotic region of a fissile nucleus, where primary fission fragments have already been formed, there arise rather high orbital angular momenta of these fragments, $L \lesssim L_m$. A virtually universal mechanism of pumping of the orbital angular momenta and spins of fission fragments was justified in [10]. This mechanism is due to a strong non-sphericity of the fragment-interaction potential in the vicinity of the scission point of a fissile nucleus and leads to a value of $L_m \approx 30$ for the maximum relative orbital angular momentum of fission fragments. So large a value of L_m is consistent with the limiting estimate obtained in [10] for the maximum value of the total spin of primary fragments, $\mathbf{F} = \mathbf{J}_1 + \mathbf{J}_2$, on the basis of experimental data on the multiplicity of prompt neutrons and on the multiplicity and multipolarity of prompt photons emitted by primary fragments, the condition that the maximum spins of these fragments are parallel, $(\mathbf{J}_1)_{\max} || (\mathbf{J}_2)_{\max}$, being satisfied.

On the basis of quantum-mechanical fission theory [9], we analyzed in [11] the angular distribution of fragments from ^{238}U photofission induced by bremsstrahlung photons of endpoint energy $E_\gamma = 5.2$ MeV, at which the experimental parameters of this distribution were determined in [12] to a fairly high degree of precision. For the maximum relative

[*]e-mail: `kadmensky@phys.vsu.ru`

orbital angular momentum in question, we found the range $25 < L_m < 40$, which correlates with the value determined in [10], $L_m \approx 30$.

The objective of the present study is to perform, within quantum-mechanical fission theory [9–11], a more detailed analysis of the angular distributions of fragments originating from the subthreshold photofission of even–even nuclei ^{232}Th, ^{234}U, ^{236}U, ^{238}U, ^{238}Pu, ^{240}Pu, and ^{242}Pu. This analysis is aimed at obtaining additional information about the value of L_m and about the physics of binary nuclear fission.

2. ANGULAR DISTRIBUTIONS OF FRAGMENTS FROM SUBTHRESHOLD PHOTOFISSION OF NUCLEI

We will perform a further analysis for the subthreshold photofission of axisymmetric deformed even–even actinide nuclei, assuming that the fission barrier has a two-humped shape [4]. At a rather low endpoint energy of the photons ($E_\gamma < 7$ MeV), the cross sections for photofission that leads to the formation of compound-nucleus states in the first well of the deformation potential decrease with increasing photon multipolarity J according to the long-wavelength law; that is,

$$\sigma_\gamma^{EJ} \approx (k_\gamma R_A)^{2(J-1)} \sigma_\gamma^{E1}; \quad \sigma_\gamma^{MJ} \approx (k_\gamma R_A)^{2J} \sigma_\gamma^{E1},$$

where k_γ is the photon wave vector and R_A is the radius of the nucleus involved, the quantity $(k_\gamma R_A)^2$ taking values in the interval 0.03–0.05 for actinide nuclei [4]. Therefore, one can disregard the contributions to the photofission cross sections from electric photons EJ for $J > 2$ and from magnetic photons MJ for $J > 1$. Subthreshold photofission via the absorption of $M1$ photons is determined by $J^\pi = 1^+$ transition fission states at the first and the second fission barrier, where J is the spin of these states and π is their parity. For axisymmetric even–even nuclei, the projection K of the spin J onto the nuclear-symmetry axis in $J^\pi = 1^+$ low-lying collective states is $K = 1$. In the region of actinide nuclei, the $J^\pi K = 1^+1$ collective state in the first well has a high excitation energy (about 1.5 MeV) with respect to the ground state, whose quantum numbers are $J^\pi K = 0^+0$. Therefore, one can expect that 1^+1 transition fission states formed at the first and the second fission barrier will also have high excitation energies with respect to 0^+0 and 2^+0 transition fission states and, in the case of subthreshold fission, very low penetration factors in relation to the penetration factors for 2^+0 transition fission states initiated in photofission by quadrupole electric photons. For the subthreshold photofission of even–even nuclei, one can therefore eliminate effects associated with the absorption of

M1 photons. At the same time, one can disregard the effect of 2^+1 fission channels initiated by the absorption of $E2$ photons, since the penetration factors for these channels involve the same smallness as the penetration factors for the 1^+1 channels.

If, for the direction of the z axis in the laboratory frame, one chooses the direction of the axis of an unpolarized-photon beam, it follows from the transverseness of the electromagnetic field that the projection M of the spin J onto the z axis of the laboratory frame in the compound state excited in the first well upon photon absorption by an even–even nucleus will have the values of $M = \pm 1$ with equal probabilities. The differential cross section for the (γ, f) subthreshold photofission of even–even nuclei that proceeds first through the stage of formation of a compound nucleus in the first well and which, thereupon, is not associated with the mechanism of delayed fission (it is induced by the radiative population of shape-isomer states [8] in the second well [6, 7]) can be represented in the form [3]

$$\sigma_{\gamma f}(\theta) \equiv \frac{d\sigma_{\gamma f}(\theta)}{d\Omega} = \sum_{J, K \geqslant 0} P^{JK} T_{MK}^J(\theta), \quad (1)$$

$$P^{JK} = \frac{\Gamma_f^{JK}}{\Gamma^J}(2 - \delta_{K,0})\sigma_\gamma^{EJ}, \quad (2)$$

where the factor $(2 - \delta_{K,0})$ takes into account a double degeneracy of $K > 0$ states, the photofission cross section $\sigma_\gamma^{EJ}(E_\gamma)$ involves only $E1$ and $E2$ photons, and the solid angle $\Omega \equiv (\theta, \varphi)$ determines the direction of fission-fragment emission in the laboratory frame. In (2), Γ^J is the total decay width of the compound state in the first well with allowance for all decay channels, including radiative ones, and Γ_f^{JK} is the partial fission width of this compound state, the latter being determined by the projection K of the spin J onto the symmetry axis of a fissile nucleus in the external region of this nucleus, where K is already an integral of the motion. It is assumed that this region coincides with the region where there occurs the transition from the outer saddle point of the deformation potential through the scission point to the space of already formed primary fission fragments, the fissile nucleus retaining its axisymmetric shape throughout this transition. The quantity Γ_f^{JK} depends in a complicated way on the properties of transition fission states at the first and the second fission barrier, the properties of collective deformation modes of motion of the nucleus, and the character of the coupling of these modes to the compound states of the nucleus in the first and the second well. Here, it is assumed that, in the compound states of the first well, all projections of the spin J onto the symmetry axis of the nucleus

undergo a uniform statistical mixing owing to the dynamical enhancement of the Coriolis interaction effect [13]. A similar idea is also often used [3, 4] for compound states in the second well, but it has yet to be rigorously justified.

The normalized (to unity) angular distribution $T^{JK}(\theta)$ of the fragments of photofission in the JK exit fission channel is independent of the spin projection $M = \pm 1$ and is usually calculated by A. Bohr's formula [3]

$$T^{JK}(\theta) = \frac{2J+1}{8\pi}[|D^J_{1K}(\omega)|^2 + |D^J_{1-K}(\omega)|^2]_{\beta=\theta},$$
(3)

where $D^J_{MK}(\omega)$ is a generalized spherical harmonic that depends on the Euler angles $\omega \equiv (\alpha, \beta, \gamma)$ determining the orientation of the symmetry axes of the fissile nucleus with respect to the axes in the laboratory frame. Within quantum-mechanical fission theory [9−11], the quantity $T^{JK}(\theta)$ takes a different form,

$$T^{JK}(\theta) = \frac{2J+1}{16\pi^2}\int d\omega[|D^J_{1K}(\omega)|^2$$ (4)
$$+ |D^J_{1-K}(\omega)|^2]F(L_m, \theta').$$

Here, $F(L_m, \theta')$ is the normalized (to unity) angular distribution of photofission fragments in the intrinsic coordinate system of the fissile nucleus,

$$F(L_m, \theta') = b(L_m)$$ (5)
$$\times \left\{\sum_{L=0}^{L_m} Y_{L0}(\xi')Y_{L0}(1)\left[\frac{1 + \pi\pi_1\pi_2(-1)^L}{2}\right]\right\}^2,$$

$$b(L_m) = \left\{\sum_{L=0}^{L_m} \frac{(2L+1)}{4\pi}\left[\frac{1 + \pi\pi_1\pi_2(-1)^L}{2}\right]^2\right\}^{-1},$$

where $\xi' = \cos\theta'$, θ' being the angle between the direction of photofission-fragment emission and the symmetry axis of the fissile nucleus. At rather high values of L_m, the distribution $F(L_m, \theta')$ does not depend on the parity π of the fissile nucleus or the parities π_1 and π_2 of fission fragments—that is, on the parity of the relative orbital angular momentum L of fission fragments. Formula (4) reduces to A. Bohr's formula (3) in the limit $L_m \to \infty$, where the distribution $F(L_m, \theta')$ reduces to the half-sum of delta functions, $[\delta(\xi' - 1) + \delta(\xi' + 1)]/2$. The properties of the angular distribution (4) were analyzed in detail elsewhere [11].

Upon the substitution of expressions (3) and (4) into (1), the differential cross section $\sigma_{\gamma f}(\theta, E_\gamma)$ can be represented in the standard form [3]

$$\sigma_{\gamma f}(\theta) = a_0 + b_0\sin^2\theta + c_0\sin^2(2\theta),$$ (6)

where the quantities a_0, b_0, and c_0 are defined as

$$a_0 = \sum_{JK}\alpha_{JK}P^{JK}, \quad b_0 = \sum_{JK}\beta_{JK}P^{JK},$$ (7)

$$c_0 = \sum_{JK}\gamma_{JK}P^{JK}.$$

The values of the coefficients α_{JK}, β_{JK}, and γ_{JK} for the cases of $L_m \to \infty$ (A. Bohr's limit), $L_m = 30$, and $L_m = 20$ are given in Table 1.

In analyzing the experimental angular distributions of photofission fragments, one usually determines the asymmetry $W_{\gamma f}(\theta) \equiv \sigma_{\gamma f}(\theta)/\sigma_{\gamma f}(90°)$ of these distributions with respect to the angle $\theta = 90°$. This asymmetry can be represented by formula (6) upon the replacement of the quantities a_0, b_0, and c_0 by the quantities

$$a = \frac{a_0}{a_0 + b_0}, \quad b = \frac{b_0}{a_0 + b_0}, \quad c = \frac{c_0}{a_0 + b_0},$$ (8)

respectively; obviously, we have $a + b = 1$.

3. ANALYSIS OF THE ANGULAR DISTRIBUTIONS OF FRAGMENTS ORIGINATING FROM THE SUBTHRESHOLD PHOTOFISSION OF NUCLEI

Let us investigate the photofission of ^{232}Th, ^{234}U, ^{236}U, ^{238}U, ^{238}Pu, ^{240}Pu, and ^{242}Pu even−even nuclei that is induced by photons of energy in the range $E_\gamma \le 7$ MeV. We select only those results of the experimental studies reported in [12, 14−18] for which relative root-mean-square deviations of the measured quantities a and c from $\langle a \rangle$ and $\langle c \rangle$ are less than 0.5.

For the ensuing analysis, we employ the quantities $G^{JK} = P^{JK}/P^{10}$, which possess the following properties: $G^{JK} > 0$, $G^{10} = 1$, $G^{11} = \Gamma_f^{11}/\Gamma_f^{10}$, and $G^{22} < G^{20}$. If we neglect, in accordance with the above estimate, the effect of 2^+1 quadrupole fission channels and eliminate the quantity G^{21} from further consideration, the substitution of formulas (7) into Eqs. (8) leads to two linear nonhomogeneous equations for the three quantities G^{11}, G^{20}, and G^{22}. By solving these equations for the quantities G^{11} and G^{20}, we obtain

$$dG^{11} = (c(\alpha_{20} + \beta_{20}) - \gamma_{20})(\alpha_{10} - a(\alpha_{10}$$ (9)
$$+ \beta_{10})) + c(\alpha_{10} + \beta_{10})(a(\alpha_{20} + \beta_{20}) - \alpha_{20})$$
$$+ G^{22}[(c(\alpha_{20} + \beta_{20}) - \gamma_{20})(\alpha_{22} - a(\alpha_{22} + \beta_{22}))$$
$$- (\gamma_{22} - c(\alpha_{22} + \beta_{22}))(a(\alpha_{20} + \beta_{20}) - \alpha_{20})],$$

$$dG^{20} = -c(\alpha_{11} + \beta_{11})(\alpha_{10} - a(\alpha_{10} + \beta_{10}))$$ (10)
$$- c(\alpha_{10} + \beta_{10})(a(\alpha_{11} + \beta_{11}) - \alpha_{11})$$
$$+ G^{22}[(\gamma_{22} - c(\alpha_{22} + \beta_{22}))(a(\alpha_{11} + \beta_{11}) - \alpha_{11})$$

Table 1. Values of the coefficients α_{JK}, β_{JK}, and γ_{JK} for $L_m \to \infty$, $L_m = 30$, and $L_m = 20$

L_m	α_{10}	α_{11}	α_{20}	α_{22}	β_{10}	β_{11}	β_{20}	β_{22}	γ_{20}	γ_{22}
∞	0	0.75	0	0	0.75	-0.375	0	0.625	0.9375	0.15625
30	0.024	0.74	0.060	0.030	0.714	-0.357	-0.022	0.592	0.854	0.142
20	0.04	0.73	0.087	0.044	0.697	-0.349	-0.033	0.576	0.815	0.136

$$- c(\alpha_{11} + \beta_{11})(\alpha_{22} - a(\alpha_{22} + \beta_{22}))],$$

$$d = c[(\alpha_{11} + \beta_{11})\alpha_{20} - \alpha_{11}(\alpha_{20} + \beta_{20})] \qquad (11)$$
$$- a(\alpha_{11} + \beta_{11})\gamma_{20} + \alpha_{11}\gamma_{20}.$$

By substituting, into these formulas, the experimental values of the quantities a and c, one can calculate G^{11} and G^{20} versus the quantities L_m and G^{22}, which are considered as parameters. Since the quantities G^{11} and G^{20} are positive by definition, a comparison of the calculated values of G^{11} and G^{20} with the conditions $G^{11} > 0$ and $G^{20} > 0$ enables one to determine the possible minimal values of L_m.

It was indicated above that, by using experimental data on the multiplicity and multipolarity of prompt photons emitted by primary fission fragments, the maximum value of the relative orbital angular momentum of fission fragments was estimated in [10] as $L_m \approx 30$. In order to test this estimate, we will consider the cases of $L_m = 30$, $L_m = 20$, and $L_m \to \infty$ (A. Bohr's limit) in our ensuing calculations.

The ratio G^{22}/G^{20} is equal to the fission-width ratio $\Gamma_f^{22}/\Gamma_f^{20}$, which is much less than unity if the axisymmetric shape the nucleus is conserved in the process of subthreshold fission. This is explained by the fact that the 2^+2 transition fission state, which is associated with the γ vibrations of a nucleus, has a rather high excitation energy (0.7 MeV [19]) with respect to the 2^+0 transition fission state. Therefore, the quantity G^{22} was varied in the interval $0 \le G^{22} \le 0.2G^{20}$, where the upper boundary was chosen to exceed, by a good margin, the possible values of G^{22}. For all cases investigated here, these variations of the quantity G^{22} lead to changes of not more than 25% in the absolute values of G^{11} and G^{20} calculated by formulas (9)–(11). Therefore, one can disregard, with a high degree of precision, the effect of G^{22} on G^{11} and G^{20} and employ a value of zero for G^{22}. This conclusion, along with the above conclusion that the effect of the 2^+1 fission channel is negligible, actually validates the procedure extensively used earlier [4] that describes the angular distributions of fragments from the subthreshold photofission of nuclei without taking into account the 2^+1 and 2^+2 fission channels.

For all cases studied here, the G^{11} and G^{20} values calculated with allowance for the experimental errors in determining a and c appear to be positive definite in A. Bohr's limit ($L_m \to \infty$). As to finite values of L_m, the situation for them proves to be more complicated, as might have been expected. One can single out cases where the values of G^{11} and G^{20} for $L_m = 30$ and $L_m = 20$ prove to be positive definite and rather close to the values of G^{11} and G^{20}, respectively, in A. Bohr's limit. These cases arise at rather large values of experimentally determined a and c and correspond to the situation where A. Bohr's formula (3) for the angular distributions of fragments is highly accurate. Table 2 gives the G^{11} and G^{20} values calculated for cases where A. Bohr's formula (3) is no longer correct, so that there arise significant distinctions between the absolute values of G^{11} and G^{20} for $L_m = 30$ and $L_m = 20$ and their counterparts in A. Bohr's limit. From Table 2, one can see that, at $L_m = 30$, the values of G^{11} and G^{20} prove to be positive definite in the majority of cases studied here, but the current experimental accuracy in determining a and c is insufficient for the root-mean-square deviations of all G^{11} and, in some cases (for example, for ^{232}Th), of G^{20} from their mean values to be much less than unity. At the same time, it turns out that, in eight of the 78 cases presented in Table 2 (at energies in the range $5.9 \le E_\gamma \le 6.4$ MeV in ^{232}Th, at energies in the range $5.75 \le E_\gamma \le 5.97$ in ^{234}U, and at an energy of $E_\gamma = 5.75$ MeV in ^{236}U), positive values of G^{11} can only be obtained by shifting the experimental values of a toward greater values by more than two standard deviations in determining a. We note in passing that, in some cases, the most recent measurements of a lead to positive definite values of G^{11}, in contrast to measurements of a that were performed previously. By way of example, we indicate that such a situation arises for ^{232}Th photofission at $E_\gamma = 6.4$ MeV, in which case the results of the more recent measurements of a that were performed in [15] differ significantly from those presented earlier in [12]. Therefore, the above situation where there appear negative values of G^{11} is likely to stem from an insufficient experimental accuracy in determining a in the region of its smallest values ($\langle a \rangle \le 0.014$

Table 2. Values of G^{11} and G^{20} for $L_m \to \infty$, $L_m = 30$, and $L_m = 20$

E_γ, MeV	c	a	$L_m = 30$		$L_m = 20$		$L_m = \infty$	
			G^{11}	G^{20}	G^{11}	G^{20}	G^{11}	G^{20}
				^{238}Pu				
5.25 [14]	1.412 ± 0.139	0.408 ± 0.103	0.368 ± 0.169	1.540 ± 0.049	0.284 ± 0.173	1.603 ± 0.050	0.523 ± 0.163	1.416 ± 0.048
5.5 [14]	1.513 ± 0.112	0.330 ± 0.063	0.240 ± 0.096	1.571 ± 0.056	0.153 ± 0.099	1.635 ± 0.057	0.399 ± 0.090	1.448 ± 0.053
5.75 [14]	0.654 ± 0.055	0.414 ± 0.037	0.431 ± 0.062	0.711 ± 0.043	0.381 ± 0.065	0.738 ± 0.044	0.523 ± 0.059	0.659 ± 0.04
6.0 [14]	0.370 ± 0.018	0.526 ± 0.011	0.644 ± 0.022	0.434 ± 0.018	0.607 ± 0.023	0.450 ± 0.018	0.714 ± 0.020	0.402 ± 0.017
				^{240}Pu				
5.45 [14]	1.147 ± 0.07	0.102 ± 0.044	-0.009 ± 0.052	1.038 ± 0.039	-0.075 ± 0.054	1.077 ± 0.04	0.109 ± 0.049	0.966 ± 0.037
5.7 [14]	0.710 ± 0.052	0.222 ± 0.034	0.160 ± 0.046	0.685 ± 0.037	0.11 ± 0.047	0.711 ± 0.038	0.251 ± 0.043	0.638 ± 0.035
5.95 [14]	0.331 ± 0.013	0.533 ± 0.010	0.660 ± 0.020	0.390 ± 0.013	0.625 ± 0.02	0.405 ± 0.013	0.727 ± 0.019	0.361 ± 0.012
				^{242}Pu				
5.0 [14]	3.702 ± 0.424	0.532 ± 0.308	0.485 ± 0.593	4.646 ± 0.530	0.275 ± 0.583	4.892 ± 0.570	0.850 ± 0.598	4.119 ± 0.402
5.25 [14]	0.965 ± 0.032	0.448 ± 0.053	0.461 ± 0.089	1.078 ± 0.003	0.396 ± 0.090	1.122 ± 0.003	0.580 ± 0.088	0.995 ± 0.001
5.35 [14]	1.018 ± 0.069	0.418 ± 0.046	0.408 ± 0.078	1.114 ± 0.042	0.341 ± 0.080	1.159 ± 0.044	0.531 ± 0.074	1.028 ± 0.040
5.5 [14]	0.734 ± 0.034	0.310 ± 0.022	0.272 ± 0.033	0.748 ± 0.025	0.219 ± 0.034	0.776 ± 0.026	0.367 ± 0.031	0.695 ± 0.023
5.75 [14]	0.422 ± 0.012	0.488 ± 0.008	0.572 ± 0.015	0.482 ± 0.011	0.532 ± 0.015	0.500 ± 0.011	0.646 ± 0.014	0.447 ± 0.010
				^{232}Th				
5.90 [14]	0.084 ± 0.014	0.010 ± 0.005	-0.028 ± 0.006	0.072 ± 0.012	-0.054 ± 0.006	0.074 ± 0.012	0.01 ± 0.005	0.068 ± 0.011
5.95 [14]	0.074 ± 0.010	0.014 ± 0.004	-0.024 ± 0.005	0.063 ± 0.008	-0.049 ± 0.005	0.066 ± 0.009	0.014 ± 0.004	0.06 ± 0.008
6.2 [14]	0.079 ± 0.010	0.012 ± 0.003	-0.026 ± 0.004	0.068 ± 0.008	-0.051 ± 0.004	0.07 ± 0.009	0.012 ± 0.003	0.064 ± 0.008
6.4 [12]	0.028 ± 0.006	0.021 ± 0.003	-0.014 ± 0.003	0.024 ± 0.005	-0.037 ± 0.004	0.025 ± 0.005	0.021 ± 0.003	0.023 ± 0.005
6.4 [15]	0.060 ± 0.040	0.060 ± 0.030	0.025 ± 0.034	0.052 ± 0.034	0 ± 0.036	0.054 ± 0.035	0.062 ± 0.032	0.049 ± 0.032
6.4 [15]	0.028 ± 0.006	0.044 ± 0.002	0.01 ± 0.002	0.024 ± 0.005	-0.014 ± 0.003	0.025 ± 0.005	0.045 ± 0.002	0.023 ± 0.005
6.5 [14]	0.022 ± 0.014	0.022 ± 0.005	-0.012 ± 0.006	0.019 ± 0.012	-0.035 ± 0.006	0.02 ± 0.012	0.022 ± 0.005	0.018 ± 0.011
6.7 [14]	0.009 ± 0.008	0.023 ± 0.002	-0.01 ± 0.003	0.008 ± 0.007	-0.033 ± 0.003	0.008 ± 0.007	0.023 ± 0.002	0.007 ± 0.006
6.9 [14]	0.020 ± 0.022	0.032 ± 0.007	-0.002 ± 0.009	0.017 ± 0.019	-0.025 ± 0.009	0.018 ± 0.02	0.033 ± 0.007	0.016 ± 0.018
7.0 [14]	0.038 ± 0.012	0.036 ± 0.004	0.001 ± 0.005	0.033 ± 0.01	-0.023 ± 0.005	0.034 ± 0.011	0.037 ± 0.004	0.031 ± 0.01
				^{234}U				
5.6 [18]	0.195 ± 0.018	0.032 ± 0.008	-0.014 ± 0.009	0.169 ± 0.015	-0.044 ± 0.01	0.175 ± 0.015	0.033 ± 0.008	0.158 ± 0.014
5.75 [16]	0.152 ± 0.012	0.025 ± 0.004	-0.018 ± 0.005	0.131 ± 0.01	-0.046 ± 0.005	0.136 ± 0.01	0.025 ± 0.004	0.123 ± 0.009
5.97 [16]	0.158 ± 0.012	0.028 ± 0.004	-0.016 ± 0.005	0.136 ± 0.01	-0.044 ± 0.005	0.141 ± 0.01	0.028 ± 0.004	0.128 ± 0.009
6.05 [16]	0.110 ± 0.014	0.041 ± 0.005	0.001 ± 0.006	0.096 ± 0.012	-0.025 ± 0.007	0.099 ± 0.012	0.042 ± 0.005	0.09 ± 0.011
6.17 [16]	0.158 ± 0.012	0.050 ± 0.004	0.007 ± 0.005	0.138 ± 0.01	-0.021 ± 0.005	0.143 ± 0.011	0.051 ± 0.004	0.13 ± 0.01
6.2 [16]	0.183 ± 0.017	0.086 ± 0.007	0.043 ± 0.009	0.163 ± 0.015	0.014 ± 0.009	0.169 ± 0.015	0.09 ± 0.008	0.153 ± 0.014
6.3 [16]	0.089 ± 0.018	0.084 ± 0.008	0.047 ± 0.01	0.079 ± 0.016	0.022 ± 0.011	0.082 ± 0.016	0.088 ± 0.009	0.074 ± 0.015
6.35 [16]	0.083 ± 0.015	0.133 ± 0.006	0.102 ± 0.008	0.076 ± 0.013	0.076 ± 0.008	0.078 ± 0.014	0.142 ± 0.007	0.071 ± 0.013
6.4 [16]	0.020 ± 0.016	0.133 ± 0.008	0.106 ± 0.01	0.018 ± 0.015	0.083 ± 0.011	0.019 ± 0.015	0.143 ± 0.009	0.017 ± 0.014
6.45 [16]	0.087 ± 0.013	0.163 ± 0.005	0.136 ± 0.007	0.081 ± 0.012	0.11 ± 0.007	0.084 ± 0.012	0.177 ± 0.006	0.076 ± 0.011
6.5 [16]	0.046 ± 0.019	0.157 ± 0.009	0.132 ± 0.012	0.042 ± 0.017	0.108 ± 0.013	0.044 ± 0.018	0.17 ± 0.011	0.04 ± 0.016
6.6 [16]	0.044 ± 0.018	0.185 ± 0.009	0.165 ± 0.012	0.041 ± 0.017	0.141 ± 0.013	0.043 ± 0.017	0.204 ± 0.011	0.039 ± 0.016
6.7 [16]	0.042 ± 0.018	0.238 ± 0.009	0.231 ± 0.013	0.041 ± 0.017	0.207 ± 0.014	0.042 ± 0.018	0.27 ± 0.012	0.038 ± 0.016

Table 2. (Contd.)

E_γ, MeV	c	a	$L_m = 30$		$L_m = 20$		$L_m = \infty$	
			G^{11}	G^{20}	G^{11}	G^{20}	G^{11}	G^{20}
				^{236}U				
4.3[15]	1.71 ± 0.35	0.72 ± 0.25	1.064 ± 0.665	2.369 ± 0.004	0.957 ± 0.677	2.481 ± 0.012	1.249 ± 0.625	2.133 ± 0.021
5.0[15]	0.250 ± 0.15	0.200 ± 0.10	0.175 ± 0.133	0.23 ± 0.129	0.143 ± 0.139	0.238 ± 0.134	0.229 ± 0.124	0.215 ± 0.121
5.1[15]	0.187 ± 0.048	0.04 ± 0.02	-0.005 ± 0.024	0.162 ± 0.040	-0.034 ± 0.0254	0.167 ± 0.042	0.041 ± 0.021	0.152 ± 0.028
5.25[15]	0.12 ± 0.04	0.06 ± 0.03	0.020 ± 0.034	0.105 ± 0.034	-0.006 ± 0.036	0.105 ± 0.035	0.062 ± 0.032	0.099 ± 0.032
5.5[15]	0.479 ± 0.016	0.048 ± 0.006	-0.018 ± 0.007	0.419 ± 0.013	-0.058 ± 0.008	0.434 ± 0.013	0.049 ± 0.006	0.393 ± 0.012
5.5[15]	0.500 ± 0.13	0.150 ± 0.07	0.094 ± 0.089	0.459 ± 0.103	0.052 ± 0.094	0.475 ± 0.106	0.165 ± 0.082	0.429 ± 0.096
5.6[15]	0.503 ± 0.028	0.040 ± 0.012	-0.027 ± 0.014	0.438 ± 0.022	-0.069 ± 0.015	0.454 ± 0.023	0.041 ± 0.013	0.411 ± 0.020
5.75[15]	0.452 ± 0.015	0.027 ± 0.005	-0.037 ± 0.006	0.391 ± 0.012	-0.076 ± 0.007	0.405 ± 0.012	0.027 ± 0.005	0.367 ± 0.011
6.0[15]	0.166 ± 0.013	0.042 ± 0.005	-0.002 ± 0.006	0.144 ± 0.011	-0.03 ± 0.006	0.149 ± 0.011	0.043 ± 0.005	0.136 ± 0.01
6.25[15]	0.110 ± 0.013	0.069 ± 0.005	0.03 ± 0.006	0.097 ± 0.011	0.004 ± 0.007	0.1 ± 0.012	0.071 ± 0.005	0.091 ± 0.011
6.5[15]	0.080 ± 0.014	0.112 ± 0.006	0.078 ± 0.008	0.072 ± 0.012	0.053 ± 0.008	0.075 ± 0.013	0.119 ± 0.007	0.068 ± 0.012
6.75[15]	0.051 ± 0.015	0.199 ± 0.008	0.181 ± 0.011	0.048 ± 0.014	0.157 ± 0.011	0.05 ± 0.014	0.221 ± 0.01	0.045 ± 0.013
				^{238}U				
4.85[12]	1.380 ± 0.134	0.231 ± 0.079	0.124 ± 0.107	1.346 ± 0.069	0.045 ± 0.11	1.399 ± 0.072	0.266 ± 0.101	1.245 ± 0.066
4.93[12]	1.350 ± 0.088	0.171 ± 0.053	0.052 ± 0.067	1.272 ± 0.045	-0.023 ± 0.069	1.322 ± 0.047	0.189 ± 0.063	1.18 ± 0.043
5.0[12]	1.139 ± 0.031	0.135 ± 0.020	0.026 ± 0.024	1.051 ± 0.017	-0.04 ± 0.025	1.091 ± 0.018	0.145 ± 0.023	0.977 ± 0.016
5.13[12]	1.026 ± 0.054	0.162 ± 0.033	0.065 ± 0.042	0.96 ± 0.033	0.003 ± 0.043	0.996 ± 0.034	0.177 ± 0.039	0.893 ± 0.031
5.2[14]	0.910 ± 0.080	0.100 ± 0.035	0.006 ± 0.043	0.821 ± 0.057	-0.051 ± 0.046	0.851 ± 0.059	0.106 ± 0.039	0.765 ± 0.053
5.2[12]	0.907 ± 0.045	0.090 ± 0.024	-0.005 ± 0.029	0.814 ± 0.03	-0.062 ± 0.03	0.844 ± 0.031	0.095 ± 0.026	0.759 ± 0.028
5.4[12]	0.306 ± 0.026	0.050 ± 0.012	-0.004 ± 0.014	0.267 ± 0.021	-0.037 ± 0.015	0.277 ± 0.022	0.051 ± 0.013	0.251 ± 0.02
5.45[14]	0.155 ± 0.021	0.038 ± 0.009	-0.005 ± 0.011	0.134 ± 0.018	-0.033 ± 0.011	0.139 ± 0.018	0.039 ± 0.009	0.126 ± 0.017
5.5[14]	0.039 ± 0.014	0.078 ± 0.005	0.045 ± 0.006	0.035 ± 0.012	0.021 ± 0.007	0.036 ± 0.013	0.081 ± 0.005	0.032 ± 0.012
5.5[12]	0.161 ± 0.007	0.040 ± 0.004	-0.004 ± 0.005	0.14 ± 0.006	-0.032 ± 0.005	0.145 ± 0.006	0.041 ± 0.004	0.131 ± 0.005
5.5[18]	0.172 ± 0.033	0.049 ± 0.013	0.005 ± 0.016	0.15 ± 0.028	-0.024 ± 0.017	0.155 ± 0.029	0.050 ± 0.014	0.141 ± 0.026
5.6[12]	0.074 ± 0.012	0.054 ± 0.005	0.017 ± 0.006	0.065 ± 0.01	-0.008 ± 0.006	0.067 ± 0.011	0.056 ± 0.005	0.061 ± 0.01
5.65[14]	0.040 ± 0.010	0.034 ± 0.005	-0.001 ± 0.006	0.035 ± 0.009	-0.025 ± 0.006	0.036 ± 0.009	0.035 ± 0.005	0.033 ± 0.008
5.65[12]	0.085 ± 0.011	0.034 ± 0.006	-0.004 ± 0.007	0.074 ± 0.009	-0.03 ± 0.007	0.076 ± 0.01	0.035 ± 0.006	0.069 ± 0.009
5.7[12]	0.041 ± 0.009	0.054 ± 0.004	0.019 ± 0.005	0.036 ± 0.008	-0.005 ± 0.005	0.037 ± 0.008	0.056 ± 0.004	0.034 ± 0.007
5.75[18]	0.043 ± 0.014	0.041 ± 0.005	0.006 ± 0.006	0.037 ± 0.012	-0.018 ± 0.007	0.039 ± 0.012	0.042 ± 0.005	0.035 ± 0.011
5.8[12]	0.052 ± 0.014	0.068 ± 0.007	0.033 ± 0.008	0.046 ± 0.012	0.009 ± 0.009	0.047 ± 0.013	0.07 ± 0.008	0.043 ± 0.011
5.9[12]	0.058 ± 0.007	0.054 ± 0.004	0.018 ± 0.005	0.051 ± 0.006	-0.006 ± 0.005	0.052 ± 0.006	0.056 ± 0.004	0.048 ± 0.006
5.97[18]	0.128 ± 0.013	0.079 ± 0.005	0.039 ± 0.006	0.113 ± 0.011	0.012 ± 0.007	0.117 ± 0.012	0.082 ± 0.005	0.107 ± 0.011
6.0[12]	0.048 ± 0.012	0.099 ± 0.006	0.066 ± 0.007	0.043 ± 0.011	0.042 ± 0.008	0.044 ± 0.011	0.104 ± 0.007	0.04 ± 0.01
6.05[18]	0.125 ± 0.016	0.087 ± 0.007	0.048 ± 0.009	0.111 ± 0.014	0.021 ± 0.009	0.115 ± 0.014	0.091 ± 0.008	0.105 ± 0.013
6.17[18]	0.123 ± 0.012	0.090 ± 0.005	0.051 ± 0.006	0.11 ± 0.01	0.024 ± 0.007	0.114 ± 0.011	0.094 ± 0.005	0.103 ± 0.010
6.2[12]	0.034 ± 0.038	0.128 ± 0.019	0.1 ± 0.024	0.031 ± 0.034	0.076 ± 0.026	0.032 ± 0.035	0.137 ± 0.022	0.029 ± 0.032
6.2[18]	0.138 ± 0.016	0.086 ± 0.007	0.046 ± 0.009	0.123 ± 0.014	0.019 ± 0.009	0.127 ± 0.014	0.090 ± 0.008	0.115 ± 0.013
6.3[18]	0.038 ± 0.018	0.110 ± 0.008	0.079 ± 0.01	0.034 ± 0.016	0.056 ± 0.011	0.035 ± 0.017	0.116 ± 0.009	0.032 ± 0.015
6.35[18]	0.032 ± 0.013	0.103 ± 0.005	0.072 ± 0.006	0.029 ± 0.012	0.049 ± 0.007	0.03 ± 0.012	0.109 ± 0.006	0.066 ± 0.009
6.4[14]	0.034 ± 0.008	0.127 ± 0.004	0.098 ± 0.005	0.031 ± 0.007	0.075 ± 0.005	0.032 ± 0.007	0.136 ± 0.005	0.029 ± 0.007
6.4[18]	0.038 ± 0.020	0.114 ± 0.009	0.084 ± 0.011	0.034 ± 0.018	0.06 ± 0.012	0.035 ± 0.019	0.121 ± 0.010	0.032 ± 0.014
6.45[18]	0.078 ± 0.011	0.111 ± 0.004	0.077 ± 0.005	0.07 ± 0.01	0.052 ± 0.006	0.073 ± 0.01	0.118 ± 0.004	0.066 ± 0.009
6.5[18]	0.052 ± 0.018	0.123 ± 0.009	0.093 ± 0.011	0.047 ± 0.016	0.068 ± 0.012	0.049 ± 0.017	0.131 ± 0.010	0.044 ± 0.015
6.6[18]	0.043 ± 0.018	0.126 ± 0.008	0.097 ± 0.01	0.039 ± 0.016	0.073 ± 0.011	0.04 ± 0.017	0.135 ± 0.009	0.037 ± 0.015
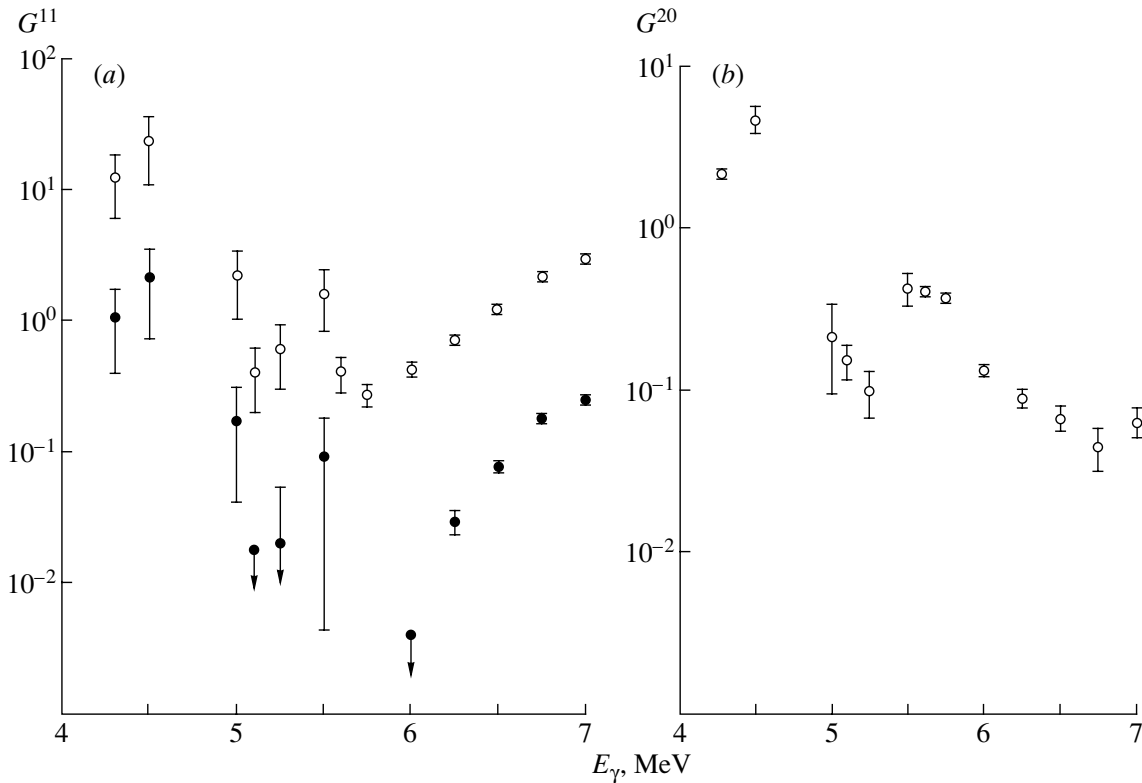
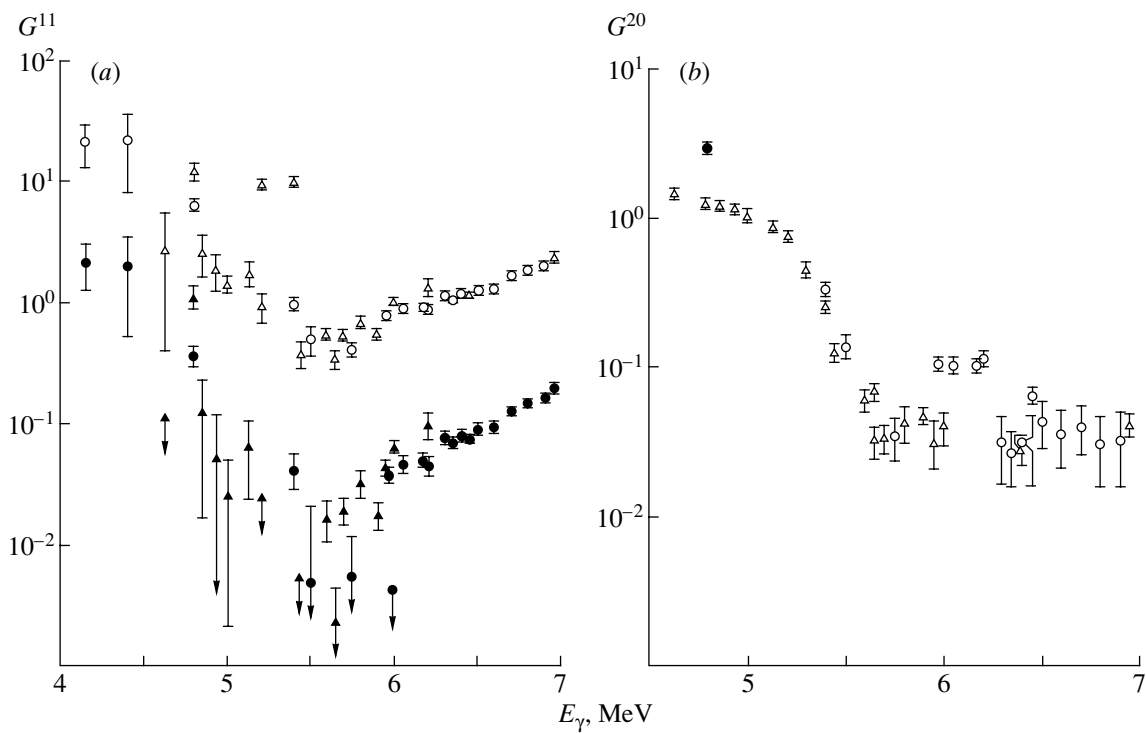**Fig. 1.** Energy dependence of (a) G^{11} and (b) G^{20} for ^{236}U (open circles) in the limit $L_m \to \infty$ and of G^{11} (closed circles) at $L_m = 30$. In this figure and those that follow, the values of G^{11} for $L_m \to \infty$ were multiplied by a factor of 10.

for ^{232}Th, $\langle a \rangle \leq 0.028$ for ^{234}U, and $\langle a \rangle \leq 0.027$ for ^{236}U) and may serve as a basis for performing more accurate investigations. From an analysis of our results for G^{11} that are presented in Table 2 for the nuclei and the energies E_γ investigated here, one can draw the conclusion that the maximum possible value of $L_m = 30$ is by and large compatible with the entire body of available experimental data. This conclusion is in accord with the results presented in [10, 11].

The situation changes radically at $L_m = 20$. From Table 2, it can be seen that, for 25 of the 78 cases studied here (at energies in the range $5.9 \leq E_\gamma \leq 7$ MeV in ^{232}Th, at energies in the range $5.75 \leq E_\gamma \leq 6.17$ MeV in ^{234}U, at energies in the range $5.5 \leq E_\gamma \leq 6$ MeV in ^{236}U, and at energies in the range $5.2 \leq E_\gamma \leq 5.65$ MeV in ^{238}U), positive values of G^{11} can be obtained only upon shifting the values found for a experimentally toward greater values by more than two standard deviations in the definition of a. It follows that, for the experimental-data array being considered, the value of $L_m = 20$ can be realized only with a probability that is negligible in relation to the probability of realization of the value of $L_m = 30$.

For all cases presented in Table 2, the values of G^{11} for $L_m = 30$ prove to be significantly smaller than the values of G^{11} that were found in A. Bohr's limit. This circumstance, which is illustrated in Figs. 1–7, results in the need for revisiting some parameters of the model of doorway states [20, 21], which was used in [4] to calculate cross sections and angular distributions of fragments from the subthreshold photofission of nuclei in A. Bohr's approximation ($L_m \to \infty$).

As to the quantities G^{20}, one can see from Table 2 that their values at $L_m = 30$ are virtually coincident with those in A. Bohr's limit. In Figs. 1–7, we therefore present the values of G^{20} for A. Bohr's limit, which tend to increase with decreasing energy E_γ and, in some cases, reach a plateau region at extremely low values of the energy E_γ, in accordance with the expected properties of the fission widths Γ_f^{10} and Γ_f^{20} in the subbarrier region [4]. Here, one can see resonance structures in the behavior of G^{20} in ^{236}U, ^{238}U, and ^{232}Th nuclei. The origin of these structures was discussed in [4] and is associated with the appearance of resonance states of the deformation fission mode in the second well of the deformation potential.

Fig. 2. Energy dependence of (a) G^{11} and (b) G^{20} for ^{238}U (open circles and triangles) in the limit $L_m \to \infty$ and (closed circles and triangles) $L_m = 30$. Presented here are experimental data from (open and closed circles) [12, 14] and (open and closed triangles) [15, 17, 18].
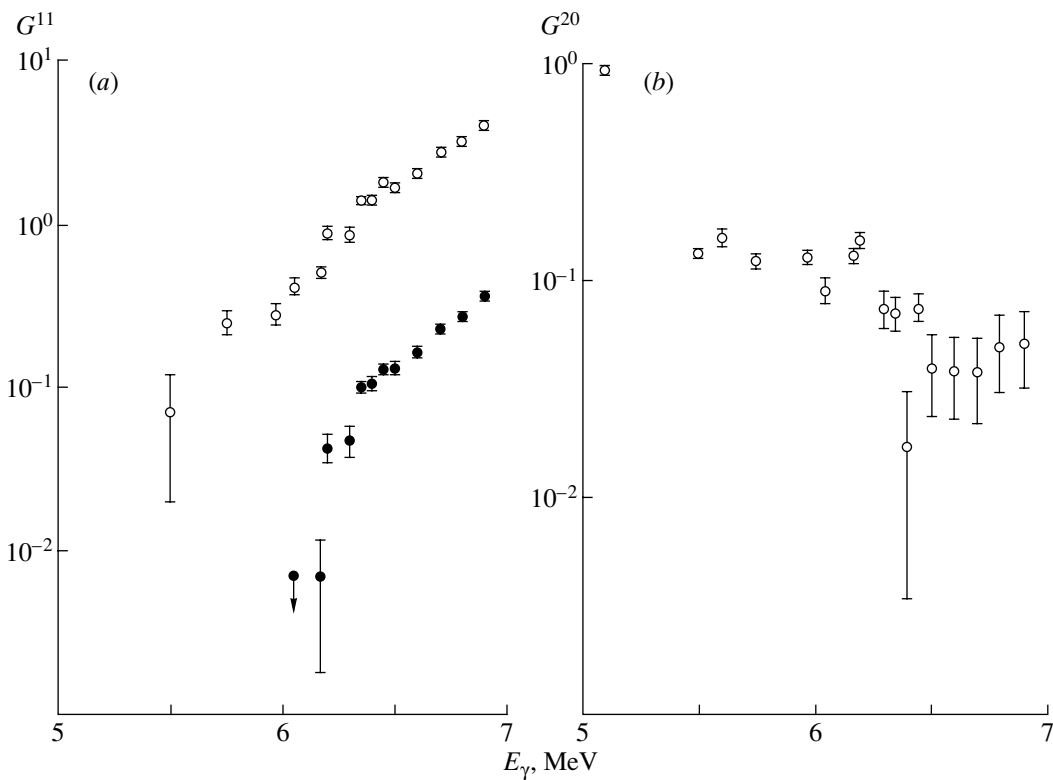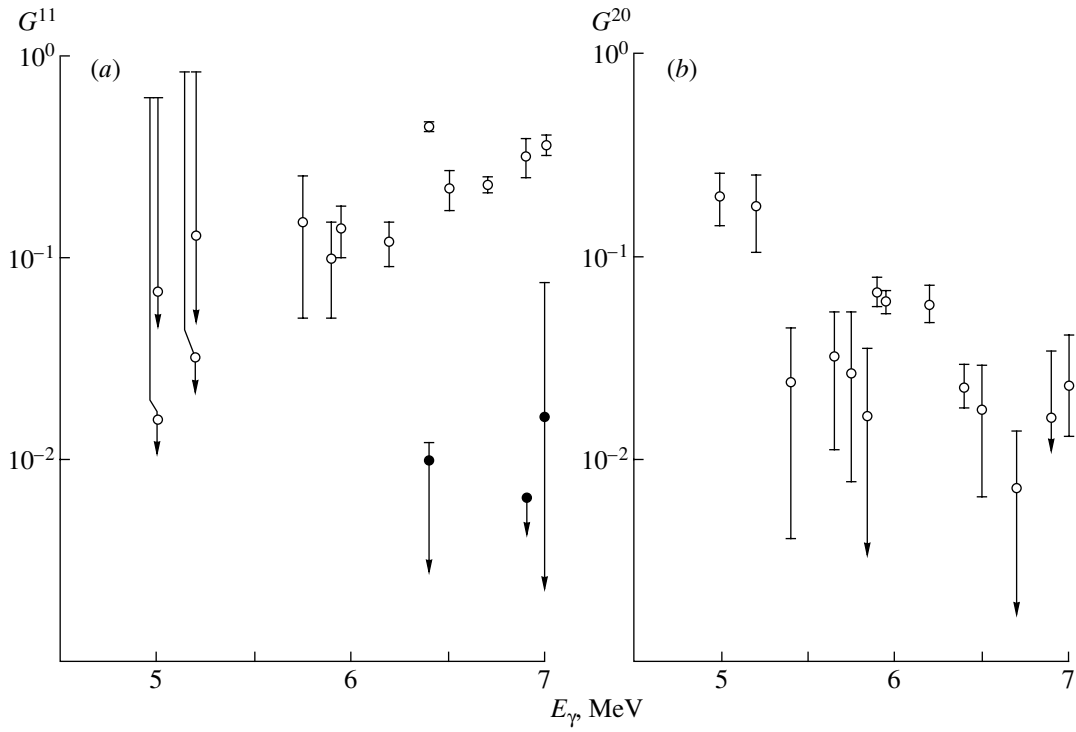

Fig. 3. As in Fig. 1, but for ^{234}U.
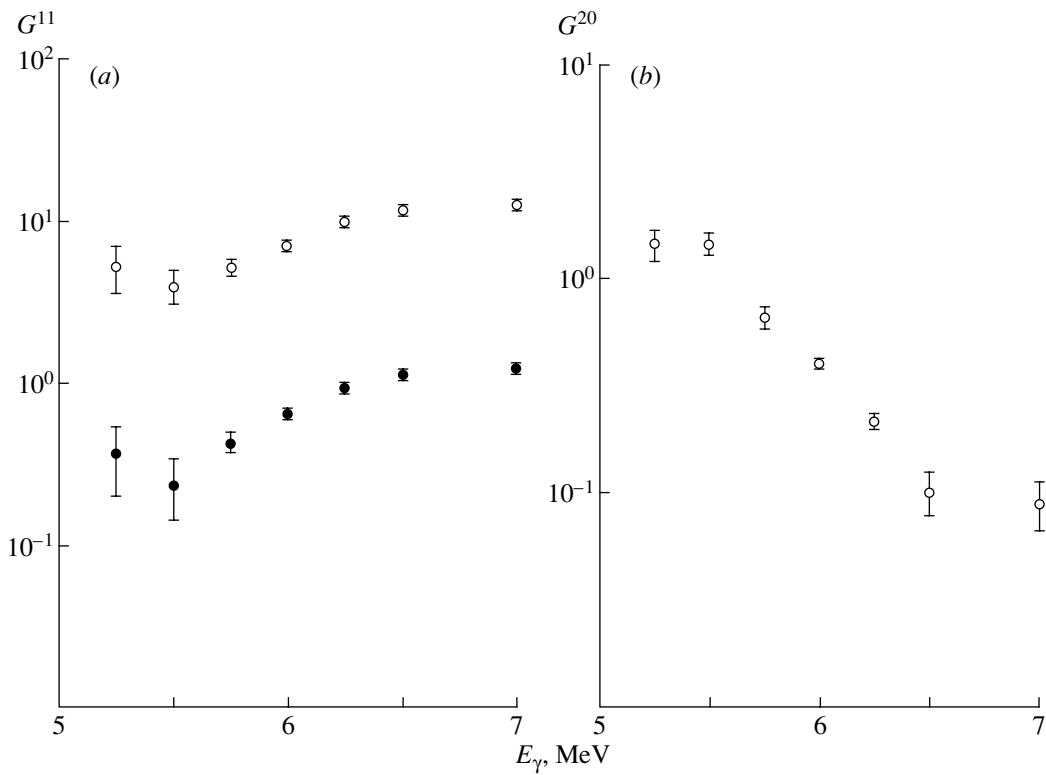
Fig. 4. As in Fig. 1, but for ^{232}Th.
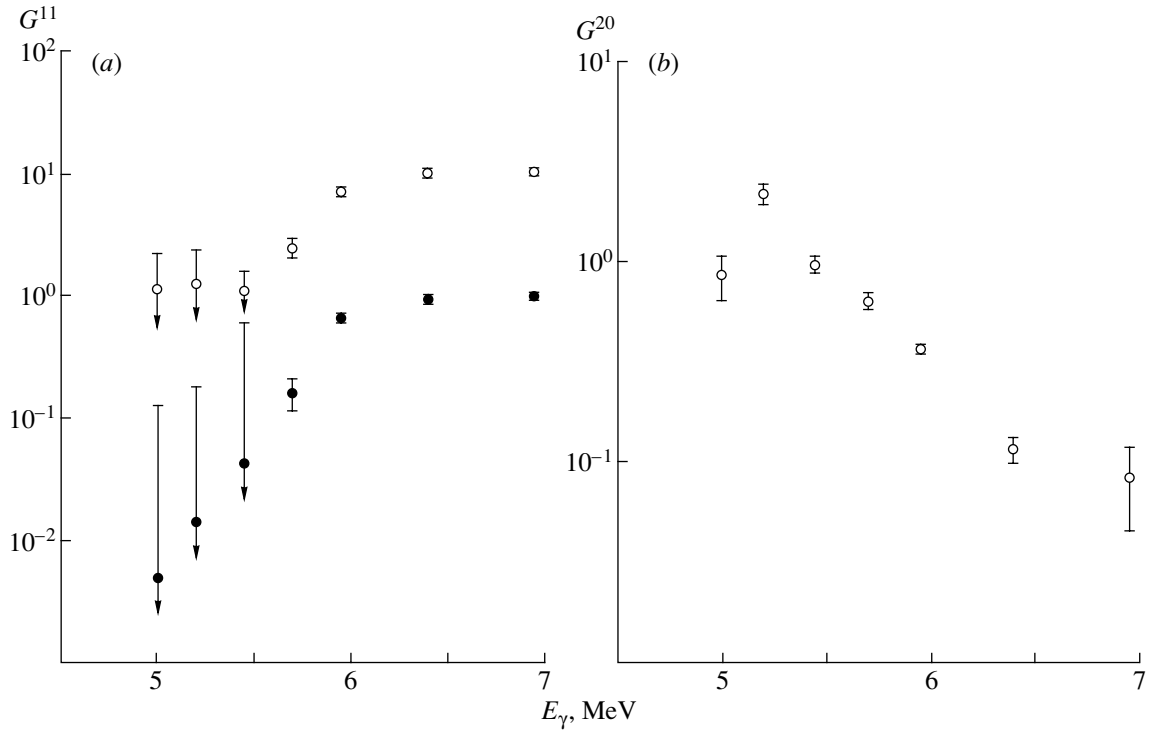

Fig. 5. As in Fig. 1, but for ^{238}Pu.

Fig. 6. As in Fig. 1, but for ^{240}Pu.
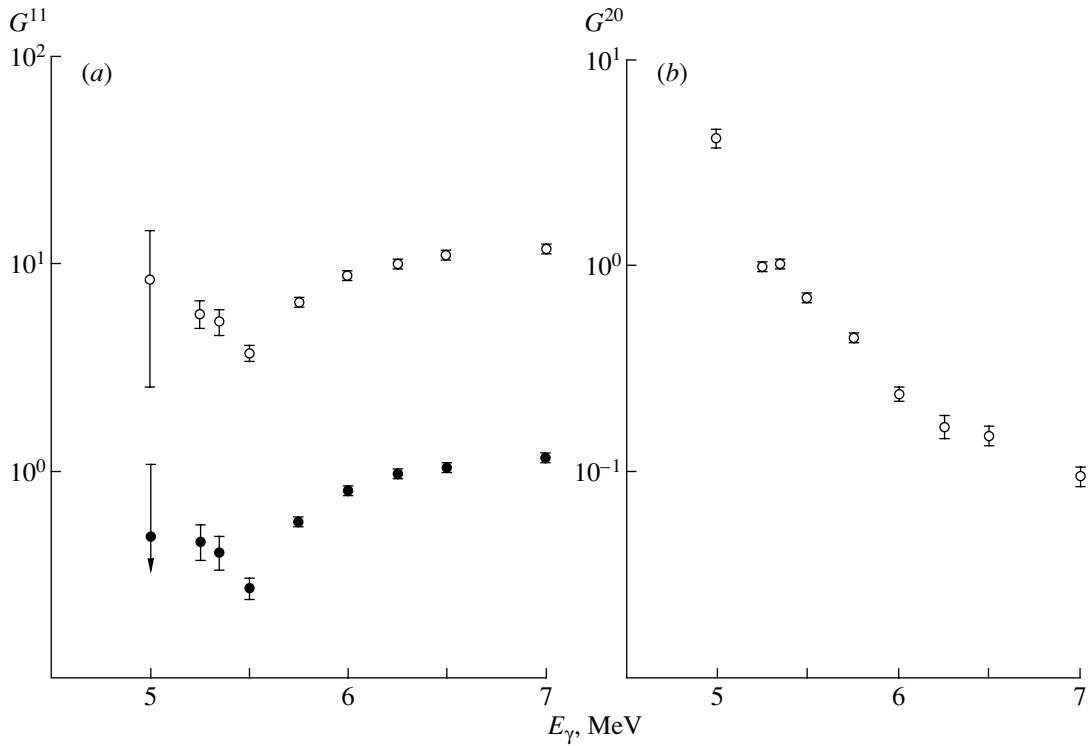
Fig. 7. As in Fig. 1, but for ^{242}Pu.

4. "ISOMERIC SHELF" IN THE ANGULAR DISTRIBUTIONS OF FRAGMENTS FROM THE SUBTHRESHOLD PHOTOFISSION OF NUCLEI

The "isomeric shelf" phenomenon discovered experimentally in analyzing the total cross sections for the subthreshold photofission of ^{238}U [6, 7] and ^{236}U [7,15] nuclei consists in the following: as one goes over from the photon endpoint energies in the region $E_\gamma > E^{is}$ to those in the range $E_\gamma \leq E^{is}$, the rate of the decrease in the photofission cross section with decreasing E_γ abruptly becomes much lower. Concurrently, the isotropic component of the angular distribution of photofission fragments grows in the region $E_\gamma \leq E^{is}$, becoming dominant at $E_\gamma \approx E_0^{is}$. An explanation of this phenomenon was proposed in [22, 4] on the basis of introducing the mechanism of delayed fission. Finding its way to the second well in the process of fission, a fissile nucleus can undergo fission either via fission without any change in energy and without delay (prompt fission) or via radiative decay accompanied by the population of a shape-isomer state and followed by fission from this state— that is, with a delay characterized by the lifetime of the nucleus in the second well (delayed fission). Since the spin of a shape isomer is zero for an even−even nucleus, the angular distribution of fragments from delayed fission is isotropic. Therefore, the quantity a_0, which appears in the definition (6) of the angular distribution of photofission fragments and which has the form (7), is replaced, upon taking into account delayed fission, by $\bar{a}_0 = (a_0 + a_0^{is})$, where a_0^{is} grows with decreasing E_γ from negligible values ($a_0^{is} \ll a_0$) for $E_\gamma > E^{is}$ to $a_0^{is} \gg b_0 \gg a_0$ at $E_\gamma = E_0^{is}$. In order to observe the isomeric-shelf effect in the angular distributions of nuclear-photofission fragments, one usually studies [4] the experimental values of the ratio $b_0/\bar{a}_0$, which can be represented in the form $b_0/\bar{a}_0 = \bar{b}/\bar{a} = (1 - \bar{a})/\bar{a} = (\bar{a})^{-1} - 1$ and which can be expressed in terms of $(\bar{a})^{-1}$ [the quantities $\bar{a}$ and $\bar{b}$ are given by formulas (8), where $\bar{a}_0$ must be substituted for a_0]. For prompt fission, $(\bar{a})^{-1} = a^{-1}$ first increases monotonically with decreasing E_γ and then reaches values that remain constant to the smallest observable energies E_γ [4]. But if one takes into account delayed fission associated with the population of a shape isomer, the behavior of $(\bar{a})^{-1}$ in response to a decrease in E_γ is the following: upon reaching a maximum at $E_\gamma \approx E^{is}$, it begins decreasing and attains a minimum in the region around $E_\gamma \approx E_0^{is}$. This effect was studied in detail by Ostapenko *et al.* [4].

In the present study, formulas (1), (2), (7), and (8), which are based on the prompt-fission mechanism,

were employed to deduce information about the values of G^{11} and G^{20}. At the same time, the experimental values of a that were used in our calculations actually correspond to the quantities $\bar{a}$ introduced above, which take into account the isomeric-shelf-induced correction a_0^{is}. As a result, the quantity G^{11} for the ^{236}U and ^{238}U nuclei (see Figs. 1, 2) first decreases with decreasing E_γ and attains a minimum, whereupon there occurs a sharp increase in G^{11} in the region of the lowest energies E_γ. This behavior of G^{11} differs from the behavior expected in the case where the prompt-fission mechanism is dominant [4] and where G^{11} first decreases with decreasing E_γ and then reaches the region of constant values. It is interesting to note that, as can be seen from Figs. 1 and 2, the regions where the isomeric shelf manifests itself for ^{236}U and ^{238}U prove to be close in A. Bohr's limit ($L_m \to \infty$) and at $L_m = 30$. From Figs. 3– 7, one can see that, for ^{234}U, ^{232}Th, ^{238}Pu, ^{240}Pu, and ^{242}Pu nuclei, the behavior of the quantity G^{11} in all regions of the energy E_γ that were studied here has a character that corresponds to the prompt-fission mechanism and which does not feature the isomeric-shelf effect. This observation is in line with the conclusions drawn in [4] from an analysis of the subthreshold photofission of ^{234}U and ^{232}Th nuclei in the region of extremely low values of the energy E_γ.

5. CONCLUSION

Within quantum-mechanical fission theory, we have analyzed the angular distributions of fragments originating from the subthreshold photofission of seven even−even nuclei. The results of this analysis have confirmed the conclusion drawn in [10, 11] that the maximum value L_m of the relative orbital angular momentum L of fission fragments cannot differ significantly from a limiting value of $L_m \approx 30$, which was obtained in [10, 11] from an analysis of the multiplicity of prompt neutrons and the multiplicity and multipolarity of prompt photons emitted by primary fission fragments. This result can be considered as an additional substantiation of the mechanism of pumping of high spins and orbital angular momenta of primary fission fragments that was proposed in [10] and which was associated with a strong nonsphericity of the potential of interaction of these fragments.

REFERENCES

1. E. J. Winhold, P. T. Demos, and I. Halpern, Phys. Rev. **87**, 1139 (1952).
2. A. Bohr, in *Proceedings of the International Conference on the Peaceful Uses of Atomic Energy, New York, 1956*, Vol. 2, p. 175.
3. A. Bohr and B. Mottelson, *Nuclear Structure* (Benjamin, New York, 1969, 1974; Moscow, 1971, 1977), Vols. 1, 2.
4. Yu. B. Ostapenko, G. N. Smirenkin, A. S. Soldatov, and Yu. M. Tsipenyuk, Fiz. Élem. Chastits At. Yadra **12**, 1364 (1981) [Sov. J. Part. Nucl. **12**, 545 (1981)].
5. S. Bjørnholm and V. M. Strutinsky, Nucl. Phys. A **136**, 1 (1969).
6. C. D. Bowman, I. G. Schröder, C. E. Dick, and H. E. Jackson, Phys. Rev. C **12**, 863 (1975).
7. V. E. Zhuchko, A. V. Ignatyuk, Yu. B. Ostapenko, *et al.*, Pis'ma Zh. Éksp. Teor. Fiz. **22**, 255 (1975) [JETP Lett. **22**, 118 (1975)].
8. S. M. Polikanov, *Shape Isomerism of Nuclei* (Atomizdat, Moscow, 1977) [in Russian].
9. S. G. Kadmensky, Yad. Fiz. **65**, 1424 (2002) [Phys. At. Nucl. **65**, 1390 (2002)].
10. S. G. Kadmensky, Yad. Fiz. **67**, 167 (2004) [Phys. At. Nucl. **67**, 170 (2004)].
11. S. G. Kadmensky and L. V. Rodionova, Yad. Fiz. **66**, 1259 (2003) [Phys. At. Nucl. **66**, 1219 (2003)].
12. A. V. Ignatyuk, N. S. Rabotnov, *et al.*, Zh. Éksp. Teor. Fiz. **61**, 1284 (1971) [Sov. Phys. JETP **34**, 684 (1971)].
13. S. G. Kadmenskiĭ, V. P. Markushev, and V. I. Furman, Yad. Fiz. **35**, 300 (1982) [Sov. J. Nucl. Phys. **35**, 166 (1982)].
14. N. S. Rabotnov, G. N. Smirenkin, A. S. Soldatov, *et al.*, Yad. Fiz. **11**, 508 (1970) [Sov. J. Nucl. Phys. **11**, 285 (1970)].
15. V. E. Zhuchko, Yu. B. Ostapenko, G. N. Smirenkin, *et al.*, Yad. Fiz. **30**, 634 (1979) [Sov. J. Nucl. Phys. **30**, 326 (1979)].
16. L. J. Lindgren, A. S. Soldatov, and Yu. M. Tsipenyuk, Yad. Fiz. **32**, 335 (1980) [Sov. J. Nucl. Phys. **32**, 173 (1980)].
17. V. E. Rudnikov, G. N. Smirenkin, A. S. Soldatov, and Sh. Yukhas, Yad. Fiz. **48**, 646 (1988) [Sov. J. Nucl. Phys. **48**, 414 (1988)].
18. P. P. Ganich, V. E. Rudnikov, D. I. Sikora, *et al.*, Yad. Fiz. **52**, 36 (1990) [Sov. J. Nucl. Phys. **52**, 23 (1990)].
19. R. Kuiken, N. J. Pattenden, and H. Postma, Nucl. Phys. A **190**, 401 (1972).
20. P. D. Goldstone and P. Paul, Phys. Rev. C **18**, 1733 (1978).
21. U. Goerlach, D. Habs, M. Just, *et al.*, Z. Phys. A **287**, 171 (1978).
22. C. D. Bowman, Phys. Rev. C **12**, 856 (1975).

Translated by A. Isaakyan

Angular Distributions of Fragments Originating from the Spontaneous Fission of Oriented Nuclei and Problem of the Conservation of the Spin Projection onto the Symmetry Axis of a Fissile Nucleus

S. G. Kadmensky[*] and L. V. Rodionova

Voronezh State University, Universitetskaya pl. 1, Voronezh, 394693 Russia
Received April 19, 2004; in final form, September 7, 2004

Abstract—The concept of transition fission states, which was successfully used to describe the angular distributions of fragments for the spontaneous and low-energy induced fission of axisymmetric nuclei, proves to be correct if the spin projection onto the symmetry axis of a fissile nucleus is an integral of the motion for the external region from the descent of the fissile nucleus from the external fission barrier to the scission point. Upon heating a fissile nucleus in this region to temperatures of $T \approx 1$ MeV (this is predicted by many theoretical models of the fission process), the Coriolis interaction uniformly mixes the possible projections of the fissile-nucleus spin for the case of low spin values, this leading to the loss of memory about transition fission states in the asymptotic region where the angular distributions of fragments are formed. Within quantum-mechanical fission theory, which takes into account deviations from A. Bohr's formula, the angular distributions of fragments are calculated for spontaneously fissile nuclei aligned by an external magnetic field at ultralow temperatures, and it is shown that an analysis of experimental angular distributions of fragments would make it possible to solve the problem of spin-projection conservation for fissile nuclei in the external region. © *2005 Pleiades Publishing, Inc.*

1. INTRODUCTION

On the basis of the observation that there is a sizable anisotropy in the angular distributions of fragments originating from the subthreshold photofission of axisymmetric deformed even−even nuclei [1], A. Bohr [2, 3] introduced the concept of transition fission states that are formed at the saddle points of the deformation potential and which are characterized by a parity π, a spin J, and its projection K onto the symmetry axis of the fissile nucleus being considered, these states corresponding to "cold" internal states of the nucleus. A generalization of this concept to the case of a two-humped fission barrier [4−7] made it possible to explain [8] basic features of experimental angular distributions of fragments for the subthreshold fission of an extensive group of even−even actinide nuclei.

Relying on quantum-mechanical fission theory [9], which employs the concept of transition fission states [2, 3], we studied [10, 11] the deviations of the experimental angular distributions of fragments for the subthreshold photofission of nuclei [8] from the predictions of A. Bohr's widely used formula [3] and found, for the maximum relative orbital angular momentum of photofission fragments (l_m), a value of $l_m \approx 30$, which is in good agreement with the

estimate of l_m obtained with allowance for the mechanism of pumping of high spins and relative orbital angular momenta of fragments (this mechanism was proposed in [12]).

The angular distributions of fragments originating from the fission of ^{236}U and ^{234}U nuclei formed upon the capture of resonance and low-energy neutrons of energy in the range $0.4 < E_n \leq 2000$ eV by, respectively, ^{235}U and ^{233}U target nuclei aligned in strong magnetic fields at ultralow temperatures were experimentally studied in [13, 14]. The results obtained in [14] by analyzing these angular distributions for the ^{234}U compound nucleus on the basis of the concept of transition fission states [2, 3] differ dramatically from the results reported by Ostapenko *et al.* [8], who analyzed the angular distributions of fragments for the photofission of the same nucleus in the same range of its excitation energies. Fission from the $J^\pi = 2^+$ compound states of ^{234}U that are excited in the reactions under study in the first well of the deformation potential of the fissile nucleus was determined exclusively by the $J^\pi K = 2^+0$ transition fission states for photofission [8] and by the $J^\pi K = 2^+1$ states for fission induced by resonance and low-energy neutrons [14].

The reason behind this distinction has yet to be clarified conclusively. In particular, it may be associated with the possibility that the interference [15]

*E-mail: kadmensky@phys.vsu.ru

between the fission amplitudes for different compound states of the fissile nucleus in the first well of the deformation potential, which have different energies and, in general, different spins, manifests itself in cross sections and in the angular distribution of fragments for nuclear fission induced by resonance and low-energy neutrons. Such an interference does not contribute to cross sections and angular distributions of fragments for photofission, since the characteristic energy interval of averaging photofission cross sections is very wide (≥ 100 keV) in the experiments reported in [8].

The very fact that there are distinctions between the results of descriptions of photofission, on one hand, and fission induced by resonance and low-energy neutrons, on the other hand, demonstrates typical difficulties that arise in extracting reliable information about fission physics in analyzing the fission of nuclei from highly excited compound states of a fissile nucleus that possess a complicated structure.

In this connection, it would be of paramount importance to implement the project [16] of studying the angular distributions of fragments for the spontaneous fission of nuclei aligned by an external magnetic field at ultralow temperatures. For anisotropy in these angular distributions to be observed, it is necessary that the ground-state spin J of the fissile nucleus satisfy the condition $J > 1/2$. This means that the nuclei being studied must be odd or odd−odd, which creates difficulties for planned experiments since the branching fractions of spontaneous fission for odd and especially odd−odd nuclei are small, falling well below the analogous branching fractions for even−even spontaneously fissile nuclei.

Investigation of the spontaneous fission of axisymmetric deformed nuclei is advantageous in that, for the ground states of these nuclei, the projection K of the spin J always takes the value $K = J$. It follows that, within the concept of transition fission states [2, 3], spontaneous fission is determined exclusively by the only deep-subbarrier transition fission state of quantum numbers $J^\pi K = J^\pi J$. This circumstance simplifies substantially the analysis of the angular distributions of fragments for the spontaneous fission of oriented nuclei in relation to the analysis of the angular distributions of fragments for fission from compound states of fissile nuclei (see above).

On the basis of quantum-mechanical fission theory [9], we demonstrated in [10] the deviations of the angular distributions of fragments for the spontaneous fission of nuclei oriented to the maximum possible degree by an external magnetic field from the predictions of A. Bohr's formula, this making it possible to determine the maximum value l_m of relative orbital angular momenta of fission fragments at

a rather high statistical accuracy of experiments that study the angular distributions in question.

The objective of the present study is to explore the problem of conservation of the spin projection K for a fissile axisymmetric nucleus in the fission process and to analyze, within quantum-mechanical fission theory [9−12], the potential of experiments that would study the angular distributions of fragments for the spontaneous fission of oriented nuclei with the aim of solving this problem.

2. PROBLEM OF CONSERVATION OF THE FISSILE-NUCLEUS-SPIN PROJECTION IN THE FISSION PROCESS

Let us consider the case where the shape of the deformed fissile nucleus in the first well of its deformation potential possesses axial symmetry. If we eliminate the effect of weak interactions, the spin J and the parity π of fissile-nucleus states will be integrals of the motion at all stages of the fission process. As to the projection K of the fissile-nucleus spin onto the symmetry axis of the fissile nucleus, it can change in the fission process because of the effect of two main factors. The first factor is associated with the possibility that, in the fission process, the nucleus undergoing fission may develop triaxial deformations specified by a nonzero parameter γ, which lead to the mixing of states characterized by different values of K. This possibility was discussed in [17]. The second factor is associated with the effect of Coriolis interaction, which, as was shown in [18, 19], undergoes a dynamical enhancement in the case of rather high excitation energies E^* of the fissile nucleus and thermalization of this energy over a large number of multiquasiparticle states (compound states) and leads to a uniform statistical mixing of the projections K of the spins J of these states.

For actinide nuclei, it is generally accepted that, as collective deformation coordinates of the nucleus undergo changes in the process of its fission, the nuclear shape retains axial symmetry. Therefore, we will disregard the effect of the first factor on the conservation of the spin projection K in the fission process. As to the second factor, which is associated with Coriolis interaction, its inclusion seems mandatory.

In calculating fission widths and the angular distributions of fragments for induced nuclear fission, use is usually made [3, 11] of the concept that, at the initial stage of the fission process—this stage involves the formation of highly excited compound states of a fissile nucleus at the first well of the deformation potential—the projections K of the spins J of these compound states are distributed uniformly at rather low values of J. As a rule, this concept is also applied [3, 11] to the compound states of the

fissile nucleus in the second well of the deformation potential. However, there is presently no consistent validation of this concept for the case of practical interest where the excitation energies of compound states in the second well are much lower than the excitation energies of the analogous states in the first well.

In describing spontaneous and low-energy induced fission of nuclei, use is extensively made of the concept of transition fission states [2, 3], which are formed at the saddle points of the deformation potential of a fissile nucleus and which are characterized by a spin J, a parity π, and a spin projection K onto the symmetry axis of the fissile nucleus. For the states being considered, the spin projection K takes a single value for the reason that, since the internal state of the fissile nucleus is cold, Coriolis mixing in K does not play any significant role at the saddle points.

For the concept of transition fission states to be operative and for these states to be crucial for the formation of fission widths and the asymptotic behavior of the fissile-nucleus wave function in the region of already formed primary fission fragments, the following condition of paramount importance must be satisfied: the spin projections K associated with transition fission states at the outer saddle point of the deformation potential must remain integrals of the motion over the entire external region of the fissile system from the descent of the nucleus from this saddle point to the point of its scission into primary fission fragments and a subsequent divergence of these fragments. This means that the fissile nucleus must remain quite cold throughout this region in order that the Coriolis interaction not come into play and not mix, with equal probabilities, all possible projections K of the fissile-nucleus spin.

The majority of modern fission models [20−27], which describe successfully the mass, charge, and energy distributions of fragments originating from the spontaneous and induced fission of various nuclei, involve the concept that, because of dissipation effects, a considerable part of the difference of the potential energies of a fissile nucleus at the outer saddle point and at the point of its scission into fragments goes into heating the fissile nucleus, whose state near the scission point is characterized by a temperature of $T \approx 1$ MeV. According to [3], the relation between the nuclear excitation energy E^* and the nuclear temperature T at rather high T is

$$E^* = aT^2, \qquad (1)$$

where $a = (A/8)$ MeV^{-1} [3]. For an $A \approx 250$ fissile nucleus, this yields the estimate $E^* \approx 30$ MeV. It was indicated above that, upon the thermalization of so high an excitation energy, Coriolis interaction in an axisymmetric nucleus leads to [18, 19] a complete

mixing of all values of the projections K of the fissile-nucleus spin J at rather low J and to the loss of memory about the spin projection in the transition fission states of the nucleus.

This conclusion contradicts the fact that there appear sizable anisotropies in the angular distributions of fragments for the subthreshold fission of nuclei [8, 10, 11] and for the fission of aligned nuclei that is induced by low-energy and resonance neutrons [12, 13]; it is also at odds with the observation of P-odd [28] and P-even [29] asymmetries in the angular distributions of fragments originating from nuclear fission induced by polarized cold neutrons, as well as with the discovery of significant fluctuations in the fission widths of neutron resonances [30]. By employing the formula obtained for the angular distributions of fragments originating from subthreshold nuclear fission [3, 8, 10, 11] and fragments originating from the fission of aligned nuclei that is induced by low-energy and resonance neutrons [13, 14], as well as the formulas for the coefficients of P-odd and P-even asymmetries in the angular distributions of fragments in nuclear fission induced by cold polarized neutrons [31−33], it can be proven rigorously that the anisotropies and the coefficients of P-odd and P-even asymmetries in the angular distributions of fission fragments vanish in the case of a uniform distribution of all projections K of the spins J of fissile-nucleus states in the vicinity of the scission point.

Upon considering that, at nuclear excitation energies in the range $E^* < 2$ MeV, the Coriolis interaction effect on the mixing of the projections K of the spins J of excited states of an $A \approx 250$ axisymmetric nucleus is weak at rather low values of J [18], the use of formula (1) makes it possible to obtain a qualitative estimate of maximum possible fissile-nucleus temperatures T_m at which the projection K of the fissile-nucleus spin J can still be considered as an integral of the motion, $T_m \leq 0.25$ MeV. This estimate contradicts the result obtained within the fission models that were proposed in [20−27] and in which, as was indicated above, the temperature T of a fissile nucleus in the vicinity of its scission point is about 1 MeV. It is of importance to develop new fission models that would be able to describe basic features of the fission process, such as the mass, charge, and energy distributions of fission fragments, and which, at the same time, would be compatible with the experimentally corroborated concept of transition fission states [2, 3].

An investigation of the angular distributions of fragments originating from the spontaneous fission of aligned nuclei may furnish additional arguments in favor of the above concept.

3. ANGULAR DISTRIBUTIONS OF FRAGMENTS FOR THE FISSION OF ALIGNED NUCLEI

Within quantum-mechanical fission theory [9–12], the normalized (to unity) angular distribution $dP^{J\pi}(\theta)/d\Omega$ of fragments originating from the spontaneous fission of axisymmetric nuclei aligned by an external magnetic field at ultralow temperatures can be represented in the form

$$\frac{dP^{J\pi}(\theta)}{d\Omega} = \sum_{K \geq 0} \frac{(2 - \delta_{K,0})\Gamma^{J\pi K}}{\Gamma^{J\pi}} \frac{dP^{J\pi K}(\theta)}{d\Omega}, \quad (2)$$

where $dP^{J\pi K}(\theta)/d\Omega$ is the angular distribution of fragments for fission from the $J\pi K$ state of the fissile nucleus,

$$\frac{dP^{J\pi K}(\theta)}{d\Omega} = \sum_{M} a_M^J T_{MK}^{J\pi}(\theta); \quad (3)$$

$\Omega \equiv (\theta, \varphi)$ is the solid angle that determines the direction of light-fission-fragment emission in the laboratory frame; $\Gamma^{J\pi K}$ is the partial fission width for the transition of the parent nucleus to the asymptotic state of spin J, parity π, and spin projection K (M) onto the symmetry axis of the nucleus (z axis in the laboratory frame); and

$$\Gamma^{J\pi} = \sum_{K>0} (2 - \delta_{K,0})\Gamma^{J\pi K}$$

is the total fission width of the parent nucleus, the factor $(2 - \delta_{K,0})$ taking into account double degeneracy of $K > 0$ states of an axisymmetric nucleus. In (3), a_M^J is a parameter that characterizes the relative population of the $J\pi M$ sublevels of the fissile nucleus, $\sum_{M=-J}^{J} a_M^J = 1$, and $T_{MK}^{J\pi}(\theta)$ is the normalized (to unity) angular distribution of fragments for fission from the $J\pi MK$ states of the fissile nucleus. For this angular distribution, we have [9, 10]

$$T_{MK}^{J\pi}(\theta) = \frac{2J+1}{16\pi^2} \int d\omega B_{MK}^J(\omega) F^2(l_m, \theta'), \quad (4)$$

$$B_{MK}^J(\omega) = |D_{MK}^J(\omega)|^2 + |D_{M-K}^J(\omega)|^2, \quad (5)$$

where θ' is the angle between the direction of light-fission-fragment emission and the symmetry axis of the fissile nucleus and $D_{MK}^J(\omega)$ is a generalized spherical harmonic, which depends on the Euler angles $\omega \equiv (\alpha, \beta, \gamma)$ determining the orientation of the symmetry axes of the fissile nucleus with respect to the axes of the laboratory frame. The function $F(l_m, \theta')$ in (4) coincides with the amplitude of the normalized (to unity) angular distribution of fission

fragments in the body frame of the fissile nucleus. Specifically, we have

$$F(l_m, \theta') = b(l_m)\left\{ \sum_{l=0}^{l_m} Y_{l0}(\theta')\sqrt{2l+1} R_l \right\}, \quad (6)$$

$$b(l_m) = \left\{ \sum_{l=0}^{l_m} (2l+1) R_l^2 \right\}^{-1/2}, \quad (7)$$

where $R_l = 1 + \pi\pi_1\pi_2(-1)^l$, l_m is the maximum value of the relative orbital angular momentum l of fission fragments, and $Y_{l0}(\theta')$ is a spherical harmonic. As follows from specific calculations, the function $F(l_m, \theta')$ at high values of l_m is virtually independent of the parity π of the fissile nucleus and the parities π_1 and π_2 of fission fragments—that is, on the parity of the relative orbital angular momentum l of fission fragments. For $l_m \to \infty$, the angular distribution $F^2(l_m, \theta')$ reduces to the sum of delta functions of the form

$$\frac{1}{4\pi}[\delta(\xi' - 1) + \delta(\xi' + 1)],$$

where $\xi' = \cos\theta'$, so that the angular distribution (4) assumes the form predicted by A. Bohr's formula [2, 3],

$$\tilde{T}_{MK}^{J\pi}(\theta) = \frac{2J+1}{8\pi} B_{MK}^J(\omega)\bigg|_{\beta=\theta}, \quad (8)$$

which is usually used [3, 8, 13, 14] in calculating the angular distributions of fission fragments.

The mechanism of pumping of relative orbital angular momenta and spins of fission fragments due to a strongly nonspherical character of the potential of interaction between primary fission fragments in the vicinity of the point where the fissile nucleus undergoes scission into fragments was proposed in [12]. This mechanism leads to a value of $l_m \approx 30$ for the maximum relative orbital angular momentum of fission fragments. This value of l_m was confirmed in [10, 11], where the angular distributions of fragments were analyzed for the subthreshold photofission of a set of even−even nuclei and will therefore be used below.

By using the multiplication theorem for spherical harmonics and the formula for transforming the spherical harmonic $Y_{l0}(\theta')$ from the body frame to the laboratory frame, we can represent the angular distribution $F^2(l_m, \theta')$ in the form

$$F^2(l_m, \theta') = \frac{[b(l_m)]^2}{\sqrt{4\pi}} \sum_{Lk} \sum_{ll'} \frac{(2l+1)(2l'+1)}{\sqrt{(2L+1)}} \quad (9)$$
$$\times |C_{ll'00}^{L0}|^2 Y_{Lk}(\theta) D_{k0}^{L*}(\omega) R_l R_{l'},$$

where $C_{ll'00}^{L0}$ is a Clebsch−Gordan coefficient.

In turn, the use of the multiplication theorem for generalized spherical harmonics makes it possible to represent the quantity $B_{MK}^J(\omega)$ in (5) as

$$B_{MK}^J(\omega) = 2 \sum_{L=0,2,4\ldots} B_{MK}^{JL} D_{00}^L(\omega), \quad (10)$$

$$B_{MK}^{JL} = (-1)^{M-K} C_{JJM-M}^{L0} C_{JJK-K}^{L0} \quad (11)$$
$$= (-1)^{2J-M-K} C_{JJM-M}^{L0} C_{JJK-K}^{L0}.$$

Performing integration in (4) with respect to ω and taking into account the explicit expressions (10) and (9) for $B_{MK}^J(\omega)$ and $F^2(l_m, \theta')$, respectively, we can recast the angular distribution $T_{MK}^{J\pi}(\theta)$ into the form

$$T_{MK}^{J\pi}(\theta) = \frac{2J+1}{4\pi} \sum_{L=0,2,4\ldots}^{2J} D_L(l_m) B_{MK}^{JL} P_L(\theta), \quad (12)$$

where $P_L(\theta)$ is a Legendre polynomial and the coefficient $D_L(l_m)$ is given by the expression

$$D_L(l_m) \quad (13)$$
$$= [b(l_m)]^2 \left\{ \sum_{ll'}^{l_m} R_l R_{l'} \frac{(2l+1)(2l'+1)}{2L+1} (C_{ll'00}^{L0})^2 \right\},$$

whence it follows that $D_L(l_m) \leq 1$ and $D_0(l_m) = 1$ for any values of l_m.

If, for the generalized spherical harmonic $D_{00}^L(\omega)$, which appears in the definition of $B_{MK}^J(\omega)$, one employs the relation $D_{00}^L(\omega)|_{\beta=\theta} = P_L(\theta)$, then the angular distribution $\tilde{T}_{MK}^{J\pi}(\theta)$ (8) in A. Bohr's limit ($l_m \to \infty$) can be represented in the form

$$\tilde{T}_{MK}^{J\pi}(\theta) = \frac{2J+1}{4\pi} \sum_{L=0,2,4\ldots}^{2J} B_{MK}^{JL} P_L(\theta). \quad (14)$$

Formula (14) can also be obtained from (12) upon considering that, in A. Bohr's limit, the quantity $D_L(l_m)$ in (13) reduces to $D_L(l_m \to \infty) = 1$ for any values of L, whence it can be seen that, at finite values of l_m, the angular distribution in (12) differs from A. Bohr's angular distribution in (14) only because of the deviation of the coefficients $D_L(l_m)$ from unity. At $l_m = 30$, the coefficients $D_L(l_m)$ are independent of the parity π of the fissile nucleus or the parities π_1 and π_2 of fission fragments, taking the values of $D_2(30) = 0.95$, $D_4(30) = 0.91$, $D_6(30) = 0.87$, $D_8(30) = 0.82$, ..., which decrease with increasing L.

Employing formula (12) and considering that, at $L = 0$, the quantity B_{MK}^{JL} is equal to $(2J+1)^{-1}$, we

can recast the angular distribution $dP^{J\pi K}(\theta)/d\Omega$ (3) into the form

$$\frac{dP^{J\pi K}(\theta)}{d\Omega} = \frac{1}{4\pi} + \frac{2J+1}{4\pi} \quad (15)$$
$$\times \sum_M a_M^J \sum_{L=2,4,\ldots} B_{MK}^{JL} D_L(l_m) P_L(\theta).$$

For a further analysis of the angular distributions (15), it is convenient to employ the quantity f_L^J that is referred to as the nuclear-orientation parameter and which is given by [34]

$$f_L^J = \left[\frac{(2J+L+1)!}{(2L+1)(2J-L)!} \right]^{-1/2} \frac{(L!)^2}{(2L)!} J^{-L} G_L^J, \quad (16)$$

where

$$G_L^J = \sum_M a_M^J (-1)^{J-M} C_{JJM-M}^{L0} \quad (17)$$

is the Fano statistical tensor. If a fissile nucleus is not oriented because of an equiprobable population of all $J\pi M$ sublevels of this nucleus at different values of M, in which case we have $a_M^J = (2J+1)^{-1}$, the Fano statistical tensor G_L^J and the nuclear-orientation parameter f_L^J become, respectively, $G_L^J = (2J+1)^{-1/2}\delta_{L,0}$ and $f_L^J = \delta_{L,0}$ by virtue of the following properties of Clebsch−Gordan coefficients:

$$\sum_M C_{JJM-M}^{L0} C_{JJ-MM}^{00} \quad (18)$$
$$= \sum_M C_{JJM-M}^{L0} (-1)^{J-M} \frac{1}{\sqrt{2J+1}} = \delta_{L,0}.$$

In this case, all of the $L \neq 0$ terms vanish in the angular distribution (15), which becomes purely isotropic,

$$\left(\frac{dP^{J\pi K}(\theta)}{d\Omega} \right)^{\text{is}} = \frac{1}{4\pi}.$$

With the aid of formulas (11), (12), (16), and (17), the angular distribution (15) can in general be represented in the form

$$\frac{dP^{J\pi K}(\theta)}{d\Omega} = \left(\frac{dP^{J\pi K}(\theta)}{d\Omega} \right)^{\text{is}} W^{J\pi K}(\theta), \quad (19)$$

where

$$W^{J\pi K}(\theta) = 1 + \sum_{L=2,4,\ldots} D_L(l_m) f_L^J A_L(J,K) P_L(\theta) \quad (20)$$

is the reduced angular distribution of fission fragments with

$$A_L(J,K) = (-1)^{J-K} C_{JJK-K}^{L0} \quad (21)$$

Orientation parameters f_L^J and coefficients $A_L(J, K)$ for $J = 7/2$ and $J = 9/2$ and various values of K versus L

L	$J = 7/2$					$J = 9/2$					
	f_L^J	$A_L(J, K)$				f_L^J	$A_L(J, K)$				
		$K = 7/2$	$K = 5/2$	$K = 3/2$	$K = 1/2$		$K = 9/2$	$K = 7/2$	$K = 5/2$	$K = 3/2$	$K = 1/2$
2	0.57	4.08	0.58	-1.75	-2.92	0.59	4.6	1.53	-0.76	-2.30	-3.07
4	0.08	7.96	-14.78	-3.41	-10.23	0.11	10.75	-13.14	-10.16	1.79	10.75
6	0.003	10.21	-51.06	91.91	-51.06	0.008	17.30	-63.43	57.67	34.60	-46.13
8						0.0002	20.85	-145.96	417.04	-583.86	291.92

$$\times \ \frac{(2J + 1)J^L(2L)!}{(L!)^2}\left[\frac{(2L + 1)(2J - L)!}{(2J + L + 1)!}\right]^{1/2}.$$

For a complete alignment of a spontaneously fissile nucleus in an external magnetic field at ultralow temperatures, in which case a_M^J becomes $a_M^J = \delta_{M, \pm J}$, depending on the sign of the gyromagnetic ratio for a fissile nucleus, the Fano tensor G_L^J (17) assumes the form

$$G_L^J = C_{JJJ-J}^{L0} = \left[\frac{(2L + 1)(2J!)^2}{(2J - L)!(2J + L + 1)!}\right]^{1/2},$$

while the nuclear-orientation parameter reduces to [34]

$$f_L^J = \frac{(L!)^2}{(2L)!}J^{-L}\frac{(2J)!}{(2J - L)!}. \tag{22}$$

The total angular distribution $dP^{J\pi}(\theta)/d\Omega$ of fragments for the spontaneous fission of oriented nuclei is obtained by substituting (19) and (20) into (2),

$$\frac{dP^{J\pi}(\theta)}{d\Omega} = \left(\frac{dP^{J\pi K}(\theta)}{d\Omega}\right)^{\text{is}}W^{J\pi}(\theta), \tag{23}$$

where the reduced angular distribution $W^{J\pi}(\theta)$ is expressed in terms of the distribution $W^{J\pi K}(\theta)$ (20) as

$$W^{J\pi}(\theta) = \sum_{K \geq 0}\frac{(2 - \delta_{K,0})\Gamma^{J\pi K}}{\Gamma^{J\pi}}W^{J\pi K}(\theta). \tag{24}$$

One can then see that, in just the same way as in the case of angular distributions of fragments for the subthreshold fission of nuclei [8, 10, 11] and fragments originating from the fission of aligned nuclei that is induced by low-energy and resonance neutrons [13, 14], the reduced angular distribution $W^{J\pi}(\theta)$ of fission fragments becomes fully isotropic and equal to

unity if the distribution of all projections K of the fissile-nucleus spin J is equiprobable in the asymptotic region, in which case the partial fission widths $\Gamma^{J\pi K}$ in (24) are independent of K. This result is associated with the property of Clebsch−Gordan coefficients that arises from (18) upon the substitution of the index K for the index M and which leads to the vanishing of all $L \neq 0$ terms in (24). This means that the discovery of a sizable anisotropy in experimental reduced angular distributions $W^{J\pi}(\theta)$ would indicate that, in the external region introduced above, the fissile nucleus being studied is not heated to significant temperatures. It would also be of interest to obtain a piece of evidence in support of an exact spin-projection conservation for a spontaneously fissile nucleus in the external region, in which case the sum over K in (24) would be dominated by the $K = J$ term.

4. ANGULAR DISTRIBUTIONS OF FRAGMENTS FOR THE SPONTANEOUS FISSION OF COMPLETELY ORIENTED NUCLEI ^{255}Es AND ^{257}Fm

A further analysis will be performed by considering spontaneous fission from the ground states of the ^{255}Es and ^{257}Fm odd nuclei that are completely oriented in an external magnetic field at ultralow temperatures and which were chosen for investigation in the project formulated in [16]. Although there have so far been no reliable measurements of the spins of these nuclei, one can conclude from the systematics of spins of neighboring odd isotopes of Es and Fm that the spins J of the ^{255}Es and ^{257}Fm nuclei are 7/2 and 9/2, respectively. Since the angular distributions of fragments in the spontaneous fission of aligned nuclei are sensitive to the spins J of these nuclei, one can obtain direct information about the spins J from an analysis of these distributions, thereby confirming
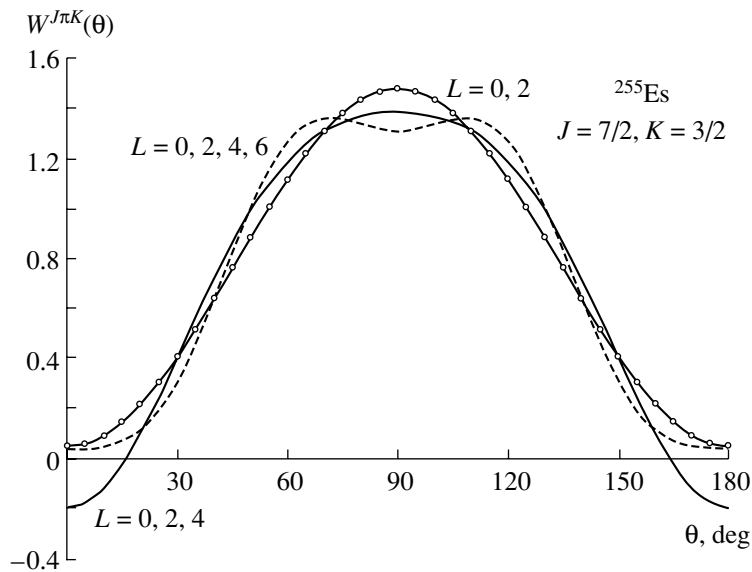
Fig. 1. Reduced angular distributions $W^{J\pi K}(\theta)$ (20) in the case of ^{255}Es for various L values included in their calculation.
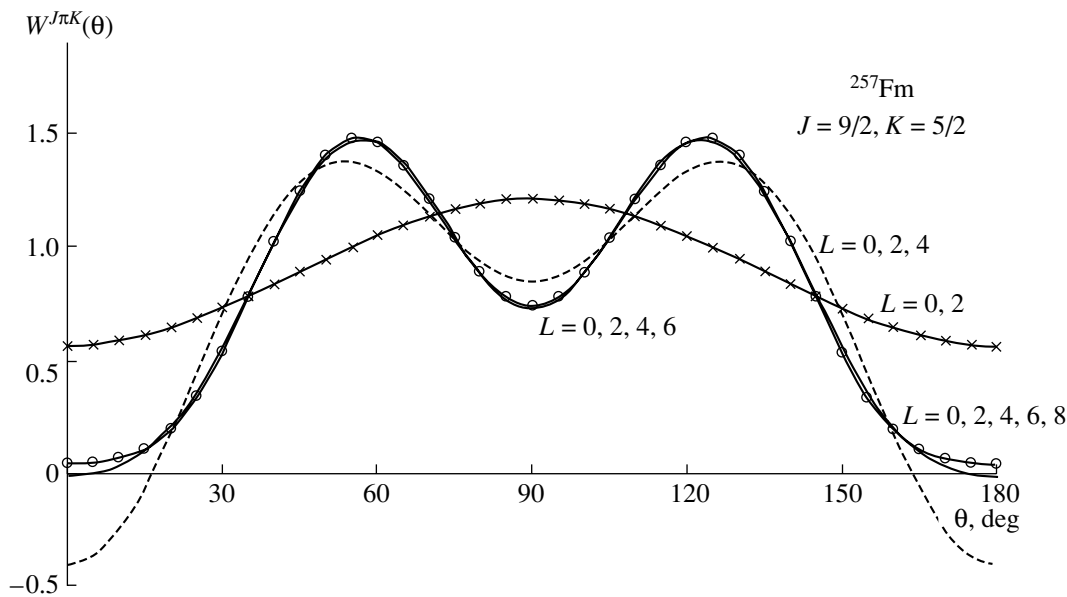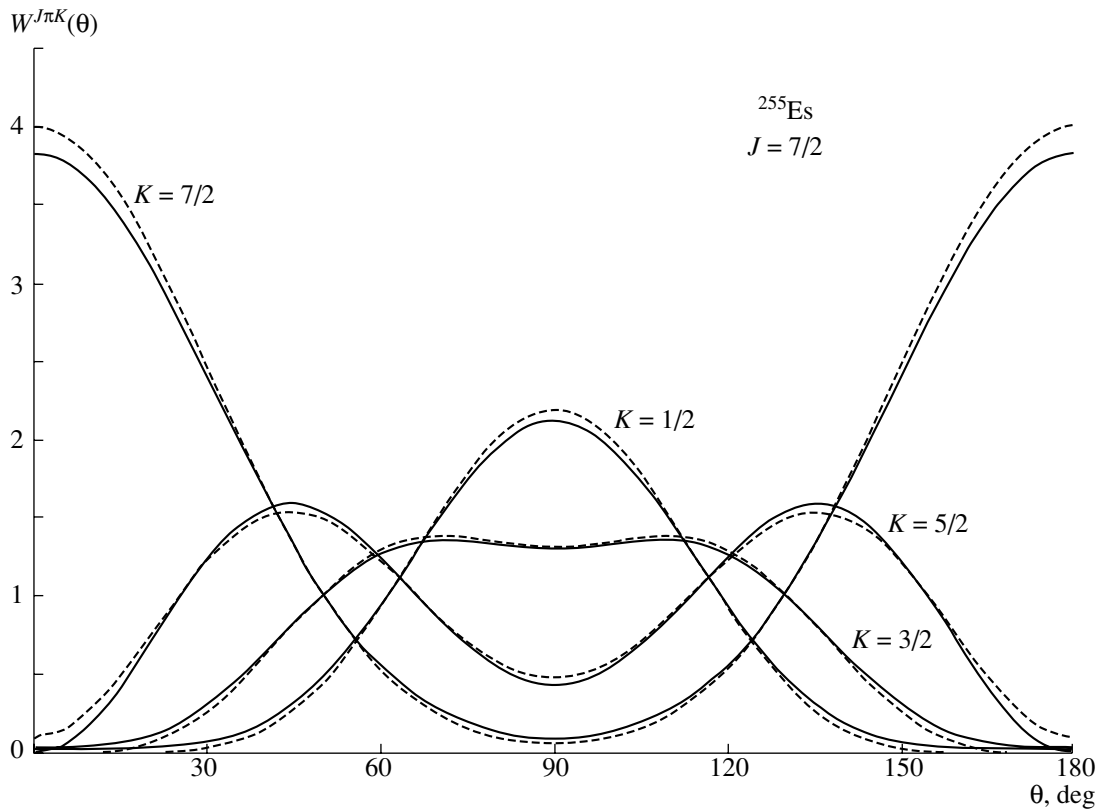

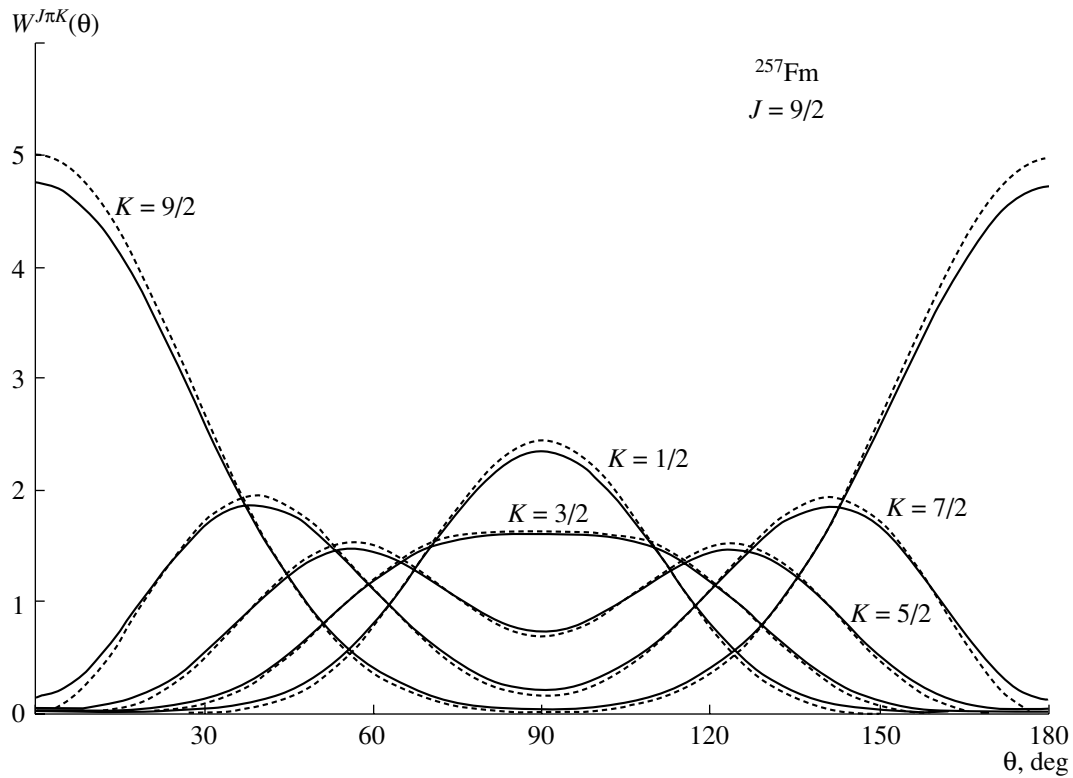**Fig. 2.** As in Fig. 1, but for ^{257}Fm.

(or disproving) the spin values proposed above for the nuclei in question.

From the table, which presents the values calculated by formulas (22) and (21) for the coefficients f_L^J and $A_L(J, K)$ at $J = 7/2$ and $J = 9/2$, one can see that the quantities f_L^J decrease with increasing L, while the coefficients $A_L(J, K)$ increase fast with increasing K. It follows that, in order to obtain rather accurate results for the reduced angular distributions $W^{J\pi K}(\theta)$ of fission fragments, one must also take into account the $L > 2$ terms in the sum over L

in (20). The calculations reveal that, in describing angular distributions of fragments for fission from the ground state of a $J = K$ fissile nucleus, one can disregard the contributions of the $L = 6$ terms for ^{255}Es and the contributions of the $L = 8$ terms for ^{257}Fm. In describing the angular distributions $W^{J\pi K}(\theta)$ for $K < J$, it is necessary to take into account all possible values of $L(L < 2J)$, this being illustrated by Figs. 1 and 2 for the example of the reduced angular distributions, respectively, at $J = 7/2$ and $K = 3/2$ and at $J = 9/2$ and $K = 5/2$. From Fig. 1, one can

Fig. 3. Reduced angular distributions $W^{J\pi K}(\theta)$ (20) in the case of ^{255}Es for various values of K. The solid and dashed curves represent the results of the calculations at, respectively, $l_m = 30$ and $l_m = \infty$ (A. Bohr's formula).

Fig. 4. As in Fig. 3, but for ^{257}Fm.

see that, at $J = 7/2$ and $K = 3/2$, the shape of the angular distribution changes markedly in the vicinity of the angle $\theta = 0°$ upon taking into account the $L = 6$ term. Figure 2 shows that, at $J = 9/2$ and $K = 5/2$, the inclusion of the $L = 8$ term is necessary since, otherwise, the distribution $W^{J\pi K}(\theta)$ takes negative values in the vicinities of the angles $0°$ and $180°$.

As can be seen from Figs. 3 and 4, the shape of the reduced angular distributions $W^{J\pi K}(\theta)$ for $J = 7/2$ and $J = 9/2$ changes strongly with K—from the distributions at low K, which have a maximum at $\theta = 90°$, to the distributions at $K = J$, which have a minimum at $\theta = 90°$. At the same time, a comparison of the data in Figs. 3 and 4 shows that, in the case of $K = J$, the distributions $W^{J\pi K}(\theta)$ change substantially upon going over from $J = 7/2$ to $J = 9/2$. Therefore, a comparison of experimental reduced angular distributions with the distributions $W^{J\pi}(\theta)$ in (24) would make it possible to determine not only the spin J of a fissile nucleus but also the spin projections K that manifest themselves in the external region of the fissile system.

Upon attaining a rather high statistical accuracy in measuring reduced angular distributions $W^{J\pi}(\theta)$, one can hope to reveal deviations of $W^{J\pi}(\theta)$ from the predictions of A. Bohr's formula (24) and to find the true value of l_m. Indeed, the angular distributions $W^{J\pi K}(\theta)$ calculated by formula (20) at $l_m = 30$ for angles around $\theta = 90°$ differ from the angular distributions calculated by A. Bohr formula (14) by factors of 1.57 and 2.66 for, respectively, $J = 7/2$ and $J = 9/2$ (see Figs. 3, 4).

5. CONCLUSION

Our analysis of the problem of conservation of the projection K of the spin J of an axisymmetric fissile nucleus at various stages of the fission process has revealed that, because of the Coriolis interaction effect, only if the fissile nucleus being considered remains cold up to the point of its scission into fission fragments do there appear noticeable anisotropies in the angular distributions of fragments for the spontaneous and low-energy induced fission of nuclei. The planned experiments to study the angular distributions of fragments originating from the spontaneous fission of oriented nuclei may furnish additional arguments in favor of the ideas developed above.

It is of importance to emphasize that the conclusions drawn from the present analysis cannot be reconciled with existing fission models, which lead to significant temperatures in the prescission configuration of a fissile nucleus.

REFERENCES

1. E. J. Winhold, P. T. Demos, and I. Halpern, Phys. Rev. **87**, 1139 (1952).
2. A. Bohr, in *Proceedings of the International Conference on the Peaceful Uses of Atomic Energy* (New York, 1956), Vol. 2.
3. A. Bohr and B. Mottelson, *Nuclear Structure*, Vol. 2: *Nuclear Deformations* (Benjamin, New York, 1975; Mir, Moscow, 1977).
4. V. M. Strutinskiĭ, Yad. Fiz. **3**, 614 (1966) [Sov. J. Nucl. Phys. **3**, 449 (1966)]; V. M. Strutinsky, Nucl. Phys. A **95**, 420 (1967).
5. J. E. Lynn, Report AERE-R5891 (1968).
6. H. Weigmann, Z. Phys. **214**, 7 (1968).
7. C. D. Bowman, Phys. Rev. C **12**, 856 (1975).
8. Yu. B. Ostapenko, G. N. Smirenkin, A. S. Soldatov, and Yu. M. Tsipenyuk, Fiz. Élem. Chastits At. Yadra **12**, 1364 (1981) [Sov. J. Part. Nucl. **12**, 545 (1981)].
9. S. G. Kadmensky, Yad. Fiz. **65**, 1424 (2002) [Phys. At. Nucl. **65**, 1390 (2002)].
10. S. G. Kadmensky and L. V. Rodionova, Yad. Fiz. **66**, 1259 (2003) [Phys. At. Nucl. **66**, 1219 (2003)].
11. S. G. Kadmensky and L. V. Rodionova, Yad. Fiz. (in press).
12. S. G. Kadmensky, Yad. Fiz. **67**, 167 (2004) [Phys. At. Nucl. **67**, 170 (2004)].
13. N. J. Pattenden and H. Postma, Nucl. Phys. A **167**, 225 (1971).
14. R. Kuiken, N. J. Pattenden, and H. Postma, Nucl. Phys. A **190**, 401 (1972).
15. W. I. Furman, in *Proceedings of FG/OM Spring Session, Geel, Belgium, 1999*, p. 248.
16. G. M. Gurevich *et al.*, in *Proceedings of the 53rd International Conference on Nuclear Spectroscopy, St. Petersburg, Russia, 2003*, p. 36.
17. L. Wilets, *Theories of Nuclear Fission* (Clarendon, Oxford, 1964; Atomizdat, Moscow, 1967).
18. S. G. Kadmenskiĭ, V. P. Markushev, and V. I. Furman, Yad. Fiz. **35**, 300 (1982) [Sov. J. Nucl. Phys. **35**, 166 (1982)].
19. S. G. Kadmenskiĭ, V. P. Markushev, Yu. P. Popov, and V. I. Furman, Yad. Fiz. **39**, 7 (1984) [Sov. J. Nucl. Phys. **39**, 4 (1984)].
20. J. R. Nix, Nucl. Phys. A **130**, 241 (1969).
21. A. V. Ignatyuk, Yad. Fiz. **9**, 357 (1969) [Sov. J. Nucl. Phys. **9**, 208 (1969)].
22. M. Brack *et al.*, Rev. Mod. Phys. **44**, 320 (1972).
23. Y. Bonch and Z. Fraenkel, Phys. Rev. C **10**, 893 (1974).

24. B. D. Wilkins *et al.*, Phys. Rev. C **14**, 1832 (1976).
25. V. A. Rubchenya and S. G. Yavshits, Yad. Fiz. **40**, 649 (1984) [Sov. J. Nucl. Phys. **40**, 416 (1984)].
26. W. Greiner, J. P. Park, and W. Schield, *Nuclear Molecules* (World Sci., Singapore, 1995).
27. T. M. Shneideman *et al.*, Phys. Rev. C **65**, 064302 (2002).
28. G. V. Danilyan *et al.*, Pis'ma Zh. Éksp. Teor. Fiz. **26**, 68 (1977) [JETP Lett. **26**, 186 (1977)].
29. A. K. Petukhov, G. A. Petrov, *et al.*, Pis'ma Zh. Éksp. Teor. Fiz. **30**, 324 (1979) [JETP Lett. **30**, 439 (1979)].
30. I. Halpern, *Nuclear Fission* (Fizmatgiz, Moscow, 1962).
31. O. P. Sushkov and V. V. Flambaum, Usp. Fiz. Nauk **136**, 3 (1982) [Sov. Phys. Usp. **25**, 1 (1982)].
32. S. G. Kadmensky, Yad. Fiz. **66**, 1739 (2003) [Phys. At. Nucl. **66**, 1691 (2003)].
33. S. G. Kadmensky, Yad. Fiz. **67**, 258 (2004) [Phys. At. Nucl. **67**, 241 (2004)].
34. *Alpha-, Beta-, and Gamma-ray Spectroscopy*, Ed. by K. Siegbahn (North-Holland, Amsterdam, 1968; Atomizdat, Moscow, 1969), Vol. 3.

Translated by A. Isaakyan

NUCLEI
Theory

Spectroscopic Factors and Barrier Penetrabilities in Cluster Radioactivity

S. N. Kuklin[1),2)], G. G. Adamian[1),3)]*, and N. V. Antonenko[1)]

Received December 2, 2004

Abstract—The cold cluster decay model is presented in the framework of a dinuclear system concept. Spectroscopic factors are extracted from barrier penetrabilities and measured half-lives. The deformation of the light cluster and residual nucleus is shown to affect the nucleus–nucleus potential and decay characteristics. Half-lives are predicted for neutron-deficient actinides and intermediate-mass nuclei. The connection between spontaneous fission and cluster radioactivity is discussed. © *2005 Pleiades Publishing, Inc.*

1. INTRODUCTION

Spontaneous binary nuclear decay is possible if this process is exothermic, i.e., occurs with positive energy release $Q > 0$. This condition is satisfied for many decay modes of numerous nuclei in the second half of the Periodic Table. Only α decay (decay supersymmetric in product masses) and/or spontaneous fission (symmetric or asymmetric decay) is primarily realized. The yields of carbon, fluorine, oxygen, neon, magnesium, and silicon isotopes are measured only for the case where one of daughter nuclei is ^{208}Pb or nuclei close to it in narrow ranges $90 \leq Z \leq 93$ and $206 \leq A \leq 212$ of the charge and mass numbers, respectively. Light clusters, as well as the α particle, are in the ground state, and the heavy residual nucleus is in the ground state or in one of low-lying states (e.g., the fine structure of the ^{223}Ra $\rightarrow$ ^{14}C + ^{209}Pb decay [1, 2]). This phenomenon is called cluster radioactivity and has many common features with α decay and cold fission in which the decay fragments are almost unexcited [1, 2]. Experiments point to the decisive role of structure effects such as the fine structure and exclusion of transitions from odd parent nuclei [1–3].

The process of cold nuclear decay can be represented in the form of the collective flow of nucleons of the initial nucleus to the daughter nuclei, when nuclei have time to occupy levels with the minimum energy. This process is accompanied with the considerable rearrangement of the parent nucleus. Such a description of cluster decay is similar to the classical description of the nuclear fission process. Models based on this description are called adiabatic or fission models [4–7]. At the same time, one can assume that a light cluster is formed on the surface of the parent nucleus. The decay of such a system consisting of two daughter nuclei does not require a significant adjustment of the system to the final decay channel. In this nonadiabatic approach [1, 2, 8, 9], α decay is well described. Thus, in adiabatic models, the shape of a fissioning nucleus is assumed to change continuously and smoothly with time, and the process is described dynamically beginning with the parent nucleus and ending with the prescission configuration. In nonadiabatic models, the probability of the almost instantaneous formation of a two-cluster system and the penetrability of the potential barrier are calculated separately.

The model discussed in this work is based on the assumption that the ground nuclear state can be represented as a superposition of cluster states and a mononucleus [10]. Cluster states are described as dinuclear systems (DNSs) [11]. A DNS decays if nuclei overcome a potential barrier preventing the instantaneous decay of the DNS. There are many methods for calculating a nucleus–nucleus potential (e.g., the proximity potential, folding potential, double-folding potential, optical potential, etc.) [1, 2, 12]. In addition, different models involve different parameters for calculating the interaction potential. The form of the potential is determined primarily by the spectroscopic factor and barrier penetrability. We use a nucleus–nucleus potential based on the double-folding procedure. The aim of this work is to extract the spectroscopic factors of clusters from the available experimental half-lives and calculated penetrabilities

[1)]Joint Institute for Nuclear Research, Dubna, Moscow oblast, 141980 Russia.
[2)]Mari State University, Ioshkar Ola, Russia.
[3)]Institute of Nuclear Physics, Academy of Sciences of Uzbekistan, Tashkent, 702132 Uzbekistan.
*e-mail: adamian@thsun1.jinr.ru
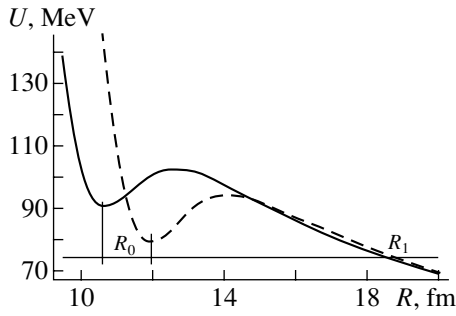
Fig. 1. Interaction potential between the ^{28}Mg and ^{206}Hg nuclei in the decay of ^{234}U. Calculations were performed for two values of the quadrupole nuclear deformation: (solid curve) $\beta_x = \beta_f = 0$ and (dashed curve) $\beta_x = 0.49$, $\beta_f = 0.05$. The horizontal straight line shows the absolute value of Q for the given decay.

of potential barriers and to predict the half-lives of neutron-deficient nuclei.

2. MODEL

Cluster decay can be described as the evolution of the system along the mass-asymmetry coordinates $\eta = (A_f - A_x)/(A_f + A_x)$ (A_f and A_x are the mass numbers of the heavy and light clusters, respectively) and along the distance R between the centers of mass of clusters. With low probability, a strongly asymmetric DNS exists in the ground nuclear state. Such a DNS decays due to tunneling through the barrier of the nucleus−nucleus potential. In the first approximation, the process can be divided into two stages: the formation of the DNS can be treated as evolution along η, and the decay of the DNS, as evolution along R. The probability S of the formation of the DNS can be found using the ground state of the Schrödinger equation in the mass asymmetry variable. The probability P of tunneling in R can be considered in the WKB approximation.

In order to calculate the characteristics of cluster decay, we use formulas similar to the formulas of α-decay theory [1]. The half-life of a nucleus with respect to cluster decay is given by the expression

$$t_x = \hbar/\Gamma_x,$$

where

$$\Gamma_x = \frac{\hbar\omega_0}{\pi} SP$$

is the decay width. The half-life can be expressed in terms of t_x as

$$T_{1/2} = t_x \ln 2 = \frac{\pi \ln 2}{\omega_0 SP}. \qquad (1)$$

In the expression, the energy $\hbar\omega_0$ related to the angular frequency is the distance between the neighboring

resonances in the classically allowed surface of the potential energy for a particular parent nucleus. In the case under consideration, this frequency is related to the frequency of zero modes in the variable η near $|\eta| = 1$. The allowed region arises because the potential energy of the α configuration is comparable or even lower (particularly for neutron-deficient nuclei) than the potential energy of the mononucleus ($|\eta| = 1$) [10]. The angular frequency has a specific value for a specific parent nucleus, but we take the mean value $\hbar\omega_0 = 1.2$ MeV [10] in calculations for all decays under consideration.

The probability of tunneling through a potential barrier in R, i.e., its penetrability P, is calculated by the formula

$$P = 1/(1 + \exp G), \qquad (2)$$

where

$$G = \frac{2}{\hbar} \int_{R_0}^{R_1} \sqrt{2m[U(R) - Q]} dR.$$

The R_0 and R_1 values are given in Fig. 1 for the interaction potential between the ^{28}Mg and ^{206}Hg nuclei, $m = m_0 A_x A_f/(A_f + A_x)$ is the reduced mass of the system (m_0 is the nucleon mass), and Q is the decay energy. The contact configuration at $R = R_0 \approx R_x(1 + \sqrt{5/(4\pi)}\beta_x) + R_f(1 + \sqrt{5/(4\pi)}\beta_f) + 0.5$ fm ($R_{x,f} = r_{0x,f} A_{x,f}^{1/3}$ are the radii of the light and heavy clusters, and $\beta_{x,f}$ are the parameters of quadrupole nuclear deformation) corresponds to the position of the local minimum of the nucleus−nucleus potential U. It is assumed that the DNS is axisymmetric, because the potential interaction energy for all other orientations of the DNS nuclei is higher. We note that only quadrupole nuclear deformation is taken into account.

The potential $U(R)$ can be represented as the sum of three terms [12]:

$$U(R) = U_{\mathrm{Coul}}(R) + U_N(R) + U_L(R), \qquad (3)$$

where $U_{\mathrm{Coul}}(R)$, $U_N(R)$, and $U_L(R) = \hbar^2 L(L + 1)/(2\Im(R))$ are the Coulomb, nuclear, and centrifugal potentials, respectively, where $\Im(R)$ is the orbital moment of inertia. Calculation of $U_N(R)$ is most difficult. Let us take it in the form of the double-folding potential:

$$U_N(R) = \int \rho_x(\mathbf{r}_x)\rho_f(\mathbf{R} - \mathbf{r}_f)F(\mathbf{r}_f - \mathbf{r}_x)d\mathbf{r}_x d\mathbf{r}_f.$$

The nucleon−nucleon forces

$$F(\mathbf{r}_f - \mathbf{r}_x)$$
$$= C_0 \left(F_{\mathrm{in}}\frac{\rho_0(\mathbf{r}_x)}{\rho_{00}} + F_{\mathrm{ex}}\left(1 - \frac{\rho_0(\mathbf{r}_x)}{\rho_{00}}\right)\right)\delta(\mathbf{r}_f - \mathbf{r}_x),$$

Table 1. Calculated penetrabilities P and spectroscopic factors S, as well as measured half-lives $T_{1/2}$; quadrupole-deformation parameters β_x and β_f of the cluster and residual nucleus, respectively [15]; and energy release Q in decay (the calculations were performed with the parameters $a_{0x} = 0.55$ fm, $a_{0f} = 0.56$ fm, $r_{0x} = 1.15$ fm, and $r_{0f} = 1.16$ fm)

$A \to A_x + A_f$	β_x	β_f	Q, MeV	$T_{1/2}$, s	P	S
^{221}Fr $\to$ ^{14}C + ^{207}Tl	-0.36	0.05	31.29	2.9×10^{14}	8.2×10^{-30}	5.2×10^{-7}
^{221}Ra $\to$ ^{14}C + ^{207}Pb	-0.36	0.03	32.29	1.5×10^{13}	8.9×10^{-28}	9.1×10^{-8}
^{222}Ra $\to$ ^{14}C + ^{208}Pb	-0.36	0.00	33.05	1.7×10^{11}	1.9×10^{-26}	3.8×10^{-7}
^{223}Ra $\to$ ^{14}C + ^{209}Pb	-0.36	0.02	31.85	7.6×10^{15}	6.0×10^{-29}	2.9×10^{-9}
^{224}Ra $\to$ ^{14}C + ^{210}Pb	-0.36	0.02	30.54	7.3×10^{15}	3.2×10^{-31}	5.3×10^{-7}
^{226}Ra $\to$ ^{14}C + ^{212}Pb	-0.36	0.02	28.21	1.7×10^{21}	1.0×10^{-36}	6.8×10^{-7}
^{225}Ac $\to$ ^{14}C + ^{211}Bi	-0.36	0.02	30.48	1.5×10^{17}	9.3×10^{-33}	8.6×10^{-9}
^{228}Th $\to$ ^{20}O + ^{208}Pb	0.26	0.00	44.72	5.4×10^{20}	7.7×10^{-29}	2.9×10^{-14}
^{230}Th $\to$ ^{24}Ne + ^{206}Hg	0.45	0.05	57.78	4.1×10^{24}	3.4×10^{-26}	5.8×10^{-21}
^{231}Pa $\to$ ^{23}F + ^{208}Pb	0.45	0.00	51.87	9.5×10^{25}	3.9×10^{-27}	3.3×10^{-21}
^{231}Pa $\to$ ^{24}Ne + ^{207}Tl	0.45	0.05	60.24	7.9×10^{22}	8.0×10^{-23}	1.9×10^{-22}
^{232}U $\to$ ^{24}Ne + ^{208}Pb	0.45	0.00	62.31	2.5×10^{20}	2.3×10^{-22}	2.1×10^{-20}
^{233}U $\to$ ^{24}Ne + ^{209}Pb	0.45	0.02	60.50	6.9×10^{24}	1.5×10^{-24}	1.1×10^{-22}
^{233}U $\to$ ^{25}Ne + ^{208}Pb	0.50	0.00	60.75	6.9×10^{24}	3.9×10^{-24}	4.4×10^{-23}
^{234}U $\to$ ^{24}Ne + ^{210}Pb	0.45	0.02	58.84	8.5×10^{25}	8.3×10^{-27}	1.7×10^{-21}
^{234}U $\to$ ^{26}Ne + ^{208}Pb	0.50	0.00	59.47	8.5×10^{25}	6.5×10^{-26}	2.1×10^{-22}
^{234}U $\to$ ^{28}Mg + ^{206}Hg	0.49	0.05	74.13	5.4×10^{25}	6.3×10^{-22}	3.5×10^{-26}
^{235}U $\to$ ^{24}Ne + ^{211}Pb	0.45	0.02	57.36	2.8×10^{27}	3.6×10^{-29}	1.2×10^{-20}
^{235}U $\to$ ^{25}Ne + ^{210}Pb	0.50	0.02	57.83	2.8×10^{27}	6.2×10^{-28}	6.5×10^{-22}
^{235}U $\to$ ^{26}Ne + ^{209}Pb	0.50	0.02	58.11	2.8×10^{27}	1.1×10^{-27}	1.5×10^{-21}
^{236}U $\to$ ^{30}Mg + ^{206}Hg	0.43	0.05	72.51	3.8×10^{27}	7.7×10^{-25}	4.0×10^{-25}
^{236}Pu $\to$ ^{28}Mg + ^{208}Pb	0.49	0.00	79.67	3.5×10^{21}	8.6×10^{-19}	4.2×10^{-25}
^{238}Pu $\to$ ^{28}Mg + ^{210}Pb	0.59	0.02	75.93	4.7×10^{25}	2.0×10^{-21}	1.3×10^{-26}
^{238}Pu $\to$ ^{30}Mg + ^{208}Pb	0.43	0.00	77.03	4.7×10^{25}	9.9×10^{-23}	2.5×10^{-24}
^{238}Pu $\to$ ^{32}Si + ^{206}Hg	0.22	0.05	91.21	1.9×10^{25}	6.3×10^{-23}	9.5×10^{-25}
^{242}Cm $\to$ ^{34}Si + ^{208}Pb	0.18	0.00	96.53	1.4×10^{23}	1.5×10^{-21}	1.5×10^{-23}

$$F_{\text{in,ex}} = \zeta_{\text{in,ex}} + \zeta'_{\text{in,ex}} \frac{A_x - 2Z_x}{A_x} \frac{A_f - 2Z_f}{A_f},$$

depend on the nuclear density, because $\rho_0(\mathbf{r}_x) = \rho_x(\mathbf{r}_x) + \rho_f(\mathbf{R} - \mathbf{r}_f)$. The constants $\zeta_{\text{in}} = 0.09$, $\zeta_{\text{ex}} = -2.59$, $\zeta'_{\text{in}} = 0.42$, $\zeta'_{\text{ex}} = 0.54$, and $C_0 = 300$ MeV fm³ are calculated by fitting the measured nuclear characteristics [13]. The spatial axisymmetric nucleon density has the form of the Woods−Saxon distribution:

$$\rho_{x,f}(\mathbf{r}) = \frac{\rho_{00}}{1 + \exp(|\mathbf{r} - \mathbf{R}_{x,f}|/a_{0x,f})},$$

where $\rho_{00} = 0.17$ fm^{-3} and $a_{0x,f}$ are the nuclear diffusivity parameters.

The Coulomb potential U_{Coul} is calculated by the formula [14]

$$U_{\text{Coul}}(R) = \frac{e^2 Z_x Z_f}{R} + \frac{3}{5} \frac{e^2 Z_x Z_f}{R^3}$$
$$\times \sum_{i=x,f} R_{0i}^2 \beta_i Y_{20}(\theta_i)$$

Table 2. Calculated penetrabilities P and spectroscopic factors S for spherical clusters and residual nuclei, as well as measured half-lives $T_{1/2}$ and energy release Q in decay (the calculations were performed with the parameters $a_{0x} = 0.55$ fm, $a_{0f} = 0.56$ fm, $r_{0x} = 1.15$ fm, and $r_{0f} = 1.16$ fm)

$A \to A_x + A_f$	Q, MeV	$T_{1/2}$, s	P	S
^{221}Fr $\to$ ^{14}C + ^{207}Tl	31.29	2.9×10^{14}	1.8×10^{-27}	2.3×10^{-9}
^{221}Ra $\to$ ^{14}C + ^{207}Pb	32.29	1.5×10^{13}	1.6×10^{-26}	5.0×10^{-9}
^{222}Ra $\to$ ^{14}C + ^{208}Pb	33.05	1.7×10^{11}	6.6×10^{-25}	1.1×10^{-8}
^{223}Ra $\to$ ^{14}C + ^{209}Pb	31.85	7.6×10^{15}	1.9×10^{-27}	8.4×10^{-11}
^{224}Ra $\to$ ^{14}C + ^{210}Pb	30.54	7.3×10^{15}	1.2×10^{-29}	1.4×10^{-8}
^{226}Ra $\to$ ^{14}C + ^{212}Pb	28.21	1.7×10^{21}	1.2×10^{-34}	5.8×10^{-9}
^{225}Ac $\to$ ^{14}C + ^{211}Bi	30.48	1.5×10^{17}	5.8×10^{-33}	1.4×10^{-8}
^{228}Th $\to$ ^{20}O + ^{208}Pb	44.72	5.4×10^{20}	1.5×10^{-31}	1.5×10^{-11}
^{230}Th $\to$ ^{24}Ne + ^{206}Hg	57.78	4.1×10^{24}	6.0×10^{-32}	4.8×10^{-15}
^{231}Pa $\to$ ^{23}F + ^{208}Pb	51.87	9.5×10^{25}	2.1×10^{-32}	6.0×10^{-16}
^{231}Pa $\to$ ^{24}Ne + ^{207}Tl	60.24	7.9×10^{22}	1.1×10^{-29}	1.4×10^{-15}
^{232}U $\to$ ^{24}Ne + ^{208}Pb	62.31	2.5×10^{20}	7.7×10^{-28}	6.3×10^{-15}
^{233}U $\to$ ^{24}Ne + ^{209}Pb	60.50	6.9×10^{24}	1.7×10^{-30}	1.0×10^{-16}
^{233}U $\to$ ^{25}Ne + ^{208}Pb	60.75	6.9×10^{24}	2.6×10^{-30}	6.7×10^{-17}
^{234}U $\to$ ^{24}Ne + ^{210}Pb	58.84	8.5×10^{25}	9.9×10^{-33}	1.4×10^{-15}
^{234}U $\to$ ^{26}Ne + ^{208}Pb	59.47	8.5×10^{25}	2.3×10^{-32}	6.0×10^{-16}
^{234}U $\to$ ^{28}Mg + ^{206}Hg	74.13	5.4×10^{25}	6.2×10^{-30}	3.5×10^{-18}
^{235}U $\to$ ^{24}Ne + ^{211}Pb	57.36	2.8×10^{27}	3.6×10^{-35}	1.2×10^{-14}
^{235}U $\to$ ^{25}Ne + ^{210}Pb	57.83	2.8×10^{27}	9.4×10^{-35}	4.3×10^{-15}
^{235}U $\to$ ^{26}Ne + ^{209}Pb	58.11	2.8×10^{27}	5.5×10^{-34}	3.2×10^{-15}
^{236}U $\to$ ^{30}Mg + ^{206}Hg	72.51	3.8×10^{27}	2.2×10^{-32}	1.4×10^{-17}
^{236}Pu $\to$ ^{28}Mg + ^{208}Pb	79.67	3.5×10^{21}	1.1×10^{-25}	3.3×10^{-18}
^{238}Pu $\to$ ^{28}Mg + ^{210}Pb	75.93	4.7×10^{25}	3.8×10^{-30}	6.9×10^{-18}
^{238}Pu $\to$ ^{30}Mg + ^{208}Pb	77.03	4.7×10^{25}	4.2×10^{-29}	6.0×10^{-18}
^{238}Pu $\to$ ^{32}Si + ^{206}Hg	91.21	1.9×10^{25}	1.2×10^{-27}	5.0×10^{-20}
^{242}Cm $\to$ ^{34}Si + ^{208}Pb	96.53	1.4×10^{23}	1.5×10^{-24}	1.5×10^{-20}

$$+ \frac{12}{35} \frac{e^2 Z_x Z_f}{R^3} \sum_{i=x,f} [R_{0i} \beta_i Y_{20}(\theta_i)]^2.$$

In terms of the measured half-lives $T_{1/2}$ and calculated penetrabilities P, the probabilities S of the formation of various clusters (spectroscopic factors) are expressed as

$$S = \frac{\pi \ln 2}{\omega_0 T_{1/2} P}. \quad (4)$$

Numerical results are given in the next section.

3. RESULTS OF THE CALCULATIONS

Figure 1 shows the nucleus–nucleus potential for the DNS ^{28}Mg + ^{206}Hg at two different values of nuclear deformation. The inclusion of quadrupole deformation changes the position and height of the barrier, as well as the depth of the local potential minimum corresponding to the DNS at the contact point; i.e., R_0 and the area under the curve $U(R) - Q$ change. As a result, penetrability P increases for $\beta_x > 0$ and decreases for $\beta_x < 0$ by one to eight orders of magnitude as compared to the values calculated

for spherical nuclei (Tables 1 and 2). Penetrability for identical clusters emitted from neighboring nuclei always increases with charge asymmetry.

If an additional degree of freedom—the angle θ_i between the emission direction of one of the nuclei ($i = x, f$) and the axial symmetry axis—is introduced, the nucleus–nucleus potential is a function of this collective variable. A change in the nucleus–nucleus potential leads to changes in the barrier penetrability P and the potential energy $U_c = B_x + B_f + U$ (B_x and B_f are the binding energies of the nuclei) of the contact configuration. As θ_i for deformed nuclei increases, P decreases and U_c increases. These dependences become sharper for large deformations and large products $Z_x Z_f$. As an example, P and U for the DNS ^{208}Pb + ^{30}Mg are shown in Fig. 2 as functions of θ_x. By definition, the state with minimum potential energy is most probable for the contact system (it has the largest spectroscopic factor). In this case, it corresponds to the cluster configuration with $\theta_i = 0$. The S value for $\theta_i = \pi/6$ is approximately 1/30 of the value for $\theta_i = 0$. The barrier penetrability is maximal for $\theta_i = 0$. Therefore, the probability SP of cluster decay is also maximal, and the main contribution to averaging of SP over θ_i comes from the vicinity of $\theta_i \approx 0$.

Analysis of the decays of odd nuclei requires the inclusion of DNS states with nonzero orbital angular momenta L. These states are effectively taken into account by the centrifugal potential U_L in nucleus–nucleus potential (3). Possible L values are determined by the conservation laws for parity and angular momentum. In particular, for the decay ^{235}U($7/2^-$) $\rightarrow$ ^{26}Ne(0^+) + ^{209}Pb($9/2^+$), L can be equal to 1, 3, 5, and 7. Figure 3 shows the dependences of the barrier penetrability on the possible orbital angular momenta for the decays ^{235}U $\rightarrow$ ^{26}Ne, ^{223}Ra $\rightarrow$ ^{14}C, and ^{229}Th $\rightarrow$ ^{21}O at $\theta = 0$ in comparison with P at $L = 0$. It is seen that, as the orbital angular momentum increases, the penetrability decreases slightly due to an increase in the moment of inertia of the system. In the decay considered above, L does not exceed 10. All calculations are performed with the inclusion of the angular momentum.

Tables 1 and 2 present spectroscopic factors S calculated by Eq. (4) using experimental data with, respectively, the inclusion and exclusion of the static quadrupole deformation of the light cluster and residual nucleus. The deformation parameters of the nuclei in the ground state are taken from experimental systematics [15], where only the absolute values of the quadrupole deformation parameters were presented. It is remarkable that, as the deformation of the light cluster is varied, S for a given channel changes strongly by more than one order of magnitude for ^{14}C
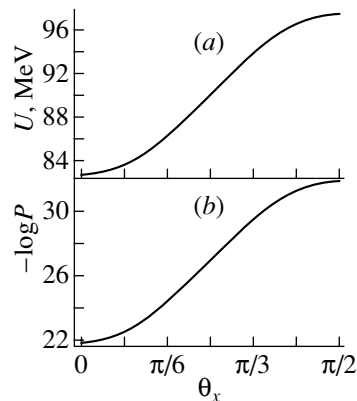
Fig. 2. (a) Contact-configuration potential U and (b) the sign-reversed logarithm of the barrier penetrability P for the dinuclear system ^{208}Pb + ^{30}Mg vs. the angle θ_x of the deviation of the light-nucleus axis of symmetry from the axis passing through the centers of masses of the nuclei.

and by seven and eight orders of magnitude for ^{24}Ne and ^{28}Mg, respectively.

According to Tables 1 and 2, the S value for ^{28}Mg is 17 orders of magnitude smaller than the value for ^{14}C. The spectroscopic factors for carbon radioactivity of the even–even isotopes ^{222,224,226}Ra as calculated including deformation are close to the respective values calculated disregarding deformation. The S value in the odd isotope ^{223}Ra is two orders of magnitude smaller than the values for the neighboring even–even isotopes. This relation indicates that structure effects are noticeable for a nuclear decay mechanism and expresses the known suppression of the emission of an even particle from an odd nucleus as compared to the neighboring even–even nuclei. This suppression explains strong deviation of the widths measured for the decays ^{221}Ra $\rightarrow$ ^{14}C + ^{207}Pb and ^{235}U $\rightarrow$ ^{24,25,26}Ne + ^{209,210,211}Pb from known dependences.

The spectroscopic factors presented in Table 1 (except for S for the decay ^{234}U $\rightarrow$ ^{28}Mg + ^{206}Hg) are one to four orders of magnitude smaller than the values for the phenomenological potential described in [16]. Our S values for ^{14}C are two orders of magnitude larger than the shell-model results [1], and our S values for ^{24}Ne, ^{28}Mg, and ^{30}Mg are two, five, and one order of magnitude lower, respectively, than the corresponding shell-model results [1]. The spectroscopic factors obtained for ^{24}Ne and ^{28}Mg in [5] are three and four orders of magnitude larger than the respective spectroscopic factors in Table 1. The spectroscopic factors obtained for ^{14}C in [5] agree well with our calculations.

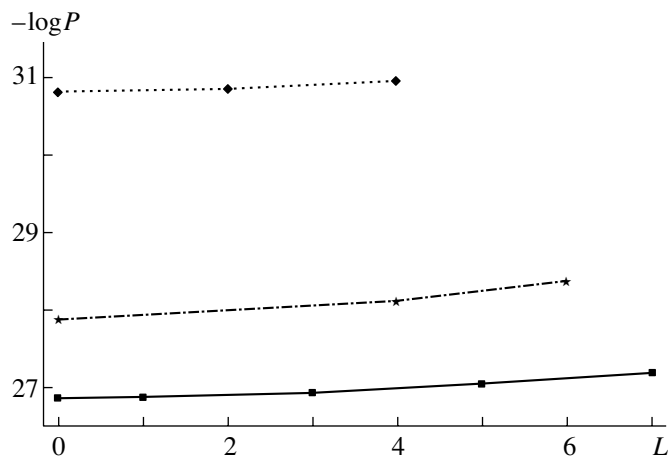Figures 4 and 5 show the spectroscopic factor S extracted from experimental data as a function of

Fig. 3. Plot of $-\log P$ vs. L for the decays ($\blacksquare$) ^{235}U $\to$ ^{26}Ne, ($\star$) ^{223}Ra $\to$ ^{14}C, and ($\blacklozenge$) ^{229}Th $\to$ ^{21}O.
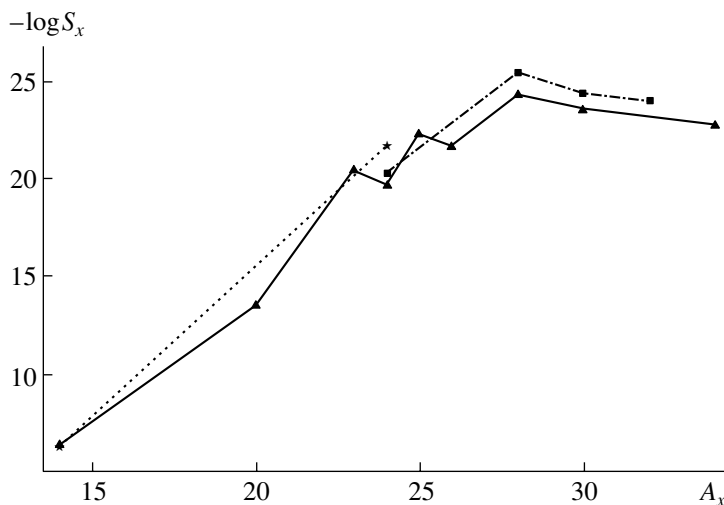

Fig. 4. Plot of $-\log S_x$, where S_x is the spectroscopic factor calculated using the measured half-life, vs. the mass A_x of the light cluster. Quadrupole deformations of clusters and the residual nuclei ($\blacktriangle$) ^{208}Pb, ($\blacksquare$) ^{206}Hg, and ($\star$) ^{207}Tl were taken into account in the calculations. The same symbols are connected by straight segments for clearness.

the cluster mass number A_x. Points connected by line segments correspond to decays with the same heavy daughter nuclei indicated in the figures. It is seen that the spectroscopic factor decreases exponentially on average as the cluster mass increases. When deformation is taken into account, decays accompanied by the emission of ^{32,34}Si and the decay ^{236}U $\to$ ^{206}Hg $+$ ^{30}Mg do not exhibit this dependence. This tendency is likely associated with the fact that these cluster configurations are beyond the Businaro–Gallone critical mass asymmetry ($Z_x \approx 8-12$), after which the potential of the DNS decreases with decreasing mass asymmetry, and the simple two-stage representation of cluster decay becomes doubtful. Moreover, new experimental data are

necessary in order to corroborate the half-life that has been already obtained [17].

Figure 6 shows the half-life as a function of barrier penetrability for "carbon," "neon," and "magnesium" radioactivity. Points for each type of radioactivity are located along the lines with approximately the same slope. This property in principle follows from Eq. (1) if the S values for the identical clusters are approximately equal to each other. This tendency is characteristic of α decay. Analysis of the resulting S values (Tables 1 and 2) shows that the spectroscopic factors for the identical clusters emitted from neighboring even–even nuclei coincide with each other within one order of magnitude. This conclusion is corroborated by microscopic calculations [1]. This fact makes it possible to predict $T_{1/2}$ values for certain decays
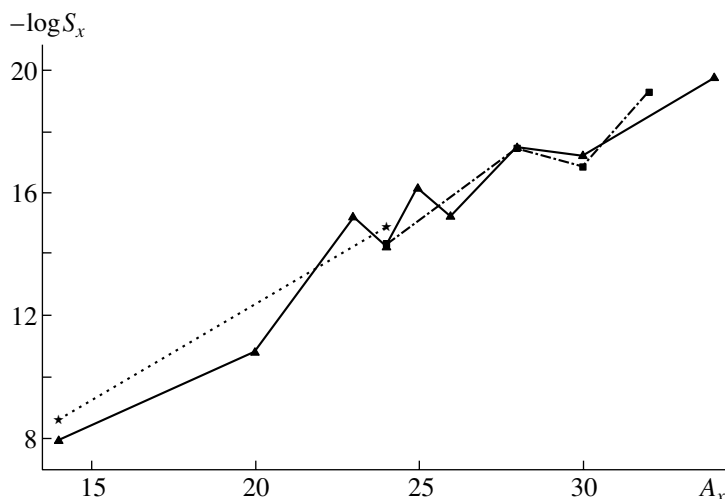
Fig. 5. The same as in Fig. 4, but for spherical residual nuclei and clusters.

(Tables 3 and 4). We use the following decays as the reference decays: $^{222}\text{Ra} \to ^{14}\text{C} + ^{208}\text{Pb}$, $^{228}\text{Th} \to ^{20}\text{O} + ^{208}\text{Pb}$, $^{232}\text{U} \to ^{24}\text{Ne} + ^{208}\text{Pb}$, $^{234}\text{U} \to ^{28}\text{Mg} + ^{206}\text{Hg}$, and $^{238}\text{Pu} \to ^{28}\text{Mg} + ^{210}\text{Pb}$. The reliability of our semiempirical predictions for even–even actinides is entirely determined by the accuracy of the measured widths of decays for neighboring reference nuclei. The S value for the decay $^{232}\text{Pa} \to ^{25}\text{Ne} + ^{207}\text{Tl}$ is calculated as the product of the spectroscopic factor of the decay $^{232}\text{U} \to ^{24}\text{Ne} + ^{208}\text{Pb}$ and the structure suppression factor $F = 10^{-1}$ for the easy cluster transition [1]. Predictions obtained for $T_{1/2}$ including (Table 3) and disregarding (Table 4) nuclear deformation differ only slightly for the same decays.

The spectroscopic factors S (Table 5) for decays in the "tin-radioactivity" region are simply obtained as the products of our spectroscopic factors for the indicated reference "lead-radioactive" nuclei and the ratios of the spectroscopic factors for the tin and lead regions as calculated in the microscopic theory [1]. The results give hope to detecting new decays with the yield of various clusters: $^{112,114,116}\text{Ba} \to ^{12}\text{C} + ^{100,102,104}\text{Sn}$, $^{118}\text{Ce} \to ^{12}\text{C} + ^{106}\text{Te}$, $^{118}\text{Ce} \to ^{16}\text{O} + ^{102}\text{Sn}$, $^{124}\text{Sm} \to ^{20}\text{Ne} + ^{104}\text{Te}$, and $^{124}\text{Sm} \to ^{24}\text{Mg} + ^{100}\text{Sn}$. For this region of nuclei, only the upper limit $T_{1/2} > 1.2 \times 10^4$ s is experimentally obtained for the decay $^{114}\text{Ba} \to ^{12}\text{C} + ^{102}\text{Sn}$ [20]. Comparison shows that our predictions (Tables 3 and 5) strongly differ from those made in [1, 2] in the tin radioactivity region. The difference arises due primarily to the difference in the barrier penetrabilities. Our predictions of $T_{1/2}$ (Table 5) for decays with the emission of the ^{12}C, ^{16}O, and ^{20}Ne nuclei from the tin radioactivity region nearly coincide with those made in [5].

In [21, 22], the possibility of fission through a quasimolecular configuration, i.e., through the mass asymmetry coordinate, was discussed. A fissioning nucleus sequentially passes through a number of stages corresponding to different DNSs. Let the spontaneous fission (s.f.) also occur through the cluster mechanism; i.e., fluctuations of the nuclear shape in the collective coordinate of mass asymmetry give rise to the formation of the initial DNS with which the system begins to evolve in the energetically allowed region of the potential surface. Thus, the transition from cluster decay to spontaneous fission occurs when the Q value for the initial DNS is equal to the potential energy $U(R_0)$ at the contact point of the nuclei. Since the system inevitably decays ($P_{\text{s.f.}} = 1$) in the process of evolution in the energetically allowed region (Q becomes much higher than the deformed Coulomb barrier $U(R_b \approx R_0 + 1 \text{ fm})$)
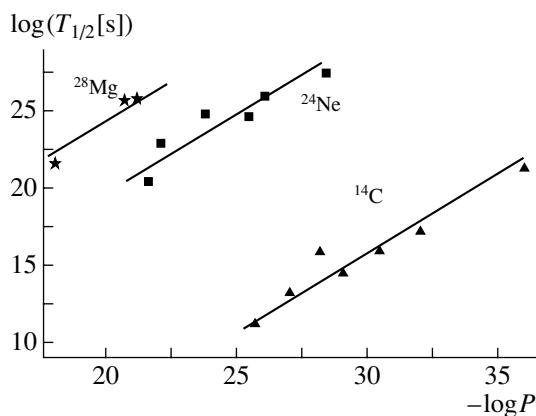

Fig. 6. Logarithm of the measured half-life $T_{1/2}$ vs. $-\log P$, where P is the calculated barrier penetrability for the light clusters (▲) ^{14}C, (■) ^{24}Ne, and (⋆) ^{28}Mg.

Table 3. Estimates of $T_{1/2}$ for certain possible decays [here, S is the spectroscopic factor taken from the same decay of the nearest reference even nucleus (see Table 1 and the main text), P is the penetrability of the nucleus−nucleus potential calculated for a given dinuclear system, and the parameters of the clusters and residual nuclei are the same as in Table 1]

$A \rightarrow A_x + A_f$	Q, MeV	S	P	$T_{1/2}$, s
^{224}Th $\rightarrow$ ^{14}C + ^{210}Po	32.9	3.8×10^{-7}	5.1×10^{-29}	2.8×10^{14}
^{226}Th $\rightarrow$ ^{14}C + ^{212}Po	30.5	3.8×10^{-7}	1.5×10^{-33}	9.5×10^{18}
^{229}Th $\rightarrow$ ^{21}O + ^{208}Pb	43.18	2.9×10^{-15}	1.3×10^{-31}	1.4×10^{22}
^{232}Pa $\rightarrow$ ^{25}Ne + ^{207}Tl	58.95	2.1×10^{-21}	1.1×10^{-23}	2.4×10^{20}
^{230}U $\rightarrow$ ^{24}Ne + ^{206}Pb	61.40	2.1×10^{-20}	3.7×10^{-23}	7.2×10^{21}
^{236}U $\rightarrow$ ^{24}Ne + ^{212}Pb	59.9	2.1×10^{-20}	4.2×10^{-25}	6.9×10^{23}
^{234}Pu $\rightarrow$ ^{24}Ne + ^{210}Po	62.3	2.1×10^{-20}	1.1×10^{-24}	2.5×10^{23}
^{234}Pu $\rightarrow$ ^{28}Mg + ^{206}Pb	79.2	1.3×10^{-26}	2.3×10^{-18}	1.9×10^{23}
^{237}Pu $\rightarrow$ ^{29}Mg + ^{208}Pb	77.51	1.3×10^{-27}	5.7×10^{-21}	7.5×10^{26}

Table 4. Estimates of $T_{1/2}$ for certain possible decays under the assumption that the clusters and residual nuclei are spherical [here, S is the spectroscopic factor taken from the same decay of the nearest reference even nucleus (see Table 1 and the main text), P is the penetrability of the nucleus−nucleus potential calculated for a given dinuclear system, and the parameters of the clusters and residual nuclei are the same as in Table 1; the data from Table 2 are used]

$A \rightarrow A_x + A_f$	Q, MeV	S	P	$T_{1/2}$, s
^{224}Th $\rightarrow$ ^{14}C + ^{210}Po	32.9	1.1×10^{-8}	5.7×10^{-27}	9.6×10^{13}
^{226}Th $\rightarrow$ ^{14}C + ^{212}Po	30.5	1.1×10^{-8}	1.6×10^{-31}	3.4×10^{18}
^{230}U $\rightarrow$ ^{24}Ne + ^{206}Pb	61.4	6.3×10^{-15}	2.6×10^{-29}	3.5×10^{22}
^{236}U $\rightarrow$ ^{24}Ne + ^{212}Pb	59.9	6.3×10^{-15}	6.2×10^{-31}	1.5×10^{24}
^{234}Pu $\rightarrow$ ^{24}Ne + ^{210}Po	62.3	6.3×10^{-15}	3.0×10^{-30}	3.1×10^{24}
^{234}Pu $\rightarrow$ ^{28}Mg + ^{206}Pb	79.2	6.9×10^{-18}	1.9×10^{-26}	4.3×10^{22}

and the measured half-lives $T_{1/2}^{\text{s.f.}}$ of actinides in spontaneous fission are known, the spectroscopic factors $S_{\text{s.f.}}$ of the initial DNS can be estimated by Eq. (4) as

$$S_{\text{s.f.}} = \frac{\pi \ln 2}{\omega_0 T_{1/2}^{\text{s.f.}}}. \qquad (5)$$

Then, $T_{1/2}^{\text{s.f.}}/T_{1/2}(A_x) = S(A_x)P(A_x)/S_{\text{s.f.}}$. Correspondingly, $T_{1/2}^{\text{s.f.}} \leq T_{1/2}(A_x)$ if $S_{\text{s.f.}} \geq S(A_x)P(A_x)$. As is known from experiments, spontaneous fission competes with cluster decay for nuclei heavier than ^{232}U. Table 6 presents the weights of the initial DNS in the wave functions of the ground state of actinides. As is seen, $S_{\text{s.f.}}$ increases with increasing charge number Z of the fissioning nucleus. This dependence is likely due to the fact that the absolute value of the potential energy of the DNS at the Businaro−Gallone point decreases with respect to the

mononucleus as Z increases. Comparison of $S_{\text{s.f.}}$ and $S(A_x)$ provides the assumption that the initial DNS is an asymmetric DNS, where the light nucleus is from the nuclear region Ca−Fe. The upper limit of this region is determined by the fact that the light nuclei ^{66}Cr, ^{66}Mn, and ^{66}Fe are observed in experiments on spontaneous fission [23]. However, the observation of light clusters is limited because their yields are low due to the low penetrabilities of the nucleus− nucleus potential barrier. With further improvement of experimental technique, the observation of such rare events will apparently become possible.

4. CONCLUSIONS

The above mechanism of cluster decay is associated with dynamic oscillations of the decaying nucleus in the mass-asymmetry coordinate. The processes of the formation of a particular DNS and its

Table 5. Estimates of the half-lives $T_{1/2}$ for tin radioactivity* (the following reference decays are used: $^{222}\text{Ra} \to {}^{14}\text{C} + {}^{208}\text{Pb}$, $^{228}\text{Th} \to {}^{20}\text{O} + {}^{208}\text{Pb}$, $^{230}\text{Th} \to {}^{24}\text{Ne} + {}^{206}\text{Hg}$, and $^{234}\text{U} \to {}^{28}\text{Mg} + {}^{206}\text{Hg}$; $\tilde{T}_{1/2}$ values are the half-lives obtained with the spectroscopic factors taken from [1]; β_x, β_f, and Q are taken from [18, 19]; and the calculations are performed with the parameters $a_{0x} = a_{0f} = 0.52$ fm, $r_{0x} = 1.15$ fm, and $r_{0f} = 1.16$ fm)

$A \to A_x + A_f$	β_x	β_f	Q, MeV	S	P	$T_{1/2}$, s	$\tilde{T}_{1/2}$, s
$^{112}\text{Ba} \to {}^{12}\text{C} + {}^{100}\text{Sn}$	0.00	0.00	22.09	2.4×10^{-6}	3.3×10^{-19}	7.2×10^{3}	5.9×10^{5}
$^{112}\text{Ba} \to {}^{12}\text{C} + {}^{100}\text{Sn}$	0.00	0.00	21.46	2.4×10^{-6}	2.0×10^{-20}	1.2×10^{5}	9.8×10^{6}
$^{114}\text{Ba} \to {}^{12}\text{C} + {}^{102}\text{Sn}$	0.00	0.00	19.00	2.4×10^{-6}	1.3×10^{-25}	1.8×10^{10}	1.5×10^{12}
$^{116}\text{Ba} \to {}^{12}\text{C} + {}^{104}\text{Sn}$	0.00	0.02	17.30	2.4×10^{-6}	1.3×10^{-29}	1.8×10^{14}	1.5×10^{16}
$^{118}\text{Ba} \to {}^{12}\text{C} + {}^{106}\text{Sn}$	0.00	0.03	15.48	2.4×10^{-6}	6.7×10^{-35}	3.5×10^{19}	2.5×10^{21}
$^{118}\text{Ce} \to {}^{12}\text{C} + {}^{106}\text{Te}$	0.00	0.12	18.00	2.4×10^{-6}	3.6×10^{-29}	6.6×10^{13}	5.4×10^{15}
$^{124}\text{Sm} \to {}^{12}\text{C} + {}^{112}\text{Ba}$	0.00	0.21	15.95	2.4×10^{-6}	2.2×10^{-39}	1.1×10^{24}	9.0×10^{25}
$^{126}\text{Sm} \to {}^{12}\text{C} + {}^{114}\text{Ba}$	0.00	0.24	16.01	2.4×10^{-6}	9.3×10^{-39}	2.5×10^{23}	2.1×10^{25}
$^{114}\text{Ba} \to {}^{16}\text{O} + {}^{98}\text{Cd}$	0.01	0.01	26.46	3.9×10^{-10}	1.5×10^{-27}	9.6×10^{15}	1.2×10^{16}
$^{116}\text{Ba} \to {}^{16}\text{O} + {}^{100}\text{Cd}$	0.01	0.02	24.11	3.9×10^{-10}	1.9×10^{-32}	7.7×10^{20}	9.6×10^{20}
$^{118}\text{Ce} \to {}^{16}\text{O} + {}^{102}\text{Sn}$	0.01	0.00	29.44	3.9×10^{-10}	1.6×10^{-24}	8.8×10^{12}	1.1×10^{13}
$^{122}\text{Nd} \to {}^{16}\text{O} + {}^{106}\text{Te}$	0.01	0.12	27.54	3.9×10^{-10}	3.2×10^{-29}	4.5×10^{17}	5.6×10^{17}
$^{124}\text{Sm} \to {}^{16}\text{O} + {}^{108}\text{Xe}$	0.01	0.15	27.44	3.9×10^{-10}	9.1×10^{-32}	1.5×10^{20}	2.0×10^{20}
$^{126}\text{Sm} \to {}^{16}\text{O} + {}^{110}\text{Xe}$	0.01	0.17	26.75	3.9×10^{-10}	6.7×10^{-33}	2.1×10^{21}	2.7×10^{21}
$^{118}\text{Ce} \to {}^{20}\text{Ne} + {}^{98}\text{Cd}$	0.36	0.01	34.54	4.1×10^{-14}	5.8×10^{-26}	2.4×10^{19}	2.0×10^{17}
$^{122}\text{Nd} \to {}^{20}\text{Ne} + {}^{102}\text{Sn}$	0.36	0.00	36.54	4.1×10^{-14}	1.8×10^{-26}	7.7×10^{18}	6.4×10^{16}
$^{124}\text{Sm} \to {}^{20}\text{Ne} + {}^{104}\text{Te}$	0.36	0.05	38.65	4.1×10^{-14}	3.7×10^{-25}	3.7×10^{17}	3.1×10^{15}
$^{126}\text{Sm} \to {}^{20}\text{Ne} + {}^{106}\text{Te}$	0.36	0.12	35.35	4.1×10^{-14}	7.0×10^{-30}	2.0×10^{22}	1.6×10^{20}
$^{122}\text{Nd} \to {}^{24}\text{Mg} + {}^{98}\text{Cd}$	0.41	0.01	46.23	3.0×10^{-19}	1.1×10^{-22}	1.6×10^{20}	3.8×10^{15}
$^{124}\text{Sm} \to {}^{24}\text{Mg} + {}^{100}\text{Sn}$	0.41	0.00	51.97	3.0×10^{-19}	3.4×10^{-18}	5.6×10^{15}	1.3×10^{11}
$^{126}\text{Sm} \to {}^{24}\text{Mg} + {}^{102}\text{Sn}$	0.41	0.00	48.94	3.0×10^{-19}	5.5×10^{-22}	3.4×10^{19}	7.8×10^{14}

* The calculation of S is explained in the main text.

Table 6. Weights of the initial dinuclear systems in the wave function of the ground state of actinides

^{A}Z	$S_{\text{s.f.}}$	^{A}Z	$S_{\text{s.f.}}$	^{A}Z	$S_{\text{s.f.}}$
^{232}U	4.8×10^{-43}	^{234}U	2.4×10^{-45}	^{236}U	1.5×10^{-45}
^{236}Pu	7.6×10^{-39}	^{238}Pu	9.5×10^{-40}	^{240}Pu	2.4×10^{-40}
^{242}Pu	5.6×10^{-40}	^{244}Pu	5.8×10^{-40}	^{246}Cm	2.1×10^{-36}

decay are considered separately. The inclusion of the positive static quadrupole nuclear deformation noticeably reduces the nucleus–nucleus potential and, correspondingly, increases the barrier penetrability by one to eight orders of magnitude. For spherical nuclei, the spectroscopic factor S decreases exponentially as A_x increases. When nuclear deformations are taken into account, the spectroscopic factors S for $A_x > 28$ differ from each other much less than the spectroscopic factors for lighter clusters, and the exponential decrease in S is violated. Final conclusions require new experiments on the detection of Si nuclei.

The half-lives $T_{1/2}$ predicted with allowance for the deformations of the light cluster and residual nucleus are nearly identical to those for spherical nuclei. The half-lives have been predicted for various clusters in the tin- and lead-radioactivity regions. The connection between spontaneous fission and cluster radioactivity in this model is discussed. The weights of the initial DNS in the wave function of the ground states of certain actinides have been estimated.

ACKNOWLEDGMENTS

REFERENCES

1. Yu. M. Tchuvil'sky, *Cluster Radioactivity* (Mosk. Gos. Univ., Moscow, 1997) [in Russian].
2. Yu. S. Zamyatin *et al.*, Fiz. Élem. Chastits At. Yadra **21**, 537 (1990) [Sov. J. Part. Nucl. **21**, 231 (1990)].
3. S. P. Tretyakova and A. A. Ogloblin, in *Proceedings of the International Symposium on Nuclei Clusters*, Ed. by R. Jolos and W. Scheid (EP Systema, Debrecen, 2003), p. 207.
4. G. A. Pik-Pichak, Yad. Fiz. **44**, 1421 (1986) [Sov. J. Nucl. Phys. **44**, 923 (1986)].
5. D. U. Poenaru *et al.*, At. Data Nucl. Data Tables **34**, 423 (1986).
6. R. K. Gupta, S. Singh, and R. K. Puri, J. Phys. G **18**, 1533 (1992).
7. D. N. Basu, Phys. Rev. C **66**, 027601 (2003).
8. S. G. Kadmenskiĭ *et al.*, Izv. Akad. Nauk SSSR, Ser. Fiz. **50**, 1786 (1986); **57** (1), 12 (1993).
9. R. Blendowske, T. Fliessbach, and H. Walliser, Nucl. Phys. A **464**, 75 (1987).
10. T. M. Shneidman *et al.*, Phys. Lett. B **526**, 322 (2002); Phys. Rev. C **67**, 014313 (2003).
11. V. V. Volkov, *Deep Inelastic Nuclear Reactions* (Énergoizdat, Moscow, 1982) [in Russian].
12. G. G. Adamian *et al.*, Int. J. Mod. Phys. E **5**, 191 (1996).
13. A. B. Migdal, *Theory of Finite Fermi Systems and Applications to Atomic Nuclei* (Nauka, Moscow, 1982; Interscience, New York, 1967).
14. C. Y. Wong, Phys. Rev. Lett. **31**, 766 (1973).
15. S. Raman *et al.*, At. Data Nucl. Data Tables **78**, 1 (2001).
16. P. R. Christensen and A. Winter, Phys. Lett. B **61B**, 19 (1976).
17. A. A. Ogloblin *et al.*, Phys. Rev. C **61**, 034301 (2000).
18. P. Moeller and J. J. Nix, At. Data Nucl. Data Tables **39**, 213 (1988); Preprint LA-UR-86-3983, LANL (Los Alamos National Library, Los Alamos, 1986).
19. J. K. Tuli, *Nuclear Wallet Cards* (BNL, New York, 2000).
20. A. Guglielmetti *et al.*, Phys. Rev. C **56**, R2912 (1997).
21. V. A. Shigin, Yad. Fiz. **3**, 756 (1966) [Phys. At. Nucl. **3**, 555 (1966)]; **14**, 695 (1971) [**14**, 391 (1971)].
22. V. V. Volkov, Yad. Fiz. **62**, 1159 (1999) [Phys. At. Nucl. **62**, 1086 (1999)].
23. D. U. Poenaru, *Nuclear Decay Modes* (IOP Publ., Bristol, 1996).

Translated by R. Tyapaev

NUCLEI
Theory

Dibaryon Model for Nuclear Force and the Properties of the 3N System[*]

V. N. Pomerantsev, V. I. Kukulin[**], V. T. Voronchev, and A. Faessler[1)]

Institute of Nuclear Physics, Moscow State University, Moscow, Russia

Received March 21, 2005

Abstract—The dibaryon model for NN interaction, which implies the formation of an intermediate six-quark bag dressed by a σ field, is applied to the $3N$ system, where it results in a new three-body force of scalar nature between the six-quark bag and a third nucleon. A new multicomponent formalism is developed to describe three-body systems with nonstatic pairwise interactions and nonnucleonic degrees of freedom. Precise variational calculations of $3N$ bound states are carried out in the dressed-bag model including the new scalar three-body force. The unified coupling constants and form factors for $2N$- and $3N$-force operators are used in the present approach, in sharp contrast to conventional meson-exchange models. It is shown that this three-body force gives at least half the $3N$ total binding energy, while the weight of nonnucleonic components in the ³H and ³He wave functions can exceed 10%. The new force model provides a very good description of $3N$ bound states with a reasonable magnitude of the σNN coupling constant. A new Coulomb $3N$ force between the third nucleon and dibaryon is found to be very important for a correct description of the Coulomb energy and rms charge radius in ³He. In view of the new results for Coulomb displacement energy obtained here for $A = 3$ nuclei, an explanation for the long-term Nolen−Schiffer paradox in nuclear physics is suggested. The role of the charge-symmetry-breaking effects in the nuclear force is discussed. © *2005 Pleiades Publishing, Inc.*

1. INTRODUCTION: CURRENT PROBLEMS IN A CONSISTENT DESCRIPTION OF 2N AND 3N SYSTEMS WITH TRADITIONAL FORCE MODELS

A few historical remarks should be made first. The current rather high activity in few-body physics started at the beginning of the 1960s, after mathematical formulation of the Faddeev equations for the three-body problem. The aim was claimed to establish unambiguously off-shell properties of the two-body t matrix, which cannot be derived from two-body scattering data only. It was hoped during that time that just accurately solving the $3N$ scattering problem would enable one to establish strong constraints for the off-shell properties of the two-nucleon t matrix. However, more than forty years has passed since then, but we are still unable to formulate such a two-nucleon t matrix that can explain fully quantitatively the properties of even $3N$ systems.

Moreover, since that time, many puzzles in few-nucleon scattering experiments have been revealed which could not be explained by the current force models based on the Yukawa concept. Among all such puzzles, we mention here only the most remarkable ones, such as the A_y puzzle in $\vec{N} + d$ and $\vec{N} + {}^3$He scattering [1, 2] and disagreements on the minima of differential cross sections (Sagara puzzle) at $E \sim 150−200$ MeV and polarization data for $N + \vec{d}$ [3], $\vec{N} + d$, $\vec{N} + \vec{d}$ [4], and $\vec{N} + {}^3$He scattering. The strongest discrepancy between current theories and respective experiments has been found in studies of the short-range NN correlations in the ³He$(e, e'pp)$ [5], ⁴He(γ, pp) [6], and ³He$(e, e'NN)$ [7] processes. In addition to these particular problems, there are more fundamental problems in the current theory of nuclear forces, e.g., strong discrepancies between the πNN, $\pi N\Delta$, and ρNN form factors used both in one-boson-exchange (OBE) models for the description of elastic and inelastic scattering and in the consistent parametrization of $2N$ and $3N$ forces [8−11]. Many of these difficulties are attributed to a rather poor knowledge of the short-range behavior of nuclear forces. This behavior was traditionally associated with vector ω-meson exchange. However, the characteristic range of this ω exchange (for $m_\omega \simeq 780$ MeV) is equal to about $\lambda_\omega \simeq 0.2−0.3$ fm; i.e., it is deeply inside the internucleon overlap region.

In fact, since Yukawa, the NN interaction is explained by a t-channel exchange of mesons between

---

[*]This article was submitted by the authors in English.

[1)]Institute for Theoretical Physics, University of Tübingen, Germany.

[**]e-mail: kukulin@nucl-th.sinp.msu.ru

two nucleons. The very successful Bonn, Nijmegen, Argonne, and other modern NN potentials prove the success of this approach. But the short- and intermediate-range region in these potentials is more parametrized than parameter-free microscopically described.

Besides the evident difficulties with the description for short-range nuclear force, there are also quite serious problems with a consistent description of basic intermediate-range attraction between nucleons. In the traditional OBE models, this attraction is described as a t-channel σ exchange with artificially enhanced σNN vertices. However, accurate modern calculations of the intermediate-range NN interaction [12, 13] within the 2π-exchange model with $\pi\pi$ s-wave interaction have revealed that this t-channel mechanism cannot give a strong intermediate-range attraction in the NN sector, which is necessary for binding of a deuteron and fitting the NN phase shifts. This conclusion has also been corroborated by recent independent calculations [14]. Thus, the t-channel mechanism of the σ-meson exchange should be replaced by some other alternative mechanism that should result in the strong intermediate-range attraction required by even the existence of nuclei.

When analyzing the deep reasons for all these failures, we must look at a most general element which is common for all the numerous NN-force models tested in few-nucleon calculations for the last 40 years. This common element is just the Yukawa concept for the strong interaction of nucleons in nuclei. Hence, if, after more than 40 years of development, we are still unable to explain quantitatively and consistently even the basic properties of $3N$ and $4N$ systems at low energies and relatively simple processes like $pp \to pp\gamma$, this concept, which is a cornerstone of all building of nuclear physics, should be analyzed critically, especially in the regions where applicability of this concept looks rather questionable.

Since the quark picture and QCD have been developed, the "nucleon–nucleon force community" is more and more convinced that, at short ranges, the quark degrees of freedom must play an important role. One of the possible mechanisms for short-range NN interaction is the formation of the six-quark ($6q$) bag (dibaryon) in the s channel. Qualitatively, many would agree with this statement. But to obtain a quantitative description of the nucleon–nucleon and the few-nucleon experimental data with this approach with the same quality as the commonly used Bonn, Nijmegen, Argonne, and other equivalent potentials is a quite different problem.

Within the $6q$ dynamics, it has long been known [15–19] that the mixing of the completely symmetric $s^6[6]$ component with the mixed-symmetry $s^4p^2[42]$ component can determine the structure of

the whole short-range interaction (in the S wave).[2] Assuming a reasonable qq-interaction model, many authors (see, e.g., [20–23]) have suggested that this mixture will result in both strong short-range repulsion (associated mainly with the s^6 component) and intermediate-range attraction (associated mainly with the above mixed-symmetry s^4p^2 component). However, recent studies [22, 23] for NN scattering on the basis of the newly developed Goldstone boson exchange qq interaction have resulted in purely repulsive NN contributions from both $s^6[6]$ and $s^4p^2[42]$ $6q$ components. There is no need to say that any quark-motivated model for the NN force with π exchange between quarks inevitably leads to the well-established Yukawa π-exchange interaction between nucleons at long distances.

Trying to solve the above problems (and to understand more deeply the mechanism for the intermediate- and short-range NN interaction), the Moscow–Tübingen group suggested replacing the conventional Yukawa meson-exchange (t-channel) mechanism (at intermediate and short ranges) with the contribution of an s-channel mechanism describing the formation of a dressed $6q$ bag in the intermediate state such as $|s^6 + \sigma\rangle$ or $|s^6 + 2\pi\rangle$ [8, 24]. It has been shown that, due to the change in the symmetry of the $6q$ state in the transition from the NN channel to the intermediate dressed-bag state, a strong scalar σ field arises around the symmetric $6q$ bag. This intensive σ field squeezes the bag and increases its density [25]. The high quark density in the symmetric $6q$ bag enhances the meson field fluctuations around the bag and thereby partially restores the chiral symmetry [26]. Therefore, the masses of constituent quarks and σ mesons decrease [8]. As a result of this phase transition, the dressed-bag mass decreases considerably (i.e., a large gain in energy arises), which manifests itself as a strong effective attraction in the NN channel at intermediate distances. The contribution of the s-channel mechanism would generally be much larger due to resonance-like enhancement.[3]

In our previous works [8, 24], on the basis of the above arguments, we proposed a new dibaryon model for the NN interaction [referred to further as the "dressed-bag model" (DBM)], which provided a quite good description of both NN phase shifts up

---

[2] We will denote the NN partial waves by capital letters ($S, P, \dots$), while the partial waves in all other cases will be denoted by lower-case letters.

[3] In the theory of nuclear reactions, the t-channel mechanism can be associated with the direct nuclear reaction, where only a few degrees of freedom are important, while the s-channel mechanism can be associated with resonance-like (or compound-nucleus-like) nuclear reactions with much larger cross sections at low energies.

to 1 GeV and the deuteron structure. The developed model includes the conventional t-channel contributions (Yukawa π and 2π exchanges) at long and intermediate distances and the s-channel contributions due to the formation of intermediate dressed-bag states at short distances. The most important distinction of such an approach from conventional models for nuclear forces is the explicit appearance of a nonnucleonic component in the total wave function of the system, which necessarily implies the presence of new three-body forces (3BF) of several kinds in the $3N$ system. These new 3BF differ from conventionally used models for three-body forces. One important aspect of the novel 3BF should be emphasized here. In conventional OBE models, the main contribution to NN attraction is due to the t-channel σ exchange. However, the 3BF models suggested until now (such as Urbana−Illinois or Tucson−Melbourne) are mainly based on the 2π exchange with intermediate Δ-isobar production, and the σ exchange either is not taken into account at all or is of little importance in these models. In contrast, the σ exchange in our approach dominates in both $2N$ and $3N$ forces. In fact, in our approach, just the unified strong σ field couples both two- and three (and more)-nucleon systems; i.e., the general pattern of the nuclear interaction appears to be more consistent.

Our recent considerations have revealed that this dibaryon mode is extremely useful in the explanation of very numerous facts and experimental results in nuclear physics, in general. We note here only a few of them.

(1) The presence of a dibaryon degree of freedom (DDF) can result in a very natural explanation of cumulative effects (e.g., the production of cumulative particles in high-energy collisions [27]).

(2) DDF leads to automatic enhancement of near-threshold cross sections for one- and two-meson production in pp, pd, etc., collisions, which is required by many modern experiments (e.g., the so-called ABC puzzle [28]). This is due to an effective enhancement of meson−dibaryon coupling as compared to meson−nucleon coupling.

(3) The incorporation of DDF makes it possible (without the artificial enhancement of meson−nucleon form factors) to share the large momentum of an incident probe (e.g., high-energy photon) among other nucleons in the target nucleus.

(4) The DDF produces in a very natural way new short-range currents required by almost all experiments associated with high momentum and energy transfers.

(5) Presence of the dressed-$6q$-bag components in nuclear wave functions leads automatically to a smooth matching between the nucleonic (at low momentum transferred) and quark currents (at very high momentum transferred) and, at the same time, results in correct counting rules at high momentum transferred.

So, it should be very important to test the above dibaryon concept of nuclear force in concise and consistent $3N$ calculations and to compare the predictions of the new model with the results of the conventional meson-exchange models.

Thus, the aim of this work is to make a comprehensive study of the properties of the $3N$ system with $2N$ and $3N$ forces given by the DBM. However, the DBM introduces explicitly nonnucleonic (quark−meson) channels. Therefore, it is necessary to introduce a self-consistent multichannel few-body formalism for the study of the $3N$ system with DBM interaction. We develop in this work such a general formalism, based on the approach which was suggested in the 1980s by Merkuriev's group [29−31] for the boundary-condition-type model for pairwise interactions. This general formalism leads immediately to a replacement of all two-body forces related to the dibaryon mechanism by the respective three (and many)-body forces, leaving a two-body character only for long-range Yukawa π and 2π exchanges, which are of little importance for the nuclear binding. Another straightforward sequence of the formalism developed here is a strong energy dependence of these many-body forces. In this work, we study all these aspects in detail by means of applications to the $3N$-system properties. The preliminary version of this work is published in [32].

This paper is organized as follows. In Section 2, we present a new general multichannel formalism for description of a two- and three-body system of particles having inner degrees of freedom. In Section 3, we give a brief description of the DBM for the NN system. In Section 4, we treat the $3N$ system with DBM interactions, including a new 3BF. In Section 5, some details of our variational method are discussed, including calculation of the matrix elements for new Coulomb 3BF. The results of our calculations for ground states of ^{3}H and ^{3}He are given in Section 6, while in Section 7 we discuss the role of the new 3BF and present a new explanation for the Coulomb displacement energy in ^{3}He within our interaction model. A comprehensive discussion of the most important results found in the work is given in Section 8. In the Conclusion, we summarize the main results of the work. In the Appendix, we give the formulas for the matrix elements of all DBM interactions taken in the Gaussian symmetrized variational basis.

2. THE GENERAL MULTICOMPONENT FORMALISM FOR 2N AND 3N SYSTEMS WITH COUPLED INTERNAL AND EXTERNAL CHANNELS

In the 1980s, the former Leningrad group (Merkuriev, Kurepin, Motovilov, Makarov, Pavlov, *et al.*) constructed and substantiated with mathematical rigor a model of strong interaction with the coupling of external and internal channels [29–31, 33]. This model was a particular realization of a general approach to interaction of particles having inner degrees of freedom. The basic physical hypothesis is that an energy-dependent interaction appears as a result of the internal structure of interacting particles.[4] A general scheme proposed by S.P. Merkuriev *et al.* was based on the assumption of existence of two independent channels: an external one, which describes the motion of particles considered as elementary bodies, i.e., neglecting their inner structure, and an internal one, which describes the dynamics of inner degrees of freedom. These channels can have quite different physical and mathematical nature and their dynamics are governed by independent Hamiltonians. The main issues here were how to define the coupling between external and internal channels and how to derive the corresponding dynamical equations (of Schrödinger or Faddeev type) for particle motion in the external channel.

In [29–31], this coupling was postulated via boundary conditions on some hypersurface. Thus, such an approach is well applicable to hybrid models for NN interaction, which were rather popular in the 1980s, e.g., the quark compound bag (QCB) model suggested by Simonov [34]. As for the $3N$ system, the formalism of incorporation of the internal channels ($6q$ bags) was proposed for the first time also within the QCB model [35]. The general scheme by Merkuriev *et al.* has allowed one to substantiate this formalism.

In QCB-like models, the coupling between the external (NN) and the inner (bag) channels was given just on some hypersurface, similarly to the well-known R-matrix approach in nuclear physics. Later on, such a general approach was applied to the two-channel Hamiltonian model, where the internal Hamiltonian had a purely discrete spectrum and the only restriction imposed on the operators coupling the external and internal channels was their boundness [33]. The above general multichannel scheme

has straightforwardly been extended to three-body problem. In particular, it has been shown for the above two models that elimination of the internal channels leads to the following recipe for embedding the energy-dependent pair interactions into the three-body problem: the replacement of the pair energy by the difference between the three-body energy and kinetic energy of the third particle: $\varepsilon_\alpha \to E - t_\alpha$ [31, 33]. It has also been proved that the resulting Faddeev equations for the external channel belong with such energy-dependent potentials to the Fredholm class and are equivalent to the four-channel Schrödinger equation.

Our aim here is to extend our new NN force model—DBM—by using the above Merkuriev *et al.* approach to the $3N$ system. There are external (nucleon–nucleon) and internal (quark–meson) channels in our model, and coupling between them is determined within a microscopic quark–meson approach. In this section, we present a general multicomponent formalism for description of systems of two and three particles having internal structure, without assuming any specific form for coupling between the external and internal channels.

2.1. Two-Body System

We assume that the total dynamics in the two-body system is governed by a self-conjugated Hamiltonian h acting in the orthogonal sum of spaces:

$$\mathcal{H} = \mathcal{H}^{\text{ex}} \oplus \mathcal{H}^{\text{in}},$$

where $\mathcal{H}^{\text{ex}}$ is the external Hilbert space of states describing motion of particles neglecting their internal structure and $\mathcal{H}^{\text{in}}$ is the internal Hilbert space corresponding to internal degrees of freedom. Thus, the total state of the system $\Psi \in \mathcal{H}$ can be written as a two-component column:

$$\Psi = \begin{pmatrix} \Psi^{\text{ex}} \in \mathcal{H}^{\text{ex}} \\ \Psi^{\text{in}} \in \mathcal{H}^{\text{in}} \end{pmatrix}.$$

The two spaces, $\mathcal{H}^{\text{ex}}$ and $\mathcal{H}^{\text{in}}$, can have quite a different nature, e.g., in the case of the NN system, Ψ^{ex} depends on the relative coordinate (or momentum) of two nucleons and their spins, while Ψ^{in} can depend on quark and meson variables. The two independent Hamiltonians are defined in each of these spaces: h^{ex} acts in $\mathcal{H}^{\text{ex}}$ and h^{in} acts in $\mathcal{H}^{\text{in}}$. Here, h^{ex} includes the kinetic energy of relative motion and some part of two-body interaction v^{ex}:

$$h^{\text{ex}} = t + v^{\text{ex}}.$$

---

[4] From a more general point of view, the explicit energy dependence of interaction reflects its nonlocality in time, while this time nonlocality, in turn, is a result of some excluded degrees of freedom. So, the explicit energy dependence is signaling some inner hidden (e.g., quark) degrees of freedom in NN interaction.

For the NN system, v^{ex} includes the peripheral part of the meson-exchange potential and Coulomb interaction between nucleons (if they are protons). Coupling between external and internal channels is determined formally by some transition operators: $h^{\mathrm{ex,in}} = (h^{\mathrm{in,ex}})^*$. Further, one can write down the total Hamiltonian h as a matrix operator,

$$h = \begin{pmatrix} h^{\mathrm{ex}} & h^{\mathrm{ex,in}} \\ h^{\mathrm{in,ex}} & h^{\mathrm{in}} \end{pmatrix}, \qquad (1)$$

not specifying so far the coupling operators (if operators h^{ex} and h^{in} are self-adjoint and $h^{\mathrm{ex,in}}$ is bounded, then the Hamiltonian h is the self-adjoint operator in $\mathcal{H}$).

Thus, one can write down the two-component Schrödinger equation

$$h\Psi = E\Psi,$$

and by excluding the internal channel wave function, one obtains an effective Schrödinger equation in the external channel

$$h^{\mathrm{eff}}(E)\Psi^{\mathrm{ex}} = E\Psi^{\mathrm{ex}} \qquad (2)$$

with an effective "pseudo-Hamiltonian":

$$h^{\mathrm{eff}}(E) = h^{\mathrm{ex}} + h^{\mathrm{ex,in}}g^{\mathrm{in}}(E)h^{\mathrm{in,ex}} = t + v^{\mathrm{ex}} + w(E), \qquad (3)$$

which depends on energy E via the resolvent of internal Hamiltonian $g^{\mathrm{in}}(E) = (E - h^{\mathrm{in}})^{-1}$. (From a mathematical point of view, an operator depending on the spectral parameter is not an operator at all, because its domain depends on the spectral parameter. Thus, this object should not be called a Hamiltonian. However, physicists do not turn their attention to this fact and use energy-dependent interactions very widely.)

Having the solution Ψ^{ex} of effective equation (2), one can "restore" the excluded internal state unambiguously:

$$\Psi^{\mathrm{in}} = g^{\mathrm{in}}(E)h^{\mathrm{in,ex}}\Psi^{\mathrm{ex}}. \qquad (4)$$

2.2. Three-Body System

In a three-body system we have three different internal spaces $\mathcal{H}_i^{\mathrm{in}}$ $(i = 1,2,3)$ and one common external space $\mathcal{H}_3^{\mathrm{ex}}$. The three-body internal space $\mathcal{H}_i^{\mathrm{in}}$ is a direct product of the two-body internal space related to the pair (jk) and single-particle space describing the motion of the third particle (i). Here, we use the conventional numbering of particles: $(ijk) = (123), (231), (312)$. The characteristic three-body Hamiltonian acts in each internal space as

$$H_i^{\mathrm{in}} = h_{jk}^{\mathrm{in}} \otimes \mathbb{I}_i + \mathbb{I}_{jk} \otimes t_i, \qquad (5)$$

$$(ijk) = (123), (231), (312)$$

where h_{jk}^{in} is the two-body internal Hamiltonian for the pair (jk), $\mathbb{I}$ is the unity operator and t_i is the kinetic energy of the third particle (i) in respect to the center of mass of the pair (jk). (Here and below we use capital letters for three-body quantities and small letters for two-body ones.)

The external three-body Hamiltonian acts in the external space $\mathcal{H}_3^{\mathrm{ex}}$ and includes the total kinetic energy T and the sum of external two-body interactions, which were incorporated into the external two-body Hamiltonians:

$$H_3^{\mathrm{ex}} = T + \sum_{i<j} v_{ij}^{\mathrm{ex}}.$$

A state in the full three-body Hilbert space

$$\mathcal{H}_3 = \mathcal{H}_3^{\mathrm{ex}} \oplus \sum_i \mathcal{H}_i^{\mathrm{in}}$$

can be written as a four-component column:

$$\Psi_3 = \begin{pmatrix} \Psi^{\mathrm{ex}} \\ \Psi_1^{\mathrm{in}} \\ \Psi_2^{\mathrm{in}} \\ \Psi_3^{\mathrm{in}} \end{pmatrix}.$$

Thus, the total Hamiltonian, H_3, of the three-body system acting in $\mathcal{H}_3$ can be written as a (4×4) matrix:

$$H_3 = \begin{pmatrix} H^{\mathrm{ex}} & H_1^{\mathrm{ex,in}} & H_2^{\mathrm{ex,in}} & H_3^{\mathrm{ex,in}} \\ H_1^{\mathrm{in,ex}} & H_1^{\mathrm{in}} & 0 & 0 \\ H_2^{\mathrm{in,ex}} & 0 & H_2^{\mathrm{in}} & 0 \\ H_3^{\mathrm{in,ex}} & 0 & 0 & H_3^{\mathrm{in}} \end{pmatrix}. \qquad (6)$$

Here, we suppose that

(i) there is no direct coupling between different internal channels $\mathcal{H}_i^{\mathrm{in}}$ and $\mathcal{H}_j^{\mathrm{in}}$ for $i \neq j$;

(ii) the channel coupling operators do not involve the third (free) particle:

$$H_i^{\mathrm{ex,in}} = h_{jk}^{\mathrm{ex,in}} \otimes \mathbb{I}_i. \qquad (7)$$

Writing the four-component Schrödinger equation with Hamiltonian (6),

$$H_3\Psi_3 = E\Psi_3, \qquad (8)$$

and excluding three internal channels from it (it is simple due to the supposed absence of direct coupling between different internal channels), one obtains an

effective Schrödinger equation for the external three-body wave function Ψ_3^{ex},

$$H_3^{\text{eff}}(E)\Psi_3^{\text{ex}} = E\Psi_3^{\text{ex}}, \qquad (9)$$

with an effective (pseudo-)Hamiltonian

$$H_3^{\text{eff}}(E) = H_3^{\text{ex}} + \sum_i H_i^{\text{ex,in}} G_i^{\text{in}}(E) H_i^{\text{in,ex}}, \qquad (10)$$

where the resolvent of internal Hamiltonian G_i^{in} is a convolution of the two-body internal resolvent g_{jk}^{in} of pair (jk) and the free motion resolvent for the third particle (i):

$$G_i^{\text{in}} = (E - H_i^{\text{in}})^{-1} \qquad (11)$$

$$= \frac{1}{2\pi i} \int_{-\infty}^{\infty} g_{jk}^{\text{in}}(z) g_i^0(E - z) dz = g_{jk}^{\text{in}}(E - t_i) \otimes \mathbb{I}_i.$$

Thus, the effective Hamiltonian in the external three-body channel takes the form

$$H^{\text{eff}} = T + \sum_{jk}\{v_{jk}^{\text{ex}} + w_{jk}(E - t_i)\}; \qquad (12)$$

i.e., the total effective interaction in the external channel of the three-body system is a sum of the two-body external potentials v_{jk}^{ex} and the two-body effective interactions with replacement of pair energy ε_i with the difference between the total three-body energy and operator for the relative-motion kinetic energy of the third particle: $\varepsilon_i \to E - t_i$.

Just this recipe for inclusion of energy-dependent pair interactions in the three-body problem is widely used in Faddeev calculations. This recipe has been rigorously proved in the works of Merkuriev *et al.* for a two-channel model without a continuous spectrum in the internal channel [33] and, in particular, for the boundary-condition model [31]. We see, however, that this result is a direct consequence of the above two assumptions and by no means is related to usage of any specific interaction model.[5]

The resulting form of the effective three-body Hamiltonian (12) is suitable for the Faddeev reduction. However, it should be emphasized that each term $W_{\beta\gamma}$ in the effective Hamiltonian (12) includes a dependence on the kinetic energy of the third particle,

i.e., each term $W_{\beta\gamma}$ is, generally speaking, a three-body force. In spite of the three-body character of such effective potentials, the corresponding Faddeev equations have the Fredholm property and are equivalent to the four-channel Schrödinger equation (it has been proved for a model with a discrete internal spectrum [33]).

2.3. A New Three-Body Force in the Three-Body System with External and Internal Channels

In each internal channel one can introduce a new interaction between the third particle and the pair as a whole. This leads to replacement of the operator for kinetic energy of the third particle t_i by some (single-particle) Hamiltonian h_i,

$$t_i \Rightarrow h_i = t_i + v_i, \qquad (13)$$

in Eq. (5) for H_i^{in}, viz.,

$$H_i^{\text{in}} = h_{jk}^{\text{in}} \otimes \mathbb{I}_i + \mathbb{I}_{jk} \otimes h_i. \qquad (14)$$

The physical meaning of such interactions will be discussed below, and here we treat only the formal aspects of their introduction. As the internal Hamiltonian (14) is still a direct sum of the two-body internal Hamiltonian and the Hamiltonian corresponding to relative motion of the third nucleon, then its resolvent can be expressed as a convolution of two subresolvents:

$$G_i^{\text{in}} = (E - H_i^{\text{in}})^{-1} = \frac{1}{2\pi i} \int_{-\infty}^{\infty} g_{jk}^{\text{in}}(z) g_i(E - z) dz, \qquad (15)$$

where $g_i(\varepsilon) = (\varepsilon - h_i)^{-1}$. Now, of course, the effective interaction in the external channel is not reduced to a sum of pairwise effective interactions with replacement $\varepsilon_i \to E - t_i$. Nevertheless, this interaction includes three terms W_{jk} and is still suitable for Faddeev reduction. But now there are no pure pairwise forces (except v_{jk}^{ex}) in the effective Hamiltonian for the external three-body channel.

Moreover, if even the external interaction v_i is disregarded at all, each term w_{jk} in the effective Hamiltonian (12) includes a dependence on the kinetic energy of the third particle, i.e., can be considered, generally speaking, as a three-body force. This dependence on the third-particle momentum reduces the strength of the effective interaction between the other two particles due to a specific energy dependence of the coupling constants (see below). Therefore, one can say that there are no pure two-body forces in the three-body system in such an approach, with the exception of that part of the interaction which is included in v^{ex} (for the NN system, it is just the peripheral part of meson exchange).

---

[5]In the literature, however, there were also discussions of the alternative variants for embedding energy-dependent pairwise force into the three-body system [36, 37]. These schemes assume that the effective total energy ε_{12} of the two-body subsystem in the three-body system is obtained from the total three-body energy E in the following way: $\varepsilon_{12} = E - t_{12} - \langle v_{13} \rangle - \langle v_{23} \rangle$, where v_{ij} is the two-body interaction between particles i and j and an averaging is assumed with the exact $3N$ wave function.

3. DRESSED-BAG MODEL FOR NN FORCES

Here, we give a brief description of the two-component DBM for the NN interaction. A detailed description has been presented in our previous papers [8, 24]. (The effective-field theory description for the dibaryon model of nuclear force has also been developed recently [38].) The main assumptions of the DBM are following:

(i) Interacting nucleons form at small and intermediate distances ($r_{NN} \sim 1$ fm) a compound state—the dibaryon or six-quark bag dressed with π, σ, and ρ fields.

(ii) The coupling of the external NN channel with this state gives the basic attractive force between nucleons at intermediate and small distances, the σ-dressed bag giving the main contribution.

Thus, nucleon–nucleon system can be found in two different phase states (channels): the NN phase and the dressed-$6q$-bag phase. In the NN (external) channel, the system is described as two nucleons interacting via OBE; in the internal $6q + \sigma$ channel, the system is treated as a $6q$ bag surrounded by a strong scalar–isoscalar σ field (a "dressed" bag).[6] The external two-nucleon Hamiltonian includes the peripheral part of one-pion- and two-pion-exchange (OPE and TPE, respectively) interaction and Coulomb interaction:

$$h^{\text{ex}} = t + \{v^{\text{OPE}} + v^{\text{TPE}}\}_{\text{(with soft cutoff)}} + v^{\text{Coul}}.$$

In the simplest version of the DBM, we used a pole approximation for the dressed-bag (internal) resolvent g^{in}:

$$g^{\text{in}}(E) = \sum_\alpha \int \frac{|\alpha, \mathbf{k}\rangle\langle\alpha, \mathbf{k}| d^3 k}{E - E_\alpha(\mathbf{k})}, \qquad (16)$$

where $|\alpha\rangle$ is the $6q$ part of the wave function for the dressed bag and $|\mathbf{k}\rangle$ represents the plane wave of the σ-meson propagation. Here, $E_\alpha(\mathbf{k})$ is the total energy of the dressed bag:

$$E_\alpha(\mathbf{k}) = m_\alpha + \varepsilon_\sigma(k), \qquad (17)$$

where

$$\varepsilon_\sigma(k) = k^2/(2m_\alpha) + \omega_\sigma(k) \simeq m_\sigma + k^2/(2\bar{m}_\sigma), \qquad (18)$$

$$\bar{m}_\sigma = \frac{m_\sigma m_\alpha}{m_\sigma + m_\alpha},$$

$\omega_\sigma(k) = \sqrt{m_\sigma^2 + k^2}$ is the relativistic energy of the σ meson, and m_σ and m_α are the masses of the σ meson and $6q$ bag, respectively.

---

[6] A full description of the NN interaction at energies $E \sim 1$ GeV still requires other fields in the bag, such as 2π, ρ, and ω.
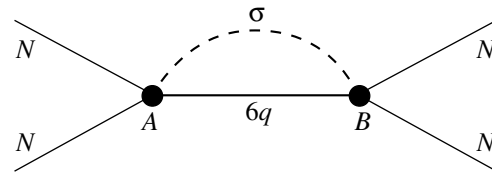
Fig. 1. Effective NN interaction induced by the production of an intermediate dressed bag.

The effective interaction $w(E)$ resulting from the coupling of the external NN channel to the intermediate dressed-bag state is illustrated by the graph in Fig. 1.

To derive the effective interaction w for the NN channel in such an approximation, knowledge of the full internal Hamiltonian h^{in} of the dressed bag, as well as the full transition operator $h^{\text{in,ex}}$, is not necessary. We need only to know how the transition operator acts on those dressed-bag states which are included in the resolvent (16): $h^{\text{in,ex}}|\alpha, \mathbf{k}\rangle$. The calculation of this quantity within a microscopic quark–meson model results in a sum of factorized terms [24]:

$$h^{\text{ex,in}}|\alpha^{JM}, \mathbf{k}\rangle = \sum_L |\varphi_L^{JM}\rangle B_L^J(\mathbf{k}), \qquad (19)$$

where $\varphi_L^{JM} \in \mathcal{H}^{\text{ex}}$ is the NN transition form factor and $B_L^J(\mathbf{k})$ is the vertex function dependent on the σ-meson momentum.

Here, we should elucidate our notation in respect to the quantum numbers of angular momenta. In general, the $6q$-state index α includes all the quantum numbers of the dressed bag, i.e., $\alpha \equiv \{J, M, S, T, L_b, L_\sigma\}$, where L_b, S, T, J, and M are the orbital angular momentum of the $6q$ bag, its spin, isospin, total angular momentum, and its projection on the z axis, respectively, and L_σ is the orbital angular momentum of the σ meson. However, in the present version of the DBM, the s-wave state of the $6q$ bag with the s^6 configuration only is taken into account, so that $L_b = 0$, $J = S$, and thus the isospin of the bag is uniquely determined by its spin. The states of the dressed bag with $L_\sigma \neq 0$ should lie higher than those with $L_\sigma = 0$. For this reason, the former states are not included in the present version of the model. Therefore, the state index α is specified here by the total angular momentum of the bag J and (if necessary) by its z projection M: $\alpha \Rightarrow \{J(M)\}$.

Thus, the effective interaction in the NN channel $w(E) \equiv h^{\text{ex,in}} g^{\text{in}}(E) h^{\text{in,ex}}$ can be written as a sum of separable terms in each partial wave:

$$w(E) = \sum_{JLL'} w_{LL'}^J(\mathbf{r}, \mathbf{r}', E), \qquad (20)$$

Table 1. Deuteron properties in the DBM and other current NN models

Model	E_d, MeV	P_D, %	r_m, fm	Q_d, fm^2	μ_d, n.m.	A_S, fm$^{-1/2}$	$\eta(D/S)$
RSC	2.22461	6.47	1.957	0.2796	0.8429	0.8776	0.0262
Moscow 99	2.22452	5.52	1.966	0.2722	0.8483	0.8844	0.0255
Bonn 2001	2.224575	4.85	1.966	0.270	0.8521	0.8846	0.0256
DBM(I) $P_{6q} = 3.66\%$	2.22454	5.22	1.9715	0.2754	0.8548	0.8864	0.02588
DBM(II) $P_{6q} = 2.5\%$	2.22459	5.31	1.970	0.2768	0.8538	0.8866	0.0263
Experiment	2.224575	−	1.971	0.2859	0.8574	0.8846	0.0263[a]

[a] An average value of the asymptotic mixing parameter η over the results of a few of the most accurate experiments is presented here (see [40−43]).

with

$$w_{LL'}^{J}(\mathbf{r}, \mathbf{r}') = \sum_{M} \varphi_L^{JM}(\mathbf{r}) \lambda_{LL'}^{J}(E) \varphi_{L'}^{JM*}(\mathbf{r}'). \quad (21)$$

The energy-dependent coupling constants $\lambda_{LL'}^{J}(E)$ appearing in Eq. (21) are directly calculated from the loop diagram shown in Fig. 1; i.e., they are expressed in terms of the loop integral of the product of two transition vertices B and the convolution of two propagators for the meson and quark bag with respect to the momentum k:

$$\lambda_{LL'}^{J}(E) = \int_0^\infty d\mathbf{k} \frac{B_L^J(\mathbf{k}) B_{L'}^{J\,*}(\mathbf{k})}{E - E_\alpha(k)}. \quad (22)$$

The vertex form factors $B_L^J(\mathbf{k})$ and the potential form factors $\varphi_L^{JM} \in \mathcal{H}^{\mathrm{ex}}$ have been calculated in the microscopic quark−meson model [8, 24].

When the NN-channel wave function Ψ^{in} is obtained by solving the Schrödinger equation with the effective Hamiltonian $h^{\mathrm{eff}}(E)$, the internal ($6qN$) component of the wave function is found from Eq. (4):

$$\Psi_{JM}^{\mathrm{in}}(E) = |\alpha^{JM}\rangle \underbrace{\sum_{L} \frac{B_L^J(\mathbf{k})}{E - E_\alpha(\mathbf{k})} \langle \varphi_L^{JM} | \Psi^{\mathrm{ex}}(E) \rangle}, \quad (23)$$

where the underlined part can be interpreted as the mesonic part of the dressed-bag wave function.

The weight of the internal dressed-bag component of the bound-state wave function (with given value J) is proportional to the norm of Ψ_{JM}^{in}:

$$\|\Psi_{JM}^{\mathrm{in}}\|^2 = \|\alpha^{JM}\|^2 \sum_{LL'} \langle \varphi_L^{JM} | \Psi^{\mathrm{ex}} \rangle \langle \Psi^{\mathrm{ex}} | \varphi_{L'}^{JM} \rangle \quad (24)$$

$$\times \underbrace{\int \frac{B_L^J(\mathbf{k}) B_{L'}^{J\,*}(\mathbf{k})}{(E - E_\alpha(\mathbf{k}))^2} d\mathbf{k}}_{I_{LL'}^J}.$$

As one can see from the comparison between Eqs. (22) and (24), the integral $I_{LL'}^J$ in Eq. (24) is equal to the energy derivative (with opposite sign) of the coupling constant $\lambda_{LL'}^J(E)$:

$$I_{LL'}^J = -\frac{d\lambda_{LL'}^J(E)}{dE},$$

and thus we get an interesting result:

$$\|\Psi^{\mathrm{in}}\|^2 \sim -\frac{d\lambda(E)}{dE};$$

i.e., the weight of the internal $6qN$ state is proportional to the energy derivative of the coupling constant of effective NN interaction. In other words, the stronger the energy dependence of the interaction in the NN channel, the larger the weight of the channel corresponding to nonnucleonic degrees of freedom. This result is in full agreement with the following well-known hypothesis: energy dependence of interaction is a sequence of underlying inner structure of interacting particles.

The total wave function of the bound state Ψ must be normalized to unity. Assuming that the external (nucleonic) part of the wave function Ψ^{ex} found from the effective Schrödinger equation has the standard normalization $\|\Psi^{\mathrm{ex}}\| = 1$, one finds that the weight of the internal part, i.e., the dressed-bag component, is equal to

$$P_{\mathrm{in}} = \frac{\|\Psi^{\mathrm{in}}\|^2}{1 + \|\Psi^{\mathrm{in}}\|^2}. \quad (25)$$

Thus, the NN interaction in the DBM approach is a sum of peripheral terms (v^{OPE} and v^{TPE}) representing OPE and TPE with soft cutoff parameter $\Lambda_{\pi NN}$ and an effective interaction $w(E)$ [see Eqs. (20), (21)], which is expressed (in a single-pole approximation) as a one-term separable potential with the energy-dependent coupling constants (22). The potential form factors $\varphi_L^{JM}(\mathbf{r})$ are taken as the conventional

harmonic oscillator wave functions $|2S\rangle$ and $|2D\rangle$.[7] Therefore, the total NN potential in the DBM model can be represented as

$$v_{NN} = v^{\text{OPE}} + v^{\text{TPE}} + v^{\text{Coul}} \qquad (26)$$
$$+ w(E) + \lambda\Gamma,$$

where $\Gamma = |\varphi_0\rangle\langle\varphi_0|$ is the projector onto $|0S\rangle$ harmonic oscillator function and the constant λ should be taken to be sufficiently large.

The model described above gives a very good description for singlet $^1S_0$ and triplet $^3S_1 - ^3D_1$ phase shifts and mixing parameter ε_1 in the energy region from zero up to 1 GeV [24]. The deuteron observables obtained in this model without any additional or free parameter are presented in Table 1 in comparison with some other NN models and experimental values. The quality of agreement with experimental data for the NN phase shifts and deuteron static properties found with the presented force model, in general, is higher than those for the modern NN potential model such as Bonn, Argonne, etc., especially for the asymptotic mixing parameter η and the deuteron quadrupole moment. The weight of the internal (dressed-bag) component in the deuteron is varied from 2.5 to 3.6% in different versions of the model [8, 24].

4. THREE-NUCLEON SYSTEM WITH DBM INTERACTION

For description of the three-body system with DBM interaction, the momentum representation is more appropriate. We will employ the same notation for functions in both the coordinate and momentum representations. The following notation for coordinates and momenta are employed: $\mathbf{r}_i$ ($\mathbf{p}_i$) is relative coordinate (momentum) of pair (jk), while $\boldsymbol{\rho}_i$ ($\mathbf{q}_i$) is the Jacobi coordinate (momentum) of the ith particle, and $\mathbf{k}$ is usually the momentum of the σ meson.

### 4.1. Effective Interaction Due to Pairwise NN Forces

One obtains an effective Hamiltonian for the external $3N$ channel according to a general recipe for transition from a two- to three-particle system:

$$H^{\text{eff}} = T + \sum_i \{v_i^{\text{ex}} + W_i(E)\}, \qquad (27)$$

where each of three effective potentials takes the form

$$W_i(E) = \delta(\mathbf{q}_i - \mathbf{q}_i')w_i(E - q_i^2/(2\bar{m})), \qquad (28)$$

---

[7] It was first suggested [39] long ago and then confirmed in detailed $6q$ microscopic calculations [15] that the $6q$ wave function in the NN channel corresponds just to $2\hbar\Omega$ excited $6q$-bag components $|s^4p^2[42]LST\rangle$, while the ground state $|s^6[6]\rangle$ describes the wave function in the bag channel.
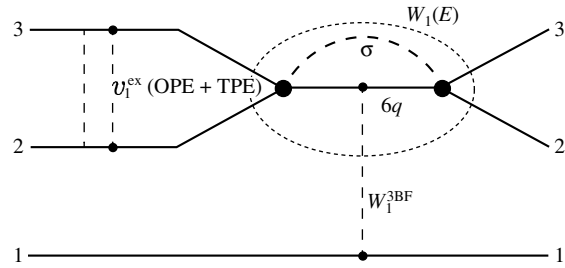
Fig. 2. Different interactions in the $3N$ system for one of three possible combinations $(1 + 23)$ of three nucleons: the peripheral two-nucleon interaction v_1^{ex} is due to OPE + TPE; the effective two-body interaction $W_1(E)$ is induced by the production of the dressed $6q$ bag and meson-exchange 3BF W_1^{3BF}.

and $\bar{m} = m_N m_\alpha/(m_N + m_\alpha)$ is a reduced mass of the nucleon and $6q$ bag. In the pole approximation, this effective interaction reduces to a sum of two-body separable potentials with the coupling constants depending on the total three-body energy E and the third-particle momentum q_i:

$$W_i(\mathbf{p}_i, \mathbf{p}_i', \mathbf{q}_i, \mathbf{q}_i'; E) = \delta(\mathbf{q}_i - \mathbf{q}_i') \qquad (29)$$
$$\times \sum_{J_i M_i L_i L_i'} \varphi_{L_i}^{J_i M_i}(\mathbf{p}_i) \lambda_{L_i L_i'}^{J_i} \left(E - \frac{q_i^2}{2\bar{m}}\right) \varphi_{L_i'}^{J_i M_i}(\mathbf{p}_i').$$

When using such an effective interaction, one must also include an additional 3BF due to the meson-exchange interaction between the dressed bag and the third nucleon (see the next subsection). The pattern of different interactions arising in the $3N$ system in such a way is illustrated in Fig. 2.

In the single-pole approximation, the internal (dressed-bag) components of the total wave function are expressed in terms of the nucleonic component $\Psi^{\text{ex}}(\mathbf{p}_i, \mathbf{q}_i)$ as

$$\Psi_i^{\text{in}}(\mathbf{k}, \mathbf{q}_i; E) = \sum_{J_i M_i L_i} |\alpha^{J_i M_i}\rangle \frac{B_{L_i}^{J_i}(\mathbf{k}) \chi_{L_i}^{J_i M_i}(\mathbf{q}_i)}{E - E_\alpha - q_i^2/(2m)}, \qquad (30)$$

where $\chi_{L_i}^{J_i M_i}(\mathbf{q}_i)$ are the overlap integrals of the external $3N$ component and the potential form factors $\varphi_{L_i}^{J_i M_i}$:

$$\chi_{L_i}^{J_i M_i}(\mathbf{q}_i) = \int \varphi_{L_i}^{J_i M_i}(\mathbf{p}_i) \Psi^{\text{ex}}(\mathbf{p}_i, \mathbf{q}_i) d\mathbf{k}_i. \qquad (31)$$

These overlap functions depend on the momentum (or coordinate), spin, and isospin of the third nucleon. For brevity, the spin−isospin parts of the overlap functions and corresponding quantum numbers are omitted unless they are needed. In Eqs. (29)−(31) and below, we keep the index i in the quantum numbers
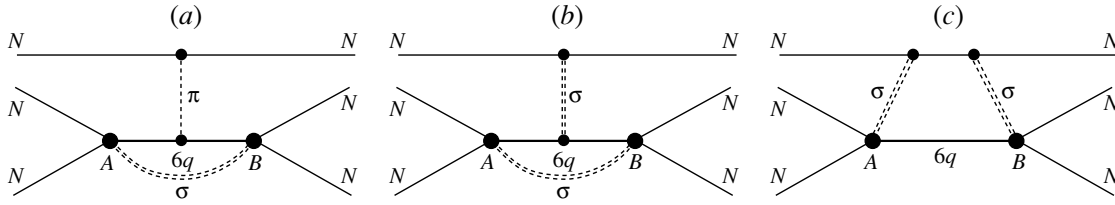
Fig. 3. The graphs corresponding to three new types of three-body force.

L_i and J_i in order to distinguish the orbital and total angular momenta attributed to the $2N$ form factors from the respective angular momenta J and L of the whole $3N$ system.

It should be noted that the angular part of the function $\chi_{L_i}^{J_i M_i}(\mathbf{q}_i)$ in Eq. (31) is not equal to $Y_{L_i M_i}(\hat{q})$. This part also includes other angular orbital momenta due to coupling of the angular momenta and spins of the dressed bag and those for the third nucleon. In the next section, we consider the spin-angular and isospin parts of the overlap functions $\chi_{L_i}^{J_i M_i}(\mathbf{q}_i)$ in more detail.

The norm of each $6qN$ component for the $3N$ bound state is determined by the sum of the integrals:

$$||\Psi_i^{\text{in}}||^2 = \sum_{J_i M_i} ||\alpha^{J_i M_i}|| \sum_{L_i L_i'} \int \chi_{L_i}^{J_i M_i}(\mathbf{q}_i) \quad (32)$$

$$\times \left\{ \int \frac{B_{L_i}^{J_i}(\mathbf{k}) B_{L_i'}^{J_i}(\mathbf{k})}{\left(E - E_\alpha - \dfrac{q_i^2}{2m}\right)^2} d\mathbf{k} \right\} \chi_{L_i'}^{J_i M_i}(\mathbf{q}_i) d\mathbf{q}_i.$$

The internal loop integral with respect to $\mathbf{k}$ in Eq. (32) (in braces) can be replaced by the energy derivative of λ_L^J:

$$\int \frac{B_{L_i}^{J_i}(\mathbf{k}) B_{L_i'}^{J_i}(\mathbf{k})}{\left(E - E_\alpha - q_i^2/(2m)\right)^2} d\mathbf{k} \quad (33)$$

$$= -\frac{d}{dE} \lambda_{L_i L_i'}^{J_i} \left(E - \frac{q_i^2}{2m}\right).$$

Thus, the weight of the $6qN$ component in the $3N$ system is determined by the same energy dependence of the coupling constants $\lambda_{LL'}^J(\varepsilon)$ as the contribution of the $6q$ component in the NN system but at a shifted energy.

Using Eq. (33), the norm of the $6qN$ component can eventually be rewritten as

$$||\Psi_i^{\text{in}}||^2 = \sum_{J_i M_i} ||\alpha^{J_i}|| \sum_{L_i L_i'} \int \chi_{L_i}^{J_i M_i}(\mathbf{q}_i) \quad (34)$$

$$\times \left(-\frac{d}{dE} \lambda_{L_i L_i'}^{J_i}(E - q_i^2/(2m)) \right) \chi_{L_i'}^{J_i M_i}(\mathbf{q}_i) d\mathbf{q}_i.$$

Due to explicit presence of the meson variables in our approach, it is generally impossible to define the wave function describing the relative motion of the third nucleon $^N\psi(q)$ in the $6qN$ channel. However, by integrating $\Psi_i^{\text{in}}(\mathbf{k}, \mathbf{q})$ with respect to the meson momentum $\mathbf{k}$, one can obtain an average momentum distribution of the third nucleon in the $6qN$ channel (i.e., that weighted with the σ-meson momentum distribution). On the basis of Eq. (33), we can attribute the meaning of the third nucleon wave function in the $6qN$ channel to the quantity

$$\tilde{\psi}_{L_i}^{J_i M_i}(\mathbf{q}_i) \quad (35)$$

$$= \left[\left(-\frac{d}{dE} \lambda_{L_i L_i'}^{J_i}(E - q_i^2/(2m)) \right) \right]^{1/2} \chi_{L_i}^{J_i M_i}(\mathbf{q}_i).$$

With this "quasi wave function," one can calculate the mean value of any operator depending on the momentum (or coordinate) of the third nucleon. We note that the derivative $-d\lambda/dE$ is always positive.

4.2. Three-Body Forces in the DBM

In this study, we employ the effective interaction (29) and take into account the interaction between the dressed bag and the third nucleon as an additional 3BF. We consider here three types of 3BF: one-meson exchange (π and σ) between the dressed bag and the third nucleon (see Figs. 3a and 3b) and the exchange by two σ mesons where the third-nucleon propagator breaks the σ loop of the two-body force—2σ process (Fig. 3c).

All these forces can be represented in the effective Hamiltonian for the external $3N$ channel as some integral operators with factorized kernels:

$$W_{(i)}^{3BF}(\mathbf{p}_i, \mathbf{p}'_i, \mathbf{q}_i, \mathbf{q}'_i; E) \qquad (36)$$

$$= \sum_{JMJ'M'LL'} \varphi_L^{JM}(\mathbf{p}_i) \,^{3BF}W_{LL'}^{JJ'}(\mathbf{q}_i, \mathbf{q}'_i; E) \varphi_{L'}^{J'M'}(\mathbf{p}'_i).$$

Therefore, matrix elements for 3BF include only the overlap functions, and thus the contribution of 3BF is proportional to the weight of the internal $6qN$ component in the total $3N$ wave function. To our knowledge, the first calculation of the 3BF contribution induced by OPE between the $6q$ bag and the third nucleon was done by Fasano and Lee [44] in the hybrid QCB model using perturbation theory. They used the model where the weight of the $6q$ component in a deuteron was about 1.7%, and thus they obtained a very small value of -0.041 MeV for the 3BF OPE contribution to the $3N$ binding energy. Our results for the OPE 3BF agree with the results obtained by Fasano and Lee (see Table 2 in Section 7), because the OPE contribution to 3BF is proportional to the weight of the $6q$ component, and in our case, it should be at least twice their calculation. However, we found that a much larger contribution comes from scalar σ-meson exchanges: one-sigma exchange (OSE) and two-sigma exchange (TSE). We emphasize that, due to (proposed) restoration of chiral symmetry in our approach, the σ-meson mass becomes about 400 MeV, and thus the effective radius of the σ-exchange interaction is not as small as that in conventional OBE models. Therefore, we cannot use perturbation theory anymore to estimate the 3BF contribution but have to do the full calculation including 3BF in the total three-body Hamiltonian.

4.2.1. One-meson exchange between the dressed bag and third nucleon. For the one-meson-exchange (OME) term, the three-body interaction $^{3BF}W_{L_iL'_i}^{J_iJ'_i}$ takes the form

$$^{OME}W_{L_iL'_i}^{J_iJ'_i}(\mathbf{q}_i, \mathbf{q}'_i; E) \qquad (37)$$

$$= \int d\mathbf{k} \frac{B_{L_i}^{J_i}(\mathbf{k})}{E - E_\alpha - q_i^2/(2m)}$$

$$\times V^{OME}(\mathbf{q}_i, \mathbf{q}'_i) \frac{B_{L'_i}^{J'_i}(\mathbf{k})}{E - E_\alpha - q_i'^2/(2m)}.$$

Therefore, the matrix element for OME can be expressed in terms of the internal "bag" components Ψ_i^{in}:

$$\langle \Psi^{ex}|OME|\Psi^{ex}\rangle = 3\langle \Psi_i^{in}|V^{OME}|\Psi_i^{in}\rangle. \qquad (38)$$

The integral with respect to the σ-meson momentum $\mathbf{k}$ (37) can be shown to be reduced to a difference of
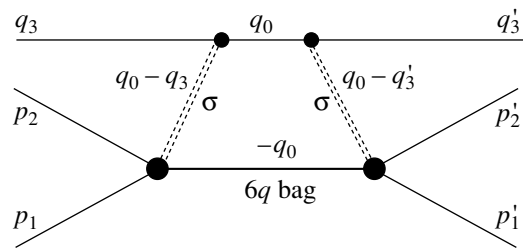

Fig. 4. The graph illustrating the three-body scalar force due to two-sigma exchange (2σ process).

the values for constant $\lambda(E - q^2/(2m))$, so that the vertex functions $B(k)$ can be excluded from formulas for OME 3BF matrix elements. The details of calculations for such matrix elements are given in the Appendix.

4.2.2. 2σ process. The 2σ process (TSE) shown in Fig. 4 also contributes significantly to 3BF. This $3N$ interaction seems less important than the OSE force, because this interaction imposes a specific kinematic restriction on the $3N$ configuration.[8]

The operator of the TSE interaction includes explicitly the vertex functions for the transitions ($NN \Longleftrightarrow 6q + \sigma$), so that these vertices cannot be excluded similarly to the case of OME. Therefore, we have to choose some form for these functions. It is natural to require that these vertices be the same as those assumed in the two-body DBM; i.e., they can be normalized by means of the coupling constants $\lambda(E)$, which, in turn, are chosen in the $2N$ sector to accurately describe NN phase shifts and deuteron properties [see below Eq. (41) for vertex normalization]. We use the Gaussian form factor for these vertices:

$$B_L^J(\mathbf{k}) = B_0^{JL} \frac{e^{-b^2k^2}}{\sqrt{2\omega_\sigma(k)}}, \qquad (39)$$

where $\mathbf{k}$ is the meson momentum and the parameter b is taken from the microscopic quark model [24]:

$$b^2 = \frac{5}{24}b_0^2, \qquad b_0 = 0.5 \text{ fm}. \qquad (40)$$

---

[8] It follows from the intuitive picture of this interaction that this force can be large only if the momentum of the third nucleon is almost opposite to the momentum of the emitted σ meson. Thus, a specific $3N$ kinematic configuration is required when two nucleons approach close to each other to form a bag, while the third nucleon has a specific space localization and momentum.

Then, the vertex constants B_0^{JL} should be found from the equation

$$\frac{1}{(2\pi)^3} \int d\mathbf{k} \frac{B_0^{JL} B_0^{JL'} e^{-2b^2 k^2}}{(E - m_\alpha - \varepsilon_\sigma(k)) \cdot 2\omega_\sigma(k)} = \lambda_{LL'}^J(E),$$

$$(41)$$

where $\lambda_{LL'}^J(E)$ are the coupling constants employed in the construction of the DBM in the $2N$ sector and are fixed by NN phase shifts. For the σNN vertices, we take also the Gaussian form factor: $g_{\sigma NN} e^{-\alpha^2 k^2}$ with $\alpha^2 = b_0^2/6$.

Then, the box diagram in Fig. 4 can be expressed in terms of the integral over the momentum $\mathbf{q}_0$ of the third nucleon in the intermediate state:

$$^{\text{TSE}}W_{LL'}^{JJ'}(\mathbf{q}, \mathbf{q}'; E) = \delta_{JJ'} g_{\sigma NN}^2 B_0^{JL} B_0^{JL'} \quad (42)$$

$$\times \frac{1}{(2\pi)^3} \int d\mathbf{q}_0 \frac{\exp[-(\alpha^2 + b^2)(\mathbf{q}_0 - \mathbf{q})^2]}{m_\sigma^2 + (\mathbf{q}_0 - \mathbf{q})^2}$$

$$\times \frac{1}{E - m_\alpha - q_0^2/(2m)} \frac{\exp[-(\alpha^2 + b^2)(\mathbf{q}_0 - \mathbf{q}')^2]}{m_\sigma^2 + (\mathbf{q}_0 - \mathbf{q}')^2}.$$

Thus, the matrix element for the total contribution of TSE eventually takes the form

$$\langle \text{TSE} \rangle = 3 \sum_{J_i M_i, L_i, L_i'} \int \chi_{L_i}^{J_i M_i}(\mathbf{q}) \quad (43)$$

$$\times {}^{\text{TSE}}W_{L_i L_i'}^{J_i J_i}(\mathbf{q}, \mathbf{q}'; E) \chi_{L_i'}^{J_i M_i}(\mathbf{q}') d\mathbf{q} d\mathbf{q}'.$$

After the partial wave decomposition, these six-dimensional integrals can be reduced to two-dimensional integrals, which are computed numerically by means of the appropriate Gaussian quadratures.

We should emphasize here that both the two-nucleon force induced by the DBM and two parts of the 3BF contribution in our approach, i.e., OSE and TSE, are all taken with unified coupling constants and unified form factors in Eqs. (37), (39)–(41), in a sharp contrast to the traditional meson-exchange models (see also Section 8).

5. VARIATIONAL CALCULATIONS OF 3N SYSTEM WITH DBM INTERACTION

The effective Schrödinger equation for the external $3N$ part of the total wave function $H^{\text{tot}}(E)\Psi^{\text{ex}}(E) = E\Psi^{\text{ex}}(E)$ with Hamiltonian

$$H^{\text{tot}}(E) = T + \sum_{i=1}^{3} \{v_i^{\text{ex}} + W_i(E) + W_i^{3\text{BF}}(E)\}$$

$$(44)$$

has been solved by variational method using an antisymmetrized Gaussian basis [45]. Because of the explicit energy dependence of the three-body total

Hamiltonian, we used an iterative procedure in respect to the total energy E for solving this equation:

$$H^{\text{tot}}(E^{(n-1)})\Psi^{\text{ex}(n)} = E^{(n)}\Psi^{\text{ex}(n)}.$$

Such iterations can be shown to converge if the energy derivative of effective interaction is negative (for our case, this condition is valid always). For our calculations, 5–7 iterations usually provide the accuracy of five decimal digits for the $3N$ binding energy.

Construction of a 3N variational basis. Here, we give the form of the basis functions used in this work and the corresponding notation for the quantum numbers. The wave function of the external $3N$ channel, Ψ^{ex}, can be written in the antisymmetrized basis as a sum of three terms:

$$\Psi^{\text{ex}} = \Psi_{\text{ex}}^{(1)} + \Psi_{\text{ex}}^{(2)} + \Psi_{\text{ex}}^{(3)}, \quad (45)$$

where the label ($i = 1, 2, 3$) enumerates one of three possible sets of the Jacobi coordinates ($\mathbf{r}_i, \boldsymbol{\rho}_i$). Every term in Eq. (45) takes the form

$$\Psi_{\text{ex}}^{(i)} = \sum_\gamma \sum_n C_n^\gamma \Phi_{\gamma n}^{(i)}. \quad (46)$$

The basis functions $\Phi_{\gamma n}^{(i)}$ are constructed from Gaussian functions and corresponding spin-angular and isospin factors:

$$\Phi_{\gamma n}^{(i)} = N_n^\gamma r_i^{\lambda_i} \rho_i^{l_i} \exp\{-\alpha_{\gamma n} r_i^2 - \beta_{\gamma n} \rho_i^2\} \quad (47)$$

$$\times \mathcal{F}_\gamma^{(i)}(\hat{\mathbf{r}}_i, \hat{\boldsymbol{\rho}}_i) \mathcal{T}_\gamma^{(i)},$$

where the spin-angular $\mathcal{F}_\gamma^{(i)}(\hat{\mathbf{r}}_i, \hat{\boldsymbol{\rho}}_i)$ and isospin $\mathcal{T}_\gamma^{(i)}$ components of the basis functions are given in the Appendix and the composite label $\gamma \equiv \gamma(i) = \{\lambda_i l_i LS_{jk} St_{jk}\}$ represents the respective set of quantum numbers for the basis functions (47): λ_i is the orbital angular momentum of the (jk) pair; l_i is the orbital angular momentum of the third nucleon (i) relative to the center of mass for the (jk) pair; L is the total orbital angular momentum of the $3N$ system; S_{jk} and t_{jk} are the spin and isospin of the (jk) pair, respectively; and S is the total spin of the system. We omit here the total angular momentum $J = 1/2$ and its z projection M, as well as the total isospin of the system $T = 1/2$ and its projection T_z (in this work, we neglect the very small contribution of the $T = 3/2$ component).

The nonlinear parameters of the basis functions $\alpha_{\gamma n}$ and $\beta_{\gamma n}$ are chosen on the Chebyshev grid, which provides the completeness of the basis and fast convergence of variational calculations [46]. As was demonstrated earlier [47], this few-body Gaussian basis is very flexible and can represent quite complicated few-body correlations. Therefore, it leads to accurate eigenvalues and eigenfunctions. The

formulas for the matrix elements of the Hamiltonian (for local NN interactions) on the antisymmetrized Gaussian basis are given in paper [45]. The matrix elements of DBM interactions on this basis are given in the Appendix.

Wave function in the internal $6qN$ channel. Having the $3N$ component Ψ_{3N} found in the above variational calculation, one can construct the inner $6qN$-channel wave function $\Psi_{in}^{(i)}$, which depends on the coordinate (or momentum) of the third nucleon and the σ-meson momentum and includes the bag wave function [see Eq. (30)]. By integrating the modulus squared of this function with respect to the meson momentum and inner variables of the bag, one obtains the density distribution of the third nucleon relative to the $6q$ bag in the $6qN$ channel. This density can be used to calculate further all observables whose operators depend on the variables of the nucleons and the bag. However, it is much more convenient and easier to deal with the quasi wave function of the third nucleon in the $6qN$ channel, which has been introduced by Eq. (35).

To calculate matrix elements of the 3BF Coulomb and OPE forces, one needs the spin−isospin part of $6qN$ components of the total wave function. Here, we give them explicitly. The potential form factors $\varphi_{L_i}^{J_i M_i}$ now include the spin−isospin part $\mathcal{Y}_{L_i S_d}^{J_i M_i}(\hat{\mathbf{p}}_i)\mathcal{T}_{t_d}^{(i)}$ with quantum numbers corresponding to the dressed bag:

$$\varphi_{L_i S_d}^{J_i M_i t_d t_{dz}} = \phi_{L_i}^{J_i}(p_i)\mathcal{Y}_{L_i S_d}^{J_i M_i}(\hat{\mathbf{p}}_i)\mathcal{T}_{t_d}^{(i)}; \qquad (48)$$

$$\mathcal{T}_{t_d}^{(i)} = |t_j t_k : t_d t_{dz}\rangle.$$

The full set of the quantum numbers labeling the form factors includes the total (J_i) and orbital (L_i) angular momenta, related to the vertex form factor, and also the spin and isospin numbers S_d, t_d, and t_{dz}, related to the dressed bag. However, since the present version of the DBM involves the bag states with zero orbital angular momentum, we have $S_d = J_i$, while the bag spin and isospin are supplementary to each other: $t_d + S_d = 1$. Hence, we will omit the quantum numbers S_d and t_d where they are unnecessary.

The total overlap function $\chi_{L_i}^{J_i M_i}(i) = \langle \varphi_{L_i}^{J_i M_i}|\Psi_{3N}\rangle$ can be written (with its spin−isospin part), e.g., as

$$\chi_{L_i}^{J_i M_i}(\mathbf{q}_i) \qquad (49)$$

$$= \sum_{l_i \mathcal{J}} \Phi_{l_i \mathcal{J}}^{J_i L_i}(q_i)\langle \mathcal{J} m_{\mathcal{J}} J_i M_i|JM\rangle$$

$$\times \mathcal{Y}_{l_i \frac{1}{2}}^{\mathcal{J} m_{\mathcal{J}}}(\hat{\mathbf{q}}_i)\langle t_d t_{dz}\tfrac{1}{2}t_{z_i}|TT_z\rangle\mathcal{T}_{\frac{1}{2}t_{z_i}}.$$

Here, J and M are the total angular momentum of the $3N$ system and its z projection; T and T_z are the total isospin of the $3N$ system and its z projection;

l_i and $\mathcal{J}$ are the orbital and total angular momenta of the third (ith) nucleon, respectively; and $\mathcal{T}_{\frac{1}{2}t_{z_i}}$ is isospinor corresponding to the third nucleon. In the present calculation for the ground states of ^{3}H and ^{3}He (with $J = 1/2$), we have considered the two lowest even partial wave components (S and D) in $3N$ wave functions only. Therefore, l_i can take only two values: 0 or 2. Moreover, the total angular momentum of the third nucleon $\mathcal{J}$ is uniquely determined by value of l_i: $\mathcal{J} = 1/2$ at $l_i = 0$ and $\mathcal{J} = 3/2$ at $\lambda_i = 2$. So, actually, there is no summation over $\mathcal{J}$ in Eq. (49).

It is easy to see that the three form factors $\varphi_{L_i}^{J_i}$ used in the present work (φ_0^0, φ_0^1, and φ_2^1) determine five radial components of the overlap function $\Phi_{l_i \mathcal{J}}^{J_i L_i}(q_i)$ and five respective components of the quasi wave function for the $6qN$ channel. To specify these components, it is sufficient to give three quantum numbers, e.g., S_d, l_i, and L_i, and we will use the notation $\Psi_{S_d l_i, L_i}^{in}(q_i)$ for these radial components:

$$\Psi_{00,0}^{in} : \left(J_i = S_d = 0, t_d = 1, L_i = 0, l_i = 0, \mathcal{J} = \frac{1}{2}\right),$$

$$\Psi_{10,0}^{in} : \left(J_i = S_d = 1, t_d = 0, L_i = 0, l_i = 0, \mathcal{J} = \frac{1}{2}\right),$$

$$\Psi_{12,0}^{in} : \left(J_i = S_d = 1, t_d = 0, L_i = 0, l_i = 2, \mathcal{J} = \frac{3}{2}\right),$$

$$\Psi_{10,2}^{in} : \left(J_i = S_d = 1, t_d = 0, L_i = 2, l_i = 0, \mathcal{J} = \frac{1}{2}\right),$$

$$\Psi_{12,2}^{in} : \left(J_i = S_d = 1, t_d = 0, L_i = 2, l_i = 2, \mathcal{J} = \frac{3}{2}\right).$$

Finally, we give a formula for the total quasi wave function in internal channel (i), separating out explicitly its spin-angular and isospin parts, which include the spin−isospin part of the bag wave function:

$$\Psi_i^{in} = \sum_{l_i S_d}\left\{\sum_{L_i}\Psi_{S_d l_i, L_i}^{in}(q_i)\right\} \qquad (50)$$

$$\times \left|l_i \tfrac{1}{2}(\mathcal{J})S_d : JM\right\rangle\left|t_d \tfrac{1}{2} : TT_z\right\rangle.$$

The explicit dependence of this function on the isospin projection T_z is important for calculation of the Coulomb matrix elements and rms charge radius.

The interaction matrix elements include the overlap integrals of the potential form factors with the basis functions $\Phi_{\gamma,n} = \Phi_{\gamma,n}^{(1)} + \Phi_{\gamma,n}^{(2)} + \Phi_{\gamma,n}^{(3)}$, where all five above components of the overlap function enter the matrix elements independently (certainly, some of the matrix elements can vanish). The explicit formulas for the above overlap functions and detailed

formulas for the matrix elements of all DBM interactions are given in the Appendix. When calculating both the normalization of the internal components and observables, the $6qN$ components distinguished only by their radial parts can be summed. Thus, only three different components of the $6qN$ quasi wave function remain: one S-wave singlet ($S_d = 0$),

$$\Psi_{00}^{\text{in}} \equiv \Psi_{00,0}^{\text{in}},$$

and two triplet ones ($S_d = 1$):

$$\Psi_{10}^{\text{in}} = \Psi_{10,0}^{\text{in}} + \Psi_{10,2}^{\text{in}}, \quad \Psi_{12}^{\text{in}} = \Psi_{12,0}^{\text{in}} + \Psi_{12,2}^{\text{in}}. \quad (51)$$

The total weight of each of the three $6qN$ components is equal to

$$P_{\text{in}}^{(i)} = ||\Psi_{00}^{\text{in}}||^2 + ||\Psi_{10}^{\text{in}}||^2 + ||\Psi_{12}^{\text{in}}||^2, \quad (52)$$
$$i = 1, 2, 3.$$

Now, let us introduce the relative weights of the individual $6qN$ components:

$$P_{S0}^{\text{in}} = \frac{||\Psi_{00}^{\text{in}}||^2}{P_{\text{in}}^{(i)}}, \quad P_{S1}^{\text{in}} = \frac{||\Psi_{10}^{\text{in}}||^2}{P_{\text{in}}^{(i)}}, \quad (53)$$

$$P_D^{\text{in}} = \frac{||\Psi_{12}^{\text{in}}||^2}{P_{\text{in}}^{(i)}}.$$

After renormalization of the full four-component wave function, the total weight of all internal components is equal to

$$P_{\text{in}} = \frac{3P_{\text{in}}^{(i)}}{1 + 3P_{\text{in}}^{(i)}} \quad (54)$$

(here, we assume that the $3N$ component of the total wave function, Ψ^{ex}, obtained from the variational calculation, is normalized to unity), while the total weight of the $3N$ component Ψ_{3N} is equal to

$$P_{\text{ex}} = \frac{1}{1 + 3P_{\text{in}}^{(i)}} = 1 - P_{\text{in}}. \quad (55)$$

It is also interesting to find the total weight of the D wave with allowance for nonnucleonic components:

$$P_D = P_D^{\text{ex}}(1 - P_{\text{in}}) + P_D^{\text{in}}P_{\text{in}}. \quad (56)$$

Numerical values of all above probabilities for internal and external components are given below in Table 2. The total weight of all $6qN$ components $P_{6qN} \equiv P_{\text{in}}$ in the $3N$ system turns out to be rather large and approaches or even exceeds 10%. Furthermore, taking into account the short-range character of these components and the much harder nucleon momentum distribution (closely associated with the first property) for these components, as well as very strong scalar three-body interaction in the internal $6qN$ channels, one can conclude that these nonnucleonic components are extremely important for the properties of nuclear systems.

6. COULOMB EFFECTS IN ^{3}He

In this section, we will demonstrate that the DBM approach leads to some new features related to the Coulomb effects in nuclei, and, in particular, in ^{3}He. First of all, the additional Coulomb force arises because the $6q$ bag and rest nucleon can have electric charges. We have found that this new Coulomb three-body force is responsible for a significant part of the total ^{3}He Coulomb energy (this three-body Coulomb force has been missed fully in previous $3N$ calculations within hybrid $6qN$ models [48]).

The second feature of the interaction model used here is the absence of the local NN short-range repulsive core. The role of this core is played by the condition of orthogonality to the confined $6q$ states forbidden in the external NN channel. This orthogonality requirement imposed on the relative-motion NN wave function is responsible for the appearance of some inner nodes and respective short-range loops in this wave function. These short-range nodes and loops lead to numerous effects and general consequences for the nuclear structure. One of these consequences is a rather strong overestimation of the Coulomb contribution when using the interaction between pointlike nucleons. Thus, it is necessary to take into account the finite radius of the nucleon charge distribution.[9]

Finally, in order to obtain an accurate Coulomb displacement energy $\Delta E_{\text{C}} = E_B(^3\text{H}) - E_B(^3\text{He})$, one should take into consideration the effects associated with the small mass difference between the proton and neutron. It is well known [49] that the above mass difference makes a rather small contribution to the difference between the ^{3}He and ^{3}H binding energies. Therefore, it was usually taken into account in a perturbation approach. However, since the average kinetic energy in our case is twice the kinetic energy in conventional force models, this correction is also expected to be much larger in our case. Hence, we present here the estimation for such a correction term without using perturbation theory.

6.1. "Smeared" Coulomb Interaction

The Gaussian charge distribution $\rho(r)$ that corresponds to the rms charge radius r_{ch} and is normalized to the total charge z, $4\pi \int \rho r^2 dr = z$, can be written as

$$\rho(r) = z \left(\frac{\alpha}{\pi}\right)^{3/2} e^{-\alpha r^2}, \quad \alpha^{-1} = \frac{2}{3}r_{\text{ch}}^2. \quad (57)$$

---

[9] We recall at this point that accounting for the finite radii of nucleons in the conventional approaches leads to fully negligible corrections to the Coulomb energy.

The Coulomb potential for the interaction between such a charge distribution $\rho(r)$ and a pointlike charged particle has the well-known form

$$V(R) = \int \frac{d\mathbf{r}\rho(r)}{|\mathbf{R} - \mathbf{r}|} = \frac{z}{R}\mathrm{erf}(R\sqrt{\alpha}).$$

We have derived here a similar formula for the Coulomb interaction between two Gaussian distributions with different widths α_1 and α_2 and rms radii r_{ch_1} and r_{ch_2}, respectively:

$$V(R; \alpha_1, \alpha_2) = \frac{z_1 z_2}{R}\mathrm{erf}(R\sqrt{\tilde{\alpha}}), \qquad (58)$$

$$\tilde{\alpha} = \frac{\alpha_1 \alpha_2}{\alpha_1 + \alpha_2}, \text{ or } \tilde{\alpha}^{-1} = \frac{2}{3}(r_{\mathrm{ch}_1}^2 + r_{\mathrm{ch}_2}^2).$$

In our calculations, we used the following charge radii for the nucleon and dibaryon:

$$(r_{\mathrm{ch}})_p = 0.87 \text{ fm}, \quad (r_{\mathrm{ch}})_{6q} = 0.6 \text{ fm}.^{10)}$$

These values lead to the "smeared" Coulomb interactions in the NN and $6qN$ channels:

$$V_{NN}^{\mathrm{Coul}}(r) = \frac{e^2}{r}\mathrm{erf}(r\sqrt{\alpha_{NN}}), \quad \alpha_{NN}^{-1/2} = 1.005 \text{ fm},$$

$$(59)$$

$$V_{\mathrm{in}}^{\mathrm{Coul}}(\rho) = \frac{e^2}{\rho}\mathrm{erf}(\rho\sqrt{\alpha_{\mathrm{in}}}), \quad \alpha_{\mathrm{in}}^{-1/2} = 0.863 \text{ fm}.$$

6.2. Matrix Elements of the Three-Body Coulomb Force

The Coulomb interaction between the charged bag and the third nucleon in the $6qN$ channel is determined by the three-particle operator with the separable kernel [see Eq. (36)]:

$$^{\mathrm{Coul}}W^{(i)}(\mathbf{p}_i, \mathbf{p}_i'; \mathbf{q}_i, \mathbf{q}_i') \qquad (60)$$

$$= \sum_{J_i M_i L_i L_i'} \varphi_{L_i}^{J_i M_i}(\mathbf{p}_i)\frac{1 + \tau_3^{(i)}}{2}$$

$$\times (1 + \hat{t}_{d_z})^{\mathrm{Coul}}W_{L_i L_i'}^{J_i}(\mathbf{q}_i, \mathbf{q}_i'; E)\varphi_{L_i'}^{J_i M_i}(\mathbf{p}_i'),$$

where $(1 + \tau_3^{(i)})/2$ is the operator of the ith nucleon charge and $1 + \hat{t}_{d_z}$ is the operator of the bag charge. It

---

10) This value is simply the rms charge radius of the $6q$ bag with the parameters given in [24]. The neutral σ field of the bag changes this value only slightly. The evident difference between the charge radii of the nucleon and dibaryon can be well understood as follows: the charge radius of the $3q$ core of the nucleon is usually taken as $r_{\mathrm{ch}}^{3q} \simeq 0.5-0.55$ fm, while remaining 0.3 fm is assumed to come from the charge distribution of the π^+ cloud surrounding the $3q$ core in the proton. In contrast, the meson cloud of the dibaryon in our approach is mainly due to the neutral scalar–isoscalar σ meson, so that the dibaryon charge distribution is characterized by the charge radius of the bare $6q$ core only.

is evident that the matrix element of the operator (60) can be expressed in terms of the integrals of the product of the overlap functions $\chi_{L_i}^{J_i M_i}(\mathbf{q}_i)$ of NN form factors and three-body basis functions. The method for calculation of such Coulomb integrals is given in the Appendix.

7. RESULTS OF CALCULATIONS

Here, we present the results of the $3N$ bound-state calculations based on two variants of the DBM.

(I) In the first version developed in [24], the dressed-bag propagator includes three loops (two loops are with pions and one loop is with the σ meson). Two of them are of the type shown in Fig. 2 of [24], in which each loop was calculated within the $^3P_0$ model for quark–meson interaction. The third loop consists of two such vertices and a convolution of the σ-meson and $6q$-bag propagators [24].

(II) In the second version, we replaced the two above pionic loops with the effective Gaussian form factor $B(k)$, which describes the direct $NN \to 6q + \sigma$ transition, i.e., the direct transition from the NN channel to the dressed-dibaryon channel.

Both versions have been fitted to the NN phase shifts in low partial waves up to an energy of 1 GeV with almost the same quality. Therefore, they can be considered on equal footing. However, version II has one important advantage. Here, the energy dependence arising from the convolution of the two propagators involved into the loop, i.e., the propagators of the σ meson and bare dibaryon, describes (with no further correction) just the energy dependence of the effective strength of the NN potential $\lambda^{(\mathrm{II})}(E)$, which is thereby taken directly from the above loop integral. In contrast, in the first version of the model, two additional $qq\pi\pi\sigma$ loops give a rather singular three-dimensional integral for $\lambda^{(\mathrm{I})}(E)$, where the energy dependence at higher energies should be corrected by a linear term.

7.1. Bound-State Energies of ^3H and ^3He and Individual Contributions to Them

The main difference between the results for both versions is that the energy dependence of $\lambda(E)$ for the second version is much weaker than that for the first one. In addition, this energy dependence leads to some decrease in the contribution of the $6qN$ component to all $3N$ observables and thus to the respective increase of the two-body force contribution as compared to the three-body force one. Table 2 presents the calculation results for the two above versions for the following characteristics: the weights of the internal $6qN$ channels and D wave in the total $3N$

Table 2. Results of the $3N$ calculations with two- and three-body forces for two variants of the DBM

Model	E, MeV	P_D, %	$P_{S'}$, %	$P_{6qN}(P_{in})$, %	Contributions to H, MeV		
					T	$T + V^{(2N)}$	$V^{(3N)}$
				^{3}H			
DBM(I) $g = 9.577$[a]	-8.482	6.87	0.67	10.99	112.8	-1.33	-7.15
DBM(II) $g = 8.673$[a]	-8.481	7.08	0.68	7.39	112.4	-3.79	-4.69
AV18 + UIX[b]	-8.48	9.3	1.05	$-$	51.4	-7.27	-1.19
				^{3}He			
DBM(I)	-7.772	6.85	0.74	10.80	110.2	-0.90	-6.88
DBM(II)	-7.789	7.06	0.75	7.26	109.9	-3.28	-4.51
AV18 + UIX[b]	-7.76	9.25	1.24	$-$	50.6	-6.54	-1.17

[a] These values of the σNN coupling constant in ^{3}H calculations have been chosen to reproduce the exact binding energy of the ^{3}H nucleus. The calculations for ^{3}He have been carried out without any free parameters.

[b] The values are taken from [50].

function, as well as the weight of the mixed-symmetry S' component (only for the $3N$ channel); the average individual contributions from the kinetic energy T, two-body interactions $V^{(2N)}$ plus the kinetic energy T, and three-body force ($V^{(3N)}$) due to OSE and TSE to the total Hamiltonian expectation.

The percentages of the D wave and the internal components given in Table 2 were obtained with incorporation of the three internal components; i.e., these values correspond to the normalization of the total (four-component) wave function of the system to unity.

To compare the predictions of the new model with the respective results for the conventional NN potential models, Table 2 also presents the results of recent calculations with the Argonne potential AV18 and Urbanna−Illinois 3BF UIX [50].

7.2. The Densities, rms Radii and Charge Distributions in ^{3}H and ^{3}He

First, we give definitions of the nucleon and charge distributions in the multichannel system.

The external $3N$ channel. The proton (ρ_p) and neutron (ρ_n) densities in this channel are defined in the standard way [51]:

$$\rho^{ex}_{\{^p_n\}}(r) \qquad (61)$$

$$= \frac{1}{N_{\{^p_n\}}} \left\langle \Psi^{ex} \sum_{i=1}^{3} \left| \frac{\delta(r - \frac{3}{2}\rho_i)}{r^2} \frac{1 \pm \tau_3^{(i)}}{2} \right| \Psi^{ex} \right\rangle$$

$$= \frac{3}{N_{\{^p_n\}}} \left\langle \Psi^{ex} \left| \frac{\delta(r - \frac{3}{2}\rho_1)}{r^2} \frac{1 \pm \tau_3^{(1)}}{2} \right| \Psi^{ex} \right\rangle,$$

where ρ_i is Jacobi coordinate in the set (i) and $N_{\{^p_n\}}$ is the number of protons (neutrons). Due to the property

$$\left\langle \Psi^{ex} \left| \sum_{i=1}^{3} \frac{1 \pm \tau_3^{(i)}}{2} \right| \Psi^{ex} \right\rangle = \left\langle \Psi^{ex} \left| \frac{3}{2} \pm \hat{T}_3 \right| \Psi^{ex} \right\rangle$$

$$= \frac{3}{2} \pm \hat{T}_3 = N_{\{^p_n\}},$$

the above densities are normalized to unity, provided that the external wave function Ψ^{ex} is also normalized to unity:

$$\int \rho^{ex}_{\{^p_n\}}(r) r^2 dr = 1.$$

The matrix element $\langle \Psi^{ex} | \tau_3^{(i)} | \Psi^{ex} \rangle$ is proportional to the z projection of the total isospin T_3; therefore, the nucleon densities can be separated into isoscalar (matter) density and isovector parts:

$$\rho_s(r) = \rho_m = \left\langle \Psi^{ex} \left| \frac{\delta\left(r - \frac{3}{2}\rho_1\right)}{r^2} \right| \Psi^{ex} \right\rangle, \quad (62)$$

$$\rho_v(r) = \frac{3}{2T_3} \left\langle \Psi^{ex} \left| \frac{\delta(r - \frac{3}{2}\rho_1)}{r^2} \tau_3^{(1)} \right| \Psi^{ex} \right\rangle. \quad (63)$$

Both latter densities are also normalized to unity. Then the nucleon densities can be expressed in terms of isoscalar and isovector densities as

$$\rho^{ex}_p(^3\text{He}) = \rho^{ex}_n(^3\text{H}) = \frac{1}{4}(3\rho_s + \rho_v), \quad (64)$$

$$\rho^{ex}_p(^3\text{H}) = \rho^{ex}_n(^3\text{He}) = \frac{1}{2}(3\rho_s - \rho_v).$$

The rms radii of the corresponding distributions are equal to

$$\langle r^2 \rangle_{\{s,v,p,n\}}^{\mathrm{ex}} = \int \rho_{\{s,v,p,n\}}^{\mathrm{ex}}(r) r^4 dr. \qquad (65)$$

The rms charge radius in the $3N$ sector is also defined conventionally:

$$\langle r_{\mathrm{ch}}^2 \rangle^{\mathrm{ex}} = \langle r^2 \rangle_p^{\mathrm{ex}} + R_p^2 + \frac{N_n}{N_p} R_n^2, \qquad (66)$$

where $R_p^2 = 0.7569$ fm^2 and $R_n^2 = -0.1161$ fm^2 are the squared charge radii of the proton and neutron, respectively.

The various types of one-particle densities (isoscalar, isovector, proton, neutron) in the external $3N$ channel for the ^{3}H and ^{3}He ground states calculated in DBM(I) are shown in Fig. 5.

Below, we present also the two-proton density for ^{3}He, which is defined usually as [52]

$$\rho_{pp}(r) = 6 \left\langle \Psi^{\mathrm{ex}} \left| \frac{\delta(r - r_1)}{r^2} \frac{1 + \tau_3^{(2)}}{2} \frac{1 + \tau_3^{(3)}}{2} \right| \Psi^{\mathrm{ex}} \right\rangle. \qquad (67)$$

This density is normalized to 2: $\int \rho_{pp}(r) r^2 dr = 2$. (As there is only a single nucleon in the $6qN$ channel, we do not attach the index "ex" to this quantity.) The two-neutron density $\rho_{nn}(r)$ for ^{3}H is defined similarly [with replacement $1 + \tau_3^{(i)} \to 1 - \tau_3^{(i)}$ in Eq. (67)]. In Fig. 6, we show both these densities for DBM(I) and also the two-proton density for ^{3}He found with the Bonn NN potential [52].

The internal $6qN$ channels. Here, we define the density (normalized to unity) of the pure nucleon distributions as

$$\rho_{\{\begin{smallmatrix}p\\n\end{smallmatrix}\}}^{\mathrm{in}}(r) \qquad (68)$$

$$= \frac{1}{N_{\{\begin{smallmatrix}p\\n\end{smallmatrix}\}}^{\mathrm{in}} P_{\mathrm{in}}^{(1)}} \left\langle \Psi_1^{\mathrm{in}} \left| \frac{\delta(r - \alpha \rho_1)}{r^2} \frac{1 \pm \tau_3^{(1)}}{2} \right| \Psi_1^{\mathrm{in}} \right\rangle,$$

where $P_{\mathrm{in}}^{(1)} = \langle \Psi_1^{\mathrm{in}} | \Psi_1^{\mathrm{in}} \rangle$ and the quantity

$$N_{\{\begin{smallmatrix}p\\n\end{smallmatrix}\}}^{\mathrm{in}} = \frac{1}{P_{\mathrm{in}}^{(1)}} \left\langle \Psi_1^{\mathrm{in}} \left| \frac{1 \pm \tau_3^{(1)}}{2} \right| \Psi_1^{\mathrm{in}} \right\rangle \qquad (69)$$

has the meaning of the average number of protons (neutrons) in the one internal $6qN$ channel (note that $N_p^{\mathrm{in}} + N_n^{\mathrm{in}} = 1$, i.e., there is only one nucleon in each internal channel). The number $N_{\{\begin{smallmatrix}p\\n\end{smallmatrix}\}}^{\mathrm{in}}$ depends on the ratio of norms of $6qN$ components with different values of isospin of the bag. Therefore, the separation of the $6qN$-channel density into isoscalar and isovector parts has no meaning.

These average numbers of nucleons in $6qN$ channel can be expressed through relative probabilities of the $6qN$ components with a definite value of isospin t, which in our case are equal to

$$P_0^{\mathrm{in}} \equiv P_{t=0}^{\mathrm{in}} = P_{S1}^{\mathrm{in}} + P_D^{\mathrm{in}}, \quad P_1^{\mathrm{in}} \equiv P_{t=1}^{\mathrm{in}} = P_{S0}^{\mathrm{in}}, \qquad (70)$$

where P_{S1}^{in}, P_D^{in}, and P_{S0}^{in} are determined by Eq. (53). Hence, $P_{t=0}^{\mathrm{in}} + P_{t=1}^{\mathrm{in}} = 1$. Then one can write the average numbers of nucleons as

$$N_p^{\mathrm{in}}(^3\mathrm{H}) = N_n^{\mathrm{in}}(^3\mathrm{He}) = \frac{2}{3} P_{t=1}^{\mathrm{in}}, \qquad (71)$$

$$N_p^{\mathrm{in}}(^3\mathrm{He}) = N_n^{\mathrm{in}}(^3\mathrm{H}) = P_{t=0}^{\mathrm{in}} + \frac{1}{3} P_{t=1}^{\mathrm{in}}.$$

The nucleon densities (61) can be expressed by a similar formula through components of the internal wave function with a definite value of isospin t.

The total densities of nucleon distributions. The total nucleon densities (normalized to unity) for the whole $3N$ system, with allowance for both the $3N$ and $6qN$ components, can now be defined as

$$\rho_{\{\begin{smallmatrix}p\\n\end{smallmatrix}\}} = \frac{(1 - P_{\mathrm{in}}) \rho_{\{\begin{smallmatrix}p\\n\end{smallmatrix}\}}^{\mathrm{ex}} N_{\{\begin{smallmatrix}p\\n\end{smallmatrix}\}} + P_{\mathrm{in}} \rho_{\{\begin{smallmatrix}p\\n\end{smallmatrix}\}}^{\mathrm{in}} N_{\{\begin{smallmatrix}p\\n\end{smallmatrix}\}}^{\mathrm{in}}}{\langle N_{\{\begin{smallmatrix}p\\n\end{smallmatrix}\}} \rangle}, \quad (72)$$

where $P_{\mathrm{in}} = 3 P_1^{\mathrm{in}} / (1 + 3 P_1^{\mathrm{in}})$ is the total weight of all three internal channels [Eq. (54)] and the denominator

$$\langle N_{\{\begin{smallmatrix}p\\n\end{smallmatrix}\}} \rangle = (1 - P_{\mathrm{in}}) N_{\{\begin{smallmatrix}p\\n\end{smallmatrix}\}} + P_{\mathrm{in}} N_{\{\begin{smallmatrix}p\\n\end{smallmatrix}\}}^{\mathrm{in}} < N_{\{\begin{smallmatrix}p\\n\end{smallmatrix}\}} \quad (73)$$

Table 3. Isospin structure of $6qN$ channel, average number of nucleons, and average mass calculated with the ground-state wave functions of ^{3}H and ^{3}He in the DBM approach

|	^{3}H		^{3}He	
	DBM(I)	DBM(II)	DBM(I)	DBM(II)
$P_{t=1}^{\mathrm{in}}$	0.6004	0.6005	0.6044	0.6044
$P_{t=0}^{\mathrm{in}}$	0.3996	0.3995	0.3956	0.3956
$3N_p^{\mathrm{in}}$	0.799	0.799	2.209	2.209
$3N_n^{\mathrm{in}}$	2.201	2.201	0.791	0.791
$\langle N_p \rangle$	0.919	0.945	1.863	1.908
$\langle N_n \rangle$	1.861	1.906	0.920	0.947
$\langle N \rangle$	2.780	2.852	2.784	2.855
$\langle m \rangle / (3 m_N)$	1.015	1.010	1.014	1.010
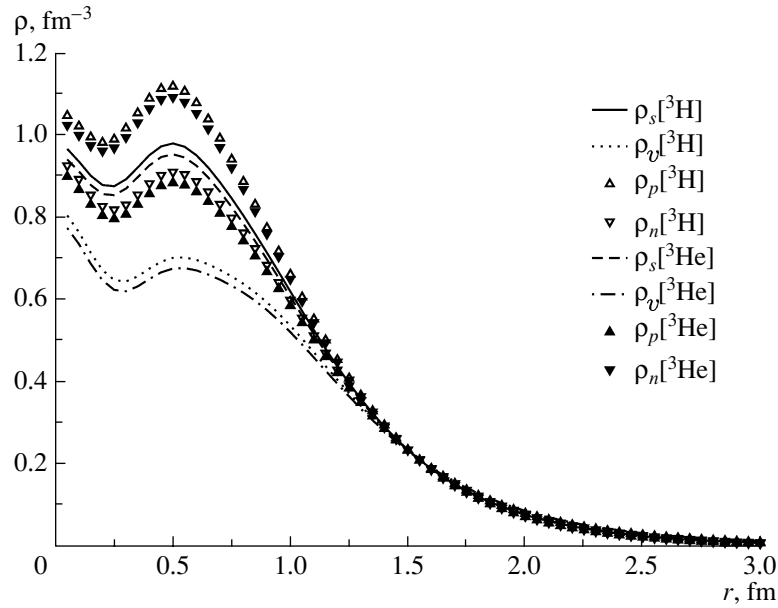
Fig. 5. The isoscalar ρ_s, isovector ρ_v, proton ρ_p, and neutron ρ_n densities in the external $3N$ channel for the ^{3}H and ^{3}He systems obtained with DBM (I).

is equal to the average number of protons (neutrons) in the whole multicomponent system. The densities of the total proton and neutron distributions and also external- and internal-channel distributions for ^{3}He calculated for DBM(I) are presented in Fig. 7.

One can also define a (normalized) density of the matter (or mass) distribution in the $6qN$ channel as

$$r^2 \rho_m^{\text{in}}(r) = \frac{1}{(m_N + m_d)P_{\text{in}}} \tag{74}$$

$$\times \langle \Psi_1^{\text{in}} | \delta(r - \alpha\rho_1)m_N + \delta(r - (1-\alpha)\rho_1)m_d | \Psi_1^{\text{in}} \rangle,$$
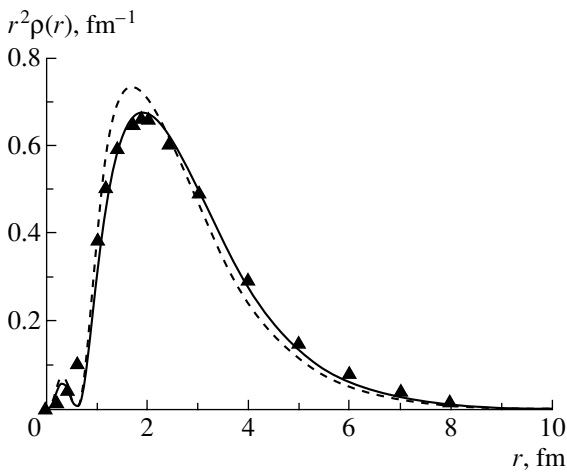
Fig. 6. The two-proton density in ^{3}He (solid curve) and the two-neutron density in ^{3}H (dashed curve) calculated with DBM (I) in comparison with the two-proton density for the Bonn potential [52] (triangles).

where $\alpha = m_d/(m_d + m_N)$, m_N is a nucleon mass, and m_d is the mass of the bag (dibaryon). Then the total matter density (normalized to unity) is equal to

$$r^2 \rho_m(r) = \frac{(1 - P_{\text{in}})\rho_m^{\text{ex}} \cdot 3m_N + P_{\text{in}}\rho_m^{\text{in}}(m_N + m_d)}{\langle m \rangle}. \tag{75}$$

The rms radius of any distribution normalized to unity is defined by Eq. (65). The denominator in Eq. (75) determines the average mass of the whole system taking into account nonnucleonic channels:

$$\langle m \rangle = (1 - P_{\text{in}})3m_N + P_{\text{in}}(m_N + m_d) \tag{76}$$

$$= 3m_N + P_{\text{in}}(m_d - 2m_N) > 3m_N.$$

In Table 3 we present some characteristics of isospin structure for wave functions in the $6qN$ channel: the relative probabilities for the components with $t = 0$ and $t = 1$ (i.e., $P_{t=0}^{\text{in}}$ and $P_{t=1}^{\text{in}}$), average numbers of protons and neutrons in all three $6qN$ components $(3\langle N_{\{^p_n\}} \rangle)$, and also the average number of nucleons $\langle N \rangle$ and the average mass $\langle m \rangle$ (divided by $3m_N$ value) in the whole four-component $3N$ system. It should be noted that the average number of nucleons in our multicomponent model, $\langle N_{\{^p_n\}} \rangle$, is always less than the numbers of nucleons in the $3N$ channel just due to the existence of the nonnucleonic components. For example, for DBM(I), the average number of protons in ^{3}H is approximately equal to the average number of neutrons in ^{3}He, viz., $\langle N_p \rangle(^3$H$) \approx \langle N_n \rangle(^3He)$, and is equal to 0.92, while the average
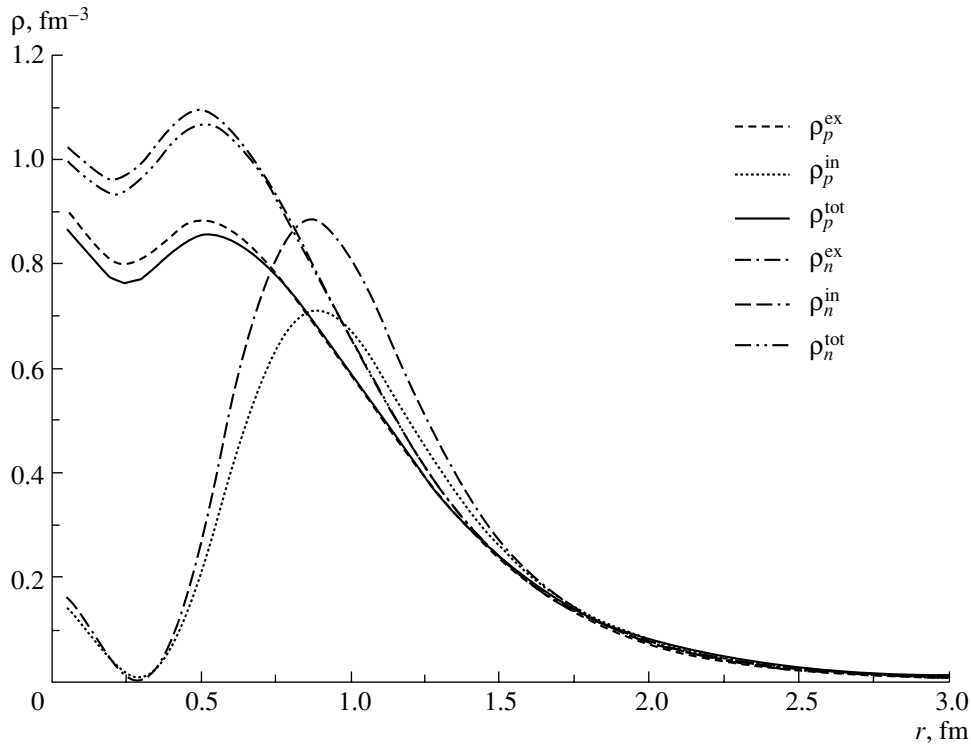
Fig. 7. The external ρ^{ex}, internal ρ^{in}, and total ρ^{tot} densities of proton and neutron distributions in ^{3}He found with DBM (I).

number of neutrons in ^{3}H is approximately equal to the average number of protons in ^{3}He, viz., $\langle N_n \rangle (^3\mathrm{H}) \approx \langle N_p \rangle (^3\mathrm{He})$, and is equal to 1.86. Hence, the average number of nucleons found with the total multicomponent ^{3}H and ^{3}He functions is also always less than 3:

$$\langle N \rangle = \langle N_p \rangle + \langle N_n \rangle = 3 - 2P_{\mathrm{in}} < 3.$$

In our DBM, $\langle N \rangle$ is equal to 2.78 and 2.85 for versions I and II, respectively.

The charge distributions. The charge distribution for the pointlike particles in the $6qN$ channel can be written as the charge density of a system consisting of a pointlike nucleon and a pointlike bag:

$$r^2 \rho^{\mathrm{in}}_{\mathrm{ch-point}}(r) = \frac{1}{Z} \left\langle \Psi^{\mathrm{in}}_1 \left| \delta(r - \alpha\rho_1)\frac{1 + \tau_3^{(1)}}{2} + \delta(r - (1-\alpha)\rho_1)(1 + \hat{t}_3) \right| \Psi^{\mathrm{in}}_1 \right\rangle, \tag{77}$$

where $1 + \hat{t}_3$ is the operator of the bag charge. The total charge radius in $6qN$ channel includes the rms radius of this pointlike distribution $\langle r^2 \rangle^{\mathrm{in}}_{\mathrm{ch-point}}$, the nucleon charge radius (R_p or R_n), and the charge bag radius R_d, which depends on the bag isospin t and its projection t_3:

$$\langle r^2 \rangle^{\mathrm{in}}_{\mathrm{ch}} = \langle r^2 \rangle^{\mathrm{in}}_{\mathrm{ch-point}} + \frac{1}{Z}\left(N^{\mathrm{in}}_p R^2_p + N^{\mathrm{in}}_n R^2_n \right. \tag{78}$$

$$\left. + \left\langle \Psi^{\mathrm{in}}_1 \left| \sum_{t,t_3} \Gamma_{t,t_3} R^2_d(t,t_3) \right| \Psi^{\mathrm{in}}_1 \right\rangle \right).$$

The last term in Eq. (78) includes the projectors Γ_{t,t_3} onto the $6q$-bag isospin state with definite values of isospin t and its projection t_3 and is equal to (for the ^{3}H and ^{3}He states with total isospin $T = 1/2$)

$$\Delta(r^2_{\mathrm{ch}})^{\mathrm{in}}_{\mathrm{bag}} \tag{79}$$

$$= \frac{1}{Z}\left\{ R^2_d(0,0)P^{\mathrm{in}}_{t=0} + \left(\frac{1}{3}R^2_d(1,0) \right. \right.$$

$$\left. \left. + \frac{2}{3}R^2_d(1,1)\delta_{T_3,\frac{1}{2}} + \frac{2}{3}R^2_d(1,-1)\delta_{T_3,-\frac{1}{2}} \right) P^{\mathrm{in}}_{t=1} \right\}.$$

The characteristic charge radius of the $6q$ bag $R^2_d(t,t_3)$

Table 4. The total rms radii (in fm) for the proton (r_p), neutron (r_n), matter (r_m), and charge ($r_{\rm ch}$) distributions in the DBM approach and their separate values for external and internal channels

Model		^{3}H				^{3}He			
		r_p	r_n	r_m	$r_{\rm ch}$	r_p	r_n	r_m	$r_{\rm ch}$
DBM(I)	$3N$	1.625	1.770	1.723	1.779	1.805	1.648	1.754	1.989
	$6qN$	1.608	1.823	1.142	1.188	1.854	1.618	1.159	1.412
	Total	1.625	1.773	1.663	1.724	1.807	1.647	1.694	1.935
DBM(II)	$3N$	1.613	1.761	1.713	1.769	1.795	1.636	1.744	1.980
	$6qN$	1.573	1.797	1.124	1.171	1.829	1.583	1.141	1.396
	Total	1.613	1.762	1.672	1.732	1.796	1.635	1.703	1.944
AV18 + UIX[a]		1.59	1.73			1.76	1.61		
Experiment		1.60[b]			1.755	1.77[b]			1.95

[a] Taken from [53].

[b] These "experimental" values are taken from [53]. They have been obtained by subtraction of the characteristic proton and neutron charge radii squared (0.743 and -0.116 fm^2, respectively) from the experimental values of the charge radii squared.

has, in general, different values in different isospin states (which is related to the different multiquark dynamics in the channels with different isospin values), but we assume in this work that their difference can be ignored, viz.,

$$R_d^2(0,0) = R_d^2(1,0) = R_d^2(1,1) = R_d^2 = b_0^2, \quad (80)$$
$$b_0 = 0.6 \text{ fm}, \text{ and } R_d^2(1,-1) = 0$$

(which corresponds to an nn bag).

With the above assumptions, the $6q$-bag contribution to the ^{3}H and ^{3}He charge radius is reduced to

$$\Delta(r_{\rm ch}^2)_{\rm bag}^{\rm in} = \frac{R_d^2}{Z}\left(P_0^{\rm in} + \frac{2+2T_3}{3}P_1^{\rm in}\right). \quad (81)$$

The rms charge radius of whole multicomponent system is defined as

$$r_{\rm ch}^2 = (1 - P_{\rm in})\langle r^2 \rangle_{\rm ch}^{\rm ex} + P_{\rm in}\langle r^2 \rangle_{\rm in}^{\rm ex}.$$

In Table 4, we give the rms radii for all the above distributions in ^{3}H and ^{3}He found in the impulse approximation, as well as the respective experimental values and results obtained for AV18($2N$) + UIX($3N$) forces. To demonstrate the separate contributions of the $3N$ and $6qN$ channels to these observables, we also present the values calculated separately with only nucleonic and $6qN$ parts of the total wave function. It is seen from Table 4 that both versions

of our model (viz., DBM(I) and DBM(II)) give quite similar values for all the radii. The most interesting point here is the importance of $6qN$-component contributions. In fact, the contribution of the $6qN$ channel shifts all the radii, i.e., $r_{\rm ch}$ and r_p in ^{3}H and ^{3}He, predicted with pure nucleonic components in our approach, much closer to the respective experimental values. For example, the value $r_{\rm ch} = 1.822$ fm calculated for ^{3}H with only the nucleonic part of the wave function is substantially larger than the respective experimental value 1.755 fm. However, an admixture of a rather compact $6qN$ component ($r_{\rm ch} = 1.22$ fm) immediately shifts the ^{3}H charge radius down to a value of 1.766 fm, which is very close to its experimental value.

Thus, the dibaryon–nucleon component works in a right way also in this aspect. It is interesting to note that, in general, the predictions of our two-phase model are quite close to those of the conventional pure nucleonic AV18 + UIX model. This means that our multichannel model is effectively similar to a conventional purely nucleonic model (at least for many static characteristics). However, this similarity will surely hold only for the characteristics that are sensitive mainly to low-momentum transfers, while the properties and processes involving high-momentum transfers will be treated in two alternative approaches in completely different ways.

7.3. Coulomb Displacement Energy and Charge-Symmetry-Breaking Effects

The problem of accurate description of Coulomb effects in ^{3}He in the current $3N$ approach of the Faddeev or variational type has attracted much attention for the last three decades (see, e.g., [49, 54] and the references therein to the earlier works). It is interesting that the Coulomb puzzle in ^{3}He, being related to the long-range interactions, is treated in a different manner in our and conventional approaches.

The ΔE_C problem dates back to the first accurate $3N$ calculations performed on the basis of the Faddeev equations with realistic NN interactions in the mid-1970s [55]. These pioneering calculations first exhibited a hardly removable difference of about 120 keV between the theoretical prediction for $\Delta E_C^{th} \simeq 640$ keV and the respective experimental value $\Delta E_C^{exp} \simeq 760$ keV. In the subsequent 30 years, numerous accurate $3N$ calculations have been performed over the world using many approaches, but this puzzle is still generally unsolved. The most plausible quantitative explanation (but yet not free of serious questions) for the puzzle has recently been suggested by Nogga *et al.* [49]. They have observed that the difference in the singlet $^1S_0$ scattering lengths of pp (nuclear part) and nn systems [originating from the effects of charge-symmetry breaking (CSB)] can increase the energy difference between the ^{3}H and ^{3}He binding energies and thus contribute to ΔE_C.

Our results obtained in this work with the DBM give an alternative explanation of the ΔE_C puzzle and other Coulomb effects in ^{3}He without any free parameter. The Coulomb displacement energies ΔE_C, together with the individual contributions to the ΔE_C value, are presented in Table 5.

We emphasize three important points where our results differ from those for conventional models.

(i) First, we found a serious difference between the conventional and our approaches in the short-range behavior of wave functions even in the nucleonic channel. Conventional $3N$ wave functions are strongly suppressed along all three interparticle coordinates r_{ij} due to the short-range local repulsive core, while our wave functions (in the $3N$ channel) have stationary nodes and short-range loops along all r_{ij} and the third Jacobi coordinates ρ_k. Such a node along the ρ coordinate is seen also in the $6qN$ relative-motion wave function. This very peculiar short-range behavior of our wave functions leads to a strong enhancement of the high-momentum components of nuclear wave functions, which is required by various modern experiments. On the other hand, these short-range radial loops lead to significant errors when using the Coulomb interaction between

Table 5. Contribution of various terms (in keV) of the Coulomb interaction to the ^{3}H$-^3$He mass difference ΔE_C

Contribution	DBM(I)	DBM(II)	AV18 + UIX
Point Coulomb $3N$ only	598	630	677
Point Coulomb $3N + 6qN$	840	782	−
Smeared Coulomb $3N$ only	547	579	648
Smeared Coulomb $3N + 6qN$	710	692	−
np mass difference	46	45	14
Nuclear CSB (see Table 6)	0	0	+65
Magnetic moments and spin−orbit[a]	17	17	17
Total	773	754	754

[a] Here we use the value for this correction from [49].

pointlike particles within our approach. Hence, we must take into account the finite radii of charge distributions in the proton and $6q$ bag. Otherwise, all Coulomb energies will be overestimated.

(ii) Another important effect following from our calculations is a quite significant contribution of the internal $6qN$ component to ΔE_C. In fact, just this interaction, which is completely missing in conventional nuclear force models, makes the main contribution (163 and 113 keV for versions I and II, respectively) to filling the gap in ΔE_C between conventional $3N$ calculations and experiment if the CSB effects are of little significance in ΔE_C.

The large magnitude of this three-body Coulomb-force contribution in our models can be explained by two factors: first, a rather short average distance $\langle \rho^2 \rangle^{1/2}$ between the $6q$ bag and the third nucleon (which enhances the Coulomb interaction in the $6qN$ channels) and, second, a relatively large weight of the $6qN$ components, where the $6q$ bag has the charge $+1$ (i.e., it is formed from an np pair). This specific Coulomb repulsion in the $6qN$ channel should also appear in all other nuclei, where the total weight of such components is about 10% or higher. Therefore, it should strongly contribute to the Coulomb displacement energies over the entire periodic table and could somehow explain the long-term Nolen−Schiffer paradox [56] in this way.

(iii) The third specific effect that has been found in this study and contributes to the quantitative explanation of ΔE_C is a strong increase in the average kinetic energy $\langle T \rangle$ of the system. This increase in $\langle T \rangle$ has already been discovered in the first early $3N$ calculations with the Moscow NN potential model [57]

Table 6. Contribution of charge-symmetry-breaking effects to the ^{3}H$-^3$He mass difference ΔE_C

a_{nn}, fm	ΔE_C, keV	
	DBM(I)	DBM(II)
-16.3	-18	-39
-18.9	$+45$	$+26$

and results in a similar nodal wave function behavior along all interparticle coordinates but without any nonnucleonic component.

The increase in $\langle T \rangle$ leads to the proportional increase in the np mass-difference correction to ΔE_C. Since the average kinetic energy in our case is twice the kinetic energy in conventional force models, this correction is expected to be also much larger in our case. Hence, we evaluate such a correction term in the following way (without using perturbation theory). In the conventional isospin formalism, one can assume that the ^{3}H and ^{3}He nuclei consist of equal-mass nucleons,

$$m = \frac{m_p + m_n}{2},$$

so that $m_p = m + \Delta m/2, m_n = m - \Delta m/2$, where $\Delta m = m_p - m_n$. The simplest way to include the correction due to the mass difference Δm is to assume that all particles in ^{3}H have the average mass

$$\bar{m}_H = \frac{2m_n + m_p}{3} = m - \frac{1}{6}\Delta m,$$

while in ^{3}He they have the different average mass

$$\bar{m}_{He} = \frac{2m_p + m_n}{3} = m + \frac{1}{6}\Delta m.$$

In spite of the smallness of the parameter $\Delta m/m$, perturbation theory in respect to this parameter does not work. So we used the average mass $\bar{m}_H$ in calculation of ^{3}H and $\bar{m}_{He}$ in calculation of ^{3}He. The contribution of this np mass difference to the ΔE_C value is given in the fifth row of Table 5. As is seen from the table, this correction is not very small in our case and contributes to ΔE_C quite significantly.

Many other effects attributed to increasing the average kinetic energy of the system will arise in our approach, e.g., numerous effects associated with the enhanced Fermi motion of nucleons in nuclei.

Charge-symmetry-breaking effects in DBM. As was noted above, the best explanation for the ΔE_C value in the framework of conventional force models published to date [49] is based on the introduction of some CSB effect, i.e., the difference between nn and pp strong interactions. At present, two alternative values of the nn scattering length are assumed:

$$a_{nn}^{(1)} = -18.7 \text{ fm and } a_{nn}^{(2)} = -16.3 \text{ fm.} \quad (82)$$

The first value has been extracted from the previous analysis of experiments $d(\pi^-, \gamma)nn$ [58] (see also [59] and references therein) and is used in all current NN potential models, while the second value in (82) has been derived from numerous three-body breakup experiments $n + d \to nnp$ done for the last three decades. In recent years, such breakup experiments are usually treated in the complete Faddeev formalism, which includes most accurately both two-body and 3BF [60]. Thus, this $a_{nn}^{(2)}$ value is considered to be quite reliable. However, the quantitative explanation for the ΔE_C value in conventional force models uses just the first value of a_{nn} as an essential point of all the construction. At the same time, the use of the second value $a_{nn}(= -16.3 \text{ fm})$ (which is not less reliable than the first one) invalidates completely the above explanation!

Therefore, in order to understand the situation more deeply and to determine the degree of sensitivity of our prediction for ΔE_C to variation in a_{nn}, we also made $3N$ calculations with two possible values of a_{nn} from Eq. (82). These calculations have been carried out with the effective values of the singlet-channel coupling constant corresponding to the V_{NqN} part of the NN force:

$$\lambda_{He}^{eff}(^1S_0) = \frac{1}{3}\lambda_{pp} + \frac{2}{3}\lambda_{np}, \quad (83)$$

$$\lambda_{H}^{eff}(^1S_0) = \frac{1}{3}\lambda_{nn} + \frac{2}{3}\lambda_{np}. \quad (84)$$

In the above calculations, we employ the value $\lambda_{np} = 328.9$ MeV, which provides an accurate description of the $^1S_0$ np phase shifts and the experimental value of the np scattering length $a_{np} = -23.74$ fm [24]. Here, for the pp channel, we use the value $\lambda_{pp} = 325.523$ MeV fitted to the well-known experimental magnitude $a_{pp} = -8.72$ fm, and for the nn channel, two λ_{nn} values corresponding to two available alternative values of the nn scattering length (82) have been tested. The calculation results are presented in Table 6.

As is seen in Tables 5 and 6, the DBM (version I) can precisely reproduce the Coulomb displacement energy ΔE_C with the lower (in modulus) value $a_{nn} = -16.3$ fm, while this model overestimates ΔE_C by 54 keV ($= 45 + 9$ keV) with the larger (in modulus) value $a_{nn} = -18.9$ fm. Thus, the DBM approach, in contrast to the conventional force models, prefers the lower (in modulus) possible value -16.3 fm of the nn scattering length, which has been extracted from very numerous $3N$ breakup experiments $n + d \to nnp$ [60].

Now, let us briefly discuss the magnitude of CSB effects in our model. The measure of CSB effects at

low energies is used to consider the difference between a_{nn} and so-called "pure nuclear" pp scattering length a_{pp}^N that is found from pp scattering data when the Coulomb potential is disregarded. The model dependence of the latter quantity was actively discussed in the 1970s−1980s [61−63]. However, the majority of modern NN potentials fitted to the experimental value $a_{pp} = -8.72$ fm results in the value $a_{pp}^N = -17.3$ fm when the Coulomb interaction is discarded. It is just the value that is adopted now as an "empirical" value of the pp scattering length [64]. Thus, the difference between this value and a_{nn} is usually considered as the measure of CSB effects. However, our model (also fitted to the same experimental value $a_{pp} = -8.72$ fm) gives a quite surprising result:

$$a_{pp}^N(\text{DBM}) = -16.57 \text{ fm}, \qquad (85)$$

which differs significantly from the above conventional value (by 0.8 fm) due to the explicit energy dependence of the NN force in our approach.

Thus, if the difference $a_{pp}^N - a_{nn}$ is still taken as the measure of CSB effects, the smallness of this difference obtained in our model attests to a small magnitude of the CSB effects, which is remarkably smaller than the values derived from conventional OBE models for the NN force.

8. DISCUSSION

The $3N$ results presented in the previous section differ significantly from the results found with any conventional model for $2N$ and $3N$ forces (based on Yukawa's meson-exchange mechanism) and also from the results obtained in the framework of hybrid models [65], which include the two-component representation of the NN wave function $\Psi = \Psi_{NN} + \Psi_{6q}$. It is convenient to discuss these differences in the following order.

(i) We found that the q^2 dependence of pair NN forces on the momentum of the third particle in the $3N$ system is more pronounced in our case than in other hybrid models [34, 48, 65, 66]: the $3N$ binding energy decreases by about 1.7 MeV, from 5.83 to 4.14 MeV, when one takes into account the q^2 dependence [32]. From a more general point of view, it means that, in our approach, pairwise NN interactions (except Yukawa OPE and TPE terms), being "embedded" into a many-body system, lose their two-particle character and become substantially many-body forces (i.e., depending on the momenta of other particles of the system).

(ii) Due to such a strong q^2 dependence (of "repulsive" character), the $3N$ system calculated including only the pairwise forces turns out to be strongly underbound ($E = -4.14$ MeV). In other words, the

"pairwise" NN forces (including their q^2 dependence on the momenta of the third nucleon) give only about half the total $3N$ binding energy, leaving the second half for the 3BF contribution. Therefore, the following question is decisively important: Can the 3BF (inevitably arising in our approach) give the large missing contribution to the $3N$ binding energy? Usefulness of the developed model for the description of nuclear systems depends directly on the answer to this important question. It is appropriate here to recall that, in the conventional 3BF models, such as Urbana−Illinois or Tucson−Melbourne, the contribution of 3BF to the total $3N$ binding energy does not exceed 1 MeV; i.e., this contribution can be considered as some correction ($\sim15\%$), although it is significant for the precise description of the $3N$ system.

(iii) Fortunately, the contribution of 3BF induced by OSE and TSE enables one to fill this 4.3-MeV gap between the two-body force contribution and experimental value. In fact, including both OSE and TSE contributions to 3BF, taken with the same coupling constants and form factors as in the driving NN-force model, together with a quite reasonable value for the σNN coupling constant, $g_{\sigma NN} = 8-10$, one obtains a $3N$ binding energy that is very close to the experimental value (see rows 1, 2 and 4, 5 in Table 2). Thus, the presented force model leads to a very reasonable binding energy for the $3N$ system, however, with the much larger (as compared to the traditional $3N$ force model) contribution of 3BF. In fact, the unification of the basic $2N$- and $3N$-force parameters provides strong support for the whole force model suggested here and is in a sharp contrast with all traditional force model based on the t-channel exchange mechanism. We remind the reader that the $2N$ and $3N$ forces in conventional approaches (where the latter is induced by an intermediate Δ-isobar production) are taken with different cutoff parameters values $\Lambda_{\pi NN}$ and $\Lambda_{\pi N\Delta}$ in the $2N$ and $3N$ sectors in order to explain the basic features of $3N$ nuclei and $N + d$ scattering! Thus, in the traditional approach, one has some serious inconsistency in parameter values for the $2N$ and $3N$ sectors.

(iv) The contributions of the pairwise and different three-body forces to the total $3N$ binding energy for ^{3}H are given in the sixth and seventh columns of Table 2. From the results presented in this table, one can conclude that just the total 3BF contribution to the $3N$ binding energy dominates and, in fact, determines the whole structure of the ^{3}H and ^{3}He ground states.[11] Moreover, comparing the entries

---

[11]It should be noted here that the relative contribution of the pairwise effective force $W(E)$ to the $3N$ binding energy decreases noticeably when including 3BF (due to strengthening of the q^2 dependence arising from the pairwise forces).

in the first and second rows and sixth and seventh columns of the table, one can see a "nonlinear" effect of self-strengthening for the 3BF contribution. In fact, the comparison of the results presented in these rows of the table (see the fourth and the seventh columns) shows clearly that the 3BF contribution to the total $3N$ binding energy is largely determined by the weight P_{in} of the $6qN$ component in the total $3N$ wave function. So, when the weight of the $6qN$ component increases, the 3BF contribution, which is related directly only to this component of the total wave function, increases accordingly. However, the enhancement of the pure attractive 3BF contribution squeezes the $3N$ system and thus reduces its rms radius, i.e., the mean distance between nucleons, which, in turn, again increases the weight of the $6qN$ component. In other words, some chain process, which strengthens the attraction in the system, arises. This process is balanced both by the weakening of the effective pairwise interaction due to the q^2 dependence and by the repulsive effect of the orthogonalizing pseudopotentials included in each pair interaction.

There are two other important stabilizing factors weakening the strong three-body attraction in the $3N$ system. The first factor is the generation of the short-range repulsive vector ω field, where all three nucleons are close to each other [25]. Since the ω meson is heavy, this field is located in the deep overlap region of all three nucleons. In the present study, we omitted the three-body contribution of this repulsive ω field. This repulsive contribution will keep the whole system from further collapse due to the strong attractive $3N$ force induced by the scalar field.

The second factor weakening slightly the effective $3N$ attraction is associated with the conservation of the number of scalar mesons generated in the $2N$- and $3N$-interaction process. The problem is that TSE giving the 3BF contribution (see Fig. 4) arises due to the break of the σ-meson loop, which induces the main $2N$ force. In other words, the σ meson generated in the transition of pair nucleons from the NN phase state to the $6q$ state is absorbed either in the $6q$ bag with closing of the loop or by the third nucleon, resulting in the 3BF contribution. Thus, the appearance of such a 3BF should weaken the attraction between nucleons in the pair. We carefully estimated the effect of the meson-number conservation for the TSE contribution on the total $3N$ binding energy. Its magnitude turned out to be rather moderate on the absolute energy scale (about $0.3-0.4$ MeV), but quite noticeable within the whole TSE contribution. However, when the total nucleon density increases (and the relative TSE contribution also increases), the effect is enhanced.

(v) Dependence of the two-body coupling constants $\lambda(\varepsilon)$ upon the average momentum of the other nucleon in the $3N$ system [see, e.g., Eq. (29)] can be interpreted generally as a density dependence of the resulting many-body force in a many-nucleon system. It is easy to show that the appearance of the energy-dependent pairwise potentials of the above-mentioned type leads unavoidably to a repulsive many-body force. In other words, the effects of the two-body interactions of this type can be reinterpreted in terms of the conventional static interaction as an additional contribution of the effective repulsive density-dependent many-body force. For example, if we remove the q^2 dependence from the coupling constant $\lambda(E - q^2/(2m))$ of our two-body force (this q^2 dependence leads to a weakening of the two-body force in a many-nucleon system, when q^2 is rising), then the neglected q^2 dependence must be compensated by an additional repulsive density-dependent effective three-body force. Thus, we can replace this energy-dependent two-body interaction by an effective static two-body potential (as is usually done) plus a repulsive density-dependent 3BF.

On the other hand, it is well known from Skirme model calculations of nuclei that just similar repulsive phenomenological density-dependent 3BF should be added to conventional $2N$ and $3N$ forces to guarantee the saturation properties of heavy nuclei. Thus, in this respect, the present force model is also in qualitative agreement with the phenomenological picture of nuclear interactions.

9. CONCLUSION

In this paper, we have developed a general formalism for the multicomponent description of the three-body system with particles having inner degrees of freedom. We have applied our new approach to studying the $3N$ system with $2N$ and $3N$ interactions based on the dressed dibaryon intermediate state and σ-field generation. It has been shown that the DBM applied to the $3N$ system inevitably results in new three-body scalar and also new (three-body) Coulomb forces due to the (strong + Coulomb) interaction between the dressed dibaryon and the third nucleon. These forces play a crucial role in the structure of few-nucleon systems and very likely in the whole nuclear dynamics. Our accurate variational calculations have demonstrated that the new 3BF gives half of the $3N$ binding energy, whereas the 3BF contribution in the traditional NN-force approaches gives about 15% of the total binding energy. Thus, the suggested approach to the $2N$ and $3N$ interactions can lead to significant revision of relative contributions of two- and many-body forces in all nuclear systems.

The developed model gives the precise value for the Coulomb displacement energy ΔE_C of the $A = 3$ system. Two basic sources of this contribution, which differ from conventional force models, should be indicated here:

the three-body Coulomb force between the dressed bag and the charged third nucleon; and

the quite significant correction to the kinetic energy of the system due to the np mass difference and high average kinetic energy.

It should be emphasized that, contrary to other studies based on conventional force models (using the $2N$ and $3N$ forces generated via the meson-exchange mechanism), this explanation does not require any noticeable CSB effect, although our model is still compatible with such effects. However, these CSB effects do not contribute remarkably to ΔE_C in our approach.

It is crucially important that the DBM leads to significant nonnucleonic components in the $3N$ wave function (8−11%), while this component in the deuteron is about 3%, which results in a reformulation of many basic effects in few-nucleon systems and other nuclei as well. It is probable that the weight of such nonnucleonic components in heavy nuclei can be even higher with an increase in the mass number and nuclear density.

There is a very specific new interplay between two- and three-body forces: the stronger the three-body force, the smaller the attractive contribution of the two-body force to the nuclear binding energy! This gives a very important stabilization in nuclei and nuclear matter. In this way, a very natural density dependence of nuclear interactions appears from the beginning. Thus, the general properties of the $3N$ system, where forces differ so much from any conventional force model, would appear also to be much different from the predictions of any conventional model and, hence, from experiment.

Therefore, it was very surprising for us to find that the static characteristics of the $3N$ system in our case turned out to be very close to the predictions of the modern force model (such as AV18 + UIX) and thus to experiment. This gives us a good test of the self-consistency and accuracy of the new force model. However, predictions of the present $2N$- and $3N$-force model in other aspects will strongly deviate from those for conventional models. First, these are the properties determined by the high-momentum components of nuclear wave functions. The point is that the system described by our multicomponent wave functions including the dibaryon components explicitly can easily absorb high-momentum transfers, which can hardly be absorbed by the system consisting of nucleons only. Therefore, to fit the experimental

data corresponding to large-momentum transfers (∼1 GeV/c), many types of meson-exchange and isobar currents are often introduced into theoretical frameworks. However, these currents are often unrelated to the underlying force model. Hence, it is rather difficult to check the self-consistency of such calculations, e.g., the validity of gauge invariance, etc.

Numerous modern experiments could corroborate these results. In particular, according to the recent $^3\text{He}(e, e'pp)$ experiments [5] and their theoretical interpretation on the basis of fully realistic $3N$ calculations, the cross sections for the $^3\text{He}(e, e'pp)$ process are underestimated by about five times with a fully realistic $3N$ model and incorporation of final-state interaction and meson-exchange currents. This important conclusion has been further confirmed in recent experiments at the Jefferson Laboratory when the incident-electron-beam energy was increased up to $E_e = 2.2$ and 4.4 GeV [7]. The data of the two different experiments give clear evidence of very strong short-range NN correlation in the ^3He ground state. This correlation still cannot be explained within the traditional pattern for the $3N$ system.

In addition, our approach has recently been partially supported [67] from the other side by considering a model for 2π production in pp collisions at $E_p = 750$ and 900 MeV. The authors have found that almost all particle energy and angular correlations (e.g., $\pi^+\pi^-$, pp, πpp, etc.) can be explained quantitatively by assuming that $\pi^+\pi^-$ production occurs through the generation of an intermediate light σ meson with the mass $m_\sigma \simeq 380$ MeV. These values generally agree with the parameters adopted in our NN model [8, 24] and drastically disagree with the values assumed in OBE and other potential models.

A very interesting general implication of the results presented here is their evident interrelation to the famous Walecka hydrodynamic model for nuclei [68]. It is well known that the Walecka model describes nuclei and nuclear matter in terms of the scalar σ and vector ω fields, where the σ field gives the attractive contribution, while the vector ω field balances this attraction by short-range repulsion. It is very important that both basic fields appear (in the model) as explicit degrees of freedom (together with relativistic nucleons), in contrast to conventional meson-exchange models for nuclear forces, where mesons appear as carriers of forces rather than as explicit field degrees of freedom. Our approach does include the σ-meson (and potentially the ω-meson) degrees of freedom in an explicit form, similarly to the Walecka model. Moreover, since the average kinetic energy of the $3N$ system in our model is high (it is much higher than that in the conventional OBE approach), nucleon motion is closer to the relativistic

case, and thus the similarity with the Walecka model gets even closer.

There is also an additional strong argument in favor of a tight interrelation between our and the above Walecka-type nuclear model. Very recently, we have formulated [38] the dibaryon model for NN interaction in terms of relativistic effective field theory with the intermediate dibaryon being represented as a color quantum string with color quark clusters at its ends. This theory includes π, σ, ρ, and ω mesons as a dressing of the dibaryon together with the $N\Delta$ and $\Delta\Delta$ loops. Thus, the $3N$ scalar force introduced in the present work "by hand" can be derived in the field-theory Lagrange language within the effective field theory. Moreover, in the mean-field approximation, this effective field theory approach, being applied to nuclei, should result in the Walecka−Serot relativistic model with the dominating collective σ field, which couples the nucleons in a nucleus together.

Thus, the alternative description given here by the new force model looks to be more self-consistent and straightforward than the conventional OBE-type models. One aspect of this new picture is evident—the present model being applied to any electromagnetic process on nuclei leads automatically to a consistent picture of the process as a whole: single-nucleon currents at low-momentum transfers, meson-exchange currents (including new meson currents) at intermediate-momentum transfers, and quark counting rules at very high momentum transfers, because the model wave function includes explicitly multinucleon, meson-exchange, and multiquark components.

From all the above-mentioned arguments, one can conclude that the dibaryon concept of nuclear force advocated in the work results in a new picture for nuclear structure and dynamics.

ACKNOWLEDGMENTS

Appendix

OVERLAP FUNCTIONS BETWEEN 3N SYMMETRIZED BASIS AND NN FORM FACTORS AND MATRIX ELEMENTS OF DBM INTERACTIONS FOR A 3N SYSTEM

1. The Construction of Basis Functions

The total wave function in the $3N$ channel with the angular momentum (J, M) and the isospin (T, T_z) is written as (below we omit the quantum numbers $JMTT_z$):

$$\Psi_{\text{ex}}^{(JMTT_z)} = \Psi_{\text{ex}}^{(1)} + \Psi_{\text{ex}}^{(2)} + \Psi_{\text{ex}}^{(3)}, \qquad (A.1)$$

$$\Psi_{\text{ex}}^{(i)} = \sum_{\gamma n} C_n^\gamma \Phi_{\gamma n}^{(i)} \qquad (i = 1, 2, 3), \qquad (A.2)$$

where

$$\Phi_{\gamma n}^{(i)}(\mathbf{r}_i, \boldsymbol{\rho}_i) = N_n^\gamma r_i^\lambda \rho_i^l \qquad (A.3)$$
$$\times \exp(-\alpha_n r_i^2 - \beta_n \rho_i^2) \mathcal{F}_\gamma^{JMTT_z}(\hat{\mathbf{r}}_i, \hat{\boldsymbol{\rho}}_i) \mathcal{T}_{t_{jk}}^{(i)}.$$

We use the following notation: $\mathbf{r}_i$ ($\mathbf{p}_i$) is the relative coordinate (momentum) of the pair (jk), while $\boldsymbol{\rho}_i$ ($\mathbf{q}_i$) is the Jacobi coordinate (momentum) of the ith particle relative to the center of mass for the pair (jk), $(i, j, k) = (1, 2, 3)$ or their cyclic permutations. Here, the composite label $\gamma = \{\lambda l L S_{jk} S t_{jk}\}$ represents the set of quantum numbers for the basis functions: the angular momenta λ and l correspond to the Jacobi coordinates $\mathbf{r}_i$ and $\boldsymbol{\rho}_i$, respectively; $S_{jk}(t_{jk})$ is the spin (isospin) of the two-body subsystem (jk); and $L(S)$ is the total orbital momentum (spin) of the system. The normalizing coefficient in (A.3) is

$$N_n^\gamma = 2^{\lambda + l + 3} \sqrt{\frac{2\alpha_n^{\lambda + 3/2} \beta_n^{l + 3/2}}{\pi (2\lambda + 1)!! (2l + 1)!!}}. \qquad (A.4)$$

The spin-angular $\mathcal{F}_\gamma$ and isospin $\mathcal{T}_{t_{jk}}^{(i)}$ parts of the basis function are defined by a standard vector-coupling scheme:

$$\mathcal{F}_\gamma^{JMTT_z} = |\{\lambda_i l_i : L\}\{s_j s_k (S_{jk}) s_i : S\} : JM\rangle, \qquad (A.5)$$

$$\mathcal{T}_{t_{jk}}^{(i)} = |t_j t_k (t_{jk}) t_i : TT_z\rangle, \qquad (A.6)$$

where $s_i(= 1/2)$ and $t_i(= 1/2)$ are the spin and isospin of the ith nucleon.

Now we define the symmetrized basis functions as

$$\Phi_{\gamma n}^{\text{sym}} = \sum_{i=1,2,3} \Phi_{\gamma n}^{(i)}, \qquad (A.7)$$

so that the total wave function in an external $(3N)$ channel takes the form

$$\Psi_{\text{ex}} = \sum_{\gamma,n} C_n^\gamma \Phi_{\gamma n}^{\text{sym}}. \qquad (A.8)$$

2. Nucleon−Nucleon Form Factors

The NN form factors in the separable DBM interaction and in the projectors $\varphi_{\lambda_i S_d}^{J_i M_i t_d t_{d_z}}(\mathbf{r}_i)$, corresponding to the orbital momentum λ_i, spin S_d, the total angular momentum (J_i, M_i), and isospin $(t_d t_{d_z})$ of the subsystem (jk) $(\mathbf{J}_i = \boldsymbol{\lambda}_i + \mathbf{S}_d)$, have the form

$$\varphi_{\lambda_i S_d}^{J_i M_i t_d t_{d_z}}(\mathbf{r}_i) \equiv \varphi_f(\mathbf{r}_i) \qquad (A.9)$$

$$= \sum_m D_m^f r_i^{\lambda_i} \exp(-\frac{1}{2}\eta_m^2 r_i^2)\mathcal{F}_f(\hat{\mathbf{r}}_i)\mathcal{T}_f^{(i)},$$

where

$$f \equiv \{\lambda_i, S_d, J_i, M_i, t_d, t_{d_z}\}, \qquad (A.10)$$

$$\mathcal{F}_f = |\lambda_i S_d : J_i M_i\rangle, \qquad \mathcal{T}_f^{(i)} = |t_j t_k : t_d t_{d_z}\rangle,$$

and D_m^f and η_m are linear and nonlinear parameters, respectively, of the Gaussian expansion. (In this Appendix, we have altered the notation for the quantum numbers of the NN form factor as compared with the main text of the paper: we have replaced $L_i \to \lambda_i$ for the orbital momentum and also included the isospin quantum numbers t_d, t_{d_z}.) In the single-pole approximation, the DBM includes only one form factor for each set f, so that index f determines the form factor uniquely. In the present version of the DBM, we use only $0S$, $2S$, and $2D$ oscillator functions as the form factors. So, we need to expand in Gaussians the $2S$ function only.

3. Overlap Integrals

The total overlap function (49)

$$\chi_{\lambda_i S_d}^{J_i M_i t_d t_{d_z}}(i) \equiv \chi_f(i) = \langle \varphi_f(i)|\Psi_{\text{ex}}\rangle \qquad (A.11)$$

$$= \sum_{\gamma n} C_n^\gamma \langle \varphi_f(i)|\Phi_{\gamma n}^{\text{sym}}\rangle$$

and also matrix elements (m.e.) of any DBM interaction include the overlap integrals between the form factors φ_f and symmetrized basis functions $\Phi_{\gamma n}^{\text{sym}}$:

$$I_{(i)}^{f,\gamma n}(\boldsymbol{\rho}_i) = \langle \varphi_f(\mathbf{r}_i)|\Phi_{\gamma n}^{\text{sym}}\rangle. \qquad (A.12)$$

This overlap integral consists of three terms:

$$I_{(i)}^{f,\gamma n} = I_{(i)i}^{f,\gamma n} + I_{(i)j}^{f,\gamma n} + I_{(i)k}^{f\gamma n}, \qquad (A.13)$$

namely, one "diagonal" $(I_{(i)i})$ and two nondiagonal ones:

$$I_{(i)j}^{f,\gamma n}(\boldsymbol{\rho}_i) = \langle \varphi_f(\mathbf{r}_i)|\Phi_{\gamma n}^{(j)}(\mathbf{r}_j, \boldsymbol{\rho}_j)\rangle = \langle \mathcal{T}_f^{(i)}|\mathcal{T}_{t_{ik}}^{(j)}\rangle \qquad (A.14)$$

$$\times \sum_m D_m^f N_n^\gamma \int r_i^{\lambda_i} \exp(-\frac{1}{2}\eta_m^2 r_i^2) r_j^\lambda \rho_j^l$$

$$\times \exp(-\alpha_n r_j^2 - \beta_n \rho_j^2)\langle \mathcal{F}_f(\hat{\mathbf{r}}_i)|\mathcal{F}_\gamma(\hat{\mathbf{r}}_j, \hat{\boldsymbol{\rho}}_j)\rangle d^3 r_i.$$

Due to symmetry of the basis functions $\Phi_{\gamma n}^{\text{sym}}$, three overlap integrals $I_{(i)}^{f,\gamma n}(\boldsymbol{\rho}_i)$ $(i = 1, 2, 3)$ are identical, so that further we present formulas for the case of $i = 2$. For example,

$$\chi_f(2) = \sum_{\gamma n} C_n^\gamma \left(I_{(2)2}^{f,\gamma n} + I_{(2)1}^{f,\gamma n} + I_{(2)3}^{f,\gamma n} \right). \quad (A.15)$$

(i) Diagonal overlap integrals $I_{(2)2}$:

$$I_{(2)2}^{f,\gamma n}(\boldsymbol{\rho}_2) = \sum_{\mathcal{J}m} G_{22}^\varepsilon \rho_2^l \qquad (A.16)$$

$$\times \exp(-\beta_n \rho_2^2)\, \mathcal{Y}_l^{\mathcal{J} J_i JM}(\hat{\boldsymbol{\rho}}_2)\delta_{t_d t_{31}}\mathcal{X}_2^{t_d t_{d_z}},$$

$$\varepsilon \equiv \{\gamma, f, \mathcal{J}, m\},$$

where

$$G_{22}^\varepsilon = \delta_{\lambda\lambda_i}\delta_{S_d S_{31}}(-1)^{\lambda+l+L} \qquad (A.17)$$

$$\times D_m^f N_n^\gamma \frac{(2\lambda+1)!!\sqrt{\pi[L][S][J_i][\mathcal{J}]}}{2^{\lambda+2}\alpha_{nm}^{\lambda+3/2}} \begin{Bmatrix} l & \frac{1}{2} & \mathcal{J} \\ \lambda & S_{31} & J_i \\ L & S & J \end{Bmatrix},$$

$$[X] \equiv 2X + 1, \qquad (A.18)$$

$$\alpha_{nm} = \alpha_n + \frac{1}{2}\eta_m^2, \qquad (A.19)$$

$$\mathcal{Y}_l^{\mathcal{J} J_i JM}(\hat{\boldsymbol{\rho}}_2) = \langle \mathcal{J}m_{\mathcal{J}} J_i M_i|JM\rangle \mathcal{Y}_{l\,1/2}^{\mathcal{J}m_{\mathcal{J}}}(\hat{\boldsymbol{\rho}}_2), \qquad (A.20)$$

$$\mathcal{X}_2^{t_d t_{d_z}} = \left\langle t_d t_{d_z} \frac{1}{2}t_{2_z}\bigg|TT_z \right\rangle |t_2 t_{2_z}\rangle. \qquad (A.21)$$

(ii) Nondiagonal overlap integrals:

$$I_{(2)1}^{f,\gamma n}(\boldsymbol{\rho}_2) = (-1)^{S_d+S_{23}} \sum_{\mathcal{J}g,t,m} G_{21}^{\tilde{\varepsilon}} \rho_2^t \qquad (A.22)$$

$$\times \exp(-\omega_{nm}\rho_2^2)\mathcal{Y}_g^{\mathcal{J} J_i JM}(\hat{\boldsymbol{\rho}}_2)\tau_{21}(t_d, t_{23})\mathcal{X}_2^{t_d t_{d_z}},$$

$$I_{(2)3}^{f,\gamma n}(\boldsymbol{\rho}_2) = (-1)^{\lambda_i+\lambda} \sum_{\mathcal{J}g,t,m} G_{21}^{\tilde{\varepsilon}} \rho_2^t \qquad (A.23)$$

$$\times \exp(-\omega_{nm}\rho_2^2)\mathcal{Y}_g^{\mathcal{J} J_i JM}(\hat{\boldsymbol{\rho}}_2)\tau_{23}(t_d, t_{12})\mathcal{X}_2^{t_d t_{d_z}},$$

where

$$\tilde{\varepsilon} \equiv \{\gamma, n, f, \mathcal{J}, g, t, m\}, \qquad (A.24)$$

$$G_{21}^{\tilde{\varepsilon}} \qquad (A.25)$$

$$= \sum_{\xi} G_{21}(\gamma, n, f, \mathcal{J}, g, m, \xi)\delta_{t,\lambda_i+\lambda+l-L_1-L_3-L_4},$$

$$\xi \equiv \{L_1, L_2, L_3, L_4, j_4, g_1, g_4\}.$$

In Eq. (A.25), the summation is carried out over all intermediate quantum numbers incorporated into the composite index ξ. Note that the overlap functions $I_{(2)1}$ and $I_{(2)3}$ are distinguished by a phase factor and isospin functions only.

The algebraic coefficients G_{21} in (A.25) are equal to

$$G_{21}(\gamma, n, f, \mathcal{J}, g, m, \xi) = (-1)^{J_i+g_1+L+1/2-J}$$
$$(A.26)$$

$$\times D_m^f N_n^\gamma A_{\lambda_i 0 L_1(\lambda_i - L_1)}^{\lambda_i L_1 0}(\mathbf{P}_{nm}) A_{\lambda l L_1 j_4}^{L L_3 L_4}(\mathbf{Q}_{nm})$$

$$\times \frac{[g_1][g_4]\sqrt{[\lambda_i][L][S][S_{23}][S_d][J_i][\lambda_i - l][j_4][\mathcal{J}]}}{(2\mu_{nm})^{\frac{L_1+L_3+L_4+3}{2}}}$$

$$\times \Gamma\left(\frac{L_1+L_3+L_4+3}{2}\right)\langle(\lambda_i - L_1)0j_40|g_0\rangle$$

$$\times \begin{Bmatrix} (\lambda_i - L_1) & L_1 & \lambda_i \\ S_0 & j & g_1 \end{Bmatrix} \begin{Bmatrix} \frac{1}{2} & \frac{1}{2} & S_{23} \\ \frac{1}{2} & S & S_d \end{Bmatrix}$$

$$\times \begin{Bmatrix} \mathcal{J} & (\lambda_i - L_1) & g_4 \\ j_4 & \frac{1}{2} & g \end{Bmatrix} \begin{Bmatrix} J & \mathcal{J} & J_i \\ (\lambda_i - L_1) & g_1 & g_4 \end{Bmatrix}$$

$$\times \begin{Bmatrix} j_4 & \frac{1}{2} & g_4 \\ L_1 & S_d & g_1 \\ L & S & J \end{Bmatrix}.$$

In formulas (A.22), (A.23), (A.26) the following notation is used:

$$\mu_{nm} = \mu_n + \frac{1}{2}\eta_m^2, \quad \omega_{nm} = \nu_n - \frac{\sigma_n^2}{4\mu_{nm}}, \quad (A.27)$$

where

$$\mu_n = \frac{1}{4}\alpha_n + \frac{3}{4}\beta_n, \quad \nu_n = \frac{3}{4}\alpha_n + \frac{1}{4}\beta_n, \quad (A.28)$$

$$\sigma_n = \frac{\sqrt{3}}{2}(\alpha_n - \beta_n).$$

The coefficients A in (A.26) are related to rotation of the basis functions from one Jacobi set to the other one:

$$A_{\lambda l j_1 j_2}^{LL_1L_2}(\hat{\mathbf{R}}) = (-1)^{\lambda+l}(R_{11})^{L_1}(R_{12})^{\lambda-L_1}(R_{21})^{L_2}$$
$$(A.29)$$

$$\times (R_{22})^{l-L_2} \begin{pmatrix} L_1 & L_2 & J_1 \\ 0 & 0 & 0 \end{pmatrix} \begin{pmatrix} \lambda - L_1 & l - L_2 & J_2 \\ 0 & 0 & 0 \end{pmatrix}$$

$$\times \sqrt{\frac{[\lambda]![l]![\lambda][l][L_1][L_2][\lambda - L_1][l - L_2][j_1][j_2]}{[L_1]![L_2]![\lambda - L_1]![l - L_2]!}}$$

$$\times \begin{Bmatrix} L_1 & \lambda - L_1 & \lambda \\ L_2 & l - L_2 & l \\ j_1 & j_2 & L \end{Bmatrix}.$$

The rotation matrices $\mathbf{P}_{nm}$ and $\mathbf{Q}_{nm}$ in (A.26) have the form

$$\mathbf{P}_{nm} = \begin{pmatrix} 1 & -\dfrac{\sigma_n}{2\mu_{nm}} \\ 0 & 1 \end{pmatrix}, \qquad (A.30)$$

$$\mathbf{Q}_{nm} = \begin{pmatrix} -\dfrac{1}{2} & -\dfrac{\sqrt{3}}{2} \\ \dfrac{\sqrt{3}}{2} & -\dfrac{1}{2} \end{pmatrix} \mathbf{P}_{nm}. \qquad (A.31)$$

The overlaps between the basic isospin functions τ_{ik} are equal to

$$\tau_{ij}(t'_{jk}, t_{ik}) \equiv \langle \mathcal{T}_{t'_{jk}}^{(i)} | \mathcal{T}_{t_{ik}}^{(j)} \rangle = \begin{cases} \delta_{t'_{jk} t_{jk}} \text{ for } i = j, \\ \\ \sqrt{(2t'_{jk}+1)(2t_{ik}+1)} \begin{Bmatrix} \frac{1}{2} & \frac{1}{2} & t'_{jk} \\ \frac{1}{2} & T & t_{ik} \end{Bmatrix} \begin{cases} (-1)^{t_{ik}} \text{ for } (ij) = (13), (21), (32), \\ (-1)^{t'_{jk}} \text{ for } (ij) = (12), (23), (31). \end{cases} \end{cases}$$
$$(A.32)$$

4. Conversion to Momentum Representation

One of the advantages of the Gaussian basis is the fact that Gaussian functions have the same form in both the coordinate and momentum representations. So expressions for the overlap integrals given below in the coordinate representation can be directly used for the calculation of m.e. of DBM interaction operators in the momentum representation. We use a "symmetrized" momentum representation:

$$f(\mathbf{p}) = \int f(\mathbf{x}) e^{i\mathbf{p}\cdot\mathbf{x}} \frac{d^3 x}{(2\pi)^{3/2}}. \qquad (A.33)$$

Therefore, due to properties of the Gaussian functions, the (normalized) basis functions $\Phi_{\gamma n}^{(i)}(\mathbf{p}_i, \mathbf{q}_i)$ in the momentum representation have the same form (A.3):

$$\Phi_{\gamma n}^{(i)}(\mathbf{p}_i, \mathbf{q}_i) \qquad (A.34)$$

$$= \tilde{N}_n^\gamma p_i^\lambda q_i^l \exp(-\tilde{\alpha}_n p_i^2 - \tilde{\beta}_n q_i^2) \mathcal{F}_\gamma^{JMTT_z}(\hat{\mathbf{p}}_i, \hat{\mathbf{q}}_i) \mathcal{T}_{t_{jk}}^{(i)},$$

where

$$\tilde{\alpha}_n = \frac{1}{4\alpha_n}, \quad \tilde{\beta}_n = \frac{1}{4\beta_n}. \qquad (A.35)$$

Moreover, as all the NN form factors (A.9) are the sums of Gaussians, the form of the overlap integrals (A.16)–(A.29) remains invariable when passing from the coordinate to momentum representation if one replaces in these formulas

$$\alpha_n \to \tilde{\alpha}_n, \quad \beta_n \to \tilde{\beta}_n, \quad \eta_m \to \tilde{\eta}_m = 1/\eta_m. \quad (A.36)$$

Below, we use the symbols with a tilde for designation of the corresponding quantities in the momentum representation, e.g., $\tilde{\alpha}_{nm} = \tilde{\alpha}_n + 1/(2\tilde{\eta}_m)$, etc.

5. Matrix Elements for DBM Operators

All quantities related to the nonnucleonic channels in the DBM can be expressed in the momentum representation as the sums of integral operators with factorized kernels [see Eq. (36)]:

$$O_{(i)}^{\mathrm{DBM}} = \varphi_{f'}(\mathbf{p}_i) O^{f'f}(\mathbf{q}'_i, \mathbf{q}_i; E) \varphi_f(\mathbf{p}_i). \quad (A.37)$$

Therefore, the m.e. of such an operator is equal to the sum of the m.e.'s for one-particle operators $O^{f'f}(\mathbf{q}'_i, \mathbf{q}_i; E)$ between the overlap functions $\chi_f(\mathbf{q}_i)$:

$$M_2 = \langle \Psi_{\mathrm{ex}} | O_{(2)}^{\mathrm{DBM}} | \Psi_{\mathrm{ex}} \rangle = \sum_{ff'} \langle \chi_{(2)}^{f'} | O_{(2)} | \chi_{(2)}^f \rangle \qquad (A.38)$$

$$= \sum_{\gamma n \gamma' n'} C_{n'}^{\gamma'} C_n^\gamma \sum_{i,j=1,2,3} M_{f\gamma n}^{f'\gamma'n'}(i2j),$$

where $M_{f\gamma n}^{f'\gamma'n'}(i2j)$ are the corresponding basis m.e.:

$$M_{f\gamma n}^{f'\gamma'n'}(i2j) = \langle I_{(2)i}^{f',\gamma'n'} | O_{(2)} | I_{(2)j}^{f,\gamma n} \rangle. \qquad (A.39)$$

Any scalar–isoscalar operator $O(\mathbf{q} - \mathbf{q}')$ which does not depend on spin and isospin variables (e.g., the DBM two-body force, the projector, the 3BF due to σ exchange, the norm of nonnucleonic component) can be expanded in spherical harmonics as

$$O(\mathbf{q}' - \mathbf{q}) = \sum_{LM} O_L(\mathbf{q}', \mathbf{q}) Y_{LM}^*(\hat{\mathbf{q}}') Y_{LM}(\hat{\mathbf{q}}). \qquad (A.40)$$

In this case, the spin-angular and isospin parts of the overlaps give

$$\sum_M \langle \mathcal{Y}_{g'}^{\mathcal{J}'J_i JM}(\hat{\mathbf{q}}') | Y_{LM}^*(\hat{\mathbf{q}}') Y_{LM}(\hat{\mathbf{q}}) | \mathcal{Y}_g^{\mathcal{J}J_i JM}(\hat{\mathbf{q}}_2) \rangle \qquad (A.41)$$

$$= \delta_{\mathcal{J}'\mathcal{J}} \delta_{g'L} \delta_{gL},$$

$$\sum_{t_{d_z}} \langle \mathcal{X}^{t'_d t'_{d_z}} | \mathcal{X}^{t_d t_{d_z}} \rangle = \delta_{t'_d t_d}. \qquad (A.42)$$

Therefore, nine m.e.'s for such an operator $M(i2j) \equiv M_{i2j}$ $(i, j = 1, 2, 3)$ can be reduced to radial integrals of four types (here, we omit the indices $f\gamma n$, $f'\gamma'n'$ for brevity):

$$M_{222} = \delta_{J'_i J_i} \delta_{l'l} \delta_{t'_{13} t_{13}} R_{222},$$

$$M_{122} = (-1)^{S_d + S'_{23}} \tau_{12}(t'_{23}, t_d) R_{122},$$

$$M_{322} = (-1)^{\lambda'_i + \lambda'} \tau_{32}(t'_{12}, t_d) R_{122},$$

$$M_{221} = (-1)^{S_d + S_{23}} \tau_{21}(t_{23}, t_d) R_{221},$$

$$M_{223} = (-1)^{\lambda_i + \lambda} \tau_{23}(t_{12}, t_d) R_{221},$$

$$M_{121} = (-1)^{S_{23} + S'_{23}} \tau_{12}(t'_{23}, t_d) \tau_{21}(t_{23}, t_d) R_{121},$$

$$M_{323} = (-1)^{\lambda + \lambda' + \lambda_i + \lambda'_i} \tau_{32}(t'_{12}, t_d) \tau_{23}(t_{12}, t_d) R_{121},$$

$$M_{123} = (-1)^{S_d + S'_{23} + \lambda_i + \lambda} \tau_{12}(t'_{23}, t_d) \tau_{23}(t_{12}, t_d) R_{121},$$

$$M_{321} = (-1)^{S_d + S_{23} + \lambda'_i + \lambda'} \tau_{32}(t'_{12}, t_d) \tau_{21}(t_{23}, t_d) R_{121}.$$

Here,

$$R_{121} \qquad (A.43)$$

$$= \sum_{\mathcal{J}\mathcal{J}'gg', mm'tt'} G_{21}^{\tilde{\varepsilon}'} G_{21}^{\tilde{\varepsilon}} \delta_{\mathcal{J}\mathcal{J}'} \delta_{gg'} R_g^{t't}(\tilde{\omega}_{n'm'}, \tilde{\omega}_{nm}; O),$$

$$R_{122} \qquad (A.44)$$

$$= \sum_{\mathcal{J}\mathcal{J}'g', mm'tt'} G_{21}^{\tilde{\varepsilon}'} G_{22}^\varepsilon \delta_{\mathcal{J}\mathcal{J}'} \delta_{g'l} R_l^{t'l}(\tilde{\omega}_{n'm'}, \tilde{\beta}_n; O),$$

$$R_{221} \tag{A.45}$$

$$= \sum_{\mathcal{J}\mathcal{J}'g,mm't} G_{22}^{\varepsilon'} G_{21}^{\tilde{\varepsilon}} \delta_{\mathcal{J}\mathcal{J}'} \delta_{gl'} R_{l'}^{l't}(\tilde{\beta}_{n'}, \tilde{\omega}_{nm}; O),$$

$$R_{222} \tag{A.46}$$

$$= \sum_{\mathcal{J}\mathcal{J}',mm'} G_{22}^{\varepsilon'} G_{22}^{\varepsilon} \delta_{\mathcal{J}\mathcal{J}'} R_l^{ll}(\tilde{\beta}_{n'}, \tilde{\beta}_n; O),$$

$$R_L^{t't}(\tilde{\omega}', \tilde{\omega}; O) \tag{A.47}$$

$$= \int_0^\infty \int_0^\infty (q')^{t'+2} q^{t+2} e^{-\tilde{\omega}'(q')^2} e^{-\tilde{\omega} q^2} O_L(q', q) dq' dq.$$

Below, we give the explicit formulas for the radial integrals $R_L^{t't}$ for all specific terms of the DBM interaction.

Projector. The total projector onto the state $\varphi_{\lambda_i, S_d}^{J_i}$ has the form

$$\Gamma^{\bar{f}} \equiv \Gamma_{\lambda_i, S_d}^{J_i} \tag{A.48}$$

$$= \sum_{M_i, t_{d_z}} |\varphi_{\lambda_i, S_d}^{J_i M_i t_d t_{d_z}}\rangle \delta(\mathbf{q} - \mathbf{q}') \langle \varphi_{\lambda_i, S_d}^{J_i M_i t_d t_{d_z}}|.$$

After expanding the δ function into partial waves,

$$\delta(\mathbf{q} - \mathbf{q}') = \sum_{LM} Y_{LM}^*(\mathbf{q}') Y_{LM}(\mathbf{q}) \delta(q - q')/q^2, \tag{A.49}$$

the corresponding operator O_L in Eq. (A.47) is reduced to

$$\Gamma_L^{\bar{f}} = \frac{\delta(q - q')}{q^2}, \tag{A.50}$$

and the radial integral for the projector takes the form

$$R_L^{t't}(\tilde{\omega}', \tilde{\omega}; \Gamma^{\bar{f}}) = \frac{\Gamma(\frac{t'+t+3}{2})}{2(\tilde{\omega}' + \tilde{\omega})^{\frac{t'+t+3}{2}}}, \tag{A.51}$$

where $\Gamma(x)$ is the gamma function.

Effective two-body DBM interaction. According to Eq. (29), the two-body DBM interaction in the $3N$ system (between nucleons 1 and 3) has the form

$$W_2 = \sum_{J_i, \lambda_i' \lambda_i} W_{\lambda_i' \lambda_i}^{J_i}(\mathbf{p}_2', \mathbf{p}_2, \mathbf{q}_2', \mathbf{q}_2; E), \tag{A.52}$$

where

$$W_{\lambda_i' \lambda_i}^{J_i} = \sum_{M_i} |\varphi_{\lambda_i', S_d}^{J_i M_i}\rangle \delta(\mathbf{q} - \mathbf{q}') \lambda_{\lambda_i' \lambda_i}^{J_i} \tag{A.53}$$

$$\times (E - q^2/(2\tilde{m})) \langle \varphi_{\lambda_i, S_d}^{J_i M_i}|;$$

therefore,

$$\left\{ W_{\lambda_i' \lambda_i}^{J_i} \right\}_L = \frac{\delta(q - q')}{q^2} \lambda_{\lambda_i' \lambda_i}^{J_i}(E - q^2/(2\tilde{m})). \tag{A.54}$$

In the present version of the DBM we employed a rational approximation for the energy dependence of the coupling constant $\lambda_{LL'}^J(E)$ [24]:

$$\lambda_{LL'}^J(E) = \lambda_{LL'}^J(0) \frac{E_0 + aE}{E_0 - E}, \tag{A.55}$$

where the parameters E_0 and a can be taken to be the same for all λ. We found that this simple rational form can reproduce quite accurately the exact energy dependence of the coupling constants $\lambda_{LL'}^J(E)$ calculated from the loop diagram in Fig. 1. Therefore, in the $3N$ system, the corresponding coupling constants $\lambda_{\lambda_i' \lambda_i}^{J_i}$ take the form

$$\lambda_{\lambda_i' \lambda_i}^{J_i}(E - q^2/(2\tilde{m})) = \lambda_{\lambda_i' \lambda_i}^{J_i}(0) \tag{A.56}$$

$$\times \left(-a + (a + 1) \frac{E_0}{E_0 - E} \frac{1}{1 + \dfrac{q^2}{2\tilde{m}(E_0 - E)}} \right).$$

The first term in Eq. (A.56) leads to the expression for the radial m.e. like (A.51). For calculating the second term, we expand the function $1/(1 + q^2)$ into a sum of Gaussians:

$$\frac{1}{1 + q^2/q_0^2} = \sum_{\mathcal{M}} \mathcal{B}_{\mathcal{M}} \exp(-\theta_{\mathcal{M}} q^2/q_0^2), \tag{A.57}$$

where $q_0^2 = 2\tilde{m}(E_0 - E) > 0$ (for $E < E_0$) and the expansion parameters $\{\mathcal{B}_{\mathcal{M}}, \theta_{\mathcal{M}}\}$ are universal constants. Then the total m.e. for two-body DBM interaction W_2 takes the form

$$R_L^{t't}(\tilde{\omega}', \tilde{\omega}; W_2^{\bar{f}'\bar{f}}) = \lambda_{\lambda_i' \lambda_i}^{J_i}(0) \tag{A.58}$$

$$\times \left(-a R_L^{t't}(\tilde{\omega}', \tilde{\omega}; \Gamma^{\bar{f}'\bar{f}}) + (a + 1) \frac{E_0}{E_0 - E} \right.$$

$$\left. \times \sum_{\mathcal{M}} \mathcal{B}_{\mathcal{M}} \frac{\Gamma(\frac{t'+t+3}{2})}{2(\tilde{\omega}' + \tilde{\omega} + \theta_{\mathcal{M}}/q_0^2)^{\frac{t'+t+3}{2}}} \right).$$

Norm of $6qN$ component. The norm of the $6qN$ component of the total $3N$ wave function determined by Eq. (34) can be expressed via a sum of the m.e.'s of the operator:

$$\mathcal{N}(\mathbf{q}', \mathbf{q}) = -\frac{d}{dE} \lambda_{\lambda_i' \lambda_i}^{J_i}(E - q^2/(2\tilde{m})) \delta(\mathbf{q}' - \mathbf{q}). \tag{A.59}$$

For the energy dependence such as in Eq. (A.55), the derivative takes the form

$$-\frac{d}{dE}\lambda(E) = \lambda(0)\frac{1}{(E_0 - E)^2}. \quad (A.60)$$

Therefore,

$$R_L^{t't}(\tilde{\omega}', \tilde{\omega}; \mathcal{N}^{\bar{f}'\bar{f}}) = \lambda_{\lambda_i'\lambda_i}^{J_i}(0)\frac{E_0(1+a)}{(E-E_0)^2} \quad (A.61)$$

$$\times \sum_{\mathcal{M}'\mathcal{M}} \mathcal{B}'_{\mathcal{M}'}\mathcal{B}_{\mathcal{M}}\frac{\Gamma(\frac{t'+t+3}{2})}{2(\tilde{\omega}' + \tilde{\omega} + (\theta_{\mathcal{M}} + \theta'_{\mathcal{M}})/q_0^2)^{\frac{t'+t+3}{2}}}.$$

Three-body force due to OME. When calculating the m.e.'s for 3BF due to OME [Eq. (37)], viz.,

$${}^{\text{OME}}W_{\lambda_i'\lambda_i}^{J_i'J_i}(\mathbf{q}_i', \mathbf{q}_i; E) \quad (A.62)$$

$$= \int d\mathbf{k}\frac{B_{\lambda_i'}^{J_i'}(\mathbf{k}')}{E - E_\alpha - \frac{q_i'^2}{2m}}V^{\text{OME}}(\mathbf{q}_i', \mathbf{q}_i)$$

$$\times \frac{B_{\lambda_i}^{J_i}(\mathbf{k})}{E - E_\alpha - \frac{q_i^2}{2m}},$$

we use a similar trick as in the calculation of the norm for the $6qN$ component. It enables us to exclude the vertex functions $B_{\lambda_i}^{J_i}(\mathbf{k})$ from the formulas for the m.e.'s. By replacing the product of propagators in the integral [over the meson momentum $\mathbf{k}$ in Eq. (A.62)] with their difference, one obtains the following expression free of the vertex functions:

$$\int \frac{B_{\lambda_i'}^{J_i}(\mathbf{k})B_{\lambda_i}^{J_i}(\mathbf{k})}{\left(E - \varepsilon(k) - \frac{q^2}{2m}\right)\left(E - \varepsilon(k) - \frac{q'^2}{2m}\right)}d\mathbf{k}$$

$$\quad (A.63)$$

$$= \frac{\lambda_{\lambda_i'\lambda_i}^{J_i}\left(E - \frac{q'^2}{2m}\right) - \lambda_{\lambda_i'\lambda_i}^{J_i}\left(E - \frac{q^2}{2m}\right)}{q'^2 - q^2}$$

$$= \Delta\lambda_{\lambda_i'\lambda_i}^{J_i}(q', q).$$

This quantity is the finite-difference analog of the derivative of λ with respect to q^2, which, in the case of the energy dependence (A.55), takes the form

$$\Delta\lambda(q', q) \quad (A.64)$$

$$= \lambda(0)E_0(1+a)\frac{1}{E - q^2/(2m)}\frac{1}{E - q'^2/(2m)}.$$

Thus, the m.e.'s for OME can be found without explicit usage of the vertex functions $B_{\lambda_i}^{J_i}(\mathbf{k})$.

Three-body force due to OSE. The exchange operator for scalar mesons does not include any spin–isospin variables. Therefore, Eq. (A.62) can be simplified and, in view of the energy dependence given in Eq. (A.55), reduces to the form

$${}^{\text{OSE}}W_{\lambda_i'\lambda_i}^{J_i'J_i}(\mathbf{q}_i', \mathbf{q}_i; E) = \delta_{J_i'J_i}\lambda_{\lambda_i'\lambda_i(0)}^{J_i} \quad (A.65)$$

$$\times E_0(1+a)\frac{1}{E - E_0 - \frac{q_i^2}{2m}}\frac{-g_{\sigma NN}^2}{(\mathbf{q}_i - \mathbf{q}_i')^2 + m_\sigma^2}$$

$$\times \frac{1}{E - E_0 - \frac{q_i'^2}{2m}}.$$

Using the expansion of the OME interaction into partial waves,

$$\frac{1}{(\mathbf{q}_i' - \mathbf{q}_i)^2 + m_\sigma^2} = \sum_{LM}Y_{LM}^*(\mathbf{q}')\frac{Q_L(z)}{2qq'}Y_{LM}(\mathbf{q}),$$

$$\quad (A.66)$$

where m_σ is the mass of the σ meson, $Q_L(z)$ is a Legendre function of the second kind, and

$$z = \frac{q'^2 + q^2 + m_\sigma^2}{2q'q},$$

one gets the following radial integral for OSE m.e.:

$$R_L^{t't}(\tilde{\omega}', \tilde{\omega}; {}^{\text{OSE}}W^{\bar{f}'\bar{f}}) \quad (A.67)$$

$$= g_{\sigma NN}^2\lambda_{\lambda_i'\lambda_i}^{J_i}(0)\frac{E_0(1+a)}{(E-E_0)^2}$$

$$\times \sum_{\mathcal{M}'\mathcal{M}} \mathcal{B}'_{\mathcal{M}'}\mathcal{B}_{\mathcal{M}}\mathcal{R}(t', \tilde{\omega}' + \theta', t, \tilde{\omega} + \theta; L, m_\sigma),$$

where

$$\mathcal{R}(t', \omega', t, \omega; L, m) \quad (A.68)$$

$$= \int\int(q')^{t'+2}e^{-\omega'q'^2}\frac{Q_L(z)}{2qq'}q^{t+2}e^{-\omega q^2}dq'dq.$$

We calculate integrals like those in Eq. (A.68) in the following way. In the integral (A.68), $t' \geq L$ and $t \geq L$, and it can be shown that $t' - L$ and $t - L$ are even numbers. Introducing the auxiliary indices k and k', so that

$$t = L + 2k, \qquad t' = L + 2k',$$

the integral (A.68) can be written as

$$\mathcal{R}(L + 2k', \omega', L + 2k, \omega; L, m) \quad (A.69)$$

$$= \left(-\frac{\partial}{\partial\omega'}\right)^{k'}\left(-\frac{\partial}{\partial\omega}\right)^k\mathcal{R}(L, \omega', L, \omega; L, m).$$

The last integral with $t = t' = L$ is easily calculated in the coordinate representation. Using the well-known

formulas

$$\frac{Q_L(\frac{q'^2+q^2+m^2}{2q'q})}{2qq'} = \int\limits_0^\infty j_L(q'\rho)\frac{e^{-m\rho}}{\rho}j_L(q\rho)\rho^2 d\rho$$

(A.70)

and

$$\sqrt{\frac{2}{\pi}}\int\limits_0^\infty e^{-\beta q^2}q^{L+2}j_L(q\rho)dq = \frac{\rho^L}{(2\beta)^{L+3/2}}e^{-\rho^2/(4\beta)},$$

(A.71)

we get the result

$$\mathcal{R}(L,\omega',L,\omega;L,m)$$

(A.72)

$$= \frac{1}{(4\omega\omega')^{L+3/2}}J_L^{\text{Yuk}}((\omega^{-1}+\omega'^{-1})/4,m),$$

where

$$J_L^{\text{Yuk}}(b,m) = \int\limits_0^\infty \rho^{2L+2}\frac{e^{-m\rho}}{\rho}e^{-b\rho^2}d\rho.$$

(A.73)

This integral of the Yukawa potential is calculated by recursions:

$$J_L^{\text{Yuk}}(b,m) = \frac{1}{m^{L+1}}Z_L(x), \quad x = \frac{m}{2\sqrt{b}},$$

(A.74)

where

$$Z_0(x) = \sqrt{\pi}xe^{x^2}(1-\text{erf}(x)),$$

(A.75)

$$Z_1(x) = 2x^2(1-Z_0(x)),$$

(A.76)

$$Z_L(x) = 2x^2((k-2)Z_{L-2}(x)-Z_{L-1}(x)).$$

(A.77)

These recursions (especially for large L) for functions $Z(x)$ and also expressions (A.75) and (A.76) for Z_0

and Z_1 cannot be used for large values of x. So, at large x, we use the following asymptotic series:

$$J_{2L}^{\text{Yuk}}(b,m)$$

(A.78)

$$= \sum_{i=0}^\infty \left(-\frac{2b}{m^2}\right)^i \frac{(2L+2i-1)!!(L+i)!}{i!},$$

$$J_{2L+1}^{\text{Yuk}}(b,m)$$

(A.79)

$$= \sum_{i=0}^\infty \left(-\frac{2b}{m^2}\right)^i \frac{(2L+2i+1)!!(L+i)!}{i!}.$$

Three-body force due to OPE. For OPE, we take the interaction operator in the standard form

$$V_{\text{OPE}}^{(i)} = -\frac{g_{\pi NN}^2}{(2m_N)^2}(\boldsymbol{\sigma}^{(i)}\cdot\mathbf{p})$$

(A.80)

$$\times\frac{1}{p^2+m_\pi^2}(\mathbf{S}_d\cdot\mathbf{p})(\boldsymbol{\tau}^{(i)}\cdot\mathbf{T}_d),$$
$$\mathbf{p} = \mathbf{q}-\mathbf{q}',$$

where $\boldsymbol{\sigma}^{(i)}$ and $\boldsymbol{\tau}^{(i)}$ are the spin and isospin operators of the third (ith) nucleon, whereas $\mathbf{S}_d$ and $\mathbf{T}_d$ are the operators of the total spin and isospin of the $6q$ bag, respectively. We found that the contribution of OPE is so small that it is sufficient to include only S waves in its evaluation. In this case, only the central part of the OPE interaction remains:

$$V_c^{\text{OPE}} = g_{\pi NN}^2 \frac{m_\pi^2}{(4m_N)^2}\frac{1}{3}(\boldsymbol{\sigma}^{(i)}\cdot\mathbf{S}_d)$$

(A.81)

$$\times(\boldsymbol{\tau}^{(i)}\cdot\mathbf{T}_d)\frac{1}{p^2+m_\pi^2}.$$

The spin–isospin m.e. is nonzero only for a singlet–triplet transition:

$$\left\langle S_d=0,T_d=1\left|\frac{1}{3}(\boldsymbol{\sigma}^{(i)}\cdot\mathbf{S}_d)(\boldsymbol{\tau}^{(i)}\cdot\mathbf{T}_d)\right|S_d=1,T_d=0\right\rangle = 4/9.$$

(A.82)

Then, the m.e. of the OPE contribution for S waves takes the form (for $S_d=0$, $S_d'=1$ or $S_d=1$, $S_d'=0$)

$$R_0^{00}(\tilde\omega',\tilde\omega;{}^{\text{OPE}}W^{\bar{f}'\bar{f}})$$

(A.83)

$$= \frac{4}{9}f_{\pi NN}^2\sqrt{\lambda_{00}^0(0)\lambda_{00}^1(0)}\frac{E_0(1+a)}{(E-E_0)^2}$$

$$\times\sum_{\mathcal{M}'\mathcal{M}}\mathcal{B}'_{\mathcal{M}'}\mathcal{B}_{\mathcal{M}}\mathcal{R}(0,\tilde\omega'+\theta',0,\tilde\omega+\theta;0,m_\pi).$$

Here, we take the vertex functions B_0^0 and B_0^1 differing

from each other only by a constant. Therefore, using Eq. (A.63), one can exclude these functions from the formula for the m.e.

Three-body Coulomb force. The m.e. of the operator for the three-body Coulomb force (60) (for pointlike charges) can be expressed in terms of integrals over the overlap functions $\chi_f(\mathbf{q})$:

$$M_{i2j}({}^{\text{Coul}}W) = e^2\sum_{J_iM_iL_iL_i'}\lambda_{L_iL_i'}^{J_i}(0)(1+a)$$

(A.84)

$$\times \int \frac{\left\langle I_{(2)i}^{f',\gamma'n'}(\mathbf{q}') \left| \frac{1+\tau_3^{(2)}}{2}(1+\hat{t}_{d_z}) \right| I_{(2)j}^{f,\gamma n}(\mathbf{q}) \right\rangle}{\left(E - E_0 - \frac{q^2}{2m}\right)(\mathbf{q} - \mathbf{q}')^2 \left(E - E_0 - \frac{q'^2}{2m}\right)} d\mathbf{q} d\mathbf{q}',$$

where $(1 + \tau_3^{(2)})/2$ is the operator of the nucleon charge (nucleon with number 2). The isospin part of this m.e. is equal to

$$\tau^{\mathrm{Coul}}(t_d) \qquad\qquad (\mathrm{A.85})$$

$$= \sum_{t_{d_z}} \left\langle \mathcal{X}^{t_d t_{d_z}} \left| \frac{1+\tau_3^{(2)}}{2}(1+t_{d_z}) \right| \mathcal{X}^{t_d} \right\rangle$$

$$= \begin{cases} 1 & \text{for } t_d = 0, \\ \dfrac{1}{3} & \text{for } t_d = 1. \end{cases}$$

Thus, for calculation of 3BF Coulomb m.e., one can apply formulas Eqs. (A.69)–(A.79) for the isoscalar operator with this additional isospin factor (A.85):

$$R_L^{t't}(\tilde{\omega}', \tilde{\omega}; {}^{\mathrm{Coul}}W^{\bar{f}'\bar{f}}) \qquad (\mathrm{A.86})$$

$$= \delta_{t'_d t_d} \tau^{\mathrm{Coul}}(t_d) e^2 \lambda_{\lambda'_i \lambda_i}^{J_i}(0) \frac{E_0(1+a)}{(E-E_0)^2}$$

$$\times \sum_{\mathcal{M}'\mathcal{M}} \mathcal{B}'_{\mathcal{M}'} \mathcal{B}_{\mathcal{M}} \mathcal{R}^{\mathrm{Coul}}(t', \tilde{\omega}' + \theta', t, \tilde{\omega} + \theta; L).$$

Here, the Coulomb integral $\mathcal{R}^{\mathrm{Coul}}(t, \omega', t, \omega; L)$ for the pointlike charges is obtained from the Yukawa integral $\mathcal{R}$ (A.68) by setting $m = 0$:

$$\mathcal{R}^{\mathrm{Coul}}(t', \omega', t, \omega; L) = \mathcal{R}(t', \omega', t, \omega; L, 0). \quad (\mathrm{A.87})$$

Hence, these Coulomb integrals are reduced by differentiating [see Eq. (A.69)] to the integrals

$$\mathcal{R}^{\mathrm{Coul}}(L, \omega', L, \omega; L) = \frac{1}{(4\omega\omega')^{L+3/2}} \qquad (\mathrm{A.88})$$

$$\times \int_0^\infty \rho^{2L+2} \frac{1}{\rho} \exp\left[-\frac{\rho^2}{4}(\omega^{-1} + \omega'^{-1})\right] d\rho$$

$$\equiv \frac{1}{(4\omega\omega')^{L+3/2}} J_L^{\mathrm{Coul}}((\omega^{-1} + \omega'^{-1})/4),$$

$$J_L^{\mathrm{Coul}}(b) = \frac{\Gamma(L+1)}{2b^{L+1}}. \qquad (\mathrm{A.89})$$

Now, we can replace the Coulomb potential $1/\rho$ between the pointlike charges in the integrand in Eq. (A.88) with the corresponding Coulomb potential between the "smeared" charges:

$$J_L^{\mathrm{Coul}}(b, a) = \int_0^\infty \rho^{2L+2} \frac{\mathrm{erf}(\rho\sqrt{a})}{\rho} e^{-b\rho^2} d\rho. \quad (\mathrm{A.90})$$

The latter integral is evaluated analytically in the form of a finite sum:

$$J_L^{\mathrm{Coul}}(b, a) = \frac{1}{2} \frac{1}{a^{L+1}} \qquad (\mathrm{A.91})$$

$$\times \sum_{k=0}^L C_L^k \frac{k!}{\left(\dfrac{b}{a}\right)^{k+1}} \frac{(2L-2k+1)!!}{2^{L-k}\left(\dfrac{b}{a}+1\right)^{L-k+1/2}},$$

where C_L^k are the binomial coefficients.

REFERENCES

1. *Proceedings of the XVIII European Conference on Few-Body Problems in Physics, Bled, Slovenia, 2002*; Few-Body Syst. Suppl. **14** (2003).
2. W. Tornow, H. Witala, and A. Kievsky, Phys. Rev. C **57**, 555 (1998); D. Hueber, Few-Body Syst. Suppl. **10**, 305 (1999); L. D. Knutson, Nucl. Phys. A **631**, 9c (1998).
3. Y. Koike and S. Ishikawa, Nucl. Phys. A **631**, 683c (1998).
4. H. O. Meyer, *Talk Presented at Symposium on Current Topics in the Field of Light Nuclei, Cracow, Poland, 1999*, p. 858 (unpublished).
5. D. L. Groep *et al.*, Phys. Rev. C **63**, 014005 (2001).
6. D. P. Watts *et al.*, Phys. Rev. C **62**, 014616 (2000).
7. L. Weinstein, Few-Body Syst. Suppl. **14**, 316 (2003).
8. V. I. Kukulin, I. T. Obukhovsky, V. N. Pomerantsev, and A. Faessler, Yad. Fiz. **64**, 1748 (2001) [Phys. At. Nucl. **64**, 1667 (2001)]; J. Phys. G **27**, 1851 (2001).
9. B. F. Gibson, Lect. Notes Phys. **260**, 511 (1986).
10. B. F. Gibson *et al.*, Few-Body Syst. **3**, 143 (1988).
11. P. Sauer, *Talk Presented at Symposium on Current Topics in the Field of Light Nuclei, Cracow, Poland, 1999*, p. 503 (unpublished).
12. N. Kaiser, R. Brockmann, and W. Weise, Nucl. Phys. A **625**, 758 (1997); N. Kaiser, S. Gerstendörfer, and W. Weise, Nucl. Phys. A **637**, 395 (1998).
13. E. Oset *et al.*, Prog. Theor. Phys. **103**, 351 (2000).
14. M. M. Kaskulov and H. Clement, Phys. Rev. C **70**, 014002 (2004); **70**, 057001 (2004).
15. A. M. Kusainov, V. G. Neudatchin, and I. T. Obukhovsky, Phys. Rev. C **44**, 2343 (1991).
16. F. Myhrer and J. Wroldsen, Rev. Mod. Phys. **60**, 629 (1988).
17. A. Faessler and F. Fernandez, Phys. Lett. B **124B**, 145 (1983); A. Faessler, F. Fernandez, G. Lübeck, and K. Shimizu, Nucl. Phys. A **402**, 555 (1983).
18. V. I. Kukulin and V. N. Pomerantsev, Prog. Theor. Phys. **88**, 159 (1992).
19. Y. Yamauchi and M. Wakamatsu, Nucl. Phys. A **457**, 621 (1986).
20. M. Oka and K. Yazaki, Nucl. Phys. A **402**, 477 (1983); E. M. Henley, L. S. Kisslinger, and G. A. Miller, Phys. Rev. C **28**, 1277 (1983); K. Bräuer, E. M. Henley, and G. A. Miller, Phys. Rev. C **34**, 1779 (1986).
21. T. Fujita *et al.*, Prog. Theor. Phys. **100**, 931 (1998).
22. Fl. Stancu, S. Pepin, and L. Ya. Glozman, Phys. Rev. C **56**, 2779 (1997).

23. D. Bartz and Fl. Stancu, Phys. Rev. C **63**, 034001 (2001).
24. V. I. Kukulin, I. T. Obukhovsky, V. N. Pomerantsev, and A. Faessler, Int. J. Mod. Phys. E **11**, 1 (2002).
25. V. I. Kukulin, Few-Body Syst. Suppl. **14**, 71 (2003).
26. T. Hatsuda and T. Kunihiro, Phys. Rep. **247**, 221 (1994); T. Hatsuda, T. Kunihiro, and H. Shimizu, Phys. Rev. Lett. **82**, 2840 (1999).
27. Yu. D. Bayukov *et al.*, Yad. Fiz. **34**, 167 (1981) [Sov. J. Nucl. Phys. **34**, 95 (1981)]; Yad. Fiz. **34**, 785 (1981) [Sov. J. Nucl. Phys. **34**, 437 (1981)]; A. V. Vlasov *et al.*, Yad. Fiz. **36**, 915 (1982) [Sov. J. Nucl. Phys. **36**, 536 (1982)].
28. T. Risser and M. D. Shuster, Phys. Lett. B **43B**, 68 (1973); C. A. Mosbacher and F. Osterfeld, Phys. Rev. C **56**, 2014 (1997); A. Gärdestig, G. Fäldt, and C. Wilkin, Phys. Lett. B **421**, 41 (1998).
29. Yu. A. Kuperin, K. A. Makarov, S. P. Merkuriev, *et al.*, Teor. Mat. Fiz. **75**, 431 (1987); **76**, 834 (1988).
30. Yu. A. Kuperin, K. A. Makarov, S. P. Merkuriev, *et al.*, J. Math. Phys. **31**, 1681 (1990).
31. Yu. A. Kuperin, K. A. Makarov, S. P. Merkuriev, *et al.*, *Quantum Scattering Theory on Energy-Dependent Potentials*, in *Properties of Few-Body and Quark−Hadron Systems* (Vilnius, 1986), Vol. 2, p. 28.
32. V. I. Kukulin, V. N. Pomerantsev, M. Kaskulov, and A. Faessler, J. Phys. G **30**, 287 (2004); V. I. Kukulin, V. N. Pomerantsev, and A. Faessler, J. Phys. G **30**, 309 (2004).
33. Yu. A. Kuperin, K. A. Makarov, S. P. Merkuriev, and A. K. Motovilov, Yad. Fiz. **48**, 358 (1988) [Sov. J. Nucl. Phys. **48**, 224 (1988)].
34. Yu. A. Simonov, Yad. Fiz. **36**, 722 (1982) [Sov. J. Nucl. Phys. **36**, 422 (1982)]; **38**, 1542 (1983) [**38**, 939 (1983)].
35. Yu. S. Kalashnikova and I. M. Narodetskii, Yad. Fiz. **46**, 1389 (1987) [Sov. J. Nucl. Phys. **46**, 820 (1987)]; Few-Body Syst. **4**, 115 (1988).
36. A. K. Motovilov, Teor. Mat. Fiz. **104**, 281 (1995).
37. E. W. Schmid, Helv. Phys. Acta **60**, 394 (1987).
38. V. I. Kukulin and M. A. Shikhalev, Yad. Fiz. **67**, 1558 (2004) [Phys. At. Nucl. **67**, 1536 (2004)].
39. V. I. Kukulin, V. M. Krasnopolsky, and V. N. Pomerantsev, in *Proceedings of the 3rd LIYaF Symposium "Nucleon−Nucleon and Hadron−Nuclear Interactions at Intermediate Energies"* (LIYaF, Leningrad, 1986), p. 103.
40. J. Horaček, J. Bok, V. M. Krasnopolskij, and V. I. Kukulin, Phys. Lett. B **172**, 1 (1986).
41. G. H. Berthold and H. Zankel, Phys. Rev. C **30**, 14 (1984).
42. M. M. Mustafa, Phys. Rev. C **47**, 473 (1993).
43. N. L. Rodning and L. D. Knutson, Phys. Rev. C **41**, 898 (1990).
44. C. Fasano and T.-S. H. Lee, Phys. Rev. C **36**, 1906 (1987); Phys. Lett. B **217**, 9 (1989).
45. E. M. Tursunov, Kh. D. Razikov, V. I. Kukulin, *et al.*, Yad. Fiz. **57**, 2155 (1994) [Phys. At. Nucl. **57**, 2075 (1994)].
46. V. T. Voronchev *et al.*, J. Phys. G **8**, 667 (1982); V. M. Krasnopol'ski *et al.*, Phys. Lett. B **121B**, 96 (1983); V. I. Kukulin *et al.*, Nucl. Phys. A **453**, 365 (1986).
47. V. I. Kukulin and V. M. Krasnopol'sky, J. Phys. G **3**, 795 (1977).
48. H. Dijk and B. L. G. Bakker, Nucl. Phys. A **494**, 438 (1989); **531**, 555 (1991).
49. A. Nogga *et al.*, Phys. Rev. C **67**, 034004 (2003).
50. S. C. Pieper, V. R. Pandharipande, R. B. Wiringa, and J. Carlson, Phys. Rev. C **64**, 014001 (2001).
51. J. L. Friar, B. F. Gibson, G. L. Payne, and C. R. Chen, Phys. Rev. C **34**, 1463 (1986).
52. B. Doyle, B. Goulard, and G. Cory, Phys. Rev. C **45**, 1444 (1992).
53. S. C. Pieper and R. B. Wiringa, Annu. Rev. Nucl. Part. Sci. **51**, 53 (2001).
54. G. L. Payne, J. L. Friar, and B. F. Gibson, Phys. Rev. C **22**, 832 (1980); J. L. Friar, B. F. Gibson, and G. L. Payne, Phys. Rev. C **35**, 1502 (1987).
55. A. Laverne and C. Gignoux, Nucl. Phys. A **203**, 597 (1973).
56. J. A. Nolen and J. P. Schiffer, Annu. Rev. Nucl. Part. Sci. **19**, 471 (1969).
57. V. I. Kukulin, V. N. Pomerantsev, A. Faessler, *et al.*, Phys. Rev. C **57**, 535 (1998).
58. C. R. Howell *et al.*, Phys. Lett. B **444**, 252 (1998).
59. I. Šlaus, Y. Akaishi, and H. Tanaka, Phys. Rep. **173**, 257 (1989).
60. V. Huhn *et al.*, Phys. Rev. C **63**, 014003 (2001); Phys. Rev. Lett. **85**, 1190 (2000).
61. P. U. Sauer and H. Walliser, J. Phys. G **3**, 1513 (1977).
62. M. Rahman and G. A. Miller, Phys. Rev. C **27**, 917 (1983).
63. S. Albeverio *et al.*, Phys. Rev. C **29**, 680 (1984).
64. R. Machleidt, Phys. Rev. C **63**, 024001 (2001).
65. B. L. G. Bakker and I. M. Narodetsky, Adv. Nucl. Phys. **21**, 1 (1994).
66. H. J. Weber, Ann. Phys. (N.Y.) **207**, 417 (1991).
67. T. Skorodko *et al.*, *Talk Presented at 8th International Workshop "MESON 2004", Cracow, Poland, 2004* (unpublished).
68. J. D. Walecka, Ann. Phys. (N.Y.) **83**, 491 (1974); B. D. Serot and J. D. Walecka, Adv. Nucl. Phys. **16**, 1 (1986); B. D. Serot, Rep. Prog. Phys. **55**, 1855 (1992).

Structure of States and Transition Rates
in the Even−Even $N = 82$ Nucleus ^{136}Xe*

V. I. Isakov[1), H. Mach[2), B. Fogelberg[2), K. I. Erokhina[3), A. J. Aas[4), and E. Hagebø[4)**

Abstract—The properties of the ^{136}Xe nucleus are theoretically investigated by using two different approaches: the two-quasiparticle RPA method and the shell-model calculation. The investigated characteristics include both the energy levels and the electromagnetic properties of ^{136}Xe. Comprehensive comparison with the experiment that includes all the currently available experimental data is performed. © 2005 Pleiades Publishing, Inc.

1. INTRODUCTION

The singly magic nuclei provide a detailed testing of model predictions for residual interaction between like nucleons and checking of different theoretical approaches for their description. Such nuclei with $N = 82$, including the ^{136}Xe, have been interesting from a theoretical viewpoint for a long time and there exist several calculations for them. The shell model was applied to these nuclides by Wildenthal in [1], while in [2−5] their properties were considered using the TD approximation accounting for the pairing correlations and particle number projection. The nature of isomerism in the even $N = 82$ isotones was cleared up by Heyde *et al.* in [6]. Paper [7] treated their properties in the framework of the generalized seniority scheme. Wildenthal [8] calculated the spectra of even and odd $N = 82$ isotones from ^{133}Sb to ^{154}Hf in the framework of the multiparticle shell model that used a restricted basis and 160 values of fitted pair matrix elements representing the effective interaction. A similar procedure, initiated due to the updated and extended experimental information on the single-proton nucleus ^{133}Sb [9] and the two-proton nucleus ^{134}Te [10], but with the full model space of the proton 50−82 shell, was also demonstrated by Blomqvist in [11], where nuclei with up to six protons added to

^{132}Sn were studied. Here, the experimental single-particle energies (except that for the $3s_{1/2}$ state) were used and the two-body matrix elements of [8] were employed as starting ones in the fitting procedure. At the same time, an extended shell-model calculation using realistic G-matrix interaction was performed for nuclei with even $Z = 52−62$, $N = 82$ in [12]. A systematic study of the $N = 82$ isotones from ^{132}Sn to ^{146}Gd based on the RPA method [13] was reported by us earlier [14].

However, the whole bulk of experimental evidence [15−26] obtained by now for ^{136}Xe, including the new data on electromagnetic properties, stimulates us to make a new theoretical review of the situation in this nuclei. We begin the interpretation of the ^{136}Xe properties also in the framework of the RPA method. The only difference with [14] is a new set of values for single-particle energies that is summarized in our work [27] and for residual interaction that was also recently used by us [28] to interpret the odd−odd $N = 83$ nucleus ^{136}I. Starting from this approach, we continue to the shell-model calculation. The intercomparison between two calculations is presented at the end of this paper.

2. BASIC RELATIONS DEFINING
THE SPECTRA OF LEVELS
AND TRANSITION PROBABILITIES IN RPA

Assuming the presence of correlations in the true ground state $|\widetilde{0}\rangle$ of an even−even nucleus, we define the creation operator $Q^+_{n,JM}$ of the one-phonon excited state $|\omega_n JM\rangle = Q^+_{n,JM}|\widetilde{0}\rangle$ as

$$Q^+_{n,JM} = \sum_{a \geq b} X^{n,J}_{j_a j_b}[\xi^+_a \xi^+_b]_{JM} - \sum_{c \geq d} Y^{n,J}_{j_c j_d}[\xi_c \xi_d]_{JM},$$

$$(1)$$

*This article was submitted by the authors in English.

$^{1)}$Petersburg Nuclear Physics Institute, Russian Academy of Sciences, Gatchina, 188350 Russia.

$^{2)}$Department of Radiation Sciences, University of Uppsala, Sweden.

$^{3)}$Ioffe Physicotechnical Institute, Russian Academy of Sciences, Politekhnicheskaya ul. 26, St. Petersburg, 194021 Russia.

$^{4)}$Department of Chemistry, University of Oslo, Norway.

**E-mail: `visakov@thd.pnpi.spb.ru`

where

$$[\xi_a^+ \xi_b^+]_{JM} = \frac{1}{\sqrt{1+\delta_{j_a j_b}}} \sum_{m_a m_b} C_{j_a m_a j_b m_b}^{JM} \xi_{j_a m_a}^+ \xi_{j_b m_b}^+, \quad (2)$$

$$[\xi_c \xi_d]_{JM} = \frac{1}{\sqrt{1+\delta_{j_c j_d}}} \quad (3)$$
$$\times \sum_{m_c m_d} C_{j_c m_c j_d m_d}^{JM} \xi_{j_c - m_c} \xi_{j_d - m_d} \varphi_c \varphi_d,$$

$$X_{j_a j_b}^{n,J} = \langle \omega_n; JM | [\xi_a^+ \xi_b^+] | 0 \rangle, \quad (4)$$

$$Y_{j_c j_d}^{n,J} = \langle \omega_n; JM | [\xi_c \xi_d] | 0 \rangle. \quad (5)$$

Here, ξ^+ are the quasiparticle operators defined by the equations

$$a_\alpha^+ = u_{|\alpha|} \xi_\alpha^+ - v_{|\alpha|} \varphi_\alpha \xi_{-\alpha} \text{ and } u_{|\alpha|}^2 + v_{|\alpha|}^2 = 1, \quad (6)$$

where $\varphi_\alpha = (-1)^{\ell_\alpha + j_\alpha - m_\alpha}$ is the phase of the particle−hole transformation (we use below the designations $u_{|\alpha|} = u_\alpha$ and $v_{|\alpha|} = v_\alpha$, omitting the magnetic quantum numbers that enter only in φ_α), and $|-\alpha\rangle$ is a state with the opposite sign of magnetic quantum number with respect to $|\alpha\rangle$.

The set of RPA equations that define the amplitudes "X" and "Y" of the states $|\omega_n, JM\rangle$ and the eigenvalues ω_n has the following form:

$$\left\| \begin{matrix} [(E-\omega)I + A] & B \\ -B & -[(E+\omega)I + A] \end{matrix} \right\| \begin{pmatrix} X \\ Y \end{pmatrix} = 0. \quad (7)$$

In Eq. (7), $E = E_{ab} = E_{j_a} + E_{j_b}$, $I_{cd,ab} = \delta_{j_a j_c} \delta_{j_b j_d}$, E_j is a quasiparticle energy, while the matrix elements of the submatrices A and B in the case of even−even nuclei look as follows:

$$A_{cd,ab} \equiv A_{j_c j_d, j_a j_b}^J = (u_{j_c} u_{j_d} u_{j_a} u_{j_b} \quad (8)$$
$$+ v_{j_c} v_{j_d} v_{j_a} v_{j_b})_a \langle j_c j_d; J | \hat{\vartheta} | j_a j_b; J \rangle_a$$
$$+ (u_{j_c} v_{j_d} u_{j_a} v_{j_b} + v_{j_c} u_{j_d} v_{j_a} u_{j_b})_a$$
$$\times \langle j_c \bar{j}_d; J | \hat{\vartheta} | j_a \bar{j}_b; J \rangle_a - (-1)^{j_a + j_b + J} (v_{j_c} u_{j_d} u_{j_a} v_{j_b}$$
$$+ u_{j_c} v_{j_d} v_{j_a} u_{j_b})_a \langle j_c \bar{j}_d; J | \hat{\vartheta} | j_b \bar{j}_a; J \rangle_a,$$

$$B_{cd,ab} \equiv B_{j_c j_d, j_a j_b}^J = (u_{j_c} u_{j_d} v_{j_a} v_{j_b} \quad (9)$$
$$+ v_{j_c} v_{j_d} u_{j_a} u_{j_b})_a \langle j_c j_d; J | \hat{\vartheta} | j_a j_b; J \rangle_a$$
$$- (u_{j_c} v_{j_d} v_{j_a} u_{j_b} + v_{j_c} u_{j_d} u_{j_a} v_{j_b})_a$$
$$\times \langle j_c \bar{j}_d; J | \hat{\vartheta} | j_a \bar{j}_b; J \rangle_a + (-1)^{j_a + j_b + J} (v_{j_c} u_{j_d} v_{j_a} u_{j_b}$$
$$+ u_{j_c} v_{j_d} u_{j_a} v_{j_b})_a \langle j_c \bar{j}_d; J | \hat{\vartheta} | j_b \bar{j}_a; J \rangle_a.$$

In Eqs. (8) and (9), ${}_a\langle j_c j_d; J | \hat{\vartheta} | j_a j_b; J \rangle_a$ and ${}_a\langle j_c \bar{j}_d; J | \hat{\vartheta} | j_a \bar{j}_b; J \rangle_a$ are the antisymmetrical matrix

elements of the effective interaction $\hat{\vartheta}$ in the particle−particle and particle−hole channels with a given spin (see [29, 30]).

From the explicit form of the system (7), there follows the normalization condition on the X and Y amplitudes, which looks like

$$\left| \sum_{a \geq b} X_{j_a j_b}^{n,J} X_{j_a j_b}^{m,J} - \sum_{c \geq d} Y_{j_c j_d}^{n,J} Y_{j_c j_d}^{m,J} \right| = \delta_{mn}, \quad (10)$$

which in terms of the RPA bosons corresponds to the condition

$$\langle \tilde{0} | Q_{n,JM} Q_{m,JM}^+ | \tilde{0} \rangle = \delta_{mn}. \quad (11)$$

In [2, 3, 14], which described systems with valence protons above the $Z = 50$, $N = 82$ shells, the interaction of the following form was used:

$$\hat{\vartheta} = V_0(\hat{P}_s + t\hat{P}_t) \exp(-\beta r_{12}^2), \quad (12)$$

where $V_0 = -33.2$ MeV, $t = 0.2$, $\beta = 0.325$ fm^{-2}, and $\hat{P}_s$ and $\hat{P}_t$ are singlet and triplet spin projectors. Here, we involve the basis that includes not only protons, but also neutrons, which gives rise to neutron particle−hole excitations and admixtures. So, now we use a more general interaction, introduced by us in [28] for description of odd−odd nuclei in the vicinity of $A = 132$, namely,

$$\hat{\vartheta} = \left[V + V_\sigma \hat{\boldsymbol{\sigma}}_1 \cdot \hat{\boldsymbol{\sigma}}_2 + V_T \hat{S}_{12} \right. \quad (13)$$
$$\left. + \left\{ V_\tau + V_{\tau\sigma} \hat{\boldsymbol{\sigma}}_1 \cdot \hat{\boldsymbol{\sigma}}_2 + V_{\tau T} \hat{S}_{12} \right\} \hat{\boldsymbol{\tau}}_1 \cdot \hat{\boldsymbol{\tau}}_2 \right] e^{-r_{12}^2/r_0^2}$$

with $r_{12} = |\mathbf{r}_1 - \mathbf{r}_2|$ and $\hat{S}_{12}$ being a tensor operator. Pair Coulomb interaction between protons was also taken into consideration. The parameters used in the calculation were the following: $V = -16.65$, $V_\sigma = 2.33$, $V_T = -3.00$, $V_\tau = 3.35$, $V_{\tau\sigma} = 4.33$, $V_{\tau T} = 3.00$ (all in MeV), and $r_0 = 1.75$ fm. With these parameters and for a system of only like nucleons, interaction (13) identically transforms into that given by Eq. (12). We also mention here that the interaction in (13) was used by us not only for calculation of the particle−particle and the particle−hole matrix elements that enter the RPA equations (7)−(9), but also for defining the pairing characteristics (u, v coefficients and the E_j values) in ^{136}Xe. Our basis included 11 proton and 5 neutron orbitals that are closest to the proton and neutron Fermi levels. Corresponding single-particle energies were either borrowed from the experiment [9, 31] or generated by the suitable phenomenological potential [27, 29, 30], if the experimental values were absent.

Considering below the electromagnetic transitions that are described by the operator $\hat{\mathcal{M}}(\lambda\mu)$,

$$\hat{\mathcal{M}}(\lambda\mu) = \sum_{i,k} \langle i|\hat{m}(\lambda\mu)|k\rangle a_i^+ a_k, \qquad (14)$$

we must distinguish between two different cases, i.e., the phonon−phonon (between the two excited states) and the phonon−ground-state transitions. In the last case, the transition matrix element reads as

$$\langle \tilde{0}||\hat{\mathcal{M}}(\lambda)||\omega_n, J\rangle = (-1)^\lambda \delta_{J\lambda}\delta_{\pi_n\pi_\lambda} \qquad (15)$$

$$\times \left[\sum_{j_a \geq j_b} X_{j_a j_b}^{n,J}(u_{j_a}v_{j_b} \pm v_{j_a}u_{j_b}) \right.$$

$$\times \frac{(-1)^{l_b}}{\sqrt{1+\delta_{j_a j_b}}} \langle j_a||\hat{m}(\lambda)||j_b\rangle$$

$$- \sum_{j_a \geq j_b} Y_{j_a j_b}^{n,J}(v_{j_a}u_{j_b} \pm u_{j_a}v_{j_b})$$

$$\times \left. \frac{(-1)^{l_b}}{\sqrt{1+\delta_{j_a j_b}}} \langle j_a||\hat{m}(\lambda)||j_b\rangle \right],$$

where the upper signs refer to T-even $(E\lambda)$ transitions, while the lower ones refer to T-odd $(M\lambda)$ transitions.

In Eq. (15), δ are the Kronecker symbols, while π_n and π_λ are the parities of the state $|\omega_n\rangle$ and of the transition operator $\hat{\mathcal{M}}(\lambda)$.

At the same time, the phonon−phonon matrix element in the case of $\lambda \neq 0$ has the form

$$\langle \omega_n, J'||\hat{\mathcal{M}}(\lambda)||\omega_m, J\rangle = [(2J+1)(2J'+1)]^{1/2} \qquad (16)$$

$$\times \sum_{j_a \geq j_b, j_c \geq j_d} \frac{\left[X_{j_a j_b}^{m,J} X_{j_c j_d}^{n,J'} \pm Y_{j_a j_b}^{m,J} Y_{j_c j_d}^{n,J'} \right]}{\sqrt{(1+\delta_{j_a j_b})(1+\delta_{j_c j_d})}}$$

$$\times \left\{ \delta_{j_b j_d} W[\lambda j_c J j_b; j_a J'](u_{j_c}u_{j_a} \mp v_{j_c}v_{j_a}) \right.$$

$$\times \langle j_c||\hat{m}(\lambda)||j_a\rangle - (-1)^{j_c+j_d+J'}\delta_{j_b j_c}$$

$$\times W[\lambda j_d J j_b; j_a J'](u_{j_d}u_{j_a} \mp v_{j_d}v_{j_a})\langle j_d||\hat{m}(\lambda)||j_a\rangle$$

$$- (-1)^{j_a+j_b+J}\delta_{j_a j_d}W[\lambda j_c J j_a; j_b J']$$

$$\times (u_{j_c}u_{j_b} \mp v_{j_c}v_{j_b})\langle j_c||\hat{m}(\lambda)||j_b\rangle$$

$$+ (-1)^{j_a+j_b+J+j_c+j_d+J'}\delta_{j_a j_c}W[\lambda j_d J j_a; j_b J']$$

$$\times \left. (u_{j_d}u_{j_b} \mp v_{j_d}v_{j_b})\langle j_d||\hat{m}(\lambda)||j_b\rangle \right\},$$

where the upper signs also refer to $E\lambda$ transitions, while the lower ones refer to $M\lambda$ transitions.

Making the calculations for transition probabilities, we used the effective charges and gyromagnetic ratios defined by us in [10, 32, 33].

3. SHELL-MODEL CALCULATIONS

The RPA method considered by us before has strong limitations, since it reproduces only states of the "two-quasiparticle" nature [see Eq. (1)] with a certain class of correlations, including the ground-state ones, taken into account. Indeed, in the energy interval that is of interest to us, one can see some other excitations, which are out of the RPA approximation. For example, the total number of 2^+ states in ^{136}Xe with excitation energies less than 3.5 MeV is at least six, while the RPA gives only four levels. The excess of 4^+ states with energies less than 3 MeV is also seen, as compared to the RPA predictions. The extra excitations offer the levels that, in the spirit of the multiparticle shell model, are nothing but states with the total seniority values s, from different possible orbitals, more than two (while the RPA states correspond to shell-model states with $s = 2$).

Below, the structure of ^{136}Xe is considered in a multiparticle shell-model approach, formally in the framework of the diagonal approximation, but with the values of interaction matrix elements obtained from the empirical data, which implicitly include the bulk of correlations.

Beginning from the lowest configuration $\{(\pi 1g_{7/2})^4\}$, we note that the RPA scheme gives us only $\{(\pi 1g_{7/2})^2, I = 0\}$ (ground state), $I = 2^+, 4^+$, and 6^+ levels, which are equivalent to the $\{7/2^4; s = 0, I = 0\}$, $\{7/2^4; s = 2, I = 2\}$, $\{7/2^4; s = 2, I = 4\}$, and $\{7/2^4; s = 2, I = 6\}$ shell-model states. However, the configuration $\{7/2^4\}$ gives rise [34] to additional seniority-four levels, namely, $\{7/2^4; s = 4, I = 2\}$, $\{7/2^4; s = 4, I = 4\}$, $\{7/2^4; s = 4, I = 5\}$, and $\{7/2^4; s = 4, I = 8\}$, which have no analog in the RPA scheme.

Consider the splitting of the configuration $\{j^n; s, \alpha, I\}$, where n is the number of particles, I is spin, s is seniority, and α is some additional quantum number (when necessary). Using the formalism of fractional parentage expansions, one may easily represent the diagonal matrix element of the interaction $\hat{\vartheta}$ in the form

$$\left\langle j^n s\alpha; I \left| \sum_{i<k}^n \hat{\vartheta}(i,k) \right| j^n s\alpha; I \right\rangle \qquad (17)$$

$$= \sum_{J_0 \text{ even}} a_{J_0}(j^n, s, \alpha; I)V_{J_0} \equiv M_I(j, n, s, \alpha),$$

where $V_{J_0} = \langle j^2 J_0|\hat{\vartheta}|j^2 J_0\rangle$. The a_{J_0} quantities are expressed via the fractional parentage and recoupling coefficients and are tabulated in [35]. We do not calculate here the V_{J_0} two-body matrix elements for the configuration $\{(\pi 1g_{7/2})^2\}$ by using some effective

Table 1. Energy levels and $E2$-transition rates, $B(E2)$, in the diagonal $\{7/2^4\}$ shell-model calculations for ^{136}Xe; all the nondiagonal matrix elements for the $M1$ operator are equal to zero (note that the calculated value of the ground-state binding energy of ^{136}Xe is equal to $\mathcal{B} = 1141.84$ MeV, which may be compared to $\mathcal{B}(^{136}\text{Xe})_{\text{exp}} = 1141.88$ MeV)

I	s	E, MeV	I_i	s_i	I_f	s_f	$B(E2; I_i s_i \to I_f s_f)$, e^2 fm^4
0	0	g.s.	2	2	0	0	215
2	2	1.279	4	4	6	2	278
4	2	1.577	4	4	4	2	229
6	2	1.691	4	4	2	2	238
4	4	1.976	2	4	4	2	106
2	4	2.204	2	4	2	2	218
5	4	2.296	5	4	6	2	164
8	4	2.664	5	4	4	2	206
			8	4	6	2	154

Table 2. Energies of the $|(\pi 1g_{7/2})^3 Js, \pi 2d_{5/2}; I\rangle$ states in ^{136}Xe; only the levels with $J = 7/2$, $s = 1$ have their analogs in the RPA calculations (note that the $L = 3$ interaction matrix element of the $\{\pi 1g_{7/2}\pi 2d_{5/2}\}$ configuration does not enter the energies of the $I = 10$ and $I = 0$ states)

J	s	I	E, MeV	J	s	I	E, MeV
7/2	1	1	2.553	9/2	3	2	3.804
		2	2.634			3	3.738
		3	2.408			4	3.698
		4	2.385			5	3.617
		5	2.421			6	3.400
		6	2.192			7	3.392
3/2	3	1	3.587	11/2	3	3	3.689
		2	3.337			4	3.855
		3	3.373			5	3.597
		4	3.318			6	3.434
						7	3.462
						8	3.233
5/2	3	0	3.483	15/2	3	5	4.193
		1	3.083			6	4.018
		2	3.181			7	4.027
		3	3.304			8	3.940
		4	3.106			9	3.591
		5	2.996			10	3.500

interaction. Instead, we define their values from the experiment by employing the ansatz based on the Koopmans theorem [36] and with account of residual interaction between the valence particles:

$$V_{J_0}((\pi 1g_{7/2})^2) = 2\mathcal{B}(^{133}\text{Sb}) - \mathcal{B}(^{132}\text{Sn}) \quad (18)$$
$$- \mathcal{B}(^{134}\text{Te}) + E_{\text{exc}}^{J_0}(^{134}\text{Te}, (\pi 1g_{7/2})^2),$$

where $\mathcal{B}$ are ground-state binding energies. Then the excitation energy of the $|(7/2)^4 s\alpha; I\rangle$ state in ^{136}Xe is given by the equation

$$E_{\text{exc}}^I(^{136}\text{Xe}; s\alpha) = \mathcal{B}(^{136}\text{Xe}) + 3\mathcal{B}(^{132}\text{Sn}) \quad (19)$$
$$- 4\mathcal{B}(^{133}\text{Sb}) + M_I(7/2, n = 4, s, \alpha)$$

(no additional quantum number α is really present in the configuration $\{7/2^4\}$).

Let us consider now the transition probabilities. If $|i\rangle \equiv |7/2^4 s_i; I_i\rangle$ and $|f\rangle \equiv |7/2^4 s_f; I_f\rangle$, then

$$\langle f || \hat{\mathcal{M}}(\lambda) || i \rangle = 4\sqrt{(2I_i + 1)(2I_f + 1)} \quad (20)$$
$$\times \sum_{s_0 J_0} \langle 7/2^3 s_0 J_0, 7/2; I_i | \} 7/2^4 s_i I_i\rangle$$
$$\times \langle 7/2^3 s_0 J_0, 7/2; I_f | \} 7/2^4 s_f I_f\rangle$$
$$\times W[I_f J_0 \lambda 7/2; 7/2 I_i] \langle \pi 1g_{7/2} || \hat{m}(\lambda) || \pi 1g_{7/2}\rangle,$$

where $\langle \ldots | \} \ldots \rangle$ are the fractional parentage coefficients. In practical calculations we used the following values of reduced matrix elements entering the right-hand side of (20):

$$\langle \pi 1g_{7/2} || \hat{m}(E2) || \pi 1g_{7/2}\rangle = -40.20|e| \text{ fm}^2,$$

corresponding to the $e_{\text{eff}}(E2) = 1.85|e|$ (see [10]) and the Woods–Saxon wave functions, while

$$\langle \pi 1g_{7/2} || \hat{m}(M1) || \pi 1g_{7/2}\rangle = 4.70\mu_N,$$

corresponding to the experimental [32] value of the ground-state magnetic moment of ^{133}Sb.

The theoretical energy levels and transition rates arising from this approach are shown in Table 1. Note that, among the nondiagonal $E2$ matrix elements only those with $\Delta s = 2$ are different from zero.

Now let us pass on to the higher lying configuration $\{j_1^3, j_2\} \equiv \{(\pi 1g_{7/2})^3, \pi 2d_{5/2}\}$. Schematically, its wave function may be represented as $|J_1, j_2; I\rangle_a$, where index a means antisymmetrization and

$$|J_1\rangle = |j_1^3 s_1, \alpha_1; J_1\rangle_a \quad (21)$$
$$= \sum_{J_0 \text{ even}} \langle j_1^2 J_0, j_1; J_1 | \} j_1^3 s_1 \alpha_1 J_1\rangle |j_1^2 J_0, j_1; J_1\rangle.$$

The diagonal matrix element of interaction for the configuration $\{j_1^3 J_1, j_2; I\}$ looks like

$$\left\langle j_1^3 s_1 \alpha_1 J_1, j_2; I \left| \sum_{i<k}^4 \hat{\vartheta}(i,k) \right| j_1^3 s_1 \alpha_1 J_1, j_2; I \right\rangle \quad (22)$$

$$= M_{J_1}(j_1, n = 3, s_1, \alpha_1) + 3(2J_1 + 1)$$
$$\times \sum_{J_0 \text{ even}; L} (2L + 1) W^2[j_1 j_2 J_0 I; L J_1]$$
$$\times \langle j_1^2 J_0, j_1; J_1 | \} j_1^3 s_1 \alpha_1 J_1 \rangle^2 \, {}_a\langle j_1 j_2 L | \hat{\vartheta} | j_1 j_2 L \rangle_a.$$

The values of ${}_a\langle j_1 j_2 L | \hat{\vartheta} | j_1 j_2 L \rangle_a$ are defined in our approach from the formula

$$_a\langle \pi 1g_{7/2} \pi 2d_{5/2} L | \hat{\vartheta} | \pi 1g_{7/2} \pi 2d_{5/2} L \rangle_a \quad (23)$$

$$= 2\mathcal{B}(^{133}\text{Sb}) - \mathcal{B}(^{132}\text{Sn}) - \mathcal{B}(^{134}\text{Te})$$
$$+ E_{\text{exc}}^L(^{134}\text{Te}, \pi 1g_{7/2} \pi 2d_{5/2}) - E_{\text{exc}}^{2d_{5/2}}(^{133}\text{Sb}),$$

where E_{exc} are the corresponding excitation energies.

At the present time, the excitation energies for all members of the $\{\pi 1g_{7/2}, \pi 2d_{5/2}\}$ multiplet in ^{134}Te, except the $L = 3$ level, are known [33]. For this level, we used the value of 2.7 MeV, obtained by us from the proper interpolation based on the parabolic rule [37, 38]. This quantity is a cause of some uncertainty in our prediction of energies, the values of which are defined from the formula

$$E_{\text{exc}}^I(^{136}\text{Xe}, s_1 J_1) = \mathcal{B}(^{136}\text{Xe}) + 3\mathcal{B}(^{132}\text{Sn}) - 4\mathcal{B}(^{133}\text{Sb}) + E_{\text{exc}}^{2d_{5/2}}(^{133}\text{Sb}) \quad (24)$$

$$+ \left\langle (\pi 1g_{7/2})^3 s_1 J_1, \pi 2d_{5/2}; I \left| \sum_{i<k}^4 \hat{\vartheta}(i,k) \right| (\pi 1g_{7/2})^3 s_1 J_1, \pi 2d_{5/2}; I \right\rangle$$

and are listed in Table 2.

Let us consider now the transitions from the state $|i\rangle = |j_1^3 s_i \alpha_i J_i, j_2; I_i\rangle$ to the $|f\rangle = |j_1^4 s_f \alpha_f I_f\rangle$ (in our case $j_1 = \pi 1g_{7/2}$ and $j_2 = \pi 2d_{5/2}$). The transition matrix element looks like

$$\langle f || \hat{\mathcal{M}}(\lambda) || i \rangle \quad (25)$$
$$= \sqrt{(2I_i + 1)(2I_f + 1)} W[I_f J_i \lambda j_2; j_1 I_i]$$
$$\times \langle j_1^3 s_i \alpha_i J_i, j_1; I_f | \} j_1^4 s_f \alpha_f I_f \rangle \langle j_1 || \hat{m}(\lambda) || j_2 \rangle.$$

At last, we show the formula for transitions within the configuration $\{j_1^3, j_2\}$, which has the form

$$\langle j_1^3 s_f \alpha_f J_f, j_2; I_f || \hat{\mathcal{M}}(\lambda) || j_1^3 s_i \alpha_i J_i, j_2; I_i \rangle \quad (26)$$
$$= \sqrt{(2I_i + 1)(2I_f + 1)}$$
$$\times \left\{ 3W[J_f j_2 \lambda I_i; I_f J_i] \langle j_1 || \hat{m}(\lambda) || j_1 \rangle \right.$$
$$\times \sum_{J_0} \langle j_1^2 J_0, j_1; J_i | \} j_1^3 s_i \alpha_i J_i \rangle$$
$$\times \langle j_1^2 J_0, j_1; J_f | \} j_1^3 s_f \alpha_f J_f \rangle$$
$$\times \sqrt{(2J_i + 1)(2J_f + 1)} W[J_f J_0 \lambda j_1; j_1 J_i]$$
$$+ W[I_f J_f \lambda j_2; j_2 I_i] \langle j_2 || \hat{m}(\lambda) || j_2 \rangle$$
$$\left. \times \delta(J_i J_f) \delta(s_i s_f) \delta(\alpha_i \alpha_f) \right\}.$$

In addition to the single-particle transition matrix elements given earlier, we now need some new ones:

$$\langle \pi 1g_{7/2} || \hat{m}(E2) || \pi 2d_{5/2} \rangle = 8.19 |e| \text{ fm}^2,$$
$$\langle \pi 2d_{5/2} || \hat{m}(E2) || \pi 2d_{5/2} \rangle = -33.82 |e| \text{ fm}^2,$$
$$\langle \pi 1g_{7/2} || \hat{m}(M1) || \pi 2d_{5/2} \rangle = -0.135 \mu_N, \text{ and}$$
$$\langle \pi 2d_{5/2} || \hat{m}(M1) || \pi 2d_{5/2} \rangle = 5.45 \mu_N.$$

All these quantities were also calculated by using the effective charges and effective $M1$ operators, defined in [10] and [33].

4. INTERCOMPARISON BETWEEN THE TWO MODELS

Coming to the consistency between both theoretical models, we again mention that, among the shell-model states, there are ones, namely, with total seniority values (from different orbitals) equal to two, which have their analogs in the RPA scheme. However, there also exist states which appear only in one approach or the other. The comparison of theoretical energies obtained in the framework of the mentioned methods with the results of experiment is demonstrated in Table 3. Parallel with our data, we show here the intercomparison with experimental results from [17, 22, 26]. As one can easily see, the total number of states in such combined method increases, as compared to only RPA or empirical limited shell-model approaches, and one can conciliate it with the

Table 3. Comparison of experimental and theoretical energy levels in ^{136}Xe (experimental states and their interpretation in the framework of approaches considered in this work are exhibited below; in the case of RPA calculations the leading components of eigenvectors are specified; all the energies are given in MeV)

$I_i^\pi; E(I_i^\pi)_{\exp}$	Phonon description	Empirical shell-model description
0_1^+; g.s.	Vacuum; g.s.	$\{(g_{7/2})^4, I = 0, s = 0\}$; g.s.
0_2^+; 2.581	Pairing vibration; 1.872	
1_1^+; 2.634	$\{g_{7/2}d_{5/2}\}$; 2.509	$\{(g_{7/2})^3, J = 7/2, s = 1, d_{5/2}; I = 1\}$; 2.553
(1_2^+); 3.212		$\{(g_{7/2})^3, J = 5/2, s = 3, d_{5/2}; I = 1\}$; 3.083
2_1^+; 1.313	$\{g_{7/2}g_{7/2}\}$; 1.301	$\{(g_{7/2})^4, s = 2, I = 2\}$; 1.279
2_2^+; 2.289		$\{(g_{7/2})^4, s = 4, I = 2\}$; 2.204
2_3^+; 2.414	$\{g_{7/2}d_{5/2}\}$; 2.315	$\{(g_{7/2})^3, J = 7/2, s = 1, d_{5/2}; I = 2\}$; 2.634
2_4^+; 2.849	$\{d_{5/2}d_{5/2}\}$; 2.528	
2_5^+; 2.869	$\{g_{7/2}d_{3/2}\}$; 3.189	
		$\{(g_{7/2})^3, J = 5/2, s = 3, d_{5/2}; I = 2\}$; 3.181
		$\{(g_{7/2})^3, J = 3/2, s = 3, d_{5/2}; I = 2\}$; 3.337
3_1^+; 2.560	$\{g_{7/2}d_{5/2}\}$; 2.384	$\{(g_{7/2})^3, J = 7/2, s = 1, d_{5/2}; I = 3\}$; 2.408
(3_2^+); 3.873	$\{g_{7/2}d_{3/2}\}$; 3.703	
		$\{(g_{7/2})^3, J = 5/2, s = 3, d_{5/2}; I = 3\}$; 3.304
4_1^+; 1.694	$\{g_{7/2}g_{7/2}\}$; 1.672	$\{(g_{7/2})^4, s = 2, I = 4\}$; 1.577
4_2^+; 2.126		$\{(g_{7/2})^4, s = 4, I = 4\}$; 1.976
4_3^+; 2.465	$\{g_{7/2}d_{5/2}\}$; 2.260	$\{(g_{7/2})^3, J = 7/2, s = 1, d_{5/2}; I = 4\}$; 2.385
5_1^+; 2.444		$\{(g_{7/2})^4, s = 4, I = 5\}$; 2.296
5_2^+; 2.608	$\{g_{7/2}d_{5/2}\}$; 2.353	$\{(g_{7/2})^3, J = 7/2, s = 1, d_{5/2}; I = 5\}$; 2.421
		$\{(g_{7/2})^3, J = 5/2, s = 3, d_{5/2}; I = 5\}$; 2.996
6_1^+; 1.892	$\{g_{7/2}g_{7/2}\}$; 1.782	$\{(g_{7/2})^4, s = 2, I = 6\}$; 1.691
6_2^+; 2.261	$\{g_{7/2}d_{5/2}\}$; 2.090	$\{(g_{7/2})^3, J = 7/2, s = 1, d_{5/2}; I = 6\}$; 2.192
8_1^+; 2.867		$\{(g_{7/2})^4, s = 4, I = 8\}$; 2.664
8_2^+; 3.229		$\{(g_{7/2})^3, J = 11/2, s = 3, d_{5/2}; I = 8\}$; 3.233
10_1^+; 3.484		$\{(g_{7/2})^3, J = 15/2, s = 3, d_{5/2}; I = 10\}$; 3.500
3_1^-; 3.275	Collective; 3.848	

experiment. Attention should also be drawn to the fact that the allied (RPA and shell-model) states have rather similar energies.

One can see from Table 3 that the second 2^+ and 4^+ levels really offer not the second RPA states, but the four-quasiparticle $\{(\pi g_{7/2})^4, s = 4\}$, i.e., two-phonon configurations. This prescription is fortified by examining the electromagnetic properties of these levels, shown among the others in Table 4. Really, if one considers the phonon 2.260-MeV state with the structure $\{g_{7/2}d_{5/2}\}$ as a 4_2^+ level, then

the $4_2^+ \rightarrow 2_1^+$ E2-transition probability is found to be small, about 0.21 W.u. (experimental value ≥ 1.7 W.u.), while the M1 $4_2^+ \rightarrow 4_1^+$ transition is rather strong, with $B(M1)$ of about 0.025 W.u. Then the ratio $\gamma(4_2^+ \rightarrow 4_1^+)/\gamma(4_2^+ \rightarrow 2_1^+)$ becomes equal to ~ 20, which also strongly contradicts the experiment, while the pattern presented in Table 4 gives the better agreement. The situation with the 2_2^+ level is more complicated. Here, if one takes as a 2_2^+ level the phonon 2.315-MeV state and as 2_3^+ level also

Table 4. Comparison of experimental and theoretical transition probabilities in ^{136}Xe (the quantities γ represent both experimental and theoretical branching ratios for the γ decays from the initial to different final states; they are normalized to 100 for the strongest decay seen in the experiment (or given by calculations), for each initial state)

$I_i^\pi \to I_f^\pi$	XL	$B(XL)_{\mathrm{exp}}^{\mathrm{a)}}$, W.u.	B(RPA), W.u.	B(sh. mod.), W.u.	γ(exp.)$^{\mathrm{b)}}$	γ(RPA)	γ(sh. mod.)
$2_1^+ \to 0_1^+$	$E2$	8.5(35)	14.5	5.2	100	100	100
$4_1^+ \to 2_1^+$	$E2$	1.29(2)	0.34	0	100	100	100
$6_1^+ \to 4_1^+$	$E2$	0.0132(5)	0.13	0	100	100	100
$4_2^+ \to 4_1^+$	$M1$	$\geq 2.8 \times 10^{-3}$		0	25(2)		4.1
	$E2$	≥ 9.2		5.5			
$4_2^+ \to 2_1^+$	$E2$	≥ 1.7		5.7	100(8)		100
$6_2^+ \to 6_1^+$	$M1$	$2.7(5) \times 10^{-3}$	0.75×10^{-1}	7.08×10^{-5}	100(6)	100	100
	$E2$	121(24)	0.29	2.55×10^{-2}			
$6_2^+ \to 4_1^+$	$E2$	0.34(7)	0.6×10^{-1}	0.67×10^{-3}	2.4(2)	0.14	1.6
$2_2^+ \to 2_1^+$	$M1$	$\geq 2.4 \times 10^{-4}$		0	25.8(14)		25
	$E2$	≥ 0.16		5.25			
$2_2^+ \to 0_1^+$	$E2$	$\geq 8.8 \times 10^{-3}$		0.28	100(5)		100$^{\mathrm{c)}}$
$5_1^+ \to 6_2^+$	$M1$	$\geq 6.5 \times 10^{-3}$		0	11(1)		0
	$E2$	≥ 121		0			
$5_1^+ \to 4_2^+$	$M1$	$\geq 1.1 \times 10^{-3}$		0	10(1)		0
	$E2$	≥ 6.9		0			
$5_1^+ \to 6_1^+$	$M1$	$\geq 2.9 \times 10^{-4}$		0	14(1)		17
	$E2$	≥ 0.6		3.95			
$5_1^+ \to 4_1^+$	$M1$	$\geq 9.3 \times 10^{-4}$		0	100(8)		100
	$E2$	≥ 1.0		4.96			
$2_3^+ \to 2_1^+$	$M1$		0.16×10^{-1}	0.25×10^{-3}	5.3(5)	10.9	6.3
	$E2$		0.133	1.14×10^{-3}			
$2_3^+ \to 0_1^+$	$E2$		1.53	0.040	100(5)	100	100
$4_3^+ \to 4_2^+$	$M1$	$1.9(8) \times 10^{-3}$		0.21×10^{-2}	22(2)		79$^{\mathrm{d)}}$
	$E2$	10.1(46)		0.24×10^{-3}			
$4_3^+ \to 4_1^+$	$M1$	$7.2(32) \times 10^{-4}$	0.25×10^{-1}	0.182×10^{-3}	100(5)	100	100
	$E2$	0.76(34)	0.88×10^{-1}	0.024			
$3_1^+ \to 2_2^+$	$M1$	$1.24(3) \times 10^{-3}$		1.11×10^{-2}	11.4(15)		12$^{\mathrm{e)}}$
	$E2$	11.0(54)		3.58×10^{-3}			
$3_1^+ \to 4_2^+$	$M1$	$9.6(46) \times 10^{-4}$		0.61×10^{-2}	35(2)		27$^{\mathrm{d)}}$
	$E2$	3.2(15)		0.50×10^{-2}			
$3_1^+ \to 4_1^+$	$M1$	$1.1(5) \times 10^{-4}$	0.56×10^{-3}	2.85×10^{-3}	30.1(19)	49	100
	$E2$	$8.7(41) \times 10^{-2}$	1.53×10^{-2}	1.68×10^{-3}			
$3_1^+ \to 2_1^+$	$M1$	$1.1(5) \times 10^{-4}$	3.72×10^{-3}	5.75×10^{-5}	100(4)	100	12
	$E2$	$4.7(22) \times 10^{-2}$	1.43×10^{-2}	2.29×10^{-2}			

Table 4. (Contd).

$I_i^\pi \to I_f^\pi$	XL	$B(XL)^{\text{a)}}_{\text{exp}}$, W.u.	B(RPA), W.u.	B(sh. mod.), W.u.	γ(exp.)[b]	γ(RPA)	γ(sh. mod.)
$5_2^+ \to 5_1^+$	$M1$	$\geq 9.2 \times 10^{-3}$		0	18.0(21)		0
	$E2$	≥ 232		0			
$5_2^+ \to 6_2^+$	$M1$	$\geq 5.1 \times 10^{-3}$	0.16	0.107	87(4)	100	100
	$E2$	≥ 28.7	0.93	0.984			
$5_2^+ \to 4_2^+$	$M1$	$\geq 1.1 \times 10^{-3}$		3.66×10^{-3}	53(3)		11[d]
	$E2$	≥ 3.3		1.52×10^{-2}			
$5_2^+ \to 6_1^+$	$M1$	$\geq 1.8 \times 10^{-4}$	3.5×10^{-3}	4.18×10^{-4}	28.3(17)	19	4
	$E2$	≥ 0.24	9.4×10^{-3}	1.85×10^{-2}			
$5_2^+ \to 4_1^+$	$M1$	$\geq 3.5 \times 10^{-4}$	5.4×10^{-3}	3.66×10^{-3}	100(5)	63	62[d]
	$E2$	≥ 0.26	7.32×10^{-2}	1.52×10^{-2}			
$1_1^+ \to 2_3^+$	$M1$	$2.2(8) \times 10^{-3}$	0.58	0.35	3.5(2)	11	47
	$E2$	29(10)	1.26	3.18			
$1_1^+ \to 2_2^+$	$M1$	$1.9(7) \times 10^{-3}$		1.64×10^{-2}	11.4(6)		9[e]
	$E2$	9.8(35)		0.15			
$1_1^+ \to 2_1^+$	$M1$	$2.9(10) \times 10^{-4}$	2.41×10^{-2}	1.46×10^{-4}	100(5)	100	8
	$E2$	0.10(4)	1.34×10^{-2}	3.99×10^{-2}			
$1_1^+ \to 0_1^+$	$M1$	$9.8(35) \times 10^{-6}$	1.35×10^{-3}	4.23×10^{-4}	26.7(12)	44	100
$8_1^+ \to 6_1^+$	$E2$			3.7			
$8_2^+ \to 6_2^+$	$E2$			4.3			
$10_1^+ \to 8_2^+$	$E2$			3.2			
$3_1^- \to 0_1^+$	$E3$	16.9	15				

a) For transitions where the mixed $M1/E2$ mode is allowed but the mixing parameter δ is not defined, the listed rates are given separately for the cases when the pure $M1$ or $E2$ mode is assumed.

b) Weighted average of branchings obtained by us [26] and the values adopted in [17].

c) Obtained as a result of the 23% admixture of 2_1^+ to 2_2^+.

d) Taking into account the 15% admixture of 4_3^+ to 4_2^+ and 4_1^+ in the amplitude.

e) By virtue of the 22% admixture of 2_3^+ to 2_2^+.

the phonon, but 2.528-MeV state, then both the transition probabilities and branching ratios can be conciliated with the experiment. However, in this case, there is no room for the $\{(g_{7/2})^4 s = 4 I = 2\}$ two-phonon state, which really is the next one, after the 2_1^+ level (see Table 3). As in the harmonic picture, there is no transition between the two-phonon and ground states; the $B(E2; 2_2^+ \to 0_1^+)$ value in the diagonal shell-model approximation is equal to zero. In order to reproduce the experimental branching from the 2_2^+ level, we must include small configuration mixing (see footnote to Table 4), which "opens" the

$2_2^+ \to 0_1^+$ transition. Small configuration mixing for other levels is also needed for better description of the branching ratios.

At present, two 5^+ levels of ^{136}Xe with excitation energies less than 3 MeV are found in the experiment [26]. At the same time, the calculations show the existence of three 5^+ states in this interval of energies. Among them, the shell-model $\{(g_{7/2})^4, s = 4, I = 5\}$ state that has the lowest energy (see Table 3) corresponds to the experimental 5_1^+ (2.444-MeV) level. Meanwhile, the identification of the structure of higher 5^+ levels is not so synonymous. We assume that the 5_2^+ (2.608-MeV)

state has the shell-model structure $\{(g_{7/2})^3, J = 7/2, s = 1, d_{5/2}; I = 5\}$, its RPA analog being of the $\{g_{7/2}d_{5/2}\}$ type. In this case, the half-life of the 5_2^+ state proves to be about ~ 3 ps as compared to the experimental value of $T_{1/2} \le 27$ ps [26], while the alternative attribution of the structure $\{(g_{7/2})^3, J = 5/2, s = 3, d_{5/2}; I = 5\}$ for this level leads to $T_{1/2} \sim 300$ ps, which contradicts the experiment.

At the present time, there exist several measurements concerning magnetic properties of the ^{136}Xe states. In [39], the magnitude of $g(4_1^+) = 0.80(15)$ was measured, while in [40] and [41] the values of $g(2_1^+)$ turned out to be $g(2_1^+) = 0.77(5)$ and $g(2_1^+) = 1.20(25)$, respectively. These numbers may be compared with the results of our RPA calculations: $g(4_1^+) = 0.81$ and $g(2_1^+) = 0.86$. We again mention here that, in calculations, we used magnetic parameters close to that from our work [33]. Unfortunately, at the present time, there is no experimental evidence on the values of quadrupole moments of states in ^{136}Xe, which are extremely dependent on the shell-model structure and the occupancy of single-particle levels.

Among the positive-parity states, we mark out the high-spin levels, where configuration mixing is small. Calculated empirical shell-model energies of these levels are very close to the experimental ones. At the same time, the theory predicts rather strong $E2$ transitions between these levels (see Table 4), which is also qualitatively confirmed by the experiment.

5. SUMMARY AND CONCLUSIONS

This work has essentially expanded our understanding of the structure of the $N = 82$ nucleus ^{136}Xe. Joint theoretical calculation of the energies of levels and their decay properties performed in the framework of two different models enabled us to make a synonymous definition of the structure for the majority of excited states in this nucleus. In our calculations, we used the minimal amount of free parameters, which we borrowed either from our own previous investigations (as in the RPA approach) or from the empirical data on other nuclei (as in the shell-model calculations). In particular, the parameters of interaction that we used in the RPA scheme agree with those used by us in other works, as well as with the parameters used by other authors for description of the $N = 82$ nuclei. Our combined theoretical approach for description of ^{136}Xe enabled us to describe most of the experimental information on this nucleus and may be successfully applied to other nuclei with one filled shell.

REFERENCES

1. B. H. Wildenthal, Phys. Rev. Lett. **22**, 1118 (1969).
2. M. Waroquier and K. Heyde, Nucl. Phys. A **164**, 113 (1971).
3. K. Heyde and M. Waroquier, Nucl. Phys. A **167**, 545 (1971).
4. M. Waroquier and K. Heyde, Z. Phys. A **268**, 11 (1974).
5. G. Wenes, K. Heyde, M. Waroquier, and P. Van Isacker, Phys. Rev. C **26**, 1692 (1982).
6. K. Heyde, M. Waroquier, and G. Vanden Berghe, Phys. Lett. B **35B**, 211 (1971).
7. O. Sholten and H. Kruse, Phys. Lett. B **125B**, 113 (1983).
8. B. H. Wildenthal, in *Proceedings of the 3rd International Spring Seminar on Nuclear Physics, Ischia, Italy, 1990*, Ed. by A. Covello (World Sci., Singapore, 1991), p. 35.
9. M. Sanchez-Vega, B. Fogelberg, H. Mach, *et al.*, Phys. Rev. Lett. **80**, 5504 (1998).
10. J. P. Omtvedt, H. Mach, B. Fogelberg, *et al.*, Phys. Rev. Lett. **75**, 3090 (1995).
11. J. Blomqvist, Acta Phys. Pol. B **30**, 697 (1999).
12. A. Holt, T. Engeland, E. Osnes, *et al.*, Nucl. Phys. A **618**, 107 (1997).
13. M. Baranger, Phys. Rev. **120**, 957 (1960).
14. K. I. Erokhina, V. I. Isakov, B. Fogelberg, and H. Mach, Preprint No. 2136, PIYaF (Petersburg Nuclear Physics Institute, Gatchina, 1996).
15. H. Mach and B. Fogelberg, Phys. Scr., T **56**, 270 (1995).
16. T. W. Burrows, Nucl. Data Sheets **52**, 273 (1987).
17. J. K. Tuli, Nucl. Data Sheets **71**, 1 (1994).
18. W. R. Western, J. C. Hill, W. L. Talbert, and W. C. Schick, Phys. Rev. C **15**, 1822 (1977).
19. P. A. Moore, P. J. Riley, C. M. Jones, *et al.*, Phys. Rev. C **1**, 1 (1970).
20. E. Achterberg, F. C. Iglesias, A. E. Jech, *et al.*, Phys. Rev. C **5**, 1759 (1972).
21. S. Sen, P. J. Riley, and T. Udagawa, Phys. Rev. C **6**, 2201 (1972).
22. P. J. Daly, P. Bhattacharyya, C. T. Zhang, *et al.*, Phys. Rev. C **59**, 3066 (1999).
23. P. F. Mantica, B. E. Zimmermann, W. B. Walters, and K. Heyde, Phys. Rev. C **43**, 1696 (1991).
24. K. Kawade, G. Battistuzzi, H. Lawin, *et al.*, Z. Phys. A **298**, 187 (1980).
25. J. A. Morman, W. C. Schick, and W. L. Talbert, Phys. Rev. C **11**, 913 (1975).
26. A. J. Aas, PhD Thesis (University of Oslo, Oslo, 1999).

27. V. I. Isakov, K. I. Erokhina, H. Mach, *et al.*, Eur. Phys. J. A **14**, 29 (2002).

28. A. J. Aas, V. I. Isakov, H. Gausemel, *et al.*, submitted to Nucl. Phys. A.

29. K. I. Erokhina and V. I. Isakov, Izv. Ross. Akad. Nauk, Ser. Fiz. **56** (11), 78 (1992).

30. K. I. Erokhina and V. I. Isakov, Yad. Fiz. **57**, 212 (1994) [Phys. At. Nucl. **57**, 198 (1994)].

31. P. Hoff, P. Baumann, A. Huck, *et al.*, Phys. Rev. Lett. **77**, 1020 (1996).

32. N. J. Stone, D. Doran, M. Lindroos, *et al.*, Phys. Rev. Lett. **78**, 820 (1997).

33. J. P. Omtvedt, B. Fogelberg, H. Mach, *et al.*, Nucl. Phys. A (in press).

34. B. F. Bayman and A. Lande, Nucl. Phys. **77**, 1 (1966).

35. I. M. Band and Yu. I. Kharitonov, At. Data Nucl. Data Tables **10** (2), 107 (1971).

36. T. H. Koopmans, Physica **1**, 104 (1933).

37. L. A. Sliv and Yu. I. Kharitonov, in *Spectroscopic and Group Theoretical Methods in Physics*, Ed. by F. Bloch *et al.* (North-Holland, Amsterdam, 1968), p. 275.

38. V. Paar, Nucl. Phys. A **331**, 16 (1979).

39. Z. Berant, A. Wolf, John C. Hill, *et al.*, Phys. Rev. C **31**, 570 (1985).

40. G. Jakob, N. Benczer-Koller, G. Kumbartzki, *et al.*, Phys. Rev. C **65**, 024316 (2002).

41. K.-H. Speidel, H. Busch, S. Kremeyer, *et al.*, Nucl. Phys. A **552**, 140 (1993).

The Nuclear Scissors Mode by Two Approaches (Wigner Function Moments versus RPA)[*]

E. B. Balbutsev[**] and P. Schuck[1)]

Joint Institute for Nuclear Research, Dubna, Moscow oblast, 141980 Russia

Received January 11, 2005

Abstract—Two complementary methods to describe the collective motion, the RPA and the method of Wigner function moments, are compared using a simple model as an example—a harmonic oscillator with quadrupole−quadrupole residual interaction. It is shown that they give identical formulas for eigenfrequencies and transition probabilities of all collective excitations of the model, including the scissors mode, which is a subject of our special attention. The normalization factor of the "synthetic" scissors state and its overlap with physical states are calculated analytically. The orthogonality of the spurious state to all physical states is proved rigorously. © 2005 Pleiades Publishing, Inc.

1. INTRODUCTION

The full analysis of the scissors mode in the framework of a solvable model [harmonic oscillator with quadrupole−quadrupole residual interaction (HO + QQ)] was given in [1]. Many obscure points in the understanding of the mode's nature were clarified: for example, its coexistence with the isovector giant quadrupole resonance (IVGQR), the decisive role of the Fermi surface deformation in its creation, and so on.

The method of Wigner function moments (WFM) was applied to derive analytic expressions for currents of both coexisting modes (this was done for the first time), their excitation energies, and magnetic and electric transition probabilities. Unexpectedly, our formulas for energies turned out to be identical to those derived by Hamamoto and Nazarewicz [2] in the framework of the RPA. This fact generated the natural motivation for this work: to check the relation between formulas for transition probabilities derived by the two methods. The obvious development of this investigation is the systematic comparison of the two approaches with the aim to establish the connection between them. The HO + QQ model is a very convenient proving ground for this kind of research, because all results can be obtained analytically. There is no need to describe the merits and demerits of the RPA—they are known very well [3]. It is necessary, however, to say a few words about the WFM. Its idea is based on the virial theorems of Chandrasekhar and

Lebovitz [4]. Instead of writing the equations of motion for microscopic amplitudes of particle−hole excitations (as in RPA), one writes the dynamical equations for various multipole phase-space moments of a nucleus. This allows one to achieve better physical interpretation of the studied phenomenon without going into its detailed microscopic structure. The WFM method was successfully applied to study isoscalar and isovector giant multipole resonances and low-lying collective modes of rotating and nonrotating nuclei with various realistic forces [5]. The results of calculations were always very close to similar results obtained with the help of the RPA. In principle, this should be expected, because the basis of both methods is the same: time-dependent Hartree−Fock (TDHF) theory and a small-amplitude approximation. On the other hand, it is evident that they are not equivalent, because one deals with equations of motion for different objects. The detailed analysis of the interplay of the two methods turns out to be useful also from a "practical" point of view: firstly, it allows one to obtain additional insight into the nature of the scissors mode; secondly, we find new exact mathematical results for the considered model.

2. THE WFM METHOD

A detailed description of the method of WFM can be found in [1, 5, 6]. Here, we recall briefly only its main points. The basis of the method is the TDHF equation for the one-body density matrix: $i\hbar\partial\hat{\rho}^\tau/\partial t = \left[\hat{H}^\tau, \hat{\rho}^\tau\right]$, where $\hat{H}^\tau$ is the one-body self-consistent Hamiltonian depending implicitly on the density matrix $\rho^\tau(\mathbf{r}_1, \mathbf{r}_2, t) = \langle\mathbf{r}_1|\hat{\rho}^\tau(t)|\mathbf{r}_2\rangle$ and τ is an isotopic

---

index. It is convenient to modify this equation, introducing the Wigner transform of the density matrix [3], known as the Wigner function $f^\tau(\mathbf{r}, \mathbf{p}, t)$:

$$\frac{\partial f^\tau}{\partial t} = \frac{2}{\hbar} \sin\left(\frac{\hbar}{2}(\nabla_{\mathbf{r}}^H \cdot \nabla_{\mathbf{p}}^f - \nabla_{\mathbf{p}}^H \cdot \nabla_{\mathbf{r}}^f)\right) H_W^\tau f^\tau, \tag{1}$$

where the upper index on the nabla operator stands for the function on which this operator acts and H_W is the Wigner transform of the Hamiltonian H.

It is shown in [5, 6] that, by integrating Eq. (1) over the phase space $\{\mathbf{p}, \mathbf{r}\}$ with the weights $x_{i_1} x_{i_2} \ldots x_{i_k} p_{i_{k+1}} \ldots p_{i_{n-1}} p_{i_n}$, where k runs from 0 to n, one can obtain a closed finite set of dynamical equations for Cartesian tensors of the rank n. Taking linear combinations of these equations, one is able to represent them through various multipole moments, which play the roles of collective variables of the problem. Here, we consider the case $n = 2$.

2.1. Model Hamiltonian, Equations of Motion

The microscopic Hamiltonian of the model is

$$H = \sum_{i=1}^{A} \left(\frac{\mathbf{p}_i^2}{2m} + \frac{1}{2}m\omega^2 \mathbf{r}_i^2\right) \tag{2}$$

$$+ \bar{\kappa} \sum_{\mu=-2}^{2} (-1)^\mu \sum_{i}^{Z} \sum_{j}^{N} q_{2\mu}(\mathbf{r}_i) q_{2-\mu}(\mathbf{r}_j)$$

$$+ \frac{1}{2}\kappa \sum_{\mu=-2}^{2} (-1)^\mu \left\{ \sum_{i \neq j}^{Z} q_{2\mu}(\mathbf{r}_i) q_{2-\mu}(\mathbf{r}_j) \right.$$

$$\left. + \sum_{i \neq j}^{N} q_{2\mu}(\mathbf{r}_i) q_{2-\mu}(\mathbf{r}_j) \right\},$$

where the quadrupole operator $q_{2\mu} = \sqrt{16\pi/5} r^2 Y_{2\mu}$, $\bar{\kappa}$ is the strength constant of the neutron−proton interaction, κ is the strength constant of the neutron−neutron and proton−proton interactions, and N and Z are the numbers of neutrons and protons, respectively. The mean field potential for protons (or neutrons) is

$$V^\tau(\mathbf{r}, t) = \frac{1}{2}m\omega^2 r^2 + \sum_{\mu=-2}^{2} (-1)^\mu Z_{2\mu}^\tau(t) q_{2-\mu}(\mathbf{r}), \tag{3}$$

where $Z_{2\mu}^n = \kappa Q_{2\mu}^n + \bar{\kappa} Q_{2\mu}^p$, $Z_{2\mu}^p = \kappa Q_{2\mu}^p + \bar{\kappa} Q_{2\mu}^n$, and the quadrupole moments $Q_{2\mu}^\tau(t)$ are defined as

$$Q_{2\mu}^\tau(t) = \int d\{\mathbf{p}, \mathbf{r}\} q_{2\mu}(\mathbf{r}) f^\tau(\mathbf{r}, \mathbf{p}, t)$$

with $\int d\{\mathbf{p}, \mathbf{r}\} \equiv 2(2\pi\hbar)^{-3} \int d^3p \int d^3r$.

Integration of Eq. (1) with the weights $r_{\lambda\mu}^2$, $(rp)_{\lambda\mu} \equiv \{r \otimes p\}_{\lambda\mu}$, and $p_{\lambda\mu}^2$ yields the following set of equations [1]:

$$\frac{d}{dt} R_{\lambda\mu}^\tau - \frac{2}{m} L_{\lambda\mu}^\tau = 0, \quad \lambda = 0, 2; \tag{4}$$

$$\frac{d}{dt} L_{\lambda\mu}^\tau - \frac{1}{m} P_{\lambda\mu}^\tau + m\omega^2 R_{\lambda\mu}^\tau$$

$$- 2\sqrt{30} \sum_{j=0}^{2} \sqrt{2j+1} \left\{ {}^{11j}_{2\lambda1} \right\} (Z_2^\tau R_j^\tau)_{\lambda\mu} = 0,$$

$$\lambda = 0, 1, 2;$$

$$\frac{d}{dt} P_{\lambda\mu}^\tau + 2m\omega^2 L_{\lambda\mu}^\tau$$

$$- 4\sqrt{30} \sum_{j=0}^{2} \sqrt{2j+1} \left\{ {}^{11j}_{2\lambda1} \right\} (Z_2^\tau L_j^\tau)_{\lambda\mu} = 0,$$

$$\lambda = 0, 2,$$

where $\left\{ {}^{11j}_{2\lambda1} \right\}$ is the Wigner $6j$ symbol, $r_{\lambda\mu}^2 \equiv \{r \otimes r\}_{\lambda\mu} = \sum_{\sigma,\nu} C_{1\sigma,1\nu}^{\lambda\mu} r_\sigma r_\nu$ is a tensor product [7], and r_ν are cyclic variables

$$r_{+1} = -(x_1 + ix_2)/\sqrt{2}, \quad r_0 = x_3,$$

$$r_{-1} = (x_1 - ix_2)/\sqrt{2}.$$

Further, the following notation is introduced:

$$R_{\lambda\mu}^\tau(t) = \int d\{\mathbf{p}, \mathbf{r}\} r_{\lambda\mu}^2 f^\tau(\mathbf{r}, \mathbf{p}, t),$$

$$L_{\lambda\mu}^\tau(t) = \int d\{\mathbf{p}, \mathbf{r}\} (rp)_{\lambda\mu} f^\tau(\mathbf{r}, \mathbf{p}, t),$$

$$P_{\lambda\mu}^\tau(t) = \int d\{\mathbf{p}, \mathbf{r}\} p_{\lambda\mu}^2 f^\tau(\mathbf{r}, \mathbf{p}, t).$$

In terms of cyclic variables $q_{2\mu} = \sqrt{6} r_{2\mu}^2$; therefore, $Q_{2\mu}^\tau = \sqrt{6} R_{2\mu}^\tau$. By definition $R_{00}^\tau = -Q_{00}^\tau/\sqrt{3}$ with $Q_{00}^\tau = N^\tau \langle r^2 \rangle$ being the mean square radius. The tensor $L_{1\nu}^\tau$ is connected with the angular momentum by the following relations: $L_{10}^\tau = \frac{i}{\sqrt{2}} I_3^\tau$, $L_{1\pm1}^\tau = \frac{1}{2}(I_2^\tau \mp iI_1^\tau)$.

We rewrite Eqs. (4) in terms of the isoscalar and isovector variables $R_{\lambda\mu} = R_{\lambda\mu}^n + R_{\lambda\mu}^p$, $\bar{R}_{\lambda\mu} = R_{\lambda\mu}^n - R_{\lambda\mu}^p$ (and so on) with the isoscalar $\kappa_0 = (\kappa + \bar{\kappa})/2$ and isovector $\kappa_1 = (\kappa - \bar{\kappa})/2$ strength constants. It is no problem to solve these equations numerically. However, we want to simplify the situation as much as possible to get the results in an analytic form that

gives us a maximum of insight into the nature of the modes.

(i) The problem is considered in a small-amplitude approximation. Writing all variables as a sum of their equilibrium value plus a small deviation,

$$R_{\lambda\mu}(t) = R_{\lambda\mu}^{\text{eq}} + \mathcal{R}_{\lambda\mu}(t), \quad P_{\lambda\mu}(t) = P_{\lambda\mu}^{\text{eq}} + \mathcal{P}_{\lambda\mu}(t),$$

$$L_{\lambda\mu}(t) = L_{\lambda\mu}^{\text{eq}} + \mathcal{L}_{\lambda\mu}(t),$$

$$\bar{R}_{\lambda\mu}(t) = \bar{R}_{\lambda\mu}^{\text{eq}} + \bar{\mathcal{R}}_{\lambda\mu}(t), \quad \bar{P}_{\lambda\mu}(t) = \bar{P}_{\lambda\mu}^{\text{eq}} + \bar{\mathcal{P}}_{\lambda\mu}(t),$$

$$\bar{L}_{\lambda\mu}(t) = \bar{L}_{\lambda\mu}^{\text{eq}} + \bar{\mathcal{L}}_{\lambda\mu}(t),$$

we linearize the equations of motion in $\mathcal{R}_{\lambda\mu}, \mathcal{P}_{\lambda\mu}, \mathcal{L}_{\lambda\mu}$ and $\bar{\mathcal{R}}_{\lambda\mu}, \bar{\mathcal{P}}_{\lambda\mu}, \bar{\mathcal{L}}_{\lambda\mu}$.

(ii) We study nonrotating nuclei, i.e., nuclei with $L_{1\nu}^{\text{eq}} = \bar{L}_{1\nu}^{\text{eq}} = 0$.

(iii) Only axially symmetric nuclei with $R_{2\pm2}^{\text{eq}} = R_{2\pm1}^{\text{eq}} = \bar{R}_{2\pm2}^{\text{eq}} = \bar{R}_{2\pm1}^{\text{eq}} = 0$ are considered.

(iv) Finally, we take

$$\bar{R}_{20}^{\text{eq}} = \bar{R}_{00}^{\text{eq}} = 0. \tag{5}$$

This means that equilibrium deformation and mean square radius of neutrons are supposed to be equal to that of protons.

Due to approximation (5), the equations for isoscalar and isovector systems are decoupled. Further, due to the axial symmetry, the angular momentum projection is a good quantum number. As a result, every set of equations splits into five independent subsets with quantum numbers $\mu = 0, \pm1, \pm2$. The detailed derivation of formulas for eigenfrequencies and transition probabilities together with all necessary explanations is given in [1]. Here, we state only the final results required for comparison with the respective results obtained in the framework of the RPA.

2.2. Isoscalar Eigenfrequencies

Let us analyze the isoscalar set of equations with $\mu = 1$:

$$\dot{\mathcal{R}}_{21} - 2\mathcal{L}_{21}/m = 0, \tag{6}$$

$$\dot{\mathcal{L}}_{21} - \mathcal{P}_{21}/m + \left[m\omega^2 + 2\kappa_0(Q_{20}^{\text{eq}} + 2Q_{00}^{\text{eq}})\right]\mathcal{R}_{21} = 0,$$

$$\dot{\mathcal{P}}_{21} + 2[m\omega^2 + \kappa_0 Q_{20}^{\text{eq}}]\mathcal{L}_{21} = 0,$$

$$\dot{\mathcal{L}}_{11} = 0.$$

Imposing the time evolution via $e^{-i\Omega t}$ for all variables, one transforms (6) into a set of algebraic equations. The eigenfrequencies are found from its characteristic equation, which reads

$$\Omega^2 \left[\Omega^2 - 4\omega^2 - \frac{6\kappa_0}{m}\left(Q_{20}^{\text{eq}} + \frac{4}{3}Q_{00}^{\text{eq}}\right)\right] = 0. \tag{7}$$

For κ_0, we take the self-consistent value $\kappa_0 = -m\bar{\omega}^2/(4Q_{00})$, where $\bar{\omega}^2 = \omega^2/(1 + 2\delta/3)$ (see Appendix A) with the standard definition of the deformation parameter $Q_{20} = Q_{00}\frac{4}{3}\delta$. Then

$$\Omega^2[\Omega^2 - 2\bar{\omega}^2(1 + \delta/3)] = 0. \tag{8}$$

The nontrivial solution of this equation gives the frequency of the $\mu = 1$ branch of the isoscalar GQR

$$\Omega^2 = \Omega_{\text{is}}^2 = 2\bar{\omega}^2(1 + \delta/3). \tag{9}$$

Taking into account relation (A.4) from Appendix A, we find that this result coincides with that of [8]. The trivial solution $\Omega = \Omega_0 = 0$ is characteristic of the nonvibrational mode, corresponding to the obvious integral of motion $\mathcal{L}_{11} = \text{const}$ responsible for the rotational degree of freedom. This is usually called the "spurious" mode.

2.3. Isovector Eigenfrequencies

The information about the scissors mode is contained in the set of isovector equations with $\mu = 1$:

$$\dot{\bar{\mathcal{R}}}_{21} - 2\bar{\mathcal{L}}_{21}/m = 0, \tag{10}$$

$$\dot{\bar{\mathcal{L}}}_{21} - \bar{\mathcal{P}}_{21}/m + \left[m\omega^2 + \kappa Q_{20}^{\text{eq}} + 4\kappa_1 Q_{00}^{\text{eq}}\right]\bar{\mathcal{R}}_{21} = 0,$$

$$\dot{\bar{\mathcal{P}}}_{21} + 2[m\omega^2 + \kappa_0 Q_{20}^{\text{eq}}]\bar{\mathcal{L}}_{21} - 6\kappa_0 Q_{20}^{\text{eq}}\bar{\mathcal{L}}_{11} = 0,$$

$$\dot{\bar{\mathcal{L}}}_{11} + 3\bar{\kappa}Q_{20}^{\text{eq}}\bar{\mathcal{R}}_{21} = 0.$$

Imposing the time evolution via $e^{-i\Omega t}$, one transforms (10) into a set of algebraic equations. Again, the eigenfrequencies are found from the characteristic equation, which reads

$$\Omega^4 - \Omega^2 \left[4\omega^2 + \frac{8}{m}\kappa_1 Q_{00}^{\text{eq}} + \frac{2}{m}(\kappa_1 + 2\kappa_0)Q_{20}^{\text{eq}}\right] \tag{11}$$

$$+ \frac{36}{m^2}(\kappa_0 - \kappa_1)\kappa_0(Q_{20}^{\text{eq}})^2 = 0.$$

Supposing, as usual, the isovector constant κ_1 to be proportional to the isoscalar one, $\kappa_1 = \alpha\kappa_0$, and taking the self-consistent value for κ_0, we finally obtain

$$\Omega^4 - 2\Omega^2\bar{\omega}^2(2 - \alpha)(1 + \delta/3) + 4\bar{\omega}^4(1 - \alpha)\delta^2 = 0. \tag{12}$$

The solutions to this equation are

$$\Omega_{\pm}^2 = \bar{\omega}^2(2 - \alpha)(1 + \delta/3) \tag{13}$$

$$\pm \sqrt{\bar{\omega}^4(2 - \alpha)^2(1 + \delta/3)^2 - 4\bar{\omega}^4(1 - \alpha)\delta^2}.$$

The solution Ω_+ gives the frequency Ω_{iv} of the $\mu = 1$ branch of the isovector GQR (IVGQR). The solution Ω_- gives the frequency Ω_{sc} of the scissors mode.

We adjust α from the fact that the IVGQR is experimentally known to lie practically at twice the

energy of the isoscalar GQR. In our model, the experimental situation is satisfied by $\alpha = -2$. Then

$$\Omega_{\text{iv}}^2 = 4\bar{\omega}^2\left(1 + \frac{\delta}{3} + \sqrt{\left(1 + \frac{\delta}{3}\right)^2 - \frac{3}{4}\delta^2}\right), \quad (14)$$

$$\Omega_{\text{sc}}^2 = 4\bar{\omega}^2\left(1 + \frac{\delta}{3} - \sqrt{\left(1 + \frac{\delta}{3}\right)^2 - \frac{3}{4}\delta^2}\right).$$

2.4. Linear Response and Transition Probabilities

A direct way of calculating the reduced transition probabilities is provided by the theory of linear response of a system to a weak external field

$$\hat{O}(t) = \hat{O}\exp(-i\Omega t) + \hat{O}^\dagger\exp(i\Omega t).$$

For magnetic excitations,

$$\hat{O} = \hat{O}_{1\mu} = -i\nabla(rY_{1\mu})\cdot[\mathbf{r}\times\nabla]\mu_N, \quad (15)$$

$$\mu_N = \frac{e\hbar}{2mc};$$

$$B(M1)_{\text{sc}} = 2|\langle\text{sc}|\hat{O}_{11}|0\rangle|^2 \quad (16)$$

$$= \frac{1-\alpha}{4\pi}\frac{m\bar{\omega}^2}{\hbar}Q_{00}\delta^2\frac{\Omega_{\text{sc}}^2 - 2(1+\delta/3)\bar{\omega}^2}{\Omega_{\text{sc}}(\Omega_{\text{sc}}^2 - \Omega_{\text{iv}}^2)}\mu_N^2,$$

$$B(M1)_{\text{iv}} = 2|\langle\text{iv}|\hat{O}_{11}|0\rangle|^2 \quad (17)$$

$$= \frac{1-\alpha}{4\pi}\frac{m\bar{\omega}^2}{\hbar}Q_{00}\delta^2\frac{\Omega_{\text{iv}}^2 - 2(1+\delta/3)\bar{\omega}^2}{\Omega_{\text{iv}}(\Omega_{\text{iv}}^2 - \Omega_{\text{sc}}^2)}\mu_N^2.$$

These two formulas can be joined into one expression by the simple transformation of the denominators. Indeed, we have from (13)

$$\pm(\Omega_{\text{iv}}^2 - \Omega_{\text{sc}}^2) = \pm(\Omega_+^2 - \Omega_-^2) \quad (18)$$

$$= \pm2\sqrt{\bar{\omega}^4(2-\alpha)^2(1+\delta/3)^2 - 4\bar{\omega}^4(1-\alpha)\delta^2}$$

$$= 2\Omega_\pm^2 - 2\bar{\omega}^2(2-\alpha)(1+\delta/3)$$

$$= 2\Omega_\pm^2 - (2-\alpha)(\omega_x^2 + \omega_z^2).$$

Using these relations in formulas (16) and (17), we obtain the expression for $B(M1)$, valid for both excitations:

$$B(M1)_\nu = 2|\langle\nu|\hat{O}_{11}|0\rangle|^2 = \frac{1-\alpha}{8\pi}\frac{m\bar{\omega}^2}{\hbar} \quad (19)$$

$$\times Q_{00}\delta^2\frac{\Omega_\nu^2 - 2(1+\delta/3)\bar{\omega}^2}{\Omega_\nu[\Omega_\nu^2 - \bar{\omega}^2(2-\alpha)(1+\delta/3)]}\mu_N^2.$$

For electric excitations, $\hat{O} = \hat{O}_{2\mu} = er^2Y_{2\mu}$,

$$B(E2)_{\text{sc}} = 2|\langle\text{sc}|\hat{O}_{21}|0\rangle|^2 \quad (20)$$

$$= \frac{e^2\hbar}{m}\frac{5}{8\pi}Q_{00}\frac{(1+\delta/3)\Omega_{\text{sc}}^2 - 2(\bar{\omega}\delta)^2}{\Omega_{\text{sc}}(\Omega_{\text{sc}}^2 - \Omega_{\text{iv}}^2)},$$

$$B(E2)_{\text{iv}} = 2|\langle\text{iv}|\hat{O}_{21}|0\rangle|^2 \quad (21)$$

$$= \frac{e^2\hbar}{m}\frac{5}{8\pi}Q_{00}\frac{(1+\delta/3)\Omega_{\text{iv}}^2 - 2(\bar{\omega}\delta)^2}{\Omega_{\text{iv}}(\Omega_{\text{iv}}^2 - \Omega_{\text{sc}}^2)},$$

$$B(E2)_{\text{is}} = 2|\langle\text{is}|\hat{O}_{21}|0\rangle|^2 \quad (22)$$

$$= \frac{e^2\hbar}{m}\frac{5}{8\pi}Q_{00}[(1+\delta/3)\Omega_{\text{is}}^2 - 2(\bar{\omega}\delta)^2]/[\Omega_{\text{is}}]^3.$$

Using relations (18) in formulas (20) and (21), we obtain the expression for $B(E2)$, valid for all three excitations:

$$B(E2)_\nu = 2|\langle\nu|\hat{O}_{21}|0\rangle|^2 \quad (23)$$

$$= \frac{e^2\hbar}{m}\frac{5}{16\pi}Q_{00}\frac{(1+\delta/3)\Omega_\nu^2 - 2(\bar{\omega}\delta)^2}{\Omega_\nu[\Omega_\nu^2 - \bar{\omega}^2(2-\alpha)(1+\delta/3)]}.$$

The isoscalar value (22) is obtained by assuming $\alpha = 1$.

3. RPA

Standard RPA equations in the notation of [3] are

$$\sum_{n,j}\{[\delta_{ij}\delta_{mn}(\epsilon_m - \epsilon_i) + \bar{v}_{mjin}]X_{nj} + \bar{v}_{mnij}Y_{nj}\}$$

$$\quad (24)$$

$$= \hbar\Omega X_{mi},$$

$$\sum_{n,j}\{\bar{v}_{ijmn}X_{nj} + [\delta_{ij}\delta_{mn}(\epsilon_m - \epsilon_i) + \bar{v}_{inmj}]Y_{nj}\}$$

$$= -\hbar\Omega Y_{mi}.$$

According to the schematic model (2), the matrix element of the residual interaction is

$$\bar{v}_{mjin} = \kappa_{\tau\tau'}D_{im}^{\tau*}D_{jn}^{\tau'}$$

with $D = q_{21} = \sqrt{16\pi/5}\,r^2Y_{21}$ and $\kappa_{\text{nn}} = \kappa_{\text{pp}} = \kappa$, $\kappa_{\text{np}} = \bar{\kappa}$. This interaction distinguishes between protons and neutrons, so we have to introduce the isospin projection indices τ, τ' into the set of RPA equations (24):

$$(\epsilon_m^\tau - \epsilon_i^\tau)X_{mi}^\tau + \sum_{n,j,\tau'}\kappa_{\tau\tau'}D_{im}^{\tau*}D_{jn}^{\tau'}X_{nj}^{\tau'} \quad (25)$$

$$+ \sum_{n,j,\tau'}\kappa_{\tau\tau'}D_{im}^{\tau*}D_{nj}^{\tau'}Y_{nj}^{\tau'} = \hbar\Omega X_{mi}^\tau,$$

$$\sum_{n,j,\tau'}\kappa_{\tau\tau'}D_{mi}^{\tau*}D_{jn}^{\tau'}X_{nj}^{\tau'} + (\epsilon_m^\tau - \epsilon_i^\tau)Y_{mi}^\tau$$

$$+ \sum_{n,j,\tau'}\kappa_{\tau\tau'}D_{mi}^{\tau*}D_{nj}^{\tau'}Y_{nj}^{\tau'} = -\hbar\Omega Y_{mi}^\tau.$$

Its solution is

$$X_{mi}^\tau = \frac{D_{im}^{\tau*}}{\hbar\Omega - \epsilon_{mi}^\tau}K^\tau, \quad Y_{mi}^\tau = -\frac{D_{mi}^{\tau*}}{\hbar\Omega + \epsilon_{mi}^\tau}K^\tau \quad (26)$$

with $\epsilon_{mi}^\tau = \epsilon_m^\tau - \epsilon_i^\tau$ and $K^\tau = \sum_{\tau'} \kappa_{\tau\tau'} C^{\tau'}$.

The constant C^τ is defined as $C^\tau = \sum_{n,j}(D_{jn}^\tau X_{nj}^\tau + D_{nj}^\tau Y_{nj}^\tau)$. Using here the above-written expressions for X_{nj}^τ and Y_{nj}^τ, one derives the useful relation

$$C^\tau = 2S^\tau K^\tau = 2S^\tau \sum_{\tau'} \kappa_{\tau\tau'} C^{\tau'}, \qquad (27)$$

where the following notation is introduced:

$$S^\tau = \sum_{mi} |D_{mi}^\tau|^2 \frac{\epsilon_{mi}^\tau}{E^2 - (\epsilon_{mi}^\tau)^2} \qquad (28)$$

with $E = \hbar\Omega$. Let us write relation (27) in detail:

$$C^{\mathrm{n}} - 2S^{\mathrm{n}}(\kappa C^{\mathrm{n}} + \bar\kappa C^{\mathrm{p}}) = 0, \qquad (29)$$
$$C^{\mathrm{p}} - 2S^{\mathrm{p}}(\bar\kappa C^{\mathrm{n}} + \kappa C^{\mathrm{p}}) = 0.$$

The condition for existence of a nontrivial solution to this set of equations leads to the secular equation

$$(1 - 2S^{\mathrm{n}}\kappa)(1 - 2S^{\mathrm{p}}\kappa) - 4S^{\mathrm{n}}S^{\mathrm{p}}\bar\kappa^2 = 0. \qquad (30)$$

Making obvious linear combinations of the two equations in (29), we write them in terms of isoscalar and isovector variables $C = C^{\mathrm{n}} + C^{\mathrm{p}}, \bar{C} = C^{\mathrm{n}} - C^{\mathrm{p}}$:

$$C - 2(S^{\mathrm{n}} + S^{\mathrm{p}})\kappa_0 C - 2(S^{\mathrm{n}} - S^{\mathrm{p}})\kappa_1 \bar{C} = 0, \quad (31)$$
$$\bar{C} - 2(S^{\mathrm{n}} - S^{\mathrm{p}})\kappa_0 C - 2(S^{\mathrm{n}} + S^{\mathrm{p}})\kappa_1 \bar{C} = 0.$$

Approximation (5) allows us to decouple equations for isoscalar and isovector variables. Really, in this case, $S^{\mathrm{n}} = S^{\mathrm{p}} \equiv S/2$; hence, we obtain two secular equations:

$$1 - 2S\kappa_0 = 0 \quad \text{or} \quad 1 - S\kappa = S\bar\kappa \qquad (32)$$

in the isoscalar case and

$$1 - 2S\kappa_1 = 0 \quad \text{or} \quad 1 - S\kappa = -S\bar\kappa \qquad (33)$$

in the isovector case, the difference between them being in the strength constants only. Having in mind the relation $\kappa_1 = \alpha\kappa_0$, we come to the conclusion that it is sufficient to analyze the isovector case only—the results for isoscalar case are obtained by assuming $\alpha = 1$.

3.1. Eigenfrequencies

The detailed expression for the isovector secular equation is

$$\frac{1}{2\kappa_1} = \sum_{mi} |D_{mi}|^2 \frac{\epsilon_{mi}}{E^2 - \epsilon_{mi}^2}. \qquad (34)$$

The operator D has only two types of nonzero matrix elements D_{mi} in the deformed oscillator basis. Matrix elements of the first type couple the states of the same major shell. All corresponding transition energies are degenerate: $\epsilon_m - \epsilon_i = \hbar(\omega_x - \omega_z) \equiv \epsilon_0$. Matrix elements of the second type couple the states of the

different major shells with $\Delta N = 2$. All corresponding transition energies are degenerate too: $\epsilon_m - \epsilon_i = \hbar(\omega_x + \omega_z) \equiv \epsilon_2$. Therefore, the secular equation can be rewritten as

$$\frac{1}{2\kappa_1} = \frac{\epsilon_0 D_0}{E^2 - \epsilon_0^2} + \frac{\epsilon_2 D_2}{E^2 - \epsilon_2^2}. \qquad (35)$$

The sums $D_0 = \sum_{mi(\Delta N=0)} |D_{mi}|^2$ and $D_2 = \sum_{mi(\Delta N=2)} |D_{mi}|^2$ can be calculated analytically (see Appendix B):

$$D_0 = \frac{Q_{00}}{m\bar\omega^2}\epsilon_0, \quad D_2 = \frac{Q_{00}}{m\bar\omega^2}\epsilon_2. \qquad (36)$$

Let us transform the secular equation (35) in the polynomial

$$E^4 - E^2[(\epsilon_0^2 + \epsilon_2^2) + 2\kappa_1(\epsilon_0 D_0 + \epsilon_2 D_2)]$$
$$+ [\epsilon_0^2\epsilon_2^2 + 2\kappa_1\epsilon_0\epsilon_2(\epsilon_0 D_2 + \epsilon_2 D_0)] = 0.$$

Using here expressions (36) for D_0 and D_2 and the self-consistent value of the strength constant (A.3), we find

$$E^4 - E^2(1 - \alpha/2)(\epsilon_0^2 + \epsilon_2^2) + (1 - \alpha)\epsilon_0^2\epsilon_2^2 = 0,$$

or

$$\Omega^4 - \Omega^2(2 - \alpha)\omega_+^2 + (1 - \alpha)\omega_-^4 = 0, \qquad (37)$$

where the notation $\omega_+^2 = \omega_x^2 + \omega_z^2$ and $\omega_-^4 = (\omega_x^2 - \omega_z^2)^2$ is introduced. This result coincides with that of [2]. By a trivial rearrangement of the terms in (37), one obtains the useful relation

$$\Omega^2(\Omega^2 - \omega_+^2) = (1 - \alpha)(\Omega^2\omega_+^2 - \omega_-^4). \qquad (38)$$

Substituting expressions (A.3) from Appendix A for ω_x^2 and ω_z^2 into (37), we reproduce formula (12) for the isovector case:

$$\Omega^4 - 2\Omega^2\bar\omega^2(2 - \alpha)(1 + \delta/3) + 4\bar\omega^4(1 - \alpha)\delta^2 = 0.$$

Taking here $\alpha = 1$, we reproduce formula (8) for the isoscalar case:

$$\Omega^4 - 2\Omega^2\bar\omega^2(1 + \delta/3) = 0.$$

3.2. B(E2) Factors

According to [3], the transition probability for a one-body operator $\hat{F} = \sum_{i=1}^A \hat{f}_i$ is calculated with the help of the formula

$$\langle 0|\hat{F}^\tau|\nu\rangle = \sum_{mi}(\hat{f}_{im}^\tau X_{mi}^{\tau,\nu} + \hat{f}_{mi}^\tau Y_{mi}^{\tau,\nu}). \qquad (39)$$

To calculate quadrupole excitations, one has to take $\hat{f}^{\mathrm{p}} = er^2 Y_{2\mu} = \tilde{e}D^{\mathrm{p}}$ with $\tilde{e} = e\sqrt{\dfrac{5}{16\pi}}$. The expressions for X_{mi}^{τ} and Y_{mi}^{τ} are given by formulas (26). Combining these results, we have

$$\langle 0|D^{\mathrm{p}}|\nu\rangle = 2\tilde{e}K_{\nu}^{\mathrm{p}} \sum_{mi} |D_{mi}^{\mathrm{p}}|^2 \frac{\epsilon_{mi}^{\mathrm{p}}}{E_{\nu}^2 - (\epsilon_{mi}^{\mathrm{p}})^2} \qquad (40)$$
$$= 2\tilde{e}K_{\nu}^{\mathrm{p}}S_{\nu}^{\mathrm{p}} = \tilde{e}C_{\nu}^{\mathrm{p}}.$$

The constant C_{ν}^{p} is determined by the normalization condition

$$\delta_{\nu,\nu'} = \sum_{mi,\tau} (X_{mi}^{\tau,\nu*} X_{mi}^{\tau,\nu'} - Y_{mi}^{\tau,\nu*} Y_{mi}^{\tau,\nu'}),$$

which gives

$$\frac{1}{(C_{\nu}^{\mathrm{p}})^2} = E_{\nu} \sum_{mi} \left[\frac{|D_{mi}^{\mathrm{p}}|^2}{(S_{\nu}^{\mathrm{p}})^2} \frac{\epsilon_{mi}^{\mathrm{p}}}{[E_{\nu}^2 - (\epsilon_{mi}^{\mathrm{p}})^2]^2} \right. \qquad (41)$$
$$\left. + \frac{(C_{\nu}^{\mathrm{n}})^2}{(C_{\nu}^{\mathrm{p}})^2} \frac{|D_{mi}^{\mathrm{n}}|^2}{(S_{\nu}^{\mathrm{n}})^2} \frac{\epsilon_{mi}^{\mathrm{n}}}{[E_{\nu}^2 - (\epsilon_{mi}^{\mathrm{n}})^2]^2} \right].$$

The ratio $C^{\mathrm{n}}/C^{\mathrm{p}}$ is determined by any of Eqs. (29):

$$\frac{C^{\mathrm{n}}}{C^{\mathrm{p}}} = \frac{1 - 2S^{\mathrm{p}}\kappa}{2S^{\mathrm{p}}\bar{\kappa}} = \frac{2S^{\mathrm{n}}\bar{\kappa}}{1 - 2S^{\mathrm{n}}\kappa}. \qquad (42)$$

Formula (41) is considerably simplified by the approximation (5), when $S^{\mathrm{p}} = S^{\mathrm{n}}$, $\epsilon_{mi}^{\mathrm{p}} = \epsilon_{mi}^{\mathrm{n}}$, and $D_{mi}^{\mathrm{p}} = D_{mi}^{\mathrm{n}}$. Applying the second parts of formulas (32) and (33), we can easily find that, in this case, $C^{\mathrm{n}}/C^{\mathrm{p}} = \pm 1$. As a result, the final expression for $B(E2)$ is

$$B(E2)_{\nu} = 2|\langle 0|D^{\mathrm{p}}|\nu\rangle|^2 \qquad (43)$$
$$= 2\tilde{e}^2 \left(16E_{\nu}\kappa_1^2 \sum_{mi} |D_{mi}|^2 \frac{\epsilon_{mi}}{(E_{\nu}^2 - \epsilon_{mi}^2)^2} \right)^{-1}.$$

With the help of formulas (36), this expression can be transformed into

$$B(E2)_{\nu} = \frac{5}{8\pi} \frac{e^2 Q_{00}}{m\bar{\omega}^2 \alpha^2 E_{\nu}} \qquad (44)$$
$$\times \left[\frac{\epsilon_0^2}{(E_{\nu}^2 - \epsilon_0^2)^2} + \frac{\epsilon_2^2}{(E_{\nu}^2 - \epsilon_2^2)^2} \right]^{-1}$$
$$= \frac{5}{8\pi} \frac{e^2 Q_{00}}{m\bar{\omega}^2 \alpha^2 E_{\nu}} \frac{(E_{\nu}^2 - \epsilon_0^2)^2 (E_{\nu}^2 - \epsilon_2^2)^2}{(E_{\nu}^2 - \epsilon_2^2)^2 \epsilon_0^2 + (E^2 - \epsilon_0^2)^2 \epsilon_2^2}$$
$$= \frac{5}{16\pi} \frac{e^2\hbar Q_{00}}{m\bar{\omega}^2 \Omega_{\nu}} \frac{(\Omega_{\nu}^2\omega_+^2 - \omega_-^4)^2}{\Omega_{\nu}^4\omega_+^2 - 2\Omega_{\nu}^2\omega_-^4 + \omega_+^2\omega_-^4}.$$

At a glance, this expression has nothing in common with (23). Nevertheless, it can be shown that they are identical. To this end, we analyze carefully the denominator of the last expression in (44). Summing

it with the secular equation (37) (multiplied by ω_+^2), which obviously does not change its value, we find after elementary combinations

$$\mathrm{Denom} = \Omega_{\nu}^4\omega_+^2 - 2\Omega_{\nu}^2\omega_-^4 + \omega_+^2\omega_-^4 \qquad (45)$$
$$+ \omega_+^2[\Omega_{\nu}^4 - \Omega_{\nu}^2(2-\alpha)\omega_+^2 + (1-\alpha)\omega_-^4]$$
$$= \omega_+^2\Omega_{\nu}^2[2\Omega_{\nu}^2 - (2-\alpha)\omega_+^2]$$
$$- \omega_-^4[2\Omega_{\nu}^2 - (2-\alpha)\omega_+^2]$$
$$= (\Omega_{\nu}^2\omega_+^2 - \omega_-^4)[2\Omega_{\nu}^2 - (2-\alpha)\omega_+^2].$$

This result allows us to write the final expression

$$B(E2)_{\nu} = \frac{5}{16\pi} \frac{e^2\hbar}{m\bar{\omega}^2} Q_{00} \frac{\Omega_{\nu}^2\omega_+^2 - \omega_-^4}{\Omega_{\nu}[2\Omega_{\nu}^2 - (2-\alpha)\omega_+^2]}, \qquad (46)$$

which coincides with (23) (we recall that $\omega_+^2 = 2\bar{\omega}^2(1 + \delta/3)$ and $\omega_-^4 = 4\delta^2\bar{\omega}^4$). By simple transformations, we can reduce this formula to the result of Hamamoto and Nazarewicz [2] (considering that they published it without the constant factor

$$\frac{5}{32\pi} \frac{e^2\hbar}{m\omega_0} Q_{00}^0).$$

3.3. B(M1) Factors

In accordance with formulas (39), (26), and (15), the magnetic transition matrix element is

$$\langle 0|\hat{O}_{11}^{\mathrm{p}}|\nu\rangle = K_{\nu}^{\mathrm{p}} \sum_{mi} \left[\frac{(\hat{O}_{11}^{\mathrm{p}})_{im} D_{im}^{\mathrm{p}*}}{E_{\nu} - \epsilon_{mi}^{\mathrm{p}}} - \frac{(\hat{O}_{11}^{\mathrm{p}})_{mi} D_{mi}^{\mathrm{p}*}}{E_{\nu} + \epsilon_{mi}^{\mathrm{p}}} \right]. \qquad (47)$$

As is shown in Appendix B, the matrix element $(O_{11}^{\mathrm{p}})_{im}$ is proportional to D_{im}^{p} [formula (B.15), Appendix B]. So, expression (47) is reduced to

$$\langle 0|\hat{O}_{11}^{\mathrm{p}}|\nu\rangle = -K_{\nu}^{\mathrm{p}} \frac{\tilde{e}\hbar}{2c\sqrt{5}} (\omega_x^2 - \omega_z^2)^{\mathrm{p}} \qquad (48)$$
$$\times \sum_{mi} \left[\frac{D_{im}^{\mathrm{p}} D_{im}^{\mathrm{p}*}}{\epsilon_{im}^{\mathrm{p}}(E_{\nu} - \epsilon_{mi}^{\mathrm{p}})} - \frac{D_{mi}^{\mathrm{p}} D_{mi}^{\mathrm{p}*}}{\epsilon_{mi}^{\mathrm{p}}(E_{\nu} + \epsilon_{mi}^{\mathrm{p}})} \right]$$
$$= K_{\nu}^{\mathrm{p}} \frac{\tilde{e}\hbar}{c\sqrt{5}} (\omega_x^2 - \omega_z^2)^{\mathrm{p}} E_{\nu} \sum_{mi} \frac{|D_{mi}^{\mathrm{p}}|^2}{\epsilon_{mi}^{\mathrm{p}}[E_{\nu}^2 - (\epsilon_{mi}^{\mathrm{p}})^2]}.$$

With the help of approximation (5) and expressions (36) for D_0 and D_2, we find

$$\langle 0|\hat{O}_{11}^{\mathrm{p}}|\nu\rangle = \frac{C_{\nu}^{\mathrm{p}}}{2S_{\nu}^{\mathrm{p}}} \frac{\tilde{e}\hbar}{c\sqrt{5}} (\omega_x^2 - \omega_z^2) \qquad (49)$$
$$\times \frac{Q_{00}}{2m\bar{\omega}^2} \left(\frac{E_{\nu}}{E_{\nu}^2 - \epsilon_0^2} + \frac{E_{\nu}}{E_{\nu}^2 - \epsilon_2^2} \right)$$
$$= -2\kappa_1 C_{\nu}^{\mathrm{p}} \frac{\tilde{e}}{c\sqrt{5}} (\omega_x^2 - \omega_z^2) \frac{Q_{00}}{m\bar{\omega}^2} \frac{\Omega_{\nu}(\Omega_{\nu}^2 - \omega_+^2)}{\alpha(\Omega_{\nu}^2\omega_+^2 - \omega_-^4)}$$

$$= \frac{C_\nu^p}{2} \frac{\tilde{e}}{c\sqrt{5}} (\omega_x^2 - \omega_z^2) \frac{1-\alpha}{\Omega_\nu}.$$

Relation (38) and the self-consistent value of the strength constant $\kappa_1 = \alpha\kappa_0$ were used at the last step. For the magnetic transition probability, we have

$$B(M1)_\nu = 2|\langle 0|\hat{O}_{11}^p|\nu\rangle|^2 \qquad (50)$$

$$= 2\frac{(C_\nu^p)^2}{4} \frac{\tilde{e}^2}{5c^2} \omega_-^4 \frac{(1-\alpha)^2}{\Omega_\nu^2} = \frac{\omega_-^4}{20c^2} \frac{(1-\alpha)^2}{\Omega_\nu^2} B(E2).$$

This relation between $B(M1)$ and $B(E2)$ was also found (to the factor $1/(20c^2)$) by Hamamoto and Nazarewicz [2]. Substituting expression (46) for $B(E2)$ into (50), we reproduce [with the help of relation (38)] formula (19).

3.4. "Synthetic" Scissors and Spurious State

The nature of collective excitations calculated by the method of WFM is ascertained quite easily by analyzing the roles of collective variables describing the phenomenon. The solution of this problem in the RPA approach is not so obvious. That is why the nature of the low-lying states has often been established by considering overlaps of these states with the "pure scissors state" [10, 11] or "synthetic state" [2], produced by the action of the scissors operator

$$S_x = \mathcal{N}^{-1}(\langle I_x^{n2}\rangle I_x^p - \langle I_x^{p2}\rangle I_x^n)$$

on the ground state:

$$|\text{Syn}\rangle = S_x|0\rangle,$$

$\mathcal{N}$ being the normalization factor. Due to axial symmetry, one can use the I_y^τ component instead of I_x^τ, or any linear combination of them, for example, the variable L_{11}^τ, which is much more convenient for us. The terms $\langle I_x^{\tau 2}\rangle$ are introduced to ensure the orthogonality of the synthetic scissors to the spurious state $|\text{Sp}\rangle = (I^n + I^p)|0\rangle$. However, we do not need these terms, because the collective states $|\nu\rangle$ of our model are already orthogonal to $|\text{Sp}\rangle$ (see below); hence, the overlaps $\langle\text{Syn}|\nu\rangle$ will be free from any admixtures of $|\text{Sp}\rangle$. So, we use the following definitions of the synthetic and spurious states:

$$|\text{Syn}\rangle = \gamma\mathcal{N}^{-1}(L_{11}^p - L_{11}^n)|0\rangle$$
$$= \mathcal{N}^{-1}(\hat{O}_{11}^p - \hat{O}_{11}^n)|0\rangle,$$
$$|\text{Sp}\rangle = (\hat{O}_{11}^p + \hat{O}_{11}^n)|0\rangle,$$

where

$$\gamma = -i\frac{e}{2mc}\sqrt{\frac{3}{2\pi}}.$$

Let us demonstrate the orthogonality of the spurious state to all the rest states $|\nu\rangle$. As the first step, it is necessary to show that the secular equation (30) has the solution $E = 0$. We need the expression for $S^\tau(E = 0) \equiv S^\tau(0)$. In accordance with (28), we have

$$S^\tau(E) = \left[\frac{\epsilon_0 D_0}{E^2 - \epsilon_0^2} + \frac{\epsilon_2 D_2}{E^2 - \epsilon_2^2}\right]^\tau,$$

$$S^\tau(0) = -\left[\frac{D_0}{\epsilon_0} + \frac{D_2}{\epsilon_2}\right]^\tau.$$

The expressions for D_0^τ and D_2^τ are easily extracted from formulas (B.10) and (B.11) (see Appendix B):

$$D_0^\tau = \frac{\hbar}{m}Q_{00}^\tau\left[\frac{1 + \frac{4}{3}\delta}{\omega_x} - \frac{1 - \frac{2}{3}\delta}{\omega_z}\right]^\tau, \qquad (51)$$

$$D_2^\tau = \frac{\hbar}{m}Q_{00}^\tau\left[\frac{1 + \frac{4}{3}\delta}{\omega_x} + \frac{1 - \frac{2}{3}\delta}{\omega_z}\right]^\tau.$$

So, we find

$$S^\tau(0) = -\frac{\hbar}{m}Q_{00}^\tau\left[\frac{1 + \frac{4}{3}\delta}{\omega_x}\left(\frac{1}{\epsilon_2} + \frac{1}{\epsilon_0}\right) \qquad (52)\right.$$

$$\left.+ \frac{1 - \frac{2}{3}\delta}{\omega_z}\left(\frac{1}{\epsilon_2} - \frac{1}{\epsilon_0}\right)\right]^\tau$$

$$= -\frac{\hbar^2}{m}\frac{4\delta^\tau Q_{00}^\tau}{\epsilon_2^\tau\epsilon_0^\tau} = -\frac{1}{m}\frac{3Q_{20}^\tau}{(\omega_x^2 - \omega_z^2)^\tau},$$

where, in accordance with (B.12) from Appendix B,

$$(\omega_x^2 - \omega_z^2)^p = -\frac{6}{m}(\kappa Q_{20}^p + \bar{\kappa}Q_{20}^n), \qquad (53)$$

$$(\omega_x^2 - \omega_z^2)^n = -\frac{6}{m}(\kappa Q_{20}^n + \bar{\kappa}Q_{20}^p),$$

and the deformation of neutrons δ^n is allowed to be different from the deformation of protons δ^p. Finally, we get

$$2S^p(0) = \frac{Q_{20}^p}{\kappa Q_{20}^p + \bar{\kappa}Q_{20}^n},$$

$$1 - 2S^p(0)\kappa = \frac{\bar{\kappa}Q_{20}^n}{\kappa Q_{20}^p + \bar{\kappa}Q_{20}^n},$$

$$2S^n(0) = \frac{Q_{20}^n}{\kappa Q_{20}^n + \bar{\kappa}Q_{20}^p},$$

$$1 - 2S^n(0)\kappa = \frac{\bar{\kappa}Q_{20}^p}{\kappa Q_{20}^n + \bar{\kappa}Q_{20}^p}.$$

It is easy to see that, substituting these expressions into (30), we obtain the identity; therefore, the secular equation has the zero solution.

At the second step, it is necessary to calculate the overlap $\langle\text{Sp}|\nu\rangle$. Summing (47) with an analogous

expression for neutrons, we get

$$\langle \mathrm{Sp}|\nu\rangle = \frac{\tilde{e}\hbar}{c\sqrt{5}}E_\nu \sum_\tau K_\nu^\tau (\omega_x^2 - \omega_z^2)^\tau \qquad (54)$$

$$\times \sum_{mi} \frac{|D_{mi}^\tau|^2}{\epsilon_{mi}^\tau (E_\nu^2 - \epsilon_{mi}^2)^\tau} = \frac{\tilde{e}\hbar}{c\sqrt{5}}E_\nu$$

$$\times \sum_\tau K_\nu^\tau (\omega_x^2 - \omega_z^2)^\tau \sum_{mi} \frac{|D_{mi}^\tau|^2 \epsilon_{mi}^\tau}{(\epsilon_{mi}^2)^\tau (E_\nu^2 - \epsilon_{mi}^2)^\tau}.$$

Applying the algebraic identity

$$\frac{1}{\epsilon^2 (E^2 - \epsilon^2)} = \frac{1}{E^2}\left(\frac{1}{\epsilon^2} + \frac{1}{E^2 - \epsilon^2}\right)$$

and remembering the definition (28) of S^τ, we can rewrite (54) as

$$\langle \mathrm{Sp}|\nu\rangle \qquad (55)$$

$$= \frac{\tilde{e}\hbar}{c\sqrt{5}E_\nu} \sum_\tau K_\nu^\tau (\omega_x^2 - \omega_z^2)^\tau (S^\tau - S^\tau(0))$$

$$= \frac{\tilde{e}\hbar}{c\sqrt{5}} \frac{K_\nu^\mathrm{p}}{E_\nu}\left[(\omega_x^2 - \omega_z^2)^\mathrm{p}(S^\mathrm{p} - S^\mathrm{p}(0))\right.$$

$$\left. + (\omega_x^2 - \omega_z^2)^\mathrm{n}(S^\mathrm{n} - S^\mathrm{n}(0))\frac{K_\nu^\mathrm{n}}{K_\nu^\mathrm{p}}\right].$$

In accordance with (27) and (42),

$$\frac{K_\nu^\mathrm{n}}{K_\nu^\mathrm{p}} = \frac{1 - 2S^\mathrm{p}\kappa}{2S^\mathrm{n}\bar{\kappa}}. \qquad (56)$$

Noting now [see formula (52)] that $(\omega_x^2 - \omega_z^2)^\tau S^\tau(0) = -\frac{3}{m}Q_{20}^\tau$ and taking into account relations (53), we find

$$\langle \mathrm{Sp}|\nu\rangle = \beta\left\{[(\kappa Q_2^\mathrm{p} + \bar{\kappa}Q_2^\mathrm{n})2S^\mathrm{p} - Q_2^\mathrm{p}]\right. \qquad (57)$$

$$\left. + [(\kappa Q_2^\mathrm{n} + \bar{\kappa}Q_2^\mathrm{p})2S^\mathrm{n} - Q_2^\mathrm{n}]\frac{1 - 2S^\mathrm{p}\kappa}{2S^\mathrm{n}\bar{\kappa}}\right\}$$

$$= \beta\left\{[(2S^\mathrm{p}\kappa - 1)Q_2^\mathrm{p} + 2S^\mathrm{p}\bar{\kappa}Q_2^\mathrm{n}]\right.$$

$$\left. + [(2S^\mathrm{n}\kappa - 1)Q_2^\mathrm{n} + 2S^\mathrm{n}\bar{\kappa}Q_2^\mathrm{p}]\frac{1 - 2S^\mathrm{p}\kappa}{2S^\mathrm{n}\bar{\kappa}}\right\}$$

$$= \beta\left\{2S^\mathrm{p}\bar{\kappa}Q_2^\mathrm{n} + (2S^\mathrm{n}\kappa - 1)Q_2^\mathrm{n}\frac{1 - 2S^\mathrm{p}\kappa}{2S^\mathrm{n}\bar{\kappa}}\right\}$$

$$= \beta\frac{Q_2^\mathrm{n}}{2S^\mathrm{n}\bar{\kappa}}\left\{2S^\mathrm{n}\bar{\kappa}2S^\mathrm{p}\bar{\kappa} - (1 - 2S^\mathrm{n}\kappa)\right.$$

$$\left. \times (1 - 2S^\mathrm{p}\kappa)\right\} = 0,$$

where

$$\beta = -\frac{3}{m}\frac{\tilde{e}\hbar}{c\sqrt{5}}\frac{K_\nu^\mathrm{p}}{E_\nu}.$$

and $Q_2 \equiv Q_{20}$. The expression in the last curly brackets obviously coincides with the secular equation (30), which proves the orthogonality of the spurious state to all physical states of the considered model. Thus, we can conclude that, strictly speaking, this is not a spurious state, but one of the exact eigenstates of the model corresponding to the integral of motion $I^\mathrm{n} + I^\mathrm{p}$. In other words [3]: "In fact, these excitations are not really spurious, but they represent a different type of motion, which has to be treated separately." The same conclusion was made by Lo Iudice [12], who solved this problem approximately with the help of several assumptions (a small deformation limit, for example).

The problem of the "spurious" state being solved, the calculation of the overlaps $\langle \mathrm{Syn}|\nu\rangle$ becomes trivial. Really, we have shown above that $\langle 0|\hat{O}_{11}^\mathrm{n} + \hat{O}_{11}^\mathrm{p}|\nu\rangle = 0$. This means that $\langle 0|\hat{O}_{11}^\mathrm{n}|\nu\rangle = -\langle 0|\hat{O}_{11}^\mathrm{p}|\nu\rangle$; then $\langle \mathrm{Syn}|\nu\rangle = \mathcal{N}^{-1}\langle 0|\hat{O}_{11}^\mathrm{p} - \hat{O}_{11}^\mathrm{n}|\nu\rangle = 2\mathcal{N}^{-1} \times \langle 0|\hat{O}_{11}^\mathrm{p}|\nu\rangle$ and

$$U^2 \equiv |\langle \mathrm{Syn}|\nu\rangle|^2 = 2\mathcal{N}^{-2}B(M1)_\nu.$$

The nontrivial part of the problem is the calculation of the normalization factor $\mathcal{N}$. It is important not to forget about the time dependence of the synthetic state, which should be determined by the external field:

$$|\mathrm{Syn}(t)\rangle = \mathcal{N}^{-1}[(\hat{O}_{11}^\mathrm{p} - \hat{O}_{11}^\mathrm{n})\exp^{-i\Omega t}$$

$$+ (\hat{O}_{11}^\mathrm{p} - \hat{O}_{11}^\mathrm{n})^\dagger \exp^{i\Omega t}]|0\rangle.$$

Then we have

$$\mathcal{N}^2 = \langle \mathrm{Syn}(t)|\mathrm{Syn}(t)\rangle \qquad (58)$$

$$= 2\langle 0|(\hat{O}_{11}^\mathrm{p} - \hat{O}_{11}^\mathrm{n})^\dagger(\hat{O}_{11}^\mathrm{p} - \hat{O}_{11}^\mathrm{n})|0\rangle$$

$$= 2\sum_{ph}\langle 0|(\hat{O}_{11}^\mathrm{p} - \hat{O}_{11}^\mathrm{n})^\dagger|ph\rangle\langle ph|(\hat{O}_{11}^\mathrm{p} - \hat{O}_{11}^\mathrm{n})|0\rangle$$

$$= 2\sum_{ph}|\langle ph|(\hat{O}_{11}^\mathrm{p} - \hat{O}_{11}^\mathrm{n})|0\rangle|^2 = 2\sum_{\tau,ph}|\langle ph|\hat{O}_{11}^\tau|0\rangle|^2.$$

With the help of relation (B.15) from Appendix B, we find

$$\mathcal{N}^2 = \frac{2}{5}\left(\frac{e\hbar}{2c}\right)^2 \sum_{\tau,\,ph}\left(\omega_-^4 \frac{|\langle ph|r^2 Y_{21}|0\rangle|^2}{\epsilon_{ph}^2}\right)^\tau \qquad (59)$$

$$= \frac{1}{8\pi}\left(\frac{e\hbar}{2c}\right)^2 \sum_\tau (\omega_-^4)^\tau \left(\frac{D_0}{\epsilon_0^2} + \frac{D_2}{\epsilon_2^2}\right)^\tau.$$

Expressions for D_0^τ, D_2^τ, ω_x^τ, and ω_z^τ are given by formulas (51) and in Appendix (B.12). To get a definite number, it is necessary to make some assumption concerning the relation between neutron and proton equilibrium characteristics. As usual, we apply the approximation (5); namely, we suppose $Q_{00}^\mathrm{n} = Q_{00}^\mathrm{p}$

and $Q_{20}^{\mathrm{n}} = Q_{20}^{\mathrm{p}}$. It is easy to check that, in this case, formulas for $\omega_{x,z}^{\tau}$ are reduced to the ones for the isoscalar case, namely, (A.3) from Appendix A, and $D_0^{\tau} = D_0/2$ and $D_2^{\tau} = D_2/2$, where D_0 and D_2 are given by (36). So, we get

$$\mathcal{N}^2 = \frac{\omega_-^4}{8\pi} \left(\frac{e\hbar}{2c}\right)^2 \frac{Q_{00}}{m\bar{\omega}^2} \left(\frac{1}{\epsilon_0} + \frac{1}{\epsilon_2}\right) \qquad (60)$$

$$= \mu_N^2 \frac{\delta}{2\pi} \frac{m\omega_x}{\hbar} Q_{00}.$$

The estimation of the overlap for ^{156}Gd with $\delta = 0.27$ gives $\mathcal{N}^2 = 34.72\mu_N^2$ and $U^2 = 0.53$, which is two times larger than the result of [10] obtained in QRPA calculations with the Skyrme forces. The disagreement can naturally be attributed to the difference in forces and especially to the lack of pair correlations in our approach (see the next section, nevertheless). In a small-deformation limit, $U^2 = \frac{1}{2}\sqrt{\frac{3}{2}} \approx 0.6$.

3.4.1. Superdeformation. A certain drawback of our approach is that, so far, we have not included the superfluidity in our description. Nevertheless, our formulas (14), (19) can be successfully used for the description of superdeformed nuclei, where the pairing is very weak [2, 9]. For example, applying them to the superdeformed nucleus ^{152}Dy ($\delta \simeq 0.6, \hbar\omega_0 = 41/A^{1/3}$ MeV), we get

$$E_{\mathrm{iv}} = 20.8\,\text{MeV}, \quad B(M1)_{\mathrm{iv}} = 15.9\mu_N^2$$

for the isovector GQR and

$$E_{\mathrm{sc}} = 4.7\,\text{MeV}, \quad B(M1)_{\mathrm{sc}} = 20.0\mu_N^2$$

for the scissors mode. There are not so many results of other calculations to compare with. As a matter of fact, there are only two papers considering this problem.

The phenomenological TRM model [9] predicts

$$E_{\mathrm{iv}} \simeq 26\,\text{MeV}, \quad B(M1)_{\mathrm{iv}} \simeq 26\mu_N^2,$$

$$E_{\mathrm{sc}} \simeq 6.1\,\text{MeV}, \quad B(M1)_{\mathrm{sc}} \simeq 22\mu_N^2.$$

The only existing microscopic calculation [2] in the framework of QRPA with separable forces gives

$$E_{\mathrm{iv}} \simeq 28\,\text{MeV}, \quad B(M1)_{\mathrm{iv}} \simeq 37\mu_N^2,$$

$$E_{\mathrm{sc}} \simeq 5\text{--}6\,\text{MeV}, \quad B(M1)_{1^+} \simeq 23\mu_N^2.$$

Here, $B(M1)_{1^+}$ denotes the total $M1$ orbital strength, carried by the calculated $K^\pi = 1^+$ QRPA excitations modes in the energy region below 20 MeV.

It is easy to see that, in the case of IVGQR, one can speak, at least, about qualitative agreement. Our results for E_{sc} and $B(M1)_{\mathrm{sc}}$ are in good agreement with that of the phenomenological model and with E_{sc} and $B(M1)_{1^+}$ of Hamamoto and Nazarewicz [2].

It is possible to extract from the histogram of [2] the value of the overlap of calculated low-lying 1^+ excitations with the synthetic scissors state: $U^2 \equiv |\langle\text{Syn}|1^+\rangle|^2 \approx 0.4$. The result of our calculation $U^2 = 0.43$ agrees with it very well. So the natural conclusion of this section is that the correct treatment of pair correlations is more important for a reasonable description of the scissors mode than the thorough choice of an interaction.

4. CONCLUSION

The properties of collective excitations (the scissors mode, isovector and isoscalar giant quadrupole resonances) of the harmonic oscillator Hamiltonian with the quadrupole–quadrupole residual interaction (HO + QQ) were studied by two methods: WFM and RPA. We have found that both methods give the same analytic expressions for energies and transition probabilities of all considered excitations. Does it mean that WFM and RPA are identical approaches? Certainly not. First of all, we have the experience of previous WFM calculations [5] with realistic forces, which show that, for example, we reproduce only centroids of giant resonances, whereas RPA describes their fine structure. Secondly, we suppose that one can find such nuclear characteristics that will be described differently by the two approaches even in this simple model. Thirdly, to establish completely (and finally) the relation between the two approaches, it is necessary to analyze the equations of motion for multipole moments from the point of view of RPA. This will be done in a subsequent publication.

There is no sense in speaking about advantages or disadvantages of one of the two discussed methods—they are complementary. Of course, RPA gives complete, exhaustive information concerning the microscopic (particle–hole) structure of collective excitations. However, sometimes, considerable additional efforts are required to understand their physical nature. On the contrary, the WFM method gives information only on the physical nature of excitations and does not touch their microscopic structure. Our results serve as a very good illustration of this situation. What do we really know about the scissors mode and IVGQR from each method? RPA says that the scissors mode is mostly created by $\Delta N = 0$ particle–hole excitations with a small admixture of $\Delta N = 2$ particle–hole excitations and vice versa for IVGQR. And this is all! One cannot even suspect the key role of the relative angular momentum in the creation of the scissors mode. On the other hand, the WFM method says that the scissors mode appears due to oscillations of the relative angular momentum with a small admixture of the quadrupole moment oscillations and vice versa for IVGQR. Further, it informs

us about the extremely important role of the Fermi surface deformation in the formation of the scissors mode.

Two new mathematical results are obtained for the HO + QQ model. We have proved exactly, without any approximations, the orthogonality of the "spurious" state to all physical states. In this sense, we have generalized the result of Lo Iudice [12], derived in a small-deformation approximation. The analytic expressions are derived for the normalization factor of the synthetic scissors state and overlaps of this state with eigenstates of the model.

Appendix A

It is known that the deformed harmonic oscillator Hamiltonian can be obtained in a Hartree approximation "by making the assumption that the isoscalar part of the QQ force builds the one-body container well" [13]. In our case, it is obtained quite easily by summing the expressions for V^p and V^n [formula (3)]:

$$V(\mathbf{r}, t) = \frac{1}{2}(V^p(\mathbf{r}, t) + V^n(\mathbf{r}, t)) \qquad (A.1)$$

$$= \frac{1}{2}m\omega^2 r^2 + \kappa_0 \sum_{\mu=-2}^{2} (-1)^\mu Q_{2\mu}(t) q_{2-\mu}(\mathbf{r}).$$

In the state of equilibrium (i.e., in the absence of an external field), $Q_{2\pm1} = Q_{2\pm2} = 0$. Using the definition [14] $Q_{20} = Q_{00}\frac{4}{3}\delta$ and the formula $q_{20} = 2z^2 - x^2 - y^2$, we obtain the potential of the anisotropic harmonic oscillator

$$V(\mathbf{r}) = \frac{m}{2}[\omega_x^2(x^2 + y^2) + \omega_z^2 z^2]$$

with oscillator frequencies

$$\omega_x^2 = \omega_y^2 = \omega^2(1 + \sigma\delta), \quad \omega_z^2 = \omega^2(1 - 2\sigma\delta),$$

where

$$\sigma = -\kappa_0 \frac{8Q_{00}}{3m\omega^2}.$$

The definition of the deformation parameter δ must be reproduced by the harmonic oscillator wave functions, which allows one to fix the value of σ. We have

$$Q_{00} = \frac{\hbar}{m}\left(\frac{\Sigma_x}{\omega_x} + \frac{\Sigma_y}{\omega_y} + \frac{\Sigma_z}{\omega_z}\right),$$

$$Q_{20} = 2\frac{\hbar}{m}\left(\frac{\Sigma_z}{\omega_z} - \frac{\Sigma_x}{\omega_x}\right),$$

where $\Sigma_x = \sum_{i=1}^{A}(n_x + 1/2)_i$ and n_x is the oscillator quantum number. Using the self-consistency condition [14]

$$\Sigma_x\omega_x = \Sigma_y\omega_y = \Sigma_z\omega_z = \Sigma_0\omega_0,$$

where Σ_0 and ω_0 are defined in the spherical case, we get

$$\frac{Q_{20}}{Q_{00}} = 2\frac{\omega_x^2 - \omega_z^2}{\omega_x^2 + 2\omega_z^2} = \frac{2\sigma\delta}{1 - \sigma\delta} = \frac{4}{3}\delta.$$

Solving the last equation with respect to σ, we find

$$\sigma = \frac{2}{3 + 2\delta}. \qquad (A.2)$$

Therefore, the oscillator frequencies and the strength constant can be written as

$$\omega_x^2 = \omega_y^2 = \bar{\omega}^2\left(1 + \frac{4}{3}\delta\right),$$

$$\omega_z^2 = \bar{\omega}^2\left(1 - \frac{2}{3}\delta\right), \quad \kappa_0 = -\frac{m\bar{\omega}^2}{4Q_{00}} \qquad (A.3)$$

with $\bar{\omega}^2 = \omega^2/(1 + \frac{2}{3}\delta)$. The condition for volume conservation $\omega_x\omega_y\omega_z = \text{const} = \omega_0^3$ makes ω δ-dependent:

$$\omega^2 = \omega_0^2\frac{1 + \frac{2}{3}\delta}{(1 + \frac{4}{3}\delta)^{2/3}(1 - \frac{2}{3}\delta)^{1/3}}.$$

So, the final expressions for oscillator frequencies are

$$\omega_x^2 = \omega_y^2 = \omega_0^2\left(\frac{1 + \frac{4}{3}\delta}{1 - \frac{2}{3}\delta}\right)^{1/3},$$

$$\omega_z^2 = \omega_0^2\left(\frac{1 - \frac{2}{3}\delta}{1 + \frac{4}{3}\delta}\right)^{2/3}.$$

It is easy to see that they correspond to the case, where the deformed density $\rho(\mathbf{r})$ is obtained from the spherical density $\rho_0(r)$ by the scale transformation [8]

$$(x, y, z) \to (xe^{\alpha/2}, ye^{\alpha/2}, ze^{-\alpha})$$

with

$$e^\alpha = \left(\frac{1 + \frac{4}{3}\delta}{1 - \frac{2}{3}\delta}\right)^{1/3}, \quad \delta = \frac{3}{2}\frac{e^{3\alpha} - 1}{e^{3\alpha} + 2}, \qquad (A.4)$$

which conserves the volume and does not destroy the self-consistency, because the density and potential are transformed in the same way.

It is necessary to note that Q_{00} also depends on δ:

$$Q_{00} = \frac{\hbar}{m}\left(\frac{\Sigma_x}{\omega_x} + \frac{\Sigma_y}{\omega_y} + \frac{\Sigma_z}{\omega_z}\right)$$

$$= \frac{\hbar}{m}\Sigma_0\omega_0\left(\frac{2}{\omega_x^2} + \frac{1}{\omega_z^2}\right)$$

$$= Q_{00}^0\frac{1}{(1 + \frac{4}{3}\delta)^{1/3}(1 - \frac{2}{3}\delta)^{2/3}},$$

where $Q_{00}^0 = A\frac{3}{5}R^2$, $R = r_0 A^{1/3}$. As a result, the final expression for the strength constant becomes

$$\kappa_0 = -\frac{m\omega_0^2}{4Q_{00}^0}\left(\frac{1 - \frac{2}{3}\delta}{1 + \frac{4}{3}\delta}\right)^{1/3} = -\frac{m\omega_0^2}{4Q_{00}^0}e^{-\alpha},$$

which coincides with the respective result of [8].

Appendix B

To calculate the sums $D_0 = \sum_{mi(\Delta N=0)}|D_{mi}|^2$ and $D_2 = \sum_{mi(\Delta N=2)}|D_{mi}|^2$, we employ the sum-rule techniques of Suzuki and Rowe [8]. The well-known harmonic oscillator relations

$$x\psi_{n_x} = \sqrt{\frac{\hbar}{2m\omega_x}}(\sqrt{n_x}\psi_{n_x-1} + \sqrt{n_x+1}\psi_{n_x+1}),$$
(B.1)

$$\hat{p}_x\psi_{n_x} = -i\sqrt{\frac{m\hbar\omega_x}{2}}(\sqrt{n_x}\psi_{n_x-1} - \sqrt{n_x+1}\psi_{n_x+1})$$

allow us to write

$$xz\psi_{n_x}\psi_{n_z}$$
(B.2)
$$= \frac{\hbar}{2m\sqrt{\omega_x\omega_z}}(\sqrt{n_x n_z}\psi_{n_x-1}\psi_{n_z-1}$$
$$+ \sqrt{(n_x+1)(n_z+1)}\psi_{n_x+1}\psi_{n_z+1}$$
$$+ \sqrt{(n_x+1)n_z}\psi_{n_x+1}\psi_{n_z-1}$$
$$+ \sqrt{n_x(n_z+1)}\psi_{n_x-1}\psi_{n_z+1}),$$

$$\frac{\hat{p}_x\hat{p}_z}{m^2\omega_x\omega_z}\psi_{n_x}\psi_{n_z}$$
$$= -\frac{\hbar}{2m\sqrt{\omega_x\omega_z}}(\sqrt{n_x n_z}\psi_{n_x-1}\psi_{n_z-1}$$
$$+ \sqrt{(n_x+1)(n_z+1)}\psi_{n_x+1}\psi_{n_z+1}$$
$$- \sqrt{(n_x+1)n_z}\psi_{n_x+1}\psi_{n_z-1}$$
$$- \sqrt{n_x(n_z+1)}\psi_{n_x-1}\psi_{n_z+1}).$$

These formulas demonstrate in an obvious way that the operators

$$P_0 = \frac{1}{2}\left(zx + \frac{1}{m^2\omega_x\omega_z}\hat{p}_x\hat{p}_z\right) \quad \text{and}$$

$$P_2 = \frac{1}{2}\left(zx - \frac{1}{m^2\omega_x\omega_z}\hat{p}_x\hat{p}_z\right)$$

contribute only to the excitation of the $\Delta N = 0$ and $\Delta N = 2$ states, respectively. Following [8], we

express the zx component of $r^2 Y_{21} = \sqrt{\frac{5}{16\pi}}D = -\sqrt{\frac{15}{8\pi}}z(x+iy)$ as

$$zx = P_0 + P_2.$$

Hence, we have

$$\epsilon_0 \sum_{mi(\Delta N=0)}\left|\left\langle 0\left|\sum_{s=1}^A z_s x_s\right|mi\right\rangle\right|^2$$
(B.3)
$$= \epsilon_0 \sum_{mi}\left|\left\langle 0\left|\sum_{s=1}^A P_0(s)\right|mi\right\rangle\right|^2$$
$$= \frac{1}{2}\left\langle 0\left|\left[\sum_{s=1}^A P_0(s), \left[H, \sum_{s=1}^A P_0(s)\right]\right]\right|0\right\rangle,$$

where $\epsilon_0 = \hbar(\omega_x - \omega_z)$. The above commutator is easily evaluated for the Hamiltonian with the potential (A.1), as

$$\left\langle 0\left|\left[\sum_{s=1}^A P_0(s), \left[H, \sum_{s=1}^A P_0(s)\right]\right]\right|0\right\rangle$$
(B.4)
$$= \frac{\hbar}{2m}\epsilon_0\left(\frac{\langle 0|\sum_{s=1}^A z_s^2|0\rangle}{\omega_x} - \frac{\langle 0|\sum_{s=1}^A x_s^2|0\rangle}{\omega_z}\right).$$

Taking into account the axial symmetry and using the definitions

$$Q_{00} = \left\langle 0\left|\sum_{s=1}^A (2x_s^2 + z_s^2)\right|0\right\rangle,$$

$$Q_{20} = 2\left\langle 0\left|\sum_{s=1}^A (z_s^2 - x_s^2)\right|0\right\rangle,$$

$$Q_{20} = Q_{00}\frac{4}{3}\delta,$$

we transform this expression to

$$\left\langle 0\left|\left[\sum_{s=1}^A P_0(s), \left[H, \sum_{s=1}^A P_0(s)\right]\right]\right|0\right\rangle$$
(B.5)
$$= \frac{\hbar}{6m}\epsilon_0 Q_{00}\left(\frac{1 + \frac{4}{3}\delta}{\omega_x} - \frac{1 - \frac{2}{3}\delta}{\omega_z}\right).$$

With the help of the self-consistent expressions for ω_x and ω_z (A.3), one comes to the following result:

$$\left\langle 0\left|\left[\sum_{s=1}^A P_0(s), \left[H, \sum_{s=1}^A P_0(s)\right]\right]\right|0\right\rangle$$
(B.6)
$$= \frac{Q_{00}}{6m}\frac{\epsilon_0^2}{\bar{\omega}^2} = \frac{\hbar^2}{6m}Q_{00}^0\left(\frac{\omega_0}{\omega_z} - \frac{\omega_0}{\omega_x}\right)^2.$$

By using the fact that the matrix elements for the zy component of r^2Y_{21} are identical to those for the zx component, because of axial symmetry, we finally obtain

$$\epsilon_0 \sum_{mi(\Delta N=0)} \left| \left\langle 0 \left| \sum_{s=1}^{A} r_s^2 Y_{21} \right| mi \right\rangle \right|^2 \qquad (B.7)$$

$$= \frac{5}{16\pi} \frac{Q_{00}}{m\bar{\omega}^2} \epsilon_0^2 = \frac{5}{16\pi} \frac{Q_{00}^0}{m} \frac{\epsilon_0^2}{\omega_0^2} \left(\frac{1 + \frac{4}{3}\delta}{1 - \frac{2}{3}\delta} \right)^{1/3}.$$

By calculating a double commutator for the P_2 operator, we find

$$\epsilon_2 \sum_{mi(\Delta N=2)} \left| \left\langle 0 \left| \sum_{s=1}^{A} r_s^2 Y_{21} \right| mi \right\rangle \right|^2 \qquad (B.8)$$

$$= \frac{5}{16\pi} \frac{Q_{00}}{m\bar{\omega}^2} \epsilon_2^2 = \frac{5}{16\pi} \frac{Q_{00}^0}{m} \frac{\epsilon_2^2}{\omega_0^2} \left(\frac{1 + \frac{4}{3}\delta}{1 - \frac{2}{3}\delta} \right)^{1/3},$$

where $\epsilon_2 = \hbar(\omega_x + \omega_z)$.

We need also the sums D_0^τ and D_2^τ calculated separately for neutron and proton systems with the mean fields V^n and V^p, respectively. The necessary formulas are easily derivable from the already obtained results. There are no reasons to require the fulfillment of the self-consistency conditions for neutrons and protons separately, so one has to use formula (B.5). The trivial change of notation gives

$$\left\langle 0 \left| \left[\sum_{s=1}^{Z} P_0(s), \left[H^p, \sum_{s=1}^{Z} P_0(s) \right] \right] \right| 0 \right\rangle \qquad (B.9)$$

$$= \frac{\hbar}{6m} \epsilon_0^p Q_{00}^p \left(\frac{1 + \frac{4}{3}\delta^p}{\omega_x^p} - \frac{1 - \frac{2}{3}\delta^p}{\omega_z^p} \right),$$

$$\epsilon_0^p \sum_{mi(\Delta N=0)} \left| \left\langle 0 \left| \sum_{s=1}^{Z} r_s^2 Y_{21} \right| mi \right\rangle \right|^2 \qquad (B.10)$$

$$= \frac{5}{16\pi} \frac{\hbar}{m} \epsilon_0^p Q_{00}^p \left(\frac{1 + \frac{4}{3}\delta^p}{\omega_x^p} - \frac{1 - \frac{2}{3}\delta^p}{\omega_z^p} \right),$$

$$\epsilon_2^p \sum_{mi(\Delta N=2)} \left| \left\langle 0 \left| \sum_{s=1}^{Z} r_s^2 Y_{21} \right| mi \right\rangle \right|^2 \qquad (B.11)$$

$$= \frac{5}{16\pi} \frac{\hbar}{m} \epsilon_2^p Q_{00}^p \left(\frac{1 + \frac{4}{3}\delta^p}{\omega_x^p} + \frac{1 - \frac{2}{3}\delta^p}{\omega_z^p} \right).$$

The nontrivial information is contained in oscillator frequencies of the mean fields V^p and V^n [formula (3)]:

$$(\omega_x^p)^2 = \omega^2 \left[1 - \frac{2}{m\omega^2}(\kappa Q_{20}^p + \bar{\kappa} Q_{20}^n) \right], \qquad (B.12)$$

$$(\omega_z^p)^2 = \omega^2 \left[1 + \frac{4}{m\omega^2}(\kappa Q_{20}^p + \bar{\kappa} Q_{20}^n) \right],$$

$$(\omega_x^n)^2 = \omega^2 \left[1 - \frac{2}{m\omega^2}(\kappa Q_{20}^n + \bar{\kappa} Q_{20}^p) \right],$$

$$(\omega_z^n)^2 = \omega^2 \left[1 + \frac{4}{m\omega^2}(\kappa Q_{20}^n + \bar{\kappa} Q_{20}^p) \right].$$

The above-written formulas can also be used to calculate the analogous sums for various components of the angular momentum. Indeed, by definition, $\hat{I}_1 = y\hat{p}_z - z\hat{p}_y$ and $\hat{I}_2 = z\hat{p}_x - x\hat{p}_z$. In accordance with (B.1), we have

$$x\hat{p}_z \psi_{n_x} \psi_{n_z} = -i\frac{\hbar}{2}\sqrt{\frac{\omega_z}{\omega_x}} \qquad (B.13)$$

$$\times \left(\sqrt{n_x n_z}\psi_{n_x-1}\psi_{n_z-1} \right.$$

$$- \sqrt{(n_x+1)(n_z+1)}\psi_{n_x+1}\psi_{n_z+1}$$

$$+ \sqrt{(n_x+1)n_z}\psi_{n_x+1}\psi_{n_z-1}$$

$$\left. - \sqrt{n_x(n_z+1)}\psi_{n_x-1}\psi_{n_z+1} \right).$$

Therefore,

$$\hat{I}_2 \psi_{n_x} \psi_{n_z} = i\frac{\hbar}{2} \left(\sqrt{\frac{\omega_z}{\omega_x}} - \sqrt{\frac{\omega_x}{\omega_z}} \right) \qquad (B.14)$$

$$\times \left(\sqrt{n_x n_z}\psi_{n_x-1}\psi_{n_z-1} \right.$$

$$\left. - \sqrt{(n_x+1)(n_z+1)}\psi_{n_x+1}\psi_{n_z+1} \right)$$

$$+ i\frac{\hbar}{2} \left(\sqrt{\frac{\omega_z}{\omega_x}} + \sqrt{\frac{\omega_x}{\omega_z}} \right)$$

$$\times \left(\sqrt{(n_x+1)n_z}\psi_{n_x+1}\psi_{n_z-1} \right.$$

$$\left. - \sqrt{n_x(n_z+1)}\psi_{n_x-1}\psi_{n_z+1} \right).$$

Having formulas (B.2) and (B.14), one derives the following expressions for matrix elements coupling the ground state with $\Delta N = 2$ and $\Delta N = 0$ excitations:

$$\langle n_x + 1, n_z + 1 | \hat{I}_2 | 0 \rangle$$

$$= i\frac{\hbar}{2} \frac{(\omega_x^2 - \omega_z^2)}{\omega_x + \omega_z} \sqrt{\frac{(n_x+1)(n_z+1)}{\omega_x \omega_z}},$$

$$\langle n_x + 1, n_z - 1 | \hat{I}_2 | 0 \rangle$$

$$= i\frac{\hbar}{2} \frac{(\omega_x^2 - \omega_z^2)}{\omega_x - \omega_z} \sqrt{\frac{(n_x+1)n_z}{\omega_x \omega_z}},$$

$$\langle n_x + 1, n_z + 1 | xz | 0 \rangle = \frac{\hbar}{2m} \sqrt{\frac{(n_x+1)(n_z+1)}{\omega_x \omega_z}},$$

$$\langle n_x + 1, n_z - 1 | xz | 0 \rangle = \frac{\hbar}{2m} \sqrt{\frac{(n_x+1)n_z}{\omega_x \omega_z}}.$$

It is easy to see that

$$\langle n_x + 1, n_z + 1|\hat{I}_2|0\rangle$$
$$= im\frac{(\omega_x^2 - \omega_z^2)}{\omega_x + \omega_z}\langle n_x + 1, n_z + 1|xz|0\rangle,$$

$$\langle n_x + 1, n_z - 1|\hat{I}_2|0\rangle$$
$$= im\frac{(\omega_x^2 - \omega_z^2)}{\omega_x - \omega_z}\langle n_x + 1, n_z - 1|xz|0\rangle.$$

Due to the degeneracy of the model, all particle–hole excitations with $\Delta N = 2$ have the same energy ϵ_2 and all particle–hole excitations with $\Delta N = 0$ have the energy ϵ_0. This fact allows one to join the last two formulas into one general expression

$$\langle \mathrm{ph}|\hat{I}_2|0\rangle = i\hbar m\frac{(\omega_x^2 - \omega_z^2)}{\epsilon_{\mathrm{ph}}}\langle \mathrm{ph}|xz|0\rangle.$$

Taking into account the axial symmetry, we can write the analogous formula for $\hat{I}_1$:

$$\langle \mathrm{ph}|\hat{I}_1|0\rangle = -i\hbar m\frac{(\omega_x^2 - \omega_z^2)}{\epsilon_{\mathrm{ph}}}\langle \mathrm{ph}|yz|0\rangle.$$

The operator $\hat{O}_{1\pm1}$ is proportional (15) to the angular momentum: $\hat{O}_{1\pm1} = -\frac{ie}{4mc}\sqrt{\frac{3}{2\pi}}(\hat{I}_2 \mp i\hat{I}_1)$. Therefore, we can write

$$\langle \mathrm{ph}|\hat{O}_{1\pm1}|0\rangle$$
$$= -\frac{e\hbar}{2c\sqrt{5}}\frac{(\omega_x^2 - \omega_z^2)}{\epsilon_{\mathrm{ph}}}\langle \mathrm{ph}|r^2 Y_{2\pm1}|0\rangle. \qquad (\text{B.15})$$

REFERENCES

1. E. B. Balbutsev and P. Schuck, Nucl. Phys. A **720**, 293 (2003); **728**, 471 (2003).
2. I. Hamamoto and W. Nazarewicz, Phys. Lett. B **297**, 25 (1992).
3. P. Ring and P. Schuck, *The Nuclear Many-Body Problem* (Springer, Berlin, 1980).
4. S. Chandrasekhar, *Ellipsoidal Figures of Equilibrium* (Yale Univ. Press, New Haven, 1969; Mir, Moscow, 1973).
5. E. B. Balbutsev, Fiz. Élem. Chastits At. Yadra **22**, 333 (1991) [Sov. J. Part. Nucl. **22**, 159 (1991)].
6. E. B. Balbutsev and P. Schuck, Nucl. Phys. A **652**, 221 (1999).
7. D. A. Varshalovich, A. N. Moskalev, and V. K. Khersonskiǐ, *Quantum Theory of Angular Momentum* (Nauka, Leningrad, 1975; World Sci., Singapore, 1988).
8. T. Suzuki and D. J. Rowe, Nucl. Phys. A **289**, 461 (1977).
9. N. Lo Iudice, Riv. Nuovo Cimento **23** (9) (2000).
10. R. R. Hilton *et al.*, in *Proceedings of the 1st International Spring Seminar on Nuclear Physics "Microscopic Approaches to Nuclear Structure," Sorrento, 1986*, Ed. by A. Covello (Editrice Compositori, Bologna, 1986), p. 357.
11. A. E. L. Dieperink and E. Moya de Guerra, Phys. Lett. B **189**, 267 (1987).
12. N. Lo Iudice, Nucl. Phys. A **605**, 61 (1996).
13. R. R. Hilton, Ann. Phys. (N.Y.) **214**, 258 (1992).
14. A. Bohr and B. Mottelson, *Nuclear Structure*, Vol. 2: *Nuclear Deformations* (Benjamin, New York, 1975; Mir, Moscow, 1977).

Experimental Arguments in Favor of Refining Model Ideas of the Cascade Gamma Decay of a Compound State of a Complex Nucleus

A. M. Sukhovoj[*], V. A. Khitrov[**], and Li Chol[***]

Joint Institute for Nuclear Research, Dubna, Moscow oblast, 141980 Russia
Received July 14, 2004; in final form, November 23, 2004

Abstract—An analysis of the entire body of data on the intensities of two-step gamma cascades studied in thermal-neutron capture for more than 50 nuclei from the range $27 \leq A \leq 199$ suggests that such processes should be described in terms of model concepts that are much more involved than those currently adopted by experimentalists. According to the results of this analysis, models of relevant parameters, such as the density of excited levels and radiative strength functions for dipole gamma transitions, should take into account more explicitly the coexistence and interaction of quasiparticle and phonon interactions. A direct inclusion of the idea that a second-order phase transition occurs and affects not only level densities but also radiative strength functions for dipole transitions may prove to be necessary. These conclusions concern primarily the excitation-energy region below a value of about $0.5B_n$. © *2005 Pleiades Publishing, Inc.*

1. INTRODUCTION

In analyzing experimental data—for example, on the cascade gamma decay of a neutron resonance— one usually uses some model ideas of the process being studied. If there exist alternative models of the process, experimentalists give preference, as a rule, to the simplest models. As the volume of experimental data increases and, what is more important, as one goes over to a previously inaccessible region of the parameters of the phenomenon under study, there arises, however, the need for invoking more involved concepts.

A large volume of experimental data on the properties of excited states from about 1 or 3 MeV to nearly B_n for more than 50 nuclei from the mass range $27 \leq A \leq 199$ was accumulated in experiments performed in Dubna, Riga, and Řež and has been comprehensively analyzed by now at the Laboratory of Neutron Physics at the Joint Institute for Nuclear Research (JINR, Dubna). This region of excitation energies (especially for deformed nuclei) has been studied for the first time in such minute detail. The entire body of resulting information gives sufficient grounds to assume that the concepts underlying the existing models of cascade gamma decays call for a radical improvement.

[*]e-mail: `suchovoj@nf.jinr.ru`
[**]e-mail: `khitrov@nf.jinr.ru`
[***]e-mail:`li@nf.jinr.ru`

One extracts two basic parameters from experimental data and then uses them to calculate nuclear-physics constants [1]. These parameters are

(i) the level density $\rho = D^{-1}$ at a given excitation energy E_{exc} for specific values of the quantum numbers characterizing the levels being considered;

(ii) the radiative strength functions

$$k = \Gamma_{\lambda i}/(E_\gamma^3 A^{2/3} D_\lambda), \qquad (1)$$

which determine the intensities of gamma transitions that deexcite the excited levels λ.

The ideas used to describe the level density range between the simplest model [2] of a noninteracting Fermi gas and the rather complicated generalized model of a superfluid nucleus [3]. Within the latter, one directly employs theoretical concepts of the phase transition in a nucleus from a superfluid to a normal state. However, there is no direct experimental information about this transition in a nucleus; in view of this, Rastopchin *et al.* [3] fixed its energy on the basis of available information about the transition of an electron gas to a superfluid state.

In order to specify the shape of the radiative strength function for an $E1$ transition having an energy E_γ and a mean width $\Gamma_{\lambda i}$ and connecting λ and i states in the excitation-energy range $0 \leq E_{\mathrm{exc}} < B_n$ in a nucleus of mass A, one usually employs one of the two known extrapolations of the giant electric dipole resonance. The spacing D_λ between the decaying states is determined either from data on neutron

resonances for primary transitions of the cascades or from the density of intermediate levels for secondary transitions of the cascades, which was obtained in one way or another.

For $M1$ transitions, models relying on the assumption that there exists a giant magnetic dipole resonance were developed in addition to the existing idea that $k(M1)$ is constant. That models of radiative strength functions are less diverse than level-density models is due to paucity of reliable experimental data on k in the range of transition energies E_γ less than B_n by several megaelectronvolts.

The relationship between $E1$ and $M1$ transition widths for $E_\gamma \approx B_n$ was determined experimentally for almost all stable target nuclei and can readily be fixed in the calculations of the parameters of a cascade gamma decay, irrespective of the model assumptions used.

Present-day theoretical ideas that make it possible to calculate ρ and k, in principle, are more realistic. However, they are hardly appropriate for analyzing experimental data. Despite this, an analysis of their conceptual framework reveals the main flaw in level-density models used to treat experimental data and to calculate nuclear-physics constants. It consists either in completely ignoring [2] or in inadequately taking into account [3] the coexistence and interaction of quasiparticle and phonon excitations in nuclei.

In any case, a solution to this problem cannot be obtained by purely theoretical methods. As before, the problem of deriving the most reliable data on ρ and k by methods that invoke model-dependent concepts to the minimum possible degree is the most important for experimentalists.

2. POTENTIAL OF THE EXPERIMENT

The possibility of obtaining completely model-independent information about ρ and k up to B_n by currently available methods of nuclear spectroscopy has yet to be realized for nuclei characterized by a high level density. The only available way to solve this problem is to select, for the corresponding parameters, values that would provide the best fit to the following observables:

(a) evaporation spectra of nucleons originating from nuclear reactions;

(b) various spectra of gamma rays emitted in these reactions;

(c) the intensities [4] of two-step cascades triggered by slow-neutron capture that connect a neutron resonance with low-lying levels of the nucleus being considered.

In the first two cases, the amplitude of the experimentally measured spectra is determined by the level density multiplied either by the photon-emission probability or by the model-dependent factor of nuclear-surface penetrability to an evaporated nucleon (nucleons). For this reason, the reliability of ρ and k values determined from the respective spectra [cases (a) and (b)] is adversely affected by a strong and irremovable correlation between the density of excited levels and the probability of emission of reaction products.

In the case of $\lambda \rightarrow i \rightarrow f$ two-step cascades, the presence of the second quantum is responsible for a different form of the functional dependence of their intensity on the energy of the primary transition of a cascade:

$$I_{\gamma\gamma} = \sum_{J,\pi}(\Gamma_{\lambda i}/\langle\Gamma_{\lambda i}\rangle m_{\lambda i})n_{\lambda i}(\Gamma_{if}/\langle\Gamma_{if}\rangle m_{if}). \quad (2)$$

The partial and total cascade-transition widths Γ, as well as the number $m(n)$ of levels excited in respective transitions in various energy ranges (the bin width that is optimal for calculations is $\Delta E \approx 50$ keV), are unambiguously determined by the functions ρ and k under the condition that gamma transitions of given multipolarities are taken into account in expression (2). This is precisely the circumstance that makes it possible to reveal, in the structure of excited states of complex nuclei, special features that are inaccessible in experiments employing different methods.

Naturally, the reliability and accuracy of the concepts that can be deduced from an analysis of $I_{\gamma\gamma}$ for the properties of the excited states of the nucleus being studied become higher as the volume of additional information included in such an analysis is enlarged. For example, one can employ known values of the total radiative width of a decaying compound state,

$$\Gamma_\lambda = \sum_i(\langle\Gamma_{\lambda i}\rangle m_{\lambda i}), \quad (3)$$

this being necessary for determining the absolute value of k (but not the shape of its dependence on E_γ). In addition, a minimum uncertainty in the sought value of ρ is ensured by taking into account the mean spacing D_λ between neutron resonances, which is determined spectroscopically by the time-of-flight method, and the known number of low-lying levels.

The use of spectroscopic data from the estimated schemes of the gamma decay of the nuclei being studied serves the same goal. Accordingly, the region of excitations under study is broken down in all calculations into a "discrete" and a "continuous" part. The parameters ρ and k, which are discussed below, are characterized by minimum fluctuations and are naturally determined only in the continuous part of excitation energies. The lower boundary of this part,

E_{dis}, is 1.5, 2.9, and 1.1 MeV in ^{60}Co, ^{118}Sn, and ^{187}W, respectively. In order to simplify the figures below, the calculated quantities are everywhere represented by lines of the same type. Since fluctuations of the calculated quantities are maximal in the discrete part of excited levels, the corresponding data are represented by broken lines.

3. EXPERIMENTAL DATA ON THE PARAMETERS OF THE CASCADE GAMMA DECAY OF A COMPLEX NUCLEUS

The accuracy to which a calculation reproduces the entire body of experimental data (it should not be lower than the accuracy of the experiments being considered) is a natural characteristic of correctness of our ideas of processes occurring in a complex nucleus. Unfortunately, it has not been possible so far to attain this degree of agreement between the theory and experiment since the volume of information accessible to an experimental determination has been insufficient.

Only four functionals can be used both to assess the intervals of probable values of ρ and k and to test the process of a cascade gamma decay. These are

(i) the total radiative width (as well as the cross sections for neutron interaction with nuclei);

(ii) the intensity of cascades in a given interval of energies of their intermediate and final levels;

(iii) the population [5] of low-lying levels by cascades involving various numbers of transitions (including the total spectra of gamma radiation);

(iv) the expected [6] number of intermediate levels of individual cascades whose intensities are below a threshold value.

Inasmuch as the first two functionals were already used in [4] to determine the quantities considered here, the values obtained for ρ and k should ensure an accurate calculation of the population of low-lying levels that was extracted in [5] from a comparison of the intensities of cascades featuring specific intermediate levels with the intensities determined independently for the primary and secondary gamma transitions of these cascades, as well as from a comparison of the total spectra of gamma radiation accompanying neutron capture and various nuclear reactions. Unfortunately, data obtained according to [4] are such that the required degree of agreement between the experiment and the calculation could not be attained.

For example, the total populations of ^{118}Sn [7] and ^{183,187}W [8] levels in the ranges between about 3 and 5 MeV and between about 1 and 3 MeV, respectively, disagree sharply with the results of the calculations not only if use is made of model-dependent values of ρ and k but also if use is made of their values obtained according to [4].

This situation manifests itself in [5] to a lesser extent for the ^{156}Gd and ^{168}Er nuclei. In these deformed nuclei, the ρ and k values determined according to [4] reproduce fairly well the experimentally determined population of low-lying levels only up to an excitation energy of about 3.5 MeV. The population of levels at higher energies cannot be estimated because there are no data from other experiments on the intensities i of gamma rays emitted in the radiative capture of thermal neutrons in the required energy intervals.

However, the calculation relying on the data from [4] reproduces the total spectra of gamma rays from the radiative capture of thermal and fast neutrons much more poorly in the region $A \sim 160$ [5] than in the region $A > 180$ (however, the results in the former region are better than their counterparts produced by models traditionally used for this purpose). As a matter of fact, this means that the ideas of cascade gamma decays are inconsistent with experimental data, at least for deformed even–even nuclei. It is natural to expect that this inconsistency will manifest itself directly in the cascade population of levels in nuclei of this type only at excitation energies in excess of about 4 MeV.

Naturally, the ρ value determined according to [4] should correspond to an independent estimate of ρ from the procedure [6] involving an approximation of the distribution of random deviations of the intensities of cascades in narrow intervals of energies of their intermediate levels from a mean value. However, the level density determined according to [4] at low excitation energies sometimes proves to be less in a number of nuclei than that obtained in [6] for zero threshold of the detection of the intensities of cascades resolved in energy (in the form of two peaks) that feature intermediate levels at energies below 3 or 4 MeV.

Of course, we cannot rule out the possibility that the existing disagreement between the measured functionals of cascade gamma decays and their counterparts calculated within conventional models is due to systematic errors in the experiment itself or in known nuclear-physics constants used in analyzing respective experimental data, but they may also be due to inadequate ideas of the properties of the process being considered.

3.1. Estimating the Possible Role of Systematic Errors in Determining ρ and k

The main qualitative conclusion that can be drawn from an analysis of the results obtained according to [4] is that it is necessary to take into account, in

greater detail than in conventional models, the co-existence and interaction of a superfluid and a normal phase of matter. An alternative idea assumes the presence of a so-called pygmy resonance in the radiative strength function [9].

The line of the most appropriate modification of our ideas concerning the properties of nuclei below the neutron binding energy cannot be chosen correctly without specifying the sources of systematic errors in the sought quantities ρ and k within various procedures for obtaining relevant experimental data and without estimating these errors.

As a matter of fact, the results obtained by applying the procedure employed in [4] may involve a significant error and, accordingly, may distort our ideas of the properties of nuclei in the energy range from 2 or 3 MeV to B_n for only three reasons. These are

(i) the presence of a regular systematic error that would result in a severalfold exaggeration of the experimental value of the cascade intensity for almost all of the 50 nuclei being studied;

(ii) the existence of two or more groups of excited states such that they all have the same spin–parity J^π (but different structures of wave functions) and that the mean intensities of two-step cascades populating them differ by more than one order of magnitude in any interval of energies of intermediate levels that is narrow against the scale of B_n;

(iii) a difference in the forms of the energy dependence of radiative strength functions for primary and secondary cascade transitions of the same multipolarity and energy (this difference should be so pronounced as to ensure that the calculated value of the ratio Γ_{if}/Γ_i for transitions to $E_f < 1$ MeV levels was on average severalfold overestimated for all cascades observed experimentally).

The effect of any of the above errors on the parameters to be determined was estimated by means of a standard formula for the transfer of errors. It becomes very difficult to estimate the resulting probable errors in the parameters ρ and k since the set of Eqs. (2) and (3) is strongly correlated and essentially nonlinear. It should be noted that, although the number of unknown quantities exceeds the number of equations in this set, the form of the functional relations between ρ and k, on one hand, and the measured intensities of the cascades and the total width, on the other hand, constrain the range of their variation quite efficiently for any excitation energies and any photon energies. (There is no such constraints for the spectra of evaporated nucleons and primary gamma transitions in any nuclear reactions.)

(1) All of the intensities obtained thus far for two-step cascades were normalized to known intensities of the strongest primary gamma transitions from the spectra of radiative thermal-neutron capture. The set of relevant data [10] on neutron capture in samples of all stable elements of natural isotopic composition was obtained in experiments performed more than 30 years ago. Nevertheless, data obtained recently by measuring the same spectra in Budapest [11] with modern γ spectrometers did not show any evidence in support of the statement that, in data presented in [10], there was a systematic error that led to a regular exaggeration of the gamma-transition intensity—for example, a severalfold exaggeration.

The root-mean-square discrepancy between the data from [10] and [11] was estimated in [12] at 20% for all of the observed gamma transitions.

Therefore, a variation of $I_{\gamma\gamma}$ within a factor of 1.2 to 1.3 with respect to the experimental intensity value both toward smaller and toward greater values gives a reasonable idea of the effect of a first-type error on the ρ and k values determined according to [4]. In the presence of a greater discrepancy between the absolute intensities of primary cascade transitions as determined in [10] and in a modern experiment, the probable systematic error in the cascade intensities increases. Accordingly, the tested cascade intensity must be increased (or decreased) to a greater extent if the intensities of maximum-energy gamma transitions in [11] are higher (or lower) than the analogous quantities used previously for the normalization of $I_{\gamma\gamma}$. The result of such an estimation is given in [13]. The basic conclusion of the analysis performed in [13] is that the discrepancy between the ρ values obtained according to [4] and those predicted by the models of a noninteracting Fermi gas cannot be explained by the systematic error in the experimental values of $I_{\gamma\gamma}$ for its maximum possible values. By way of example, we indicate that, of 14 nuclei for which a direct comparison of the spectra of gamma rays from radiative thermal-neutron capture is possible, the $I_{\gamma\gamma}$ values found previously were underestimated by a factor of about 2 in relation to those obtained with the aid of data from [11] for ^{114}Cd and ^{124}Te. For ^{182}Ta and ^{192}Ir, they are overestimated by a factor of about 1.5, the mean intensity in the high-energy section of the spectra of radiative thermal-neutron capture being identical for the remaining 10 nuclei. If one assumes that the data presented in [11] involve a systematic error much less than that in the earlier data compared with them [4], then the amplitude of fluctuations of the difference between the ρ and k values determined according to the procedure employed in [4] and the model concepts existing for them will increase somewhat for the former two nuclei and decrease insignificantly for the latter two.

(2) Experiments of all types known to date have one special feature in common—they are plagued by

an irremovable ambiguity in ρ and k values determined from them. The uncertainties in the sought parameters ρ and k depend greatly on the volume of information that one invokes and on the procedure used to analyze it.

By way of example, we indicate that, in the experimentally measured distributions of the intensities of cascades whose total energy is equal to a few megaelectronvolts, the order in which the two gamma transitions occur cannot be determined by means of experimental equipment exclusively. As a result, such spectra can be faithfully reproduced ($\chi^2/f < 1$) by using a very wide variety of the functional dependences $\rho = F(E_{\mathrm{exc}})$ and $k = \phi(E_\gamma)$. Moreover, the maximum value of either parameter may severalfold exceed its minimal value. This uncertainty can be reduced only by establishing the order in which the transitions follow each other in a cascade. For this, it is necessary to isolate that section in the experimental spectra which is equal to the sum of the intensities of all possible cascades where the primary-transition energy lies in a preset interval. At the present time, this problem can be solved [14] by means of the nuclear-spectroscopy technique and by using data accumulated in relevant experiments.

In the experimental spectrum of two-step cascades such that $E_1 + E_2 = \mathrm{const}$, one usually observes (in the form of pairs of resolved peaks) not less than 90 to 95% of the intensity of cascades going to $E_i \leq 0.5B_n$ levels at a nearly zero level of background. The dependence $I_{\gamma\gamma} = F(E_1)$ obtained according to the method used in [14] involves a systematic error that is caused by a nonzero threshold for individual-cascade detection. It decreases asymptotically with increasing efficiency of germanium detectors used to record coincidences.

A method for estimating the error in determining [14] the shape of the functional dependence $I_{\gamma\gamma} = F(E_1)$ was described in [6]. It consists in extrapolating the cumulative sums of random values of cascade intensities to zero value of the experimental-sensitivity threshold. For a present-day experiment, the threshold cascade-intensity value below which such an extrapolation should be performed does not exceed, as a rule, approximately 10^{-4} events per decay.

Therefore, the relative error in the dominant part of the dependences $I_{\gamma\gamma} = F(E_1)$ obtained according to [14] is in fact smaller than the error in absolute cascade intensities if random deviations of the cascade intensities from their mean values have a variance whose magnitude does not exceed that which was used in [6].

If this is not so and if the majority of the $E_1 < 0.5B_n$ cascades have intensities below the sensitivity threshold of their detection, the relative error in determining the dependence $I_{\gamma\gamma} = F(E_1)$ may increase. There are presently no specific data that would suggest the presence or absence of this effect. But if the mean intensity of cascades does indeed depend greatly on the structure of their intermediate level, then the prevalent ideas of the process being studied [which are reflected in Eqs. (2) and (3)] would require a refinement more pronounced than that which is associated with taking into account the previously unobserved [4] stepwise structure in the level density.

(3) The question of whether the level density does indeed have a stepwise structure and whether it is due to [3, 15] the rupture of some Cooper pairs of nucleons is directly related to the problem of assessing the degree to which radiative strength functions depend on the structure of levels excited by a gamma transition.

Indirect pieces of evidence that $R = k(E_\gamma, E_\lambda)/k(E_\gamma, E_i) \neq \mathrm{const}$ for transitions that have the same multipolarity and energy, but which occur in the deexcitation of levels having different excitation energies E_λ and E_i, were first obtained in [5] in an attempt at describing the total spectra of gamma radiation in the capture of thermal and fast neutrons. It was found that, for the accuracy of the reproduction of these spectra in the calculations to be improved, the radiative strength functions for secondary gamma transitions must feature a weaker dependence on the emitted-photon energy than their counterparts for primary transitions.

The most detailed, albeit still indirect, data on the behavior of a nucleus in the region of the stepwise structure and on the expected change in the radiative strength functions come from an analysis of the total and cascade populations of levels at excitation energies up to 3 or 4 MeV in heavy nuclei (^{181}Hf and ^{183,184,185,187}W) and at somewhat higher energies in nuclei of lower mass, such as ^{60}Co and ^{118}Sn.

The intensity of an arbitrary cascade, $i_{\gamma\gamma}$, is related to the intensities of its primary and secondary transitions, i_1 and i_2, respectively, by the equation

$$i_{\gamma\gamma} = i_1 i_2 / \sum i_2. \tag{4}$$

By applying this equation to the entire body of experimental data on the aforementioned intensities, we can determine (see Fig. 1) the total population $P = \sum i_2$ of about 100 or more intermediate levels of the cascades in any nucleus among those that have been studied to date by the method of summation of the amplitudes of coinciding pulses. In the presence of maximally comprehensive data on i_1 and i_2, this can be done for the excitation energies of intermediate cascade levels up to 3 or 4 MeV or even for higher
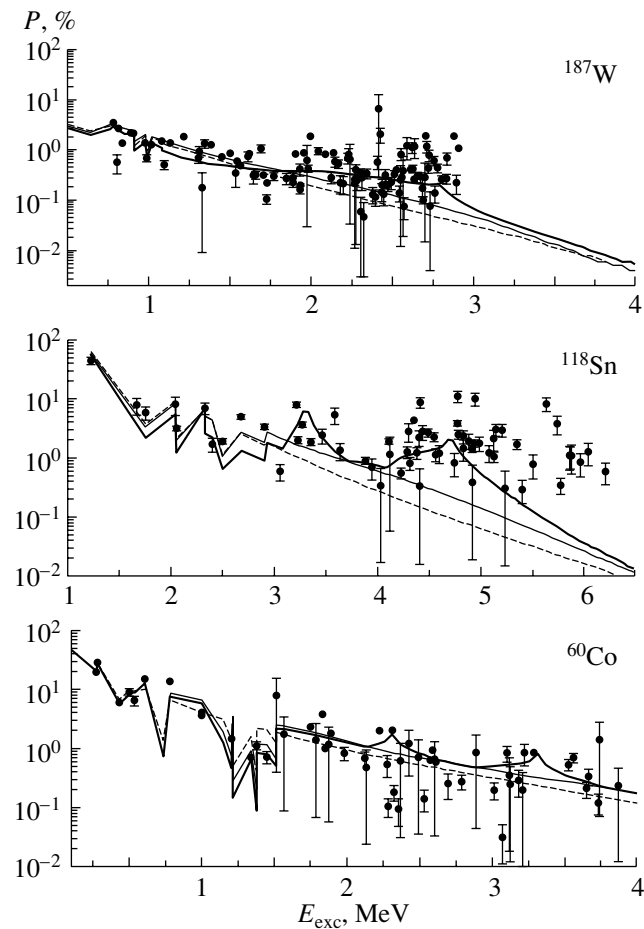
Fig. 1. Total population P of intermediate levels of two-step cascades in ^{187}W, ^{118}Sn, and ^{60}Co nuclei: (points) experimental data; (thin lines) results of the calculation with the ρ and k values obtained according to the procedure used in [4]; (dashed lines) results of the calculation based on the models proposed in [2, 17]; and (thick lines) results of the calculation employing the level density from [4], the corresponding strength functions being modified according to expressions (5) and (6).

energies, but, if there are no such data, the populations in question can be determined up to much lower energies [5].

The difference of P and the intensity i_1 of the primary transition to each of these levels is equal to the sum of their populations by two-step, three-step, etc., cascades. It can be calculated by using various assumptions on the density of levels excited in thermal-neutron capture and on radiative strength functions for cascade gamma transitions. This may be done, for example, within the existing models of these parameters or possible hypotheses concerning them (including the k and ρ values obtained according to [4]).

At the present time, the populations of all (without exception) intermediate levels of two-step cascades can hardly be determined even at moderate excitation energies (because of the presence of the detection threshold for the intensities of the cascades, $i_{\gamma\gamma}$, and for the respective gamma transitions, i_1 and i_2);

therefore, it is reasonable to compare experimental and calculated results for $P - i_1$ values summed over a moderately narrow interval of excitation energies and consider these sums as a lower bound for each of the intervals. As an example, we present below the results of such a comparison for the compound nuclei ^{60}Co, ^{118}Sn, and ^{187}W (Fig. 2). Among 17 nuclei accessible to the data-analysis method described below, they were chosen because the population in them was determined for the maximum number of intermediate levels of the cascades, because their masses differ to the maximum possible degree, and because they represent the three possible combinations of parities of the numbers of neutrons and protons in a compound nucleus.

The degree of the discrepancy between the calculated total population P (see Fig. 1) and its precise value is determined both by the incompleteness of data on the intensities of cascades and transitions and by the possible strong effect of the structure of the wave function for an excited level on the probability
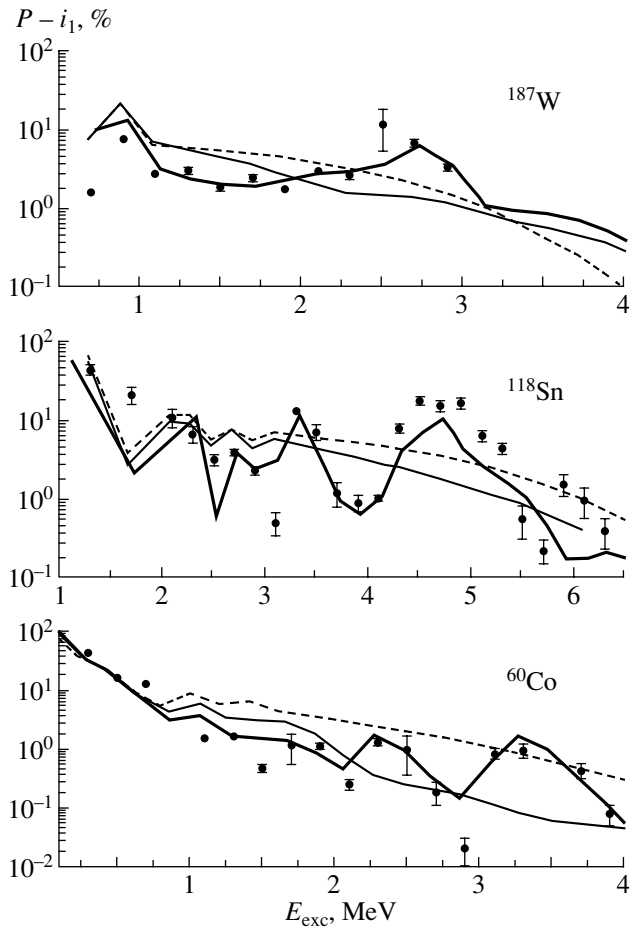
Fig. 2. Total cascade population of intermediate levels of cascades in ^{187}W, ^{118}Sn, and ^{60}Co nuclei. The notation for the curves is identical to that in Fig. 1.

Fig. 3. Sums of the intensities of two-step cascades in ^{187}W, ^{118}Sn, and ^{60}Co nuclei over intervals of width 0.5 MeV versus the primary-cascade-transition energy. The dashed curve represents the results of the calculation according to expression (2) for the set of models from [2] and [17].

of its cascade population. The need for taking this possibility into account follows from the fact that the cascade population of levels at excitation energies above 1 to 3 MeV changes strongly from one level to another. This is suggested by very strong fluctuations of the populations of neighboring levels.

In the isotopes being considered, primary dipole transitions of two-step cascades excite $J = 1/2, 3/2$ levels in ^{187}W, $J = 0-2$ levels in ^{118}Sn, and $J = 2-5$ levels in ^{60}Co. Since the entire body of data on two-step cascades can be described only with allowance for electric and magnetic dipole transitions, a further analysis is performed under the assumption that they excite levels of both parities. The fractions of captured neutrons in one or another spin channel for cobalt and tin were taken into account in all calculations on the basis of data from [16].

The cascade population of any level is determined not only by the total intensity of all two-step cascades but also by the intensity of three- and four-

step cascades, which deexcite levels from a wider spin window than two-step cascades. Therefore, it seems incorrect to relate, on the basis of the data in Fig. 1, the difference in the population of neighboring intermediate levels of the cascades to the difference in their spins exclusively [as is usually done, for example, in analyzing data on $(n, n'\gamma)$ reactions].

The number of available versions of the functional dependences of strength functions and level densities on, respectively, the photon energy and the excitation energy of a level is quite large. However, general regularities of the change in the population of levels in response to a change in their excitation energy can be revealed by using only three versions of calculations:

(i) The level density is predicted by any version of the model of a noninteracting Fermi gas; the $E1$ radiative strength function is specified by known extrapolations of a giant electric dipole resonance to the

region below B_n; and $k(M1) = \text{const}$, $k(M1)/k(E1)$ being normalized to the experimental value.

(ii) One employs ρ and k values [4] that faithfully reproduce the intensities of two-step cascades versus the energy of their primary transition (Fig. 3).

(iii) One chooses the set of values for the level density and the strength function in such a way as to reproduce simultaneously precise values of $I_{\gamma\gamma} = F(E_1)$ and Γ_γ and to reproduce the values of $P - i_1$ to the highest possible precision. In order to solve this problem exactly, it would be necessary to specify the form of the dependence of $k(E1)$ and $k(M1)$ not only on the photon energy but also on the excitation energy of a nucleus for electric and magnetic transitions individually. (Naturally, the state of the art in the experiment presently gives little hope to obtain this information in the near future.) A possible approximate solution is to multiply the function k for the first photon of a cascade—it depends only on the energy E_γ—by some correcting function $h = f(E_\gamma, E_{\text{exc}})$ for all subsequent photons of the cascades.

Through this choice of the form of the dependence of radiative strength functions on the energy U of a level excited by a gamma transition, $U = E_{\text{exc}} - E_\gamma$, one can also effectively introduce, in the iteration process proposed in [4], additional experimental information about the distinctions between the forms of the energy dependence of strength functions for primary and secondary gamma transitions, concurrently retaining the efficiency of this iteration process and a relatively high rate of convergence to values of $\chi^2/f < 1$ for the calculated cascade intensity.

An implementation of version (iii) is possible in an iterative regime: for the k values obtained according to [4], one selects a functional dependence that changes the values of the strength functions for secondary transitions with respect to the strength function from [4] is such a way as to reproduce the values of $P - i_1$ to the highest possible degree of precision. For this, it is quite sufficient to multiply the strength functions for secondary gamma transitions to levels below some boundary excitation energy by a function h that involves a few very narrow peaks. It is very convenient to specify the dependence of the shapes of these peaks on the nuclear excitation energy U by analogy with the heat capacity of a uniform system at the point U_c of a second-order phase transition as

$$h = 1 + \alpha(\ln|U_c - U_1| - \ln|U_c - U|) \quad (5)$$

$$\text{in the case of } U < U_c,$$

and as

$$h = 1 + \alpha(\ln|U_c - U_2| - \ln|U_c - U|) \quad (6)$$

$$\text{in the case of } U > U_c$$

$k(E1) + k(M1)$, 10^{-9} MeV^{-3}
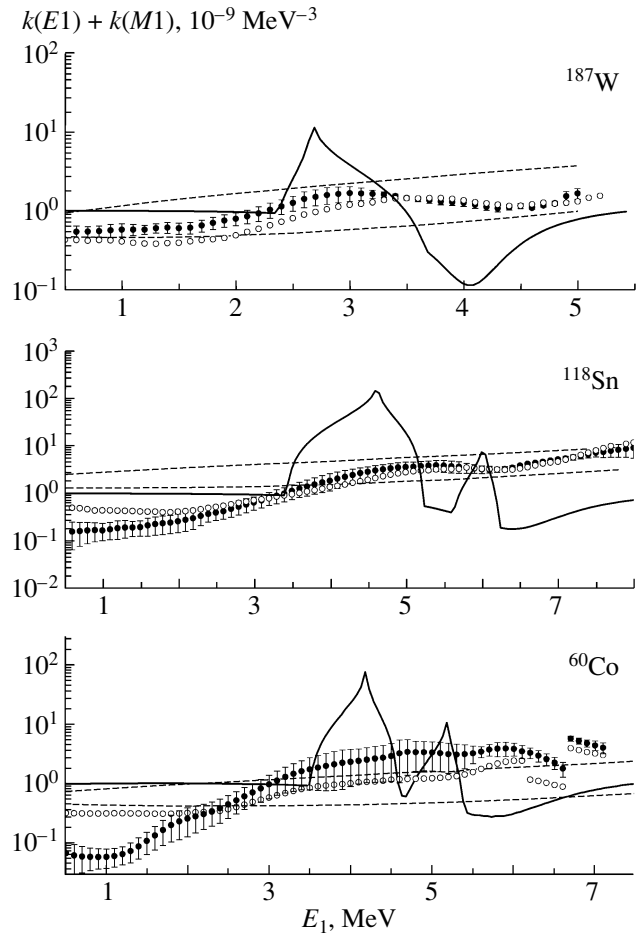
Fig. 4. Sums of radiative strength functions that correspond to primary electric and magnetic dipole transitions of cascades and which make it possible to reproduce faithfully their intensity with allowance for the probable distinction between their values and the values of the strength functions for secondary transitions in the cases of (closed circles) h given by Eqs. (5) and (6) and (open circles) $h = \text{const}$. The upper and lower dashed curves represent the predictions of the models proposed in [17] and [18], respectively; $k(M1) = \text{const}$. The thick curve corresponds to the function h for gamma transitions to the levels at E_i.

with some parameters α, U_1, U_2, and U_c. The condition $(U_c - U_1) \neq (U_2 - U_c)$ ensures, if necessary, the asymmetry of peaks and a somewhat closer reproduction of the cascade population of levels at the tails of the peaks than, for example, in the case of a Lorentzian curve.

With decreasing excitation energy U, the parameter α must increase (for example, linearly), in the best of the versions tested here, from zero at $U = B_n$ to some maximum value shown in Figs. 4 and 5. The positions of the peaks and their amplitude and shape are quite unambiguously determined by $P - i_1$. The results found for the correcting functions are then
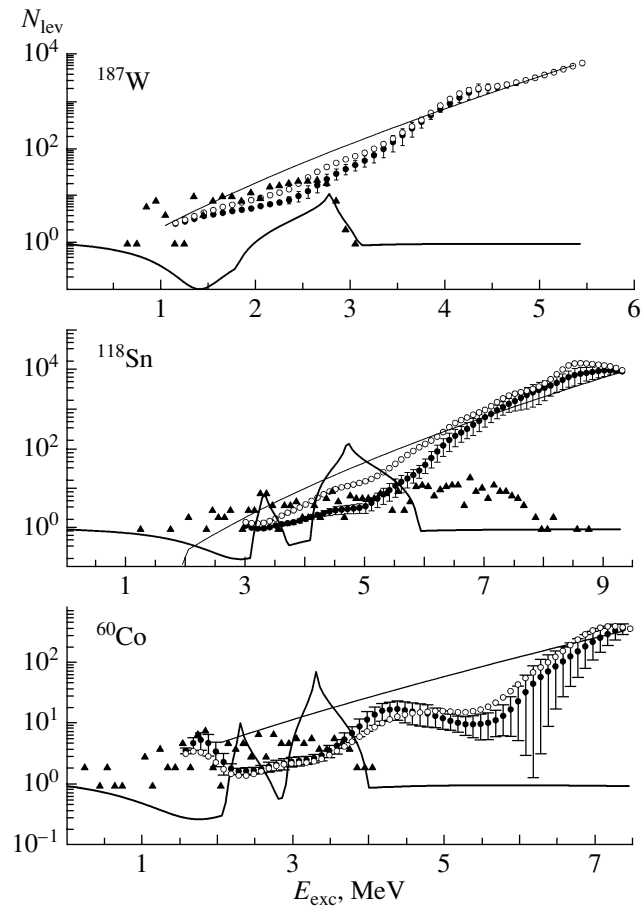
Fig. 5. Total number of all intermediate levels of two-step cascades for the cases of (closed circles with error bars) h given by Eqs. (5) and (6) and (open circles) $h = $ const. The thin and thick curves represent, respectively, the predictions of the model proposed in [2] and the best correcting function h, while the triangles correspond to the observed number of intermediate levels in the allowed cascades. The width of the summation interval is 100 keV.

included in the analysis according to [4] in order to determine ρ and k values faithfully reproducing the cascade intensities. The values of the latter are given in Fig. 3, while the corresponding strength functions and level densities are displayed in Figs. 4 and 5, respectively. After that, this cycle can be repeated—not more than once if use is made of the hypothesis that the distortions of the values of $k(E1)$ and $k(M1)$ grow linearly with decreasing energy of decaying levels and a few times for the version where $\alpha = $ const. In order to minimize the number of adjustable parameters, it was assumed that the correcting functions in Figs. 4 and 5 are identical for electric and magnetic gamma transitions.

The growth of the parameter α with decreasing energy of a decaying nucleus reduces the derivative dk/dE_γ, this being in perfect agreement with the conclusions drawn in [5] from a comparison of the total experimental and calculated spectra for the radiative capture of thermal and fast neutrons. The possibility of consistently describing all experimental

data within the approximations used gives sufficient grounds to expect that the cascade-gamma-decay parameters found according to [4] reflect basic special features of actual level densities and strength functions, so that these features must remain unchanged as the total uncertainty in the determination of the parameters in question is reduced further. By and large, the impossibility of explaining, in terms of known systematic errors, the discrepancy between the experimental functionals of cascade gamma decay and their counterparts calculated according to data from [4] provides the main argument in support of the need for invoking more involved model ideas of the properties of heavy nuclei (first of all, deformed nuclei) at excitation energies below 5 to 8 MeV than those currently used by experimentalists.

4. OBSERVED PATTERN OF THE CASCADE GAMMA DECAY OF A NEUTRON RESONANCE IN A COMPLEX NUCLEUS

The largest volume of the most detailed information about the properties of heavy nuclei in their

excitation-energy range $1-2 < E_{\text{exc}} < B_n$ [MeV] has been obtained to date by studying two-step cascades following thermal-neutron capture. Since one or a few neutron resonances are effectively excited in this process, it can be conjectured that the possible effect of the structure of levels on the process being considered does not fully manifest itself or is specific and local. In particular, the possible correlation between the reduced neutronic width of a compound state and part of partial radiative widths with respect to primary transitions of its decay may result in that the shape and the amplitude of the dependence $I_{\gamma\gamma} = F(E_1)$ change significantly in relation to what we see in Fig. 3 (this being accompanied by a change in the ρ and k values determined according to [4]). Nevertheless, the observed effects are fragments of the total pattern of the change in and the complication of the structure of an excited nucleus and call for an explanation even in this hypothetical case.

To date, experimentalists have found three rather general and previously unknown effects indicating that the properties of nuclei in the excitation-energy region being considered are more intricate than what is embedded in the existing models. These are

(i) an extremely strong effect of the structure of excited levels on the cascade gamma decay of a neutron resonance in the excitation-energy region extending at least to half the neutron binding energy (see Fig. 2);

(ii) a pronounced stepwise structure in the density of intermediate levels of observed two-step cascades in the region around $0.5B_n$ plus an increase in $k(E1) + k(M1)$ both for primary and for secondary transitions, which completely correlates in the excitation energy with this structure;

(iii) nearly equal spacings between the intermediate states (or their close multiplets) of the most intense cascades [intervals that stand out are observed at least for triplets of intermediate levels of the cascades (or for their multiplets), and, at least, two such nearly equidistant "bands" can be singled out in spectroscopic experimental data (see Fig. 6); for a first approximation, the parameter of equidistance is proportional to the number of boson pairs in unfilled nucleon shells].

The equidistant character of the spectrum may be an indication that the structures of the wave functions for intermediate levels of the cascades feature large components corresponding to the existence of one, two, or more phonons—that is, this fact may suggest that excitations of the boson type have a significant effect on cascade gamma decay at energies of cascade levels at least below a value of about $0.5B_n$.

A sizable increase in the strength functions for secondary gamma transitions to levels in the region of the stepwise structure also counts in favor of local

and strong variation in the properties of nuclei in a bounded region of its excitations, and it is this change in the intrinsic properties of the system that is peculiar to the occurrence of a second-order phase transition.

4.1. ^{60}Co Odd−Odd Nucleus

This is the only nucleus that contains odd numbers of protons and neutrons and for which available data on the spectra of gamma rays made it possible to obtain information about the populations of levels at energies up to about 4 MeV. Moreover, this nucleus is rather heavy, so that, in simulating the gamma decay of a compound state for it, it would be natural to expect comparatively small fluctuations of values determined for respective radiative strength functions and level densities. At the same time, the effect of the structure of intermediate levels of the cascades on their intensity exhibits itself quite nontrivially in this nucleus. In just the same way as in heavier near-magic nuclei, the intensity of cascades featuring low-energy primary transitions is much lower than their counterparts for cascades where primary transitions are high-energy. Although the present-day version of the procedure proposed in [4] takes into account quite efficiently a considerable local increase in $I_{\gamma\gamma}$ in individual intervals of energies of intermediate levels of the cascades (see Fig. 3), this complicates quite significantly the iterative process [4] of searches for the interval of ρ and k values that ensure a faithful reproduction of the experimental intensities of the cascades, and we cannot rule out the possibility that this circumstance would lead to the emergence of an additional systematic error in the values found for ρ and k.

The widest interval of possible values of spins characterizing intermediate levels of the cascades leads to maximum fluctuations of both the experimental and the calculated population of the levels. The values of P for each of the levels appearing in the known decay scheme are shown below E_{dis} in Fig. 1. Above it, only its spin-averaged value is given to avoid encumbering the figure. For P values summed over a narrow interval of excitation energies, all three versions of the calculation of populations (see Subsection 3.1) yield results differing insignificantly. However, quite a sizable discrepancy between the calculated and experimental values of $P - i_1$ for the level density [2] is a very strong argument against employing the ideas of the model of a noninteracting Fermi gas in attempts at constructing a precise description of the cascade gamma decay of this odd−odd nucleus.

Yet, it should be noted that quite a significant distinction between the best values of k and their counterparts predicted by the models proposed in [17, 18]

$I_{\gamma\gamma}$, keV^{-1} per 10^4 decays
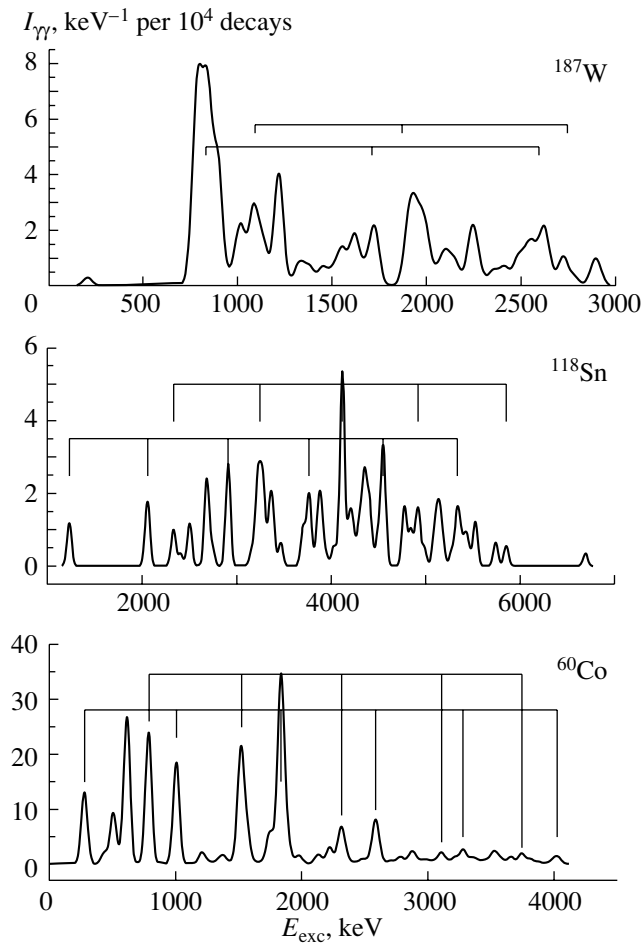
Fig. 6. Possible "bands" of nearly equidistant intermediate levels of the most intense cascades and their multiplets (intensities of the strongest cascades are smoothed by using a Gaussian curve of mean width $\sigma = 50$ keV).

(this is manifested to the same degree in other odd−odd nuclei as well [4]) indicates that the model concepts used are sharply at odds with experimental results for nuclei of this type and that this discrepancy is probably of a general character.

4.2. ^{118}Sn Even−Even Nucleus

The populations of intermediate levels of the cascades were determined on the basis of available data on the spectra of gamma rays in the even−even compound nuclei ^{74}Ge, ^{118}Sn, and ^{184}W up to energies of $E_{\mathrm{exc}} > 4$ MeV and ^{114}Cd, ^{124}Te, ^{150}Sm, ^{156,158}Gd, ^{168}Er, and ^{196}Pt up to $E_{\mathrm{exc}} \approx 3$ MeV. In the first three of these nuclei, the function h increases greatly in the region $E_{\mathrm{exc}} \geq 4$ MeV. Only in this way can one reduce significantly the discrepancy between the calculated and experimental distributions of $P - i_1$. At the same time, the distributions $P = f(E_{\mathrm{exc}})$ feature a significant noncompensated excess of the experimental population of levels above the results of all model calculations. This discrepancy is an additional

argument in support of the above assumption that unpaired nucleons have a pronounced effect on the mean probability of photon emission below B_n and the statement that the conditions under which the calculations are performed are inadequate to the phenomenon being studied.

4.3. ^{187}W Even−Odd Nucleus

Available data on the intensities of individual two-step cascades and on the spectra of gamma rays originating from radiative thermal-neutron capture made it possible to obtain a vast body of information about the populations of levels in ^{181}Hf and ^{183,185,187}W and a smaller amount of information for ^{165}Dy and ^{175}Yb. For all of these nuclei, the cascade population $P - i_1$ could not be reproduced without taking into account local peaks in the function h, but the value found in this case for α is not as great as that for even−even compound nuclei.

5. UNEXPLAINED EFFECTS IN CASCADE GAMMA DECAY

The entire body of data and parameters concerning gamma-decay processes that comes from the investigation of two-step cascades has not yet furnished a completely consistent pattern of such processes. For example, the distinction between the level density required for reproducing experimental $I_{\gamma\gamma}$ values that was obtained according to the procedure proposed in [4] or according to its modification where $R = k(E_\gamma, E_\lambda)/k(E_\gamma, E_i) \neq$ const and the level density estimated according to the procedure used in [6] has yet to be explained.

Of course, the number of intermediate levels of cascades that is extrapolated to zero value of their detection threshold in the form of two peaks resolved in energy may correspond to experimental data only under conditions that would ensure the correctness of the application of the Porter–Thomas distribution [19] to describing [6] the distribution of random values of the intensities of primary transitions in the region of their smallest values. This assumption may be erroneous, for example, in the case where the distribution of terms for the primary-transition amplitude differs from a normal distribution owing to an excess of terms having the same sign.

An alternative possibility consists in that primary or secondary gamma transitions (or both of them) of the same multipolarity and nearly the same energy fluctuate with respect to different mean widths. As to their markedly different values, they are determined by a specific structure of the excited (decaying) intermediate level of the cascades. In this case, it is natural to assume that a nucleus features excited states forming two systems different in properties and that these systems go over to each other in response to a change in the nuclear excitation energy. Among intermediate levels of the cascades, those whose wave functions involve dominant components of the multiquasiparticle or the phonon type may be candidates for this role.

There are no obstacles of fundamental character for taking into account this possibility in expressions (2) and (3), but it is impossible to verify this assumption without additional experimental information. The possibilities of such a verification are estimated in Section 7.

6. POSSIBLE FORM OF A MORE INVOLVED MODEL OF CASCADE GAMMA DECAY AND METHODS FOR AN EXPERIMENTAL DETERMINATION OF ITS PARAMETERS

All experimental data that we have obtained to date for the cascade gamma decay of compound nuclear states are indicative of a strong dependence of this process on the structure of excited levels. First of all, these data rule out the possibility of reproducing its parameters to a precision of present-day experiments on the basis of employing, for the level density, model concepts like those in the model of a noninteracting Fermi gas or some other model concepts that lead to ρ values close to that in [2]. This conclusion [4] is in line with the results of our present analysis (see Fig. 5); moreover, it also follows directly and independently from the maximum discrepancy between the experimental and calculated total populations of relevant levels (see Fig. 1).

Yet another conclusion of considerable importance from our analysis of experimental data is that it is necessary to take directly into account, within models of the level density and radiative widths, large-scale effects associated with the influence of the nuclear structure on these parameters up to an excitation energy of about $0.5B_n$ or higher. This conclusion follows from the impossibility of faithfully reproducing the sums of cascade populations of levels (see Fig. 2) with the aid of the ρ and k values deduced from the analysis performed in [4]. The degree to which the details of the nuclear structure should be taken into account in model concepts will of course depend on the degree of discrepancies between the calculated functionals of cascade gamma decay and their counterparts determined experimentally.

The entire body of experimental data accumulated thus far gives sufficient grounds to put forth the hypothesis that model concepts of the process being studied should be refined by taking into account more directly and precisely the interplay of the superfluid and normal phases in a nucleus. However, the following questions would remain open in all probability:

(a) Is the present-day experimental level of understanding of cascade gamma decay sufficient for creating new models of level densities and radiative strength functions?

(b) Is it possible to obtain all experimental data that are required for fully parametrizing such models?

The following points may form the basis of new model concepts:

(i) The transition of a nucleus from a superfluid to a normal phase with increasing excitation energy of the nucleus occurs well below the neutron binding energy for its values within some range.

(ii) The probability of excitation of levels whose wave functions involve both quasiparticle and vibrational components depends on the relationship between their contributions to the normalization (in particular, on the position of the excited level with respect to the energy of the presumed phase transition).

Since the spins of neutron resonances are low, one can skip, for the majority of deformed nuclei, the

question of a possible distinction between the probabilities of excitation and decay of levels of rotational bands, on one hand, and the analogous values for bandheads, on the other hand, paying no attention, at this stage, to the effect of rotational excitations on cascade gamma decay, at least in slow-neutron capture by even–even targets. It is very unlikely that attempts at taking into account the first point would run into difficulties of a fundamental character. It can be incorporated by various methods, including extremely simple ones. This is illustrated by the attempt made in [20] to create some phenomenological version of the level-density model. By using the concept of the heat capacity of nuclear matter and by applying, to nuclei, the ideas of the form of its variation with energy in the region of a second-order phase transition that were inferred from the study of superfluidity in liquid helium, it was shown in [20] that the use of this, extremely simple, modification of models belonging to the type in [2] makes it possible to reproduce stepwise structures in the level density.

Unfortunately, it is then necessary to solve the following problems:

(a) a determination of the phenomenological dependence of the nuclear heat capacity for a mixture of a normal and superfluid phase in the presence of unpaired nucleons;

(b) the inclusion of the expected dependence of mean partial widths with respect to gamma transitions on the energies of a decaying and an excited level that are characterized by wave functions of different structures.

That an increase in the sums of radiative strength functions and a decrease in the level density (the latter is necessary for the dependence of the intensity of a cascade on the energy of its intermediate level to be reproduced in the calculations) occur synchronously may suggest the need for taking into account the relationship between these two nuclear parameters. In particular, the set of available data [4] on level densities and radiative strength functions for cascade gamma transitions gives sufficient grounds to assume that these parameters may depend on the parity of the number of nucleons in a compound nucleus (number of excited quasiparticles). This is one of the possible (in principle) explanations for the significant discrepancy between the absolute values of radiative strength functions for even–even and odd–odd nuclei that was observed in [4].

Yet another problem that was not solved in [20] consists in the need for directly including the density of vibrational levels in the modified version of the Fermi gas model. This problem requires a dedicated analysis within the generalized model of a superfluid nucleus, since, within the existing version, the model

cannot reproduce the intensities $I_{\gamma\gamma}$ for all nuclei being studied, most likely because of an approximately twofold overestimation of the energy of the phase transition from a superfluid to a normal state. It is also necessary to revisit its ideas of the thermodynamic parameters of a nucleus below the point of the phase transition for a lower phase-transition energy.

The possibilities for going over to more involved model concepts of radiative strength functions for performing a more precise analysis of experimental data are severely restricted by the absence of reliable data on the probability of photon emission in a wide interval of photon energies and a wide interval of excitation energies of decaying levels. For primary transitions of the cascades, the values obtained in [4] for $k(E1) + k(M1)$ have a minimum possible, albeit actually unknown, discrepancy with the sought value. Data presented in [5] give every reason to assume that, as the excitation energy of a nucleus decreases, the sum of the $E1$ and $M1$ strength functions features a weaker dependence on the photon energy than for primary transitions of neutron-resonance decay. This comment is probably quite correct for strongly deformed nuclei, but is may be insufficiently accurate, say, for spherical and transition nuclei from the regions around $A \sim 100$ and around $A \sim 190$, respectively.

Of course, questions like that of the number of broken Cooper pairs at an excitation energy of 3 to 4 MeV for a deformed rare-earth nucleus and that of the effect of the phonon components of a decaying level at an excitation energy above the region of the presumed phase transition remain unresolved experimentally.

The procedures developed thus far for studying excited nuclear states by means of two-step cascades do not have restrictions of a fundamental origin [4, 6, 13] on the accuracy in determining their parameters nearly over the entire region of excitations of intermediate and final levels, at least in the capture of thermal neutrons and neutrons of "filtered" beams from stationary nuclear reactors. In attempts at deriving more precise ideas of the properties of complex nuclei below the neutron binding energy and at developing new phenomenological models of the nucleus, the existing experimental procedures may prove to be insufficient, however, primarily because of the absence of detailed experimental data on the intensities of two-step cascades to $E_f > 1$ MeV final levels.

7. POSSIBILITIES OF EXPERIMENTAL TESTS OF NEW IDEAS

A direct observation of enhanced secondary gamma transitions to levels in the region of "stepwise" struc-

tures is the most pressing experimental problem of the near future.

In order to prove directly a local enhancement of radiative strength functions for gamma transitions to levels at an excitation energy of about 3 MeV in a deformed heavy even−odd nucleus, it is necessary to determine the reduced relative probability of gamma transitions from higher lying levels in the interval of E_γ from a few hundred kiloelectrovolts to a few megaelectronvolts. This problem cannot be solved by means of classical nuclear spectroscopy by using any types of existing detectors and procedures for determining the energies of excited levels and their decay modes.

The only realistic possibility to solve it is to measure experimentally the distribution of the intensities of two-step cascades to all possible final levels up to an excitation energy of about 3 MeV or higher in a deformed heavy even−odd nucleus. For even−even and lighter spherical nuclei, the energy of these levels must somewhat exceed 4 to 5 MeV. In accumulating useful statistics of a few thousand events for each spectrum where $E_1 + E_2 = B_n - E_f = \text{const}$, some fraction of secondary gamma transitions will be resolved in energy in these spectra in the form of pairs of isolated peaks. By using presently elaborate procedures, one will be able to determine, from these data, the intensities of individual secondary gamma transitions to $E_f \leq 3{-}4$ MeV levels, thereby obtaining a set of values for the reduced probabilities of gamma transitions that makes it possible to assess directly the shape of the energy dependence of strength functions in the excitation-energy region of interest to us.

The special features of the energy dependence of the observed population of levels gives sufficient grounds to expect a maximum increase in k values for secondary transitions of the cascades in even−even nuclei and a less pronounced increase in even−odd nuclei.

The only reason why such spectra have not been recorded [21] so far is that, in the spectra of the sums of amplitudes of coinciding pulses, the corresponding peaks of ever decreasing area appear against an ever increasing Compton background. In principle, the problem in question can be tackled by means of a procedure where cases of a simultaneous absorption of the total energy of three photons sequentially emitted to the ground and low-lying states of a nucleus are isolated in the form of peaks in the spectrum of sums of amplitudes of three coinciding peaks. Since the energies of secondary transitions of two-step cascades are known (and can be found in the same experiment), it proves to be possible to determine, from the cases of detection of the total energy of three sequentially emitted photons, the distributions of the intensities of two-step cascades to $E_f > 1$ MeV final levels.

The required result can be attained with recording systems formed by at least three high-purity germanium detectors or by only two such spectrometers in the case where the Compton background is suppressed. Experimental data reported by Bondarenko *et al.* [21] make it possible to obtain a preliminary estimate of the required degree of suppression of the Compton background: the suppression factor must not be less than 10 for each detector. In one version or another, the efficiency of the detectors used must be commensurate with the efficiency of modern crystal ball detectors.

8. CONCLUSION

The results of experiments performed thus far in Dubna, Riga, and Řež to study two-step cascades in thermal-neutron capture and the results of their analysis carried out at the Laboratory of Neutron Physics at JINR have revealed that various functionals of the cascade gamma decay of nuclei that have a high level density cannot be reproduced, to a precision of present-day experiments, by a calculation that employs only the existing ideas of the factors determining this process. The set of available data and their interpretation indicates that it is necessary to elaborate on the model concepts of this process that underlie an analysis of any experiment in this region of low-energy nuclear physics. The most probable line of such a modification is to take into account more precisely, in new models of ρ and k, the coexistence of quasiparticle and phonon excitations in a nucleus and the effect of their interplay on the level density and on the probability of gamma decay, including a direct use of the idea that there exists a second-order phase transition in a nucleus between a superfluid and a normal state.

REFERENCES

1. *Handbook for Calculation of Nuclear Reaction Data*, IAEA-TECDOC-1034 (Vienna, 1998).
2. W. Dilg *et al.*, Nucl. Phys. A **217**, 269 (1973).
3. E. M. Rastopchin, M. I. Svirin, and G. N. Smirenkin, Yad. Fiz. **52**, 1258 (1990) [Sov. J. Nucl. Phys. **52**, 799 (1990)].
4. É. V. Vasilieva, A. M. Sukhovoj, and V. A. Khitrov, Yad. Fiz. **64**, 195 (2001) [Phys. At. Nucl. **64**, 153 (2001)]; V. A. Khitrov and A. M. Sukhovoj, INDC(CCP)-435, IAEA (Vienna, 2002), p. 21; nucl-ex/0110017.
5. A. M. Sukhovoj, V. A. Khitrov, and E. P. Grigor'ev, INDC(CCP)-432, IAEA (Vienna, 2002), p. 115.
6. A. M. Sukhovoj, and V. A. Khitrov, Yad. Fiz. **62**, 24 (1999) [Phys. At. Nucl. **62**, 19 (1999)].
7. J. Honzátko, V. A. Khitrov, C. Panteleev, *et al.*, Preprint No. E3-2003-88, JINR (Joint Inst. Nucl. Res., Dubna, 2003); nucl-ex/0305020.

8. V. A. Bondarenko, J. Honzátko, V. A. Khitrov, *et al.*, in *Proceedings of the XI International Seminar on Interaction of Neutrons with Nuclei, Dubna, Russia, 2003* (JINR, Dubna, 2003), E3-2004-9, p. 73.

9. M. Igashira *et al.*, Nucl. Phys. A **457**, 301 (1986).

10. M. A. Lone, R. A. Leavitt, and D. A. Harrison, Nucl. Data Tables **26**, 511 (1981).

11. http://www-nds.iaea.org/pgaa/egaf.html

12. G. L. Molnar *et al.*, Appl. Radiat. Isot. **53**, 527 (2000).

13. V. A. Khitrov, Li Chol, and A. M. Sukhovoj, in *Proceedings of the XI International Seminar on Interaction of Neutrons with Nuclei, Dubna, 2003* (JINR, Dubna, 2003), E3-2003-9, p. 98.

14. S. T. Boneva *et al.*, Z. Phys. A **338**, 319 (1991); Nucl. Phys. A **589**, 293 (1995).

15. A. V. Ignatyuk and Yu. V. Sokolov, Yad. Fiz. **19**, 1229 (1974) [Sov. J. Nucl. Phys. **19**, 628 (1974)].

16. S. F. Mughabghab, M. Davadeenom, and N. E. Holden, *Neutron Cross Sections* (Academic, New York, 1984), Vol. 1, Part A.

17. P. Axel, Phys. Rev. **126**, 671 (1962); J. M. Blatt and V. F. Weisskopf, *Theoretical Nuclear Physics* (Wiley, New York, 1952; Inostrannaya Literatura, Moscow, 1954).

18. S. G. Kadmenskiĭ, V. P. Markushev, and V. I. Furman, Yad. Fiz. **37**, 277 (1983) [Sov. J. Nucl. Phys. **37**, 165 (1983)].

19. C. F. Porter and R. G. Thomas, Phys. Rev. **104**, 483 (1956).

20. A. M. Sukhovoj and V. A. Khitrov, Izv. Ross. Akad. Nauk, Ser. Fiz. **61**, 2068 (1997).

21. V. A. Bondarenko, J. Honzátko, V. A. Khitrov, *et al.*, Fizika B (Zagreb) **11**, 201 (2002).

Translated by A. Isaakyan

=============== **NUCLEI** ===============
Theory

Static and Statistical Properties of Hot Rotating Nuclei in a Macroscopic Temperature-Dependent Finite-Range Model

E. G. Ryabov* and   G. D. Adeev**

Omsk State University, pr. Mira 55A, Omsk, 644077 Russia
Received May 13, 2004; in final form, October 29, 2004

Abstract—A macroscopic temperature-dependent model that takes into account nuclear forces of finite range is used to calculate the static and statistical properties of hot rotating compound nuclei. The level-density parameter is approximated by an expression of the leptodermous type. The resulting expansion coefficients are in good agreement with their counterparts proposed previously by A.V. Ignatyuk and his colleagues. The effect of taking simultaneously into account the temperature of a nucleus and its angular momentum on the quantities under study, such as the heights and positions of fission barriers and the effective moments of inertia of nuclei at the barrier, is considered, and the importance of doing this is demonstrated. The fissility parameter $(Z^2/A)_{\mathrm{crit}}$ and the position of the Businaro–Gallone point are studied versus temperature. It is found that, with increasing temperature, both parameters are shifted to the region of lighter nuclei. It is shown that the inclusion of temperature leads to qualitatively the same effects as the inclusion of the angular momentum of a nucleus, but, quantitatively, thermal excitation leads to smaller effects than rotational excitation. © *2005 Pleiades Publishing, Inc.*

1. INTRODUCTION

In recent decades, there has appeared the possibility of experimentally studying the fission of nuclei formed in heavy-ion reactions. This has given impetus to theoretical investigations into processes involving the formation and decay of nuclei characterized by high angular momenta and relatively high excitation energies [1−12]. In this case, a theoretical consideration includes a quantitative estimate of the effect of excitation energy and angular momentum on the evolution of the shapes of a fissile compound nucleus. This information makes it possible to describe the fission of rotating heavy nuclei and the competition between fusion and fission in heavy-ion reactions. In particular, the theoretically predicted probability of the formation of relatively stable superheavy nuclei depends primarily on excitation energy and angular momentum. The answer to the question of whether the nucleus formed will exist, prior to undergoing fission, long enough to be recorded experimentally is determined precisely by these quantities.

In theoretical calculations, the most comprehensive and precise information about the effect of the temperature and rotation of a nucleus on its properties can of course be obtained within microscopic approaches, such as the Hartree−Fock method [9], the extended Thomas−Fermi method [3, 4, 7, 12], or

relativistic mean-field theory [13, 14]. However, such calculations are complicated and cumbersome even at the present-day level of development of computational techniques. By using a simpler macroscopic− microscopic approach proposed by Strutinsky [15], Diebel *et al.* [1] calculated fission barriers and critical angular momenta for excited nuclear systems. However, an approach that is based on the liquid-drop model of the nucleus is the simplest and the most successfully used in fission dynamics. Despite its more than half-century history, the liquid-drop model, albeit having undergone a number of modifications and improvements, remained essentially macroscopic. For many years, the fact that the temperature of a compound nuclear system was not taken into account in this model has been a significant drawback of the model. The absence of vast experimental data generally used to determine the parameters of the liquid-drop model (nuclear binding energies in the ground state and fission barriers, some fusion barriers, an equivalent nuclear radius, as well as the diffuseness of the charge distribution) for hot nuclei was an excuse for this situation to some extent. In determining the coefficients used in the model, one has had to rely, in this case, on the results of microscopic calculations performed, for example, within the extended temperature-dependent Thomas−Fermi method [3]. It is the approach that was used in [2, 4, 7, 10, 16]. The rotating-liquid-drop model that takes into account nuclear forces of finite range and the diffuseness of the nuclear density [17, 18] is widely

*e-mail: ryabov@org.omskreg.ru
**e-mail: adeev@univer.omsk.su

used both in dynamical and in statistical approaches to nuclear fission. It was generalized to the case of hot nuclei by Krappe in [16]. Within the macroscopic approach (the very applicability of this approach is determined by nuclear excitation and rotation), this finally makes it possible to take into account adequately and self-consistently the effect of both the angular momentum and the temperature of a compound system on the statistical properties of nuclei, on one hand, and on fission dynamics, on the other hand. It should be emphasized that the parameters of this model were determined by Krappe on the basis of calculations within the microscopic Thomas–Fermi method (a detailed description of this procedure can be found in [16]).

In the earlier studies reported in [1–5, 7, 9, 10] and mentioned above, temperature effects and the rotation of a nucleus were not taken simultaneously into account in determining static and statistical properties of nuclei (fission barriers B_f; level-density parameters in the ground state and at the barrier, a_n and a_f, respectively; effective moments of inertia, J_{eff}; and critical angular momenta L_{crit}). The importance of taking these effects into account cannot be overestimated, but this does not reduce the value of the previous investigations.

Some preliminary results of an analysis of the properties of the temperature-dependent finite-range liquid-drop model were described by our group in [19]. The present article is aimed at more detailed calculations and discussions.

2. TEMPERATURE-DEPENDENT FINITE-RANGE LIQUID-DROP MODEL

Hot rotating compound nuclei produced in heavy-ion reactions form a thermodynamic system. Naturally, various parameters of this system and its stability conditions must be determined by some of its thermodynamic potentials, either the free energy [16] or entropy [20]. The choice of one thermodynamic potential or another is a matter of taste and convenience in performing calculations since they are related by the well-known equation $F(\mathbf{q}, T) = E(\mathbf{q}, T) - TS$.

For a set of collective coordinates $\mathbf{q}$ describing the nuclear shape, we choose geometric parameters of the nuclear shape—that is, $\mathbf{q} = \{c, h, \alpha'\}$. In doing this, we employ a modified version of the well-known $\{c, h, \alpha\}$ parametrization from [21]. The parametrization used here in the equation determining the profile function differs from the original $\{c, h, \alpha\}$ parametrization in that the former involves a new mass-asymmetry parameter α' that is related to α by the scale transformation [22]

$$\alpha' = \alpha c^3. \tag{1}$$

Within the parametrization being considered, the shape of the nuclear surface in terms of cylindrical coordinates is given by the equation [21, 23]

$$\rho_s^2(z) = \begin{cases} c^{-2} \left(c^2 - z^2\right) \left(A_s c^2 + B z^2 + \alpha' z/c^2\right), & B \geq 0, \\ c^{-2} \left(c^2 - z^2\right) \left(A_s c^2 + \alpha' z/c^2\right) \exp(B c z^2), & B < 0, \end{cases} \tag{2}$$

where z is the coordinate along the symmetry axis and ρ_s is the value of the coordinate ρ at the nuclear surface. The quantities A_s and B are expressed in terms of the nuclear-shape parameters (c, h) as

$$B = 2h + (c-1)/2;$$

$$A_s = \begin{cases} c^{-3} - B/5, & B \geq 0, \\ -\dfrac{4}{3} \dfrac{B}{\exp(Bc^3) + (1 + 1/(2Bc^3)) \sqrt{-\pi Bc^3} \operatorname{erf}(\sqrt{-Bc^3})}, & B < 0. \end{cases} \tag{3}$$

In Eqs. (1)–(3), c is the elongation parameter ($2c$ is the elongation of a nucleus), h is a parameter that specifies the neck thickness at a given elongation, and α' is the mass-asymmetry parameter. Shapes that are symmetric with respect to the $z = 0$ plane correspond to the case of $\alpha' = 0$.

A formula for the free energy was proposed in [16] on the basis of the finite-range liquid-drop model. The free energy of a nucleus as a function of the mass

Table 1. Coefficients in Eq. (4) [values at zero temperature (first row) and temperature coefficient x_i (second row)]

	r_0	a	a_d	a_v	k_v	a_s	k_s
$a_i(0)$	1.16	0.68	0.7	16.0	1.911	21.13	2.3
$10^3 x_i \,[\mathrm{MeV}^{-2}]$	-0.736	-7.37	-7.37	-3.22	5.61	4.81	-14.79

number $A = N + Z$, the neutron excess per nucleon [$I = (N - Z)/A$], temperature, and the collective coordinates $\mathbf{q}$ characterizing the nuclear shape has the form [16]

$$F(A, Z, \mathbf{q}, T, L) = -a_v(1 - k_v I^2)A \qquad (4)$$
$$+ a_s(1 - k_s I^2)B_n(\mathbf{q})A^{2/3}$$
$$+ c_0 A^0 + a_{\mathrm{C}} \frac{Z^2}{A^{1/3}} B_{\mathrm{C}}(\mathbf{q})$$
$$- a_c \frac{5}{4}\left(\frac{3}{2\pi}\right)^{2/3} \frac{Z^{4/3}}{A^{1/3}} + \frac{\hbar^2 L(L+1)}{2J(\mathbf{q})},$$

where a_v, a_s, and a_{C} are the parameters of the volume, surface, and Coulomb energies in the finite-range liquid-drop model at zero temperature, while k_v and k_s are, respectively, the volume and the surface parameter of the symmetry energy. The dependence on the deformation in Eq. (4) is determined by the functionals $B_n(\mathbf{q})$, $B_{\mathrm{C}}(\mathbf{q})$, and $J(\mathbf{q})$:

$$B_n(\mathbf{q}) = \frac{1}{8\pi^2 a^4 r_0^2 A^{2/3}} \qquad (5)$$
$$\times \int_V \int_{V'} \left(2 - \frac{|\mathbf{r} - \mathbf{r}'|}{a}\right) \frac{\exp\left(-|\mathbf{r} - \mathbf{r}'|/a\right)}{|\mathbf{r} - \mathbf{r}'|/a} d\mathbf{r}\,d\mathbf{r}',$$

$$B_{\mathrm{C}}(\mathbf{q}) = \frac{15}{32\pi^2 r_0^5 A^{5/3}} \qquad (6)$$
$$\times \int_V \int_{V'} \left[1 - \left(1 + \frac{|\mathbf{r} - \mathbf{r}'|}{2a_d}\right)\right.$$
$$\times \left. \exp\left(-\frac{|\mathbf{r} - \mathbf{r}'|}{a_d}\right)\right] \frac{d\mathbf{r}\,d\mathbf{r}'}{|\mathbf{r} - \mathbf{r}'|}.$$

One can easily see that the functionals in (5) and (6) are in fact the nuclear-energy and the Coulomb energy functional within the finite-range liquid-drop model [18]. The last term in (4) is the rotational energy involving the deformation-dependent rigid-body moment of inertia of a nucleus with allowance for the diffuseness of the nuclear density (perfect analog of the rotational energy in the finite-range liquid-drop model [18]).

The temperature dependence of the seven coefficients appearing in Eq. (4), a_v, a_s, k_v, k_s, r_0, a, and a_d, is parametrized in the form [16]

$$a_i(T) = a_i(T = 0)(1 - x_i T^2), \qquad (7)$$

which can be considered as adequate for $T \leq 4$ MeV [3]. Information about the temperature coefficients x_i was obtained from self-consistent microscopic calculations on the basis of the extended Thomas–Fermi method with the SkM^* interaction for the effective interaction between nucleons [3, 4]. In [16], the results of these calculations for the thermodynamic Gibbs potential were used to derive formula (4). The values of 14 parameters that were obtained in [16] and which are used in the present study are given in Table 1.

Considering a nucleus within the Fermi gas model, using thermodynamic relations, and knowing the free energy, one can obtain both the entropy and the level-density parameter:

$$S(\mathbf{q}, T) = -\left(\frac{\partial F(\mathbf{q}, T)}{\partial T}\right)_V, \quad a(\mathbf{q}, T) = \frac{S(\mathbf{q}, T)}{2T}. \qquad (8)$$

Within the Fermi gas model, we also have the relation

$$E_{\mathrm{int}}(\mathbf{q}, T) = E(\mathbf{q}, T) - E(\mathbf{q}, T = 0) = a(\mathbf{q})T^2, \qquad (9)$$

where $E_{\mathrm{int}}(\mathbf{q}, T)$ and $E(\mathbf{q}, T)$ are, respectively, the internal energy of the system and its total excitation energy, while $a(\mathbf{q})$ is the level-density parameter. From formulas (8) and (9), it follows, among other things, that the temperature dependence of the free energy has the form

$$F(\mathbf{q}, T) = V(\mathbf{q}) - a(\mathbf{q})T^2, \qquad (10)$$

where $V(\mathbf{q})$ is the potential energy of the nucleus at $T = 0$ $(V(\mathbf{q}) = F(\mathbf{q}, T = 0))$. The microscopic calculations performed in [3] within the extended temperature-dependent Thomas–Fermi method revealed that Eq. (10) for the free energy F provides quite an accurate approximation in the region $T \leq 4$ MeV.

Table 2. Coefficients a_v and a_s obtained in the present study by using a one-, a two-, and a three-dimensional grid and in [24, 27]

	a_v, MeV^{-1}	a_s, MeV^{-1}
one-dimensional	0.0603	0.1186
two-dimensional	0.0600	0.1210
three-dimensional	0.0598	0.1218
[24]	0.073	0.095
[27]	0.0685	0.274

3. RESULTS OF THE CALCULATIONS AND DISCUSSIONS

3.1. Asymptotic Level-Density Parameter

The level-density parameter a is one of the most important features of an excited nucleus considered within the Fermi gas model [24, 25]. By using the thermodynamic relations (8) and (9) and formula (4), we can determine the level-density parameter within the liquid-drop model that takes into account nuclear forces of finite range and nuclear excitations. In this case, an implicit dependence of a on the nuclear deformation is specified by the dependence of the free energy F appearing in Eqs. (8) and (9) on the collective coordinates.

At the same time, the dependence of the level-density parameter on the deformation of a nucleus is often represented by a leptodermous-type expansion of the form [24−27]

$$a(\mathbf{q}) = a_v A + a_s A^{2/3} B_s(\mathbf{q}). \qquad (11)$$

In this equation, A is the mass number of the fissile nucleus and the dimensionless factor $B_s(\mathbf{q})$ specifies the area of the deformed-nucleus surface in units of the surface of a sphere having the same volume—the surface-energy functional in the model of a liquid drop having a sharp surface [28]. Among a number of sets of the parameters a_v and a_s in the dependence given by (11), use is most frequently made of that which was proposed by Ignatyuk *et al.* [24] ($a_v = 0.073\,\mathrm{MeV}^{-1}$ and $a_s = 0.095\,\mathrm{MeV}^{-1}$) and that which was recommended by Töke and Swiatecki [27] ($a_v = 0.0685\,\mathrm{MeV}^{-1}$ and $a_s = 4a_v$).

For two values of the nuclear temperature, Fig. 1 shows the level-density parameters versus deformation (elongation) that were calculated by formula (11) with the coefficients borrowed from [24] and [27] and by formulas (4) and (8) within the liquid-drop model taking into account nuclear forces of finite range and

nuclear excitations. We note that the level-density parameter $a(\mathbf{q})$ calculated on the basis of the liquid-drop-model version used here weakly depends on temperature. The same result was obtained in [16] for spherical nuclei. Because of this, we further assume that the level-density parameter in the finite-range liquid-drop model is temperature-independent.

We approximated the deformation dependence of the level-density parameter in the finite-range liquid-drop model by the widely used expression (11). In order to obtain the approximation coefficients a_v and a_s, we used 70 nuclei along the beta-stability line from $Z = 47$ to $Z = 116$. The equation determining the beta-stable nuclei has the form [29]

$$Z = \frac{A}{2}\left(1 - \frac{0.4A}{A + 200}\right). \qquad (12)$$

In constructing the approximation in question, we employed the least squares method and took into account all nuclear shapes, with the exception of scission shapes whose neck radius was smaller than $0.3R_0$ (R_0 is the radius of the original spherical nucleus). The results of the approximation are given in Table 2. The coefficients a_v and a_s were estimated for the one- ($h = \alpha' = 0$), two- ($\alpha' = 0$), and three-dimensional cases. It can easily be seen that the coefficients are not sensitive to the dimensionality of the grid used in the approximation; therefore, all of the results discussed below were obtained with the coefficients calculated with a three-dimensional grid.

A variation of the approximate coefficients a_v and a_s along the beta-stability line is shown in Fig. 2a. It can be seen that the value of a_v is in fact constant, while the coefficient a_s decreases by 20% as Z varies from 47 to 116. It can be concluded from Figs. 2b and 2c that our approximation is quite correct within the range of nuclear deformations under consideration. The coefficient a_s specifies the dependence of the level-density parameter on deformation; hence, it is of importance for statistical and dynamical models of nuclear fission. The value obtained for this coefficient in the approximation proposed here is close to that from [24], $a_s = 0.095\,\mathrm{MeV}^{-1}$, and differs by a factor of more than two from the value of $a_s = 0.274\,\mathrm{MeV}^{-1}$ from [27]. The second coefficient, a_v, takes approximately the same value in all of the approximations considered here.

For the ground states of the nuclei lying along the beta-stability line, Fig. 3 displays the level-density parameter as a function of the mass number. From this figure, one can see that the results of the calculations with Ignatyuk's coefficients [24] and the results of the calculations performed within the temperature-dependent liquid-drop model are in better agreement with the values obtained on the
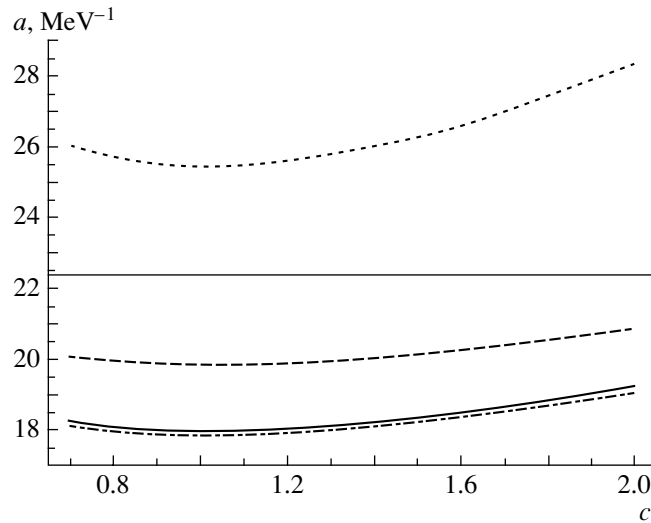
Fig. 1. Level-density parameter as a function of deformation for the ^{224}Th nucleus: results for the liquid-drop model taking into account nuclear forces of finite range and nuclear excitations at (solid curve) $T = 0.001$ MeV and (dash-dotted curve) $T = 4$ MeV, for the case of (dashed curve) Ignatyuk's coefficients and (dotted curve) Töke–Swiatecki coefficients, and for the case of (thin straight line) $a(\mathbf{q}) = A/10$.
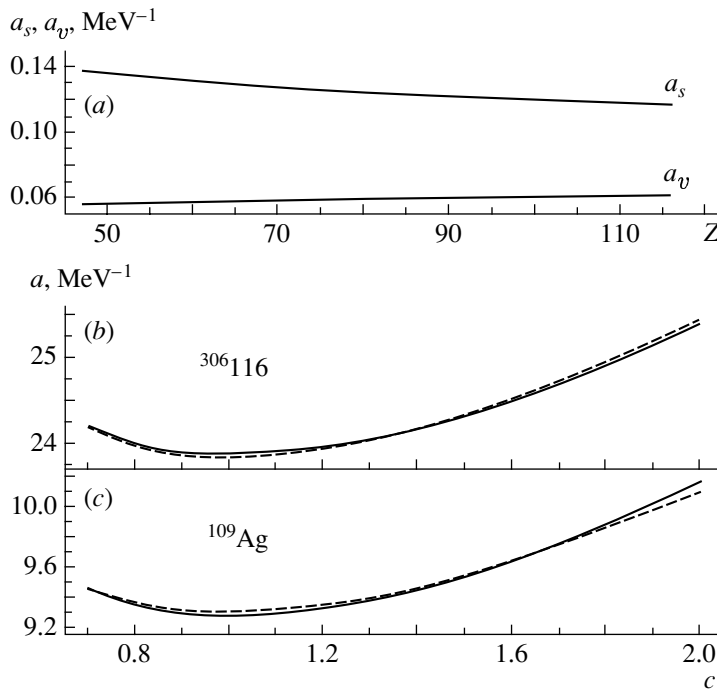
Fig. 2. (a) Coefficients a_v and a_s as obtained here from an approximation along the beta-stability line; (b, c) level-density parameter as a function of deformation for the element $^{306}116$ and for ^{109}Ag within the finite-range liquid-drop model (solid curves) and its approximation (dashed curves) (for these nuclei, the accuracy of the approximation is the lowest).

basis of microscopic approaches than with those that were calculated by employing the set of Töke–Swiatecki parameters [27]. In turn, the curve for the level-density parameters that was calculated with Ignatyuk's coefficients is virtually coincident with the results obtained within relativistic mean-field theory [14]. Since the parameters of the temperature-dependent finite-range liquid-drop model were determined in [16] on the basis of an approximation of the results obtained within the extended Thomas–Fermi method by using effective Skyrme interaction forces SkM^*, the curves corresponding to them in Fig. 3 coincide.

a, MeV^{-1}
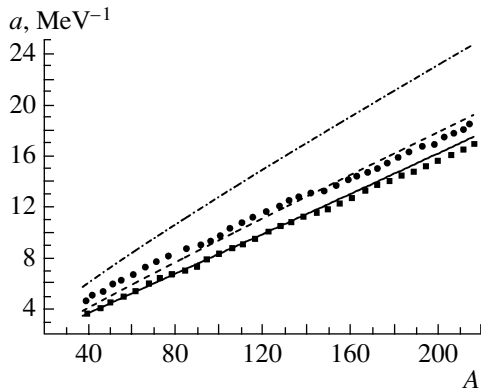
Fig. 3. Level-density parameter for some nuclei along the beta-stability line in the ground state: (dash-dotted curve) results within the finite-range liquid-drop model [16], (solid curve) results obtained with Ignatyuk's coefficients [24], and (dashed curve) results obtained with Töke–Swiatecki's coefficients [27]. The boxes represent the level-density parameter as a function of the mass number for beta-stable nuclei according to calculations within the extended Thomas–Fermi method with effective-interaction Skyrme forces SkM^* [4], while the circles correspond to self-consistent calculations within relativistic mean-field theory [14].

B_f, MeV
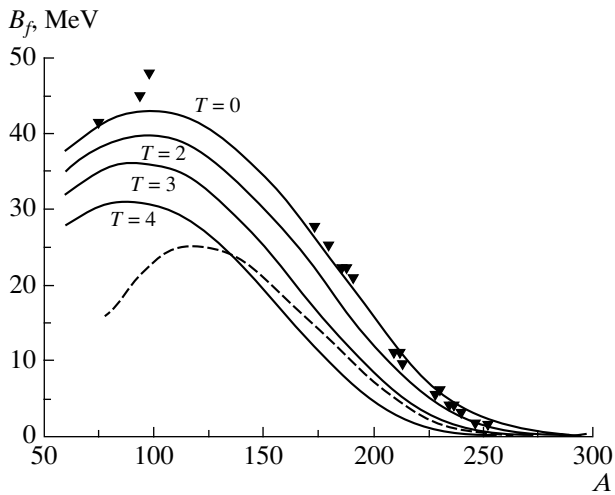
Fig. 4. Fission barriers in hot beta-stable nuclei at various temperatures T and $L = 0$ (solid curves, the temperature being indicated in MeV) and at $T = 2$ MeV and $L = 40\hbar$ (dashed curve). The triangles represent experimental data reported in [12] corrected with allowance for shell effects.

3.2. Effect of the Temperature of a Nucleus and Its Angular Momentum on the Barrier Height

For nuclei formed in heavy-ion reactions, fission barriers (B_f) play an important role in their fusion—fission dynamics. The height and position of the barrier determine not only the character of a nuclear process—fast fission, quasifission, or the existence of

superdeformed nuclei—but also, in the case of the decay of an equilibrium compound nucleus, the competition between the processes of fission and particle emission. It should be noted that the angular distribution of fission fragments also depends on the effective moment of inertia of a fissile nucleus at the barrier (J_{eff}), this moment of inertia being determined by the saddle-point configuration of the nucleus.

The effect of nuclear rotation on the fission process is well known [18, 30]: the fission barrier decreases, disappearing at some value of the angular momentum (L_{crit}); the ground state of the nucleus with respect to the main fission coordinate (c, which is the elongation parameter of the nucleus) is shifted toward the scission point, while the saddle point is, on the contrary, shifted toward the ground state, these effects becoming more pronounced with increasing angular momentum of the rotating nucleus.

However, the inclusion of temperature effects is no less important [2–5, 9]. It should be noted that only a few studies have been devoted to a macroscopic treatment of the temperature dependence of fission barriers (among those that were mentioned above, there are [2, 6, 7, 31]). If, in a theoretical description, we want to approach the pattern observed in heavy-ion reactions, we must take self-consistently into account both factors (temperature and angular momentum), considering a hot rotating nucleus [1, 7, 10, 11] within a unified model.

In analyzing the temperature or the angular-momentum dependence of static and statistical properties of nuclei, we will assume here and below that a factor whose magnitude and variation are not discussed is constant and is equal to zero.

For hot beta-stable nuclei, Fig. 4 presents the dependence of the fission barriers on the mass number. Here, the triangles represent experimental data from [12] that were corrected with allowance for shell effects. As was indicated in [2], the liquid-drop model is inapplicable in the region of medium-mass and light nuclei, this being by and large confirmed by overestimated values of theoretically predicted barriers in the region of light nuclei (see Fig. 4). Qualitative agreement between the temperature dependence of the barrier height (a decrease in B_f with increasing temperature) and data obtained in [2, 10] is worthy of note, albeit the barriers calculated in the present study are systematically below those data. The same conclusions can be drawn from a comparison of our results for the temperature dependence of barriers in heavy and superheavy nuclei with the results reported in [1], where use was made of Strutinsky's macroscopic—microscopic approach. At the same time, good qualitative agreement is obtained for barrier heights if a comparison is performed with

the results of calculations based on the Thomas–Fermi method [7, 12], although an interaction differing from the SkM^* interaction was used for an effective nucleon–nucleon potential. As might have been expected, the results of our calculations at zero temperature for barriers agree with the barriers in the finite-range liquid-drop model employing Sierk's parameters [18] (in Fig. 4, the respective curves are indistinguishable). The dashed curve, which represents the barrier heights for the same beta-stable nuclei of temperature 2 MeV whose rotation is characterized by an angular momentum of $L = 40\hbar$, illustrates vividly the need for simultaneously taking into account the rotation of a nucleus and its thermal excitation. The difference in the barrier heights as calculated with and without allowance for the rotation of a hot nucleus becomes ever more pronounced with decreasing mass number of nuclei.

The effect of simultaneously taking into account the thermal excitation of a nucleus and its rotation as a discrete unit is illustrated in Fig. 5a, where the effect that both factors considered in the present study (a decrease in the barrier height with increasing nuclear temperature and angular momentum of nuclear rotation) exert on the barrier is shown for the ^{240}Pu nucleus. It is worth mentioning that an increase in the angular momentum produces a greater effect, the temperature effect becoming less pronounced with increasing L. For a comparison of our results with data of Garcias et $al.$ [7], who considered the effect of the same two factors on the fission barrier in ^{240}Pu within the Thomas–Fermi method, to be complete, we approximated the dependence of B_f on T and L by the expression (dashed curve in Fig. 5a)

$$B_f = 3.889 - (1.544 \times 10^{-3}L^2 - 5.71 \times 10^{-6}L^3) \quad (13)$$

$$- (5.03 \times 10^{-1} - 0.63 \times 10^{-4}L^2)T^2$$

$$+ 0.068T^3 \text{ [MeV]},$$

which is similar to expression (2) from [7].

In contrast to the quadratic dependence in [7], we obtained a cubic temperature dependence of the barrier height (it descends slowly as the temperature approaches the values of $T = T_c$, at which the barrier disappears). A cubic temperature dependence is observed for barriers in all of the nuclei considered in the present study and is a general feature peculiar to the finite-range model of a hot liquid drop [16]. Barriers for symmetric binary fission that were calculated in [6], where diffuseness was simulated in terms of the "proximity" energy [32] and where the temperature dependence was constructed on the basis of data from [5], also have a cubic temperature dependence.

Following the same line of reasoning as Garcias et $al.$ [7] and employing the approximate relation (13),
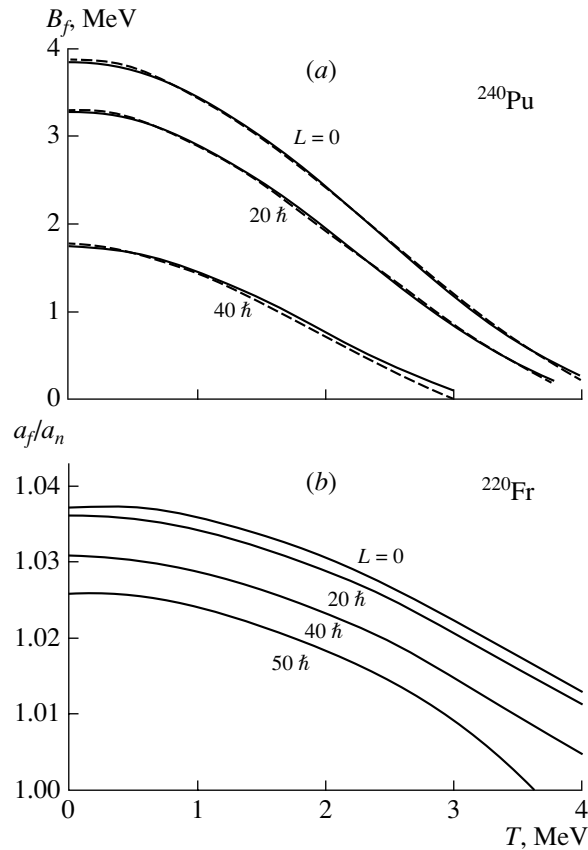
Fig. 5. (a) Fission barrier for ^{240}Pu as a function of the temperature and angular momentum of a compound nucleus: (solid curves) results of a theoretical calculation by formula (4) and (dashed curves) approximation by expression (13); (b) ratio a_f/a_n as a function of the temperature and angular momentum of the ^{220}Fr nucleus according to calculations by formulas (4), (8), and (9) for the saddle-point configuration and for the ground state of the nucleus.

we can conclude that temperature effects are only slightly correlated with nuclear-rotation effects (the term proportional to L^2T^2 is only a slight correction). The coefficients in the approximation are very close to the values obtained in [7], naturally with the exception of that term in (13) which is cubic in temperature. The fact that there is no such term in relation (2) from [7] may be due to the following: although the authors of [7] relied on the Thomas–Fermi method realized with an effective nucleon–nucleon interaction of the SkM^* type, they calculated the effective Weizsäcker coefficient ($\beta/36$) in the expansion in powers of $\hbar^2$ with the value of $\beta = 1.6$ rather than with the value of $\beta = 1$, which is usually used. A detailed discussion of the effect of this factor is beyond the scope of the present study. We note that a cubic character of the temperature dependence of the barrier height was also observed in [10], where use was made of the generalized liquid-drop model

due to Myers and Swiatecki [28] and the "proximity" energy (for details, see [10] and references therein). Although the fission barriers calculated in [10] are systematically higher than those that were obtained in the present study, their temperature and angular-momentum dependences are similar: with increasing angular momentum, the temperature effect becomes weaker.

The critical angular momentum L_{crit} characterizes the fission stability of a nucleus with respect to rotation [30]. Strictly speaking, this is the angular-momentum value at which the fission barrier in a compound nucleus vanishes. Since this feature is determined by the barrier height, which in turn decreases with increasing nuclear temperature, as we have seen above, L_{crit} must decrease as the nucleus being considered is heated. The critical angular momentum as a function of the mass number A for beta-stable nuclei is displayed in Fig. 6a for various values of the temperature. It seems quite natural that, at $T = 0$, the critical angular momentum determined in the present study is consistent with L_{crit} calculated by Sierk [18] on the basis of the finite-range liquid-drop model. Since L_{crit} only decreases upon taking into account nuclear temperature, there is no agreement, over the whole temperature range, with the critical-angular-momentum values calculated for superheavy elements within the macroscopic−microscopic approach proposed in [1] (see Table 3 in [1]). We obtained L_{crit} values close to zero even at zero temperature, while, at $T = 1.5$ MeV, L_{crit} [1] is about a few tens of $\hbar$ units (yet, these values were obtained with allowance for shell effects).

Our estimates of L_{crit} also fall systematically short of data reported in [10], where, with increasing mass number, the critical angular momentum decreases in the region of heavy nuclei faster than its counterpart calculated here. For the ^{190}Hg nucleus, we found agreement to within $1\hbar$ for L_{crit} with the results of Myers and Swiatecki [12], who employed the Thomas−Fermi formalism to calculate the barriers. A comparison with data from [7] reveals that, for ^{240}Pu, the values that we obtained for the critical angular momentum are systematically greater—for example, $62\hbar$ versus $50\hbar$ at zero temperature and $40\hbar$ versus $32\hbar$ at $T = 2$ MeV. However, this fact is not unexpected, highlighting the validity of our statement that it is necessary to consider simultaneously the effect of the temperature of a nucleus and the effect of its rotation on the static properties of a compound nuclear system. It is the difference in the character of the temperature dependence of the barriers (we obtained here a cubic dependence, which descends with increasing angular momentum, while it is quadratic in [7]) that is responsible for the difference in L_{crit}.

3.3. Effect of Temperature and Angular Momentum on the Saddle-Point Configuration of a Fissile Nucleus and on Features Depending on It

The saddle-point configuration of a fissile nucleus is the shape that this nucleus assumes at the saddle point. The saddle point determines the position of the fission barrier on the quasisurface that specifies the collective-coordinate dependence of the free energy of the nucleus being considered and is a point of conditional equilibrium (a maximum with respect to the main fission coordinate c and a minimum with respect to other coordinates). Accordingly, the barrier height is defined as the difference of the free energy at the saddle point and the minimum value of the free energy. In turn, the point of minimum specifies the coordinates of the ground state of the nucleus. In the case of the $\{c, h, \alpha'\}$ parametrization, which is used here, the position of the saddle point in the space of collective coordinates is determined by three quantities, c_{sd}, h_{sd}, and α'_{sd}. From the outset, we took zero value for the coordinate α'_{sd}, since it is well known that, within the model of a rotating liquid drop [18, 33], asymmetric shapes of a fissile nucleus are less favorable energetically for nuclei lying on the right of the Businaro−Gallone point (medium-mass and heavy nuclei), so that, for the saddle point, the profile of the free-energy surface along the coordinate α' has the shape of a parabola with a minimum at $\alpha' = 0$. For light nuclei (which lie on the left of the Businaro−Gallone point), the profile in question has, on the contrary, the shape of an inverted parabola with a maximum at $\alpha' = 0$. In this case, searches for a minimum in the mass-asymmetry coordinate involve the problem of grid finiteness in this coordinate. In order to circumvent this problem, we made the following "simplification" in our calculations: we set to zero the mass-asymmetry coordinate at the saddle point, α'_{sd}, for all nuclei studied here. This simplification is consistent with the experimentally observed fact that symmetric fission is dominant for hot nuclei [33].

On the basis of our calculations, we can draw the following conclusion: similarly to the case of a decrease in the barrier height, the position of the barrier is most strongly affected by temperature and angular momentum in the region of heavy nuclei; on the contrary, the lighter the nucleus, the weaker the effect of these two factors. By way of example, we indicate that, at any temperature considered here (not higher than 4 MeV), the saddle-point configuration of nuclei lighter than ^{122}Te is virtually independent of either a thermal or a rotational excitation. If, however, the temperature range is bounded from above by the value of 2 MeV, this effect is observed for nuclei lighter than ^{156}Gd. A similar pattern emerges in the case of
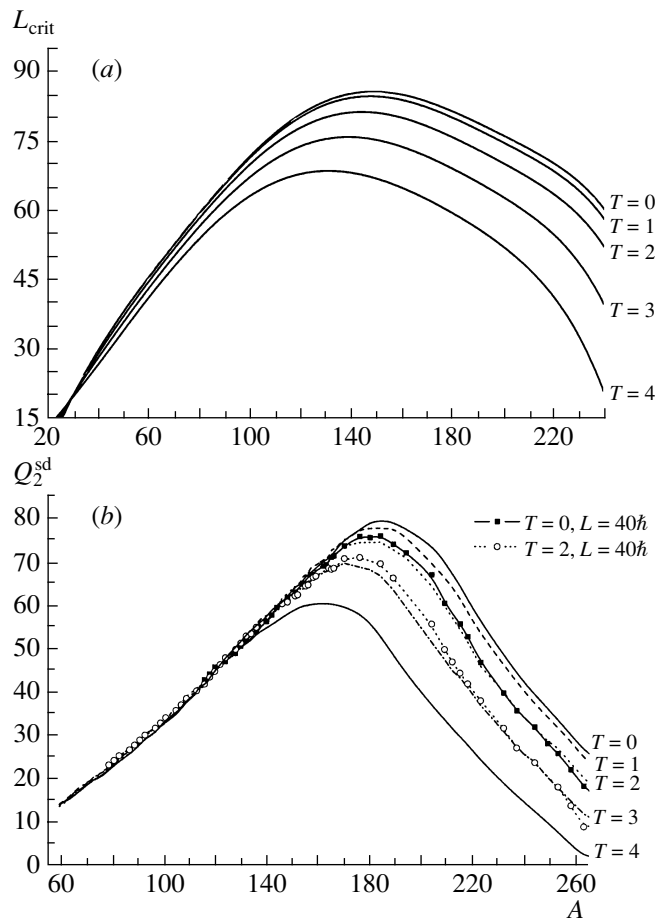
Fig. 6. (*a*) Critical angular momentum L_{crit} (in $\hbar$ units) as a function of the mass number A for beta-stable nuclei at various values of the temperature T (in MeV); (*b*) quadrupole moment in the saddle-point configuration of a nucleus, Q_2^{sd} (in barns), as a function of the mass number A for beta-stable nuclei at various values of the temperature.

varying the angular momentum at a constant temperature.

The above is illustrated in Fig. 6*b*, where the temperature dependence of the quadrupole moment in saddle-point configurations is shown for beta-stable nuclei. In order to compare the effect of rotation of a nucleus on the saddle-point configuration and the effect of its heating, curves drawn through boxes and circles are also displayed in Fig. 6*b*. They correspond to the saddle-point configurations of nuclei at the angular momentum of $L = 40\hbar$ and the temperatures of $T = 0$ and 2 MeV (solid and dashed curves, respectively). One can see that the heating of a non-rotating nucleus to a temperature of 2 MeV and the rotation of a cold nucleus at the angular momentum of $40\hbar$ lead to approximately identical saddle-point configurations of fissile beta-stable nuclei. Similar conclusions can also be drawn for the $T = 3$, $L = 0$ and $T = 2$, $L = 40\hbar$ cases. We note that the pattern observed here is in qualitative agreement with the results obtained in [2, 7].

It is impossible to compare directly the results of our calculations for saddle-point configurations with experimental data. However, this can be done indirectly via a comparison of nuclear-shape-dependent quantities at the barrier (such as the ratio of the level-density parameters at the barrier and in the ground state, a_f/a_n, and the effective moment of inertia at the barrier, J_{eff}).

The importance of the ratio a_f/a_n in a statistical simulation of fission reactions induced by heavy ions is well known [34, 35]. Governing neutron emission, as a matter of fact, this parameter determines, along with the barrier height, the fissility of a compound nucleus. The difference in a_f and a_n is a macroscopic effect, which is described within the liquid-drop model, the origin of this effect being related in theory to the effect of the nuclear surface and shape on the level density [24, 27]. Although the ratio a_f/a_n is close to unity, even a change of a few percent in it changes the ratio of the mean neutronic and fission
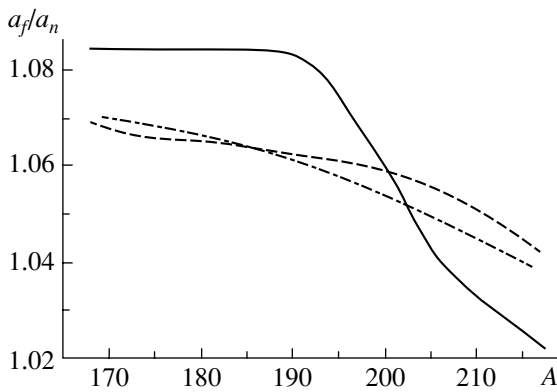
a_f/a_n

Fig. 7. Ratio a_f/a_n for preactinide nuclei along the beta-stability line: (solid curve) averaged empirical estimates from [37], (dashed curve) results based on relation (11) with Ignatyuk's coefficients [24], and (dash-dotted curve) results of our calculation (see main body of the text for the angular-momentum and temperature values at which we performed this calculation).

decay widths by a value that grows with increasing excitation energy [36].

The aforementioned effect of the change in the position of the saddle point in the space of collective variables in response to a change in the temperature and angular momentum naturally leads to a variation in the ratio a_f/a_n. Moreover, the conclusions on the character of the dependence of the barrier heights on T and L fully apply to the ratio a_f/a_n: it decreases both in response to an increase in the angular momentum and in response to an increase in the temperature (see, for example, Fig. 5b). Although this decrease is as small as about a few percent, it can substantially affect, as has already been mentioned, the results of statistical calculations for reactions involving the fission of compound nuclei. We note that the lighter the nucleus involved, the weaker the temperature dependence of a_f/a_n; on the contrary, it becomes more important to take into account nuclear rotation.

On the basis of an analysis of the fissility of compound preactinide nuclei bombarded with charged particles, Ignatyuk *et al.* [37] estimated the averaged empirical ratio a_f/a_n (the results are shown by the solid curve in Fig. 7). The dashed curve in this figure represents the ratio a_f/a_n calculated for preactinide nuclei on the basis of relation (11) with Ignatyuk's coefficients [24] without explicitly taking into account the temperature and angular-momentum dependences. The dash-dotted curve corresponds to our calculation for the same nucleus with allowance for the excitation energy (which specifies the nuclear temperature according to the relation $T = \sqrt{E_{\mathrm{int}}/a}$, where E_{int} is the internal energy of the nucleus

being considered) at an angular momentum fixed at $L = 20\hbar$ (this choice was motivated by the fact that, in the reactions being studied, the fission process is induced by light charged particles, so that the formation of a compound nucleus that would carry a high angular momentum is improbable). From Fig. 7, one can see that the results obtained within the above two theoretical approaches (dashed and dash-dotted curves) agree quite well, but that the two curves deviate markedly from the empirical dependence. According to [35], the scatter of the results of different theoretical analyses [24, 27] for the ratio a_f/a_n, as well as the scatter of its experimental values, may be as large as 15%. A large arbitrariness in describing the level density of excited nuclei in the studies of different authors may be one of the reasons for this uncertainty. By way of illustration, we indicate that, in [38], the ratio a_f/a_n changes in response to going over from one phenomenological systematics of level densities to another in analyzing the ratio of the fission and neutronic width.

The barrier heights and the ratios a_f/a_n determined by Krappe within the rotating-liquid-drop model generalized to the case of hot nuclei have not yet been used in statistical calculations. However, the study of Newton *et al.* [39], who calculated the mean prescission neutron multiplicity for ^{181}Ta $+ {}^{19}$F and ^{159}Tb $+ {}^{19}$F reactions on the basis of the statistical model, is worthy of note. In order to calculate the temperature-dependent barrier heights, use was made of data from [7, 8], while the parameter a_f/a_n was adjusted to fit the fission cross sections calculated for the above two reaction types to their experimental counterparts. Also, the a_f/a_n value at which the agreement with experimental data on neutron multiplicities is good was estimated in [39], but use was made there of the barriers that were calculated by the Thomas–Fermi method [3, 4] and which are actually equivalent to the barriers determined within the model considered here. The value of $a_f/a_n = 0.97$, which was obtained by using the barriers from [7, 8], proves to be less than its counterpart in the case of the barriers from [3, 4] ($a_f/a_n = 1.00$). So small a value, which is less than unity, is at odds with some results obtained in a number of studies [24, 35–37], where a statistical description of level densities in nuclei led to $a_f/a_n > 1$. In view of this, the self-consistency of the calculations employing the barriers from [3, 4] and resulting in a greater value of a_f/a_n is less disputable. The problem of consistency of the model concepts and arbitrariness in choosing the ratio a_f/a_n can be fully solved by employing barriers and level-density-parameter ratios (a_f/a_n) determined within a unified model—for example, that which was considered in the present study.
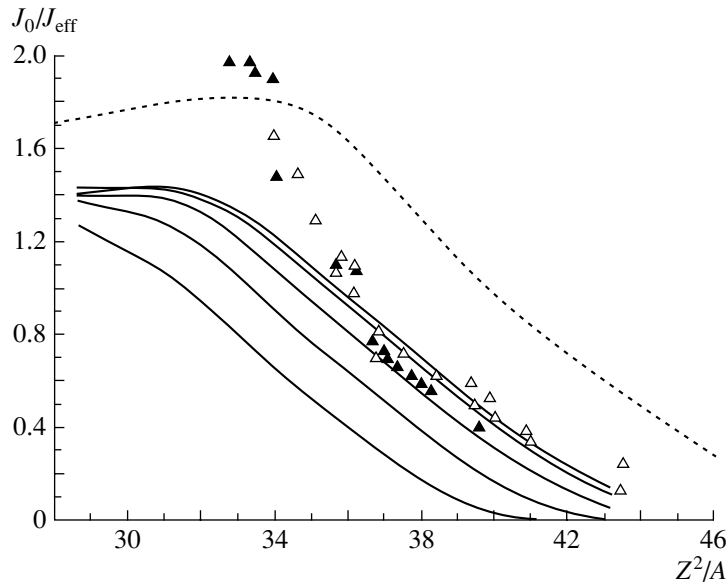
Fig. 8. Inverse effective moments of inertia J_{eff}^{-1} for nuclei along the beta-stability line: (solid curves) results of Krappe's calculation [16] within the temperature-dependent macroscopic finite-range liquid-drop model [at the temperature values of 0, 1, 2, 3, and 4 MeV (from up down), the angular momentum being set to zero], (dotted curve) results of the calculation on the basis of the rotating-liquid-drop model due to Cohen, Plasil, and Swiatecki [30], and (points) J_{eff}^{-1} values obtained from an analysis of experimental data on the angular anisotropy of fission fragments: (open triangles) experimental data on heavy-ion reactions [40] and (closed triangles) results of an experimental analysis from [41].

The effective moment of inertia J_{eff} at the saddle point is yet another feature that is determined by the position of the barrier. The inverse of J_{eff} is given by

$$\frac{1}{J_{\text{eff}}} = \frac{1}{J_{\parallel}} - \frac{1}{J_{\perp}}, \qquad (14)$$

where $J_{\parallel}$ and $J_{\perp}$ are the moments of inertia of the nucleus under consideration with respect to the symmetry axis and the axis orthogonal to it (nuclear-rotation axis), correspondingly. As a rule, the effective moment of inertia is measured in units of J_0, which is the moment of inertia of a sphere of the same volume.

The experimental value of the effective moment of inertia can be obtained from an analysis of the anisotropy of the angular distribution of fission fragments. This was precisely the method that was used calculate the J_{eff}^{-1} values represented by closed and open triangles in Fig. 8. This figure displays the fissility-parameter dependence of J_{eff} for nuclei along the beta-stability line. The effective moments of inertia calculated here on the basis of the Krappe model [16] for various values of the temperature are shown by the solid curves in the figure. The dotted curve, which represents the results of the calculations based on the model of a liquid drop with a sharp surface [30], lies markedly higher. The curve calculated with the Sierk coefficients [18] coincides with the solid curve, which corresponds to the temperature value of $T = 0$. This comes as no surprise since the positions of the saddle points coincide in these models at zero temperature, while the moments of inertia are calculated in the rigid-body approximation. From Fig. 8, one can see that the experimental data being considered are in better agreement with the results of our calculations, while, for $Z^2/A < 36$, the J_{eff}^{-1} values obtained from the analysis of experimental data lie considerably higher than the curves that we obtained and comply better with the Cohen–Plasil–Swiatecki model [30]. The existence of experimental points below the solid curve, which corresponds to zero temperature ($T = 0$) is worthy of special note: if one considers that, within the model used here, an increase in the angular momentum of a nucleus at fixed temperature also leads to a decrease in J_{eff}^{-1}, the experimental values are reproduced at specific values of T and L, this counting in favor of the model that we apply, which takes into account the temperature dependence of relevant parameters.

The analysis of experimental data that was performed in [40, 41] and which is illustrated in Fig. 8 did not take into account the emission of prescission neutrons. This shortcoming was remedied in [42], where the data are given with allowance for prefission neutrons. However, these corrected data do not change the conclusions that we have drawn above. Anyway, overall agreement between a theoretical description and experimental data could not be achieved. The model used here is more realistic than the idealized

Cohen−Plasil−Swiatecki model of a liquid drop with a sharp surface [30] and takes into account the temperature dependence of the liquid-drop parameters. As was indicated in [43], the quantitative disagreement may be due both to an approximate character of the Halpern−Strutinsky statistical theory of angular-distribution formation [44] and to the uncertainty in some parameters used in analyzing experimental data (for example, a variation in the level-density parameter in [41]).

By calculating the effective moment of inertia, one can determine, for the ratio (Z^2/A), the critical value $(Z^2/A)_{\text{crit}}$ at which a nucleus loses stability with respect to fission, this being a parameter of paramount importance for nuclear physics. For nuclei characterized by this value of (Z^2/A), the saddle-point deformation coincides with that in the ground state and $J_{\text{eff}} \to \infty$, the ratio J_0/J_{eff} tending to zero. Within the model considered here, $(Z^2/A)_{\text{crit}}$ develops a temperature and an angular-momentum dependence, as all of the other static parameters that we explored in this study do. This circumstance becomes obvious if one recalls that the parameter $(Z^2/A)_{\text{crit}}$ is determined in terms of the ratio of the surface and Coulomb constants of the liquid-drop model, a_s and a_C, which depend explicitly on temperature in the model being considered; as to the angular momentum, its effect is due to the shift of the saddle point, at which we calculate J_{eff}^{-1}. An excitation of a nucleus (both of a thermal and a rotational character) leads to a shift of $(Z^2/A)_{\text{crit}}$ toward the region of lighter nuclei, the effect of the two factors being approximately identical. By way of example, we indicate that, at zero temperature, the change in temperature from 0 to 4 MeV leads to the reduction of $(Z^2/A)_{\text{crit}}$ from 44.5 to 40.5; at zero temperature, approximately the same values correspond to a variation in the angular momentum from $L = 0$ to $L = 60\hbar$. The value that we obtained at $T = 0$ is in good agreement with the predictions of other realistic liquid-drop models [18, 45]. The experimental estimates obtained in [41] for $(Z^2/A)_{\text{crit}}$ on the basis of determining J_{eff} from an analysis of the angular anisotropies of fission fragments are different for different sets of nuclei and for different values of the nuclear-level-density parameter that were used in that analysis. The estimate $(Z^2/A)_{\text{crit}} = 44.3−44.9$ [41], which is in good agreement with the results of our calculations and which is markedly less than the value of $(Z^2/A)_{\text{crit}} \simeq 50$, predicted by the model of a liquid drop with a sharp surface, seems the most plausible.

3.4. Stiffness with Respect to a Mass-Asymmetry Variation in the Nuclear Shape within the Model of Hot Rotating Nuclei

In the fission of $Z^2/A < 32$ nuclei whose rotation is not very fast (low values of L), the "dynamics of motion" of a nucleus from the saddle to the scission point does not play any significant role [46]. In this case, the static properties of the potential-energy surface of a deformed nucleus play the most important role in a theoretical analysis of the fission process. In describing the potential energy within the liquid-drop model, the stiffness (stability) of nuclei with respect to mass-asymmetric deformations (shape variations), $\partial^2 V/\partial \eta^2$ [46], is one of the main parameters.

For the mass-asymmetry coordinate η, we followed Strutinsky's definition [45]

$$\eta = 2 \frac{V_{\text{l}} - V_{\text{r}}}{V_{\text{l}} + V_{\text{r}}}, \qquad (15)$$

where V_{l} and V_{r} are the volumes of those parts of the asymmetric body representing the nucleus being considered that are, respectively, on the left and on the right of the midpoint of the neck. It was indicated above that, in our calculations, we used the parameter α' for the coordinate describing the mass asymmetry of the nucleus; therefore, we calculated the stiffness by the formula

$$\frac{\partial^2 F}{\partial \eta^2} = \frac{\partial^2 F}{\partial \alpha'^2} \left(\frac{\partial \alpha'}{\partial \eta} \right)^2. \qquad (16)$$

We calculated the second factor in this formula by employing Eq. (15) and the expressions chosen for the volumes V_{l} and V_{r} of the left- and right-hand parts in accordance with the parametrization being considered.

On the basis of the liquid-drop model involving temperature-dependent parameters, we calculated here stiffness for hot nuclei, employing the free energy F instead of the potential energy V. This enables us to assess the effect of temperature on the magnitude of stiffness for the case of mass-asymmetric deformations and on the critical points of the stiffness curve. The results are presented in Fig. 9. In this figure, the experimental data are given only for the region $Z^2/A < 31$, since, for $Z^2/A > 32$ nuclei, the saddle and scission points differ significantly, as was indicated in [46, 47], while the experimental values of the stiffness for them lie higher, corresponding to some point that is intermediate between the saddle and scission points. This range of nuclei will not be considered in the present analysis.

In [46−48], it was indicated that, in the interval $Z^2/A \sim 20−30$, the finite-range liquid-drop model involving Sierk's coefficients provides the best description of experimental data. In those studies, the
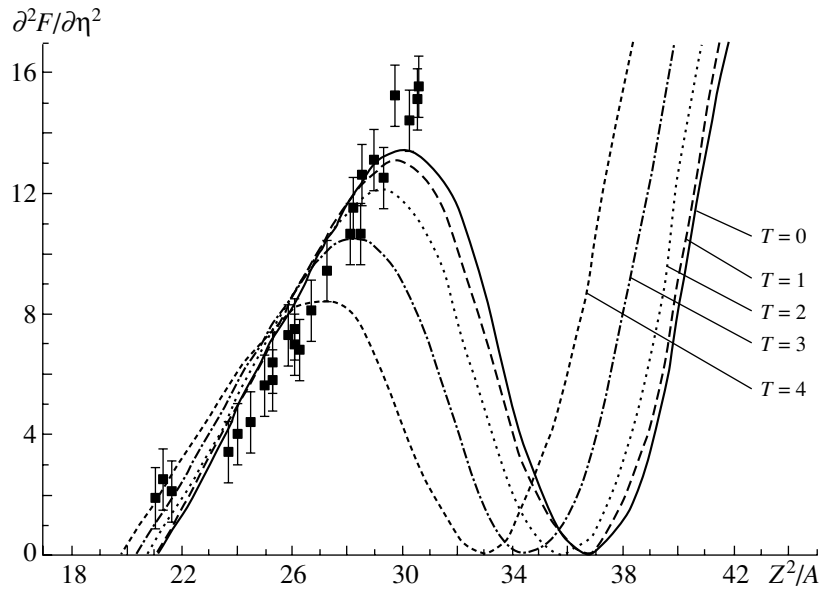
Fig. 9. Stiffness of fissile nuclei at the saddle point, $\partial^2 F/\partial\eta^2$ (in MeV), for nuclei along the beta-stability line at various values of the temperature T (in MeV). Boxes represent the results obtained by analyzing experimental data from [48].

position of the Businaro–Gallone point, where a nucleus completely loses stability against a mass-asymmetric deformation (the stiffness vanishes), was determined to be $(Z^2/A)_{\rm BG} = 22.0 \pm 0.6$. It should be noted that the theoretical curves calculated in [46–48] were obtained with the set of coefficients from [17] rather than with the set of constants proposed by Sierk in [18]. Our results at zero temperature agree with the results obtained on the basis of the Sierk model with the constants from [18]. The value of $(Z^2/A)_{\rm BG} = 21.1$, which was found in the present study, depends greatly on the set of constants used. For example, $(Z^2/A)_{\rm BG} = 21.6$ if use is made of the parameter set from [17]. This is less than the estimate 22 ± 0.6 from [46–48], but the difference is likely to be due to employing different nuclear-shape parametrizations in the respective calculations (generalized Cassini ovals in [49] versus the $\{c, h, \alpha'\}$ parametrization in the present study). For a more detailed discussion of all uncertainties associated with the analysis of experimental data and with the calculation of the stiffness on the basis of these data in [46–48], the interested reader is referred to [47].

From Fig. 9, one can see that an increase in the temperature leads to a shift of the Businaro–Gallone point toward the region of lighter nuclei, with the result that, at $T = 4$ MeV, $(Z^2/A)_{\rm BG} = 19.8$. Similar behavior was obtained in [31] within the model of a rotating liquid drop with allowance for "proximity" forces [32]. It was also found there that, up to the temperature of 2 MeV, the position of the Businaro–Gallone point remains unchanged on the fissility axis

x ($x = (Z^2/A)/(Z^2/A)_{\rm crit}$). We will arrive at the same conclusion if, in calculating the fissility parameter x, we take into account the temperature dependence of $(Z^2/A)_{\rm crit}$ described in the preceding section. However, it is worth noting that, within the model being considered, the decrease in $(Z^2/A)_{\rm crit}$ with increasing temperature is faster than the decrease in $(Z^2/A)_{\rm BG}$, since, as the temperature increases from $T = 2$ to 4 MeV, the position of the Businaro–Gallone point on the fissility axis, $x_{\rm BG}$, changes from 0.47 to 0.49. But in [31], the situation was qualitatively different: an increase in the temperature there led to a sizable decrease in $x_{\rm BG}$.

A second critical point on the curve of the stiffness with respect to mass-asymmetric nuclear-shape variations is the point of maximum; at $T = 0$, it occurs at $Z^2/A \sim 30$ (see Fig. 9). As was found in [47, 48], this point of inflection on the curve of the stiffness plotted against Z^2/A corresponds to a change in the sign of the derivative $d\sigma_M^2/dL^2$—this means that, with increasing angular momentum, the variance of the mass distribution decreases for nuclei characterized by Z^2/A values on the left of this point and increases for nuclei characterized by Z^2/A values on the right of it. Figure 9 clearly shows that, as the temperature is elevated from 0 to 4 MeV, the position of the maximum is shifted from $Z^2/A \sim 30$ to 27.

The effect of the angular momentum on the stiffness with respect to mass-asymmetric nuclear-shape variations was studied in detail by Rusanov *et al.* [46]. Their conclusions that the Businaro–Gallone point

and the point of maximum are shifted toward the region of light nuclei, this corresponding to an effective increase in the masses of nuclei, also apply to the results obtained within the model being considered. This comes as no surprise since the potential energy of a rotating drop was calculated in [46] on the basis of the Sierk model [18], which is equivalent to the zero-temperature Krappe model, which was used here. Analyzing and comparing the results obtained in [46] and in the present study, we would like to emphasize that the rotation of a nucleus has a substantially stronger effect than temperature on the position of the Businaro—Gallone point. This was also observed in [47, 48] in analyzing experimentally determined stiffnesses.

4. SUMMARY AND OUTLOOK

In calculating static and statistical properties of hot nuclei, we have applied the temperature-dependent macroscopic model that takes into account nuclear forces of finite range.

The main coefficients of the model that were obtained by Krappe [16] on the basis of approximating the results of calculations within the microscopic Thomas—Fermi method feature an explicit temperature dependence. Within a unified approach, we have therefore been able to calculate self-consistently both fission barriers and level-density parameters. The importance of this self-consistency was previously highlighted in [19]. By relying on the temperature-dependent finite-range liquid-drop model, we have approximated the level-density parameter by a leptodermous-type equation. The values that we have obtained for the coefficients, $a_v = 0.0598\ \text{MeV}^{-1}$ and $a_s = 0.1218\ \text{MeV}^{-1}$, agree well with the coefficients obtained in [24]. These coefficient values can be of use both in a statistical and in a dynamical simulation of the fission process on the basis of the finite-range liquid-drop model.

By way of example, we have calculated barrier heights in nuclei and have determined their saddle-point configurations and ratios a_f/a_n. From these examples, it is obvious that, in theoretically describing heavy-ion fusion—fission reactions (where the aforementioned parameters play a crucial role), it is necessary to take into account the effect of both the temperature and the rotation of a nascent compound nuclear system. In the majority of cases, the effect of the angular momentum proves to be more sizable, but it weakens with increasing temperature.

As matter of fact, the liquid-drop-model version used here, which involves the coefficients that were determined on the basis of microscopic calculations, remains macroscopic. Its applicability range, as well as the applicability range of any other macroscopic

version of the liquid-drop model, embraces nuclei heated to such an extent that single-particle pairing and shell effects can be disregarded. For superheavy nuclei, shell corrections play a significant role; therefore, the liquid-drop-model version due to Krappe is inapplicable to such nuclei. The model that we have considered here does not reproduce the results obtained in [1]: for superheavy elements, there are no stable states characterized by a relatively high temperature and high angular momenta.

The results that we have obtained here for the effective moments of inertia at the saddle point are in good agreement with experimental estimates only for $Z^2/A > 36$ nuclei. For $Z^2/A \sim 33$—34 nuclei, the model of a liquid drop with a sharp surface leads to better agreement. However, the parameter $(Z^2/A)_{\text{crit}}$ extracted from information about J_{eff} within the model of a liquid drop with a sharp surface appears to be $(Z^2/A)_{\text{crit}} \sim 50$, which is markedly larger than experimental estimates, 44.3—44.9, which, in turn, are well reproduced by the temperature-dependent finite-range liquid-drop model that was generalized by Krappe and which has been used in the present study.

In calculating the stiffness of nuclei, we have focused our attention primarily on temperature effects. With increasing temperature, the Businaro—Gallone point is shifted toward the region of light nuclei on the Z^2/A axis, this corresponding to the results reported in [31]. As in [31], the increase in the temperature from 0 to 2 MeV does not change the position of the Businaro—Gallone point on the x axis, but, in contrast to the results of Haddad and Royer [31], a further increase in the temperature leads, in our case, to an increase in $x_{\text{BG}} = (Z^2/A)_{\text{BG}}/(Z^2/A)_{\text{crit}}$, this being due to a faster decrease in the parameter $(Z^2/A)_{\text{crit}}$ with increasing temperature. This circumstance confirms once again the importance of consistently applying nuclear models in theoretical calculations.

Summarizing the aforesaid, we emphasize that, even within the best (at least at the present time) version of the liquid-drop model, one can hardly reproduce experimental data over the whole range of mass numbers. In view of this, our present conclusions concerning the simultaneous effect of an increase in the temperature and angular momentum of a fissile nucleus are only qualitative. In order to perform a more detailed quantitative comparison with experimental data, one needs dynamical calculations that would employ the temperature-dependent macroscopic model featuring finite-range nuclear forces that has been studied here. That the application of this model in our future dynamical calculations would be quite straightforward explains our attention to it and partly justifies the qualitative

character of the results that we obtained for the static and statistical features of fissile nuclei.

REFERENCES

1. M. Diebel, K. Albrecht, and R. Hasse, Nucl. Phys. A **355**, 66 (1981).
2. M. Pi, X. Viñas, and M. Barranco, Phys. Rev. C **26** (2), 733 (1982).
3. M. Brack, C. Guet, and H. B. Håkansson, Phys. Rep. **123**, 275 (1985).
4. C. Guet, E. Strumberger, and M. Brack, Phys. Lett. B **205**, 427 (1988).
5. H. R. Jaqaman, Phys. Rev. C **40**, 1677 (1989).
6. G. X. Dai, J. B. Natowitz, R. Wada, *et al.*, Nucl. Phys. A **568**, 601 (1994).
7. F. Garcias, M. Barranco, H. S. Wio, *et al.*, Phys. Rev. C **40**, 1522 (1989).
8. F. Garcias, M. Barranco, J. Nemeth, *et al.*, Nucl. Phys. A **495**, 169 (1989).
9. J. Bartel and P. Quentin, Phys. Lett. B **152B**, 29 (1985).
10. G. Royer and J. Mignen, J. Phys. G **18**, 1781 (1992).
11. J. Bartel, K. Mahboub, J. Richert, and K. Pomorski, Z. Phys. A **354**, 59 (1996).
12. W. D. Myers and W. J. Swiatecki, Nucl. Phys. A **601**, 141 (1996).
13. P. Ring, Prog. Part. Nucl. Phys. **37**, 193 (1996).
14. B. Nerlo-Pomorska, K. Pomorski, J. Bartel, and K. Dietrich, Phys. Rev. C **66**, 051302 (2002).
15. B. M. Strutinsky, Nucl. Phys. A **95**, 420 (1967); **122**, 1 (1968).
16. H. J. Krappe, Phys. Rev. C **59**, 2640 (1999).
17. H. J. Krappe, J. R. Nix, and A. J. Sierk, Phys. Rev. C **20**, 992 (1979).
18. A. J. Sierk, Phys. Rev. C **33**, 2039 (1986).
19. A. V. Karpov, P. N. Nadtochy, E. G. Ryabov, and G. D. Adeev, J. Phys. G **29**, 2365 (2003).
20. P. Fröbrich and I. I. Gontchar, Phys. Rep. **292**, 131 (1998).
21. M. Brack, J. Damgaard, A. S. Jensen, *et al.*, Rev. Mod. Phys. **44**, 320 (1972).
22. A. Mamdouh, J. M. Pearson, M. Rayet, and F. Tondeur, Nucl. Phys. A **644**, 389 (1998).
23. A. V. Karpov, P. N. Nadtochy, D. V. Vanin, and G. D. Adeev, Phys. Rev. C **63**, 054610 (2001).
24. A. V. Ignatyuk, M. G. Itkis, V. N. Okolovich, *et al.*, Yad. Fiz. **21**, 1185 (1975) [Sov. J. Nucl. Phys. **21**, 616 (1975)].
25. A. V. Ignatyuk, *Statistical Properties of Excited Nuclei* (Énergoatomizdat, Moscow, 1983).
26. R. Balian and C. Bloch, Ann. Phys. (N.Y.) **60**, 401 (1970).
27. J. Töke and W. J. Swiatecki, Nucl. Phys. A **372**, 141 (1981).
28. W. D. Myers and W. J. Swiatecki, Ark. Fys. **36**, 343 (1967).
29. A. E. S. Green, *Nuclear Physics* (McGraw-Hill, New York, 1985), p. 185.
30. S. Cohen, F. Plasil, and W. J. Swiatecki, Ann. Phys. (N.Y.) **82**, 557 (1974).
31. F. Haddad and G. Royer, J. Phys. G **21**, 1357 (1995).
32. J. Blocki, J. Randrup, W. J. Swiatecki, and C. F. Tsang, Ann. Phys. (N.Y.) **105**, 427 (1977).
33. M. G. Itkis, V. N. Okolovich, A. Ya. Rusanov, and G. N. Smirenkin, Fiz. Élem. Chastits At. Yadra **19**, 701 (1988) [Sov. J. Part. Nucl. **19**, 301 (1988)].
34. J. O. Newton, Fiz. Élem. Chastits At. Yadra **21**, 821 (1990) [Sov. J. Part. Nucl. **21**, 349 (1990)].
35. E. M. Rastopchin, Yu. B. Ostapenko, M. I. Svirin, and G. N. Smirenkin, Yad. Fiz. **49**, 24 (1989) [Sov. J. Nucl. Phys. **49**, 15 (1989)].
36. G. A. Pik-Pichak, *Physics of Nuclear Fission* (Gosatomizdat, Moscow, 1962) [in Russian].
37. A. V. Ignatyuk, G. N. Smirenkin, M. G. Itkis, *et al.*, Fiz. Élem. Chastits At. Yadra **16**, 709 (1985) [Sov. J. Part. Nucl. **16**, 307 (1985)].
38. A. S. Iljinov, M. V. Mebel, *et al.*, Nucl. Phys. A **543**, 517 (1992).
39. J. O. Newton, D. G. Popescu, and J. R. Leigh, Phys. Rev. C **42**, 1772 (1990).
40. S. A. Karamyan, I. V. Kuznetsov, Yu. A. Muzychka, *et al.*, Yad. Fiz. **6**, 494 (1966) [Sov. J. Nucl. Phys. **6**, 360 (1967)].
41. R. F. Reising, G. L. Bate, and J. R. Huizenga, Phys. Rev. **141** (3), 1161 (1966).
42. W. U. Schröder and J. R. Huizenga, Nucl. Phys. A **502**, 473c (1989).
43. Yu. Ts. Oganessian and Yu. A. Lazarev, in *Treatise on Heavy Ion Science*, Ed. by D. A. Bromley (Plenum, New York, 1985), Vol. 4, p. 1.
44. I. Halpern and V. M. Strutinsky, in *Proceedings of the Second United Nations International Conference on the Peaceful Uses of Atomic Energy, Geneva, Switzerland, 1957* (United Nations, Geneva, 1958), p. 408.
45. V. M. Strutinskiǐ, Zh. Éksp. Teor. Fiz. **45**, 1891 (1963) [Sov. Phys. JETP **18**, 1298 (1963)].
46. A. Ya. Rusanov, V. V. Pashkevich, and M. G. Itkis, Yad. Fiz. **62**, 595 (1999) [Phys. At. Nucl. **62**, 547 (1999)].
47. M. G. Itkis and A. Ya. Rusanov, Fiz. Élem. Chastits At. Yadra **29**, 389 (1998) [Phys. Part. Nucl. **29**, 160 (1998)].
48. M. G. Itkis, Yu. A. Muzychka, Yu. Ts. Oganessian, *et al.*, Yad. Fiz. **58**, 2140 (1995) [Phys. At. Nucl. **58**, 2026 (1995)].
49. V. V. Pashkevich, Nucl. Phys. A **169**, 275 (1971).

Translated by A. Isaakyan

NUCLEI
Theory

Interaction of Gold Nuclei with Photoemulsion Nuclei at Energies in the Range 100−1200 MeV per Nucleon and Cascade−Evaporation Model

S. D. Bogdanov[1], E. Ya. Shablya[1]*, S. Vokal[2], V. F. Kosmach[1], and V. A. Plyuschev[3]

Received September 9, 2004; in final form, March 10, 2005

Abstract—The interaction of gold nuclei with photoemulsion nuclei at energies in the range 100−1200 MeV per nucleon was studied experimentally. A consistent comparison of the experimental data obtained in this way with the results of the calculations based on the cascade−evaporation model is performed. © *2005 Pleiades Publishing, Inc.*

INTRODUCTION

On the basis of the nuclear-photoemulsion method, the propagation of heavy (gold) nuclei through a homogeneous medium is studied here under conditions of a complete experiment in the energy range 100−1200 MeV per nucleon. Also, the features of the interactions between ^{197}Au nuclei and photoemulsion nuclei are calculated within the cascade−evaporation model [1], this including an analysis of the multiplicities of secondary particles versus the basic properties of the process. Further, our experimental data are compared with the results of the calculations.

A similar investigation of the applicability of the cascade−evaporation model to describing the interactions of lighter nuclei (Ne, Ar, Fe) with photoemulsion nuclei in the same energy range was previously performed in [2−5].

EXPERIMENT AND CALCULATIONS

In order to obtain quantitative results, we employed a photoemulsion chamber formed by 34 layers of BR-2 photoemulsion having a standard composition (3.148×10^{22} H, 1.412×10^{22} C, 0.396×10^{22} N, 0.956×10^{22} O, 0.004×10^{22} S, 0.002×10^{22} I, 1.031×10^{22} Br, and 1.036×10^{22} Ag nuclei per 1 cm^3). The dimensions of each layer were close to $10 \times 10 \times 0.05$ cm^3. The chamber was irradiated with

^{197}Au nuclei accelerated at the Bevalac accelerator (Berkeley, USA) to an energy of 1147.2 MeV per nucleon. In the irradiation, the mean fluence ranged between 500 and 2000 particles per 1 cm^2. The details of the development and primary treatment of the results obtained in the chamber are given elsewhere [6, 7].

By using the method of fast and slow scanning, 1122 tracks were traced from their entrance into the emulsion to their stop or interaction. As a result, 585 interactions of ^{197}Au nuclei over the energy range 0−1147 MeV per nucleon were found over a length of 30 m. Among these, we processed 332 inelastic interactions of ^{197}Au nuclei whose mean energy ranged between 100 and 1147 MeV per nucleon. The procedure employed here to process interactions was described in [8, 9]. In processing data on projectile disintegration, we were able to determine the charges of all projectile fragments and their polar and azimuthal emission angles.

For a sample comprising 108 inelastic interactions of ^{197}Au nuclei whose mean energy fell within the range 741.2 ± 19.8 MeV per nucleon, we measured the production angles, ionization losses, and free paths of all charged secondaries (the sample included 4444 particles).

In addition, we processed 173 nonrelativistic interactions of ^{197}Au nuclei where the atomic number of a fragment in excess of 20 was determined by the residual free path of the fragment [8], measurements for other charged particles not being performed.

The calculated statistical sample was obtained by generating the interactions between ^{197}Au nuclei of energy 700 MeV per nucleon and individual emulsion nuclei (^{1}H, ^{12}C, ^{14}N, ^{16}O, ^{80}Br, ^{107}Ag) on the basis of the Monte Carlo method and by subsequently performing summation with weights corresponding

---

[1] St. Petersburg State Polytechnical University, Politekhnicheskaya ul. 29, St. Petersburg, 195251 Russia.
[2] Joint Institute for Nuclear Research, Dubna, Moscow oblast, 141980 Russia; University of P.J. Šafárik, Jesenná 5, SK-041 54 Košice, Slovak Republic.
[3] Khlopin Radium Institute, Vtoroĭ Murinskiĭ pr. 28, St. Petersburg, 194021 Russia.
*e-mail: `shey79@mail.ru`

to the calculated cross sections and the composition of the emulsion. In doing this, we took into account meson-production processes, a Lorentz contraction, and the effect of the Pauli exclusion principle at the fast (first) stage and the effect exerted by the change in the nuclear-matter density in the course of cascade propagation. The deexcitation of nuclear residues after the completion of the fast stage (the second stage, which is slow) is described on the basis of the statistical model. The total statistical sample obtained within the cascade−evaporation model comprised 1000 events.

INELASTIC-INTERACTION FREE PATHS OF ^{197}Au NUCLEI

On the basis of our experimental measurements, inelastic-interaction free paths of ^{197}Au nuclei in BR-2 nuclear photoemulsion were determined in the energy ranges 100−400, 400−900, 900−1200, and 100−1200 MeV per nucleon. The results obtained in this way are given in Fig. 1. Also shown in this figure are experimental results reported in [10], where Ilford-G5 emulsions and ^{197}Au nuclei were used for targets and projectiles, respectively.

Among a great variety of models for calculating cross sections for inelastic nucleus−nucleus interactions, we choose the Karol model [11] and the Bradt−Peters model [12], according to which we calculated the cross sections for the interaction of photoemulsion nuclei with ^{197}Au nuclei and the corresponding inelastic-interaction free paths for BR-2 photoemulsion in the energy range between 100 and 1200 MeV per nucleon. In this calculation, we took into account the change in the energy of the nuclei as they traverse emulsion layers and the corresponding change in the mean cross section for nucleon−nucleon interactions.

From the experimental data and from the results of the calculations (see Fig. 1), it follows that, although the cross sections for nucleon−nucleon interactions exhibit a pronounced energy dependence in the energy range being considered, the inelastic-interaction free paths of ^{197}Au nuclei in a nuclear photoemulsion are rather weakly dependent on the projectile energy. The experimental data obtained here and in [10] prove to be quite close to each other if one takes into account the distinctions between the composition and densities of BR-2 and Ilford-G5 emulsions. The calculations lead to larger cross sections for the interactions of gold nuclei and, consequently, to shorter free paths. The observed discrepancies between the calculated and measured results may be due to missing few-prong events in the experiments or to employing inaccurate values of adjustable parameters in the above models or to both of these factors.
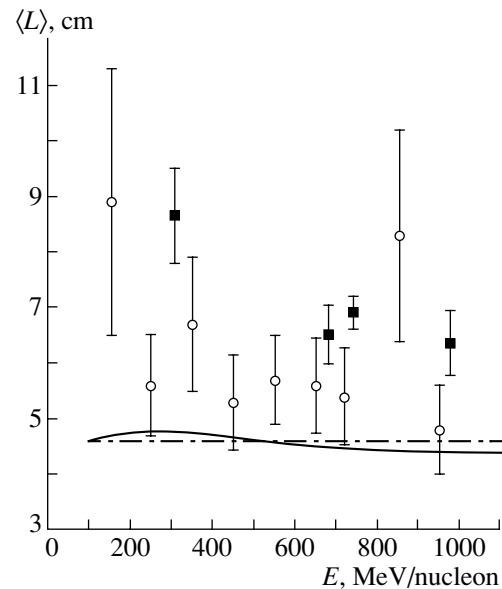
Fig. 1. Inelastic-interaction mean free paths $\langle L \rangle$ of ^{197}Au nuclei in emulsion versus the projectile energy E: (closed boxes) our present experimental data, (open circles) experimental data from [10], (solid curve) results of the calculation based on the model proposed in [11], and (dash-dotted line) results of the calculation within the model considered in [12].

MULTIPLICITIES OF SECONDARY PARTICLES

For a further analysis of our data, all secondaries were partitioned into the following groups:

(i) the group of $(g + s)$ particles defined as first-stage particles, which comprise singly charged target fragments of energy $E \geq 26$ MeV per nucleon, product mesons, and singly charged projectile fragments whose transverse momentum exceeds 222.6 MeV/c (this corresponds to $E \geq 26$ MeV per nucleon in the transverse direction);

(ii) the group of b particles defined as target fragments of energy in the range $E \leq 26$ MeV per nucleon (their free path is shorter than 3 mm), which are emitted predominantly at the second reaction stage;

(iii) the group of $(s' + g' + b')$ particles having energies in the region $E \geq 26$ MeV per nucleon and transverse momenta below 222.6 MeV/c per nucleon, this group including singly (s'), doubly (g'), and multiply (b', $Z \geq 3$) charged projectile fragments.

In each interaction event, we determined the multiplicities of particles belonging to the above groups, the total number N of charged secondaries, and their total charge $Z_{\text{int.ch.}}$ (in electron-charge units). This made it possible to obtain particle-number distributions in disintegration events induced by gold ions of energy 0.741 GeV per nucleon and correlations

Table 1. Multiplicity (in number of particles per interaction event) of charged secondaries produced in the interactions between ^{197}Au nuclei of mean energy 0.741 GeV per nucleon and photoemulsion nuclei

Interaction type	$\langle N_{g+s} \rangle$	$\langle N_b \rangle$	$\langle N_{s'+g'+b'} \rangle$	$\langle N \rangle$	$\langle Z_{\text{int.ch.}} \rangle$
^{197}Au + Em	21.71 ± 0.45	3.24 ± 0.17	16.24 ± 0.39	41.19 ± 0.62	91.97 ± 0.92
	(19.06)	(3.94)	(13.04)	(36.03)	(95.08)
^{197}Au + H	0.82 ± 0.27	0.09 ± 0.09	6.27 ± 0.76	7.18 ± 0.81	80.00 ± 2.69
	(1.34)	(0.02)	(4.14)	(5.49)	(80.02)
^{197}Au + CNO	13.39 ± 0.57	0.49 ± 0.11	20.51 ± 0.71	34.39 ± 0.92	82.51 ± 1.42
	(10.74)	(1.75)	(15.26)	(27.75)	(87.56)
^{197}Au + AgBr	31.91 ± 0.76	5.88 ± 0.32	15.07 ± 0.52	52.86 ± 0.97	101.25 ± 1.34
	(35.52)	(7.85)	(16.33)	(59.70)	(118.40)

between the numbers of different-type particles in an interaction event.

Table 1 gives the mean multiplicities of secondary particles, $\langle N_{g+s} \rangle$, $\langle N_b \rangle$, and $\langle N_{s'+g'+b'} \rangle$, and the mean multiplicity of all charged secondaries, $\langle N \rangle$, in the interactions of nuclei having various masses and energies, as well as the mean value of the total charge in an interaction event, $\langle Z_{\text{int.ch.}} \rangle$. We note that the statistical errors in the values calculated on the basis of the cascade–evaporation model (these values are given in parentheses) are approximately three times less than the experimental errors; therefore, they are not presented here.

From Table 1 and from the data obtained previously for the interactions of lighter nuclei (Ne, Ar, Fe) [2–5], it follows that an increase in the mass of colliding particles has the greatest effect on the number of particles produced at the first stage of the process. For interactions of energy below 1 GeV per nucleon, the mean multiplicity of $(g + s)$ particles is proportional to the product of the masses of interacting nuclei that is raised to a power close to 0.7, $\langle N_{g+s} \rangle \sim (A_{\text{pr}} A_{\text{tar}})^{0.7}$. Also, the total interaction charge $\langle Z_{\text{int.ch.}} \rangle$ increases with increasing dimensions of interacting nuclei. We note that $\langle Z_{\text{int.ch.}} \rangle$ does not include the target-nucleus charge, which was not detected in our experiment. The masses of interacting nuclei have a weaker effect on the mean multiplicity of all charged secondaries, $\langle N \rangle$, than on $\langle N_{g+s} \rangle$. For interactions of energy below 1 GeV per nucleon, $\langle N \rangle$ is approximately proportional to $(A_{\text{pr}} A_{\text{tar}})^{0.5}$.

As can be seen from Table 1, the results obtained by the Monte Carlo method for the mean multiplicities of $(g + s)$, b, and $(s' + g' + b')$ particles and for the mean multiplicity of all charged secondaries, as well as for the total interaction charge, are close to their experimental counterparts, describing the increase in the particle multiplicity and in $\langle Z_{\text{int.ch.}} \rangle$ with increasing mass of colliding particles.

A comparison of our experimental data with the results reported in [2, 3] revealed that the mean multiplicity of b particles is virtually independent of the projectile mass in the mass range 20–197 amu. For example, the increase in the projectile mass by a factor of 10—from that of ^{20}Ne to that of ^{197}Au—leads to only a 15% increase in the multiplicity of b particles in the interaction with heavy emulsion nuclei, the multiplicity of b particles in the interactions with light emulsion nuclei even decreasing.

In order to clarify the possible reasons behind this behavior of the multiplicity of b particles, we plotted the mean multiplicity of b particles as a function of the multiplicity of $(g + s)$ particles in disintegration events induced by the interaction between ^{197}Au nuclei of energy 0.741 GeV per nucleon and photoemulsion nuclei (see Fig. 2). Figure 2 also displays the results of the calculations based on the cascade–evaporation model that were performed for ^{197}Au nuclei of energy 0.7 GeV per nucleon and the results presented in [2, 3] for the interactions of ^{20}Ne and ^{40}Ar nuclei whose energies were, respectively, 0.28 and 0.27 GeV per nucleon.

From the data in Fig. 2, it follows that, up to a value of $N_{g+s} \approx 40$, $\langle N_b \rangle$ grows almost linearly with N_{g+s} in the interactions of gold nuclei. The emission of each of the $(g + s)$ particles (a particle that escaped from the nucleus under consideration at the fast stage) leads, on average, to an additional emission of 0.2 to 0.3 of a b particle. In the region $N_{g+s} > 40$, a decrease in the mean multiplicity of b particles with increasing multiplicity of $(g + s)$ particles is observed in disintegration events involving heavy target nuclei.
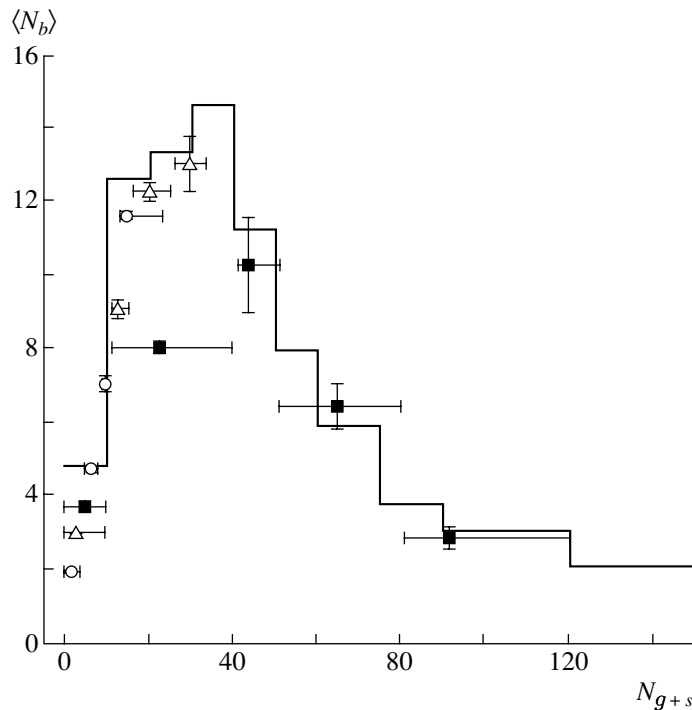
Fig. 2. Experimental correlations between the mean multiplicity of b particles and the multiplicity of fast $(g+s)$ particles in disintegration events induced by the interactions of (closed boxes) ^{197}Au nuclei of energy 0.741 GeV per nucleon, (open circles) ^{20}Ne nuclei of energy 0.28 GeV per nucleon, and (open triangles) ^{40}Ar nuclei of energy 0.27 GeV per nucleon with photoemulsion nuclei. The histogram represents the respective correlation calculated on the basis of the cascade−evaporation model for ^{197}Au nuclei of energy 0.7 GeV per nucleon.

Experiments with light projectiles of ^{20}Ne and ^{40}Ar exhibited an increase in $\langle N_b \rangle$ with increasing N_{g+s}; however, the respective correlation dependences did not show (see Fig. 2) a decrease in $\langle N_b \rangle$ as N_{g+s} grows further since there were no interactions characterized by $N_{g+s} > 40$. We also note that, in the interaction of 660-MeV protons with heavy emulsion nuclei, the number of emitted $(g+s)$ particles does not exceed three, the mean multiplicity being 1.03 particles per interaction event [12].

The simplest way to explain the observed form of the $\langle N_b \rangle (N_{g+s})$ correlation, which characterizes the interplay of the slow and the fast reaction stage, is to take into account effects that are associated with the "finiteness" of a heavy target nucleus. If the heavy target nucleus of ^{107}Ag loses 35 to 47 protons at the first reaction stage, there will be no sizable target-nucleus residue, with the result that the multiplicity of b particles will not be large. Previously, the observed effect of finiteness of a heavy target nucleus was not found in the projectile-mass range between 2 and 56 amu, since the required number of nucleons could not be knocked out of a heavy photoemulsion nucleus because of small projectile dimensions. In our opinion, the experimentally observed fact that the mean multiplicity of b particles in interactions involving light nuclei decreases as one goes over from neon to gold projectiles can also be explained by the finiteness effect. Upon undergoing a collision with gold nucleons, the bulk of the nucleons of light nuclei go over to the energy region above 26 MeV per nucleon.

The histogram in Fig. 2 represents the results of the calculations based on the cascade−evaporation model. One can easily see that this model provides a fairly good description of the complicated experimental dependence $\langle N_b \rangle (N_{g+s})$, including the experimentally observed effect of finiteness of a heavy target nucleus.

TARGET-NUCLEUS FRAGMENTATION

For each target-nucleus fragment (b particle), we determined here the polar (θ) and azimuthal (ψ) emission angles and its free path in the photoemulsion. Under the assumption that all b particles are protons, we found angular, energy, and momentum properties of each b particle. The mean values of the multiplicity $(\langle N_b \rangle)$, polar emission angle, ratio of the number of particles emitted into the forward hemisphere to the number of particles emitted into the backward hemisphere (forward/backward), and longitudinal and transverse momenta ($\langle P_{\parallel} \rangle$ and $\langle P_{\perp} \rangle$, respectively) are given in Table 2 for the interactions of gold

Table 2. Properties of target fragments of energy in the range $E \leq 26$ MeV per nucleon that are emitted at the second reaction stage

Target nucleus	$\langle N_b \rangle$, part./int.	$\langle \theta \rangle$, deg	Forward/backward	$\langle E \rangle$, MeV/nucleon	$\langle P_\| \rangle$, MeV/c	$\langle P_\perp \rangle$, MeV/c
Au, $E = 0.741$ GeV/nucleon						
Em	3.24 ± 0.17	77.81 ± 1.91	1.76 ± 0.09	9.23 ± 0.37	26.26 ± 3.92	94.96 ± 2.62
	(3.94)	(80.03)	(1.59)	(9.72)	(19.6)	(94.29)
C, N, O	0.49 ± 0.11	64.63 ± 5.14	5.67 ± 0.58	5.25 ± 1.15	36.76 ± 9.31	71.92 ± 9.15
	(1.76)	(84.30)	(1.38)	(7.24)	(13.67)	(79.02)
Ag, Br	5.88 ± 0.32	78.71 ± 2.00	1.65 ± 0.09	9.47 ± 0.38	25.43 ± 4.12	96.36 ± 2.71
	(7.85)	(79.32)	(1.62)	(10.14)	(20.54)	(96.93)
Au, $E_{\mathrm{int}} \leq 0.873$ GeV/nucleon						
Ag, Br	5.53 ± 0.43	75.85 ± 0.23	1.77 ± 0.13	9.92 ± 0.04	30.31 ± 0.47	96.54 ± 0.30
Au, $E_{\mathrm{int}} > 0.873$ GeV/nucleon						
Ag, Br	6.27 ± 0.49	81.62 ± 0.21	1.55 ± 0.13	9.01 ± 0.04	20.46 ± 0.43	96.17 ± 0.30

nuclei at an average energy of 741 MeV per nucleon. The results of the calculations within the cascade–evaporation model are presented in parentheses.

From Table 2, one can see that a change in the target mass by nearly a factor of 7 (in going over from C, N, and O to Ag and Br) leads to an increase in the multiplicity of b particles by almost a factor of 12, the energy by a factor of 1.8, and the transverse momentum by a factor of 1.3. Concurrently, the forward orientation becomes less pronounced—the forward/backward ratio decreases by almost a factor of 3.5, $\langle P_\| \rangle$ decreases by a factor of 1.5, and the polar emission angle increases by a factor of 1.2.

The results of the calculations within the cascade–evaporation model are in satisfactory agreement with the experimentally determined properties of b particles in interactions with heavy photoemulsion nuclei, the discrepancies being within 5 to 10%. The calculations describe qualitatively the dependences of the multiplicity, energy, and transverse momentum of low-energy protons on the target-nucleus mass.

In order to analyze the effect of the projectile velocity on the properties of b particles, the entire body of data on interactions with heavy photoemulsion nuclei was partitioned into two groups where the interaction energies were $E_{\mathrm{int}} \leqslant 873$ MeV per nucleon and $E_{\mathrm{int}} > 873$ MeV per nucleon (samples containing identical numbers of b particles). The properties of b particles belonging to these samples are also given in Table 2. One can see that, with decreasing projectile velocity, the forward orientation of b particles becomes more pronounced, the longitudinal momentum component increasing by a factor of 1.5. The mean

emission angle decreases by 20%. This effect was previously observed in [2–5], where it was explained by the contribution of first-stage particles to the energy region $E < 26$ MeV per nucleon, this contribution increasing as the projectile energy decreases.

The measurements of the free paths and of the azimuthal and polar emission angles in our experiment made it possible to determine the 3-momentum components for each of the b particles. For our analysis, we choose $P_z(P_\|)$, which is the momentum component along the direction of projectile motion, and $P_x(P_\perp \cos \psi)$, which is the projection of the momentum onto an axis in the azimuthal plane that is orthogonal to the direction of projectile motion.

In Fig. 3, we present the results obtained for the distributions of b particles with respect to these 3-momentum components from our measurements (Figs. 3a, 3c) and from the calculations within the cascade–evaporation model (Figs. 3b, 3d). Both the experimental and the measured distributions are close to Gaussian distributions, this giving sufficient grounds to consider a system that emits particles isotropically and which has a characteristic temperature and moves at a specific velocity. The effective temperature of the system emitting particles can be estimated by assuming that the distribution of singly charged particles with respect to each 3-momentum component is described by a Gaussian distribution characterized by the parameter $\sigma = (2/\pi)^{0.5} \langle P_\perp \rangle$, the variance being related to the temperature by the equation $T_0 = \sigma^2/m$. Both for the experimental events and for their counterparts calculated within the cascade–evaporation model, the estimates performed
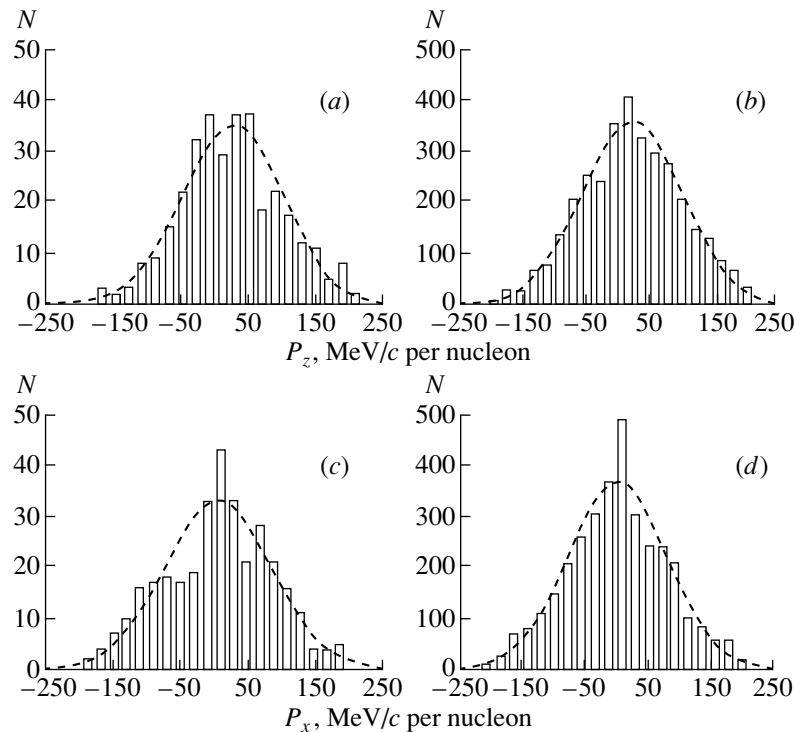
Fig. 3. Distributions of b particles with respect to two 3-momentum components (P_z, P_x) in the interactions of ^{197}Au nuclei with photoemulsion nuclei at an average energy of 0.741 GeV per nucleon. The histograms represent experimental data in Figs. 3a and 3c and the results of the calculations within the cascade–evaporation model in Figs. 3b and 3d. The dashed curves correspond to approximations by a Gaussian distribution.

for the interaction with heavy nuclei yield a value of about 6 MeV for the effective particle-emission temperature and a value of $\langle \beta_\parallel \rangle = 0.025$ of the speed of light for the velocity in question.

PROJECTILE-NUCLEUS FRAGMENTATION

For the interactions of gold nuclei with photoemulsion nuclei at an average energy of 741 MeV per nucleon, Table 3 gives the mean multiplicities of doubly and multiply charged fragments ($\langle N_{g'} \rangle$ and $\langle N_{b'} \rangle$, respectively), the mean multiplicities of multiply charged fragments in various charge intervals (columns 4–6), and the mean charge of $Z \geq 3$ fragments ($\langle Z_{\text{fr}} \rangle$). The respective values obtained from the calculations within the cascade–evaporation model are presented in parentheses.

From an analysis of the data in this table on the multiplicity of b' particles, one can easily see that there are two regions both in the calculated data and in the experimental data at $E \approx 700$ MeV per nucleon: these are the region of fragment charges close to the projectile charge ($Z = 61-79$), where the calculated values exceed considerably their experimental counterparts, and the fragment-charge region $Z = 3-20$, where the calculation predicts fragment yields below

the experimental data. By way of example, we indicate that, in the first region, the adequate calculated data for our statistical sample (1000 events) at a projectile energy of about 700 MeV per nucleon should have been only 180 fragments instead of 590 actually obtained in the calculation—that is, the discrepancy in this region of fragment atomic numbers is as great as a factor of 3. In the region $Z = 3-20$, the experimental data differ from the results of the calculations by a factor of 18.

The data that we obtained show that the model applied here is unable to take adequately into account the multifragmentation and fission of excited heavy nuclear residues. As a result, the calculations involve virtually no interactions leading to the emission of two or more heavy fragments. The mean multiplicity of heavy fragments of the incident nucleus ^{197}Au was 1.7 to 2.7 particles per interaction event in the experiment (see Table 3), whereas its calculated value amounted to unity. An increase in the probability of the multifragmentation and fission of excited projectile fragments within the model would lead to an increase in the multiplicity of fragments in the range $Z = 3-20$ and would increase, by and large, the multiplicity of $Z \geq 3$ fragments in the interactions of nuclei, and this would make it possible to describe the experimental data more adequately.

Table 3. Multiplicity of multiply charged projectile fragments formed in the interaction of ^{197}Au nuclei with photoemulsion nuclei at an average energy of 0.741 GeV per nucleon

Target nucleus	$\langle N_{g'} \rangle$, part./int.	$\langle N_{b'} \rangle$, part./int.	Intervals in Z			$\langle Z_{\mathrm{fr}} \rangle$, el. ch.
			3−20	21−60	61−79	
Em	4.76 ± 0.21	2.52 ± 0.15	1.74 ± 0.13	0.62 ± 0.08	0.16 ± 0.04	18.79 ± 0.26
	(1.97)	(1.00)	(0.08)	(0.35)	(0.57)	(58.10)
H	2.27 ± 0.46	1.73 ± 0.40	0.27 ± 0.16	1.09 ± 0.31	0.36 ± 0.18	41.53 ± 1.48
	(0.91)	(1.00)	(0.00)	(0.03)	(0.97)	(74.70)
C, N, O	5.83 ± 0.38	3.37 ± 0.29	2.68 ± 0.26	0.63 ± 0.12	0.05 ± 0.03	13.38 ± 0.31
	(2.52)	(1.00)	(0.06)	(0.39)	(0.56)	(57.66)
Ag, Br	4.46 ± 0.28	2.05 ± 0.19	1.34 ± 0.15	0.52 ± 0.10	0.21 ± 0.06	21.51 ± 0.43
	(2.14)	(1.00)	(0.14)	(0.51)	(0.35)	(49.04)

In order to separate fission events from the whole array of processed events of ^{197}Au disintegration at an energy of 0.741 GeV per nucleon, we selected four events that involved at least two fast projectile fragments carrying $Z_{\mathrm{fr}} \geq 20$ elementary charge units each. Thus, the ratio of the cross section for the formation of two massive fragments to the total inelastic cross section was 0.037 ± 0.010, which is close to the probability of the binary fission of ^{197}Au nuclei that is induced by high-energy protons (3−5% [12]).

CONCLUSION

New experimental and calculated data have been obtained for inelastic-interaction free paths of ^{197}Au nuclei in photoemulsion and for the multiplicities of various charged secondaries produced in the inelastic interaction of gold nuclei with photoemulsion nuclei at energies in the range 100−1147 MeV per nucleon, as well as for the angular, energy, and momentum properties of these particles. The fragmentation of target and projectile nuclei has been considered. The properties of the interaction have been analyzed versus the energy of interacting nuclei.

For particles emitted at the slow stage, we have discovered the effect of finiteness of heavy photoemulsion nuclei in their interaction with gold ions. This effect was not observed previously in the projectile-mass range between 2 and 56 amu. The behavior of particles originating at the second stage of the process from target nuclei can be described quite accurately within the model of a thermalized source that emits particles isotropically and which has an effective temperature of about 6 MeV and moves at a velocity of $\langle \beta_{||} \rangle = 0.025$ of the speed of light.

In studying projectile fragments, we have found that the main discrepancy between the calculated and experimental data consists in that the calculation underestimates significantly the probability of the disintegration of a fast nucleus into several $Z \geq 3$ fragments, with the result that the charge spectra of ^{197}Au fragments appear to be distorted. Otherwise, the results of the calculations within the cascade−evaporation model describe qualitatively and quantitatively (to within 10 to 15%) our experimental data, including correlation dependences and the angular, energy, and momentum features of charged secondaries versus the target mass and particle type.

REFERENCES

1. S. D. Bogdanov, S. S. Bogdanov, V. F. Kosmach, *et al.*, Izv. Akad. Nauk, Ser. Fiz. **60**, 132 (1996).
2. V. E. Dudkin, E. E. Kovalev, N. A. Nefedov, *et al.*, Nucl. Phys. A **568**, 906 (1994).
3. S. D. Bogdanov, V. F. Kosmach, V. M. Molchanov, and V. A. Plyushchev, Izv. Akad. Nauk, Ser. Fiz. **63**, 427 (1999).
4. V. A. Bakaev, S. D. Bogdanov, S. S. Bogdanov, *et al.*, Izv. Akad. Nauk, Ser. Fiz. **64**, 2144 (2000).

5. S. D. Bogdanov, S. S. Bogdanov, V. E. Dudkin, *et al.*, Nucl. Tracks Radiat. Meas. **25**, 111 (1995).

6. S. D. Bogdanov, S. S. Bogdanov, E. E. Zhurkin, and V. F. Kosmach, Zh. Éksp. Teor. Fiz. **115,** 404 (1999) [JETP **88**, 220 (1999)].

7. V. A. Bakaev, S. D. Bogdanov, S. S. Bogdanov, *et al.*, Surf. Inv. **13**, 681 (1998).

8. V. A. Bakaev, S. D. Bogdanov, S. S. Bogdanov, *et al.*, Poverkhnost, No. 4, 41 (2003).

9. V. A. Bakaev, S. D. Bogdanov, S. S. Bogdanov, *et al.*, Poverkhnost, No. 4, 45 (2004).

10. C. J. Waddington and P. S. Freier, Phys. Rev. C **31**, 888 (1985).

11. P. J. Karol, Phys. Rev. C **11,** 1203 (1975).

12. V. S. Barashenkov and V. D. Toneev, *Interactions of High-Energy Particles and Nuclei with Nuclei* (Atomizdat, Moscow, 1972) [in Russian].

Translated by A. Isaakyan

ELEMENTARY PARTICLES AND FIELDS
Experiment

Some Special Features of the Momentum Spectrum of Protons Produced in ^{16}Op Collisions at a Momentum of 3.25 GeV/c per Nucleon

E. Kh. Bazarov, V. V. Glagolev[1]), K. G. Gulamov, S. L. Lutpullaev, K. Olimov*, Kh. Sh. Khamidov[2]), A. A. Yuldashev, and B. S. Yuldashev[2])

Institute for Physics and Technology, Fizika—Solntse Research and Production Association, Uzbek Academy of Sciences, ul. Timiryazeva 2b, Tashkent, 700084 Republic of Uzbekistan
Received August 10, 2004; in final form, December 2, 2004

Abstract—The momentum features of protons originating from ^{16}Op collisions at a momentum of 3.25 GeV/c per nucleon are analyzed. It is shown that the degree of excitation of the fragmenting nucleus affects predominantly the shape of the momentum spectrum of protons emitted into the backward hemisphere in the rest frame of the projectile nucleus and partly the shape of the spectra of protons emitted into the forward hemisphere and formed via the mechanisms of Fermi breakup and evaporation. © 2005 Pleiades Publishing, Inc.

It is well known that the formation of light fragments like ^{1}H$_1$, ^{2}H$_1$, ^{3}H$_1$, and ^{3}He$_2$ is a feature peculiar to the nuclear-fragmentation process [1]. In particular, it was proven experimentally that the bulk of protons are formed at the initial, fast, stage of high-energy hadron—nucleus and nucleus—nucleus interactions. At the same time, the cross section for nucleon production appeared to be commensurate with the inelastic nuclear-reaction cross section. In view of this, more information about the dynamics of the nuclear-fragmentation process can be deduced from an analysis of the production of light fragments than from an analysis of the production of heavy fragments. Since it is quite straightforward to identify secondary protons and to measure their kinematical features, they have been explored fairly well. Nevertheless, correlations in the production of protons and multiply charged fragments in relativistic hadron—nucleus collisions have not yet received adequate study.

In [2], it was shown that the shape of the momentum spectrum of protons produced in ^{16}Op collisions at a momentum of 3.25 GeV/c per nucleon depends on the degree of excitation of the fragmenting oxygen nucleus. It was also shown there that the mechanism of the production of relatively fast protons ($p > 0.45$ GeV/c) traveling in the forward hemisphere in the rest frame of the projectile nucleus is independent

of either the energy or the mass number of the fragmenting nucleus.

The present study, which is a continuation of the analysis reported in [2], is devoted to a more detailed exploration of correlations between the properties of the momentum spectrum of protons and the degree of excitation of the oxygen nucleus.

The experimental data subjected to the present analysis were obtained by exposing the 1-m hydrogen bubble chamber of the Laboratory for High Energies at the Joint Institute for Nuclear Research (JINR, Dubna) to a beam of ^{16}O nuclei accelerated at the Dubna synchrophasotron to a momentum of 3.25 GeV/c per nucleon. This data sample consisted of 11 098 measured ^{16}Op events. The methodological aspects of our experiment are described in [3—5].

The total charge of multiply charged ($z_f \geq 2$) fragments ($\sum z_f$) can be considered as a measure of the degree of excitation of the fragmenting oxygen nucleus. In this connection, it is of interest to explore the effect of the degree of excitation of a fragmenting nucleus on the momentum features of protons. We will now consider the dependence of the mean momentum of protons emitted into the forward and backward hemispheres (forward and backward protons, respectively) in the rest frame of the oxygen nucleus on the total charge of multiply charged fragments. This dependence is shown in Fig. 1. From Fig. 1a, one can see that, within the statistical errors, the mean momentum of forward protons is everywhere (with the exception of the point at $\sum z_f = 6$) independent of $\sum z_f$—that is, of the degree of excitation of the fragmenting nucleus. The solid curve represents the

[1])Joint Institute for Nuclear Research, Dubna, Moscow oblast, 141980 Russia.
[2])Institute of Nuclear Physics, Uzbek Academy of Sciences, pos. Ulughbek, Tashkent, 702132 Republic of Uzbekistan.
*E-mail: `olimov@uzsci.net`

result obtained (without allowance for the experimental point at $\sum z_f = 6$) by approximating the experimental data by a function of the form

$$\langle p \rangle = \alpha. \tag{1}$$

It can be seen that this approximation describes fairly well the fact that the mean momentum of forward protons is independent of the total charge of multiply charged fragments. The fitted value of the parameter α proved to be 435.9 ± 4.0 MeV/c at $\chi^2 = 0.74$ per five degrees of freedom, this corresponding to a 98% confidence level. We also note that, within the statistical errors, the standard deviations for the momentum spectra of forward protons remain unchanged for these groups of events ($\sum = 273.7 \pm 2.9$ MeV/c). If, in approximating the experimental data by expression (1), one includes the point at $\sum z_f = 6$ (the dotted curve in Fig. 1a), then $\alpha = 425.0 \pm 3.0$ MeV/c at $\chi^2 = 14.96$ per six degrees of freedom, this corresponding to a 2% confidence level. Thus, one can conclude that the deviation of the experimental point at $\sum z_f = 6$ from $\langle p \rangle$ is significant in relation to other values of the total charge of multiply charged fragments.

The observed decrease of about 10% in the mean momentum of forward protons at $\sum z_f = 6$ in relation to $\langle p \rangle$ at other values of $\sum z_f$ can be explained by a relatively large contribution of the evaporation mechanism to the spectrum of forward protons in these events. This can be qualitatively interpreted as follows. By virtue of the isotopic invariance of strong interaction, the probabilities of pp and pn interactions are identical since the projectile nucleus contains equal numbers of protons and neutrons. Further, the processes of multiple intranuclear rescattering can be disregarded since events in which the total charge is 6 or 7 are due to peripheral $^{16}\mathrm{O}p$ collisions. In the case where $\sum z_f = 7$, the observed proton is, with identical probabilities, a product of either a direct knockout or evaporation. For the group of $\sum z_f = 6$ events, the final state features two protons; of these, one is due to evaporation, while the other may be, with a probability of 0.5, a knock-on proton, as in the case of $\sum z_f = 7$. This is precisely the circumstance that leads to an increased fraction of evaporated protons in the $\sum z_f = 6$ group and, accordingly, to a decrease in the mean momentum in this group.

From Fig. 1b, one can see that, with increasing total charge of multiply charged fragments, the mean momentum of backward protons decreases monotonically, which is likely to be due to an increase in the fraction of evaporated protons. It should be noted that the contribution of cascade protons to the spectrum of backward protons can be disregarded. With increasing total charge, the standard deviations for
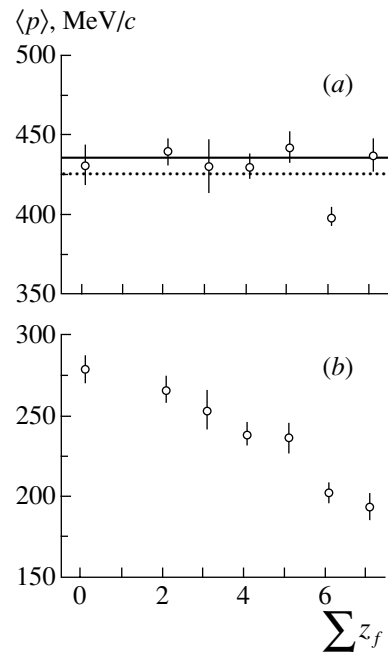
Fig. 1. Mean total momenta of (a) forward and (b) backward protons in the rest frame of the oxygen nucleus versus the total charge, $\sum z_f$, of multiply charged fragments.

the momentum distributions decrease almost linearly; that is, the momentum spectra in question become narrower.

Here, it is also of interest to study the dependence of the shapes of the forward- and backward-proton momentum spectra on the degree of excitation of the oxygen nucleus. Figure 2 shows the ratios R of the forward- and backward-proton momentum spectra for various groups of events to the total spectra of, respectively, forward and backward protons. The Roman numerals there indicate the numbers of groups corresponding to different values of $\sum z_f$. Because of scarce statistics of $\sum z_f = 0$ and $\sum z_f = 3$ events, they were combined with events characterized by close total charges of multiply charged fragments— that is, with $\sum z_f = 2$ and $\sum z_f = 4$ events, respectively. Thus, groups I, II, III, IV, and V contain, respectively, $\sum z_f = 0$–2, $\sum z_f = 3$–4, $\sum z_f = 5$, $\sum z_f = 6$, and $\sum z_f = 7$ events.

As follows from Fig. 2a, the ratios R display a significant momentum dependence only in the region $p < 0.25$ GeV/c, which corresponds to the spectrum of evaporated protons. One can see that the dependence of R on p is linear; however, the slope of the respective straight lines changes from negative values for groups I–III to positive values for groups IV and V, reflecting the dynamics of changes in the relative yields of protons of different origin versus momentum.

R, arb. units
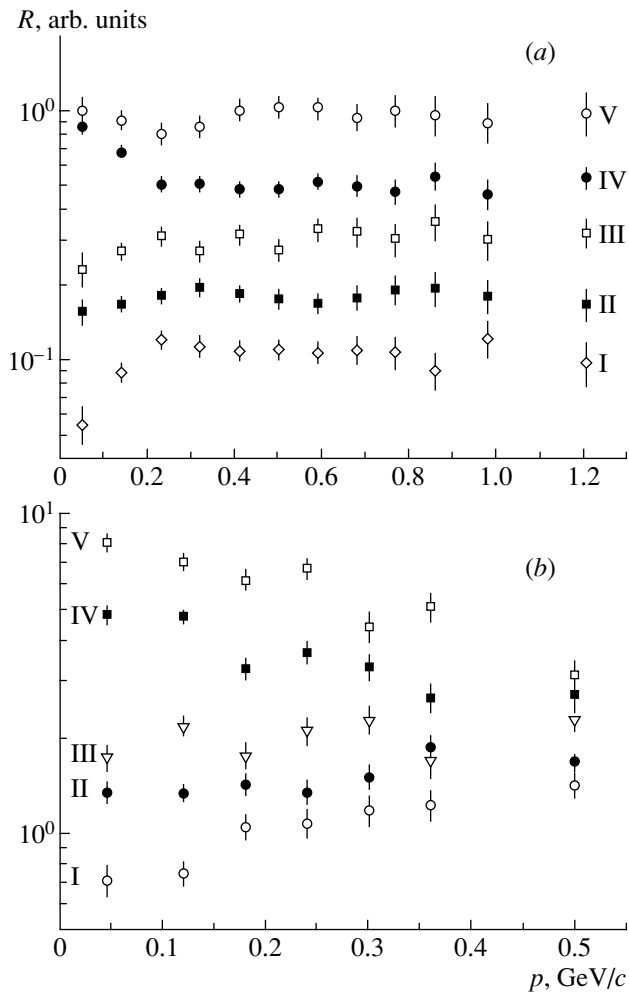
Fig. 2. Ratios R of (*a*) forward- and (*b*) backward-proton momentum spectra in the rest frame of the oxygen nucleus for various charge groups of events to the total momentum spectra of, respectively, forward and backward protons.

In the region $p > 0.25$ GeV/c, where there are virtually no evaporated protons, R is independent of p within the statistical errors. Thus, one can conclude that the degree of excitation of the projectile nucleus changes the shape of the spectrum of forward protons that do not originate from a cascade.

From Fig. 2*a*, one can also see that the fraction of evaporated protons is maximal in group IV—that is, in the case where $\sum z_f = 6$. The bulk of events in this group involve the formation of one sextuply charged fragment and three doubly charged fragments.

The ratio R for backward protons displays an interesting momentum dependence (Fig. 2*b*). For groups I and II, R increases slowly with increasing momentum over the entire region of the spectrum; for

group III, R remains virtually unchanged, within the statistical errors, over the entire momentum range; for groups IV and V, R decreases monotonically with increasing momentum.

From the experimental data considered above, it follows that the degree of excitation of the fragmenting nucleus affects differently the shapes of the momentum spectra of forward and backward protons. A substantial effect of the degree of excitation of the fragmenting nucleus on the shape of the momentum spectrum of backward protons can be explained by the origin of these protons. Protons emitted into the backward hemisphere are predominantly produced via evaporation and Fermi breakup, these mechanisms being directly associated with the degree of excitation of the fragmenting nucleus, as is observed experimentally. In addition to these mechanisms, intranuclear-cascade processes make a significant contribution to the production of forward protons. It is interesting to note that, although there is an interrelation between the degree of excitation of the fragmenting nucleus and the multiplicity of the intranuclear cascade, the former has no effect on the shape of the momentum spectrum of protons of this origin.

Thus, we can conclude that the degree of excitation of the fragmenting nucleus has a substantial effect only on the shape of the momentum spectrum of backward protons and affects partly the shape of the spectra of forward protons that do not originate from a cascade. The observed decrease in the mean momentum of forward protons at $\sum z_f = 6$ in relation to other charge groups is due to an increased fraction of evaporated protons.

REFERENCES

1. V. I. Zagrebaev and Yu. E. Penionzhkevich, Fiz. Élem. Chastits At. Yadra **24**, 295 (1993) [Phys. Part. Nucl. **24**, 125 (1993)].
2. É. Kh. Bazarov, V. V. Glagolev, K. G. Gulamov, *et al.*, Yad. Fiz. **67**, 736 (2004) [Phys. At. Nucl. **67**, 708 (2004)].
3. V. V. Glagolev, K. G. Gulamov, M. Yu. Kratenko, *et al.*, Pis'ma Zh. Éksp. Teor. Fiz. **58**, 497 (1993) [JETP Lett. **58**, 497 (1993)].
4. V. V. Glagolev, K. G. Gulamov, M. Yu. Kratenko, *et al.*, Pis'ma Zh. Éksp. Teor. Fiz. **59**, 316 (1994) [JETP Lett. **59**, 336 (1994)].
5. V. V. Glagolev, K. G. Gulamov, M. Yu. Kratenko, *et al.*, Yad. Fiz. **58**, 2005 (1995) [Phys. At. Nucl. **58**, 1896 (1995)].

Translated by A. Isaakyan

ELEMENTARY PARTICLES AND FIELDS
Experiment

On the Energy Spectrum of Protons Produced in ¹⁶Op Collisions at a Momentum of 3.25 GeV/c per Nucleon

E. Kh. Bazarov

Institute for Physics and Technology, Fizika–Solntse Research and Production Association, Uzbek Academy of Sciences, ul. Timiryazeva 2b, Tashkent, 700084 Republic of Uzbekistan
Received August 10, 2004; in final form, December 2, 2004

Abstract—New experimental data concerning the mechanisms of the production of protons originating as fragments from oxygen-nucleus interactions in a hydrogen bubble chamber at high energies are presented. It is shown that anomalies observed in the energy spectrum of protons at kinetic energies in the range $T = 70-90$ MeV are associated with the absorption of slow pions by a quasideuteron nucleon pair. © 2005 Pleiades Publishing, Inc.

According to present-day theoretical ideas, the production of the lightest nuclear fragments, nucleons (protons and neutrons), can proceed at all stages of hadron−nucleus interaction at high energies, which is an extremely intricate process. Such nucleons may emerge at the stage of an intranuclear cascade or from the decay of excited multinucleon fragments; also, they may be products of either evaporation or an explosive decay (Fermi breakup) of a thermalized residual nucleus. The interaction of primary particles with intranuclear systems, where nucleons occur at very short distances (≤ 1 fm), may in principle lead to the formation of so-called cumulative nucleons—that is, nucleons whose momenta have values forbidden by the usual kinematics of particle scattering on free intranuclear nucleons (with allowance for their Fermi motion). In particular, relatively energetic nucleons appearing as fragments may originate from the absorption of slow product pions by quasideuteron nucleon pairs in a nucleus via the reaction

$$\pi + \langle\langle d \rangle\rangle \to N + N. \tag{1}$$

If the energy of the pion involved is rather high, the final state may involve isobars. Such reactions, if they indeed occur, may result in the formation of cumulative nucleons.

Previously, a structure in the momentum spectrum of protons emitted in the backward hemisphere in the laboratory frame was discovered in [1−3] in pNe interactions at 300 GeV/c and in π^-C collisions at 4 and 40 GeV/c—more specifically, the differential cross section as a function of the proton momentum was found there to deviate from a monotonic behavior in the region $p \approx 0.3-0.5$ GeV/c. It was shown that

the observed structure is the result of pion or meson-resonance absorption by strongly bound few-nucleon systems.

The present study is devoted to exploring the energy spectrum of protons originating as oxygen-nucleus fragments from ¹⁶Op interactions at a momentum 3.25 GeV/c per nucleon. It is a continuation of the series of investigations into the mechanisms of relativistic-hydrogen-nucleus fragmentation with the aid of the 1-m liquid-hydrogen bubble chamber at the Joint Institute for Nuclear Research (JINR, Dubna). It should be noted that the use of a liquid bubble chamber in a magnetic field proved to be an efficient method for studying many features of the fragmentation process under conditions of 4π geometry. The methodological issues concerning the identification of particles and fragments were described in detail elsewhere [4−7].

The experimental data presented below are based on a statistical sample of about 15 000 measured ¹⁶Op events. In analyzing the energy spectra of the protons, a clear mass separation of fragments was ensured by considering only those events in which the measured length of tracks of fast singly charged particles in the fiducial volume of the chamber exceeded 35 cm. In the case of this selection, the mean error in momentum measurements was less than 3% for ¹H and ²H and 5% for ³H. The following momentum intervals were introduced in order to perform a mass identification of these fragments: $p = 4.75-7.75$ GeV/c for ²H and $p > 7.8$ GeV/c for ³H. All singly charged positive particles in the momentum range $2.0 \leq p \leq 4.75$ GeV/c were classified as protons, since the production of positively charged pions is kinematically impossible in the momentum

Number of protons
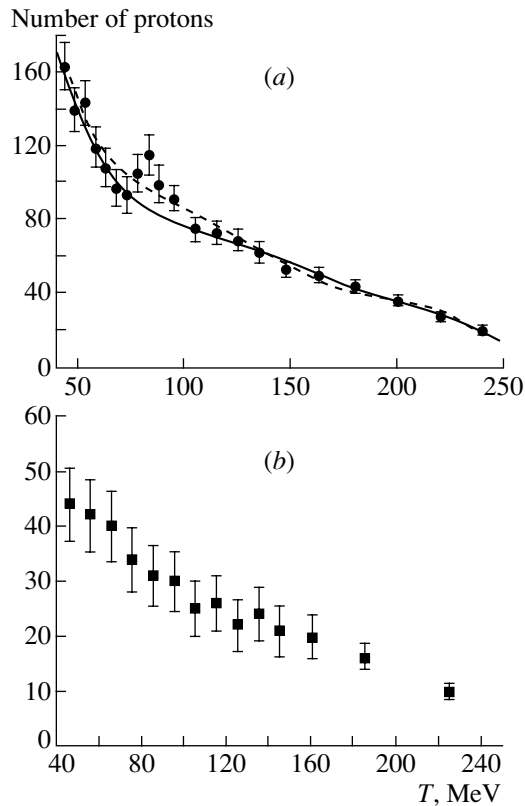
Fig. 1. Kinetic-energy distribution of protons appearing as fragments in channels where the total charge of multiply charged fragments falls within the range $5 \leq \sum z_f \leq 7$: (a) results for events not involving deuteron production and (b) results for events involving the production of at least one deuteron.

region $p > 2$ GeV/c. It should be noted that all multiply charged fragments of the projectile nucleus were unambiguously identified by the charge value. This made it possible to study the fragmentation process in individual topological channels. In describing and discussing the results obtained here, all energy features of protons are presented below in the antilaboratory frame—that is, in the rest frame of the oxygen nucleus.

As was shown in [7], the distribution of the invariant structure function $f(T)$ with respect to the proton kinetic energy has a sharply descending character as the energy increases in the region $T \leq 10$ MeV, but, at higher energies, the slope of the spectrum decreases; in the region $T > 50$ MeV, the shape of the spectrum approaches that of an exponential. In the region $T \approx 60-90$ MeV, the inclusive kinetic-energy spectrum of protons exhibits a deviation from monotononicity in its descending part. This structure manifests itself most clearly in topological channels where the total charge of multiply charged fragments falls within the range $5 \leq \sum z_f \leq 7$. For two groups of events belonging to these channels, Fig. 1 displays

the kinetic-energy distribution of protons appearing as fragments (in the range $40 < T < 250$ MeV). The groups are defined in such a way that events of one group feature no deuterons (Fig. 1a), while events of the other group feature at least one deuteron (Fig. 1b). From Fig. 1a, one can see that the distribution for the first group exhibits a structure that involves a sizable peak. The solid curve represents the result of approximating the spectrum beyond the interval $70 < T < 110$ MeV by a Legendre polynomial of fifth degree. One can see that beyond this interval, the spectrum in question has a monotonically decreasing character and is very well reproduced by this polynomial ($\chi^2 = 3.18$ per 11 degrees of freedom, this corresponding to a more than 99% confidence level). The dashed curve in Fig. 1a represents the result of approximating all experimental points by a Legendre polynomial of fifth degree. We see that the description of the experimental data deteriorates upon the inclusion of the interval $70 < T < 110$ MeV ($\chi^2 = 17.5$ per 15 degrees of freedom, this corresponding to a less than 30% confidence level). This suggests that the structure observed in the interval $70 < T < 110$ MeV is reliable.

The position of the peak maximum at $T \approx 80 \pm 5$ MeV in Fig. 1a agrees well with the assumption that some of the protons are produced in the decays of a quasideuteron nucleon pair upon the absorption of a slow pion. In this case, it is natural to expect that, in channels involving deuteron production, the probability of observing protons formed in reactions of pion absorption by quasideuteron nucleon pairs in a nucleus ($\pi + \langle\langle d \rangle\rangle \rightarrow N + p$) is strongly suppressed. Indeed, one can see from Fig. 1b that, in events involving deuteron production, there are no anomalies in the range $T \approx 70-90$ MeV. In passing, we emphasize that the presence or absence of three-nucleon fragments (^{3}H and ^{3}He nuclei), which could be formed upon the fusion of a deuteron with another nucleon from a cascade [7], has virtually no effect on the result.

The absence of a sizable peak in topological channels where the total charge of $z_f \geq 2$ fragments is less than five can be explained qualitatively as follows. Since a greater number of intranuclear collisions and a disintegration of the primary nucleus to a greater degree occur in those channels, protons formed in reaction (1) lose their initial kinematical parameters, the energy spectrum of these protons being strongly smeared.

Thus, we can conclude that the structure observed in the energy spectrum of protons in the range $T \approx 70-90$ MeV is associated with the decay of a two-nucleon system upon the absorption of a slow pion.

ACKNOWLEDGMENTS

REFERENCES

1. S. O. Edgorov, S. L. Lutpullaev, A. A. Yuldashev, and B. S. Yuldashev, Yad. Fiz. **55**, 2962 (1992) [Sov. J. Nucl. Phys. **55**, 1656 (1992)].
2. V. M. Asaturyan *et al.*, Nucl. Phys. A **496**, 770 (1989).
3. D. Armutliĭski, A. P. Gasparyan, V. G. Grishin, *et al.*, Yad. Fiz. **46**, 1712 (1987) [Sov. J. Nucl. Phys. **46**, 1023 (1987)].
4. V. V. Glagolev, K. G. Gulamov, M. Yu. Kratenko, *et al.*, Yad. Fiz. **58**, 2005 (1995) [Phys. At. Nucl. **58**, 1896 (1995)].
5. V. V. Glagolev, K. G. Gulamov, M. Yu. Kratenko, *et al.*, Pis'ma Zh. Éksp. Teor. Fiz. **59**, 316 (1994) [JETP Lett. **59**, 336 (1994)].
6. K. G. Gulamov, V. D. Lipin, S. L. Lutpullaev, *et al.*, Yad. Fiz. **59**, 1042 (1996) [Phys. At. Nucl. **59**, 997 (1996)].
7. V. V. Glagolev, K. G. Gulamov, V. D. Lipin, *et al.*, Yad. Fiz. **62**, 1472 (1999) [Phys. At. Nucl. **62**, 1388 (1999)].

Translated by A. Isaakyan

<center>

ELEMENTARY PARTICLES AND FIELDS
Theory

Decay $\phi(1020) \to \gamma f_0(980)$: Analysis in the Nonrelativistic Quark Model Approach*

</center>

A. V. Anisovich, V. V. Anisovich, V. N. Markov, V. A. Nikonov, and A. V. Sarantsev

Petersburg Nuclear Physics Institute, Russian Academy of Sciences, Gatchina, 188350 Russia
Received May 18, 2004; in final form, January 17, 2005

Abstract—We demonstrate the possibility of a good description of the processes $\phi(1020) \to \gamma \pi \pi$ and $\phi(1020) \to \gamma f_0(980)$ within the framework of the nonrelativistic quark model assuming $f_0(980)$ to be a dominantly quark−antiquark system. Different mechanisms of the radiative decay, that is, the emission of a photon by the constituent quark (additive quark model) and charge-exchange current, are considered. We also discuss the status of the threshold theorem applied to the studied reactions, namely, the behavior of the decay amplitude at $M_{\pi\pi} \to m_\phi$ and $m_{f_0} \to m_\phi$. In conclusion, the arguments favoring the $q\bar{q}$ origin of $f_0(980)$ are listed. © *2005 Pleiades Publishing, Inc.*

1. INTRODUCTION

The K-matrix analysis of meson spectra [1−3] and meson systematics [4, 5] point determinately to the quark−antiquark origin of $f_0(980)$. However, there exist hypotheses where $f_0(980)$ is interpreted as a four-quark state [6], $K\bar{K}$ molecule [7], or vacuum scalar [8]. The radiative and weak decays involving $f_0(980)$ may be a decisive tool for understanding the nature of $f_0(980)$.

In the present paper, the reaction $\phi(1020) \to \gamma f_0(980)$ is considered in terms of a nonrelativistic quark model assuming $f_0(980)$ to be dominantly the $q\bar{q}$ state. The nonrelativistic quark model is a good approach for the description of the lowest $q\bar{q}$ states of pseudoscalar and vector nonets, so one may hope that the lowest scalar $q\bar{q}$ states are described with reasonable accuracy as well. The choice of a nonrelativistic approach for the analysis of the reaction $\phi(1020) \to \gamma f_0(980)$ was motivated by the fact that, in its framework, we can take account of not only the additive-quark-model processes (emission of a photon by a constituent quark) but also those beyond it within the use of the dipole formula (photon emission by the charge-exchange current gives such an example). The dipole formula for the radiative transition of a vector state to a scalar one, $V \to \gamma S$, was applied before for the calculation of reactions with heavy quarks (see [9, 10] and references therein). Still, a straightforward application of the dipole formula to the reaction $\phi(1020) \to \gamma f_0(980)$ is hardly possible since the $f_0(980)$ surely cannot be represented as a stable particle: this resonance is characterized by two

poles lying on two different sheets of the complex-M plane, at $M = 1020 - 40i$ MeV and $M = 960 - 200i$ MeV. It should be emphasized that these two poles are important for the description of $f_0(980)$. Therefore, we use the method below as follows: we calculate the radiative transition to a stable bare f_0 state (this is $f_0^{\text{bare}}(700 \pm 100)$); its parameters were obtained in the K-matrix analysis [1]. In this way, we find out the description of the process $\phi(1020) \to \gamma f_0^{\text{bare}}(700 \pm 100)$, and furthermore, we switch on the hadronic decays and determine the transition $\phi(1020) \to \gamma \pi \pi$; just the residue in the pole of this amplitude is the radiative transition amplitude $\phi(1020) \to \gamma f_0(980)$. Hence, we obtain a successful description of data for $\phi(1020) \to \gamma \pi \pi$ and $\phi(1020) \to \gamma f_0(980)$ within the assumption that $f_0(980)$ is dominated by the quark−antiquark state.

The conclusion about the nature of $f_0(980)$ cannot be based on the study of one reaction only but should be motivated by the whole aggregate of data. In the article, we also list the other processes, which provide us with arguments in favor of the dominant $q\bar{q}$ structure of $f_0(980)$.

Section 2 is introductive: here, we consider a simple model for the description of composite vector (V) and scalar (S) particles, the composite particles consisting of one-flavor quark, charge-exchange currents being absent. In such a model, the decay transition $V \to \gamma S$ is completely determined by the additive-quark-model process: a photon is emitted only by one or another constituent quark. Two alternative representations of the $V \to \gamma S$ decay amplitude are given, namely, the standard additive-quark-model formula and that of a photon dipole emission; in the latter, the factor $\omega = m_V - m_S$ is written in

---

explicit form. The comparison of these two representations helps us to formulate the problem of application of the threshold theorem [11] to the reaction $V \to \gamma S$. Using a simple example with exponential wave functions, we demonstrate that the ω^3 factor occurs in the partial decay width when the transition $V \to \gamma S$ is considered in terms of the additive quark model.

The threshold theorem has a straightforward formulation for the stable V and S states, but it is not the case for resonances, which are the main objects of our present study. That is why we intend to reformulate the threshold theorem as the requirement of amplitude analyticity—this is given in Section 3 on the basis of [12]. Working with nonstable particles, when V and S are resonances, the $V \to \gamma S$ amplitude should be determined as a residue of a more general amplitude, with stable particles in the initial and final states. For example, the $\phi(1020) \to \gamma f_0(980)$ amplitude should be defined as a residue of the $e^+e^- \to \gamma\pi\pi$ amplitude in the poles corresponding to resonances $\phi(1020)$ and $f_0(980)$ (the ϕ pole in the e^+e^- channel and the f_0 pole in the $\pi\pi$ channel). The only residue in the pole defines the universal amplitude which does not depend on the considered reaction.

In Section 4, we discuss the reaction $\phi \to \gamma f_0$ for the case when the f_0 is a multicomponent system and f_0 and ϕ are stable states with respect to hadronic decays. The analysis of meson spectra (e.g., see the latest K-matrix analyses [1, 5]) definitely tells us that the f_0 mesons are the mixture of the quarkonium ($n\bar{n} = (u\bar{u} + d\bar{d})/\sqrt{2}$ and $s\bar{s}$) and gluonium components. Such a multichannel structure of f_0 states reveals itself in the existence of the t-channel charge-exchange currents. Therefore, the transition $\phi \to \gamma f_0$ goes via two mechanisms: the photon emission by constituent quarks (additive-quark-model process) and charge-exchange current. We write down the formulas for the amplitudes initiated by these two mechanisms. The equality to zero of the whole amplitude at small mass difference of ϕ and f_0, $A_{\phi \to \gamma f_0} \sim \omega$ at $\omega \to 0$, resulted from the cancellation of contributions of these two mechanisms. We also give a dipole representation of the transition amplitude, where $A_{\phi \to \gamma f_0}$ is determined through the mean transition radius and mass difference $(m_\phi - m_{f_0})$.

Section 5 is devoted to the reaction $\phi(1020) \to \gamma f_0(980)$. First, we discuss whether it is possible to treat $f_0(980)$ as a stable particle. Our answer is "no"; in fact, the $f_0(980)$ is an unstable particle characterized by two poles located near the $K\bar{K}$ threshold. As was stressed above, strong transitions $f_0(980) \to \pi\pi$, $K\bar{K}$ reveal themselves in the two amplitude poles, which are located on different sheets of the complex-M plane, at $M = 1020 - 40i$ MeV

and $M = 960 - 200i$ MeV, and these two poles are important for the description of $f_0(980)$. The essential role of the second pole is seen by considering the $\pi\pi$ spectrum in $\phi(1020) \to \gamma\pi\pi$ (Section 6): the visible width of the pick in the $\pi\pi$ spectrum is of the order of 150 MeV, and the spectrum decreases slowly with a further decrease in $M_{\pi\pi}$.

Another problem to be discussed is the choice of method for the consideration of radiative decay amplitude. One can work within two alternative representations for the $A_{\phi \to \gamma f_0}$ amplitude. One representation uses the additive quark model complemented with the contribution from the charge-exchange current processes. Whence the additive-quark-model amplitude can be calculated rather definitely, at least for the lowest $q\bar{q}$ states, the charge-exchange current processes are vaguely determined.

The other way to deal with the transition amplitude consists in using the dipole emission formulas, where the amplitude is defined by the mean transition radius and factor $(m_\phi - m_{f_0})$. For the lowest $q\bar{q}$ states, we have a good estimate of the radius. But there is a problem of the determination of the factor $(m_\phi - m_{f_0})$, because the $f_0(980)$ is an unstable particle characterized by two poles. The pole $M = 960 - 200i$ MeV is disposed on the same sheet of the complex-M plane as the pole of ϕ meson, and the distance $|m_\phi - m_{f_0}|$ is ~ 200 MeV, while the pole $M = 1020 - 40i$ MeV is located on another sheet, and the distance from the ϕ meson is ~ 70 MeV, which is also not small on the hadronic scale. The problem is what the mass difference factor means in the case of complex masses and which pole should be used to characterize this mass difference.

To succeed in the description of the decay $\phi(1020) \to \gamma f_0(980)$, we use the results of the K-matrix analysis of the $IJ^{PC} = 00^{++}$ wave [1]. The fact is that, on the one hand, the K-matrix analysis allows us to get the experimentally based information on masses and full widths of resonances together with the pole residues needed for the decay couplings and partial widths. On the other hand, the knowledge of the K-matrix amplitude enables us to trace the evolution of states by switching on/off the decay channels. In such a way, one may obtain the characteristics of the bare states, which are predecessors of real resonances. With such characteristics, one can perform a reverse procedure: to retrace the transformation of the amplitude written in terms of bare states to the amplitude corresponding to the transition to a real resonance. Just this procedure has been applied in Section 5 for the calculation of the decay amplitude $\phi(1020) \to \gamma f_0(980)$.

Therefore, within the framework of the nonrelativistic quark model, we have calculated the reaction $\phi(1020) \to \gamma f_0^{\text{bare}}(n)$, where $f_0^{\text{bare}}(n)$ are bare states found in [1]. Furthermore, with the K-matrix technique, we have taken account of the decays $f_0^{\text{bare}}(n) \to \pi\pi, K\bar{K}$, thus having calculated the reaction $\phi(1020) \to \gamma\pi\pi$ and the amplitude of $\phi(1020) \to \gamma f_0(980)$ (the pole residue in the $\pi\pi$ channel). In this way, we see that the main contribution is given by the transition $\phi(1020) \to \gamma f_0^{\text{bare}}(700 \pm 100)$. The characteristics of $f_0^{\text{bare}}(700 \pm 100)$ are fixed by the K-matrix analysis [1]: this is a $q\bar{q}$ state close to the flavor octet and it is just the predecessor of $f_0(980)$. In the framework of this approach, we succeed in the description of data for the reactions $\phi(1020) \to \gamma f_0(980)$ (Section 5) and $\phi(1020) \to \gamma\pi\pi$ (Section 6).

Let us note that such a method, the use of bare states for the calculation of meson spectra, has been applied before for the study of weak hadronic decays $D^+ \to \pi^+\pi^+\pi^-$ [13] and description of the $\pi\pi$ spectra in photon–photon collisions $\gamma\gamma \to \pi\pi$ [14].

The question of what the accuracy of the additive quark model is in the description of the reactions $\phi(1020) \to \gamma f_0^{\text{bare}}(700 \pm 100)$ and $\phi(1020) \to \gamma f_0(980)$ is discussed in Section 7. We compare the results of the calculation of the $\phi(1020) \to \gamma f_0^{\text{bare}}(700 \pm 100)$ reaction by using the dipole formula with that of the additive quark model. It is seen that, within error bars given by the K-matrix analysis [1], the results coincide. Still, one should emphasize that the dipole-calculation accuracy is low, which is due to a large error in the determination of the bare-state masses. The coincidence of results in the dipole and additive-quark-model formulas should point to a small contribution of processes which violate additivity, such as photon emission by the charge-exchange current: this smallness is natural, provided the hadrons are characterized by two sizes, namely, the hadron radius ($R_h \sim R_{\text{conf}}$) and constituent-quark radius (r_q) under the condition $r_q^2 \ll R_h^2$ (see [15] and references therein).

The performed analysis demonstrates that the reaction $\phi(1020) \to \gamma f_0(980)$ does not produce any difficulty with the interpretation of $f_0(980)$ as a $q\bar{q}$ state. Still, to draw a conclusion about the content of $f(980)$, we list in Section 8 the arguments in favor of the $q\bar{q}$ origin of $f_0(980)$.

2. THE PROCESS $V \to \gamma S$ WITHIN THE NONRELATIVISTIC ADDITIVE QUARK MODEL

Here, in the framework of the nonrelativistic quark model, we consider the transition $V \to \gamma S$ in the case when the charge-current-exchange forces are absent and the $V \to \gamma S$ amplitude is given by the additive-quark-model contribution.

2.1. Wave Functions for Vector and Scalar Composite Particles

The $q\bar{q}$ wave functions of vector and scalar particles are defined as follows:

$$\Psi_{V\mu}(\mathbf{k}) = \sigma_\mu \psi_V(k^2), \tag{1}$$
$$\Psi_S(\mathbf{k}) = (\boldsymbol{\sigma} \cdot \mathbf{k})\psi_S(k^2),$$

where, by using Pauli matrices, the spin factors are singled out. The blocks dependent on the relative momentum squared are related to the vertices in the following way:

$$\psi_V(k^2) = \frac{\sqrt{m}}{2} \frac{G_V(k^2)}{k^2 + m\varepsilon_V}, \tag{2}$$
$$\psi_S(k^2) = \frac{1}{2\sqrt{m}} \frac{G_S(k^2)}{k^2 + m\varepsilon_V}.$$

Here, m is the quark mass, and ε is the composite-system binding energy: $\varepsilon_V = 2m - m_V$ and $\varepsilon_S = 2m - m_S$, where m_V and m_S are the masses of bound states. The normalization condition for the wave functions reads

$$\int \frac{d^3k}{(2\pi)^3} \text{Sp}_2 \left[\Psi_S^+(\mathbf{k})\Psi_S(\mathbf{k})\right] \tag{3}$$
$$= \int \frac{d^3k}{(2\pi)^3} \psi_S^2(k^2) \text{Sp}_2[(\boldsymbol{\sigma} \cdot \mathbf{k})(\boldsymbol{\sigma} \cdot \mathbf{k})] = 1,$$

$$\int \frac{d^3k}{(2\pi)^3} \text{Sp}_2 \left[\Psi_{V\mu}^+(\mathbf{k})\Psi_{V\mu'}(\mathbf{k})\right]$$
$$= \int \frac{d^3k}{(2\pi)^3} \psi_V^2(k^2) \text{Sp}_2[\sigma_\mu \sigma_{\mu'}] = \delta_{\mu\mu'}.$$

2.2. Amplitude within the Additive Quark Model

When a photon is emitted by a quark or antiquark, the $V \to \gamma S$ process is described by the triangle diagram (see Fig. 1a) that is actually the contribution from the additive quark model. Relativistic consideration of the triangle diagram is presented in [16, 17], while the discussion of the nonrelativistic approximation is given in [12, 18] (recall that, in [18], the corresponding wave functions were determined in another way, namely, $\psi_V(k^2) = G_V(k^2)(4k^2 + 4m\varepsilon_V)^{-1}$ and $\psi_S(k^2) = G_S(k^2)(4k^2 + 4m\varepsilon_S)^{-1}$).

In terms of wave functions (1), the triangle-diagram contribution reads

$$\epsilon_\mu^{(V)}\epsilon_\alpha^{(\gamma)} A_{\mu\alpha}^{V \to \gamma S} = eZ_{V \to \gamma S}\epsilon_\mu^{(V)}\epsilon_\alpha^{(\gamma)} F_{\mu\alpha}^{V \to \gamma S}, \tag{4}$$
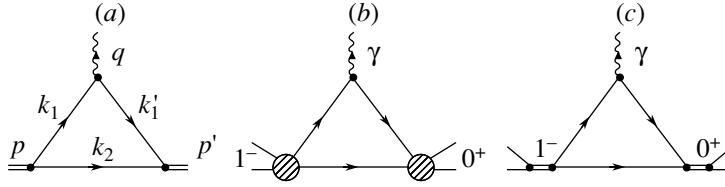
Fig. 1. Transitions $V \to \gamma S$ in the additive quark model.

$$F_{\mu\alpha}^{V\to\gamma S} = \int \frac{d^3k}{(2\pi)^3} \mathrm{Sp}_2\left[\Psi_S^+(\mathbf{k}) 4k_\alpha \Psi_{V\mu}(\mathbf{k})\right].$$

Here, $\epsilon_\mu^{(V)}$ and $\epsilon_\alpha^{(\gamma)}$ are polarization vectors for V and γ: $\epsilon_\mu^{(V)} p_{V\mu} = 0$ and $\epsilon_\alpha^{(\gamma)} q_\alpha = 0$. The charge factor $Z_{V\to\gamma S}$ being different for different reactions is specified below (see also [16, 17]). The expression for the transition amplitude (4) can be simplified after the substitution in the integrand

$$\mathrm{Sp}_2[\sigma_\mu(\boldsymbol{\sigma}\cdot\mathbf{k})]k_\alpha \to \frac{2}{3}k^2 g_{\mu\alpha}^{\perp\perp}, \qquad (5)$$

where $g_{\mu\alpha}^{\perp\perp}$ is the metric tensor in the space orthogonal to total momentum of the vector particle p_V and photon q. The substitution (5) results in

$$A_{\mu\alpha}^{V\to\gamma S} = e g_{\mu\alpha}^{\perp\perp} A_{V\to\gamma S}, \qquad (6)$$

where

$$A_{V\to\gamma S} = Z_{V\to\gamma S} \int_0^\infty \frac{dk^2}{\pi} \psi_S(k^2)\psi_V(k^2)\frac{2}{3\pi}k^3. \quad (7)$$

The amplitudes $A_{\mu\alpha}^{V\to\gamma S}$ and $A_{V\to\gamma S}$ were used in [16, 17] for the decay amplitude $\phi(1020) \to \gamma f_0(980)$ within the relativistic treatment of the quark transitions.

However, for our purpose, it would be suitable not to deal with Eq. (7) but use the form factor $F_{\mu\alpha}^{V\to\gamma S}$ of Eq. (4) rewritten in the coordinate representation. One has

$$\Psi_{V\mu}(\mathbf{k}) = \int d^3r\, e^{i\mathbf{k}\cdot\mathbf{r}}\Psi_{V\mu}(\mathbf{r}), \qquad (8)$$

$$\Psi_S(\mathbf{k}) = \int d^3r\, e^{i\mathbf{k}\cdot\mathbf{r}}\,\Psi_S(\mathbf{r}).$$

Then the form factor $F_{\mu\alpha}^{V\to\gamma S}$ can be represented as follows:

$$F_{\mu\alpha}^{V\to\gamma S} = \int d^3r\, \mathrm{Sp}_2\left[\Psi_S^+(\mathbf{r})\cdot 4k_\alpha \Psi_{V\mu}(\mathbf{r})\right], \quad (9)$$

where k_α is the operator: $k_\alpha = -i\nabla_\alpha$. This operator can be written as the commutator of r_α and $-\nabla^2/m = T$ (kinetic energy):

$$2im(Tr_\alpha - r_\alpha T) = 4(-i\nabla_\alpha). \qquad (10)$$

Let us consider the case when the quark−quark interaction is rather simple, say, it depends on the relative interquark distance with the potential $U(r)$. For vector and scalar composite systems, we also use an additional simplifying assumption: vector and scalar mesons consist of quarks of the same flavor ($q\bar{q}$). Then we have the Hamiltonian

$$H = -\frac{\nabla^2}{m} + U(r) \qquad (11)$$

and can rewrite (10) as

$$2im(Hr_\alpha - r_\alpha H) = 4(-i\nabla_\alpha). \qquad (12)$$

After substituting the commutator in (9), the transition form factor for the reaction $V \to \gamma S$ reads

$$F_{\mu\alpha}^{V\to\gamma S} = \int d^3r\, \mathrm{Sp}_2\left[\Psi_S^+(\mathbf{r})r_\alpha \Psi_{V\mu}(\mathbf{r})\right] \qquad (13)$$

$$\times 2im(\varepsilon_V - \varepsilon_S).$$

Here, we have used the fact that $(H + \varepsilon_V)\Psi_V = 0$ and $(H + \varepsilon_S)\Psi_S = 0$.

The factor $(\varepsilon_V - \varepsilon_S)$ on the right-hand side of (13) is a manifestation of the threshold theorem: at $\varepsilon_V - \varepsilon_S = m_S - m_V \to 0$, the form factor $F_{\mu\alpha}^{V\to\gamma S}$ goes to zero. Actually, in the additive quark model, the amplitude of the $V \to \gamma S$ transition, being determined by the process of Fig. 1a, cannot be zero if V and S are basic states with radial quantum number $n = 1$: in this case, the wave functions $\psi_V(k^2)$ and $\psi_S(k^2)$ do not change sign, and the right-hand side of (7) does not equal zero. In order to clarify this point, let us consider as an example the exponential approximation for the wave functions $\psi_V(k^2)$ and $\psi_S(k^2)$.

2.3. Basic Vector and Scalar $q\bar{q}$ States: An Example of the Exponential Approach to Wave Functions

We parametrize the ground-state wave functions of scalar and vector particles as follows:

$$\Psi_{V_\mu}(r) = \sigma_\mu \psi_V(r^2), \qquad (14)$$

$$\psi_V(r^2) = \frac{1}{2^{5/4}\pi^{3/4}b_V^{3/4}}\exp\left[-\frac{r^2}{4b_V}\right],$$

$$\Psi_S(r) = (\boldsymbol{\sigma}\cdot\mathbf{r})\psi_S(r^2),$$

$$\psi_S(r^2) = \frac{i}{2^{5/4}\pi^{3/4}b_S^{5/4}\sqrt{3}}\exp\left[-\frac{r^2}{4b_S}\right].$$

The wave functions with $n = 1$ have no nodes; numerical factors take account of the normalization conditions

$$\int d^3r \,\mathrm{Sp}_2\left[\Psi_S^+(r)\Psi_S(r)\right] = 1, \qquad (15)$$

$$\int d^3r \,\mathrm{Sp}_2\left[\Psi_{V\mu}^+(r)\Psi_{V\mu'}(r)\right] = \delta_{\mu\mu'}.$$

With exponential wave functions, the matrix element for $V \to \gamma S$ given by the additive-quark-model diagram [Eq. (9)] is equal to

$$\epsilon_\mu^{(V)}\epsilon_\alpha^{(\gamma)}F_{\mu\alpha}^{V\to\gamma S}(\text{additive}) \qquad (16)$$

$$= (\epsilon^{(V)}\epsilon^{(\gamma)})\frac{2^{7/2}}{\sqrt{3}}\frac{b_V^{3/4}b_S^{5/4}}{(b_V+b_S)^{5/2}}.$$

The formula for $F_{\mu\alpha}^{V\to\gamma S}$ written in the framework of dipole emission [Eq. (13)] reads

$$\epsilon_\mu^{(V)}\epsilon_\alpha^{(\gamma)}F_{\mu\alpha}^{V\to\gamma S}(\text{dipole}) \qquad (17)$$

$$= (\epsilon^{(V)}\epsilon^{(\gamma)})\frac{2^{7/2}}{\sqrt{3}}\frac{b_V^{7/4}b_S^{5/4}}{(b_V+b_S)^{5/2}}m(m_V - m_S).$$

In the case under consideration [one-flavor quarks with the Hamiltonian given by Eq. (11)], Eqs. (16) and (17) coincide, $F_{\mu\alpha}^{V\to\gamma S}(\text{additive}) = F_{\mu\alpha}^{V\to\gamma S}(\text{dipole})$; therefore,

$$m(m_V - m_S) = b_V^{-1}, \qquad (18)$$

which means that the factor $(\varepsilon_S - \varepsilon_V)$ on the right-hand side of (13) relates to the difference between the V and S levels and is defined by b_V only. In this way, the form factor $F_{\mu\alpha}^{V\to\gamma S}$ goes to zero only when b_V (or b_S) tends to infinity.

The considered example does not mean that the threshold theorem for the reaction $V \to \gamma S$ does not work; this tells us only that we should interpret and use it carefully. In the next section, we discuss how to formulate the threshold theorem based on the requirement of amplitude analyticity, thus getting more information on its applicability.

3. ANALYTICITY OF THE AMPLITUDE AND THE THRESHOLD THEOREM

The threshold theorem can be formulated as the requirement of analyticity of the amplitude. To clarify this statement, we consider here not only the transition of the bound states but also a more general process shown in Fig. 1b, where the interacting constituents being in the vector $J^P = 1^-$ state emit a photon and then turn into the scalar $J^P = 0^+$ state. This amplitude has as a subprocess a bound-state transition. Namely, the blocks for the rescattering of constituents in Fig. 1b contain the poles related to bound states (see Fig. 1c), and the residues in these poles determine the bound-state transition amplitude (triangle diagram shown as intermediate block in Fig. 1c).

With the notation for invariant mass squares in the initial and final states of Fig. 1b as follows:

$$P_V^2 = s_V, \qquad P_S^2 = s_S, \qquad (19)$$

we can write the spin structures for this more general transition $V \to \gamma S$. The standard representation of this amplitude is

$$A_{\mu\alpha}^{V\to\gamma S}(s_V, s_S, q^2 \to 0) \qquad (20)$$

$$= \left(g_{\mu\alpha} - \frac{2q_\mu P_{V\alpha}}{s_V - s_S}\right)A_{V\to\gamma S}(s_V, s_S, 0).$$

Here, we stress that the amplitude $A_{V\to\gamma S}$ describes the emission of a real photon, $q^2 = 0$. In (20), it was taken into account that $(P_V q) = (s_V - s_S)/2$. The requirement of analyticity, i.e., the absence of a pole at $s_V = s_S$, leads to the condition

$$\left[A_{V\to\gamma S}(s_V, s_S, 0)\right]_{s_V\to s_S} \to 0, \qquad (21)$$

which is the threshold theorem for the transition amplitude $V \to \gamma S$.

It should be now emphasized that the form of the spin factor in Eq. (20) is not unique. Alternatively, one can write the spin factor as the metric tensor $g_{\mu\alpha}^{\perp\perp}$ working in the space orthogonal to P_V and q, i.e., $P_{V\mu}g_{\mu\alpha}^{\perp\perp} = 0$ and $g_{\mu\alpha}^{\perp\perp}q_\alpha = 0$ [see Eq. (5)]. This metric tensor reads

$$g_{\mu\alpha}^{\perp\perp}(0) = g_{\mu\alpha} + \frac{4s_V}{(s_V - s_S)^2}q_\mu q_\alpha \qquad (22)$$

$$- \frac{2}{s_V - s_S}(P_{V\mu}q_\alpha + q_\mu P_{V\alpha}),$$

and we have used it in Eq. (6). The uncertainty in the choice of spin factor is due to the fact that the difference

$$g_{\mu\alpha}^{\perp\perp}(0) - \left(g_{\mu\alpha} - \frac{2q_\mu P_{V\alpha}}{s_V - s_S}\right) = 4L_{\mu\alpha}(0), \qquad (23)$$

where

$$L_{\mu\alpha}(0) = \frac{s_V}{(s_V - s_S)^2}q_\mu q_\alpha - \frac{1}{2(s_V - s_S)}P_{V\mu}q_\alpha, \qquad (24)$$

is the nilpotent operator [12]:

$$L_{\mu\alpha}(0)L_{\mu\alpha}(0) = 0. \qquad (25)$$

The addition of the nilpotent operator $L_{\mu\alpha}(0)$ to spin factor of the transition amplitude $V \rightarrow \gamma S$ does not change the expression $A_{V \rightarrow \gamma S}(s_V, s_S, 0)$ (see [12] for more detail). Here, in discussing the analytical structure of the amplitude, it is convenient to work with the operator (20), since it is the least cumbersome.

Consider now the reaction $V \rightarrow \gamma S$ (V and S being quark–antiquark bound states), say, of the type of $\phi \rightarrow \gamma f_0$ or $\phi \rightarrow \gamma a_0$. Because of the confinement, the quarks are not the particles which form the $|\text{in}\rangle$ and $\langle \text{out}|$ states; therefore, the amplitudes like $A_{\phi \rightarrow \gamma f_0}$ are to be defined as the amplitude residue for the process with the scattering of the stable particles, for example, for $e^+e^- \rightarrow \gamma\pi^+\pi^-$ (see Fig. 2):

$$A_{\mu\alpha}^{e^+e^- \rightarrow \gamma\pi^+\pi^-}(s_V, s_S, 0) = \left(g_{\mu\alpha} - \frac{2q_\mu P_{V\alpha}}{s_V - s_S} \right) \tag{26}$$

$$\times \left[G_{e^+e^- \rightarrow \phi} \frac{A_{\phi \rightarrow \gamma f_0}(m_\phi^2, m_{f_0}^2, 0)}{(s_V - m_\phi^2)(s_S - m_{f_0}^2)} g_{f_0 \rightarrow \pi^+\pi^-} \right.$$

$$\left. + B(s_V, s_S, 0) \right].$$

We see that $A(m_\phi^2, m_{f_0}^2, 0)$, up to the factors $G_{e^+e^- \rightarrow \phi}$ and $g_{f_0 \rightarrow \pi^+\pi^-}$, is the residue in the amplitude poles $s_V = m_\phi^2$ and $s_S = m_{f_0}^2$: just this value supplies us with the transition amplitude for the reactions with bound states $\phi \rightarrow \gamma f_0$. If we deal with stable composite particles, in other words, if ϕ and f_0 can be included in the set of fields $|\text{in}\rangle$ and $\langle \text{out}|$, the transition amplitude $\phi \rightarrow \gamma f_0$ can be written in a form similar to (20):

$$A_{\mu\alpha}^{\phi \rightarrow \gamma f_0}(m_\phi^2, m_{f_0}^2, 0) \tag{27}$$

$$= \left(g_{\mu\alpha} - \frac{2q_\mu p_\alpha}{m_\phi^2 - m_{f_0}^2} \right) A_{\phi \rightarrow \gamma f_0}\left(m_\phi^2, m_{f_0}^2, 0 \right),$$

where we have substituted $P_V \rightarrow p$. For $A_{\phi \rightarrow \gamma f_0}\left(m_\phi^2, m_{f_0}^2, 0 \right)$, the threshold theorem is fulfilled:

$$\left[A_{\phi \rightarrow \gamma f_0}(m_\phi^2, m_{f_0}^2, 0) \right]_{m_\phi^2 \rightarrow m_{f_0}^2} \sim m_\phi^2 - m_{f_0}^2; \tag{28}$$

this means that the threshold theorem of Eq. (28) reveals itself as a requirement of analyticity of the amplitude $\phi \rightarrow \gamma f_0$ determined by Eq. (27).

Let us emphasize again that formula (27) has been written for the ϕ and f_0 mesons assuming them to be stable; i.e., they can be treated as the states which belong to the sets $|\text{in}\rangle$ and $\langle \text{out}|$. However, by considering the process $\phi \rightarrow \gamma f_0$, we deal with resonances, not stable particles, and whether this assumption is valid for resonances is a question which deserves
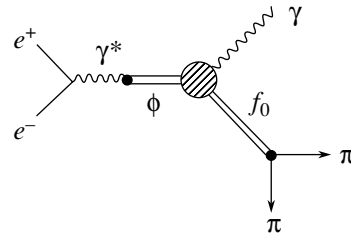
Fig. 2. Process $e^+e^- \rightarrow \gamma\pi\pi$: residues in the e^+e^- and $\pi\pi$ channels determine the $\phi \rightarrow \gamma f_0$ amplitude.

special discussion. We shall come back to this point below, and now let us investigate how the requirement (28) is realized in quantum mechanics when ϕ and f_0 are stable particles.

4. QUANTUM MECHANICS CONSIDERATION OF THE REACTION $\phi \rightarrow \gamma f_0$ WITH ϕ AND f_0 BEING STABLE PARTICLES

In Section 2, we have considered the model for the reaction $V \rightarrow \gamma S$ when V and S are formed by quarks of the same flavor (one-channel model for V and S). The one-channel approach for $\phi(1020)$ (the dominance of $s\bar{s}$ component) looks acceptable, though for f_0 mesons it is definitely not so: scalar–isoscalar states are multicomponent ones.

The existence of several components in the f_0 mesons changes the situation with the $\phi \rightarrow \gamma f_0$ decays. First, the mixing of different components may result in close values of masses of the low-lying vector and scalar mesons. Second, Eqs. (9) and (13) for the $\phi \rightarrow \gamma f_0$ decay turn out to be nonequivalent because of the photon emission by the t-channel exchange currents.

Here, we consider in detail a simple model for ϕ and f_0: the ϕ meson is treated as an $s\bar{s}$ system, with no admixture of the nonstrange quarkonium, $n\bar{n} = (u\bar{u} + d\bar{d})/\sqrt{2}$, nor gluonium ($gg$), while the f_0 meson is a mixture of $s\bar{s}$ and gg.

This model can be considered as a guide for the study of the reaction $\phi(1020) \rightarrow \gamma f_0(980)$. Indeed, the $\phi(1020)$ is an almost pure $s\bar{s}$ state; the admixture of the $n\bar{n}$ component in $\phi(1020)$ is small, $\leq 5\%$, and it can be neglected in a rough estimate of the $\phi(1020) \rightarrow \gamma f_0(980)$ decay.

The resonance $f_0(980)$ is a multicomponent state. Analysis of the $IJ^{PC} = 00^{++}$ wave in the K-matrix fit to the data for meson spectra $\pi\pi$, $K\bar{K}$, $\eta\eta$, $\eta\eta'$, $\pi\pi\pi$ gives the following constraints for the $s\bar{s}$, $n\bar{n}$, and gg components in $f_0(980)$ [1, 5]:

$$50\% \lesssim W_{s\bar{s}}[f_0(980)] < 100\%, \tag{29}$$
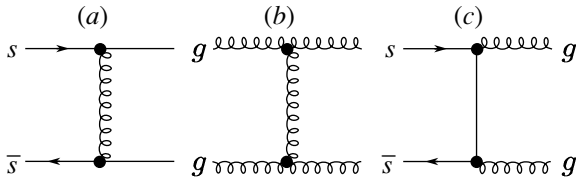
Fig. 3. Examples of diagrams which contribute to the potentials $U_{s\bar{s}\to s\bar{s}}(r)$, $U_{gg\to gg}(r)$, and $U_{s\bar{s}\to gg}(\mathbf{r})$.

$$0 \lesssim W_{n\bar{n}}[f_0(980)] < 50\%,$$
$$0 \lesssim W_{gg}[f_0(980)] < 25\%.$$

Also, the $f_0(980)$ may contain a long-range $K\bar{K}$ component, on the level of $10-20\%$.

The restrictions (29) permit the variant when the probability for the $n\bar{n}$ component is small and $f_0(980)$ is a mixture of $s\bar{s}$ and gg only. Bearing this variant in mind, we consider such a two-component model for ϕ and f_0 supposing these particles are stable in respect to hadronic decays.

It is not difficult to generalize our consideration for the three-component f_0 state ($n\bar{n}$, $s\bar{s}$, and gg); the corresponding formulas are given in this section too.

4.1. Two-Component Model ($s\bar{s}$, gg) for f_0 and ϕ

Now let us discuss the model where f_0 has two components only: strange quarkonium ($s\bar{s}$ in the P wave) and gluonium (gg in the S wave). The spin structure of the $s\bar{s}$ wave function is written in Section 2: it contains the factor $(\boldsymbol{\sigma} \cdot \mathbf{r})$ in the coordinate representation. For the gg system, we have δ_{ab} or, in terms of polarization vectors, the convolution $(\boldsymbol{\epsilon}_1^{(g)} \boldsymbol{\epsilon}_2^{(g)})$. Here, we consider a simple interaction when the potential does not depend on spin variables—in this case, one may forget about the vector structure of gg working as if the gluon component consists of spinless particles. As concerns ϕ, it is considered as a pure $s\bar{s}$ state in the S wave, with the wave-function spin factor $\sim \sigma_\mu$ (see Section 2). So, the wave functions of f_0 and ϕ mesons are written as follows:

$$\hat{\Psi}_{f_0}(\mathbf{r}) = \begin{pmatrix} \Psi_{f_0(s\bar{s})}(\mathbf{r}) \\ \Psi_{f_0(gg)}(r) \end{pmatrix} = \begin{pmatrix} (\boldsymbol{\sigma} \cdot \mathbf{r})\psi_{f_0(s\bar{s})}(r) \\ \psi_{f_0(gg)}(r) \end{pmatrix},$$
$$(30)$$

$$\hat{\Psi}_{\phi\mu}(\mathbf{r}) = \begin{pmatrix} \Psi_{\phi(s\bar{s})\mu}(\mathbf{r}) \\ \Psi_{\phi(gg)\mu}(r) \end{pmatrix} = \begin{pmatrix} \sigma_\mu \psi_{\phi(s\bar{s})}(r) \\ 0 \end{pmatrix}.$$

The normalization condition is given by Eq. (15) with the obvious replacement $\Psi_S \to \hat{\Psi}_{f_0}$ and $\Psi_{V\mu} \to \hat{\Psi}_{\phi\mu}$.

The Schrödinger equation for the two-component states, $s\bar{s}$ and gg, reads

$$\left| \begin{matrix} \frac{k^2}{m} + U_{s\bar{s}\to s\bar{s}}(r) & U_{s\bar{s}\to gg}(\mathbf{r}) \\ U_{s\bar{s}\to gg}^+(\mathbf{r}) & \frac{k^2}{m_g} + U_{gg\to gg}(r) \end{matrix} \right| \quad (31)$$

$$\times \begin{pmatrix} \Psi_{s\bar{s}}(\mathbf{r}) \\ \Psi_{gg}(\mathbf{r}) \end{pmatrix} = E \begin{pmatrix} \Psi_{s\bar{s}}(\mathbf{r}) \\ \Psi_{gg}(\mathbf{r}) \end{pmatrix}.$$

Furthermore, we denote the Hamiltonian on the left-hand side of (31) as H_0.

We set the gg component in ϕ to zero. It means that the potential $U_{s\bar{s}\to gg}(\mathbf{r})$ satisfies the following constraints:

$$\langle 0^+ s\bar{s}|U_{s\bar{s}\to gg}(\mathbf{r})|0^+ gg\rangle \neq 0, \quad (32)$$
$$\langle 1^- s\bar{s}|U_{s\bar{s}\to gg}(\mathbf{r})|1^- gg\rangle = 0.$$

These constraints do not look surprising for mesons in the region $1.0-1.5$ GeV because the scalar glueball is located just in this mass region, while the vector one has considerably higher mass, ~ 2.5 GeV [19].

The t-exchange diagrams shown in Figs. 3a, 3b, and 3c are an example of interaction leading to the potentials $U_{s\bar{s}\to s\bar{s}}(r)$, $U_{gg\to gg}(r)$, and $U_{s\bar{s}\to gg}(\mathbf{r})$. The potential $U_{s\bar{s}\to gg}(\mathbf{r})$ contains the t-channel charge exchange.

4.1.1. Dipole emission of the photon in $\phi \to \gamma f_0$ decay. The Hamiltonian for the interaction of an electromagnetic field with two-component composite systems (quarkonium and gluonium components) is presented in the Appendix.

For the transition $V \to \gamma S$, keeping the terms proportional to the charge e, we have the following operator for the dipole emission:

$$\hat{d}_\alpha = \left| \begin{matrix} 2k_\alpha & ir_\alpha U_{s\bar{s}\to gg}(\mathbf{r}) \\ -ir_\alpha U_{s\bar{s}\to gg}^+(\mathbf{r}) & 0 \end{matrix} \right|. \quad (33)$$

The transition form factor is given by a formula similar to Eq. (9) for the one-channel case; it reads

$$F_{\mu\alpha}^{\phi\to\gamma f_0} = \int d^3r \mathrm{Sp}_2 \left[\hat{\Psi}_{f_0}^+(\mathbf{r}) 2\hat{d}_\alpha \hat{\Psi}_{\phi\mu}(\mathbf{r}) \right]. \quad (34)$$

Drawing explicitly the two-component wave functions, one can rewrite Eq. (34) as follows:

$$F_{\mu\alpha}^{\phi\to\gamma f_0} = \int d^3r \mathrm{Sp}_2 \left[\Psi_{f_0(s\bar{s})}^+(\mathbf{r}) 4k_\alpha \Psi_{\phi(s\bar{s})\mu}(\mathbf{r}) \right]$$
$$(35)$$
$$+ \int d^3r \mathrm{Sp}_2 \left[\Psi_{f_0(gg)}^+(\mathbf{r}) \right.$$
$$\left. \times (-ir_\alpha U_{gg\to s\bar{s}}(\mathbf{r})) \Psi_{\phi(s\bar{s})\mu}(\mathbf{r}) \right].$$

The first term on the right-hand side of (35), with the operator $4k_\alpha$, is responsible for the interaction of a photon with constituent quark that is the additive-quark-model contribution, while the term $(-ir_\alpha U_{gg \to s\bar{s}}(\mathbf{r}))$ describes interaction of the photon with the charge flowing through the t channel—this term describes the photon interaction with the fermion-exchange current.

Let us return to Eq. (34) and rewrite it in a form similar to (13). One can see that

$$im\left(\hat{H}_0 \hat{r}_\alpha - \hat{r}_\alpha \hat{H}_0\right) = \hat{d}_\alpha, \tag{36}$$

where $\hat{H}_0$ is the Hamiltonian for composite systems written on the left-hand side of (31), and the operator $\hat{r}_\alpha$ is determined as

$$\hat{r}_\alpha = \begin{pmatrix} r_\alpha & 0 \\ 0 & 0 \end{pmatrix}. \tag{37}$$

Substituting Eq. (36) into (34), we have

$$F_{\mu\alpha}^{\phi \to \gamma f_0} = \int d^3r \tag{38}$$
$$\times \mathrm{Sp}_2\left[(\boldsymbol{\sigma} \cdot \mathbf{r})\psi_{f_0(s\bar{s})}(r)r_\alpha \sigma_\mu \psi_{\phi(s\bar{s})}(r)\right]$$
$$\times 2im(\varepsilon_\phi - \varepsilon_{f_0}).$$

This formula for the dipole emission of a photon is similar to that of (13) for the one-channel model.

4.1.2. Partial width of the decay $\phi \to \gamma f_0$. The partial width of the decay $\phi \to f_0$ in the case when ϕ is a pure $s\bar{s}$ state is determined by the following formula:

$$m_\phi \Gamma_{\phi \to \gamma f_0} = \frac{1}{6}\alpha \frac{m_\phi^2 - m_{f_0}^2}{m_\phi^2}\left|A_{\phi \to \gamma f_0(s\bar{s})}\right|^2, \tag{39}$$

where $\alpha = 1/137$ and the $A_{\phi \to \gamma f_0(s\bar{s})}$ amplitude is determined by Eq. (6) (here, it is specified that we deal with $s\bar{s}$ quarks in the intermediate state).

4.2. Three-Component Model ($s\bar{s}, n\bar{n}, gg$) for f_0 and ϕ

The above formula can be easily generalized for the case when f_0 is the three-component system ($s\bar{s}, n\bar{n}, gg$) and ϕ is the two-component one ($s\bar{s}, n\bar{n}$), while gg is supposed to be negligibly small. We have two transition form factors:

$$F_{\mu\alpha}^{\phi \to \gamma f_0(s\bar{s})} \tag{40}$$
$$= \int d^3r \mathrm{Sp}_2\left[(\boldsymbol{\sigma} \cdot \mathbf{r})\psi_{f_0(s\bar{s})}(r)r_\alpha \sigma_\mu \psi_{\phi(s\bar{s})}(r)\right]$$
$$\times 2im(\varepsilon_\phi - \varepsilon_{f_0})$$

and

$$F_{\mu\alpha}^{\phi \to \gamma f_0(n\bar{n})} \tag{41}$$
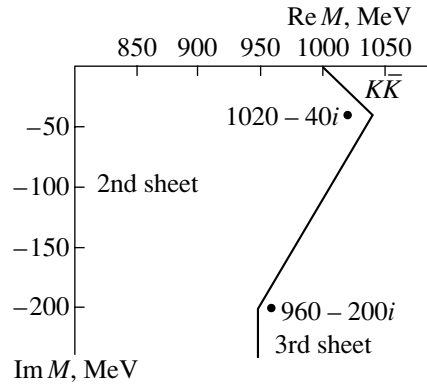
Fig. 4. Complex-M plane and location of the poles corresponding to $f_0(980)$; the cut related to the $K\bar{K}$ threshold is shown as a broken line.

$$= \int d^3r \mathrm{Sp}_2\left[(\boldsymbol{\sigma} \cdot \mathbf{r})\psi_{f_0(n\bar{n})}(r)r_\alpha \sigma_\mu \psi_{\phi(n\bar{n})}(r)\right]$$
$$\times 2im(\varepsilon_\phi - \varepsilon_{f_0}).$$

The partial width reads

$$m_\phi \Gamma_{\phi \to \gamma f_0} = \frac{1}{6}\alpha \frac{m_\phi^2 - m_{f_0}^2}{m_\phi^2} \tag{42}$$
$$\times \left|A_{\phi \to \gamma f_0(s\bar{s})} + A_{\phi \to \gamma f_0(n\bar{n})}\right|^2,$$

with $A_{\phi \to \gamma f_0}$ defined by Eqs. (4) and (6). The charge factors, which were separated in Eq. (4), are equal to

$$Z_{\phi \to \gamma f_0}^{(s\bar{s})} = -\frac{2}{3}, \qquad Z_{\phi \to \gamma f_0}^{(n\bar{n})} = \frac{1}{3}; \tag{43}$$

they include the combinatorics factor 2 related to two diagrams with photon emission by a quark and antiquark (see [16, 17] for more detail).

5. DECAY $\phi(1020) \to \gamma f_0(980)$

The vector meson $\phi(1020)$ has a rather small decay width, $\Gamma_{\phi(1020)} \simeq 4.5$ MeV; from this point of view, there is no doubt that treating $\phi(1020)$ as a stable particle is reasonable. As to $f_0(980)$, the picture is not so determinate. In the PDG compilation [20], the $f_0(980)$ width is given in the interval $40 \leq \Gamma_{f_0(980)} \leq 100$ MeV, and the width uncertainty is related not to the data inaccuracy (experimental data are rather good) but to a vague definition of the width.

The mass and width of the resonance are determined by the pole position in the complex-mass plane, $M = m - i\Gamma/2$—just this magnitude is a universal characteristic of the resonance.

5.1. The $f_0(980)$: Position of Poles

The definition of the $f_0(980)$ width is aggravated by the $K\bar{K}$ threshold singularity that leads to the existence of two poles, not one. According to the K-matrix analyses [1, 5], there are two poles in the $IJ^{PC} = 00^{++}$ wave at $s \sim 1.0$ GeV^2,

$$M^{\mathrm{I}} \simeq 1020 - 40i \text{ GeV}, \tag{44}$$

$$M^{\mathrm{II}} \simeq 960 - 200i \text{ GeV},$$

which are located on different complex-M sheets related to the $K\bar{K}$ threshold (see Fig. 4). By switching off the decay $f_0(980) \to K\bar{K}$, both poles begin to move toward one another, and they coincide completely after switching off the $K\bar{K}$ channel. Usually, when one discusses the $f_0(980)$, the resonance is characterized by the closest pole, M^{I}. However, when we are interested in how far from each other the $\phi(1020)$ and $f_0(980)$ are, one should not forget about the second pole.

Keeping in mind the existence of two poles, one should accept that $\phi(1020)$ and $f_0(980)$ are considerably "separated" from each other, and the $f_0(980)$ resonance can hardly be represented as a stable particle—we return to this point once more in Section 6 in discussing the $\pi\pi$ spectrum in $\phi(1020) \to \gamma\pi\pi$.

5.2. Switching off Decay Channels: Bare States in K-Matrix Analysis of the $IJ^{PC} = 00^{++}$ Wave

A significant trait of the K-matrix analysis is that it also gives us, along with the characteristics of real resonances, the positions of levels before the onset of the decay channels, i.e., it determines the bare states. In addition, the K-matrix analysis allows one to observe the transform of bare states into real resonances. The onset of the decay channels is regulated by the parameter x, and the value $x = 0$ corresponds to the bare state (amplitude pole on the ReM axis) and the value $x = 1$ stands for the resonance observed experimentally. In Fig. 5, one can see such a transform of the 00^{++}-amplitude poles by switching off the decays $f_0 \to \pi\pi, K\bar{K}, \eta\eta, \eta\eta', \pi\pi\pi\pi$. It is seen that, after switching off the decay channels, the $f_0(980)$ turns into a stable state, approximately 300 MeV lower:

$$f_0(980) \longrightarrow f_0^{\mathrm{bare}}(700 \pm 100). \tag{45}$$

The transform of bare states into real resonances can be illustrated by Fig. 6 for the levels in the potential well: bare states are the levels in a well with an impenetrable wall (Fig. 6a); at the onset of the decay channels (underbarrier transitions, Fig. 6b), the stable levels transform into real resonances.

Figure 7 demonstrates the evolution of coupling constants at the onset of the decay channels: following [21], relative changes of the coupling constants are shown for $f_0(980)$ after switching on/off the decay channels.

Let us bring attention to a rapid increase in the coupling constant $f_0 \to K\bar{K}$ on the evolution curve $f_0^{\mathrm{bare}}(700) - f_0(980)$ in the region $x \sim 0.8{-}1.0$, where $\gamma(x = 1.0) - \gamma(x = 0.8) \simeq 0.2$ (see Fig. 7). Actually, this increase allows one to estimate a possible admixture of the long-range $K\bar{K}$ component in the $f_0(980)$: it cannot be greater than 20%.

5.3. Calculation of the $\phi(1020) \to \gamma f_0(980)$ Decay Amplitude

The above discussion of the location of the amplitude poles of $f_0(980)$, as well as the movement of poles by switching off the decay channels, tells us definitely that the smallness of the amplitude of the $\phi(1020) \to \gamma f_0(980)$ decay due to a visible proximity of masses of vector and scalar particles is rather questionable. As to $f_0(980)$, its poles "dived" into the complex plane, on the average by ~ 100 MeV (40 MeV for one pole and 200 MeV for another). But when we intend to represent $f_0(980)$ as a stable level, one should bear in mind that the mass of the stable level is below the mass of $\phi(1020)$ by ~ 300 MeV (this value is given by the K-matrix analysis). In both cases, we deal with shifts in the mass scale of the order of the pion mass, which is hardly small on the hadronic scale.

The K-matrix amplitude of the 00^{++} wave reconstructed in [1] gives us the possibility to trace the evolution of the transition form factor $\phi(1020) \to \gamma f_0^{\mathrm{bare}}(700 \pm 100)$ during the transformation of the bare state $f_0^{\mathrm{bare}}(700 \pm 100)$ into the $f_0(980)$ resonance. Using diagrammatic language, one can say that the evolution of the form factor $F_{\phi \to \gamma f_0}^{(\mathrm{bare})}$ is due to the processes shown in Fig. 8: the ϕ meson goes into $f_0^{\mathrm{bare}}(n)$, with the emission of a photon; then $f_0^{\mathrm{bare}}(n)$ decays into mesons $f_0^{\mathrm{bare}}(n) \to hh = \pi\pi$, $K\bar{K}$, $\eta\eta$, $\eta\eta'$, $\pi\pi\pi\pi$. The decay yields may rescatter, thus coming to final states.

The residue of the amplitude pole $\phi(1020) \to \gamma\pi\pi$ gives us the transition amplitude $\phi(1020) \to \gamma f_0(980)$. So, in the K-matrix representation, the amplitude of the reaction $\phi(1020) \to \gamma\pi\pi$ (Fig. 8) reads

$$A_{\phi(1020)\to\gamma\pi\pi}(s) = \sum_{a,n} \frac{F_{\phi(1020)\to\gamma f_0^{\mathrm{bare}}(n)}^{(\mathrm{bare})}}{M_n^2 - s} g_a^{\mathrm{bare}}(n) \tag{46}$$
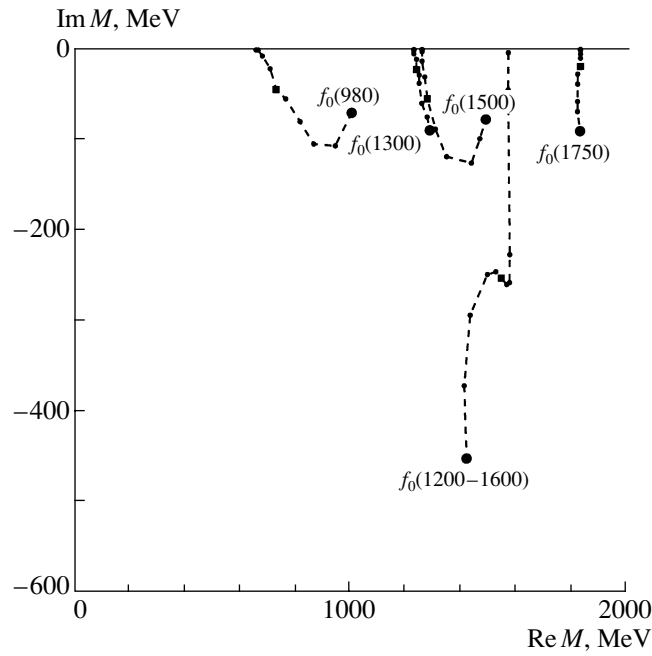
Fig. 5. Complex-M plane: trajectories of poles corresponding to the states $f_0(980)$, $f_0(1300)$, $f_0(1500)$, $f_0(1750)$, $f_0(1200-1600)$ within a uniform onset of the decay channels. The value $x = 0.5$ is marked by a square point.
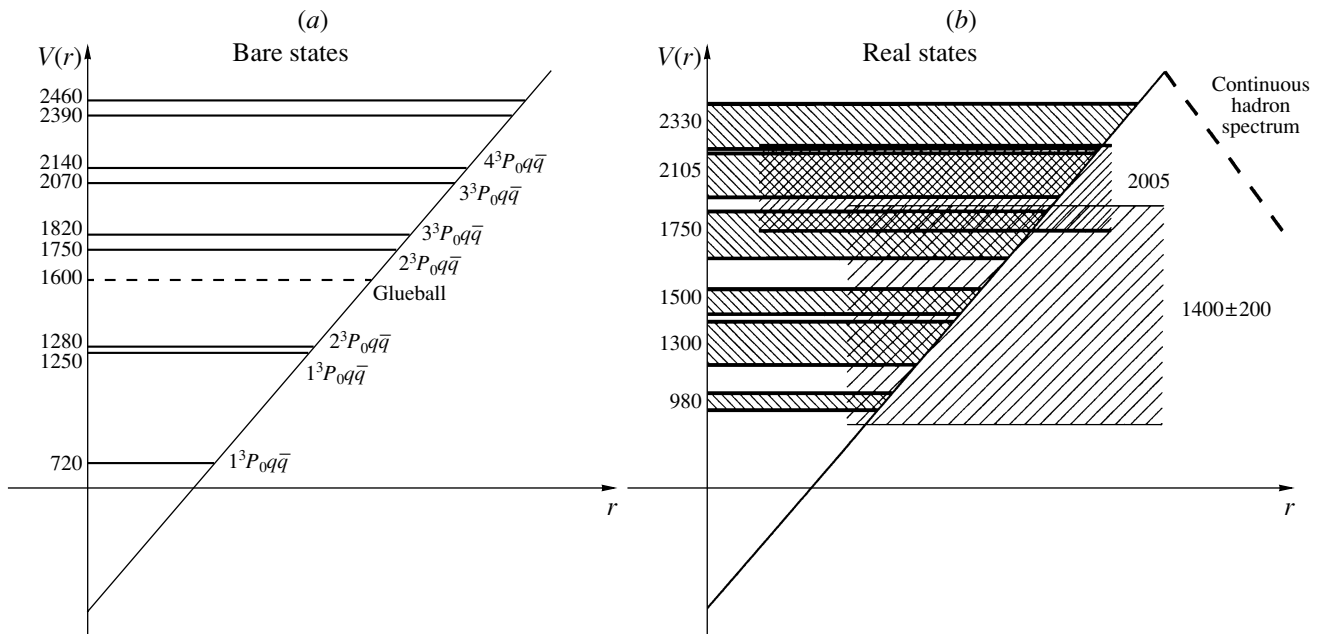

Fig. 6. The f_0 levels in the potential well depending on the onset of the decay channels: bare states (a) and real resonances (b).

$$\times \left(\frac{1}{1 - i\hat{\rho}(s)\hat{K}(s)} \right)_{a,\pi\pi}.$$

Here, M_n is the mass of the bare state, and $g_a^{\text{bare}}(n)$ is the coupling for the transition $f_0^{\text{bare}}(n) \to a$, where $a = \pi\pi$, $K\bar{K}$, $\eta\eta$, $\eta\eta'$, $\pi\pi\pi\pi$. The matrix element

$(1 - i\hat{\rho}(s)\hat{K}(s))^{-1}$ takes account of the rescatterings of the formed mesons. Here, $\hat{\rho}(s)$ is the diagonal matrix of phase spaces for hadronic states (for example, for the $\pi\pi$ system, it reads $\rho_{\pi\pi}(s) = \sqrt{(s - 4m_\pi^2)/s}$), and the K-matrix elements $K_{ab}(s)$ contain the poles
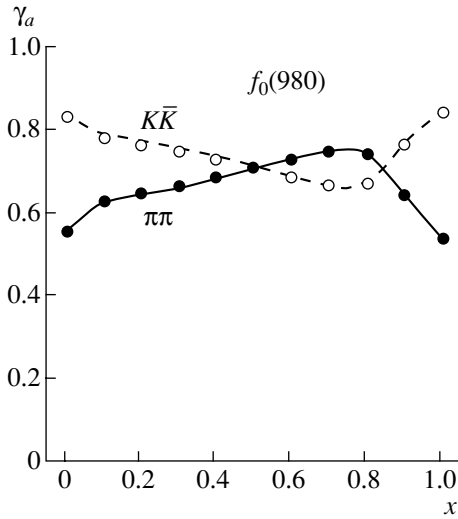
Fig. 7. The evolution of normalized coupling constants $\gamma_a = g_a/\sqrt{\sum_b g_b^2}$ at the onset of the decay channels for $f_0(980)$.

corresponding to the bare states:

$$K_{ab}(s) = \sum_n \frac{g_a^{\text{bare}}(n)g_b^{\text{bare}}(n)}{M_n^2 - s} + f_{ab}(s). \qquad (47)$$

The function $f_{ab}(s)$ is analytical in the right-hand half-plane of the complex-s plane, at $\text{Re}\, s > 0$ (see [1] for more detail).

Near the pole corresponding to the f_0 resonance (resonance poles are contained in the factor $(1 - i\hat{\rho}(s)\hat{K}(s))^{-1}$), the amplitude $\phi(1020) \to \gamma\pi\pi$ is written as follows:

$$A_{\phi(1020)\to\gamma\pi\pi}(s) \qquad (48)$$

$$\simeq \frac{A_{\phi(1020)\to\gamma f_0(980)}}{M_{f_0(980)}^2 - s} g_{f_0(980)\to\pi\pi} + \text{smooth terms},$$

where $M_{f_0(980)}$ is the complex-valued resonance mass: $M_{f_0(980)} \to M^{\text{I}} \simeq 1020 - 40i$ MeV for the first pole, and $M_{f_0(980)} \to M^{\text{II}} \simeq 960 - 200i$ MeV for the second one. The transition amplitude $A_{\phi(1020)\to\gamma f_0(980)}$ is different for different poles; the $g_{f_0(980)\to\pi\pi}$ couplings are different as well.

We see that the radiative transition $\phi(1020) \to \gamma f_0(980)$ is determined by two amplitudes,

$$A_{\phi(1020)\to\gamma f_0(M^{\text{I}})} \equiv A^{\text{I}}_{\phi(1020)\to\gamma f_0(980)},$$

$$A_{\phi(1020)\to\gamma f_0(M^{\text{II}})} \equiv A^{\text{II}}_{\phi(1020)\to\gamma f_0(980)},$$

and just these amplitudes are the subject of our interest. The amplitudes $A^{\text{I}}_{\phi(1020)\to\gamma f_0(980)}$ and

$A^{\text{II}}_{\phi(1020)\to\gamma f_0(980)}$ may be represented as the sum of contributions from different bare states:

$$A^{\text{I}}_{\phi(1020)\to\gamma f_0(980)} \qquad (49)$$

$$= \sum_n \zeta_n^{(\text{I})}[f_0(980)]F^{(\text{bare})}_{\phi(1020)\to\gamma f_0^{\text{bare}}(n)},$$

$$A^{\text{II}}_{\phi(1020)\to\gamma f_0(980)}$$

$$= \sum_n \zeta_n^{(\text{II})}[f_0(980)]F^{(\text{bare})}_{\phi(1020)\to\gamma f_0^{\text{bare}}(n)}.$$

To calculate the constants $\zeta_n[f_0(m_R)]$, we use the K-matrix solution for the 00^{++}-wave amplitude denoted in [1] as II-2. In this solution, there are five bare states $f_0^{\text{bare}}(n)$ in the mass interval 290–1950 MeV: four of them are members of the $q\bar{q}$ nonets ($1^3P_0 q\bar{q}$ and $2^3P_0 q\bar{q}$) and the fifth state is the glueball. Namely:

$$1^3P_0 q\bar{q} : f_0^{\text{bare}}(700 \pm 100), f_0^{\text{bare}}(1220 \pm 30), \quad (50)$$

$$2^3P_0 q\bar{q} : f_0^{\text{bare}}(1230 \pm 40), f_0^{\text{bare}}(1800 \pm 40),$$

$$\text{glueball} : f_0^{\text{bare}}(1580 \pm 50).$$

For the first pole of the $f_0(980)$ resonance located at $M[f_0(980)] = 1020 - 40i$ MeV, the renormalization constants are as follows:

$$\zeta_{700}^{(\text{I})}[f_0(980)] = 0.62\exp(-144°i), \qquad (51)$$

$$\zeta_{1220}^{(\text{I})}[f_0(980)] = 0.37\exp(-41°i),$$

$$\zeta_{1230}^{(\text{I})}[f_0(980)] = 0.19\exp(1°i),$$

$$\zeta_{1800}^{(\text{I})}[f_0(980)] = 0.02\exp(-112°i),$$

$$\zeta_{1580}^{(\text{I})}[f_0(980)] = 0.02\exp(5°i).$$

These constants are complex-valued. One should pay attention to the fact that the phases of constants $\zeta_{700}^{(\text{I})}[f_0(980)]$ and $\zeta_{1220}^{(\text{I})}[f_0(980)]$ have a relative shift close to 90°. This means that the contributions from $f_0^{\text{bare}}(700 \pm 100)$ and $f_0^{\text{bare}}(1220 \pm 30)$ (which are members of the basic $1^3P_0 q\bar{q}$ nonet) do not interfere in practice in the calculation of probability for the decay $\phi(1020) \to \gamma f_0(980)$.

Actually, one may neglect the bare states $f_0^{\text{bare}}(1230)$, $f_0^{\text{bare}}(1800)$, $f_0^{\text{bare}}(1580)$ in the calculation of the $\phi(1020) \to \gamma f_0(980)$ reaction because the form factors for the production of radial excited states are noticeably suppressed (see [17]):

$$\left| F^{(\text{bare})}_{\phi(1020)\to\gamma f_0(2^3P_0 q\bar{q})} \right| \ll \left| F^{(\text{bare})}_{\phi(1020)\to\gamma f_0(1^3P_0 q\bar{q})} \right|.$$

In addition, the coefficients $\zeta_{1230}^{(\text{I})}[f_0(980)]$ $\zeta_{1800}^{(\text{I})}[f_0(980)]$ are also comparatively small [see (51)].

The second pole located on the third sheet, $M[f_0(980)] = 960 - 200i$ MeV, has renormalizing
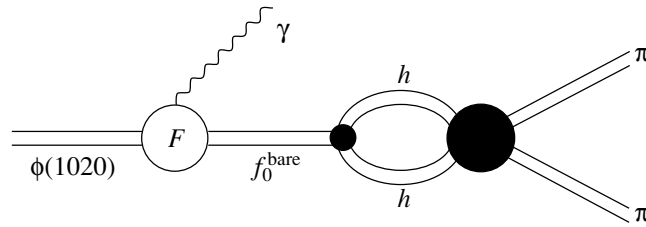
Fig. 8. Diagram for the transition $\phi(1020) \to \gamma\pi\pi$ in the K-matrix representation, Eq. (46).

constants as follows:

$$\zeta_{700}^{(II)}[f_0(980)] = 1.00 \exp(6°i), \qquad (52)$$

$$\zeta_{1220}^{(II)}[f_0(980)] = 0.33 \exp(113°i),$$

$$\zeta_{1230}^{(II)}[f_0(980)] = 0.32 \exp(148°i),$$

$$\zeta_{1800}^{(II)}[f_0(980)] = 0.08 \exp(4°i),$$

$$\zeta_{1580}^{(II)}[f_0(980)] = 0.04 \exp(98°i).$$

Here, as before, the transitions $\phi(1020) \to \gamma f_0^{\text{bare}}(1230)$, $\gamma f_0^{\text{bare}}(1580)$, $\gamma f_0^{\text{bare}}(1800)$ are negligibly small.

In $\phi(1020)$, the admixture of the $n\bar{n}$ component is small. In the estimates given below, we assume $\phi(1020)$ to be a pure $s\bar{s}$ state. The bare states $f_0^{\text{bare}}(700)$ and $f_0^{\text{bare}}(1220)$ are mixtures of the $n\bar{n}$ and $s\bar{s}$ components,

$$n\bar{n} \cos\varphi + s\bar{s} \sin\varphi,$$

and, according to [1], the mixing angles are as follows:

$$\varphi\left[f_0^{\text{bare}}(700)\right] = -70° \pm 10°, \qquad (53)$$

$$\varphi\left[f_0^{\text{bare}}(1220)\right] = 20° \pm 10°.$$

Because of that, the transition amplitude for $\phi(1020) \to \gamma f_0(980)$ reads

$$A_{\phi(1020)\to\gamma f_0(980)}^{N} \qquad (54)$$

$$\simeq \zeta_{700}^{(N)}[f_0(980)] \sin\varphi\left[f_0^{\text{bare}}(700)\right]$$

$$\times F_{\phi(1020)\to\gamma f_0^{\text{bare}}(700)}^{(\text{bare})}$$

$$+ \zeta_{1220}^{(N)}[f_0(980)] \sin\varphi\left[f_0^{\text{bare}}(1220)\right]$$

$$\times F_{\phi(1020)\to\gamma f_0^{\text{bare}}(1220)}^{(\text{bare})}.$$

Here, $\zeta_{700}^{(N)}[f_0(980)]$ and $\zeta_{1220}^{(N)}[f_0(980)]$ ($N = $ I, II) are given by formulas (51), (52). One can see that numerically the factor $\zeta_{1220}[f_0(980)] \sin\varphi \times \left[f_0^{\text{bare}}(1220)\right]$ is small, and we may neglect the second term on the right-hand side of (54). Then, for the pole which is

the closest one to the real axis ($1020 - 40i$ MeV), one has

$$A_{\phi(1020)\to\gamma f_0(980)}^{I} \qquad (55)$$

$$\simeq (0.58 \pm 0.04) F_{\phi(1020)\to\gamma f_0^{\text{bare}}(700)}^{(\text{bare})},$$

and for the distant one ($960 - 200i$ MeV),

$$A_{\phi(1020)\to\gamma f_0(980)}^{II} \qquad (56)$$

$$\simeq (0.92 \pm 0.06) F_{\phi(1020)\to\gamma f_0^{\text{bare}}(700)}^{(\text{bare})}.$$

We see that, in practice, the $A_{\phi(1020)\to\gamma f_0(980)}^{II}$ amplitude does not change its value during the evolution from bare state to resonance, while the decrease in $A_{\phi(1020)\to\gamma f_0(980)}^{I}$ is significant.

5.4. Comparison to Data

Comparing the above-written formulas to experimental data, we have parametrized the wave functions of the $q\bar{q}$ states in the simplest, exponent-type, form (see Section 2.3). For $\phi(1020)$, we accept its mean radius square to be close to the pion radius, $R_{\phi(1020)}^2 \simeq R_\pi^2$: both states are members of the same 36-plet. This value of the mean radius square for $\phi(1020)$ fixes its wave function by $b_\phi = 10$ GeV^{-2}.

For $f_0^{\text{bare}}(700)$, we change the value b_{f_0} in the interval

$$5 \le b_{f_0}^{(\text{bare})} \le 15 \text{ GeV}^{-2},$$

which corresponds to the interval $(0.5-1.5)R_\pi^2$ of the mean radius square of $f_0^{(\text{bare})}(700)$.

Using the branching ratios [22, 23]

$$\text{BR}[\phi(1020) \to \gamma f_0(980)] \qquad (57)$$

$$= (3.5 \pm 0.3_{-0.5}^{+1.3}) \times 10^{-4},$$

$$\text{BR}[\phi(1020) \to \gamma f_0(980)]$$

$$= (2.90 \pm 0.21 \pm 1.54) \times 10^{-4},$$

and the definition of the radiative decay width,

$$m_\phi \Gamma_{\phi\to\gamma f_0} = \frac{1}{6} \alpha \frac{m_\phi^2 - m_{f_0}^2}{m_\phi^2} |A_{\phi\to\gamma f_0}|^2,$$
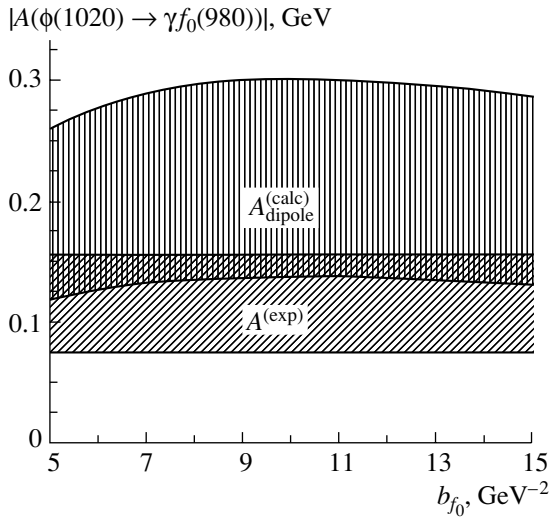
Fig. 9. Amplitudes for the decay $\phi(1020) \to \gamma f_0(980)$: the calculated amplitude $A_{\text{dipole}}^{\text{(calc)}}$ vs. the experimental one $A^{\text{(exp)}}$.

we have the following experimental value for the decay amplitude:

$$A_{\phi(1020)\to\gamma f_0(980)}^{\text{(exp)}} = 0.115 \pm 0.040 \text{ GeV}. \qquad (58)$$

Here, $\alpha = 1/137$, $m_\phi = 1.02$ GeV, and $m_{f_0} = 0.975$ GeV (the mass reported in [22, 23] for the measured $\gamma f_0(980)$ signal) and $\Gamma_{\text{tot}}[\phi(1020)] = 4.26 \pm 0.05$ MeV [20]. The right-hand side of (58) should be compared with $A_{\phi(1020)\to\gamma f_0(980)}$ calculated with Eqs. (17), (38), and (55):

$$A_{\phi(1020)\to\gamma f_0(980)}^{\text{(calc)}} \text{ (dipole)} \qquad (59)$$

$$\simeq (0.58 \pm 0.04)\sqrt{W_{q\bar{q}}[f_0^{\text{bare}}(700)]} Z_{\phi\to\gamma f_0}^{(s\bar{s})}$$

$$\times \frac{2^{7/2}}{\sqrt{3}} \frac{b_\phi^{7/4} b_{f_0}^{5/4}}{(b_\phi + b_{f_0})^{5/2}} m_s \left[m_\phi - (0.7 \pm 0.1) \text{ GeV} \right].$$

Recall that, in (59), the factor (0.58 ± 0.04) takes into account the change of the transition amplitude caused by the final-state hadron interaction, Eq. (55). The probability to find the quark–antiquark component in the bare state $f_0^{\text{bare}}(700)$ is denoted as $W_{q\bar{q}}[f_0^{\text{bare}}(700)]$: one can guess that it is of the order of 80–90%, or even more. The mass of the strange constituent quark is equal to $m_s \simeq 0.5$ GeV. The wave functions of $\phi(1020)$ and $f_0^{\text{bare}}(700)$ are parametrized as exponents: we fix $b_\phi = 10$ GeV^{-2} (which gives for the mean radius of $\phi(1020)$ a value of the order of the pion radius, $R_\phi \simeq R_\pi$) and vary b_{f_0} in the interval 5–15 GeV^{-2}.

The comparison of the data (58) to the calculated amplitude is shown in Fig. 9. We see that the calcu-
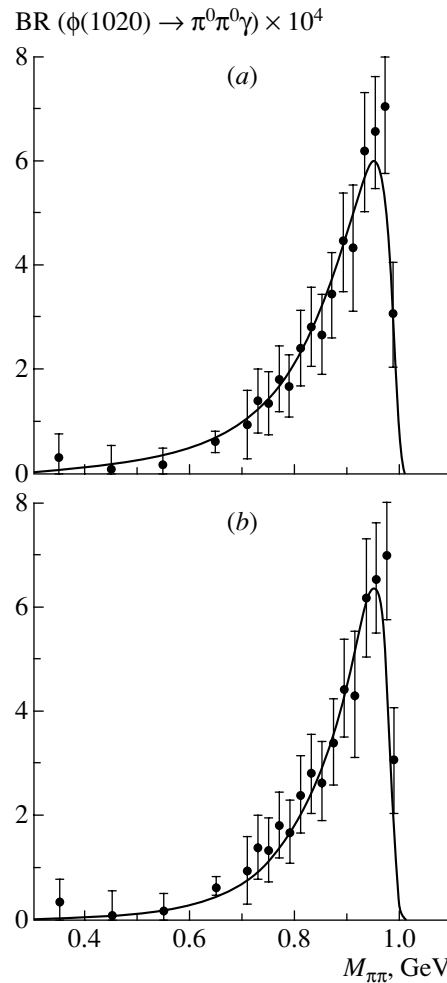
Fig. 10. The $\pi\pi$ spectrum of the reaction $\phi(1020) \to \gamma\pi\pi$ calculated with the Flatté formula (*a*) and Eq. (68) (*b*).

lated amplitude (59) is in a perfect agreement with data when $M f_0^{\text{bare}} \simeq 750$–$800$ MeV, which is just inside the error bars given by the K-matrix analysis [1].

6. PION–PION SPECTRUM IN $\phi(1020) \to \gamma\pi\pi$

The $f_0(980)$ resonance is seen in the reaction $\phi(1020) \to \gamma\pi\pi$ as a peak at the edge of the $\pi\pi$ spectrum. So, it is rather enlightening to calculate the $\pi\pi$ spectrum to be sure that its description agrees both with the quark-model calculation of the form factor $F_{\phi(1020)\to\gamma f_0(980)}$ and with the threshold theorem (cross section tending to zero as ω^3 at $\omega \to 0$, where $\omega = m_\phi - M_{\pi\pi}$).

The partial cross section of the decay $\phi(1020) \to \gamma\pi^0\pi^0$ is given by the following formula:

$$\frac{d\Gamma_{\phi(1020)\to\gamma\pi^0\pi^0}}{dM_{\pi\pi}} = \frac{1}{3}\Gamma_{\phi(1020)\to\gamma f_0(980)} \qquad (60)$$

$$\times \frac{m_\phi^2 - M_{\pi\pi}^2}{m_\phi^2 - m_{f_0}^2} \frac{2M_{\pi\pi}}{\pi} \rho_{\pi\pi}$$

$$\times \left| \frac{g_\pi}{M_0^2 - M_{\pi\pi}^2 - ig_\pi^2 \rho_{\pi\pi} - ig_K^2 \rho_{K\bar{K}}} + B(M_{\pi\pi}^2) \right|^2 .$$

The factor $1/3$ in front of the right-hand side of (60) is associated with the $\pi^0\pi^0$ channel: $\Gamma_{\phi(1020)\to\gamma\pi^0\pi^0} = (1/3)\Gamma_{\phi(1020)\to\gamma\pi\pi}$. Here, for the description of the $f_0(980)$, we use the Flatté formula [24] with the phase-space factors

$$\rho_{\pi\pi} = \frac{1}{M_0} \sqrt{M_{\pi\pi}^2 - 4m_\pi^2}, \qquad (61)$$

$$\rho_{K\bar{K}} = \frac{1}{M_0} \sqrt{M_{\pi\pi}^2 - 4m_K^2}. \qquad$$

At $M_{\pi\pi}^2 < 4m_K^2$, one should replace $\sqrt{M_{\pi\pi}^2 - 4m_K^2} \to i\sqrt{4m_K^2 - M_{\pi\pi}^2}$. In line with [22, 23, 25], we use the Flatté formula with the parameters

$$g_\pi^2 = 0.12 \text{ GeV}^2, \quad g_K^2 = 0.27 \text{ GeV}^2, \qquad (62)$$
$$M_0 = 0.975 \text{ GeV}.$$

The threshold theorem requires

$$\left[\frac{g_\pi}{M_0^2 - M_{\pi\pi}^2 - ig_\pi^2 \rho_{\pi\pi} - ig_K^2 \rho_{K\bar{K}}} \right. \qquad (63)$$
$$\left. + B(M_{\pi\pi}^2) \right]_{M_{\pi\pi}\to m_\phi} \sim M_{\pi\pi} - m_\phi,$$

which gives a constraint for the background term $B(M_{\pi\pi}^2)$. The term $B(M_{\pi\pi}^2)$ is parametrized in the form

$$B(M_{\pi\pi}^2) = C\left[1 + a(M_{\pi\pi}^2 - m_\phi^2)\right] \qquad (64)$$
$$\times \exp\left[-\frac{m_\phi^2 - M_{\pi\pi}^2}{\mu^2}\right],$$

and the parameter C is fixed by the constraint

$$\left[\frac{g_\pi}{M_0^2 - M_{\pi\pi}^2 - ig_\pi^2 \rho_{\pi\pi} - ig_K^2 \rho_{K\bar{K}}} + C \right]_{M_{\pi\pi}=m_\phi} = 0. \qquad (65)$$

Fitting to the $\pi^0\pi^0$ spectrum [22] (see Fig. 10a), we have the following values for other parameters:

$$\frac{1}{a} = -0.2 \text{ GeV}^2, \quad \mu = 0.388 \text{ GeV}. \qquad (66)$$

For $\Gamma_{\phi(1020)\to\gamma f_0(980)}$ entering (60), we have used $A_{\phi(1020)\to\gamma f_0(980)} = 0.13$ GeV, which satisfies both (58) and (59).

The Flatté formula gives us a rather rough description of the $\pi\pi$ amplitude around the $f_0(980)$ resonance. A more precise description may be obtained by using in addition the nonzero transition length for $\pi\pi \to K\bar{K}$ [21]. For this case, we have formulas analogous to Eq. (60), after replacing the resonance factor

$$\frac{g_\pi}{M_0^2 - M_{\pi\pi}^2 - ig_\pi^2 \rho_{\pi\pi} - ig_K^2 \rho_{K\bar{K}}} \qquad (67)$$

by the following one:

$$\frac{g_\pi + i\rho_{K\bar{K}} g_K f}{M_0^2 - M_{\pi\pi}^2 - ig_\pi^2 \rho_{\pi\pi} - i\rho_{K\bar{K}}[g_K^2 + i\rho_{\pi\pi}(2g_\pi g_K f + f^2(M_0^2 - M_{\pi\pi}^2))]}. \qquad (68)$$

The parameters found in [21] are equal to

$$g_\pi = 0.386 \text{ GeV}, \quad g_K = 0.447 \text{ GeV}, \qquad (69)$$
$$M_0 = 0.975 \text{ GeV}, \quad f = 0.516.$$

The transition length $a_{\pi\pi\to K\bar{K}}$ is determined by the parameter f as follows: $a_{\pi\pi\to K\bar{K}} = 2f/M_0$.

The description of the $\pi^0\pi^0$ spectra [22] within the resonance formulas (68) is demonstrated in Fig. 10b. In this fit, we have the following parameters for $B(M_{\pi\pi}^2)$:

$$a = 0, \quad \mu = 0.507 \text{ GeV}. \qquad (70)$$

In this variant of the fitting to spectra, we also used $A_{\phi(1020)\to\gamma f_0(980)} = 0.13$ GeV.

Let us emphasize that the visible width of the $f_0(980)$ signal in the $\pi\pi$ spectrum is comparatively large, ~ 150 MeV, which is related to an essential contribution of the second pole at $960 - 200i$ MeV.

7. THE ADDITIVE QUARK MODEL, DOES IT WORK?

Let us point to the two aspects of this question. One is the problem of the applicability of the additive quark model to the production of the resonance $f_0(980)$; the other is the production of the bare state $f_0^{\text{bare}}(700 \pm 100)$.
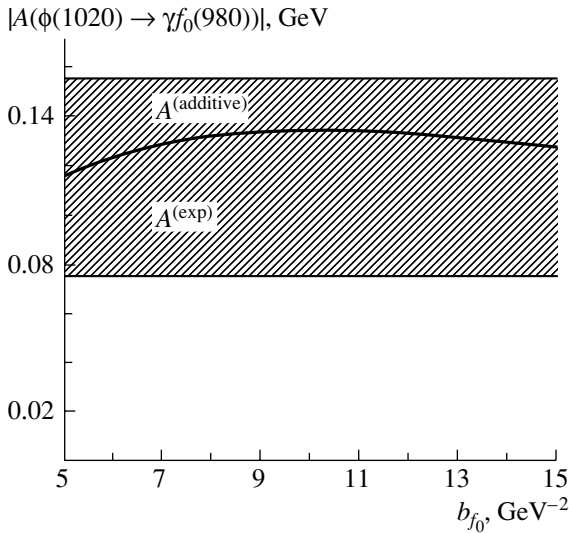
$|A(\phi(1020) \to \gamma f_0(980))|$, GeV

Fig. 11. The additive quark-model-amplitude (72) for $\phi(1020) \to \gamma f_0(980)$ vs. $A^{(\exp)}_{\phi(1020) \to \gamma f_0(980)}$.

7.1. Process $\phi(1020) \to \gamma f_0^{bare}(700 \pm 100)$

The additive quark model describes well the production of the bare state $f_0^{\rm bare}(700 \pm 100)$, provided its mass is in the region $750-800$ MeV. To see it, consider Eq. (38) for $F^{\phi \to \gamma f_0}_{\mu\alpha}$(dipole), or Eq. (17), where the exponential representation of the quark wave functions is used. Formula (17) takes into account both the additive-quark-model processes and photon emission by the charge-exchange current, while Eq. (16) gives us the triangle-diagram contribution within the additive quark model. The contribution of the charge-exchange current is small when

$$m_s[m_\phi - M_{f_0^{\rm bare}}] \simeq \frac{1}{b_\phi}. \tag{71}$$

At $m_s = 0.5$ GeV and $b_\phi = 10$ GeV^{-2}, the equality (71) is almost fulfilled, when $M_{f_0^{\rm bare}} \simeq 0.8$ GeV. Such a magnitude is allowed by the K-matrix fit [1], which gives $M_{f_0^{\rm bare}} = 0.7 \pm 0.1$ GeV.

However, let us emphasize that the error bars ± 0.1 GeV are rather large in the difference $m_\phi - M_{f_0^{\rm bare}}$: with the lower possible limit $M_{f_0^{\rm bare}} = 0.6$ GeV, we face a two-times disagreement in Eq. (71). Still, one may hardly hope that the K-matrix analysis of the 00^{++} wave would provide us with a tighter restriction for the mass of this bare state, since a large uncertainty in the definition of $M_{f_0^{\rm bare}}$ is not related to the data accuracy but to the problem of the light σ-meson existence (see the discussions in [5, 26–28] and references therein).

The use of $F^{\phi \to \gamma f_0}_{\mu\alpha}$(additive), Eq. (16), for the calculation of $A^{(\rm calc)}_{\phi(1020) \to \gamma f_0(980)}$ results in agreement with experimental data. Thus, we have

$$A^{(\rm calc)}_{\phi(1020) \to \gamma f_0(980)}(\text{additive}) \tag{72}$$

$$\simeq (0.58 \pm 0.04)\sqrt{W_{q\bar{q}}[f_0^{\rm bare}(700)]} Z^{(s\bar{s})}_{\phi \to \gamma f_0}$$

$$\times \frac{2^{7/2}}{\sqrt{3}} \frac{b_\phi^{3/4} b_{f_0}^{5/4}}{(b_\phi + b_{f_0})^{5/2}}.$$

In Fig. 11, one can see $A^{(\rm calc)}_{\phi(1020) \to \gamma f_0(980)}(\text{additive})$ versus $A^{(\exp)}_{\phi(1020) \to \gamma f_0(980)}$: there is good agreement with data.

The existence of two characteristic sizes in a hadron, namely, hadronic radius and that of the constituent quark, may be the reason why the contribution of the charge-exchange current is small in the reaction $\phi(1020) \to \gamma f_0^{\rm bare}(700)$. The relatively small radius of the constituent quark assumes that charge-exchange interaction $s\bar{s} \to gg \to n\bar{n}$ is a short-range one, which causes a smallness of the second term on the right-hand side of (35).

The hadronic size is defined by the confinement radius $R_h \sim R_{\rm conf}$, which is of the order of 1 fm for light hadrons. The constituent-quark size r_q is much smaller; it is defined, as one may believe, by the relatively large mass of the soft gluon (experimental data [29] and lattice calculations [30] give us $m_g \sim 700-1000$ MeV). So, we get $r_q^2/R_h^2 \sim 0.1-0.2$; the same value follows from the analysis of soft hadron collisions (see [15, 31] and references therein).

7.2. Process $\phi(1020) \to \gamma f_0(980)$

The two sizes, r_q^2 and R_h^2, being accepted, the additive-quark-model contribution dominates the reaction $\phi(1020) \to \gamma f_0(980)$ too, thus allowing direct use of the triangle diagram of Fig. 1a for the calculation of this process. Such calculations were performed in [17], revealing reasonable agreement with data. Once again it should be emphasized that the triangle diagram contribution does not have a particular smallness related to a deceptive proximity of $\phi(1020)$ and $f_0(980)$. In addition, as was explained above, the poles associated with these resonances are separated from each other in the complex-M plane by nonsmall distances on the hadronic scale.

In the literature, there exist rather opposite statements about the possibility to describe the reaction $\phi(1020) \to \gamma f_0(980)$ within the framework of the hypothesis of the $q\bar{q}$ nature of $f_0(980)$. Using the QCD sum-rule technique, the authors of [32] evaluated
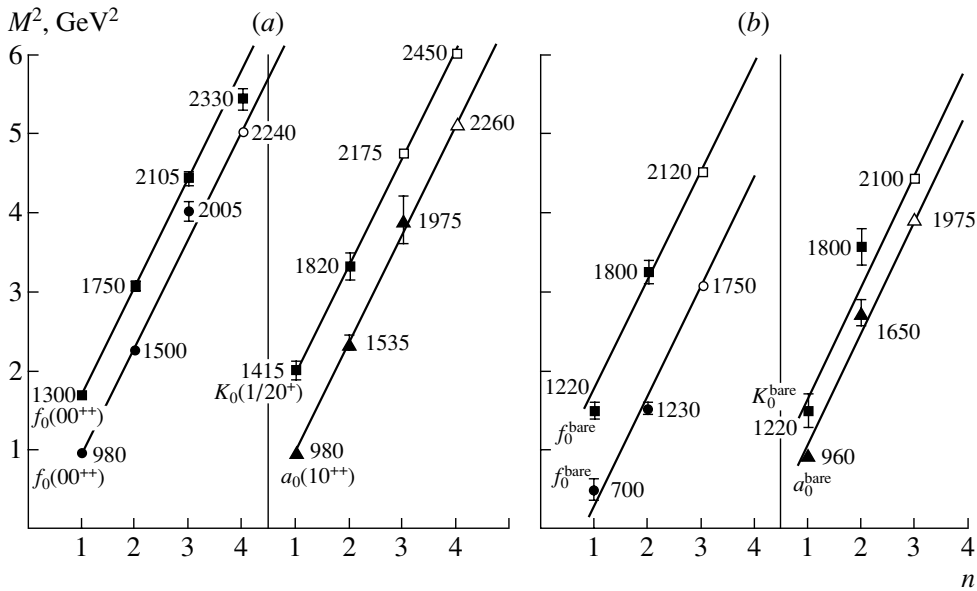
Fig. 12. Linear trajectories on the (n, M^2) plane for bare states (a) and scalar resonances (b).

the rate of the decay $\phi(1020) \to \gamma f_0(980)$, with fair agreement with data, supposing a sizeable $s\bar{s}$ component in the $f_0(980)$.

The results of the calculation performed in [33] in the framework of the additive quark model do not agree with data on the reaction $\phi(1020) \to \gamma f_0(980)$. This calculation, though similar to those of [16, 17], led to a different result, so it would be instructive to compare model parameters used in these two approaches.

In [33] as well as in [16, 17], the exponential parametrization of the wave function was used; however, the slopes b_ϕ and b_{f_0} in [33] were considerably smaller (constituent quark masses are smaller too). In [33], $b_{s\bar{s}} = 2.9$ GeV^{-2} and $b_{u\bar{u}} = b_{d\bar{d}} = 3.7$ GeV^{-2} ($m_u = m_d = 220$ MeV, $m_s = 450$ MeV), while in [16, 17] $b_\phi \simeq 10$ GeV^{-2} and $b_\phi \sim b_{f_0}$ ($m_u = m_d = 350$ MeV, $m_s = 500$ MeV). In addition, in [33], the scheme of mixing of f_0 states was used that was suggested in [33, 35], where the transitions $f_0^{\text{bare}} \to$ real mesons were not accounted for. Still, as was emphasized above (Section 5.2), just the transitions $f_0^{\text{bare}} \to \pi\pi, K\bar{K}, \eta\eta, \pi\pi\pi\pi$ afford the final disposition of poles in the complex plane, for they are responsible for the resonance mass shift of the order of 100 MeV (see Fig. 5).

In our opinion, the failure of the $q\bar{q}$ model demonstrated in [33] can attest only to the fact that not any model enables the description of radiative decays. The $q\bar{q}$ model should be based on the whole set of experimental data but not on the reproduction of several levels of the lowest states.

8. CONCLUSIONS

Correct determination of the origin of $f_0(980)$ is a key for understanding the status of the light σ and classification of heavier mesons $f_0(1300)$, $f_0(1500)$, $f_0(1750)$, and the broad state $f_0(1200-1600)$.

We have shown that experimental data on the reaction $\phi(1020) \to \gamma f_0(980)$ do not contradict the suggestion about the dominance of the quark–antiquark component in the $f_0(980)$. However, as was emphasized in the Introduction, the final conclusion about the origin of $f_0(980)$ should be made on the basis of the whole availability of arguments, so let us enumerate them briefly.

(1) There are data on the hadronic decays of the lowest mesons, and the most reliable information on scalar resonances is given by the K-matrix analysis. Summing up, one can state that, according to the K-matrix analysis [1], the lowest states $f_0(980)$, $f_0(1300)$, $a_0(980)$, $K_0(1430)$ are the descendants of bare mesons, which have created the 1^3P_0 multiplet. Because of that, all the decays, namely,

$$f_0(980) \to \pi\pi, K\bar{K}, \qquad (73)$$
$$f_0(1300) \to \pi\pi, K\bar{K}, \eta\eta,$$
$$a_0(980) \to K\bar{K}, \pi\eta,$$
$$K_0(1430) \to K\pi,$$

are described by two parameters only in the leading terms of the $1/N_c$ expansion, which are the universal coupling constant and mixing angle for the $n\bar{n}$ and $s\bar{s}$ components in the scalar–isoscalar sector.

(2) Another argument is the systematics of scalar states on linear trajectories on the (n, M^2) plane. For scalar mesons, the trajectories are shown in Fig. 12a—one can see that $f_0(980)$ lies comfortably on a linear trajectory, together with the other scalars. Such trajectories are formed not only for the scalar sector but also for all aggregate of data (see [4, 5]), and all the trajectories are characterized by a universal slope.

Similar $q\bar{q}$ trajectories exist in the (J, M^2) plane too, and $f_0(980)$ belongs to one of them.

(3) The alternative to the $q\bar{q}$ system may be the four-quark $q\bar{q}q\bar{q}$ or molecular $K\bar{K}$ structure [6, 7, 36, 37]. Such a nature of $f_0(980)$ would mean that $f_0(980)$ was a loosely bound system, but the experiment tells us that this is not so. The point is that

(i) $f_0(980)$ is easily produced at large momenta transferred to the nucleon in the reaction $\pi^- p \to f_0(980)n$ [38, 39],

(ii) $f_0(980)$ is produced in Z^0-boson decays [40],

(iii) $f_0(980)$ is produced in central pp collisions at high energies [41].

Were the $f_0(980)$ a loosely bound system, these processes would be suppressed.

(4) The $f_0(980)$ resonance is produced in hadronic decays of the D_s meson, $D_s^+ \to \pi^+ f_0(980)$, with a probability comparable with that for the transition $D_s^+ \to \pi^+ \phi(1020)$ [42]. These two reactions are due to the weak decay of the c quark, $c \to \pi^+ s$; as to $f_0(980)$, it is formed, like $\phi(1020)$, by the $s\bar{s}$ system in the transition $s\bar{s} \to f_0(980)$. The calculation of this process [43] shows us that the $f_0(980)$ yield in the reaction $D_s^+ \to \pi^+ f_0(980)$ can be reliably calculated under the assumption that $f_0(980)$ is close to the $q\bar{q}$ flavor octet.

The study of $D_s^+ \to \pi^+ f_0(980)$ decay in [44−46] also led to the conclusion about the $s\bar{s}$ nature of $f_0(980)$.

(5) Concerning radiative decays with the formation of $f_0(980)$, we see that the transition $\phi(1020) \to \gamma f_0(980)$ can be well described within the approach of the additive quark model, with the dominant $q\bar{q}$ component in the $f_0(980)$. Another radiative decay, $f_0(980) \to \gamma\gamma$, the partial width of which was measured [47], can also be treated in terms of the $q\bar{q}$ structure of $f_0(980)$ [16, 48]. The values of partial widths in both decays support the conclusion made in [1] that the flavor content of $f_0(980)$ is close to the octet one.

ACKNOWLEDGMENTS

Appendix

DIPOLE EMISSION OF PHOTON

To describe the interaction of a composite system with an electromagnetic field, we consider the full Hamiltonian

$$\hat{H}(0) = \begin{vmatrix} \dfrac{k_1^2}{2m} + \dfrac{k_2^2}{2m} + U_{s\bar{s} \to s\bar{s}}(\mathbf{r}_1 - \mathbf{r}_2) & \widehat{U}_{s\bar{s} \to gg}(\mathbf{r}_1 - \mathbf{r}_2) \\ \widehat{U}_{s\bar{s} \to gg}(\mathbf{r}_1 - \mathbf{r}_2) & \dfrac{k_1^2}{2m_g} + \dfrac{k_2^2}{2m_g} + U_{gg \to gg}(\mathbf{r}_1 - \mathbf{r}_2) \end{vmatrix}. \tag{A.1}$$

Here, the coordinates $(\mathbf{r}_a)$ and momenta $(\mathbf{k}_a = -i\nabla_a)$ of the constituents are related to the characteristics of the relative movement, entering (31), as follows:

$$\mathbf{r}_1 = \mathbf{r} + \frac{1}{2}\mathbf{R}, \quad \mathbf{r}_2 = -\frac{1}{2}\mathbf{r} + \mathbf{R}, \tag{A.2}$$

$$\mathbf{k}_1 = \mathbf{k} + \frac{1}{2}\mathbf{P}, \quad \mathbf{k}_2 = -\frac{1}{2}\mathbf{k} + \mathbf{P}.$$

The electromagnetic interaction is included by substituting in (8) as follows:

$$\mathbf{k}_1^2 \to (\mathbf{k}_1 - e_1\mathbf{A}(r_1))^2, \tag{A.3}$$

$$\mathbf{k}_2^2 \to (\mathbf{k}_2 - e_2\mathbf{A}(r_2))^2,$$

$$\widehat{U}_{s\bar{s} \to gg}(\mathbf{r}_1 - \mathbf{r}_2) \to \widehat{U}_{s\bar{s} \to gg}(\mathbf{r}_1 - \mathbf{r}_2)$$

$$\times \exp \left[ie_1 \int\limits_{-\infty}^{\mathbf{r}_1} dr'_\alpha A_\alpha(r') + ie_2 \int\limits_{-\infty}^{\mathbf{r}_2} dr'_\alpha A_\alpha(r') \right],$$

with $e_1 = -e_2 = e_s$. After that, we obtain the gauge-invariant Hamiltonian $\hat{H}(A)$:

$$\hat{H}(\mathbf{A}) = \hat{\chi}^+ \hat{H}(\mathbf{A} + \nabla\chi)\hat{\chi}, \qquad (A.4)$$

where $\mathbf{A} + \nabla\chi$ means the substitution

$$\mathbf{A}(r_a) \to \mathbf{A}(r_a) + \nabla\chi(r_a), \qquad (A.5)$$

and matrix $\hat{\chi}$ reads

$$\hat{\chi} = \begin{vmatrix} \exp[ie_s\chi(r_1) - ie_s\chi(r_2)] & 0 \\ 0 & 1 \end{vmatrix}. \qquad (A.6)$$

For the transition $\phi \to \gamma f_0$, keeping the terms proportional to the s-quark charge, e_s, we have the following operator for the dipole emission:

$$\hat{d}_\alpha = \begin{vmatrix} 2(k_{1\alpha} - k_{2\alpha}) & i(r_{1\alpha} - r_{2\alpha})\hat{U}_{s\bar{s} \to gg}(\mathbf{r}_1 - \mathbf{r}_2) \\ -i(r_{1\alpha} - r_{2\alpha})\hat{U}_{s\bar{s} \to gg}(\mathbf{r}_1 - \mathbf{r}_2) & 0 \end{vmatrix}. \qquad (A.7)$$

There exist other mechanisms of photon emission which, being beyond the additive quark model, lead us to the dipole formula for $V \to \gamma S$ transition; an example is given by $(\mathbf{L} \cdot \mathbf{S})$ interaction in the quark–antiquark component [9, 10, 49]. The short-range $(\mathbf{L} \cdot \mathbf{S})$ interaction in the $q\bar{q}$ systems was discussed [50, 51] as a source of the nonet splitting. Actually, the pointlike $(\mathbf{L} \cdot \mathbf{S})$ interaction gives (v/c) corrections to the nonrelativistic approach. In the relativistic quark model approaches based on the Bethe–Salpeter equation, the gluon-exchange forces result in similar nonet splitting as for the $(\mathbf{L} \cdot \mathbf{S})$ interaction (see, for example, [52]).

REFERENCES

1. V. V. Anisovich and A. V. Sarantsev, Eur. Phys. J. A **16**, 229 (2003).
2. V. V. Anisovich, A. A. Kondashov, Yu. D. Prokoshkin, *et al.*, Yad. Fiz. **63**, 1489 (2000) [Phys. At. Nucl. **63**, 1410 (2000)].
3. V. V. Anisovich and A. V. Sarantsev, Phys. Lett. B **382**, 429 (1996); V. V. Anisovich, Yu. D. Prokoshkin, and A. V. Sarantsev, Phys. Lett. B **389**, 388 (1996).
4. A. V. Anisovich, V. V. Anisovich, and A. V. Sarantsev, Phys. Rev. D **62**, 051502 (2000); V. V. Anisovich, hep-ph/0310165.
5. V. V. Anisovich, Usp. Fiz. Nauk **174**, 49 (2004) [Phys. Usp. **47**, 45 (2004)]; hep-ph/0208123, v3.
6. R. L. Jaffe, Phys. Rev. D **15**, 267 (1977).
7. J. Weinshtein and N. Isgur, Phys. Rev. D **41**, 2236 (1990).
8. F. E. Close *et al.*, Phys. Lett. B **319**, 291 (1993).
9. N. Byers and R. McClary, Phys. Rev. D **28**, 1692 (1983).
10. A. LeYaouanc, L. Oliver, O. Pene, and J. C. Raynal, Z. Phys. C **40**, 77 (1988).
11. A. J. F. Siegert, Phys. Rev. **52**, 787 (1937).
12. V. V. Anisovich and M. A. Matveev, Yad. Fiz. **67**, 634 (2004); hep-ph/0303119.
13. S. Malvezzi, *Talk Presented at "Hadron-03," Aschaffensburg, Germany, August–September, 2003.*
14. A. V. Anisovich and V. V. Anisovich, Phys. Lett. B **467**, 289 (1999).
15. V. V. Anisovich, M. N. Kobrinsky, J. Nyiri, and Yu. M. Shabelski, *Quark Model and High-Energy Collisions*, 2nd ed. (World Sci., Singapore, 2004).
16. A. V. Anisovich, V. V. Anisovich, and V. A. Nikonov, Eur. Phys. J. A **12**, 103 (2001).
17. A. V. Anisovich, V. V. Anisovich, V. N. Markov, and V. A. Nikonov, Yad. Fiz. **65**, 523 (2002) [Phys. At. Nucl. **65**, 497 (2002)].
18. A. V. Anisovich, V. V. Anisovich, and V. A. Nikonov, hep-ph/0305216.
19. G. S. Bali *et al.*, Phys. Lett. B **309**, 378 (1993); J. Sexton, A. Vaccarino, and D. Weingarten, Phys. Rev. Lett. **75**, 4563 (1995); C. J. Morningstar and M. Peardon, Phys. Rev. D **56**, 4043 (1997).
20. PDG (D. E. Groom *et al.*), Eur. Phys. J. C **15**, 1 (2000).
21. V. V. Anisovich, V. A. Nikonov, and A. V. Sarantsev, Yad. Fiz. **65**, 1583 (2002) [Phys. At. Nucl. **65**, 1545 (2002)]; **66**, 772 (2003) [**66**, 741 (2003)].
22. M. N. Achasov *et al.*, Phys. Lett. B **485**, 349 (2000).
23. R. R. Akhmetshin *et al.*, Phys. Lett. B **462**, 380 (1999).
24. S. M. Flatté, Phys. Lett. B **63B**, 224 (1976).
25. A. V. Sarantsev, private communication.
26. S. F. Tuan, hep-ph/0303248.
27. E. van Beveren *et al.*, Mod. Phys. Lett. A **17**, 1673 (2002).
28. W. Ochs and P. Minkowski, Nucl. Phys. B (Proc. Suppl.) **121**, 123 (2003).
29. G. Parisi and R. Petronzio, Phys. Lett. B **94B**, 51 (1980); M. Consoli and J. H. Field, Phys. Rev. D **49**, 1293 (1994).

30. D. B. Leinweber *et al.*, Phys. Rev. D **58**, 031501 (1998).
31. L. G. Dakhno and V. A. Nikonov, Eur. Phys. J. A **5**, 209 (1999).
32. F. De Fazio and M. R. Pennington, Phys. Lett. B **521**, 15 (2001).
33. M. A. DeWitt, H. M. Choi, and C. R. Ji, Phys. Rev. D **68**, 054026 (2003).
34. W. Lee and D. Weingarten, Phys. Rev. D **61**, 014015 (2000).
35. F. E. Close and A. Kirk, Eur. Phys. J. C **21**, 531 (2001).
36. F. E. Close, Int. J. Mod. Phys. A **17**, 3239 (2002).
37. N. N. Achasov, AIP Conf. Proc. **619**, 112 (2002).
38. D. Alde *et al.*, Z. Phys. C **66**, 375 (1995); Yu. D. Prokoshkin *et al.*, Dokl. Akad. Nauk **342**, 473 (1995) [Phys. Dokl. **40**, 266 (1995)].
39. J. Gunter *et al.* (E852 Collab.), Phys. Rev. D **64**, 072003 (2001).
40. K. Ackerstaff *et al.*, Eur. Phys. J. C **4**, 19 (1998).
41. D. Barberis *et al.*, Phys. Lett. B **453**, 325 (1999).
42. E. M. Aitala *et al.*, Phys. Rev. Lett. **86**, 765 (2001).
43. V. V. Anisovich, L. G. Dakhno, and V. A. Nikonov, hep-ph/0302137.
44. P. Minkowski and W. Ochs, Nucl. Phys. B (Proc. Suppl.) **121**, 119 (2003).
45. F. Kleefeld *et al.*, Phys. Rev. D **66**, 034007 (2002).
46. A. Deandrea *et al.*, Phys. Lett. B **502**, 79 (2001).
47. M. Boglione and M. R. Pennington, Eur. Phys. J. C **9**, 11 (1999).
48. A. V. Anisovich, V. V. Anisovich, M. A. Matveev, and V. A. Nikonov, Yad. Fiz. **66**, 946 (2003) [Phys. At. Nucl. **66**, 914 (2003)].
49. Yu. S. Kalashnikova, private communication.
50. Ya. B. Zeldovich and A. D. Sakharov, Yad. Fiz. **4**, 395 (1966) [Phys. At. Nucl. **4**, 283 (1966)].
51. A. De Rujula, H. Georgi, and S. L. Glashow, Phys. Rev. D **12**, 147 (1975).
52. R. Ricken, M. Koll, D. Merten, *et al.*, Eur. Phys. J. A **9**, 221 (2000).

====== **ELEMENTARY PARTICLES AND FIELDS** ======
Theory

Quark−Antiquark Composite Systems: the Bethe−Salpeter Equation in the Spectral-Integration Technique in the Case of Different Quark Masses*

A. V. Anisovich, V. V. Anisovich**, V. N. Markov, M. A. Matveev, and A. V. Sarantsev

Petersburg Nuclear Physics Institute,
Russian Academy of Sciences, Gatchina, 188350 Russia
Received May 24, 2004; in final form, December 22, 2004

Abstract—The Bethe−Salpeter equations for quark−antiquark composite systems with different quark masses, such as $q\bar{s}$ (with $q = u,d$), $q\bar{Q}$, and $s\bar{Q}$ (with $Q = c, b$), are written in terms of spectral integrals. For mesons characterized by the mass M, spin J, and radial quantum number n, the equations are written for the (n, M^2) trajectories with fixed J. The mixing between states with different quark spin S and angular momentum L is also discussed. © *2005 Pleiades Publishing, Inc.*

1. INTRODUCTION

The relativistic description of quark−antiquark states is a necessary step for meson systematics and the search for exotic states. The standard way to take account of relativistic effects is to use the Bethe−Salpeter equation [1]. Different versions of the Bethe−Salpeter equations applied to the description of quark−antiquark systems may be found in [2−6]. In the present paper, we develop the approach suggested in [7] for the Bethe−Salpeter equation written for quark−antiquark systems in terms of spectral integrals. In [7], the systems of quarks with equal masses have been considered, such as $u\bar{u}, u\bar{d}, d\bar{d}$, and $s\bar{s}$. In this paper, the systems with unequal masses, like $q\bar{s}$ ($q = u, d$) and $q\bar{Q}$ ($Q = c, b$), are treated.

A detailed presentation of the spectral-integration method as well as the emphasis on its advantages was given in [7], so we need not repeat ourselves. Let us only stress a particular feature of the method: it is rather easy to control the quark−gluonium content of the composite system that is rather important for the search for exotics. Another advantage consists in the easy treatment of the systems with high spins.

Similarly to [7], we present here the equations for the group of states lying on the (n, M^2) trajectory. Such trajectories are linear, and they are suitable for the reconstruction of interaction between quarks at large distances. We hope, by investigating high-spin quark−antiquark states, to obtain decisive information on the structure of forces in the region of $r \sim R_{\text{conf}}$.

*This article was submitted by the authors in English.
**e-mail: `anisovic@thd.pnpi.spb.ru`

In this paper, we present final formulas for the (n, M^2) trajectories; the details of the calculations may be found in [7]. It should be immediately emphasized that the case of different masses requires more cumbersome calculations. In particular, the mixing of states with $J = L, S = 0$ and $J = L, S = 1$ should be accounted for (here, L and S are the orbital momentum and spin of quarks, respectively).

Note that, for systems with equal quark masses, we have already obtained numerical results for a set of the (n, M^2) trajectories such as a_0, a_1, a_2, π, ρ, and b_1. So, we hope that we have elaborated a rather efficient technique allowing us to find realistic wave functions for the quark−antiquark systems. Certain aspects of numerical solutions of the Bethe−Salpeter equations in terms of the spectral integrals are discussed in [8].

The paper is organized as follows. In Section 2, we define the quantities entering the Bethe−Salpeter equation: for equal masses, they were introduced in [7]; now, we expand the definition for unequal masses. In Section 3, the equations for the (n, M^2) trajectories are considered for two different cases, for $J = L, S = 0$ and $J = L, S = 1$ states. The technicalities related to the trace calculations of loop diagrams as well as trace factor convolutions are considered in Appendices A and B.

2. QUARK−ANTIQUARK COMPOSITE SYSTEMS

In the spectral integral technique, the Bethe−Salpeter equation for the wave function of the $q_1\bar{q}_2$

system with the total momentum J, angular momentum $L = |\mathbf{J} - \mathbf{S}|$, and quark−antiquark spin S can be schematically written as

$$\left(s - M^2\right) \widehat{\Psi}_{(n)\mu_1\ldots\mu_J}^{(S,L,J)}(k_\perp) \qquad (1)$$

$$= \int \frac{d^3 k'_\perp}{(2\pi)^3} \Phi(s') \widehat{V}\left(s, s', (k_\perp k'_\perp)\right) (\hat{k}'_1 + m_1)$$

$$\times \widehat{\Psi}_{(n)\,\mu_1\ldots\mu_J}^{(S,L,J)}(k'_\perp)(-\hat{k}'_2 + m_2),$$

where the quarks are mass-on-shell: $k_1^2 = k_1'^2 = m_1^2$ and $k_2^2 = k_2'^2 = m_2^2$. We use the following notation:

$$k = \frac{1}{2}\left(k_1 - k_2\right), \quad P = k_1 + k_2, \qquad (2)$$

$$k' = \frac{1}{2}\left(k'_1 - k'_2\right), \quad P' = k'_1 + k'_2,$$

$$P^2 = s, \quad P'^2 = s', \quad k_\mu^\perp = k_\nu g_{\nu\mu}^\perp, \quad k_\mu'^\perp = k'_\nu g_{\nu\mu}^\perp.$$

The phase-space integral is written as

$$ds' \frac{d^3 k'_1}{2k'_{10}} \frac{d^3 k'_2}{2k'_{20}} \delta^{(4)}(P' - k'_1 - k'_2) = \frac{d^3 k'_\perp}{(2\pi)^3} \Phi(s'), \quad (3)$$

$$\Phi(s') = \frac{2s'\sqrt{s'}}{s'^2 - (m_1^2 - m_2^2)^2}.$$

The wave function reads

$$\widehat{\Psi}_{(n)\mu_1\ldots\mu_J}^{(S,L,J)}(k_\perp) = Q_{\mu_1\ldots\mu_J}^{(S,L,J)}(k_\perp)\psi_n^{(S,L,J)}(k_\perp^2). \quad (4)$$

Here, $Q_{\mu_1\ldots\mu_J}^{(S,L,J)}(k_\perp)$ are the moment operators for fermion−antifermion systems [9] defined as follows:

$$Q_{\mu_1\mu_2\ldots\mu_J}^{(0,J,J)}(k_\perp) = i\gamma_5 X_{\mu_1\ldots\mu_J}^{(J)}(k_\perp), \qquad (5)$$

$$Q_{\mu_1\ldots\mu_J}^{(1,J+1,J)}(k_\perp) = \gamma_\alpha^\perp X_{\mu_1\ldots\mu_J\alpha}^{(J+1)}(k_\perp),$$

$$Q_{\mu_1\ldots\mu_J}^{(1,J,J)}(k_\perp) = \varepsilon_{\alpha\nu_1\nu_2\nu_3}\gamma_\alpha^\perp P_{\nu_1} Z_{\nu_2\mu_1\ldots\mu_J,\nu_3}^{(J)}(k_\perp),$$

$$Q_{\mu_1\ldots\mu_J}^{(1,J-1,J)}(k_\perp) = \gamma_\alpha^\perp Z_{\mu_1\ldots\mu_J,\alpha}^{(J-1)}(k_\perp),$$

where

$$X_{\mu_1\ldots\mu_J}^{(J)}(k_\perp) = \frac{(2J-1)!!}{J!} \qquad (6)$$

$$\times \left[k_{\mu_1}^\perp k_{\mu_2}^\perp k_{\mu_3}^\perp k_{\mu_4}^\perp \ldots k_{\mu_J}^\perp - \frac{k_\perp^2}{2J-1} \right.$$

$$\times \left(g_{\mu_1\mu_2}^\perp k_{\mu_3}^\perp k_{\mu_4}^\perp \ldots k_{\mu_J}^\perp \right.$$

$$\left. + g_{\mu_1\mu_3}^\perp k_{\mu_2}^\perp k_{\mu_4}^\perp \ldots k_{\mu_J}^\perp + \ldots \right)$$

$$+ \frac{k_\perp^4}{(2J-1)(2J-3)}$$

$$\times \left(g_{\mu_1\mu_2}^\perp g_{\mu_3\mu_4}^\perp k_{\mu_5}^\perp k_{\mu_6}^\perp \ldots k_{\mu_J}^\perp \right.$$

$$\left. + g_{\mu_1\mu_2}^\perp g_{\mu_3\mu_5}^\perp k_{\mu_4}^\perp k_{\mu_6}^\perp \ldots k_{\mu_J}^\perp + \ldots \right) + \ldots \Bigg],$$

$$Z_{\mu_1\ldots\mu_J,\alpha}^{(J-1)}(k_\perp) = \frac{2J-1}{L^2}$$

$$\times \left(\sum_{i=1}^{J} X_{\mu_1\ldots\mu_{i-1}\mu_{i+1}\ldots\mu_J}^{(J-1)}(k_\perp) g_{\mu_i\alpha}^\perp - \frac{2}{2J-1} \right.$$

$$\times \left. \sum_{\substack{i,j=1\\i<j}}^{J} g_{\mu_i\mu_j}^\perp X_{\mu_1\ldots\mu_{i-1}\mu_{i+1}\ldots\mu_{j-1}\mu_{j+1}\ldots\mu_J\alpha}^{(J-1)}(k_\perp) \right).$$

The potential operator can be represented as a sum of the t-channel operators:

$$\widehat{V}\left(s, s', (k_\perp k'_\perp)\right) \qquad (7)$$

$$= \sum_I V_I^{(0)}\left(s, s', (k_\perp k'_\perp)\right) \widehat{O}_I \otimes \widehat{O}_I,$$

$$\widehat{O}_I = I, \gamma_\mu, i\sigma_{\mu\nu}, i\gamma_\mu\gamma_5, \gamma_5.$$

To write the spectral-integral equations, we are to transform the t-channel potential operator $\widehat{V}(s, s', (k_\perp k'_\perp))$ into the s-channel ones as follows:

$$\widehat{V}\left(s, s', (k_\perp k'_\perp)\right) \qquad (8)$$

$$= \sum_I \sum_c \widehat{V}_I^{(0)}\left(s, s', (k_\perp k'_\perp)\right) C_{Ic}(\widehat{F}_c \otimes \widehat{F}_c),$$

where C_{Ic} are coefficients of the Fierz matrix

$$C = \begin{pmatrix} \dfrac{1}{4} & \dfrac{1}{4} & \dfrac{1}{8} & \dfrac{1}{4} & \dfrac{1}{4} \\ 1 & -\dfrac{1}{2} & 0 & \dfrac{1}{2} & -1 \\ 3 & 0 & -\dfrac{1}{2} & 0 & 3 \\ 1 & \dfrac{1}{2} & 0 & -\dfrac{1}{2} & -1 \\ \dfrac{1}{4} & -\dfrac{1}{4} & \dfrac{1}{8} & -\dfrac{1}{4} & \dfrac{1}{4} \end{pmatrix}. \qquad (9)$$

Here, the summation is assumed in the $i\sigma_{\mu\nu} \otimes i\sigma_{\mu\nu}$ structure for all indices. Denoting

$$V_c\left(s, s', (k_\perp k'_\perp)\right) = \sum_I \widehat{V}_I^{(0)}\left(s, s', (k_\perp k'_\perp)\right) C_{Ic},$$

$$(10)$$

we have

$$\widehat{V}\left(s, s', (k_\perp k'_\perp)\right) \qquad (11)$$

$$= \sum_c (\widehat{F}_c \otimes \widehat{F}_c) V_c\left(s, s', (k_\perp k'_\perp)\right)$$

$$= (I \otimes I) V_S\left(s, s', (k_\perp k'_\perp)\right)$$

$$+ (\gamma_\mu \otimes \gamma_\mu) V_V\left(s, s', (k_\perp k'_\perp)\right)$$

$$+ (i\sigma_{\mu\nu} \otimes i\sigma_{\mu\nu}) V_T \left(s, s', (k_\perp k'_\perp)\right)$$
$$+ (i\gamma_\mu \gamma_5 \otimes i\gamma_\mu \gamma_5) V_A \left(s, s', (k_\perp k'_\perp)\right)$$
$$+ (\gamma_5 \otimes \gamma_5) V_P \left(s, s', (k_\perp k'_\perp)\right).$$

Let us multiply Eq. (1) by the operator $Q^{(S,L,J)}_{\mu_1...\mu_J}(k_\perp)$ and convolute over the spin–momentum indices:

$$\left(s - M^2\right) \mathrm{tr} \Bigg[\widehat{\Psi}^{(S,L,J)}_{(n)\mu_1...\mu_J}(k_\perp)(\widehat{k}_1 + m_1) \qquad (12)$$

$$\times Q^{(S,L,J)}_{\mu_1...\mu_J}(k_\perp)(-\widehat{k}_2 + m_2)\Bigg]$$

$$= \sum_c \mathrm{tr}\left[\widehat{F}_c(\widehat{k}_1 + m_1) Q^{(S,L,J)}_{\mu_1...\mu_J}(k_\perp)(-\widehat{k}_2 + m_2)\right]$$

$$\times \int \frac{d^3 k'_\perp}{(2\pi)^3} \, \Phi(s') V_c \left(s, s', (k_\perp k'_\perp)\right)$$

$$\times \mathrm{tr}\left[(\widehat{k}'_1 + m_1)\widehat{F}_c(-\widehat{k}'_2 + m_2)\widehat{\Psi}^{(S,L,J)}_{(n)\mu_1...\mu_J}(k'_\perp)\right].$$

We have four states with the $q_1\bar{q}_2$ spins $S = 0$ and $S = 1$:

(i) $S = 0$; $L = J$;

(ii) $S = 1$; $L = J + 1, J, J - 1$,

which are mixed and form two final states. The wave functions read

for $S = 0, 1$, $J = L$,

$$\widehat{\Psi}^{(S_i,J,J)}_{(n)\mu_1...\mu_J}(k_\perp) = C_i \widehat{\Psi}^{(0,J,J)}_{(n)\mu_1...\mu_J}(k_\perp) \qquad (13)$$

$$+ D_i \widehat{\Psi}^{(1,J,J)}_{(n)\mu_1...\mu_J}(k_\perp),$$

where C_i and D_i are the mixing coefficients with $i = 1, 2$;

for $S = 1, L = J \pm 1, J$,

$$\widehat{\Psi}^{(1,(J\pm1)_j,J)}_{(n)\mu_1...\mu_J}(k_\perp) \qquad (14)$$

$$= A_j \widehat{\Psi}^{(1,J-1,J)}_{(n)\mu_1...\mu_J}(k_\perp) + B_j \widehat{\Psi}^{(1,J+1,J)}_{(n)\mu_1...\mu_J}(k_\perp),$$

where A_j and B_j are the mixing coefficients with $j = 1, 2$.

These wave functions are normalized:

$$\int \frac{d^3 k_\perp}{(2\pi)^3}\Phi(s)(-1) \qquad (15)$$

$$\times \mathrm{tr}\Bigg[\widehat{\Psi}^{(S',L'_{j'},J')}_{(n')\mu_1...\mu_J}(k_\perp)(\widehat{k}_1 + m_1)\widehat{\Psi}^{(S,L_j,J)}_{(n)\mu_1...\mu_J}(k_\perp)$$

$$\times (-\widehat{k}_2 + m_2)\Bigg] = (-1)^J \delta_{S'S}\delta_{L'_{j'}L_j}\delta_{J'J}\delta_{n'n}.$$

3. EQUATIONS FOR (n, M^2) TRAJECTORIES

In this section, we write the trajectories for $J = L, S = 0, 1$ and $J = L \pm 1, S = 1$ states.

3.1. The Equation for the $S = 0, 1$, $J = L$ State

There are two equations for the two states with $S = 0, 1$ and $J = L$. Their wave functions are denoted as $C_i \widehat{\Psi}^{(0,J,J)}_{(n)\mu_1...\mu_J}(k_\perp) + D_i \widehat{\Psi}^{(1,J,J)}_{(n)\mu_1...\mu_J}(k_\perp)$, with $i = 1, 2$. These wave functions are orthogonal to each other. Normalization and orthogonality conditions give three constraints for four mixing parameters C_i and D_i.

Each wave function obeys two equations:

$$(s - M^2)X^{(J)}_{\mu_1...\mu_J}(k_\perp) \qquad (16)$$

$$\times \mathrm{tr}\Bigg[\left(i\gamma_5 C_i X^{(J)}_{\mu_1...\mu_J}(k_\perp)\psi^{(0,J,J)}_n(k^2_\perp)\right.$$

$$\left. + \gamma^\perp_\alpha D_i \varepsilon_{\alpha\nu_1\nu_2\nu_3} P_{\nu_1} Z^{(J)}_{\nu_2\mu_1...\mu_J,\nu_3}(k_\perp)\psi^{(1,J,J)}_n(k^2_\perp)\right)$$

$$\times (\widehat{k}_1 + m_1)i\gamma_5(-\widehat{k}_2 + m_2)\Bigg] = X^{(J)}_{\mu_1...\mu_J}(k_\perp)$$

$$\times \sum_c \mathrm{tr}\left[\widehat{F}_c(\widehat{k}_1 + m_1)i\gamma_5(-\widehat{k}_2 + m_2)\right]$$

$$\times \int \frac{d^3 k'_\perp}{(2\pi)^3}\Phi(s')V_c\left(s, s', (k_\perp k'_\perp)\right)$$

$$\times \mathrm{tr}\Bigg[\left(i\gamma_5 C_i X^{(J)}_{\mu_1...\mu_J}(k'_\perp)\psi^{(0,J,J)}_n(k'^2_\perp)\right.$$

$$\left. + \gamma^\perp_{\alpha'} D_i \varepsilon_{\alpha'\nu_1\nu_2\nu_3} P'_{\nu_1} Z^{(J)}_{\nu_2\mu_1...\mu_J,\nu_3}(k'_\perp)\psi^{(1,J,J)}_n(k'^2_\perp)\right)$$

$$\times (\widehat{k}'_1 + m_1)\widehat{F}_c(-\widehat{k}'_2 + m_2)\Bigg]$$

and

$$(s - M^2)\,\varepsilon_{\beta\nu_1\nu_2\nu_3} P_{\nu_1} Z^{(J)}_{\nu_2\mu_1...\mu_J,\nu_3}(k_\perp) \qquad (17)$$

$$\times \mathrm{tr}\Bigg[\left(i\gamma_5 C_i X^{(J)}_{\mu_1...\mu_J}(k_\perp)\psi^{(0,J,J)}_n(k^2_\perp)\right.$$

$$\left. + \gamma^\perp_\alpha D_i \varepsilon_{\alpha\nu_1\nu_2\nu_3} P_{\nu_1} Z^{(J)}_{\nu_2\mu_1...\mu_J,\nu_3}(k_\perp)\psi^{(1,J,J)}_n(k^2_\perp)\right)$$

$$\times (\widehat{k}_1 + m_1)\gamma^\perp_\beta(-\widehat{k}_2 + m_2)\Bigg]$$

$$= \varepsilon_{\beta'\nu_1\nu_2\nu_3} P_{\nu_1} Z^{(J)}_{\nu_2\mu_1...\mu_J,\nu_3}(k_\perp)$$

$$\times \sum_c \mathrm{tr}\left[\widehat{F}_c(\widehat{k}_1 + m_1)\gamma^\perp_{\beta'}(-\widehat{k}_2 + m_2)\right]$$

$$\times \int \frac{d^3 k'_\perp}{(2\pi)^3}\Phi(s')V_c\left(s, s', (k_\perp k'_\perp)\right)$$

$$\times \mathrm{tr}\Bigg[\left(i\gamma_5 C_i X^{(J)}_{\mu_1...\mu_J}(k'_\perp)\psi^{(0,J,J)}_n(k'^2_\perp)\right.$$

$$\left. + \gamma^\perp_{\alpha'} D_i \varepsilon_{\alpha'\nu_1\nu_2\nu_3} P'_{\nu_1} Z^{(J)}_{\nu_2\mu_1...\mu_J,\nu_3}(k'_\perp)\psi^{(1,J,J)}_n(k'^2_\perp)\right)$$

$$\times (\widehat{k}'_1 + m_1)\widehat{F}_c(-\widehat{k}'_2 + m_2)\Bigg].$$

Now consider the left-hand side of Eq. (16). Using the traces written in Appendix A and convolution of operators from Appendix B, we have

$$X^{(J)}_{\mu_1...\mu_J}(k_\perp)\mathrm{tr}\left[i\gamma_5(\widehat{k}_1 + m_1)i\gamma_5(-\widehat{k}_2 + m_2)\right]$$

$$\times X^{(J)}_{\mu_1...\mu_J}(k_\perp) = -2(s - \Delta^2)\alpha(J)k_\perp^{2J},$$

$$X^{(J)}_{\mu_1...\mu_J}(k_\perp) \qquad (18)$$

$$\times \mathrm{tr}\left[\gamma_\alpha^\perp(\widehat{k}_1 + m_1)i\gamma_5(-\widehat{k}_2 + m_2)\right]$$

$$\times \varepsilon_{\alpha\nu_1\nu_2\nu_3}P_{\nu_1}Z^{(J)}_{\nu_2\mu_1...\mu_J,\nu_3}(k_\perp) = 0.$$

Here and below, we use the following notation: $\delta = m_2 - m_1, \sigma = m_2 + m_1$. Also, the left-hand side of (17) contains two convolutions:

$$\varepsilon_{\beta\nu_1\nu_2\nu_3}P_{\nu_1}Z^{(J)}_{\nu_2\mu_1...\mu_J,\nu_3}(k_\perp) \qquad (19)$$

$$\times \mathrm{tr}\left[i\gamma_5(\widehat{k}_1 + m_1)\gamma_\beta^\perp(-\widehat{k}_2 + m_2)\right]$$

$$\times X^{(J)}_{\mu_1...\mu_J}(k_\perp) = 0,$$

$$\varepsilon_{\beta\nu_1\nu_2\nu_3}P_{\nu_1}Z^{(J)}_{\nu_2\mu_1...\mu_J,\nu_3}(k_\perp)$$

$$\times \mathrm{tr}\left[\gamma_\alpha^\perp(\widehat{k}_1 + m_1)\gamma_\beta^\perp(-\widehat{k}_2 + m_2)\right]$$

$$\times \varepsilon_{\alpha\nu_1\nu_2\nu_3}P_{\nu_1}Z^{(J)}_{\nu_2\mu_1...\mu_J,\nu_3}(k_\perp)$$

$$= -2s(s - \Delta^2)\frac{J(2J + 3)^2}{(J + 1)^3}\alpha(J)k_\perp^{2J}.$$

The right-hand side of Eq. (17) is calculated in two steps. First, we summarize over c:

$$A\left(s, s', (k_\perp k_\perp')\right) \qquad (20)$$

$$= \sum_{c=T,A,P} A_c\left(s, s', (k_\perp k_\perp')\right)V_c\left(s, s', (k_\perp k_\perp')\right)$$

$$= \sum_{c=T,A,P} \mathrm{tr}\left[\widehat{F}_c(\widehat{k}_1 + m_1)i\gamma_5(-\widehat{k}_2 + m_2)\right]$$

$$\times \mathrm{tr}\left[i\gamma_5(\widehat{k}_1' + m_1)\widehat{F}_c(-\widehat{k}_2' + m_2)\right]$$

$$\times V_c\left(s, s', (k_\perp k_\perp')\right),$$

$$B_{\beta'\alpha'}\left(s, s', (k_\perp k_\perp')\right) \qquad (21)$$

$$= \sum_{c=T,A,V,S} (B_c)_{\beta'\alpha'}\left(s, s', (k_\perp k_\perp')\right)$$

$$\times V_c\left(s, s', (k_\perp k_\perp')\right)$$

$$= \sum_{c=T,A,V,S} \mathrm{tr}\left[\widehat{F}_c(\widehat{k}_1 + m_1)\gamma_{\beta'}^\perp(-\widehat{k}_2 + m_2)\right]$$

$$\times \mathrm{tr}\left[\gamma_{\alpha'}^\perp(\widehat{k}_1' + m_1)\widehat{F}_c(-\widehat{k}_2' + m_2)\right]$$

$$\times V_c\left(s, s', (k_\perp k_\perp')\right),$$

and

$$C_{\alpha'}\left(s, s', (k_\perp k_\perp')\right) \qquad (22)$$

$$= \sum_{c=T,A} C_{\alpha'}^c\left(s, s', (k_\perp k_\perp')\right)V_c\left(s, s', (k_\perp k_\perp')\right)$$

$$= \sum_{c=T,A} \mathrm{tr}\left[\widehat{F}_c(\widehat{k}_1 + m_1)i\gamma_5(-\widehat{k}_2 + m_2)\right]$$

$$\times \mathrm{tr}\left[\gamma_{\alpha'}^\perp(\widehat{k}_1' + m_1)\widehat{F}_c(-\widehat{k}_2' + m_2)\right]$$

$$\times V_c\left(s, s', (k_\perp k_\perp')\right).$$

In Appendix A, the trace calculations are presented, and the values $A_c\left(s, s', (k_\perp k_\perp')\right)$, $C_c\left(s, s', (k_\perp k_\perp')\right)$ are given. So, after the summation, A_c, B_c, C_c are written as follows:

$$A\left(s, s', (k_\perp k_\perp')\right) \qquad (23)$$

$$= \sum_{c=T,A,P} A_c\left(s, s', (k_\perp k_\perp')\right)V_c\left(s, s', (k_\perp k_\perp')\right)$$

$$= -16(k_\perp k_\perp')\left[2\sqrt{ss'}V_T\left(s, s', (k_\perp k_\perp')\right)\right.$$

$$\left. + \Delta^2 V_A\left(s, s', (k_\perp k_\perp')\right)\right] - 4(s - \Delta^2)(s' - \Delta^2)$$

$$\times \left[\frac{\sigma\sigma'}{\sqrt{ss'}}V_A\left(s, s', (k_\perp k_\perp')\right) + V_P\left(s, s', (k_\perp k_\perp')\right)\right],$$

$$B_{\beta'\alpha'}\left(s, s', (k_\perp k_\perp')\right) \qquad (24)$$

$$= \sum_{c=T,A,V,S} (B_c)_{\beta'\alpha'}\left(s, s', (k_\perp k_\perp')\right)$$

$$\times V_c\left(s, s', (k_\perp k_\perp')\right)$$

$$= 4g_{\beta'\alpha'}^\perp\left[(s - \Delta^2)(s' - \Delta^2)\right.$$

$$\times \left(V_V\left(s, s', (k_\perp k_\perp')\right)\right.$$

$$\left.+ 2\frac{\sigma^2}{\sqrt{ss'}}V_T\left(s, s', (k_\perp k_\perp')\right)\right)$$

$$+ 4\sqrt{k_\perp^2}\sqrt{k_\perp'^2}z\left(\sqrt{ss'}V_A\left(s, s', (k_\perp k_\perp')\right)\right.$$

$$\left.\left. + 2\Delta^2 V_T\left(s, s', (k_\perp k_\perp')\right)\right)\right]$$

$$+ 16k_{\beta'}^\perp k_{\alpha'}'^\perp\left[\left(\sigma^2 V_S\left(s, s', (k_\perp k_\perp')\right)\right.\right.$$

$$\left.\left.+ \frac{\sigma^2\Delta^2}{\sqrt{ss'}}V_V\left(s, s', (k_\perp k_\perp')\right)\right)\right.$$

$$\left.+ 4\sqrt{k_\perp^2}\sqrt{k_\perp'^2}zV_V\left(s, s', (k_\perp k_\perp')\right)\right]$$

$$- 16k_{\beta'}'^\perp k_{\alpha'}^\perp\left[\sqrt{ss'}V_A\left(s, s', (k_\perp k_\perp')\right)\right.$$

$$\left.+ 2\Delta^2 V_T\left(s, s', (k_\perp k_\perp')\right)\right]$$

$$+ 16k_{\beta'}^\perp k_{\alpha'}^\perp\left(s' - \Delta^2\right)V_V\left(s, s', (k_\perp k_\perp')\right)$$

$$+ 16k_{\beta'}'^\perp k_{\alpha'}'^\perp\left(s - \Delta^2\right)V_V\left(s, s', (k_\perp k_\perp')\right),$$

and

$$C_{\alpha'}\left(s, s', (k_\perp k'_\perp)\right) \qquad (25)$$

$$= \sum_{c=T,A} C^c_{\alpha'}\left(s, s', (k_\perp k'_\perp)\right) V_c\left(s, s', (k_\perp k'_\perp)\right)$$

$$= 8\big[2\Delta\varepsilon_{\alpha'kk'P'}V_A\left(s, s', (k_\perp k'_\perp)\right)$$

$$+ \sigma\varepsilon_{\alpha'Pk'P'}V_A\left(s, s', (k_\perp k'_\perp)\right)$$

$$+ 4\Delta\varepsilon_{\alpha'Pkk'}V_T\left(s, s', (k_\perp k'_\perp)\right)$$

$$+ 2\sigma\varepsilon_{\alpha'PkP'}V_T\left(s, s', (k_\perp k'_\perp)\right)\big].$$

Here we used a shorthand notation: $\varepsilon_{\alpha'kk'P'} \equiv k_\beta k'_\mu P'_\nu \varepsilon_{\alpha'\beta\mu\nu}$. Second, the convolution of operators is performed by using equations of Appendix B and recurrent formulas for the Legendre polynomials

$$zP_J(z) = \frac{J+1}{2J+1}P_{J+1}(z) + \frac{J}{2J+1}P_{J-1}(z),$$

which allows us to represent the Bethe−Salpeter equation in terms of the Legendre polynomials. As a result, we get

$$X^{(J)}_{\mu_1\ldots\mu_J}(k_\perp)A\left(s, s', (k_\perp k'_\perp)\right) X^{(J)}_{\mu_1\ldots\mu_J}(k'_\perp) \quad (26)$$

$$= -4\alpha(J)\left(\sqrt{k_\perp^2}\sqrt{k_\perp'^2}\right)^J$$

$$\times \Bigg[4\frac{J+1}{2J+1}\sqrt{k_\perp^2}\sqrt{k_\perp'^2}\Big(2\sqrt{ss'}V_T\left(s, s', (k_\perp k'_\perp)\right)$$

$$+ \Delta^2 V_A\left(s, s', (k_\perp k'_\perp)\right)\Big)P_{J+1}(z)$$

$$+ (s - \Delta^2)(s' - \Delta^2)$$

$$\times \Bigg(\frac{\sigma^2}{\sqrt{ss'}}V_A\left(s, s', (k_\perp k'_\perp)\right)$$

$$+ V_P\left(s, s', (k_\perp k'_\perp)\right)\Bigg)$$

$$\times P_J(z) + 4\frac{J}{2J+1}\sqrt{k_\perp^2}\sqrt{k_\perp'^2}$$

$$\times \Big(2\sqrt{ss'}V_T\left(s, s', (k_\perp k'_\perp)\right)$$

$$+ \Delta^2 V_A\left(s, s', (k_\perp k'_\perp)\right)\Big)P_{J-1}(z)\Bigg]$$

and

$$X^{(J)}_{\mu_1\ldots\mu_J}(k_\perp)C_{\alpha'}\left(s, s', (k_\perp k'_\perp)\right) \qquad (27)$$

$$\times \varepsilon_{\alpha'\nu_1\nu_2\nu_3}P'_{\nu_1}Z^{(J)}_{\nu_2\mu_1\ldots\mu_J,\nu_3}(k'_\perp)$$

$$= 16\frac{2J+3}{J+1}\alpha(J)\left(\sqrt{k_\perp^2}\sqrt{k_\perp'^2}\right)^{J+1}$$

$$\times \left(\frac{2}{J+1}P'_J(z) - JP_{J+1}(z)\right)$$

$$\times \left(s'\Delta V_A\left(s, s', (k_\perp k'_\perp)\right)\right.$$

$$\left.+ 2\Delta\sqrt{ss'}V_T\left(s, s', (k_\perp k'_\perp)\right)\right).$$

For the right-hand side of (17), we have

$$\varepsilon_{\beta'\nu_1\nu_2\nu_3}P_{\nu_1}Z^{(J)}_{\nu_2\mu_1\ldots\mu_J,\nu_3}(k_\perp) \qquad (28)$$

$$\times C_{\beta'}\left(s, s', (k_\perp k'_\perp)\right) X^{(J)}_{\mu_1\ldots\mu_J}(k'_\perp)$$

$$= 16\frac{2J+3}{J+1}\alpha(J)\left(\sqrt{k_\perp^2}\sqrt{k_\perp'^2}\right)^{J+1}$$

$$\times \left(\frac{2}{J+1}P'_J(z) - JP_{J+1}(z)\right)$$

$$\times \left(s\Delta V_A\left(s, s', (k_\perp k'_\perp)\right)\right.$$

$$\left.+ 2\Delta\sqrt{ss'}V_T\left(s, s', (k_\perp k'_\perp)\right)\right)$$

and

$$\varepsilon_{\beta'\nu_1\nu_2\nu_3}P_{\nu_1}Z^{(J)}_{\nu_2\mu_1\ldots\mu_J,\nu_3}(k_\perp) \qquad (29)$$

$$\times B_{\beta'\alpha'}\left(s, s', (k_\perp k'_\perp)\right)\varepsilon_{\alpha'\nu_1\nu_2\nu_3}$$

$$\times P'_{\nu_1}Z^{(J)}_{\nu_2\mu_1\ldots\mu_J,\nu_3}(k'_\perp)$$

$$= -4\sqrt{ss'}\frac{J(2J+3)^2}{(J+1)^3}\alpha(J)\left(\sqrt{k_\perp^2}\sqrt{k_\perp'^2}\right)^J$$

$$\times \Bigg[4\frac{J}{2J+1}\sqrt{k_\perp^2}\sqrt{k_\perp'^2}\Big(\sqrt{ss'}V_A\left(s, s', (k_\perp k'_\perp)\right)$$

$$+ 2\Delta^2 V_T\left(s, s', (k_\perp k'_\perp)\right)\Big)P_{J+1}(z)$$

$$+ (s - \Delta^2)(s' - \Delta^2)\Big(V_V\left(s, s', (k_\perp k'_\perp)\right)$$

$$+ 2\frac{\sigma^2}{\sqrt{ss'}}V_T\left(s, s', (k_\perp k'_\perp)\right)\Big)P_J(z)$$

$$+ 4\frac{J+1}{2J+1}\sqrt{k_\perp^2}\sqrt{k_\perp'^2}\Big(\sqrt{ss'}V_A\left(s, s', (k_\perp k'_\perp)\right)$$

$$+ 2\Delta^2 V_T\left(s, s', (k_\perp k'_\perp)\right)\Big)P_{J-1}(z)\Bigg].$$

Expanding the interaction block in a series of Legendre polynomials,

$$V_c\left(s, s', (k_\perp k'_\perp)\right) = \sum_J V^{(J)}_c\left(s, s'\right)P_J(z) \quad (30)$$

$$= \sum_J \widetilde{V}^{(J)}_c\left(s, s'\right)\alpha(J)\left(-\sqrt{k_\perp^2}\sqrt{k_\perp'^2}\right)^J P_J(z),$$

and integrating over angle variables on the right-hand side by taking account of the standard normalization condition $\int_{-1}^{1} \frac{dz}{2} P_J^2(z) = 1/(2J+1)$, we have finally

$$(s - M^2)\left[(s - \Delta^2)\psi_n^{(0,J,J)}(s)C_i\right] \qquad (31)$$

$$= \int\limits_{(m_1+m_2)^2}^{\infty} \frac{ds'}{\pi}\rho(s') \cdot 2(-k_\perp'^2)^J \psi_n^{(0,J,J)}(s')C_j$$

$$\times \left[-4\xi(J+1)\frac{J+1}{2J+1}k_\perp^2 k_\perp'^2 \right.$$

$$\times \left(2\sqrt{ss'}\widetilde{V}_T^{(J+1)}(s,s') + \Delta^2\widetilde{V}_A^{(J+1)}(s,s')\right)$$

$$+ \xi(J)(s-\Delta^2)(s'-\Delta^2)$$

$$\times \left(\frac{\sigma^2}{\sqrt{ss'}}\widetilde{V}_A^{(J)}(s,s') + \widetilde{V}_P^{(J)}(s,s')\right)$$

$$- 4\xi(J-1)\frac{J}{2J+1}$$

$$\times \left. \left(2\sqrt{ss'}\widetilde{V}_T^{(J-1)}(s,s') + \Delta^2\widetilde{V}_A^{(J-1)}(s,s')\right)\right]$$

$$- \int\limits_{(m_1+m_2)^2}^{\infty} \frac{ds'}{\pi}\rho(s') \cdot 8\frac{2J+3}{J+1}k_\perp^2(-k_\perp'^2)^{J+1}$$

$$\times \psi_n^{(1,J,J)}(s')D_j\left[\frac{2}{J+1}\sum_a(2J-4a-1)\right.$$

$$\times \xi(J-2a-1)\left(-\sqrt{k_\perp^2}\sqrt{k_\perp'^2}\right)^{-2(a+1)}$$

$$\times \left(s'\Delta\widetilde{V}_A^{(J-2a-1)}(s,s')\right.$$

$$\left. + 2\Delta\sqrt{ss'}\widetilde{V}_T^{(J-2a-1)}(s,s')\right)$$

$$- J\xi(J+1)\left(s'\Delta\widetilde{V}_A^{(J+1)}(s,s')\right.$$

$$\left.\left. + 2\Delta'\sqrt{ss'}\widetilde{V}_T^{(J+1)}(s,s')\right)\right],$$

where

$$P_J'(z) = \sum_a(2J-4a-1)P_{J-2a-1}(z). \qquad (32)$$

Equation (17) reads

$$(s-M^2)\left[s(s-\Delta^2)\frac{J(2J+3)^2}{(J+1)^3}\psi_n^{(1,J,J)}(s)D_i\right] \qquad (33)$$

$$= - \int\limits_{(m_1+m_2)^2}^{\infty} \frac{ds'}{\pi}\rho(s') \cdot 8\frac{2J+3}{J+1}k_\perp^2(-k_\perp'^2)^{J+1}$$

$$\times \psi_n^{(0,J,J)}(s')D_j\left(\frac{2}{J+1}\sum_a(2J-4a-1)\right.$$

$$\times \xi(J-2a-1)\left(-\sqrt{k_\perp^2}\sqrt{k_\perp'^2}\right)^{-2(a+1)}$$

$$\times \left(s\Delta\widetilde{V}_A^{(J-2a-1)}(s,s')\right.$$

$$\left. + 2\Delta\sqrt{ss'}\widetilde{V}_T^{(J-2a-1)}(s,s')\right)$$

$$- J\xi(J+1)\left(s\Delta\widetilde{V}_A^{J+1}(s,s')\right.$$

$$\left.\left. + 2\Delta\sqrt{ss'}\widetilde{V}_T^{J+1}(s,s')\right)\right)$$

$$+ \int\limits_{(m_1+m_2)^2}^{\infty} \frac{ds'}{\pi}\rho(s') \cdot 2\sqrt{ss'}\frac{J(2J+3)^2}{(J+1)^3}(-k_\perp'^2)^J$$

$$\times \psi_n^{(1,J,J)}(s')D_j\left[-4\xi(J+1)\frac{J}{2J+1}k_\perp^2 k_\perp'^2\right.$$

$$\times \left(\sqrt{ss'}\widetilde{V}_A^{(J+1)}(s,s') + 2\Delta^2\widetilde{V}_T^{(J+1)}(s,s')\right)$$

$$+ \xi(J)(s-\Delta^2)(s'-\Delta^2)$$

$$\times \left(2\frac{\sigma^2}{\sqrt{ss'}}\widetilde{V}_T^{(J)}(s,s') + \widetilde{V}_V^{(J)}(s,s')\right)$$

$$- 4\xi(J-1)\frac{J+1}{2J+1}$$

$$\times \left. \left(\sqrt{ss'}\widetilde{V}_A^{(J-1)}(s,s') + 2\Delta^2\widetilde{V}_T^{(J-1)}(s,s')\right)\right].$$

The normalization and orthogonality conditions look as follows:

$$\int\limits_{(m_2+m_1)^2}^{\infty} \frac{ds}{\pi}\rho(s)\left[C_i^2\left(\psi_n^{(0,J,J)}(k_\perp^2)\right)^2 \cdot 2\alpha(J)\right. \qquad (34)$$

$$\times (-k_\perp^2)^J(s-\Delta^2) + D_i^2\left(\psi_n^{(1,J,J)}(k_\perp^2)\right)^2$$

$$\left. \times 2\alpha(J)(-k_\perp^2)^J s(s-\Delta^2)\frac{J(2J+3)^2}{(J+1)^3}\right] = 1,$$

$$i = 1,2,$$

and

$$\int\limits_{(m_2+m_1)^2}^{\infty} \frac{ds}{\pi}\rho(s)\left[C_1C_2\left(\psi_n^{(0,J,J)}(k_\perp^2)\right)^2 \cdot 2\alpha(J)\right.$$

$$(35)$$

$$\times \left(-k_\perp^2\right)^J \left(s - \Delta^2\right) + D_1 D_2 \left(\psi_n^{(1,J,J)}(k_\perp^2)\right)^2$$

$$\times 2\alpha(J)(-k_\perp^2)^J s \left(s - \Delta^2\right) \frac{J(2J+3)^2}{(J+1)^3}\right] = 0.$$

As the result of our calculations, we observe the mixing of singlet ($J = L$, $S = 0$) and triplet ($J = L$, $S = 1$) states and that is proportional to the quark mass difference. This is a consequence of C-parity breaking for the quark−antiquark system with nonequal quark masses. The best known examples of such a system is K and B mesons.

The mixing between $S = 1$, $J = L$ and $S = 0$, $J = L$ states gives rise to a system of equations where, for states with total spin J, we need to know all lower projections of the potential on the Legendre polynomials, not only the $J + 1$, J, $J - 1$ ones.

3.2. The Equations for the S = 1, J = L ± 1 States

We have two equations for the two states with $S = 1$ and $J = L \pm 1$. Their wave functions are denoted as $A_j \widehat{\Psi}_{(n)\mu_1\ldots\mu_J}^{(1,J-1,J)}(k_\perp) + B_j \widehat{\Psi}_{(n)\mu_1\ldots\mu_J}^{(1,J+1,J)}(k_\perp)$, with $j = 1, 2$. These wave functions are orthogonal. The normalization and orthogonality conditions give three constraints for four mixing parameters A_j and B_j.

Each wave function obeys two equations:

$$\left(s - M^2\right) X_{\mu_1\ldots\mu_J\beta}^{(J+1)}(k_\perp) \qquad (36)$$

$$\times \text{tr}\left[\gamma_\alpha^\perp(\widehat{k}_1 + m_1)\gamma_\beta^\perp(-\widehat{k}_2 + m_2)\right]$$

$$\times \left(A_j Z_{\mu_1\ldots\mu_J,\alpha}^{(J-1)}(k_\perp)\psi_n^{(1,J-1,J)}(k_\perp^2)\right.$$

$$\left. + B_j X_{\mu_1\ldots\mu_J\alpha}^{(J+1)}(k_\perp)\psi_n^{(1,J+1,J)}(k_\perp^2)\right)$$

$$= X_{\mu_1\ldots\mu_J\beta'}^{(J+1)}(k_\perp)$$

$$\times \sum_c \text{tr}\left[\widehat{F}_c(\widehat{k}_1 + m_1)\gamma_{\beta'}^\perp(-\widehat{k}_2 + m_2)\right]$$

$$\times \int \frac{d^3k_\perp'}{(2\pi)^3}V_c\left(s, s', (k_\perp k_\perp')\right)$$

$$\times \text{tr}\left[\gamma_{\alpha'}^\perp(\widehat{k}_1' + m_1)\widehat{F}_c(-\widehat{k}_2' + m_2)\right]$$

$$\times \left(A_j Z_{\mu_1\ldots\mu_J,\alpha'}^{(J-1)}(k_\perp')\psi_n^{(1,J-1,J)}(k_\perp'^2)\right.$$

$$\left. + B_j X_{\mu_1\ldots\mu_J\alpha'}^{(J+1)}(k_\perp')\psi_n^{(1,J+1,J)}(k_\perp'^2)\right)$$

and

$$\left(s - M^2\right) Z_{\mu_1\ldots\mu_J,\beta}^{(J-1)}(k_\perp) \qquad (37)$$

$$\times \text{tr}\left[\gamma_\alpha^\perp(\widehat{k}_1 + m_1)\gamma_\beta^\perp(-\widehat{k}_2 + m_2)\right]$$

$$\times \left(A_j Z_{\mu_1\ldots\mu_J,\alpha}^{(J-1)}(k_\perp)\psi_n^{(1,J-1,J)}(k_\perp^2)\right.$$

$$\left. + B_j X_{\mu_1\ldots\mu_J\alpha}^{(J+1)}(k_\perp)\psi_n^{(1,J+1,J)}(k_\perp^2)\right)$$

$$= Z_{\mu_1\ldots\mu_J,\beta'}^{(J-1)}(k_\perp)$$

$$\times \sum_c \text{tr}\left[\widehat{F}_c(\widehat{k}_1 + m_1)\gamma_{\beta'}^\perp(-\widehat{k}_2 + m_2)\right]$$

$$\times \int \frac{d^3k_\perp'}{(2\pi)^3}V_c\left(s, s', (k_\perp k_\perp')\right)$$

$$\times \text{tr}\left[\gamma_{\alpha'}^\perp(\widehat{k}_1' + m_1)\widehat{F}_c(-\widehat{k}_2' + m_2)\right]$$

$$\times \left(A_j Z_{\mu_1\ldots\mu_J,\alpha'}^{(J-1)}(k_\perp')\psi_n^{(1,J-1,J)}(k_\perp'^2)\right.$$

$$\left. + B_j X_{\mu_1\ldots\mu_J\alpha'}^{(J+1)}(k_\perp')\psi_n^{(1,J+1,J)}(k_\perp'^2)\right).$$

First, consider Eq. (36). On the left-hand side of (36), one has two convolutions:

$$X_{\mu_1\ldots\mu_J\beta}^{(J+1)}(k_\perp)\text{tr}\left[\gamma_\alpha^\perp(\widehat{k}_1 + m_1)\right. \qquad (38)$$

$$\left.\times \gamma_\beta^\perp(-\widehat{k}_2 + m_2)\right] X_{\mu_1\ldots\mu_J\alpha}^{(J+1)}(k_\perp)$$

$$= 2\alpha(J)k_\perp^{2(J+1)}\left[\frac{2J+1}{J+1}(s - \Delta^2) + 4k_\perp^2\right],$$

$$X_{\mu_1\ldots\mu_J\beta}^{(J+1)}(k_\perp)\text{tr}\left[\gamma_\alpha^\perp(\widehat{k}_1 + m_1)\gamma_\beta^\perp(-\widehat{k}_2 + m_2)\right]$$

$$\times Z_{\mu_1\ldots\mu_J,\alpha}^{(J-1)}(k_\perp) = 8\alpha(J)k_\perp^{2(J+1)}.$$

Also, the left-hand side of (37) contains two convolutions:

$$Z_{\mu_1\ldots\mu_J,\beta}^{(J-1)}(k_\perp)\text{tr}\left[\gamma_\alpha^\perp(\widehat{k}_1 + m_1)\gamma_\beta^\perp(-\widehat{k}_2 + m_2)\right] \qquad (39)$$

$$\times X_{\mu_1\ldots\mu_J\alpha}^{(J+1)}(k_\perp) = 8\alpha(J)k_\perp^{2(J+1)},$$

$$Z_{\mu_1\ldots\mu_J,\beta}^{(J-1)}(k_\perp)\text{tr}\left[\gamma_\alpha^\perp(\widehat{k}_1 + m_1)\right.$$

$$\left.\times \gamma_\beta^\perp(-\widehat{k}_2 + m_2)\right] Z_{\mu_1\ldots\mu_J,\alpha}^{(J-1)}(k_\perp)$$

$$= 2\alpha(J)k_\perp^{2(J-1)}\left[\frac{2J+1}{J}(s - \Delta^2) + 4k_\perp^2\right].$$

The right-hand sides of Eqs. (36) and (37) are determined by the convolutions of the trace factor $B_{\beta'\alpha'}\left(s, s', (k_\perp k_\perp')\right)$ [see Eqs. (24)] with angular-momentum wave functions; the corresponding formulas may be found in Appendix B. Taking them into account, one has for the right-hand side of (36)

$$X_{\mu_1\ldots\mu_J\beta'}^{(J+1)}(k_\perp)B_{\beta'\alpha'}\left(s, s', (k_\perp k_\perp')\right) X_{\mu_1\ldots\mu_J\alpha'}^{(J+1)}(k_\perp')$$

$$\qquad (40)$$

$$= 4\alpha(J)\left(\sqrt{k_\perp^2}\sqrt{k_\perp'^2}\right)^{J+1}$$

$$\times \left(\left[\frac{2J+1}{J+1}(s-\Delta^2)(s'-\Delta^2) \right. \right.$$

$$\times \left(V_V(s,s',(k_\perp k'_\perp)) + 2\frac{\sigma^2}{\sqrt{ss'}}V_T(s,s',(k_\perp k'_\perp)) \right)$$

$$+ 4(s'-\Delta^2)k_\perp^2 V_V(s,s',(k_\perp k'_\perp))$$

$$+ 4(s-\Delta^2)k'^2_\perp V_V(s,s',(k_\perp k'_\perp))$$

$$\left. + 16\frac{J+1}{2J+1}k_\perp^2 k'^2_\perp V_V(s,s',(k_\perp k'_\perp)) \right]$$

$$\times P_{J+1}(z) + 4 \left[\sigma^2 V_S(s,s',(k_\perp k'_\perp)) \right.$$

$$+ \frac{\sigma^2\Delta^2}{\sqrt{ss'}}V_V(s,s',(k_\perp k'_\perp))$$

$$+ \frac{J}{J+1}\left(\sqrt{ss'}V_A(s,s',(k_\perp k'_\perp)) \right.$$

$$\left. \left. + 2\Delta^2 V_T(s,s',(k_\perp k'_\perp)) \right) \right] \sqrt{k_\perp^2}\sqrt{k'^2_\perp}P_J(z)$$

$$\left. + 16\frac{J}{2J+1}k_\perp^2 k'^2_\perp V_V(s,s',(k_\perp k'_\perp))P_{J-1}(z) \right)$$

and

$$X^{(J+1)}_{\mu_1...\mu_J\beta'}(k_\perp)B_{\beta'\alpha'}\left(s,s',(k_\perp k'_\perp)\right) \qquad (41)$$

$$\times Z^{(J-1)}_{\mu_1...\mu_J,\alpha'}(k'_\perp) = 16\alpha(J)k_\perp^2$$

$$\times \left(\sqrt{k_\perp^2}\sqrt{k'^2_\perp} \right)^{J-1} \left(\left[s-\Delta^2 + 4\frac{J+1}{2J+1}k_\perp^2 \right] \right.$$

$$\times k'^2_\perp V_V(s,s',(k_\perp k'_\perp))P_{J+1}(z)$$

$$+ \left[\sigma^2 V_S(s,s',(k_\perp k'_\perp)) + \frac{\sigma^2\Delta^2}{\sqrt{ss'}}V_V(s,s',(k_\perp k'_\perp)) \right.$$

$$- \sqrt{ss'}V_A(s,s',(k_\perp k'_\perp))$$

$$\left. - 2\Delta^2 V_T(s,s',(k_\perp k'_\perp)) \right]$$

$$\times \sqrt{k_\perp^2}\sqrt{k'^2_\perp}P_J(z) + \left[s'-\Delta^2 + 4\frac{J}{2J+1}k'^2_\perp \right]$$

$$\left. \times k_\perp^2 V_V(s,s',(k_\perp k'_\perp))P_{J-1}(z) \right).$$

For the right-hand side of (37),

$$Z^{(J-1)}_{\mu_1...\mu_J,\beta'}(k_\perp)B_{\beta'\alpha'}\left(s,s',(k_\perp k'_\perp)\right) \qquad (42)$$

$$\times X^{(J+1)}_{\mu_1...\mu_J\alpha'}(k'_\perp) = 16\alpha(J)k'^2_\perp \left(\sqrt{k_\perp^2}\sqrt{k'^2_\perp} \right)^{J-1}$$

$$\times \left(\left[s'-\Delta^2 + 4\frac{J+1}{2J+1}k'^2_\perp \right] \right.$$

$$\times k_\perp^2 V_V(s,s',(k_\perp k'_\perp))P_{J+1}(z)$$

$$+ \left[\sigma^2 V_S(s,s',(k_\perp k'_\perp)) + \frac{\sigma^2\Delta^2}{\sqrt{ss'}}V_V(s,s',(k_\perp k'_\perp)) \right.$$

$$- \sqrt{ss'}V_A(s,s',(k_\perp k'_\perp)) - 2\Delta^2 V_T(s,s',(k_\perp k'_\perp)) \right]$$

$$\times \sqrt{k_\perp^2}\sqrt{k'^2_\perp}P_J(z) + \left[s-\Delta^2 + 4\frac{J}{2J+1}k_\perp^2 \right]$$

$$\left. \times k'^2_\perp V_V(s,s',(k_\perp k'_\perp))P_{J-1}(z) \right),$$

and

$$Z^{(J-1)}_{\mu_1...\mu_J,\beta'}(k_\perp)B_{\beta'\alpha'}\left(s,s',(k_\perp k'_\perp)\right) \qquad (43)$$

$$\times Z^{(J-1)}_{\mu_1...\mu_J,\alpha'}(k'_\perp) = 4\alpha(J) \left(\sqrt{k_\perp^2}\sqrt{k'^2_\perp} \right)^{J-1}$$

$$\times \left(16\frac{J+1}{2J+1}k_\perp^2 k'^2_\perp V_V(s,s',(k_\perp k'_\perp))P_{J+1}(z) \right.$$

$$+ 4 \left[\sigma^2 V_S(s,s',(k_\perp k'_\perp)) \right.$$

$$+ \frac{\sigma^2\Delta^2}{\sqrt{ss'}}V_V(s,s',(k_\perp k'_\perp))$$

$$+ \frac{J+1}{J}\left(\sqrt{ss'}V_A(s,s',(k_\perp k'_\perp)) \right.$$

$$\left. \left. + 2\Delta^2 V_T(s,s',(k_\perp k'_\perp)) \right) \right] \sqrt{k_\perp^2}\sqrt{k'^2_\perp}P_J(z)$$

$$+ \left[\frac{2J+1}{J}(s-\Delta^2)(s'-\Delta^2) \right.$$

$$\times \left(V_V(s,s',(k_\perp k'_\perp)) + 2\frac{\sigma^2}{\sqrt{ss'}}V_T(s,s',(k_\perp k'_\perp)) \right)$$

$$+ 4(s'-\Delta^2)k_\perp^2 V_V(s,s',(k_\perp k'_\perp))$$

$$+ 4(s-\Delta^2)k'^2_\perp V_V(s,s',(k_\perp k'_\perp))$$

$$\left. \left. + 16\frac{J}{2J+1}k_\perp^2 k'^2_\perp V_V(s,s',(k_\perp k'_\perp)) \right] P_{J-1}(z) \right).$$

On the right-hand sides of Eqs. (36) and (37), we expand the interaction block in a series of Legendre polynomials and integrate over angle variables: $\int_{-1}^{1} dz/2$. As a result, Eq. (36) reads

$$(s-M^2)\left[4\psi_n^{(1,J-1,J)}(s)A_j \right. \qquad (44)$$

$$+ \left(\frac{2J+1}{J+1}(s-\Delta^2) + 4k_\perp^2 \right) \psi_n^{(1,J+1,J)}(s) B_j \Bigg]$$

$$= \int\limits_{(m_1+m_2)^2}^{\infty} \frac{ds'}{\pi} \rho(s') \cdot 8(-k_\perp'^2)^{J-1}$$

$$\times \psi_n^{(1,J-1,J)}(s') A_j \Bigg(\xi(J+1) k_\perp'^4$$

$$\times \left(s - \Delta^2 + 4\frac{J+1}{2J+1} k_\perp^2 \right) \widetilde{V}_V^{(J+1)}(s,s')$$

$$- \xi(J) k_\perp'^2 \Bigg[\sigma^2 \widetilde{V}_S^{(J)}(s,s') + \frac{\sigma^2\Delta^2}{\sqrt{ss'}} \widetilde{V}_V^{(J)}(s,s')$$

$$- \sqrt{ss'}\widetilde{V}_A^{(J)}(s,s') - 2\Delta^2 \widetilde{V}_T^{(J)}(s,s') \Bigg] + \xi(J-1)$$

$$\times \left[s' - \Delta^2 + 4\frac{J}{2J+1} k_\perp'^2 \right] \widetilde{V}_V^{(J-1)}(s,s') \Bigg)$$

$$+ \int\limits_{(m_1+m_2)^2}^{\infty} \frac{ds'}{\pi} \rho(s') \cdot 2(-k_\perp'^2)^{J+1} \psi_n^{(1,J+1,J)}(k_\perp'^2)$$

$$\times B_j \Bigg(\xi(J+1) \Bigg[\frac{2J+1}{J+1}(s-\Delta^2)(s'-\Delta^2)$$

$$\times \left(\widetilde{V}_V^{(J+1)}(s,s') + 2\frac{\sigma^2}{\sqrt{ss'}} \widetilde{V}_T^{(J+1)}(s,s') \right)$$

$$+ 4(s'-\Delta^2) k_\perp^2 \widetilde{V}_V^{(J+1)}(s,s')$$

$$+ 4(s-\Delta^2) k_\perp'^2 \widetilde{V}_V^{(J+1)}(s,s')$$

$$+ 16\frac{J+1}{2J+1} k_\perp^2 k_\perp'^2 \widetilde{V}_V^{(J+1)}(s,s') \Bigg]$$

$$- 4\xi(J) \Bigg[\sigma^2 \widetilde{V}_S^{(J)}(s,s') + \frac{\sigma^2\Delta^2}{\sqrt{ss'}} \widetilde{V}_V^{(J)}(s,s')$$

$$+ \frac{J}{J+1} \left(\sqrt{ss'}\widetilde{V}_A^{(J)}(s,s') + 2\Delta^2 \widetilde{V}_T^{(J)}(s,s') \right) \Bigg]$$

$$+ 16\xi(J-1)\frac{J}{2J+1} \widetilde{V}_V^{(J-1)}(s,s') \Bigg).$$

The second equation, (37), reads

$$(s-M^2) \Bigg[\left(\frac{2J+1}{J}(s-\Delta^2) + 4k_\perp^2 \right) \qquad (45)$$

$$\times \psi_n^{(1,J-1,J)}(s) A_j + 4k_\perp^4 \psi_n^{(1,J+1,J)}(s) B_j \Bigg]$$

$$= \int\limits_{(m_1+m_2)^2}^{\infty} \frac{ds'}{\pi} \rho(s') \cdot 2(-k_\perp'^2)^{J-1} \psi_n^{(1,J-1,J)}(s') A_j$$

$$\times \Bigg(16\xi(J+1)\frac{J+1}{2J+1} k_\perp^4 k_\perp'^4 \widetilde{V}_V^{(J+1)}(s,s')$$

$$- 4\xi(J) k_\perp^2 k_\perp'^2 \Bigg[\sigma^2 \widetilde{V}_S^{(J)}(s,s')$$

$$+ \frac{\sigma^2\Delta^2}{\sqrt{ss'}} \widetilde{V}_V^{(J)}(s,s') + \frac{J+1}{J}$$

$$\times \left(\sqrt{ss'}\widetilde{V}_A^{(J)}(s,s') + 2\Delta^2 \widetilde{V}_T^{(J)}(s,s') \right) \Bigg]$$

$$+ \xi(J-1) \Bigg[\frac{2J+1}{J}(s-\Delta^2)(s'-\Delta^2)$$

$$\times \left(\widetilde{V}_V^{(J-1)}(s,s') + 2\frac{\sigma^2}{\sqrt{ss'}} \widetilde{V}_T^{(J-1)}(s,s') \right)$$

$$+ 4(s'-\Delta^2) k_\perp^2 \widetilde{V}_V^{(J-1)}(s,s')$$

$$+ 4(s-\Delta^2) k_\perp'^2 \widetilde{V}_V^{(J-1)}(s,s')$$

$$+ 16\frac{J}{2J+1} k_\perp^2 k_\perp'^2 \widetilde{V}_V^{(J-1)}(s,s') \Bigg] \Bigg)$$

$$+ \int\limits_{(m_1+m_2)^2}^{\infty} \frac{ds'}{\pi} \rho(s') \cdot 8(-k_\perp'^2)^{J+1} \psi_n^{(1,J+1,J)}(s') B_j$$

$$\times \Bigg(\xi(J+1) k_\perp^4 \left[s' - \Delta^2 + 4\frac{J+1}{2J+1} k_\perp'^2 \right]$$

$$\times \widetilde{V}_V^{(J+1)}(s,s') - \xi(J) k_\perp^2$$

$$\times \Bigg[\sigma^2 \widetilde{V}_S^{(J)}(s,s') + \frac{\sigma^2\Delta^2}{\sqrt{ss'}} \widetilde{V}_V^{(J)}(s,s')$$

$$- \sqrt{ss'}\widetilde{V}_A^{(J)}(s,s') - 2\Delta^2 \widetilde{V}_T^{(J)}(s,s') \Bigg]$$

$$+ \xi(J-1) \left[s - \Delta^2 + 4\frac{J}{2J+1} k_\perp^2 \right] \widetilde{V}_V^{(J-1)}(s,s') \Bigg).$$

The normalization and orthogonality conditions are

$$\int\limits_{(m_2+m_1)^2}^{\infty} \frac{ds}{\pi} \rho(s) \Bigg[A_j^2 \left(\psi_n^{(1,J-1,J)}(k_\perp^2) \right)^2 \qquad (46)$$

$$\times 2\alpha(J)(-k_\perp^2)^{(J-1)}$$

$$\times \left(\frac{2J+1}{J}(s-\Delta^2) + 4k_\perp^2 \right)$$

$$+ 2A_j B_j \psi_n^{(1,J-1,J)}(k_\perp^2) \psi_n^{(1,J+1,J)}(k_\perp^2) 8\alpha(J)$$

$$\times (-k_\perp^2)^{(J+1)} + B_j^2 \left(\psi_n^{(1,J+1,J)}(k_\perp^2) \right)^2$$

$$\times 2\alpha(J)(-k_\perp^2)^{(J+1)}$$

$$\times \left(\frac{2J+1}{J+1}(s-\Delta^2) + 4k_\perp^2 \right) \Bigg] = 1$$

for $j = 1, 2$, and

$$\int\limits_{(m_2+m_1)^2}^{\infty} \frac{ds}{\pi} \rho(s) \left[A_1 A_2 \left(\psi_n^{(1,J-1,J)}(k_\perp^2) \right)^2 \right. \quad (47)$$

$$\times 2\alpha(J)(-k_\perp^2)^{(J-1)} \left(\frac{2J+1}{J}(s - \Delta^2) + 4k_\perp^2 \right)$$

$$+ (A_1 B_2 + A_2 B_1) \psi_n^{(1,J-1,J)}(k_\perp^2)$$

$$\times \psi_n^{(1,J+1,J)}(k_\perp^2) \cdot 8\alpha(J)(-k_\perp^2)^{(J+1)}$$

$$+ B_1 B_2 \left(\psi_n^{(1,J+1,J)}(k_\perp^2) \right)^2 \cdot 2\alpha(J)(-k_\perp^2)^{(J+1)}$$

$$\left. \times \left(\frac{2J+1}{J+1}(s - \Delta^2) + 4k_\perp^2 \right) \right] = 0.$$

Let us emphasize again: all the above equations are written for $J > 0$.

4. CONCLUSION

We have presented the Bethe−Salpeter equations for the quark−antiquark systems when the quark and antiquark have different masses. The main difference from the equal-mass case is that there is the mixture of states $J = L$, $S = 0$ and $J = L$, $S = 1$ and that is proportional to the quark-mass difference. The mixing between $S = 1$, $J = L$ and $S = 0$, $J = L$ states gives rise to a strongly correlated system of equations. In the equation for states with total spin J, we need to know all lower projections of the potential on the Legendre polynomials, not only the $J + 1$, J, $J − 1$ ones. The numerical study of these equations is now in progress.

ACKNOWLEDGMENTS

Appendix A

TRACES FOR LOOP DIAGRAMS

Here, we present the traces used in the calculation of loop diagrams. Recall that, in the spectral-integral representation, there is no energy conservation, $s \neq s'$, where $P^2 = s$, $P'^2 = s'$, but all constituents are mass-on-shell:

$$k_1^2 = m_1^2, \quad k_2^2 = m_2^2, \quad k_1'^2 = m_1^2, \quad k_2'^2 = m_2^2.$$

We have used the notation for the quark momenta

$$k_\nu = \frac{1}{2}(k_1 - k_2)_\nu, \quad k_\nu' = \frac{1}{2}(k_1' - k_2')_\nu, \quad (A.1)$$

$$k_\mu^\perp = k_\nu g_{\nu\mu}^\perp, \quad k_\mu'^\perp = k_\nu' g_{\nu\mu}^\perp,$$

$$k_\mu = \frac{m_1^2 - m_2^2}{2s} P_\mu + k_\mu^\perp, \quad k_\mu' = \frac{m_1^2 - m_2^2}{2s'} P_\mu' + k_\mu'^\perp,$$

and for the quark masses

$$\Delta = m_2 - m_1, \quad \sigma = m_2 + m_1. \quad (A.2)$$

We work with the following definition of the matrices:

$$\gamma_5 = -i\gamma^0\gamma^1\gamma^2\gamma^3, \quad \sigma_{\mu\nu} = \frac{1}{2}[\gamma_\mu\gamma_\nu].$$

TRACES FOR THE $S = 0$ STATES

For the $S = 0$ states, we have the following nonzero traces:

$$T_P' = \text{tr}\left[i\gamma_5(\hat{k}_1' + m_1)\gamma_5(-\hat{k}_2' + m_2)\right] \quad (A.3)$$

$$= 2i(s' - (m_2 - m_1)^2),$$

$$T_A' = \text{tr}\left[i\gamma_5(\hat{k}_1' + m_1)i\gamma_\mu\gamma_5(-\hat{k}_2' + m_2)\right]$$

$$= -2\left[2k_\mu'(m_2 - m_1) + P_\mu'(m_2 + m_1)\right],$$

$$T_T' = \text{tr}\left[i\gamma_5(\hat{k}_1' + m_1)i\sigma_{\mu\nu}(-\hat{k}_2' + m_2)\right]$$

$$= -4i\varepsilon_{\mu\nu\alpha\beta}P_\alpha'k_\beta'$$

and

$$T_P = \text{tr}\left[i\gamma_5(-\hat{k}_2 + m_2)\gamma_5(\hat{k}_1 + m_1)\right] \quad (A.4)$$

$$= 2i(s - (m_2 - m_1)^2),$$

$$T_A = \text{tr}\left[i\gamma_5(-\hat{k}_2 + m_2)i\gamma_\mu\gamma_5(\hat{k}_1 + m_1)\right]$$

$$= 2\left[2k_\mu(m_2 - m_1) + P_\mu(m_2 + m_1)\right],$$

$$T_T = \text{tr}\left[i\gamma_5(-\hat{k}_2 + m_2)i\sigma_{\mu\nu}(\hat{k}_1 + m_1)\right]$$

$$= 4i\varepsilon_{\mu\nu\alpha\beta}P_\alpha k_\beta.$$

The convolutions of the traces $A_P = (T_P T_P')$, $A_A = (T_A T_A')$, $A_T = (T_T T_T')$ are equal to

$$A_P = -4(s - \Delta^2)(s' - \Delta^2), \quad (A.5)$$

$$A_A = -16\Delta^2 \sqrt{k_\perp^2 \, k_\perp'^2} z - 4 \frac{\sigma^2}{\sqrt{ss'}}(s-\Delta^2)(s'-\Delta^2),$$

$$A_T = -32\sqrt{ss'}\sqrt{k_\perp^2 \, k_\perp'^2} z.$$

TRACES FOR THE $S=1$ STATES

For the $S=1$ states, the traces are equal to

$$T_S' = \mathrm{tr}\left[\gamma_{\alpha'}^{\perp}(\hat{k}_1' + m_1)(-\hat{k}_2' + m_2)\right] \quad\quad (A.6)$$

$$= 4k_{\alpha'}'^{\perp}(m_2 + m_1),$$

$$T_V' = \mathrm{tr}\left[\gamma_{\alpha'}^{\perp}(\hat{k}_1' + m_1)\gamma_\mu(-\hat{k}_2' + m_2)\right]$$

$$= 2\left(g_{\alpha'\mu}^{\perp}(s' - (m_2 - m_1)^2) + 4k_{\alpha'}'^{\perp}k_\mu'\right),$$

$$T_A' = \mathrm{tr}\left[\gamma_{\alpha'}^{\perp}(\hat{k}_1' + m_1)i\gamma_\mu^{\perp}\gamma_5(-\hat{k}_2' + m_2)\right]$$

$$= 4\varepsilon_{\alpha'\mu\alpha\beta}k_\alpha' P_\beta',$$

$$T_T' = \mathrm{tr}\left[\gamma_{\alpha'}^{\perp}(\hat{k}_1' + m_1)i\sigma_{\mu\nu}(-\hat{k}_2' + m_2)\right]$$

$$= 2i\left[2(m_2 - m_1)\left(g_{\alpha'\nu}^{\perp}k_\mu' - g_{\alpha'\mu}^{\perp}k_\nu'\right)\right.$$

$$\left.+ (m_1 + m_2)\left(g_{\alpha'\nu}^{\perp}P_\mu' - g_{\alpha'\mu}^{\perp}P_\nu'\right)\right]$$

and

$$T_S = \mathrm{tr}\left[\gamma_{\beta'}^{\perp}(-\hat{k}_2 + m_2)(\hat{k}_1 + m_1)\right] \quad\quad (A.7)$$

$$= 4k_{\beta'}^{\perp}(m_1 + m_2),$$

$$T_V = \mathrm{tr}\left[\gamma_{\beta'}^{\perp}(-\hat{k}_2 + m_2)\gamma_\mu(\hat{k}_1 + m_1)\right]$$

$$= 2\left[g_{\mu\beta'}^{\perp}(s - (m_2 - m_1)^2) + 4k_{\beta'}^{\perp}k_\mu\right],$$

$$T_A = \mathrm{tr}\left[\gamma_{\beta'}^{\perp}(-\hat{k}_2 + m_2)i\gamma_\mu\gamma_5(\hat{k}_1 + m_1)\right]$$

$$= -4\varepsilon_{\beta'\mu\alpha\beta}k_\alpha P_\beta,$$

$$T_T = \mathrm{tr}\left[\gamma_{\beta'}^{\perp}(-\hat{k}_2 + m_2)i\sigma_{\mu\nu}(\hat{k}_1 + m_1)\right]$$

$$= 2i\left[2(m_2 - m_1)(g_{\beta'\mu}^{\perp}k_\nu - g_{\beta'\nu}^{\perp}k_\mu)\right.$$

$$\left.+ (m_2 + m_1)\left(g_{\beta'\mu}^{\perp}P_\nu - g_{\beta'\nu}^{\perp}P_\mu\right)\right].$$

The corresponding convolution $B_S = (T_c T_c')$ reads

$$(B_S)_{\beta'\alpha'} = 16 k_{\beta'}^{\perp} k_{\alpha'}'^{\perp}\sigma^2, \quad\quad (A.8)$$

$$(B_V)_{\beta'\alpha'} = 4\left[\left(g_{\beta'\alpha'}^{\perp}(s-\Delta^2)(s'-\Delta^2)\right.\right.$$

$$+ 16k_{\beta'}^{\perp}k_{\alpha'}'^{\perp}\sqrt{k_\perp^2 \, k_\perp'^2} z + 4k_{\beta'}^{\perp}k_{\alpha'}'^{\perp}(s'-\Delta^2)$$

$$\left.\left.+ 4k_{\beta'}'^{\perp}k_{\alpha'}'^{\perp}(s-\Delta^2) + 4k_{\beta'}^{\perp}k_{\alpha'}'^{\perp}\frac{\sigma^2\Delta^2}{\sqrt{ss'}}\right)\right],$$

$$(B_A)_{\beta'\alpha'} = -16\sqrt{ss'}\left[k_{\beta'}'^{\perp}k_{\alpha'}^{\perp} - g_{\beta'\alpha'}^{\perp}\sqrt{k_\perp^2 \, k_\perp'^2} z\right],$$

$$(B_T)_{\beta'\alpha'} = -8\left[4\Delta^2\left(k_{\beta'}'^{\perp}k_{\alpha'}^{\perp} - g_{\beta'\alpha'}^{\perp}\sqrt{k_\perp^2 \, k_\perp'^2} z\right)\right.$$

$$\left.- g_{\beta'\alpha'}^{\perp}\frac{\sigma^2}{\sqrt{ss'}}(s-\Delta^2)(s'-\Delta^2)\right].$$

Appendix B

CONVOLUTIONS OF TRACE FACTORS

Here, we present the convolutions of the angular-momentum factors. Let z be

$$z = \frac{(k_\perp k_\perp')}{\sqrt{k_\perp^2}\sqrt{k_\perp'^2}}. \quad\quad (A.9)$$

The convolutions for the $S=1$ states read

$$X_{\mu_1\mu_2\ldots\mu_J}^{(J)}(k_\perp)X_{\mu_1\mu_2\ldots\mu_J}^{(J)}(k_\perp') \quad\quad (A.10)$$

$$= \alpha(J)\left(\sqrt{k_\perp^2}\sqrt{k_\perp'^2}\right)^J P_J(z).$$

Analogous convolutions for $S=1$ states are written as follows:

$$X_{\mu_1\mu_2\ldots\mu_J\beta}^{(J+1)}(k_\perp)X_{\mu_1\mu_2\ldots\mu_J\alpha}^{(J+1)}(k_\perp') \quad\quad (A.11)$$

$$= \frac{\alpha(J)}{J+1}\left(\sqrt{k_\perp^2}\sqrt{k_\perp'^2}\right)^J\left[\frac{\sqrt{k_\perp'^2}}{\sqrt{k_\perp^2}}A_{P_{J,J+1}}(z)k_\beta^{\perp}k_\alpha^{\perp}\right.$$

$$+ \frac{\sqrt{k_\perp^2}}{\sqrt{k_\perp'^2}}B_{P_{J,J+1}}(z)k_\beta'^{\perp}k_\alpha'^{\perp}$$

$$+ C_{P_{J,J+1}}(z)k_\beta^{\perp}k_\alpha'^{\perp} + D_{P_{J,J+1}}(z)k_\beta'^{\perp}k_\alpha^{\perp}$$

$$\left.+ \left(\sqrt{k_\perp^2}\sqrt{k_\perp'^2}\right)E_{P_{J,J+1}}(z)g_{\beta\alpha}^{\perp}\right],$$

$$X_{\mu_1\mu_2\ldots\mu_J\beta}^{(J+1)}(k_\perp)Z_{\mu_1\mu_2\ldots\mu_J,\alpha}^{(J-1)}(k_\perp') \quad\quad (A.12)$$

$$= -\frac{\alpha(J)}{J}\frac{1}{k_\perp'^2}\left(\sqrt{k_\perp^2}\sqrt{k_\perp'^2}\right)^J$$

$$\times\left[\frac{\sqrt{k_\perp'^2}}{\sqrt{k_\perp^2}}A_{P_{J,J+1}}(z)k_\beta^\perp k_\alpha^\perp + \frac{\sqrt{k_\perp^2}}{\sqrt{k_\perp'^2}}\right.$$

$$\times\left(B_{P_{J,J+1}}(z) - (2J+1)A_J(z)\right)k_\beta'^\perp k_\alpha'^\perp$$

$$+ \left(C_{P_{J,J+1}}(z) - (2J+1)B_J(z)\right)k_\beta^\perp k_\alpha'^\perp$$

$$+ D_{P_{J,J+1}}(z)k_\beta'^\perp k_\alpha^\perp$$

$$\left. + \left(\sqrt{k_\perp^2}\sqrt{k_\perp'^2}\right)E_{P_{J,J+1}}(z)g_{\beta\alpha}^\perp\right],$$

$$Z_{\mu_1\mu_2...\mu_J,\beta}^{(J-1)}(k_\perp)Z_{\mu_1\mu_2...\mu_J,\alpha}^{(J-1)}(k_\perp') \qquad (A.13)$$

$$= \frac{J+1}{J^2}\alpha(J)\left(\sqrt{k_\perp^2}\sqrt{k_\perp'^2}\right)^{J-2}$$

$$\times\left[\frac{\sqrt{k_\perp'^2}}{\sqrt{k_\perp^2}}\left(A_{P_{J,J+1}}(z) - (2J+1)A_J(z)\right)k_\beta^\perp k_\alpha^\perp\right.$$

$$+ \frac{\sqrt{k_\perp^2}}{\sqrt{k_\perp'^2}}\left(B_{P_{J,J+1}}(z) - (2J+1)A_J(z)\right)k_\beta'^\perp k_\alpha'^\perp$$

$$+ \left(C_{P_{J,J+1}}(z) + \frac{(2J+1)^2}{J+1}P_J(z)\right.$$

$$\left. - 2(2J+1)B_J(z)\right)k_\beta^\perp k_\alpha'^\perp + D_{P_{J,J+1}}(z)k_\beta'^\perp k_\alpha^\perp$$

$$\left. + \left(\sqrt{k_\perp^2}\sqrt{k_\perp'^2}\right)E_{P_{J,J+1}}(z)g_{\beta\alpha}^\perp\right],$$

$$C_{P_{J,J+1}}(z) = \frac{\left[(1-J)z^2 + (J+1)\right]P_J(z) + \left[(2J+1)z^2 - (2J+3)\right]zP_{J+1}(z)}{(1-z^2)^2},$$

$$D_{P_{J,J+1}}(z) = \frac{\left[(J+2)z^2 - J\right]P_J(z) - 2zP_{J+1}(z)}{(1-z^2)^2},$$

$$E_{P_{J,J+1}}(z) = \frac{zP_J(z) - P_{J+1}(z)}{(1-z^2)}.$$

For the factors $K_\beta X_{\mu_1\mu_2...\mu_J\beta}^{(J+1)}(k_\perp) \times X_{\mu_1\mu_2...\mu_J\alpha}^{(J+1)}(k_\perp')K_\alpha$, where $K = k, k'$, we need more complicated convolutions, namely:

$$k_\beta X_{\mu_1\mu_2...\mu_J\beta}^{(J+1)}(k_\perp)X_{\mu_1\mu_2...\mu_J\alpha}^{(J+1)}(k_\perp')k_\alpha$$

$$= k_\perp^2\alpha(J)\left(\sqrt{k_\perp^2}\sqrt{k_\perp'^2}\right)^{J+1}P_{J+1}(z),$$

$$\varepsilon_{\beta\nu_1\nu_2\nu_3}P_{\nu_1}Z_{\nu_2\mu_1...\mu_J,\nu_3}^{(J)}(k_\perp) \qquad (A.14)$$

$$\times \varepsilon_{\alpha\lambda_1\lambda_2\lambda_3}P_{\lambda_1}'Z_{\lambda_2\mu_1...\mu_J,\lambda_3}^{(J)}(k_\perp')$$

$$= \frac{(2J+3)^2}{(J+1)^3}\alpha(J)\left(\sqrt{k_\perp^2}\sqrt{k_\perp'^2}\right)^{J-1}(PP')$$

$$\times\left[-\sqrt{k_\perp^2}\sqrt{k_\perp'^2}\left((z^2-1)D_{P_{J,J+1}}(z)\right.\right.$$

$$\left. + zE_{P_{J,J+1}}(z)\right)g_{\beta\alpha}^\perp - D_{P_{J,J+1}}(z)$$

$$\times\left(\frac{\sqrt{k_\perp'^2}}{\sqrt{k_\perp^2}}k_\beta^\perp k_\alpha^\perp + \frac{\sqrt{k_\perp^2}}{\sqrt{k_\perp'^2}}k_\beta'^\perp k_\alpha'^\perp - zk_\beta^\perp k_\alpha'^\perp\right)$$

$$\left. + \left(zD_{P_{J,J+1}}(z) + E_{P_{J,J+1}}(z)\right)k_\beta'^\perp k_\alpha^\perp\right],$$

and

$$X_{\mu_1...\mu_J}^{(J)}(k_\perp)\varepsilon_{\alpha\nu_1\nu_2\nu_3}P_{\nu_1}'Z_{\nu_2\mu_1...\mu_J,\nu_3}^{(J)}(k_\perp') \quad (A.15)$$

$$= \frac{2J+3}{J+1}\alpha(J)\left(\sqrt{k_\perp^2}\sqrt{k_\perp'^2}\right)^{J-1}A_{P_{J,J+1}}(z)\varepsilon_{\alpha P'kk'}.$$

Here,

$$A_{P_{J,J+1}}(z) = B_{P_{J,J+1}}(z) \qquad (A.16)$$

$$= -\frac{2zP_J(z) + \left[Jz^2 - (J+2)\right]P_{J+1}(z)}{(1-z^2)^2},$$

$$k_\beta X_{\mu_1\mu_2...\mu_J\beta}^{(J+1)}(k_\perp)X_{\mu_1\mu_2...\mu_J\alpha}^{(J+1)}(k_\perp')k_\alpha'$$

$$= \alpha(J)\left(\sqrt{k_\perp^2}\sqrt{k_\perp'^2}\right)^{J+2}P_J(z),$$

$$k_\beta' X_{\mu_1\mu_2...\mu_J\beta}^{(J+1)}(k_\perp)X_{\mu_1\mu_2...\mu_J\alpha}^{(J+1)}(k_\perp')k_\alpha'$$

$$= k_\perp'^2\alpha(J)\left(\sqrt{k_\perp^2}\sqrt{k_\perp'^2}\right)^{J+1}P_{J+1}(z),$$

$$k_\beta' X_{\mu_1\mu_2...\mu_J\beta}^{(J+1)}(k_\perp)X_{\mu_1\mu_2...\mu_J\alpha}^{(J+1)}(k_\perp')k_\alpha$$

$$= \alpha(J)\left(\sqrt{k_\perp^2}\sqrt{k_\perp'^2}\right)^{J+2}$$

$$\times \left[\frac{2J+1}{J+1} z P_{J+1}(z) - \frac{J}{J+1} P_J(z) \right],$$

$$g_{\beta\alpha}^{\perp} X^{(J+1)}_{\mu_1\mu_2...\mu_J\beta}(k_\perp) X^{(J+1)}_{\mu_1\mu_2...\mu_J\alpha}(k'_\perp)$$

$$= \frac{2J+1}{J+1} \alpha(J) \left(\sqrt{k_\perp^2} \sqrt{k_\perp'^2} \right)^{J+1} P_{J+1}(z);$$

as well as for the factors $K_\beta X^{(J+1)}_{\mu_1\mu_2...\mu_J\beta}(k_\perp) \times Z^{(J-1)}_{\mu_1\mu_2...\mu_J,\alpha}(k'_\perp) K_\alpha$:

$$k_\beta X^{(J+1)}_{\mu_1\mu_2...\mu_J\beta}(k_\perp) Z^{(J-1)}_{\mu_1\mu_2...\mu_J,\alpha}(k'_\perp) k_\alpha$$

$$= k_\perp^4 \alpha(J) \left(\sqrt{k_\perp^2} \sqrt{k_\perp'^2} \right)^{J-1} P_{J-1}(z),$$

$$k_\beta X^{(J+1)}_{\mu_1\mu_2...\mu_J\beta}(k_\perp) Z^{(J-1)}_{\mu_1\mu_2...\mu_J,\alpha}(k'_\perp) k'_\alpha$$

$$= k_\perp^2 \alpha(J) \left(\sqrt{k_\perp^2} \sqrt{k_\perp'^2} \right)^{J} P_J(z),$$

$$k'_\beta X^{(J+1)}_{\mu_1\mu_2...\mu_J\beta}(k_\perp) Z^{(J-1)}_{\mu_1\mu_2...\mu_J,\alpha}(k'_\perp) k'_\alpha$$

$$= \alpha(J) \left(\sqrt{k_\perp^2} \sqrt{k_\perp'^2} \right)^{J+1} P_{J+1}(z),$$

$$k'_\beta X^{(J+1)}_{\mu_1\mu_2...\mu_J\beta}(k_\perp) Z^{(J-1)}_{\mu_1\mu_2...\mu_J,\alpha}(k'_\perp) k_\alpha$$

$$= k_\perp^2 \alpha(J) \left(\sqrt{k_\perp^2} \sqrt{k_\perp'^2} \right)^{J} P_J(z),$$

$$g_{\beta\alpha}^{\perp} X^{(J+1)}_{\mu_1\mu_2...\mu_J\beta}(k_\perp) Z^{(J-1)}_{\mu_1\mu_2...\mu_J,\alpha}(k'_\perp) = 0;$$

and for the factors $K_\beta Z^{(J-1)}_{\mu_1\mu_2...\mu_J,\beta}(k_\perp) \times Z^{(J-1)}_{\mu_1\mu_2...\mu_J,\alpha}(k'_\perp) K_\alpha$:

$$k_\beta Z^{(J-1)}_{\mu_1\mu_2...\mu_J,\beta}(k_\perp) Z^{(J-1)}_{\mu_1\mu_2...\mu_J,\alpha}(k'_\perp) k_\alpha$$

$$= k_\perp^2 \alpha(J) \left(\sqrt{k_\perp^2} \sqrt{k_\perp'^2} \right)^{J-1} P_{J-1}(z),$$

$$k_\beta Z^{(J-1)}_{\mu_1\mu_2...\mu_J,\beta}(k_\perp) Z^{(J-1)}_{\mu_1\mu_2...\mu_J,\alpha}(k'_\perp) k'_\alpha$$

$$= \alpha(J) \left(\sqrt{k_\perp^2} \sqrt{k_\perp'^2} \right)^{J} P_J(z),$$

$$k'_\beta Z^{(J-1)}_{\mu_1\mu_2...\mu_J,\beta}(k_\perp) Z^{(J-1)}_{\mu_1\mu_2...\mu_J,\alpha}(k'_\perp) k'_\alpha$$

$$= k_\perp'^2 \alpha(J) \left(\sqrt{k_\perp^2} \sqrt{k_\perp'^2} \right)^{J-1} P_{J-1}(z),$$

$$k'_\beta Z^{(J-1)}_{\mu_1\mu_2...\mu_J,\beta}(k_\perp) Z^{(J-1)}_{\mu_1\mu_2...\mu_J,\alpha}(k'_\perp) k_\alpha$$

$$= \alpha(J) \left(\sqrt{k_\perp^2} \sqrt{k_\perp'^2} \right)^{J}$$

$$\times \left[\frac{2J+1}{J} z P_{J-1}(z) - \frac{J+1}{J} P_J(z) \right],$$

$$g_{\beta\alpha}^{\perp} Z^{(J-1)}_{\mu_1\mu_2...\mu_J,\beta}(k_\perp) Z^{(J-1)}_{\mu_1\mu_2...\mu_J,\alpha}(k'_\perp)$$

$$= \frac{2J+1}{J} \alpha(J) \left(\sqrt{k_\perp^2} \sqrt{k_\perp'^2} \right)^{J-1} P_{J-1}(z);$$

and for the factors $K_\beta \varepsilon_{\beta\nu_1\nu_2\nu_3} P_{\nu_1} Z^{(J)}_{\nu_2\mu_1...\mu_J,\nu_3}(k_\perp) \times \varepsilon_{\alpha\lambda_1\lambda_2\lambda_3} P'_{\lambda_1} Z^{(J)}_{\lambda_2\mu_1...\mu_J,\lambda_3}(k'_\perp) K_\alpha$:

$$k_\beta \varepsilon_{\beta\nu_1\nu_2\nu_3} P_{\nu_1} Z^{(J)}_{\nu_2\mu_1...\mu_J,\nu_3}(k_\perp)$$

$$\times \varepsilon_{\alpha\lambda_1\lambda_2\lambda_3} P'_{\lambda_1} Z^{(J)}_{\lambda_2\mu_1...\mu_J,\lambda_3}(k'_\perp) k_\alpha = 0,$$

$$k_\beta \varepsilon_{\beta\nu_1\nu_2\nu_3} P_{\nu_1} Z^{(J)}_{\nu_2\mu_1...\mu_J,\nu_3}(k_\perp)$$

$$\times \varepsilon_{\alpha\lambda_1\lambda_2\lambda_3} P'_{\lambda_1} Z^{(J)}_{\lambda_2\mu_1...\mu_J,\lambda_3}(k'_\perp) k'_\alpha = 0,$$

$$k'_\beta \varepsilon_{\beta\nu_1\nu_2\nu_3} P_{\nu_1} Z^{(J)}_{\nu_2\mu_1...\mu_J,\nu_3}(k_\perp)$$

$$\times \varepsilon_{\alpha\lambda_1\lambda_2\lambda_3} P'_{\lambda_1} Z^{(J)}_{\lambda_2\mu_1...\mu_J,\lambda_3}(k'_\perp) k'_\alpha = 0,$$

$$k'_\beta \varepsilon_{\beta\nu_1\nu_2\nu_3} P_{\nu_1} Z^{(J)}_{\nu_2\mu_1...\mu_J,\nu_3}(k_\perp)$$

$$\times \varepsilon_{\alpha\lambda_1\lambda_2\lambda_3} P'_{\lambda_1} Z^{(J)}_{\lambda_2\mu_1...\mu_J,\lambda_3}(k'_\perp) k_\alpha$$

$$= \frac{(2J+3)^2}{(J+1)^3} \alpha(J) \left(\sqrt{k_\perp^2} \sqrt{k_\perp'^2} \right)^{J+1}$$

$$\times (PP') \left[z P_J(z) - P_{J+1}(z) \right],$$

$$g_{\beta\alpha}^{\perp} \varepsilon_{\beta\nu_1\nu_2\nu_3} P_{\nu_1} Z^{(J)}_{\nu_2\mu_1...\mu_J,\nu_3}(k_\perp)$$

$$\times \varepsilon_{\alpha\lambda_1\lambda_2\lambda_3} P'_{\lambda_1} Z^{(J)}_{\lambda_2\mu_1...\mu_J,\lambda_3}(k'_\perp)$$

$$= -\frac{J(2J+3)^2}{(J+1)^3} \alpha(J) \left(\sqrt{k_\perp^2} \sqrt{k_\perp'^2} \right)^{J} (PP') P_J(z).$$

Considering the Bethe−Salpeter equation with unequal masses, one may face the problem of the definition of the momentum transfer squared t in the interaction block (this means the relation between z, t) when retardation effects are accounted for. We think that the most convenient form, symmetrical under the permutation of the indices $1 \Longleftrightarrow 2$, was suggested in [10]:

$$t = (k'_1 - k_1)_\mu (k_2 - k'_2)_\mu. \qquad (A.17)$$

The other variants of accounting for retardation effects may be found in [11, 12]; see also discussion in [10].

REFERENCES

1. E. Salpeter and H. A. Bethe, Phys. Rev. **84**, 1232 (1951); E. Salpeter, Phys. Rev. **91**, 994 (1953).
2. D. Merten, R. Ricken, M. Koll, *et al.*, Eur. Phys. J. A **13**, 477 (2002).
3. R. Ricken, M. Koll, D. Merten, *et al.*, Eur. Phys. J. A **9**, 221 (2000); **9**, 79 (2000).
4. M. Harada, M. Kurachi, and K. Yamawaki, Phys. Rev. D **68**, 076001 (2003).
5. A. D. Lahiff and I. R. Afnan, Phys. Rev. C **66**, 044001 (2002).

6. R. Alkofer, P. Watson, and H. Weigel, Phys. Rev. D **65**, 094026 (2002).

7. A. V. Anisovich, V. V. Anisovich, V. N. Markov, *et al.*, Yad. Fiz. **67**, 794 (2004) [Phys. At. Nucl. **67**, 773 (2004)]; hep-ph/0208150.

8. V. N. Markov, in *Proceedings of the XXXIII PNPI Winter School "The Bethe−Salpeter Equation for the Meson Quark−Antiquark States," 2003*.

9. A. V. Anisovich, V. V. Anisovich, V. N. Markov, *et al.*, J. Phys. G **28**, 15 (2002).

10. H. Hershbach, Phys. Rev. C **50**, 2562 (1994); Phys. Rev. A **46**, 3657 (1992).

11. F. Gross and J. Milana, Phys. Rev. D **43**, 2401 (1991).

12. K. M. Maung, D. E. Kahana, and J. W. Norbury, Can. J. Phys. **70**, 86 (1992).

ELEMENTARY PARTICLES AND FIELDS
Theory

Electroproduction of $D^{*\pm}$ Mesons at High Energies

V. A. Saleev[*] and D. V. Vasin[**]

Samara State University, ul. Akademika Pavlova 1, Samara, 443011 Russia
Received February 4, 2004; in final form, August 18, 2004

Abstract—A comparative analysis of the predictions of the collinear parton model and the k_T-factorization approach is performed for the case of the D^*-meson electroproduction at the HERA ep collider. It is shown that, owing to effectively taking into account, in noncollinear distributions, next-order corrections in the strong coupling constant α_s, the k_T-factorization approach increases, in contrast to the predictions of the collinear parton model, the absolute value of the cross sections for charmed-meson electroproduction by approximately a factor of 1.5 to 2. As a result, the agreement with experimental data is improved. This is not so only for the pseudorapidity spectrum, whose shape differs considerably from the experimental one and depends greatly on the choice of parametrization of the noncollinear gluon distribution within the proton.
© 2005 Pleiades Publishing, Inc.

1. INTRODUCTION

The cross sections for photo- and electroproduction of D^* mesons have been calculated many times within the k_T-factorization approach (see, for example, the discussion on the results of the Small-x Collaboration in [1]). However, there are still a large number of disputable aspects in the k_T-factorization approach, the ambiguities in their interpretation substantially affecting the results. Previous calculations of D^*-meson spectra ensured fairly good agreement with experimental data [1] via optimizing the choice of parameters of the approach (which include the quark masses and the renormalization scale) and the choice of parametrization for the noncollinear gluon distribution in the proton. The objective of the present study is to perform a unified calculation of the spectra for D^*-meson photo- and electroproduction in order to assess the uncertainty that is inherent in the approach because it is necessary to choose the parametrization for the noncollinear gluon distribution in the proton. Moreover, analytic expressions that describe the squares of the absolute values of amplitudes for partonic subprocesses within the k_T-factorization approach and which are convenient for numerical calculations are given for the first time in this article, this being of paramount importance for a comparison with the results obtained by other authors. Our results are compared below with available data on various spectra (with respect to p_T, η, W, x_{Bj}, and Q), whereas the comparison in the literature is usually performed only for the p_T and η spectra.

[*]e-mail: `Saleev@ssu.samara.ru`
[**]e-mail: `Vasin@ssu.samara.ru`

At some values of kinematical parameters, our present results for the D^*-meson-production spectra differ by a factor of 1.5 to 2 from the results of our previous study [2], where an embarrassing error was made at the stage of numerical calculations. An improved version of the study reported in [2] was presented in the form of a preprint [3].

2. FORMALISM OF THE k_T-FACTORIZATION APPROACH

At the present time, there exist two approaches to describing high-energy processes that lead to the production of hadrons containing heavy quarks. These are the collinear parton model and the k_T-factorization approach, which is also known as the theory of semihard processes. Either approach is based on the hypothesis that the effects of long- and short-distance physics factorize in hard processes.

In the collinear parton model, it is assumed that the cross section for the hadronic process being considered—$\sigma(ep \to D^*X, s)$ in the present case—and the cross section for the corresponding partonic subprocess, $\hat{\sigma}(eg \to D^*X, \hat{s})$, are related by the equation

$$\sigma^{\mathrm{PM}}(ep \to D^*X, s) \qquad (1)$$
$$= \int dx G(x, \mu^2)\hat{\sigma}(eg \to D^*X, \hat{s}),$$

where $\hat{s} = xs$, s is the square of the total energy of the participant electron and proton in their c.m. frame, $G(x, \mu^2)$ is the collinear gluon distribution in the proton, $k = xp_N$ is the gluon 4-momentum, x is the proton-momentum fraction carried by the gluon,

and μ^2 is the characteristic scale of the hard scattering process. Within perturbative QCD, the evolution of the gluon distribution $G(x, \mu^2)$ is described by the Dokshitzer−Gribov−Lipatov−Altarelli−Parisi evolution equation [4].

Within the k_T-factorization approach, the partonic and hadronic cross sections are related by the equation

$$\sigma^{\mathrm{KT}}(ep \to D^*X, s) = \int \frac{dx}{x} \int d\mathbf{k}_T^2 \qquad (2)$$

$$\times \int \frac{d\varphi}{2\pi} \Phi(x, \mathbf{k}_T^2, \mu^2)\hat{\sigma}(eg^* \to D^*X, \hat{s}),$$

where $\hat{\sigma}(eg^* \to D^*X, \hat{s})$ is the cross section for D^*-meson production in electron scattering on a Reggeized gluon, $k = xp_N + k_T$ is the gluon 4-momentum, $k_T = (0, \mathbf{k}_T, 0)$ is the transverse gluon 4-momentum, $k^2 = k_T^2 = -\mathbf{k}_T^2$ is the virtuality of the primary gluon, $p_N = E_N(1, 0, 0, 1)$ is the 4-momentum of the primary proton, $\hat{s} = xs - \mathbf{k}_T^2$, φ is the azimuthal angle in the xy plane between the vector $\mathbf{k}_T$ and the fixed x axis ($\mathbf{p}_{D^*} \in xz$, the z axis being aligned with the ep-reaction axis), and $\Phi(x, \mathbf{k}_T^2, \mu^2)$ is the noncollinear distribution of Reggeized gluons in the proton. The QCD evolution of the noncollinear gluon distribution $\Phi(x, \mathbf{k}_T^2, \mu^2)$ is described by the Balitsky−Fadin−Kuraev−Lipatov [5] or the Ciafaloni−Catani−Fiorani−Marchesini [6] evolution equation. It is usually assumed that the function describing the noncollinear distribution of gluons in the proton and satisfying the Balitsky−Fadin−Kuraev−Lipatov evolution equation [5] can be related to the collinear gluon distribution $G(x, \mu^2)$ in the proton as follows:

$$xG(x, \mu^2) = \int\limits_0^{\mu^2} \Phi(x, \mathbf{k}_T^2, \mu^2) d\mathbf{k}_T^2. \qquad (3)$$

The need for reconstructing the gauge invariance of amplitudes for hard scattering processes involving Reggeized gluons leads to effective Feynman rules [7], where the polarization vector of primary off-shell gluons is represented in the form

$$\varepsilon^\mu(k_T) = \frac{k_T^\mu}{|\mathbf{k}_T|}. \qquad (4)$$

At the stage of numerical calculations, use is made of the GRV LO parametrization [8] of the collinear gluon distribution $G(x, \mu^2)$ in the proton. In the case of calculations within the k_T-factorization approach, we employed the following parametrizations for the unintegrated (noncollinear) gluon distribution $\Phi(x, \mathbf{k}_T^2, \mu^2)$ in the proton: the JB parametrization

from the study of Blumlein [9], the JS parametrization from the study of Jung and Salam [10], and the KMR parametrization from the study of Kimber, Martin, and Ryskin [11].

For the sake of comparison, Figs. 1 and 2 display unintegrated gluon distributions in the proton versus x at fixed $\mathbf{k}_T^2$ (Fig. 1) and versus $\mathbf{k}_T^2$ at fixed x (Fig. 2). One can see that, in the x region around $x \sim m_c/\sqrt{s}$ and the transverse-momentum region around $\mathbf{k}_T^2 \approx 50$ GeV^2 (and these are the regions in which we are interested), the parametrizations in question differ substantially.

3. FRAGMENTATION FUNCTION

The production of D^* mesons, which consist of a heavy c quark and a light $\bar{u}$ ($\bar{d}$) antiquark, is described phenomenologically on the basis of the fragmentation model [2, 12−14] by introducing a universal fragmentation function $D_{c \to D^*}(z, \mu^2)$ for c-quark fragmentation into a D^* meson or on the basis of the fusion model [15, 16].

At high energies, the cross sections for c-quark and D^*-meson production in the fragmentation model are related by the equation

$$d\sigma(ep \to D^*X) \qquad (5)$$

$$= \int D_{c \to D^*}(z, \mu^2) dz \cdot d\sigma(ep \to cX),$$

where $D_{c \to D^*}(z, \mu^2)$ is the above fragmentation function, μ^2 is the characteristic scale of the hard scattering process, and z is the fragmentation parameter.

The probability of c-quark fragmentation into a $D^{*\pm}$ meson is given by

$$\omega_{c \to D^{*\pm}} = \int\limits_0^1 D_{c \to D^{*\pm}}(z, \mu^2) dz. \qquad (6)$$

According to data of the OPAL Collaboration [17], we have

$$\omega_{c \to D^{*\pm}} = 0.222 \pm 0.014. \qquad (7)$$

In the present study, we use the Peterson phenomenological scaling fragmentation function [18]

$$D_{c \to D^*}(z) = N \frac{z(1-z)^2}{[(1-z)^2 + \epsilon z]^2}. \qquad (8)$$

In the limit of massless quarks and hadrons, the fragmentation parameter z relates the c-quark and D^*-meson 4-momenta as follows:

$$p_{D^*} = zp_c. \qquad (9)$$

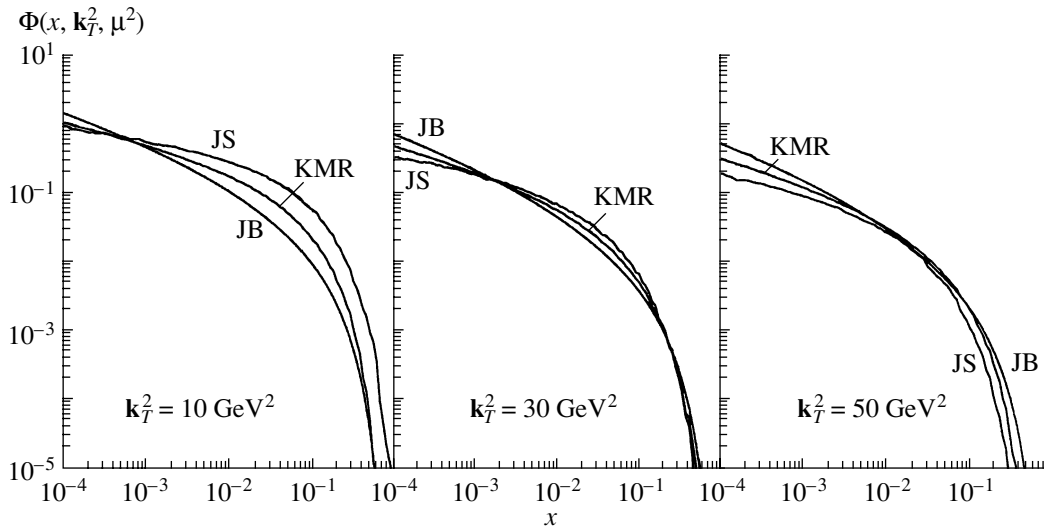Experimental data on $D^{*\pm}$-meson production at the HERA ep collider correspond to the region $p \geq m_c$,

$\Phi(x, \mathbf{k}_T^2, \mu^2)$

Fig. 1. Unintegrated gluon distribution $\Phi(x, \mathbf{k}_T^2, \mu^2)$ in the proton versus x at $\mathbf{k}_T^2 = 10, 30$, and 50 GeV^2 for $\mu = 10$ GeV.

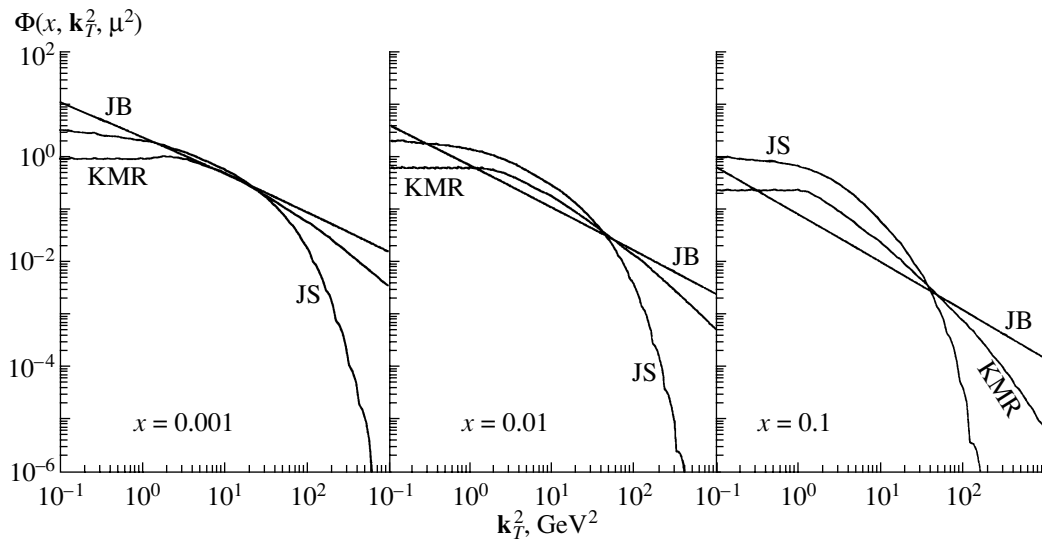$\Phi(x, \mathbf{k}_T^2, \mu^2)$

Fig. 2. Unintegrated gluon distribution $\Phi(x, \mathbf{k}_T^2, \mu^2)$ in the proton versus $\mathbf{k}_T^2$ at $x = 0.001, 0.01$, and 0.1 for $\mu = 10$ GeV.

so that the use of the massless approximation is not quite correct; therefore, we employ a different definition of the fragmentation parameter z,

$$z = \frac{E_{D^*} + |\mathbf{p}_{D^*}|}{E_c + |\mathbf{p}_c|}, \qquad (10)$$

assuming that

$$\theta_{D^*} = \theta_c, \qquad (11)$$

where θ_{D^*} and θ_c are, respectively, the D^*-meson and c-quark emission angles in the laboratory frame. This assumption is justified by the fact that the c-quark mass is approximately equal to the $D^{*\pm}$-meson mass, $m_c \approx m_{D^{*\pm}}$ ($m_{D^{*\pm}} = 2.010$ GeV [19]); therefore, the c quark does not change the direction of its motion in

the fragmentation process. For the sake of definiteness, we set the c-quark mass to $m_c = 1.5$ GeV in our numerical calculations.

Alternative definitions of the fragmentation parameter z are also possible, for example,

$$\mathbf{p}_{D^*} = z\mathbf{p}_c. \qquad (12)$$

As was shown in [20], the definitions in (9), (10), and (12) lead to virtually identical spectra of D^* mesons over a wide range of kinematical variables.

A definition of z close to that in (10) was used in [21–24] to extract the $c \to D^*$ fragmentation function in the processes of electro- and photoproduction

on protons; namely,

$$z = \frac{E_{D^*} + |\mathbf{p}_{D^*}|}{2E_{\text{had}}}, \tag{13}$$

where E_{had} is the total energy of the hadron jet.

For the free parameter of the Peterson fragmentation function [18], a fit to experimental data on $D^{*\pm}$-meson production in e^+e^- annihilation gives the value of $\epsilon = 0.036$ [25] in the model that takes into account the c-quark mass and the value of $\epsilon = 0.116$ [12, 26] in the model of massless c quarks. We use the value

$$\epsilon = 0.06, \tag{14}$$

which is in accord with the analysis in [21].

4. DEEP-INELASTIC SCATTERING

4.1. Cross Section for the Process
$e + p \rightarrow e + D^* + X$

By using relations (1), (2), and (5) and the definition of the fragmentation parameter z in the form specified by Eqs. (10) and (11), one can rewrite the quadruple-differential production cross section in the parton model as

$$\frac{d\sigma^{\text{PM}}(ep \rightarrow eD^*X)}{d\eta_{D^*}d|\mathbf{p}_{D^*T}|dQ^2dW^2} \tag{15}$$

$$= \int dz D_{c \rightarrow D^*}(z, \mu^2) G(x, \mu^2)$$

$$\times \int d\varphi_c \frac{1}{(2\pi)^4} \frac{|\mathbf{p}_c||\mathbf{p}_{cT}|}{2E_{D^*}} \frac{1}{s|y-a|} \frac{\overline{|M(eg \rightarrow ec\bar{c})|^2}}{8xs^2},$$

where Q^2 is the photon virtuality; $x_{\text{Bj}} = Q^2/(ys)$ is the Bjorken variable; $y = (W^2 + Q^2)/s$; W is the energy of photon−proton interaction in the c.m. frame; φ_c is the polar angle between the directions of p_{cT} and the fixed axis x ($p'_e \in xz$); p'_e is the 4-momentum of the final electron; η is the pseudorapidity,

$$\eta = -\ln\tan\frac{\theta}{2}; \tag{16}$$

$\mu^2 = m^2_{D^*} + p^2_{D^*T} + Q^2$ is the characteristic scale of the hard interaction; and, for other quantities, we use the notation

$$x = \frac{Q^2 + 2|\mathbf{p}_{cT}|Q\beta_1 + syb}{s|y-a|}, \tag{17}$$

$$\beta_1 = \cos\varphi_c, \tag{18}$$

$$a = \frac{E_c - p_{cz}}{2E_e}, \tag{19}$$

$$b = \frac{E_c + p_{cz}}{2E_N}. \tag{20}$$

In the k_T-factorization approach, we have

$$\frac{d\sigma^{\text{KT}}(ep \rightarrow eD^*X)}{d\eta_{D^*}d|\mathbf{p}_{D^*T}|dQ^2dW^2} \tag{21}$$

$$= \int dz D_{c \rightarrow D^*}(z, \mu^2) \int \frac{d\varphi}{2\pi} \int d\mathbf{k}_T^2 \frac{\Phi(x, \mathbf{k}_T^2, \mu^2)}{x}$$

$$\times \int d\varphi_c \frac{1}{(2\pi)^4} \frac{|\mathbf{p}_c||\mathbf{p}_{cT}|}{2E_{D^*}} \frac{1}{s|y-a|} \frac{\overline{|M(eg^* \rightarrow ec\bar{c})|^2}}{8xs^2},$$

where

$$x = \frac{|\mathbf{k}_T|^2 + Q^2 + 2|\mathbf{k}_T||\mathbf{q}_T|\beta_2 - 2|\mathbf{p}_{cT}||\mathbf{k}_T|\beta_3 + 2|\mathbf{p}_{cT}||\mathbf{q}_T|\beta_1 + s(yb + av)}{s|y-a|}, \tag{22}$$

$$v = -Q^2/s, \tag{23}$$

$$|\mathbf{q}_T| = Q\sqrt{1-y}, \tag{24}$$

$$\beta_2 = \cos\varphi, \tag{25}$$

$$\beta_3 = \cos(\varphi - \varphi_c). \tag{26}$$

To go over from one set of differential cross sections to another, one can employ the formulas

$$\frac{d^3p'_e}{2E'_e} = \frac{dQ^2dW^2d\varphi'_e}{4s} = \frac{dydQ^2d\varphi'_e}{4} \tag{27}$$

$$= \frac{ydx_{\text{Bj}}dQ^2d\varphi'_e}{4x_{\text{Bj}}},$$

where E'_e is the energy of the final electron and φ'_e is the azimuthal angle of final-electron emission.

In the high-energy region ($x_{\text{Bj}} \ll 1$, $Q^2 \ll s$), the electroproduction cross section can be represented as the convolution of the photoproduction cross section $\hat{\sigma}(\gamma^*g^* \rightarrow c\bar{c})$ and the equivalent-virtual-photon spectrum $f_{\gamma^*/e}(y, Q^2)$; that is,

$$\frac{d\sigma^{\text{KTQT}}(ep \rightarrow eD^*X)}{d\eta_{D^*}d|\mathbf{p}_{D^*T}|dQ^2dW^2} \tag{28}$$

$$= \int dz D_{c \rightarrow D^*}(z, \mu^2) \int \frac{d\varphi}{2\pi} \int d\mathbf{k}_T^2 \frac{\Phi(x, \mathbf{k}_T^2, \mu^2)}{x}$$

$$\times \int d\varphi_c f_{\gamma^*/e}(y,Q^2) \frac{1}{(2\pi)^2} \frac{|\mathbf{p}_c||\mathbf{p}_{cT}|}{2E_{D^*}}$$

$$\times \frac{1}{s|y-a|} \frac{\overline{|M(\gamma^*g^* \to ec\bar{c})|^2}}{2xys^2},$$

where $q_T = (0, \mathbf{q}_T, 0)$ is the transverse momentum of the virtual photon, $q_T^2 = -Q^2$; $q = yp_e + q_T$ is the 4-momentum of the virtual photon; $p_e = E_e(1, 0, 0, -1)$ is the 4-momentum of the initial electron; φ_c is the polar angle between the directions of p_{cT} and the fixed x axis ($q \in xz$); and $f_{\gamma^*/e}(y, Q^2)$ is the equivalent-virtual-photon spectrum, which can be represented in the form [27]

$$f_{\gamma^*/e}(y, Q^2) = \frac{\alpha}{2\pi}\Big(\frac{1+(1-y)^2}{yQ^2} - \frac{2m_e^2 y}{Q^4}\Big). \quad (29)$$

In this approximation, the polarization tensor of virtual photons is given by

$$L_e^{\mu\nu}(q) = q_T^\mu q_T^\nu / Q^2. \quad (30)$$

4.2. Amplitudes of Parton Subprocesses

Let us introduce the notation

$$\tilde{t} = \hat{t} - m_c^2, \quad (31)$$

$$\tilde{u} = \hat{u} - m_c^2 \quad (32)$$

and set

$$f_{kk} = |\mathbf{k}_T|^2, \quad f_{kp} = \beta_3|\mathbf{k}_T||\mathbf{p}_{cT}|, \quad (33)$$
$$f_{kq} = \beta_2|\mathbf{k}_T||\mathbf{q}_T|,$$
$$f_{pp} = \beta_3^2|\mathbf{p}_{cT}|^2, \quad f_{pq} = \beta_2\beta_3|\mathbf{p}_{cT}||\mathbf{q}_T|,$$
$$f_{qq} = \beta_2^2|\mathbf{q}_T|^2.$$

For the electroproduction of a pair of c quarks on a Yang–Mills gluon via the process

$$e + g \to e + c + \bar{c}, \quad (34)$$

the result obtained upon averaging the absolute value of the amplitude over the electron and gluon polarizations and over the color states of the initial gluon has the form

$$\overline{|M(eg \to ec\bar{c})|^2} \quad (35)$$
$$= 32\alpha^2 \alpha_s e_c^2 \pi^3 (M_{11}^a + 2M_{12}^a + M_{22}^a),$$

where

$$M_{11}^a = -\frac{4}{Q^4\tilde{t}^2}\Big[m_c^4\big(4Q^2 + s(6b+x)\big) \quad (36)$$

$$+ s\hat{t}\big((Q^2+\hat{t})x + b(\hat{t}+\hat{u}+2sx)\big)$$

$$- m_c^2\big(2Q^4 + Q^2 s(4b+x)$$

$$+ s(4b^2s + 7b\hat{t} + b\hat{u} + 2bsx + 2\hat{t}x)\big)\Big],$$

$$M_{12}^a = \frac{2}{Q^4\tilde{t}\tilde{u}}\Big[2Q^6 - 4m_c^4(Q^2 - 2sx) \quad (37)$$

$$+ 2Q^4(2bs + \hat{t} - sx) + Q^2\Big(2s^2(2b^2 - 2bx + x^2)$$

$$+ \hat{t}(2bs - \hat{u} - sx) - \hat{u}(2bs - \hat{u} - 3sx)\Big)$$

$$+ s(-b\hat{t}^2 + b\hat{u}^2 - 2bs\hat{t}x + \hat{t}^2x + 2bs\hat{u}x + 3\hat{t}\hat{u}x$$

$$+ 2s\hat{t}x^2) - m_c^2\Big(2Q^4 - Q^2(8bs + \hat{t} - 5\hat{u} - 6sx)$$

$$+ s\big(2b(4s(x-b) - 3(\hat{t} - \hat{u})) + 9\hat{t}x$$

$$+ 3\hat{u}x + 2sx^2\big)\Big)\Big],$$

$$M_{22}^a = \frac{4}{Q^4\tilde{u}^2}\Big[\hat{u}\big(-Q^4 + Q^2(-\hat{s} + sx) \quad (38)$$

$$+ s(b\hat{t} + b\hat{u} + 2bsx - \hat{t}x - 2\hat{u}x - 2sx^2)\big)$$

$$+ m_c^4 s(6b - 7x) + m_c^2\big(3Q^4 + Q^2(4bs + \hat{s}$$

$$- 4\hat{u} - 5sx) + s(4b^2s - b\hat{t} - 7b\hat{u} - 10bsx + \hat{t}x$$

$$+ 9\hat{u}x + 6sx^2)\big)\Big].$$

Here, $\hat{s}$, $\hat{t}$, and $\hat{u}$ are the standard Mandelstam variables for the process $\gamma^* + g \to c + \bar{c}$.

For the electroproduction of c quarks on a Reggeized gluon via the process

$$e + g^* \to e + c + \bar{c}, \quad (39)$$

the result analogously obtained by averaging the square of the absolute value of the amplitude over the electron polarizations and over the color states of the initial gluon is

$$\overline{|M(eg^* \to ec\bar{c})|^2} \quad (40)$$
$$= 64\alpha^2 \alpha_s e_c^2 \pi^3 (M_{11}^b + 2M_{12}^b + M_{22}^b),$$

where

$$M_{11}^b = \frac{2s}{Q^4\tilde{t}^2}\Big[\big(v(Q^2 - 2m_c^2 + 2bs + \tilde{t}) \quad (41)$$

$$- 2b^2 s\big)(f_{kk} - 4f_{kp} - 4f_{kq} + 4f_{pp}$$

$$+ 8f_{pq} + 4f_{qq}) - b\tilde{t}(f_{kk} - 8f_{kp} - 4f_{kq} + 8f_{pp}$$

$$+ f_{pq} + 4f_{qq} + Q^2 + \hat{s}) - x\tilde{t}(\tilde{t} + Q^2 + 2bs)\Big],$$

$$M_{12}^b = -\frac{s}{Q^4\tilde{t}\tilde{u}}\Big[4bs(b - x - v)(4f_{pp} - 4f_{kp}) \quad (42)$$

$$+ f_{kk} + 4f_{pq} - 2f_{kq}) - 4b\tilde{u}(f_{qq} + 2f_{pq} - f_{kq})$$

$$- 2x\tilde{t}(4f_{pp} - 4f_{kp} + f_{kk} + 2f_{pq}) + (\hat{u} - \hat{t})$$

$$\times \Big(b(\hat{s} + Q^2) + \tilde{u} + 3vf_{kk}\Big) + v\Big(2sx\big(4f_{pp}$$

$$- 4f_{kp} + f_{kk} + 4f_{pq}) - 4m_c^2(f_{kk} + f_{qq} - 4f_{pp}$$
$$- 7f_{pq}) + 4\hat{u}(f_{pp} + f_{qq} - 4f_{kp} - 2f_{kq})$$
$$- 4\hat{s}(2f_{kp} + 2f_{pq} + f_{kq}) - 2Q^2(4f_{pp} + 8f_{pq}$$
$$+ f_{kk}) - 4\hat{t}(f_{pp} + 3f_{pq}) + 2f_{kk}(f_{kk} - 8f_{kp}$$
$$- 4f_{kq} + 4f_{pp} + 2f_{qq})\Big) + x\Big((Q^2 + \tilde{t})$$
$$\times (2sx + \tilde{t} + \tilde{u}) + 2s(b(\hat{t} - \hat{u}) + v\tilde{u})$$
$$+ 2(m_c^2(\hat{u} + \hat{t}) - m_c^4 - \hat{t}\hat{u})\Big)\Big],$$

$$M_{22}^b = -\frac{2s}{Q^4 \tilde{u}^2}\Big[\Big(2s(x-b)(x-b-v) \qquad (43)$$
$$- Q^2 v\Big)(f_{kk} - 4f_{kp} + 4f_{pp}) + 4\hat{u}v(-f_{kp} + f_{pp}$$
$$+ f_{pq}) + \tilde{u}(x-b)(f_{kk} - 8f_{kp} + 8f_{pp} + 4f_{pq})$$
$$+ 2m_c^2 v(f_{kk} - 2f_{kp} + 2f_{pp} - 2f_{pq})$$
$$+ \tilde{u}(Q^2 + \hat{s})(b-v) + x\tilde{u}\Big(\tilde{u} - \hat{s} + 2s(x-b+v)\Big)\Big].$$

Upon averaging over the color states of the initial gluon, the square of the absolute value of the amplitude for the photoproduction of c quarks by a virtual photon on a Reggeized gluon via the process

$$\gamma^* + g^* \to c + \bar{c} \qquad (44)$$

takes the form

$$\overline{|M(\gamma^* g^* \to c\bar{c})|^2} \qquad (45)$$
$$= 8\alpha\alpha_s e_c^2 \pi^2 (M_{11}^c + 2M_{12}^c + M_{22}^c),$$

where

$$M_{11}^c = -\frac{2}{\tilde{t}^2}\Big[(f_{kk} + 4f_{pp} + \tilde{t})Q^2 \qquad (46)$$
$$- (f_{kk} - m_c^2 + \hat{s})m_c^2 - 4|\mathbf{p}_{cT}|Q\Big(|\mathbf{k}_T|Q$$
$$+ (\tilde{t} + 2Q^2)\beta_2\Big)\beta_3 + 4(\tilde{t} + Q^2)(|\mathbf{k}_T|Q\beta_2 + Q^2\beta_2^2)$$
$$- (Q^2 + \hat{u})\hat{t} - 4|\mathbf{p}_{cT}|\Big(4f_{pp}Q\beta_1 + (\tilde{t} + 4Q^2)|\mathbf{k}_T|$$
$$\times \beta_2 + 2(\tilde{t} + 2Q^2)Q\beta_2^2 - 2|\mathbf{p}_{cT}|(2|\mathbf{k}_T|Q$$
$$+ (\tilde{t} + 4Q^2)\beta_2)\beta_3 + Qf_{kk}\Big) + 4|\mathbf{p}_{cT}|^2$$
$$\times \beta_1^2\Big(f_{kk} + 2Q^2 + 4|\mathbf{k}_T|Q\beta_2 + 2Q^2(\cos 2\varphi)$$
$$- 4f_{kp} - 4|\mathbf{p}_{cT}|(Q\beta_1 - Q\cos(2\varphi - \varphi_c)$$
$$+ |\mathbf{p}_{cT}|\beta_3)\Big)\Big],$$

$$M_{12}^c = -\frac{2}{\tilde{t}\tilde{u}}\Big[-\tilde{t}\tilde{u} + 2(\tilde{u} + f_{kk})(\tilde{t} + Q^2)\beta_2^2 \qquad (47)$$
$$+ f_{kk}Q^2 - 2\hat{s}|\mathbf{k}_T|Q\beta_2 - 2|\mathbf{p}_{cT}|\Big(2(\tilde{t} + 2Q^2)|\mathbf{k}_T|$$

$$\times \beta_2 - (\hat{s} - 3f_{kk} - Q^2)Q\beta_2 + 2|\mathbf{k}_T|Q^2\Big)\beta_3$$
$$+ 4f_{pp}Q\Big(Q + 2|\mathbf{k}_T|\beta_2\Big) - 2|\mathbf{p}_{cT}|\Big((f_{kk} + 3Q^2$$
$$- \hat{s})|\mathbf{k}_T|\beta_2 + 2f_{kk}Q + 2(\tilde{u} + 2f_{kk})Q\beta_2^2$$
$$- 2|\mathbf{p}_{cT}|(4|\mathbf{k}_T|Q + (3f_{kk} + 3Q^2 - \hat{s})\beta_2$$
$$+ 4|\mathbf{k}_T|Q\beta_2)\beta_3 + 8f_{pp}(Q + |\mathbf{k}_T|\beta_2)\Big)\beta_1$$
$$+ 4|\mathbf{p}_{cT}|^2\Big(2|\mathbf{p}_{cT}|\beta_3 - |\mathbf{k}_T|\Big)$$
$$\times \Big(-|\mathbf{k}_T| - 2Q\beta_2 + 2|\mathbf{p}_{cT}|\beta_3\Big)\beta_1^2\Big],$$

$$M_{22}^c = -\frac{2}{\tilde{u}^2}\Big[f_{kk}(\tilde{u} + Q^2) - (\hat{t} + f_{kk})\hat{u} \qquad (48)$$
$$+ 4(|\mathbf{k}_T|Q\beta_2 + f_{kk}\beta_2^2)(\tilde{u} + f_{kk}) - m_c^2(\hat{s} - m_c^2$$
$$+ Q^2) - 4|\mathbf{p}_{cT}|\Big(Q(\tilde{u} + 4f_{kk})\beta_2$$
$$+ 2|\mathbf{k}_T|(\tilde{u} + 2f_{kk})\beta_2 + |\mathbf{k}_T|Q^2\Big)\beta_3$$
$$+ 4f_{pp}\Big(Q^2 + 4|\mathbf{k}_T|Q\beta_2 + 4f_{kk}\beta_2\Big)$$
$$+ 4|\mathbf{p}_{cT}|^2\Big(|\mathbf{k}_T| - 2|\mathbf{p}_{cT}|\beta_3\Big)^2\beta_1^2$$
$$- 4|\mathbf{p}_{cT}|\beta_1\Big(-|\mathbf{k}_T| + 2|\mathbf{p}_{cT}|\beta_3\Big)\Big(-|\mathbf{k}_T|Q$$
$$- (\tilde{u} + 2f_{kk})\beta_2 + 2|\mathbf{p}_{cT}|Q\beta_3 + 2|\mathbf{k}_T||\mathbf{p}_{cT}|$$
$$\times \cos(2\varphi - \varphi_c) + 2|\mathbf{k}_T||\mathbf{p}_{cT}|\beta_1\Big)\Big].$$

We have tested analytically that, in the limit $|\mathbf{k}_T| \to 0$ and upon averaging over the azimuthal angle φ, the amplitudes for the processes involving a Reggeized initial gluon reduce exactly to the amplitudes for the process involving a real gluon in the initial state. By way of example, we indicate that, for the processes in (34) and (39),

$$\overline{|M(eg \to ec\bar{c})|^2} = \lim_{|\mathbf{k}_T| \to 0} \int_0^{2\pi} \frac{d\varphi}{2\pi} \overline{|M(eg^* \to ec\bar{c})|^2},$$
$$(49)$$

where φ is the angle between the fixed axis x and the vector $\mathbf{k}_T$.

4.3. Results of the Calculations

In this section, we compare theoretical predictions made within various approaches and experimental data obtained at the HERA collider for the spectra of $D^{*\pm}$ mesons in ep interactions at the energies of $E_N = 820$ GeV and $E_e = 27.5$ GeV. The experimental data of the ZEUS Collaboration [23] are presented in the form of various spectra of $D^{*\pm}$ mesons versus

the variable $y = Q^2/(x_{\mathrm{Bj}}s) = (Q^2 + W^2)/s$ in the interval $0.02 < y < 0.7$, the photon 4-momentum squared Q^2 in the interval $1 < Q^2 < 600 \text{ GeV}^2$, the transverse momentum p_{D^*T} in the interval $1.5 < p_{D^*T} < 15$ GeV, and the pseudorapidity η in the interval $|\eta| < 1.5$.

Figure 3 shows the results of the present calculations for the p_T spectrum of D^* mesons. One can see that the curves obtained within the k_T-factorization approach lie above (by a factor of 1.5 to 2) the predictions of the collinear parton model; this is not so only for the curve obtained in calculations on the basis of the KMR parametrization [11] for the unintegrated distribution of gluons in the proton.

It should be noted that the numerical results obtained with the aid of formulas (21) and (28) within the k_T-factorization approach are virtually coincident. Thus, we see that, within the k_T-factorization approach and in the parton model, the use of the Williams–Weizsäcker spectrum (29) for equivalent virtual photons is possible and is correct in the kinematical region $Q^2 \geq 1 \text{ GeV}^2$.

Figure 4a shows the results of the present calculations for the η spectrum of D^* mesons. In this spectrum, the discrepancies between the predictions obtained with the different parametrizations of the unintegrated distribution of gluons in the proton are the most pronounced. The discrepancies between the theoretical predictions and the experimental data are due to the uncertainty in the choice of parametrization for the distribution of Reggeized gluons in the proton. The curve obtained by using the JS parametrization [10] describes most precisely the shape of the spectrum, it but underestimates its absolute value.

In Fig. 4c, we display the results of the present calculations for the Q^2 spectrum of D^* mesons. One can see that, in this spectrum, the discrepancy between the results obtained by applying the different parametrizations and approaches is the most pronounced in the region of low Q^2; therefore; it is necessary to investigate processes in which $Q^2 < 1 \text{ GeV}^2$—that is, photoproduction processes. This will be done in the next section of the present study.

In Fig. 4d, the results of the calculation of the differential cross section for the production of D^* mesons are displayed in the form of the spectrum in the Bjorken variable x_{Bj}. The relationship between the predictions of various models is analogous to that for the spectra considered above. The curves obtained with the JB parametrization [9] provide the best description of the experimental data.

Figure 4b shows the results of our present calculations for the W spectrum of D^* mesons. In this spectrum, the predictions of the parton model lie above
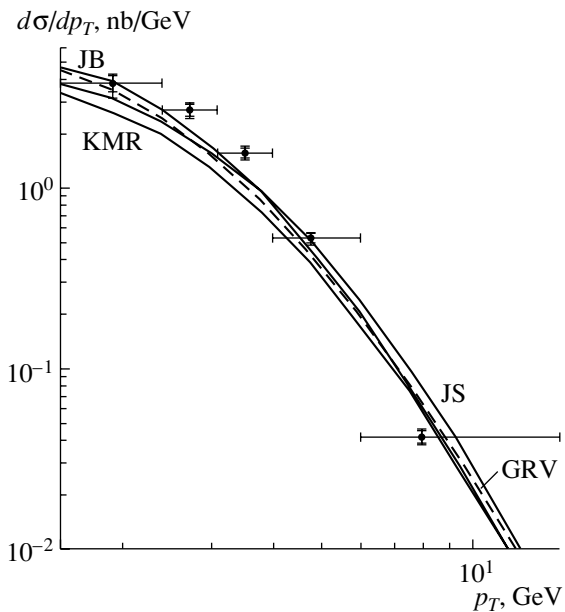

Fig. 3. Differential cross section for the deep-inelastic electroproduction of D^* mesons as a function of the transverse momentum p_{D^*T}.

the predictions of the k_T-factorization approach supplemented with the KMR parametrization [11]. This spectrum exhibits the lowest sensitivity to the choice of approach and provides a testing ground for comparing different gluon distributions. One can see that none of the parametrizations (JB [9], JS [10], KMR [11], or GRV LO [8]) is universal.

5. PHOTOPRODUCTION

5.1. Cross Section for the Process $\gamma + p \to D^* + X$

Along with experiments to study the deep-inelastic electroproduction of D^* mesons, the ZEUS [22] and H1 [21] Collaborations performed measurements in the region of low photon virtualities, $Q^2 < 1 \text{ GeV}^2$.

In the region of low Q^2, the cross section for D^*-meson electroproduction in the process $e + p \to e + D^* + X$ can be expressed in terms of the cross section for D^*-meson photoproduction by real photons in the process $\gamma + p \to D^* + X$ as

$$\sigma(ep \to eD^*X) \qquad (50)$$

$$= \int \sigma(\gamma p \to D^*X) \cdot f_{\gamma/e}(y)dy,$$

where $f_{\gamma/e}(y)$ determines the virtual-photon spectrum (29) integrated with respect to Q^2 within the kinematical limits from $Q^2_{\min}$ to $Q^2_{\max}$ ($Q^2_{\min} = m_e^2 y^2/(1-y)$ is the lower kinematical limit, while $Q^2_{\max}$ is the upper kinematical limit of the cut on the photon virtuality) and $y = W^2/s$.
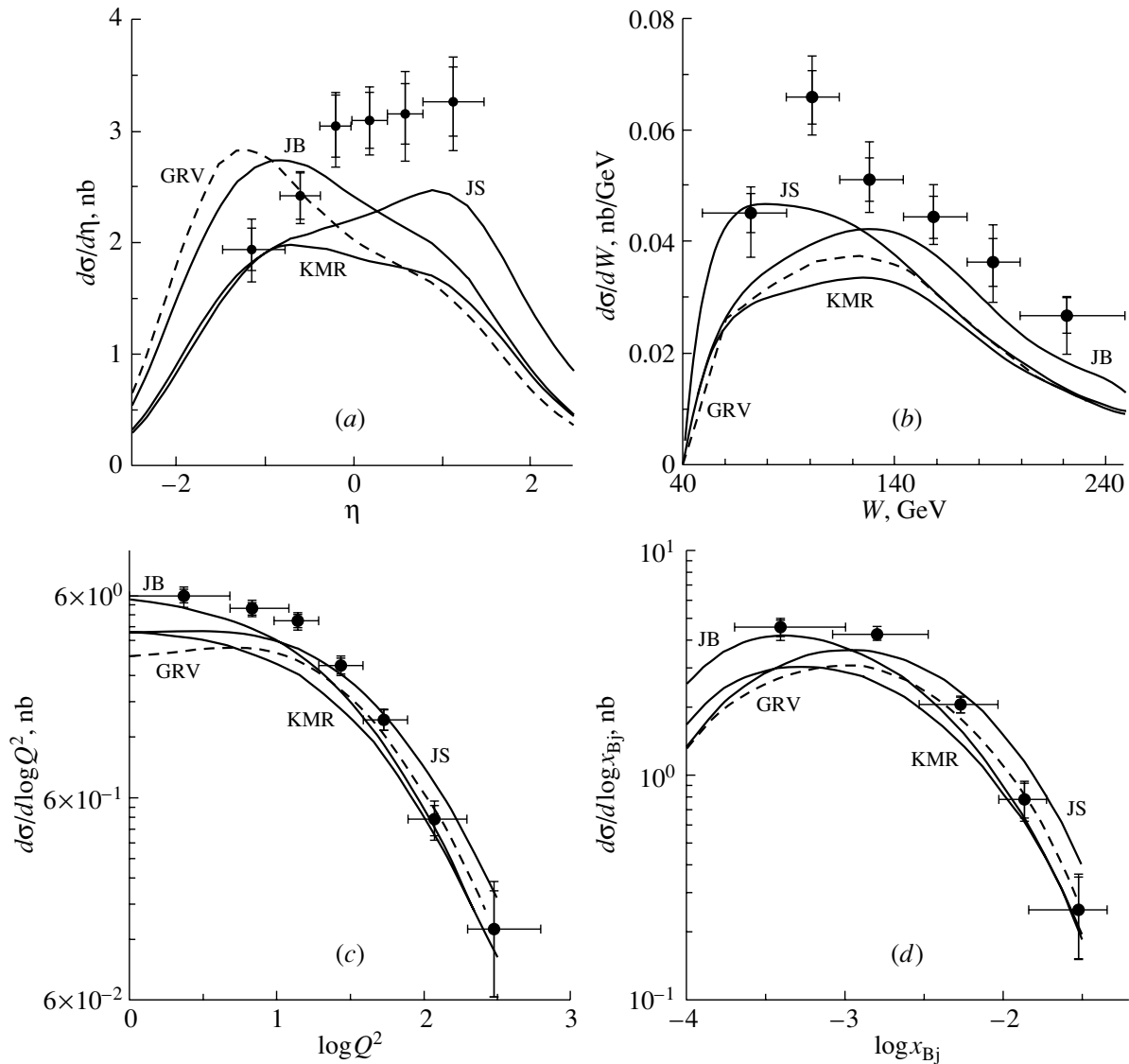
Fig. 4. Differential cross section for the deep-inelastic electroproduction of D^* mesons as a function of various variables.

The Williams–Weizsäcker spectrum of quasireal photons can be derived by performing integration of (29) with respect to Q^2 [28]. The result is

$$f_{\gamma/e}(y) = \frac{\alpha}{2\pi} \left[\frac{1 + (1-y)^2}{y} \log \frac{Q^2_{\max}}{Q^2_{\min}} \right. \tag{51}$$

$$\left. + 2m_e^2 y \left(\frac{1}{Q^2_{\min}} - \frac{1}{Q^2_{\max}} \right) \right].$$

By using the relation between the cross sections at the hadron level and at the quark level as determined by Eq. (5), the relation between the hadron process and the parton subprocess as determined by Eq. (1) in the parton model and by Eq. (2) in the k_T-factorization approach, and the definition of the fragmentation parameter z in the form specified by Eqs. (10) and (11), one can obtain the double-

differential production cross section within the parton model and within the k_T-factorization approach.

In the parton model, we have

$$\frac{d\sigma^{\mathrm{PM}}(ep \to eD^*X)}{d\eta_{D^*} dp_{D^*T}} \tag{52}$$

$$= \int dy f_{\gamma/e}(y) \int \frac{dz}{z} D_{c \to D^*}(z, \mu^2) G(x, \mu^2)$$

$$\times \frac{2|\mathbf{p}_c||\mathbf{p}_{cT}|}{E_c(W^2 - 2E_N(E_c - p_{cz}))} \frac{\overline{|M(\gamma g \to c\bar{c})|^2}}{16\pi x W^2},$$

where $y_{\min} = W^2_{\min}/s$ and $y_{\max} = W^2_{\max}/s$ are, correspondingly the lower and the upper limit of integration with respect to y; W is the energy of photon–proton interaction in the c.m. frame; and $\mu^2 = m_{D^*}^2 + p_{D^*T}^2$ is the characteristic scale of hard interaction.

Within the k_T-factorization approach, the double-differential cross section in question takes the form

$$\frac{d\sigma^{\mathrm{KT}}(ep \to eD^*X)}{d\eta_{D^*}\,dp_{D^*T}} \qquad (53)$$

$$= \int dy\, f_{\gamma/e}(y) \int \frac{dz}{z} D_{c \to D^*}(z, \mu^2)$$

$$\times \int \frac{d\varphi}{2\pi} \int d\mathbf{k}_T^2 \frac{\Phi(x, \mathbf{k}_T^2, \mu^2)}{x}$$

$$\times \frac{2|\mathbf{p}_c||\mathbf{p}_{cT}|}{E_c(W^2 - 2E_N(E_c - p_{cz}))} \frac{\overline{|M(\gamma g^* \to c\bar{c})|^2}}{16\pi x W^2},$$

where $q = y p_e$ is the 4-momentum of the real photon; $q^2 = 0$; and $k = x p_N + k_T$ is the 4-momentum of the Reggeized gluon, $k^2 = k_T^2 = -|\mathbf{k}_T|^2$.

5.2. Amplitudes of Parton Subprocesses

For the process

$$\gamma + g \to c + \bar{c}, \qquad (54)$$

the result of averaging the square of the absolute value of the amplitude over the photon and gluon polarizations and over the color states of the initial gluon is well known and can be represented in the form [29]

$$\overline{|M(\gamma g \to c\bar{c})|^2} \qquad (55)$$

$$= 16\pi^2 e_c^2 \alpha_s \alpha \left[-4\left(\frac{m_c^2}{\tilde{t}} + \frac{m_c^2}{\tilde{u}}\right)^2 \right.$$

$$\left. - 4\left(\frac{m_c^2}{\tilde{t}} + \frac{m_c^2}{\tilde{u}}\right) + \frac{\tilde{u}}{\tilde{t}} + \frac{\tilde{t}}{\tilde{u}} \right].$$

For the analogous process involving a Reggeized gluon,

$$\gamma + g^* \to c + \bar{c}, \qquad (56)$$

the averaging of the square of the absolute value of the respective amplitude over the photon polarization and over the color states of the initial gluon was performed in [2]. The result can be written in the form

$$\overline{|M(\gamma g^* \to c\bar{c})|^2} = \frac{-16\pi^2 e_c^2 \alpha_s \alpha}{\tilde{t}^2 \tilde{u}^2} \qquad (57)$$

$$\times \left[m_c^2 \left(2m_c^6 - (8\mathbf{p}_T^2 + m_c^2 + 3\mathbf{k}_T^2)\mathbf{k}_T^4 \right. \right.$$

$$+ 4m_c^2 \mathbf{p}_T^2 \mathbf{k}_T^2 - (4m_c^4 + 5\mathbf{k}_T^4 + 12\mathbf{p}_T^2 \mathbf{k}_T^2)\hat{s}$$

$$\left. + (3m_c^2 - 4\mathbf{p}_T^2 - 3\mathbf{k}_T^2)\hat{s}^2 - \hat{s}^3 \right)$$

$$+ \left(4m_c^4(3\hat{s} - 2m_c^2) + (\hat{s} + 4\mathbf{p}_T^2 + \mathbf{k}_T^2 + 2m_c^2)\mathbf{k}_T^4 \right.$$

$$\left. + 4\mathbf{p}_T^2 \mathbf{k}_T^2(\hat{s} - 2m_c^2) + (s + \mathbf{k}_T^2 - 6m_c^2)\hat{s}^2 \right)\hat{t}$$

$$+ \left(4\mathbf{p}_T^2 \mathbf{k}_T^2 - \mathbf{k}_T^4 + 3(-2m_c^2 + s)^2 \right)\hat{t}^2 + 2\hat{t}^4$$

$$- 4(2m_c^2 - \hat{s})\hat{t}^3 + 4|\mathbf{p}_T| \left(|\mathbf{k}_T|\cos\varphi \left[-2m_c^6 \right. \right.$$

$$- (\mathbf{k}_T^2 - \hat{s} - 2\hat{t})\hat{t}(m_c^2 - \tilde{u}) + m_c^4(\mathbf{k}_T^2 + 3\hat{s} + 6\hat{t})$$

$$\left. + m_c^2\left(3\mathbf{k}_T^4 + \hat{s}^2 - 6\hat{s}\hat{t} + \mathbf{k}_T^2(4\hat{s} - 2\hat{t}) - 6\hat{t}^2 \right) \right]$$

$$+ \cos(2\varphi)|\mathbf{p}_T|\left[m_c^4 \mathbf{k}_T^2 + \mathbf{k}_T^2 \hat{t}(m_c^2 - \tilde{u}) \right.$$

$$\left. \left. \left. - m_c^2\left(2\mathbf{k}_T^4 + \hat{s}^2 + \mathbf{k}_T^2(3\hat{s} + 2\hat{t}) \right) \right] \right) \right].$$

If we use the polarization vector of the Reggeized gluon in the form

$$\varepsilon^\mu(x, k_T) = -\frac{x p_N^\mu}{|\mathbf{k}_T|}, \qquad (58)$$

the amplitude squared appears to be [30, 31]

$$\overline{|M(\gamma g^* \to c\bar{c})|^2} \qquad (59)$$

$$= 16\pi^2 e_c^2 \alpha_s \alpha (\hat{s} + \mathbf{k}_T^2)^2 \left[\frac{\alpha_1^2 + \alpha_2^2}{(\hat{t} - m_c^2)(\hat{u} - m_c^2)} \right.$$

$$\left. - \frac{2m_c^2}{\mathbf{k}_T^2}\left(\frac{\alpha_1}{\hat{u} - m_c^2} - \frac{\alpha_2}{\hat{t} - m_c^2} \right)^2 \right],$$

where

$$\alpha_1 = \frac{m_c^2 + \mathbf{p}_{cT}^2}{m_c^2 - \hat{t}}, \qquad (60)$$

$$\alpha_2 = \frac{m_c^2 + \mathbf{p}_{\bar{c}T}^2}{m_c^2 - \hat{u}}; \qquad (61)$$

$\mathbf{p}_{cT}$ and $\mathbf{p}_{\bar{c}T}$ are the transverse momenta of the c and $\bar{c}$ quarks, respectively; and $\mathbf{k}_T = \mathbf{p}_{cT} + \mathbf{p}_{\bar{c}T}$ is the transverse momentum of the Reggeized gluon.

Formula (59) can be reduced to the form (57), whereby the gauge-invariance of the amplitude for the process involving a Reggeized gluon is confirmed.

In the limit $|\mathbf{k}_T| \to 0$, the matrix element involving a Reggeized gluon reduces to the matrix element involving a real gluon, as this occurred in the case of electroproduction. Specifically, we have

$$\overline{|M(\gamma g \to c\bar{c})|^2} = \lim_{|\mathbf{k}_T| \to 0} \int_0^{2\pi} \frac{d\varphi}{2\pi}\overline{|M(\gamma g^* \to c\bar{c})|^2},$$

$$(62)$$

where φ is the angle between the fixed axis x and the vector $\mathbf{k}_T$.
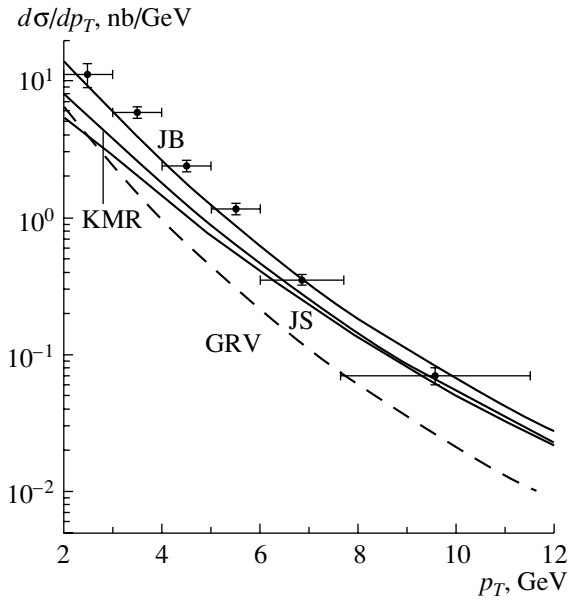
$d\sigma/dp_T$, nb/GeV

Fig. 5. Differential cross section for the photoproduction of D^* mesons as a function of the transverse momentum p_{D^*T}.

5.3. Results of the Calculations

In this section, we compare the theoretical predictions obtained within various approaches with experimental data on the spectra of $D^{*\pm}$-meson photoproduction in ep interactions at the HERA collider for the energies of $E_N = 820$ GeV and $E_e = 27.5$ GeV. Experimental data of the H1 [21] and ZEUS [22] Collaborations are represented in the form of various spectra of $D^{*\pm}$ mesons—specifically, the spectrum with respect to W in the range $130 < W < 280$ GeV, the spectrum with respect to the square of the photon 4-momentum in the range $Q^2 < 1$ GeV^2, the spectrum with respect to the transverse momentum in the range $1.5 < p_{D^*T} < 15$ GeV, and the spectrum with respect to the pseudorapidity in the range $|\eta| < 1.5$.

Figure 5 shows the results of our calculations for the p_T spectrum of D^* mesons. One can see that the curves calculated within the k_T-factorization approach lie higher (by a factor of 2 to 3) than the predictions of the collinear parton model.

It should be noted that the respective calculations for D^*-meson photoproduction can be directly performed by the formulas that describe D^*-meson electroproduction, in which case integration with respect to Q^2 in formulas (15), (21), and (28) must be performed from $Q^2_{\min}$ to $Q^2_{\max} = 1$ GeV^2. We have verified this statement by means of numerical calculations, and this proved the applicability of the method of equivalent photons both in the parton model and in the k_T-factorization approach.
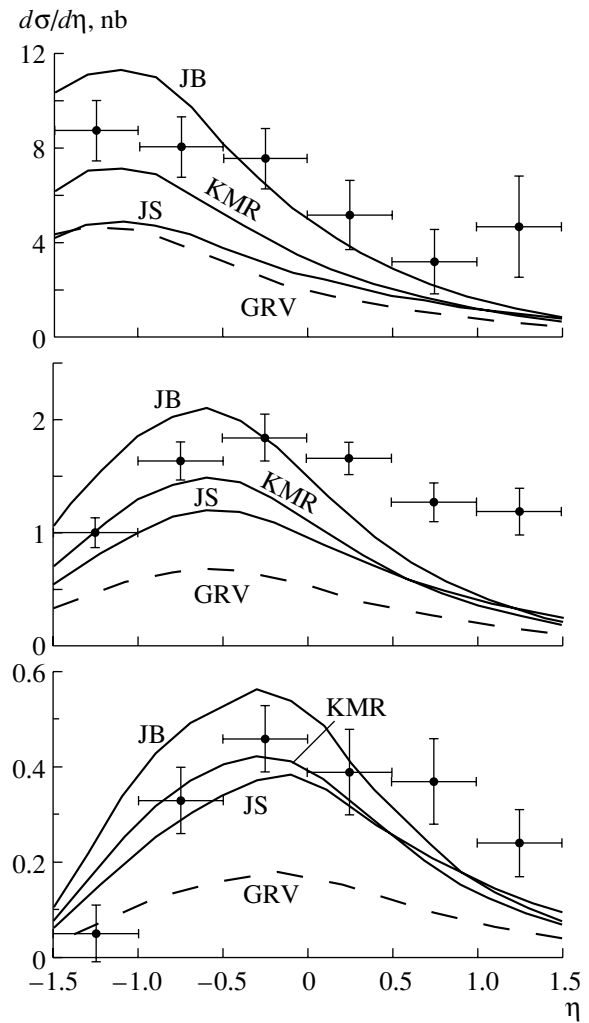
$d\sigma/d\eta$, nb

Fig. 6. Differential cross section for D^*-meson photoproduction as a function of the pseudorapidity η_{D^*} at various cuts on the transverse momentum of D^* mesons [$p_{D^*T} > 2, 4, 6$ GeV (from top to bottom)] and for W from the interval $130 < W < 280$ GeV.

Figure 6 displays the results of the present calculations for the η spectra of D^* mesons for various cuts on the D^*-meson transverse momentum p_{D^*T}. This spectrum demonstrates most clearly the distinctions between the predictions obtained by using the different parametrizations of unintegrated gluon distributions in the proton. Our results agree with the results reported in [13] if use is made of the JB parametrization [9].

Figure 7 shows the results of the present calculations for the W spectra of D^* mesons for various cuts on the D^*-meson transverse momentum p_{D^*T}. There are no experimental data on the W spectra in D^*-meson photoproduction, a significant scatter (by a factor of 2 to 3) of the theoretical predictions calling for experimental tests. A comparison with experimental data would make it possible to assess

uncertainties that are associated with the choice of various parametrizations for the noncollinear gluon distribution in the proton.

6. CONCLUSIONS

In the present study, we have shown that only for a specific choice of parametrization for the noncollinear gluon distribution in the proton do calculations with parton amplitudes in the leading order in the strong coupling constant within the k_T-factorization approach describe experimental data on $D^{*\pm}$-meson electro- and photoproduction at the HERA collider energies better than calculations within the collinear parton model (see also [3, 32]).

Our results for the p_T and η spectra of D^* mesons in photoproduction processes are in good agreement with the results obtained in [13], where the JB parametrization [9] was used for the noncollinear gluon distribution.

The main sources of uncertainties in theoretical calculations are the following: (i) the existing arbitrariness in the choice of c-quark mass (1.3– 1.8 GeV), a variation in the c-quark mass leading to a 30% change in the result (this is in accord with the results obtained in [14]); (ii) the uncertainties in the choice of fragmentation function and of the fragmentation parameter, they being about 15%; (iii) the errors in measuring the parameter ϵ in the fragmentation function for the transformation of a c quark into a $D^{*\pm}$ meson, which are about 25% of the result; (iv) the distinctions (by a factor of 1.5 to 2.5) between the predictions obtained by using different parametrizations of the unintegrated gluon distribution in the proton; and (v) the choice of renormalization scale μ^2 in the running strong coupling constant, this leading to a change in the total cross section by a factor of 1.5 to 2. By way of example, we indicate that, in [13, 14, 33], the argument of the running coupling constant was set to the Reggeized gluon virtuality $\mu^2 = \mathbf{k}_T^2$. Concurrently, the value of α_s is fixed in the region of low $\mathbf{k}_T^2$ ($\alpha_s(\mathbf{k}_T^2) = \alpha_{s,\max} \simeq 0.5$), or integration with respect to $\mathbf{k}_T^2$ is performed over the region $\mathbf{k}_T^2 \geq Q_0^2 \simeq 2$ GeV^2. In either case, one has to invoke additional assumptions and introduce new phenomenological parameters. Moreover, such a choice for processes involving a few Reggeized gluons or a few quark–gluon interaction vertices some of which have no bearing on a Reggeized gluon may lead to a violation of the gauge-invariance condition for the amplitudes if different values of μ^2 are chosen for different vertices. In the present calculations, we have set $\mu^2 = m_{D^*}^2 + \mathbf{p}_T^2 + Q^2$, where $Q^2 \to 0$ in the case of photoproduction.

$d\sigma/dW$, nb/GeV
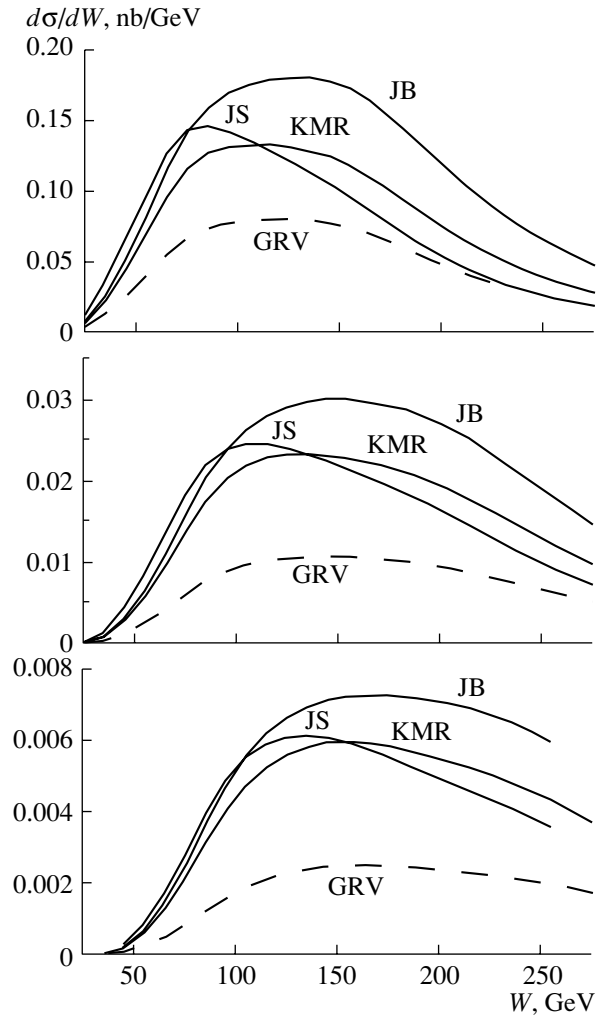
Fig. 7. Differential cross section for the photoproduction of D^* mesons as a function of the total energy W of the photon–proton interaction in the c.m. frame for various cuts on the transverse momentum of D^* mesons [$p_{D^*T} > 2, 4, 6$ GeV (from top to bottom)] and for $|\eta_{D^*}| < 1.5$.

We note that the choice of μ^2 with allowance for $\mathbf{k}_T^2$ in the quark–gluon interaction vertex, $\mu^2 = m_{D^*}^2 + \mathbf{p}_T^2 + Q^2 + \mathbf{k}_T^2$, introduces virtually no changes in the results because of a low power of α_s in the square of the absolute value of the $eg^* \to ec\bar{c}$ matrix element, a weak logarithmic dependence in $\alpha_s(\mu^2)$ at high μ^2, and a relatively small contribution from the region of high $\mathbf{k}_T^2$ due to the decrease in the unintegrated distributions with increasing $\mathbf{k}_T^2$.

ACKNOWLEDGMENTS

REFERENCES

1. Small-x Collab. (B. Andersson *et al.*), Eur. Phys. J. C **25**, 77 (2002).
2. V. A. Saleev and D. V. Vasin, Phys. Lett. B **548**, 161 (2002).
3. V. A. Saleev and D. V. Vasin, hep-ph/0209220 v2.
4. V. N. Gribov and L. N. Lipatov, Yad. Fiz. **15**, 781 (1972) [Sov. J. Nucl. Phys. **15**, 438 (1972)]; Yu. L. Dokshitser, Zh. Éksp. Teor. Fiz. **73**, 1216 (1977) [Sov. Phys. JETP **46**, 641 (1977)]; G. Altarelli and G. Parisi, Nucl. Phys. B **126**, 298 (1977).
5. E. A. Kuraev, L. N. Lipatov, and V. S. Fadin, Zh. Éksp. Teor. Fiz. **71**, 840 (1976) [Sov. Phys. JETP **44**, 443 (1976)]; I. I. Balitsky and L. N. Lipatov, Sov. J. Nucl. Phys. **28**, 822 (1978).
6. M. Ciafaloni, Nucl. Phys. B **296**, 49 (1988); S. Catani, F. Fiorani, and G. Marchesini, Phys. Lett. B **234**, 339 (1990); G. Marchesini, Nucl. Phys. B **445**, 49 (1995).
7. J. C. Collins and R. K. Ellis, Nucl. Phys. B **360**, 3 (1991).
8. M. Glück, E. Reya, and A. Vogt, Z. Phys. C **67**, 433 (1995).
9. J. Blumlein, DESY 95-121 (1995).
10. H. Jung and G. P. Salam, Eur. Phys. J. C **19**, 351 (2001).
11. M. A. Kimber, A. D. Martin, and M. G. Ryskin, Phys. Rev. D **63**, 114027 (2001).
12. B. A. Kniehl, G. Kramer, and M. Spira, Z. Phys. C **76**, 689 (1997).
13. S. P. Baranov, H. Jung, and N. P. Zotov, hep-ph/9910210.
14. S. P. Baranov, H. Jung, L. Jonsson, *et al.*, Eur. Phys. J. C **24**, 425 (2002); S. P. Baranov, H. Jung, and N. P. Zotov, Nucl. Phys. B (Proc. Suppl.) **99**, 192 (2001).
15. A. V. Berezhnoy, V. V. Kiselev, and A. K. Likhoded, hep-ph/9901333; Yad. Fiz. **63**, 1682 (2000) [Phys. At. Nucl. **63**, 1595 (2000)].
16. M. Kramer, Prog. Part. Nucl. Phys. **47**, 141 (2001); E. Braaten and T. C. Yuan, Phys. Rev. D **52**, 6627 (1995).
17. OPAL Collab. (R. Akers *et al.*), Z. Phys. C **67**, 27 (1995).
18. C. Peterson, D. Schlatter, I. Schmitt, and P. M. Zerwas, Phys. Rev. D **27**, 105 (1983).
19. Rev. Part. Phys. (Meson Particle Listing), Phys. Rev. D **54**, 468 (1996).
20. K. Anikeev *et al.*, Fermilab-Pub-01/197 (2001).
21. H1 Collab. (C. Adolf *et al.*), Nucl. Phys. B **545**, 21 (1999).
22. ZEUS Collab. (J. Breitweg *et al.*), Eur. Phys. J. C **6**, 67 (1999).
23. ZEUS Collab. (J. Breitweg *et al.*), Eur. Phys. J. C **12**, 35 (2000).
24. ZEUS Collab. (J. Breitweg *et al.*), Phys. Lett. B **481**, 213 (2000).
25. P. Nason and C. Oleari, Phys. Lett. B **447**, 327 (1999).
26. J. Binnewies, B. A. Kniehl, and G. Kramer, Phys. Rev. D **58**, 014014 (1998).
27. C. F. Weizsäcker, Z. Phys. **88**, 612 (1934); E. J. Williams, Phys. Rev. **45**, 729 (1934).
28. S. Frixione *et al.*, Phys. Lett. B **319**, 339 (1993).
29. J. Babcock, D. Sivers, and S. Wolfram, Phys. Rev. D **18**, 162 (1978).
30. S. Catani, M. Ciafaloni, and F. Hautmann, Nucl. Phys. B **366**, 135 (1991).
31. V. A. Saleev and N. P. Zotov, Mod. Phys. Lett. A **11**, 25 (1996).
32. V. A. Saleev and D. V. Vasin, Phys. Rev. D **68**, 114013 (2003).
33. A. V. Lipatov, V. A. Saleev, and N. P. Zotov, Mod. Phys. Lett. A **15**, 1727 (2000).

Translated by A. Isaakyan

ELEMENTARY PARTICLES AND FIELDS
Theory

Quark Regge Trajectory in Two Loops from Unitarity Relations*

A. V. Bogdan** and V. S. Fadin***

Budker Institute for Nuclear Physics, Siberian Division,
Russian Academy of Sciences, Novosibirsk, 630090 Russia;
Novosibirsk State University, Novosibirsk, 630090 Russia
Received April 15, 2004; in final form, February 28, 2005

Abstract—The two-loop quark Regge trajectory is obtained at arbitrary spacetime dimension D using the s-channel unitarity conditions. Although explicit calculations are performed for massless quarks, the method used allows one to find the trajectory for massive quarks as well. At $D \to 4$, the trajectory turns into one derived earlier from the high-energy limit of the two-loop amplitude for the quark−gluon scattering. The comparison of two expressions obtained by quite different methods serves as a strict cross check of many intermediate results used in the calculations, and their agreement gives strong evidence of accuracy of these results. © 2005 Pleiades Publishing, Inc.

1. INTRODUCTION

Perturbative QCD is widely used for the description of semihard [1] as well as hard processes [2]. But whereas the theory of the latter is clear and plain, a lot of problems remain unsolved for the former processes. The applicability of perturbation theory, improved by the renormalization group, to a hard process with a large typical virtuality Q^2 is justified by the smallness of the strong coupling constant $\alpha_s(Q^2)$. In the semihard case, however, smallness of the ratio x of the typical virtuality Q^2 to the squared c.m.s. energy s requires resummation of the terms strengthened by powers of $\ln(1/x)$. In the scattering channel, this problem is related to the theoretical description of high-energy amplitudes at fixed (not growing with s) momentum transfer t. It turns out, that the Gribov−Regge theory of complex angular momenta, which was developed much before the appearance of QCD, is eminently suitable for description of the QCD amplitudes, due to the remarkable property of QCD—Reggeization of its elementary particles, gluons and quarks [3−6]. The Reggeization means, in particular, that, with account of radiative corrections in the high-energy limit, the s dependence of QCD amplitudes with gluon (G) or quark (Q) quantum numbers in the t channel is given by Regge factors $(s)^{j_P(t)}$, with $P = G$ or $P = Q$, accordingly. The functions $j_P(t)$

with the property $j_P(m_P^2) = s_P$ (m_P and s_P are respective mass and spin values), called Regge trajectory, describe the motion of poles of the corresponding t-channel partial waves in the complex angular momentum plane. In this respect, QCD sharply differs from QED, where only amplitudes with electron exchange in the t channel [7], but not with photon one [8], acquire the Regge factors.

The Reggeization phenomenon is extremely important at high energy. The gluon Reggeization is especially significant, since gluon exchanges in the t channel provide nondecreasing cross sections at large s. In particular, the gluon Reggeization constitutes the basis of the famous BFKL approach [5, 9] to the theoretical description of high-energy processes in QCD. Initially, the BFKL approach was formulated in the leading logarithmic approximation (LLA). Now it is developed in the next-to-leading order (NLO) (for references, see, for instance, [10]) since LLA is not sufficiently reliable, especially because this approximation does not fix scales either longitudinal (for s) or transverse (for running coupling α_s) momenta. This development extensively uses gluon Reggeization, which has been proved in LLA [11], but in the next-to-leading approximation (NLA) still remains a hypothesis, although it has successfully passed through a set of stringent tests on self-consistency (see, for instance, [12] and references therein). Accordingly, the NLO gluon Regge trajectory and Reggeized gluon vertices are calculated; moreover, a way for the proof of gluon Reggeization in the NLA is outlined (see, e.g., [10] and references therein).

---
*This article was submitted by the authors in English.
**e-mail: A.V.Bogdan@inp.nsk.su
***e-mail: Fadin@inp.nsk.su
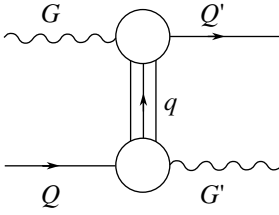
Fig. 1. Schematic representation of the backward quark–gluon scattering process $G + Q \to Q' + G'$. The triple line denotes an intermediate t-channel state with momentum $q = p_Q - p_{G'} = p_{Q'} - p_G$.

Along with the Pomeron, which appears in the BFKL approach as a compound state of two Reggeized gluons, the hadron phenomenology requires Reggeons, which can be constructed in QCD as colorless states of Reggeized quarks and antiquarks. It demands further development of Reggeized quark theory, which remains in a worse state than Reggeized gluon theory, although noticeable progress was achieved in recent years. In particular, multiparticle Reggeon vertices required in the NLA were found [13] and the NLO corrections to the LLA vertices were calculated [14, 15] assuming quark Reggeization in NLA. Note that the Reggeization hypothesis is extremely powerful; but in the quark case, it actually was not proved even in the LLA, where merely its self-consistency was shown, in all orders of α_s but only in a particular case of elastic quark–gluon scattering [6]. Recently, the hypothesis was tested at the NLO in order of α_s^2 in [16], where its compatibility with the two-loop amplitude for the quark–gluon scattering was exhibited and the NLO correction to the quark trajectory was found in the limit of the spacetime dimension D tending to the physical value $D = 4$.

In this paper, we investigate the quark Reggeization in the NLO by the method based on the s-channel unitarity and the analyticity of scattering amplitudes, which was developed for analysis of processes with gluon exchanges [4, 5] and was already successfully applied to processes with fermion exchanges [6]. The two-loop quark trajectory at arbitrary spacetime dimension D is obtained as a particular result of the investigation. At $D \to 4$, the trajectory goes into one derived in [16]. This agreement testifies to the accuracy of many intermediate results used in both derivations. In the method used here, the trajectory is obtained from the requirement of the compatibility of the Reggeized form of the amplitudes with the s-channel unitarity at the two-loop level. A possible generalization of this requirement to all orders of perturbation theory should give the "bootstrap" conditions on the Reggeized quark vertices and the trajectory in QCD. Verification of them will

give a strict test for quark Reggeization. A proof of the Reggeization is also possible in this way.

The calculation of the two-loop corrections to the quark trajectory is performed explicitly for massless quarks; but the method used here allows one to do it for massive quarks as well, since all necessary one-loop Reggeon vertices for the massive case are known now.

The paper is organized as follows. In the next section, all necessary notation is introduced and the method of calculation is discussed. Section 3 is devoted to the calculation of the two-particle contribution to the s-channel discontinuity of the quark–gluon scattering amplitude. The contribution of the three-particle intermediate state is calculated in Section 4. The final expressions for the discontinuity and the two-loop corrections to the quark trajectory are presented and discussed in Section 5. For convenience, the integrals encountered in Sections 3 and 4 are listed in Appendices A and B, respectively. Details of the calculation of a new nontrivial integral arising in present calculations are given in Appendix C.

2. NOTATION AND METHOD OF CALCULATION

Let us consider the backward quark–gluon scattering process (see Fig. 1) in the limit of large (tending to infinity) c.m.s. energy and fixed momentum transfer $t \equiv q^2 = (p_Q - p_{G'})^2$.

We use the Sudakov decomposition of momenta

$$p = \beta p_1 + \alpha p_2 + p_\perp,$$

$$p_1^2 = p_2^2 = 0, \quad (p_1 + p_2)^2 = s, \tag{1}$$
$$s\alpha\beta = p^2 - p_\perp^2,$$

supposing that the momenta $p_G, p_{Q'}$ and $p_Q, p_{G'}$ are close to the light-cone momenta p_1 and p_2, respectively, that is,

$$\beta_G \sim \beta_{Q'} \sim \alpha_Q \sim \alpha_{G'} \simeq 1, \tag{2}$$

$$\beta_Q \simeq \beta_{G'} \simeq \alpha_G \simeq \alpha_{Q'} \sim \frac{|t|}{s},$$

and all transverse momenta are limited, so that $q \simeq q_\perp$. We do not suppose that p_1 and p_2 are contained in the initial momentum plane, in order to maintain symmetry between cross channels and to make more evident substitutions for transitions between channels. For a gluon having momentum k_a (k_b) with predominant component along p_1 (p_2), we use physical polarization vectors in the light-cone gauge $e(k_a)p_2 = 0$ ($e(k_b)p_1 = 0$), so that

$$e(k_a) = e(k_a)_\perp - \frac{(e(k_a)k_a)_\perp}{k_a p_2} p_2, \tag{3}$$

$$e(k_b) = e(k_b)_\perp - \frac{(e(k_b)k_b)_\perp}{k_b p_1} p_1,$$

where $(ab)_\perp$ means $(a_\perp b_\perp)$. Furthermore, since with our choice of gauges gluon polarization vectors are expressed in terms of their transverse components, from this point forward, we will use only these components, without explicit indications, so that everywhere below e means $e_\perp$. The same we will do for the momentum transfer q.

The large-s and fixed-t limit of scattering amplitudes is related to quantum numbers in the t channel. For the gauge group $SU(N_c)$, the t-channel color state of the process depicted in Fig. 1 contains three irreducible representations of the color group (for QCD with $N_c = 3$, it is $\underline{3} \oplus \underline{\bar{6}} \oplus \underline{15}$). Therefore, it is natural to decompose the quark–gluon scattering amplitude into three parts, in accordance with the representations [6, 16]. At the same time, in the Gribov–Regge theory, each part must be decomposed into two pieces according to the new quantum number—signature—which is introduced in the theory. Besides quantum numbers, commonly used for particle classification, a Reggeon has definite signature, positive or negative, which is actually a parity of the t-channel partial waves with respect to the substitution $\cos\theta_t \to -\cos\theta_t$ (which turns into $s \to u = -s$ in the limit of large s and fixed t). Consequently, there are six terms $A_\chi^{(\pm)}$, $\chi = \underline{3}, \underline{\bar{6}}$, and $\underline{15}$ in full decomposition [6, 16] of the quark–gluon scattering amplitude. As is known [6], in the LLA only one of the positive signature amplitudes, namely $A_{\underline{3}}^{(+)}$, does survive; and at the same time, it has the Reggeized form. This is not so for the negative signature amplitudes. The Bethe–Salpeter-type equation obtained for them in the LLA [6] does not have a simple Regge-type solution (in fact, no solution has been found at all). Note that they are not actually leading in each order of perturbation theory, because leading logarithms cancel in them as the result of antisymmetry with respect to the exchange $s \to u = -s$. Below, we consider only the amplitudes of positive signature. As we will see, in the NLA, as well as in the LLA, only amplitudes with a color triplet in the t channel survive among them. For quark–gluon scattering, the contribution of the Reggeized quark can be represented as [here and below, we write symbols of initial (final) particles as lower (upper) indices of scattering amplitudes and place first the particles with momenta close to p_1]

$$\mathcal{R}_{GQ}^{Q'G'} = \Gamma_{Q'G} \frac{1}{m_Q - \hat{q}} \frac{1}{2} \tag{4}$$

$$\times \left[\left(\frac{-s}{-t}\right)^{\delta_T(\hat{q})} + \left(\frac{s}{-t}\right)^{\delta_T(\hat{q})} \right] \Gamma_{G'Q},$$

where $\Gamma_{Q'G}$ and $\Gamma_{G'Q}$ are effective vertices for interaction of particles (quarks and gluons) with the Reggeized quark; we call them PPR vertices, and we call $\delta_T(\hat{q})$ the quark trajectory. Strictly speaking, for massive quarks, there are two trajectories, in accordance with two possible parity states for an off-mass-shell quark. These trajectories are determined by eigenvalues of $\delta_T(\hat{q})$. We perform actual calculations for the massless case, when $\delta_T(\hat{q})$ depends in fact not on $\hat{q}$, but on $\hat{q}^2 = t$, and write it as $\delta_T(t)$. Note, however, that the PPR vertices $\Gamma_{Q'G}$ and $\Gamma_{G'Q}$ are known now for massive quarks [15], so that all consideration presented below can be transferred to the massive case in a straightforward way.

We demonstrate that the Reggeized form (4) is compatible with the s-channel unitarity and obtain the NLO contribution to the trajectory δ_T. More precisely, we calculate, using the unitarity relation, both logarithmic and nonlogarithmic terms in the two-loop s-channel discontinuity of the backward quark–gluon scattering amplitude with positive signature and prove that only color triplet t-channel states contribute to the discontinuity. It means that only the color triplet part $A_{\underline{3}}^{(+)}$ of the amplitude survives at NLO as well as at LO. We compare the calculated discontinuity with the discontinuity of the Reggeized quark contribution (4). The logarithmic terms of confronted discontinuities turn out to be equal. The nonlogarithmic terms in the discontinuity of (4) are expressed through the one-loop corrections to the PPR vertices, which are known, and the two-loop correction to the trajectory, which makes it possible to obtain the last correction.

For massless quarks, the PPR vertices entering in (4) have the form [14]

$$\Gamma_{Q'G} = -g\bar{u}(p_{Q'})t^G \tag{5}$$

$$\times \left[\hat{e}_G(1 + \delta_e(t)) + \frac{(e_G q)\hat{q}}{q^2} \delta_q(t) \right],$$

$$\Gamma_{G'Q} = -g\left[\hat{e}_{G'}^*(1 + \delta_e(t)) + \frac{(e_{G'}^* q)\hat{q}}{q^2} \delta_q(t) \right]$$

$$\times t^{G'} u(p_Q).$$

Here, t^G and $t^{G'}$ are the color group generators in the fundamental representation; we omit color wave functions for gluons and assume that they are included in $u(p_Q)$, $\bar{u}(p_{Q'})$ for quarks. The one-loop corrections $\delta_e(t)$, $\delta_q(t)$ can be written as

$$\delta_e(t) = \omega^{(1)}(t)\delta_e^{(1)}, \quad \delta_q(t) = \omega^{(1)}(t)\delta_q^{(1)}, \tag{6}$$

where

$$\delta_e^{(1)} = \frac{C_F}{2N_c}\left(\frac{1}{\epsilon} - \frac{3(1-\epsilon)}{2(1+2\epsilon)} \right) \tag{7}$$

$$+ \psi(1) + \psi(1 - \epsilon) - 2\psi(1 + \epsilon) \Bigg) + \frac{1}{2\epsilon} - \frac{\epsilon}{2(1 + 2\epsilon)},$$

$$\delta_q^{(1)} = \frac{\epsilon}{2(1 + 2\epsilon)} \left(1 + \frac{1}{N_c^2}\right),$$

$\psi(x) = \Gamma'(x)/\Gamma(x)$ is the logarithmic derivative of the Euler gamma function, and $\omega^{(1)}(t)$ is the one-loop gluon Regge trajectory:

$$\omega^{(1)}(t) = -\frac{2N_c}{\epsilon} \frac{g_s^2}{(4\pi)^{2+\epsilon}} \left(\frac{\mu^2}{-t}\right)^{-\epsilon} \Gamma_\epsilon, \qquad (8)$$

$$\Gamma_\epsilon = \frac{\Gamma^2(1 + \epsilon)\Gamma(1 - \epsilon)}{\Gamma(1 + 2\epsilon)}.$$

We use conventional dimensional regularization; the spacetime dimension $D = 4 + 2\epsilon$ and $g_s = g\mu^\epsilon$ is the dimensionless bare coupling constant.

To avoid uncertainties, let us note that the vertices $\Gamma_{G\bar{Q}}$ and $\Gamma_{\bar{Q}G'}$ are obtained from (5) by the substitutions $\bar{u}(p_{Q'}) \to \bar{v}(p_{\bar{Q}}), e_G \to e_G^*$ and $u(p_Q) \to v(p_{\bar{Q}}), e_{G'}^* \to e_{G'}$, respectively.

Representing the quark trajectory as

$$\delta_T(t) = \frac{\omega^{(1)}(t)}{N_c} \delta_T^{(1)} + \frac{1}{2} \left(\frac{\omega^{(1)}(t)}{N_c}\right)^2 \delta_T^{(2)}, \qquad (9)$$

where $\delta_T^{(1)} = C_F$ [6], and the two-loop s-channel discontinuity of the Reggeized quark contribution (4) as

$$\left[\mathcal{R}_{GQ}^{Q'G'}(\text{two-loop})\right]_s \qquad (10)$$

$$= \frac{i\pi g^2}{t} \frac{1}{2} \left(\frac{\omega^{(1)}(t)}{N_c}\right)^2 \bar{u}(p_{Q'}) t^G t^{G'} \Delta_R u(p_Q),$$

we have from (4), (5), (9), and (6)

$$\Delta_R = \delta_T^{(2)} \hat{\mathcal{Q}} + 2C_F \qquad (11)$$

$$\times \left(2N_c \delta_e^{(1)} + C_F \ln \frac{s}{-t}\right) \hat{\mathcal{Q}} + 2C_F N_c \delta_q^{(1)} \hat{\mathcal{E}},$$

where

$$\hat{\mathcal{Q}} = \hat{e}_G \hat{q} \hat{e}_{G'}^*, \quad \hat{\mathcal{E}} = \hat{e}_G(e_{G'}^* q) + \hat{e}_{G'}^*(e_G q), \qquad (12)$$

and $\delta_e^{(1)}$, $\delta_q^{(1)}$ are given by (7).

Below we calculate the discontinuity $\left[\left(A^{(+)}\right)_{GQ}^{Q'G'} (\text{two-loop})\right]_s$ of the backward quark–gluon scattering amplitude with positive signature from the s-channel unitarity condition. We show that it has the same color structure as $\left[\mathcal{R}_{GQ}^{Q'G'} (\text{two-loop})\right]_s$ (10); i.e., in this approximation, only the color triplet state survives in the positive signature. Writing the calculated discontinuity in the same form as the

right-hand side of (10) with Δ_s instead of Δ_R, we see that Δ_s has the same helicity structure as Δ_R (11) and that their logarithmic terms coincide; moreover, the nonlogarithmic terms at the helicity nonconserving structure $\hat{\mathcal{E}}$ also coincide. After that, the requirement of equality of the nonlogarithmic terms at the helicity conserving structure $\hat{\mathcal{Q}}$ gives us $\delta_T^{(2)}$.

The calculation of Δ_s is the main content of this paper. It is determined from the s-channel unitarity relation:

$$\left[\left(A^{(+)}\right)_{GQ}^{Q'G'} (\text{two-loop})\right]_s \qquad (13)$$

$$= \frac{i\pi g^2}{t} \frac{1}{2} \left(\frac{\omega^{(1)}(t)}{N_c}\right)^2 \bar{u}(p_{Q'}) t^G t^{G'} \Delta_s u(p_Q)$$

$$= iP^{(+)} \sum_n \int d\Phi_n A_{GQ}^n \left(A_{Q'G'}^n\right)^*,$$

where Φ_n is the n-particle phase-space element and $P^{(+)}$ is the positive signature projector. The summation is performed over two- and three-particle intermediate states; accordingly, we represent the discontinuity as the sum of two contributions

$$\Delta_s = \Delta_s^{(2)} + \Delta_s^{(3)}. \qquad (14)$$

The projection on the positive signature means the half-sum of the s-channel discontinuities for the direct ($GQ \to Q'G'$) and crossed ($G\tilde{G} \to Q'\bar{Q}'$) processes. More precisely, if one represents the discontinuity of the direct processes as $\langle Q'G'|M|GQ\rangle$, where $|GQ\rangle$ is a spin and color quark–gluon wave function, and the discontinuity for the process $G\tilde{G} \to Q'\bar{Q}'$ with $p_{\tilde{G}} = p_Q$, $p_{\bar{Q}'} = p_{G'}$ as $\langle Q'\bar{Q}'|M_c|G\tilde{G}\rangle$, then the projection on the positive signature is $\langle Q'G'|(M + M_c)/2|GQ\rangle$. Note that, calculating Δ_s, we always use the fact that the rightmost $\hat{p}_2$ and leftmost $\hat{p}_1$ in M and M_c give negligible contributions because of the Dirac equation.

3. TWO-PARTICLE CONTRIBUTION TO THE DISCONTINUITY

In the direct channel, a two-particle intermediate state can be solely a quark–gluon one. Since only limited transverse momenta of intermediate particles are important in the unitarity relation (we will see it directly; actually, it is a consequence of the renormalizability), non-negligible contributions are given by two nonoverlapping kinematical regions. In one of them, the intermediate gluon momentum is close to p_G (see Fig. 2a), and in another, it is close to p_Q
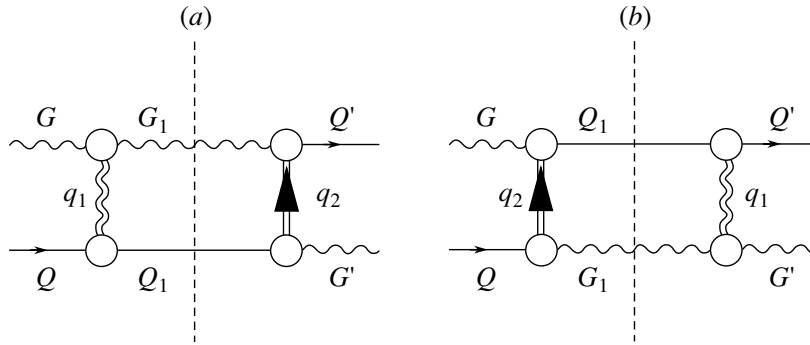
Fig. 2. Schematic representation of the two-particle contribution to the s-channel discontinuity of the backward quark–gluon scattering amplitude. The double lines represent Reggeized quark and gluon, and the blobs, PPR vertices.

(Fig. 2b). In both cases, the amplitudes on the right-hand side of the unitarity relation (13) are in Regge-type kinematics.

As we need to calculate the two-loop contribution to the discontinuity, one of them has to be taken in the Born approximation and another one in the one-loop approximation. An important point is that since Born amplitudes are real, only real parts of one-loop amplitudes are essential for the calculation of the discontinuity. Therefore, required amplitudes are determined by Reggeized quark and gluon contributions. Moreover, we can use $A_n^{Q'G'}$ instead of $\left(A_{Q'G'}^n\right)^*$, as imaginary parts of the amplitudes are not important.

The amplitudes with t-channel quarks can be obtained by evident substitutions from (4). Using Eqs. (5), (6), for the process $G + Q \to Q' + G'$, we have with required accuracy

$$A_{GQ}^{Q'G'} = \frac{g^2}{-q^2}\bar{u}(p_{Q'})t^G t^{G'}\Bigg\{\hat{e}_G\hat{q}\hat{e}_{G'}^* \qquad (15)$$

$$\times\left[1 + \omega^{(1)}(q^2)\left(2\delta_e^{(1)} + \frac{C_F}{N_c}\ln\frac{s}{-q^2}\right)\right]$$

$$+ \omega^{(1)}(q^2)\delta_q^{(1)}\left[\hat{e}_G(e_{G'}^*q) + (e_Gq)\hat{e}_{G'}^*\right]\Bigg\}u(p_Q),$$

where $q = p_Q - p_{G'}$.

In the following, in the amplitudes on the right-hand side of (13), we denote Reggeized gluon and quark momenta q_1 and q_2, respectively, $q_1 + q_2 = q$, and Reggeized gluon color index r. Since $q_1 \simeq q_{1\perp}, q_2 \simeq q_{2\perp}$, everywhere below we omit the sign $\perp$ at $q_{1,2}$, so that q_i means $q_{i\perp}, i = 1, 2$.

Amplitudes for processes $AB \to A'B'$ with gluon exchanges with our accuracy are written as

$$\mathcal{A}_{AB}^{A'B'} = \frac{2s}{q_1^2}\Gamma_{A'A}^r\left(1 + \omega^{(1)}(q_1^2)\ln\frac{s}{-q_1^2}\right)\Gamma_{B'B}^r,$$
$$(16)$$

where $\Gamma_{A'A}^r$ and $\Gamma_{B'B}^r$ are Reggeized gluon vertices, which can be found in [12]. In the direct channel, we need quark–gluon scattering amplitudes. For the process $G + Q \to G_1 + Q_1$ (see the left part of Fig. 2a), we obtain

$$A_{GQ}^{G_1Q_1} = \frac{2g^2 s}{q_1^2}T_{G_1G}^r\bar{u}(p_{Q_1})t^r\frac{\hat{p}_1}{s}u(p_Q) \qquad (17)$$

$$\times\Bigg\{-(e_{G_1}^*e_G)\Big[1 + \omega^{(1)}(q_1^2)$$

$$\times\left(\delta_G^{(1+)} + \delta_G^{(1-)} + \delta_Q^{(1)} + \ln\frac{s}{-q_1^2}\right)\Big]$$

$$+ \omega^{(1)}(q_1^2)(D-2)\frac{(e_{G_1}^*q_1)(e_Gq_1)}{q_1^2}\delta_G^{(1-)}\Bigg\},$$

where $T_{G_1G}^r$ are color generators in the adjoint representation; $q_1 = (p_{G_1} - p_G)_\perp$; δ_Q represents the one-loop corrections to the quark–quark–Reggeon vertex,

$$\delta_Q^{(1)} = \frac{1}{2}\Bigg[\frac{1}{\epsilon} + \psi(1-\epsilon) + \psi(1) - 2\psi(1+\epsilon) \quad (18)$$

$$+ \frac{2+\epsilon}{2(1+2\epsilon)(3+2\epsilon)} - \frac{1}{2N_c^2}\left(1 + \frac{2}{\epsilon(1+2\epsilon)}\right)$$

$$- \frac{n_f}{N_c}\frac{1+\epsilon}{(1+2\epsilon)(3+2\epsilon)}\Bigg],$$

n_f being the number of quark flavors; and $\delta_G^{(1+)}$ and $\delta_G^{(1-)}$ represent helicity-conserving and helicity-violating corrections to the gluon–gluon–Reggeon vertex,

$$\delta_G^{(1+)} = \frac{1}{2}\Bigg[\frac{2}{\epsilon} + \psi(1-\epsilon) + \psi(1) \qquad (19)$$

$$- 2\psi(1+\epsilon) - \frac{9(1+\epsilon)^2 + 2}{2(1+\epsilon)(1+2\epsilon)(3+2\epsilon)}$$

$$+ \frac{n_f}{N_c} \frac{(1+\epsilon)^3 + \epsilon^2}{(1+\epsilon)^2(1+2\epsilon)(3+2\epsilon)} \Bigg],$$

$$\delta_G^{(1-)} = \frac{\epsilon}{2(1+\epsilon)(1+2\epsilon)(3+2\epsilon)}$$

$$\times \left(-1 + \frac{n_f}{N_c(1+\epsilon)} \right).$$

Note that, in order to obtain $A_{Q_1 G_1}^{Q'G'}$ (see the right part of Fig. 2b) from (17), one has to change $\hat{p}_1$ to $\hat{p}_2$ besides evident substitution of symbols.

In addition to the presented amplitudes, in the crossed channel, we need gluon–gluon and quark–antiquark forward scattering amplitudes (see Fig. 3).

The first (see the left part of Fig. 3a) is written as

$$A_{G\tilde{G}}^{G_1\tilde{G}_1} = \frac{2g^2 s}{q_1^2} T_{G_1 G}^r T_{\tilde{G}_1 \tilde{G}}^r \Bigg\{ (e_{G_1}^* e_G)(e_{\tilde{G}_1}^* e_{\tilde{G}}) \left[1 + \omega^{(1)}(q_1^2) \left(2\delta_G^{(1+)} + 2\delta_G^{(1-)} + \ln\frac{s}{-q_1^2} \right) \right] \tag{20}$$

$$- \omega^{(1)}(q_1^2)(D-2) \frac{\left((e_{G_1}^* e_G)(e_{\tilde{G}_1}^* q_1)(e_{\tilde{G}} q_1) + (e_{G_1}^* q_1)(e_G q_1)(e_{\tilde{G}_1}^* e_{\tilde{G}}) \right)}{q_1^2} \delta_G^{(1-)} \Bigg\},$$

and the second (see the right part of Fig. 3b)

$$A_{Q_1 \bar{Q}_1}^{Q'\bar{Q}'} = -\frac{2g^2 s}{q_1^2} \bar{u}(p_{Q'}) t^r \frac{\hat{p}_2}{s} u(p_{Q_1}) \bar{v}(p_{\bar{Q}_1}) \tag{21}$$

$$\times t^r \frac{\hat{p}_1}{s} v(p_{\bar{Q}'}) \left[1 + \omega^{(1)}(q_1^2) \left(2\delta_Q^{(1)} + \ln\frac{s}{-q_1^2} \right) \right].$$

Before starting with the calculation, let us show that only a color triplet state survives in the discontinuity, due to cancellation of contributions of all other color states in the direct and crossed channels. In fact, this cancellation has the same nature as in the leading order [6]. The point is that, if a one-loop contribution is taken for one of the PPR vertices in Figs. 2 and 3, then all other vertices must be taken at NLO in the Born approximation. Therefore, either both lower or both upper vertices are Born ones. Let us consider the first case. Since the upper parts of the diagrams Fig. 2a and Fig. 3a are equal, contributions to $M + M_c$ from the lower lines enter as the sum

$$\gamma_\perp^\mu t^{G'} \sum_\lambda u^\lambda(p_{Q_1}) \bar{u}^\lambda(p_{Q_1}) t^r \frac{\hat{p}_1}{s} \tag{22}$$

$$- \sum_\lambda \hat{e}_{\tilde{G}_1}^\lambda t^{\tilde{G}_1} \left(e_{\tilde{G}_1}^\lambda \right)^{*\mu} T_{\tilde{G}_1 G'}^r = \gamma_\perp^\mu t^r t^{G'}.$$

Here, we have omitted terms with leftmost $\hat{p}_1$ because of the reason explained above and have taken the same Lorentz and color indices of the gluons G' and $\tilde{G}$ as we do not write their wave functions. It is easy to see that the lower lines of Fig. 2b and Fig. 3b give in sum the same result. Since $t^r t^{G'}$ projects the t-channel quark–gluon state on a color triplet, it

means that contributions of other color states cancel in the sum of the direct and cross channels. The case when both upper vertices are Born ones can be considered quite analogously. One can come to the same conclusion seeing that sum of contributions of Fig. 2a and Fig. 3b, as well as Fig. 2b and Fig. 3a, is proportional to $t^G t^r$. It is not difficult to understand that the cancellation of color states different from a triplet is not restricted by the considered diagrams or by the two-loop approximation, but is a general property of the NLA, as well as the LLA.

Since we have shown that only a color triplet survives in the t channel, we can write

$$P_3^{(+)} \sum_{P_1 P_2} A_{GQ}^{P_1 P_2} \left(A_{Q'G'}^{P_1 P_2} \right)^* \tag{23}$$

$$= g^4 \omega^{(1)}(t) s \bar{u}(p_{Q'}) t^G t^{G'} \mathcal{M}^{(2)} u(p_Q).$$

With the amplitudes listed above, calculation of $\mathcal{M}^{(2)}$ is straightforward. Dividing it into two pieces, $\mathcal{M}^{(2)} = \mathcal{M}_Q^{(2)} + \mathcal{M}_G^{(2)}$, one of which contains one-loop corrections for a quark channel and another for a gluon channel, we obtain

$$\mathcal{M}_Q^{(2)} = \left(\frac{q^2}{q_2^2} \right)^{-\epsilon} \frac{C_F}{q_1^2 q_2^2} \tag{24}$$

$$\times \Bigg\{ \left(2\delta_e^{(1)} + \frac{C_F}{N_c} \ln\frac{s}{-q_2^2} \right) \hat{e}_G \hat{q}_2 \hat{e}_{G'}^*$$

$$+ \delta_q^{(1)} [\hat{e}_G (e_{G'}^* q_2) + (e_G q_2) \hat{e}_{G'}^*] \Bigg\}$$
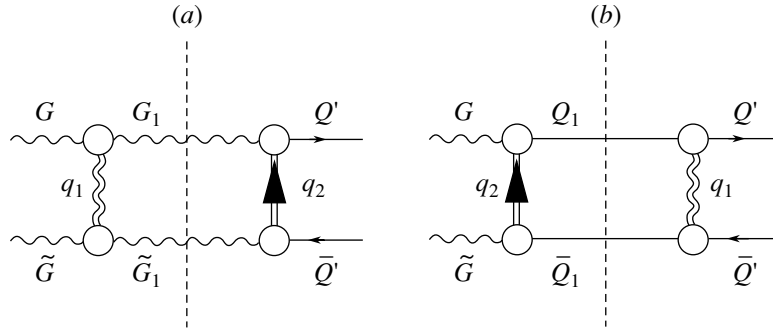
Fig. 3. Schematic representation of the two-particle contribution to the cross-channel discontinuity of the backward quark−gluon scattering amplitude.

and

$$\mathcal{M}_G^{(2)} = \left(\frac{q^2}{q_1^2}\right)^{-\epsilon} \frac{1}{q_2^2 q_1^2} \left\{ \left[-\frac{1}{N_c}\delta_Q^{(1)} \right. \right. \tag{25}$$

$$+ N_c \left(\delta_G^{(1+)} + \delta_G^{(1-)}\right) + C_F \ln\frac{s}{-q_1^2} \bigg]$$

$$\times \hat{e}_G \hat{q}_2 \hat{e}_{G'}^* - \frac{N_c}{2}\frac{D-2}{q_1^2}\delta_G^{(1-)}$$

$$\times [\hat{e}_G\hat{q}_2\hat{q}_1(e_{G'}^* q_1) + (e_G q_1)\hat{q}_1\hat{q}_2\hat{e}_{G'}^*] \bigg\}.$$

Integration over the phase-space element $d\Phi_2 = d^{D-2}q_2/(2s(2\pi)^{D-2})$ is quite simple. The integrals are well convergent at large $|q_2|$, so that the integration region can be expanded to infinity. For convenience of the reader, we present necessary formulas in Appendix A. As a result, we obtain for the two-particle contribution to Δ_s

$$\Delta_s^{(2)} = \frac{2N_c\epsilon(-q^2)^{1-\epsilon}}{\Gamma_\epsilon \pi^{(D-2)/2}} \int d^{D-2}q_2 \mathcal{M}^{(2)} \tag{26}$$

$$= 2N_c X_\Gamma \bigg\{ 2C_F\delta_e^{(1)} + \frac{N_c}{2}\left(\delta_G^{(1+)} - \frac{2\epsilon}{1-\epsilon}\delta_G^{(1-)}\right)$$

$$- \frac{1}{2N_c}\delta_Q^{(1)} + \frac{C_F^2}{N_c}\left(\ln\frac{s}{-t} + \Psi_1\right)$$

$$+ \frac{C_F}{2}\left(\ln\frac{s}{-t} + \Psi_1 + \frac{1}{2\epsilon}\right)\bigg\}\hat{\mathcal{Q}}$$

$$+ X_\Gamma \left\{ C_F\delta_q^{(1)} + N_c\frac{\epsilon(1+\epsilon)}{1-\epsilon}\delta_G^{(1-)}\right\}\hat{\mathcal{E}},$$

where

$$X_\Gamma = \frac{\Gamma(1-2\epsilon)\Gamma^2(1+2\epsilon)}{\Gamma(1+\epsilon)\Gamma(1+3\epsilon)\Gamma^2(1-\epsilon)}, \tag{27}$$

and

$$\Psi_1 = \psi(1-2\epsilon) + \psi(1+3\epsilon) \tag{28}$$
$$- \psi(1+2\epsilon) - \psi(1-\epsilon).$$

4. THREE-PARTICLE CONTRIBUTION TO THE DISCONTINUITY

Let us denote intermediate particles in the unitarity condition (13) P_j and their momenta $k_j, j = 1-3$. Just as before, only limited transverse momenta are important. As for longitudinal momenta, let us set (without loss of generality) $\alpha_3 \simeq 1$; that is, for the direct process $G + Q \to Q' + G'$, a particle P_3 is produced in the fragmentation region of the initial quark (note that, for the crossed process $G + \tilde{G} \to Q' + \bar{Q}'$, it is the region of $\tilde{G}$ fragmentation). Then $\beta_1 + \beta_2 \simeq 1$; i.e., at least one of the particles $P_i, i = 1, 2$, is produced in the gluon fragmentation region. Let it be P_1; then $\beta_1 \sim 1$, but β_2 can vary from $\beta_2 \sim 1$ (which means P_2 as well as P_1 is produced in the gluon fragmentation region) to $\beta_2 \sim |k_{2\perp}^2|/s$ (which means $\alpha_2 \sim 1$, i.e., P_2 is in the quark fragmentation region). Of course, the same with substitution $1 \leftrightarrow 2$ can be said for the case when in the gluon fragmentation region particle P_2 is produced. Note that region $1 \gg \beta_i \gg |k_{i\perp}^2|/s$ is usually called multi-Regge or central region for a particle P_i. But this region does not require separate consideration, because amplitudes for production of P_i in any of the fragmentation regions are applicable in it. Actually, natural bounds for domains of applicability of these amplitudes are $\alpha_i \ll 1$ for the gluon and $\beta_i \ll 1$ for the quark fragmentation regions. Therefore, it is sufficient to consider two regions: $1 \geq \beta_i \geq \sqrt{|k_{i\perp}^2|/s}$ and

$1 \geq \alpha_i \geq \sqrt{|k_{i\perp}^2|/s}$. For brevity, we will say that, in the first (second) case, there are two particles in the gluon (quark) fragmentation region. Moreover, the symmetry with respect to $\alpha \leftrightarrow \beta$ in the definition of the regions permits one to consider only one of them. Indeed, as regards the inverse reaction $(Q' + G' \to G + Q)$, the names of the regions must be changed; therefore their contribution to the discontinuity is related by the substitutions $Q \leftrightarrow Q', G \leftrightarrow G'$ and com-

plex conjugation. We will consider the gluon fragmentation region.

In this region, amplitudes on the right-hand side of the unitarity relation (13) can be written, in accordance with our agreement about notation, as

$$A_{AB}^{P_1P_2P_3} = \frac{2s}{q_1^2} \Gamma_{\{P_1P_2\}A}^r \Gamma_{P_3B}^r \qquad (29)$$

and

$$A_{AB}^{P_1P_2P_3} = \Gamma_{\{P_1P_2\}A} \frac{-\hat{q}_2}{q_2^2} \Gamma_{P_3B} \qquad (30)$$

for gluon and quark exchanges, respectively, with the same vertices $\Gamma_{P_3B}^r$ and Γ_{P_3B} as for the elastic amplitudes, but taken now in the Born approximation only. Therefore, as well as in the two-particle contribution, only the t-channel color triplet survives in positive signature since

$$P^{(+)} \sum_{P_3} \Gamma_{P_3Q}^r (\Gamma_{P_3G'}^r)^* \qquad (31)$$

$$= -P^{(+)} \sum_{P_3} \Gamma_{P_3Q} (\Gamma_{P_3G'}^r)^* = -\frac{g^2}{2} t^r t^{G'} \hat{e}_{G'}^* u(p_Q).$$

The vertices $\Gamma_{\{P_1P_2\}A}^r$ and $\Gamma_{\{P_1P_2\}A}$ can be found in [12] and [13], respectively. Actually, they can be easily calculated since are given by Born amplitudes for processes $A + R \to P_1 + P_2$, where R is either a gluon (for $\Gamma_{\{P_1P_2\}A}^r$) with momentum q_1, color index r, and polarization vector p_2/s (p_1/s) for a particle A with predominant momentum components along p_1 (p_2) or a quark (for $\Gamma_{\{P_1P_2\}A}$) with momentum q_2 and omitted quark wave function. An important point is that the corresponding light-cone gauge [see (3)] must be taken not only for real gluons, but for virtual ones as well. Note that the Hermitian property of Born amplitudes gives the relations

$$\left(\Gamma_{\{P_1P_2\}Q'}^r\right)^* = \Gamma_{Q'\{P_1P_2\}}^r, \qquad (32)$$

$$\left(\Gamma_{\{P_1P_2\}Q'}\right)^\dagger = \Gamma_{Q'\{P_1P_2\}} \gamma^0,$$

which we use in the following.

Let us denote

$$\sum_{P_1P_2} \left(\Gamma_{\{P_1P_2\}G}^r \Gamma_{Q'\{P_1P_2\}} - \Gamma_{\{P_1P_2\}G} \Gamma_{Q'\{P_1P_2\}}^r\right) t^r$$

$$\qquad (33)$$

$$= g^4 \bar{u}(p_{Q'}) t^G F_G .$$

The particles P_1 and P_2 can be two gluons (G_1G_2), quark and gluon (Q_1G_2), and quark and antiquark ($Q_1\bar{Q}_2$). Evidently, only the first (second) term on the left-hand side of (33) contributes in the first and third cases (in the second case). Using the fact that the

phase-space element $d\Phi_3$ in the gluon fragmentation region looks like

$$d\Phi_3 = \delta(1 - \beta_1 - \beta_2) \frac{d\beta_1 d\beta_2}{4s\beta_1\beta_2} \frac{d^{D-2}k_1 d^{D-2}k_2}{(2\pi)^{2D-3}}, \quad (34)$$

with the help of (29)–(31), we obtain the contribution of this region to Δ_s (13) in the form

$$\Delta_s^{(3)G} = -\frac{\epsilon^2(-q^2)^{1-2\epsilon}}{\pi^{(D-2)}\Gamma_\epsilon^2} \int \frac{d\beta_1 d\beta_2}{\beta_1\beta_2} \qquad (35)$$

$$\times \frac{d^{D-2}k_1 d^{D-2}k_2}{q_1^2 q_2^2} F_G \hat{q}_2 \hat{e}_{G'}^* \delta(1 - \beta_1 - \beta_2)$$

$$\times \theta\left(\beta_1 - \sqrt{\frac{|k_{1\perp}^2|}{s}}\right) \theta\left(\beta_2 - \sqrt{\frac{|k_{2\perp}^2|}{s}}\right),$$

where q_1 and q_2 are the momenta of t-channel gluon and quark, respectively, $q_1 + q_2 = q$. As was already pointed out, the total three-particle contribution can be written then as

$$\Delta_s^{(3)} = \Delta_s^{(3)G} + \bar{\Delta}_s^{(3)G}(G \to G'), \qquad (36)$$

where $\bar{\Delta} = \gamma^0 \Delta^\dagger \gamma^0$. Note that logarithms of s appear in $\Delta_s^{(3)G}$ from integration over β_i of those terms in F_G which do not go to zero at $\beta_i \to 0$. It is always possible to rewrite F_G as a sum of terms which go to zero either at $\beta_1 = 0$ or at $\beta_2 = 0$. For the first (second) of them, the limitation $\beta_1 > \sqrt{|k_{1\perp}^2|/s}$ ($\beta_2 > \sqrt{|k_{2\perp}^2|/s}$) can be taken away; the change of variables $k_{1\perp} = \beta_1 l_{1\perp}$ ($k_{2\perp} = \beta_2 l_{2\perp}$) often turns out to be useful, and we meet integrals

$$\int_{\sqrt{|k_{i\perp}^2|/s}}^1 \frac{d\beta_i}{\beta_i}(1 - \beta_i)^\delta \qquad (37)$$

$$= \frac{1}{2}\ln\frac{s}{|k_{i\perp}^2|} + \psi(1) - \psi(\delta + 1),$$

where δ is proportional to ϵ.

Calculation of integrals without $\ln|k_{i\perp}^2|$ does not present a problem. The list of basis integrals is presented in Appendix B. On the contrary, two of the integrals with $\ln|k_{i\perp}^2|$ cannot be expressed in terms of elementary functions at arbitrary ϵ. Besides the integral I_0 [see (46)] already encountered in the calculations of the two-loop gluon Regge trajectory, here we meet a new nontrivial integral I_1 [see (47)] below, which is considered in Appendix C.

In the following, we will use Eqs. (33), (35), (36) and the notation

$$k_{iG} = (k_i - \beta_i p_G)_\perp, \quad k_{iQ'} = (k_i - \beta_i p_{Q'})_\perp, \quad (38)$$

$$k_{12} = -k_{21} = (\beta_2 k_1 - \beta_1 k_2)_\perp.$$

It is easy to understand that k_{iA} $(i = 1, 2)$ is the transverse part of k_i with respect to the p_A, p_2 plane, multiplied by β_A.

Since the integration in (35) is symmetric with respect to exchange $k_1 \leftrightarrow k_2$, we will systematically omit in F_G contributions antisymmetric in relation to this exchange, without further reminding.

4.1. Fragmentation into Two Gluons

The vertex for production of the gluons G_1, G_2 with color indices i_1, i_2 by the initial gluon G can be written as

$$\Gamma^r_{\{G_1 G_2\}G} = g^2 \left\{ (T^G T^r)_{i_1 i_2} \left[\gamma^{\mu\nu}(k_{1G}) \right. \right. \tag{39}$$

$$\left. \left. - \gamma^{\mu\nu}(k_{12}) \right] e_{1\mu}^* e_{2\nu}^* + (1 \leftrightarrow 2) \right\},$$

where

$$\gamma^{\mu\nu}(p) = \frac{2}{p^2} \left[\beta_1 \beta_2 g_\perp^{\mu\nu}(e_G p) - \beta_1 e_G^\mu p^\nu - \beta_2 p^\mu e_G^\nu \right].$$

The vertex for a quark exchange can be taken in [13]. Using Sudakov parametrization and omitting terms with rightmost $\hat{p}_2$, we have for it

$$\Gamma_{Q'\{G_1 G_2\}} = -g^2 \bar{u}(p_{Q'}) \tag{40}$$

$$\times \left\{ t^{i_1} t^{i_2} \left[\gamma_{12}^{\mu\nu} - \gamma_{[12]}^{\mu\nu} \right] e_{1\mu} e_{2\nu} + (1 \leftrightarrow 2) \right\},$$

where

$$\gamma_{12}^{\mu\nu} = \frac{1}{k_{1Q'}^2} \left(\beta_1 \hat{k}_{1Q'} \gamma_\perp^\mu - 2 k_{1Q'}^\mu \right) \gamma_\perp^\nu, \tag{41}$$

$$\gamma_{[12]}^{\mu\nu} = \frac{2}{k_{12}^2} \left[\beta_1 \beta_2 g_\perp^{\mu\nu} \hat{k}_{12} - \beta_1 \gamma_\perp^\mu k_{12}^\nu - \beta_2 k_{12}^\mu \gamma_\perp^\nu \right].$$

Note that the lower indices of $\gamma^{\mu\nu}$ vertices in (40) are determined by sequences of color matrices in corresponding group factors, and square brackets in $\gamma_{[12]}^{\mu\nu}$ emphasize its antisymmetry with respect to the permutation $1 \leftrightarrow 2$, as well as its relation to the color factor $[t^{i_1} t^{i_2}]$.

As was pointed out already, only the first term on the left-hand side of (33) contributes in the case of two-gluon production. Putting there the vertices (39) and (40) and performing summation over spin and color of intermediate gluons, after simple color algebra, we obtain for the two-gluon contribution to F_G

$$F_G^{GG} = -\frac{N_c^2}{4} \left[(\gamma_{\mu\nu}(k_{1G}) - \gamma_{\mu\nu}(k_{12})) \right. \tag{42}$$

$$\left. \times \left(\gamma_{12}^{\mu\nu} - \gamma_{[12]}^{\mu\nu} \right) + (1 \leftrightarrow 2) \right].$$

One should pay attention that all terms in (42) correspond to planar diagrams. It is an important property of a color triplet state in the t channel which greatly simplifies calculations.

The convolutions entering in (42) give

$$\gamma_{\mu\nu}(p) \gamma_{12}^{\mu\nu} = \frac{2}{k_{1Q'}^2 p^2} \{ \hat{e}_G [2\beta_2 (k_{1Q'} p) \tag{43}$$

$$+ \beta_1 (1 - 2\beta_2) \hat{k}_{1Q'} \hat{p}] + 4\beta_1 \beta_2 (e_G k_{1Q'}) \hat{p}$$

$$+ \beta_1 \beta_2 [\beta_1 (D - 2) - 4] (e_G p) \hat{k}_{1Q'} \};$$

$$\gamma_{\mu\nu}(p) \gamma_{[12]}^{\mu\nu} = \frac{-4}{k_{12}^2 p^2} \tag{44}$$

$$\times \{ \beta_1 \beta_2 (2 - \beta_1 \beta_2 (D - 2)) (e_G p) \hat{k}_{12}$$

$$- 2\beta_1 \beta_2 (e_G k_{12}) \hat{p} - (1 - 2\beta_1 \beta_2) (k_{12} p) \hat{e}_G \}.$$

We obtain the two-gluon contribution in $\Delta_s^{(3)G}$ by substituting (42) into (35) and performing integration. Note that, if we integrate over all phase space in (35), we have to take into account equivalence of produced gluons by the factor $1/2!$. With account of the quark fragmentation region according to (36), we obtain, denoting the contributions related to the terms $\gamma_{\mu\nu}(p) \gamma_N^{\mu\nu}$ in F_G^{QQ} (42) by Δ_{N*p},

$$\Delta_{12*k_{1G}} = \frac{N_c^2}{4} \left\{ 2 \left[\frac{2}{\epsilon} - \frac{3}{1 + 2\epsilon} + \Psi_2 \right. \right. \tag{45}$$

$$\left. \left. + \ln \frac{s}{-t} + \frac{5}{2\epsilon} X_\Gamma + \frac{1}{2} (I_0 + I_1) \right] \hat{\mathcal{Q}} + \frac{2\epsilon}{1 + 2\epsilon} \hat{\mathcal{E}} \right\};$$

$$\Delta_{12*k_{12}} = \frac{N_c^2}{4} X_\Gamma$$

$$\times \left\{ 2 \left[\frac{3}{1 + 2\epsilon} - \frac{3}{\epsilon} - \ln \frac{s}{-t} - \Psi \right] \hat{\mathcal{Q}} - \frac{2\epsilon}{1 + 2\epsilon} \hat{\mathcal{E}} \right\};$$

$$\Delta_{[12]*k_{12}} = 0;$$

$$\Delta_{[12]*k_{1G}} = -\frac{N_c^2}{4} X_\Gamma \left\{ 2 \left[\ln \frac{s}{-t} + \Psi + \frac{5}{2\epsilon} \right. \right.$$

$$\left. - \frac{4}{1 + 2\epsilon} + \frac{1}{(1 - \epsilon)(1 + 2\epsilon)(3 + 2\epsilon)} \right] \hat{\mathcal{Q}}$$

$$\left. - \frac{4\epsilon^2}{(3 + 2\epsilon)(1 - \epsilon)(1 + 2\epsilon)} \hat{\mathcal{E}} \right\},$$

where

$$I_0 = -\frac{\epsilon^2 (-q^2)^{1-2\epsilon}}{\Gamma_\epsilon^2 \pi^{(D-2)}} \tag{46}$$

$$\times \int \frac{d^{D-2} k_1 d^{D-2} k_2 q^2}{k_{1\perp}^2 (k_1 - q)_\perp^2 k_{2\perp}^2 (k_2 - q)_\perp^2} \ln \frac{q^2}{(k_1 - k_2)_\perp^2},$$

$$I_1 = -\frac{\epsilon^2 (-q^2)^{1-2\epsilon}}{\Gamma_\epsilon^2 \pi^{(D-2)}} \qquad (47)$$

$$\times \int \frac{d^{D-2}k_1 d^{D-2}k_2 (k_1 - k_2)_\perp^2}{k_{1\perp}^2 (k_1 - q)_\perp^2 k_{2\perp}^2 (k_2 - q)_\perp^2} \ln \frac{q^2}{(k_1 - k_2)_\perp^2}.$$

Here and below, we use the notation

$$\Psi_2 = 2[\psi(1) - \psi(1 + 2\epsilon)], \qquad (48)$$

$$\Psi = \psi(1 - 2\epsilon) + \psi(1 + 3\epsilon)$$
$$- \psi(1 + \epsilon) - \psi(1) + \Psi_2.$$

The contribution Δ_s^{GG} of fragmentation into two gluons to $\Delta_s^{(3)}$ is

$$\Delta_s^{GG} = \Delta_{12*k_{1G}} + \Delta_{12*k_{12}} + \Delta_{[12]*k_{1G}}. \qquad (49)$$

4.2. Fragmentation into Quark and Gluon

Let us denote particles produced in the gluon fragmentation region Q_1 and G_2 and their momenta k_1 and k_2, respectively. The vertex $\Gamma_{\{Q_1G_1\}G}$ can be obtained by crossing and appropriate substitutions from $\Gamma_{Q'\{G_1G_2\}}$ (40). We will represent it as

$$\Gamma_{\{Q_1G_2\}G} = -g^2 \bar{u}(k_1) \qquad (50)$$

$$\times \left\{ t^G t^{i_2} \left[\gamma_{G2}^\nu - \gamma_{[G2]}^\nu \right] e_{2\nu}^* \right.$$

$$\left. + t^{i_2} t^G \left[\gamma_{2G}^\mu + \gamma_{[G2]}^\mu \right] e_{2\mu}^* \right\},$$

where γ_{G2}^ν, $\gamma_{[G2]}^\nu$, and γ_{2G}^ν, are obtained from $\gamma_{12}^{\mu\nu}$, $\gamma_{[12]}^{\mu\nu}$, and $\gamma_{21}^{\nu\mu}$, respectively, by the substitutions

$$\beta_1 \to \frac{1}{\beta_1}, \quad \beta_2 \to -\frac{\beta_2}{\beta_1}, \quad k_{1Q'} \to -\frac{k_{1G}}{\beta_1}, \qquad (51)$$

$$k_{12} \to \frac{k_{2G}}{\beta_1}, \quad k_{2Q'} \to \frac{k_{12}}{\beta_1}$$

and convolution with e_G^μ. The vertex $\Gamma_{Q'\{Q_1G_2\}}^r$ can be found in [12] and represented as

$$\Gamma_{Q'\{Q_1G_2\}}^r = g^2 \bar{u}(p_{Q'}) \frac{\hat{p}_2}{s} \qquad (52)$$

$$\times \{ t^{i_2} t^r (L_\mu(k_{2Q'}) + L_\mu(k_{1Q'}))$$

$$+ t^r t^{i_2} (L_\mu(k_{12}) - L_\mu(k_{1Q'})) \} e_2^\mu u(k_1),$$

where

$$L^\mu(p) = \frac{\beta_2 \hat{p} \gamma_\perp^\mu - 2p^\mu}{p^2}. \qquad (53)$$

In the case of quark–gluon production, only the second term on the left-hand side of (33) contributes.

Using vertices (50) and (52), we obtain for the quark–gluon contribution to F_G after summation over spin and color

$$F_G^{QG} = -\beta_1 \sum_{ij} L_\mu(k_{ij}) \qquad (54)$$

$$\times \left[C_{G2}^{ij} \gamma_{G2}^\mu + C_{2G}^{ij} \gamma_{2G}^\mu + C_{[G2]}^{ij} \gamma_{[G2]}^\mu \right],$$

where ij takes on values $1Q'$, $2Q'$, 12 and

$$C_{G2}^{1Q'} = \frac{1}{4}, \quad C_{G2}^{2Q'} = \frac{1}{4}\left(1 + \frac{1}{N_c^2}\right), \qquad (55)$$

$$C_{G2}^{12} = \frac{1}{4N_c^2};$$

$$C_{2G}^{1Q'} = \frac{1}{4}, \quad C_{2G}^{2Q'} = \frac{1}{4N_c^2},$$

$$C_{2G}^{12} = -\frac{1}{4}\left(1 - \frac{1}{N_c^2}\right);$$

$$C_{[G2]}^{1Q'} = 0, \quad C_{[G2]}^{2Q'} = -\frac{1}{4}, \quad C_{[G2]}^{12} = -\frac{1}{4}.$$

Note that the term $C_{G2}^{2Q'} L_\mu(k_{2Q'}) \gamma_{G2}^\mu$ here corresponds to a nonplanar diagram and leads to a complicated integral. Fortunately, it is canceled by the respective contribution from quark–antiquark production, as we will see in the next subsection.

For the products $L_\mu(p) \gamma_{mn}^\mu$, we have after some simplifications

$$L_\mu(p) \gamma_{G2}^\mu = \frac{1}{k_{1G}^2 p^2} \{ 2\beta_1 \beta_2 (D - 2) \qquad (56)$$

$$\times (e_G k_{1G}) \hat{p} - \beta_2 (D - 6) \hat{p} \hat{k}_{1G} \hat{e}_G - 2\hat{e}_G \hat{k}_{1G} \hat{p} \};$$

$$L_\mu(p) \gamma_{2G}^\mu = \frac{1}{k_{12}^2 p^2}$$

$$\times \{ \beta_2 (\beta_2 (D - 2) - 4) \hat{p} \hat{k}_{12} + 4(k_{12}p) \} \hat{e}_G;$$

$$L_\mu(p) \gamma_{[G2]}^\mu = \frac{2\beta_2}{k_{2G}^2 p^2} \left\{ \left(\frac{\beta_2}{\beta_1} - 1 \right) \hat{e}_G \hat{p} \hat{k}_{2G} \right.$$

$$+ (\beta_2 (D - 2) - 4)(e_G k_{2G}) \hat{p}$$

$$\left. + \frac{2}{\beta_2} (k_{2G}p) \hat{e}_G + 4(e_G p) \hat{k}_{2G} \right\}.$$

The quark–gluon contribution to $\Delta_s^{(3)G}$ is given by (35) with (54) instead of F_G. Denoting by $\Delta_{mn\cdot ij}$ the contributions proportional C_{mn}^{ij} in (54), after integration, we obtain for them with account of the quark fragmentation region according to (36)

$$\Delta_{G2\cdot 1Q'} = \frac{1}{4}\left\{ 2\left[\frac{3 - 2\epsilon}{1 + 2\epsilon} - \Psi_2 - \ln \frac{s}{-t} \right. \right. \qquad (57)$$

$$-\frac{5}{2\epsilon}X_\Gamma - \frac{1}{2}(I_0 + I_1)\Big]\hat{\mathcal{Q}} + \frac{2\epsilon}{1+2\epsilon}\hat{\mathcal{E}}\Big\};$$

$$\Delta_{G2\cdot12} = \frac{1}{4N_c^2}X_\Gamma$$

$$\times \Big\{-2\Big[\ln\frac{s}{-t} + \Psi + \frac{1}{\epsilon} - \frac{3-2\epsilon}{1+2\epsilon}\Big]\hat{\mathcal{Q}} + \frac{2\epsilon}{1+2\epsilon}\hat{\mathcal{E}}\Big\};$$

$$\Delta_{2G\cdot1Q'} = \frac{1}{4}X_\Gamma$$

$$\times \Big\{2\Big[\ln\frac{s}{-t} + \Psi + \frac{3}{2\epsilon} - \frac{3}{2(1+2\epsilon)}\Big]\Big\}\hat{\mathcal{Q}};$$

$$\Delta_{2G\cdot2Q'} = \frac{1}{4N_c^2}X_\Gamma\Big\{2\Big[\frac{3-2\epsilon}{2(1+2\epsilon)} - \frac{1}{\epsilon}\Big]\Big\}\hat{\mathcal{Q}};$$

$$\Delta_{2G\cdot12} = 0;$$

$$\Delta_{[G2]\cdot2Q'} = \frac{1}{4}\Big\{-2\Big[-\frac{3}{1+2\epsilon} + \frac{2}{\epsilon} + \Psi_2$$

$$+ \ln\frac{s}{-t} - \frac{X_\Gamma}{\epsilon} - \frac{1}{2}I_1\Big]\hat{\mathcal{Q}} - \frac{2\epsilon}{1+2\epsilon}\hat{\mathcal{E}}\Big\};$$

$$\Delta_{[G2]\cdot12} = \frac{1}{4}X_\Gamma\Big\{2\Big[\ln\frac{s}{-t} + \Psi$$

$$+ \frac{3}{\epsilon} - \frac{3}{1+2\epsilon}\Big]\hat{\mathcal{Q}} + \frac{2\epsilon}{1+2\epsilon}\hat{\mathcal{E}}\Big\}.$$

The contribution $\Delta_{G2\cdot2Q'}$ is not presented here since it is canceled with the respective contribution from quark−antiquark production, as was pointed out. The quark−gluon contribution to $\Delta_s^{(3)}$ is given by

$$\Delta_s^{QG} = \sum_{ij,mn}\Delta_{mn\cdot ij}, \quad ij = 1Q', 2Q', 12; \quad (58)$$

$$mn = G2, 2G, [G2].$$

4.3. Fragmentation into Quark−Antiquark Pair

As well as in the two-gluon case, only the first term on the left-hand side of (33) exists. We denote the momenta of particles Q_1 and $\bar{Q}_2$ in the gluon fragmentation region k_1 and k_2, respectively. The vertex $\Gamma^r_{\{Q_1\bar{Q}_2\}G}$ can be obtained by crossing and corresponding substitutions from $\Gamma^r_{Q'\{Q_1G_2\}}$ (52):

$$\Gamma^r_{\{Q_1\bar{Q}_2\}G} = g^2\bar{u}(k_1)\frac{\hat{p}_2}{s}\Big\{t^Gt^r\Big(L(k_{1G}) \quad (59)$$

$$- L(k_{12})\Big) + t^rt^G\big(L(k_{12}) + L(k_{2G})\big)\Big\}v(k_2),$$

where

$$L(p) = \frac{-\hat{p}\hat{e}_G + 2\beta_1(pe_G)}{p^2}. \quad (60)$$

The vertex $\Gamma_{Q'\{Q_1\bar{Q}_2\}}$ can be obtained from [13]; a direct calculation does not encounter difficulties either. We have

$$\Gamma_{Q'\{Q_1\bar{Q}_2\}} = g^2\Big[\bar{v}(k_2)t^c\gamma^\sigma u(k_1)\bar{u}(p_{Q'})t^cA_\sigma \quad (61)$$

$$- \bar{u}(p_{Q'})t^c\gamma^\sigma u(k_1)\cdot\bar{v}(k_2)t^cB_\sigma\delta_{Q_1Q}\Big],$$

where δ_{Q_1Q} shows that the last contribution exists only when an intermediate quark has the same flavor as the initial one, and the values A_σ and B_σ can be written as

$$A^\sigma = \frac{-\beta_1\beta_2}{k_{12}^2}\Big(\gamma_\perp^\sigma - (\hat{k}_1 + \hat{k}_2)_\perp\frac{2p_2^\sigma}{s}\Big); \quad (62)$$

$$B^\sigma = \frac{\beta_1}{k_{1Q'}^2}\Big(\gamma_\perp^\sigma + (\hat{k}_1 - \hat{p}_{Q'})_\perp\frac{2p_2^\sigma}{s\beta_2}\Big).$$

By substituting the vertices (59) and (61) into (33), after summation over spin and color states of intermediate particles, we obtain for the quark−antiquark contribution to F_G

$$F_G^{QQ} = \sum_{ij}\Big[C_A^{ij}\mathrm{tr}\Big(\hat{k}_1\frac{\hat{p}_2}{s}L(k_{ij})\hat{k}_2\gamma_\sigma\Big)A^\sigma \quad (63)$$

$$- C_B^{ij}\gamma_\sigma\hat{k}_1\frac{\hat{p}_2}{s}L(k_{ij})\hat{k}_2B^\sigma\Big],$$

where ij takes on values $1G, 2G, 12$ and

$$C_A^{1G} = \frac{N_c}{8}n_f, \quad C_A^{2G} = -\frac{N_c}{8}n_f, \quad C_A^{12} = -\frac{N_c}{4}n_f;$$
$$(64)$$

$$C_B^{1G} = \frac{1}{4N_c^2}, \quad C_B^{2G} = \frac{1}{4}\Big(1 + \frac{1}{N_c^2}\Big), \quad C_B^{12} = \frac{1}{4}.$$

Taking into account, as usual, external Dirac spinors, we obtain

$$\mathrm{tr}\Big(\hat{k}_1\frac{\hat{p}_2}{s}L(p)\hat{k}_2\gamma_\sigma\Big)A^\sigma = \frac{2\beta_1\beta_2}{p^2k_{12}^2} \quad (65)$$

$$\times \Big((k_{12}p)\hat{e}_G - (e_Gk_{12})\hat{p} + (1-4\beta_1\beta_2)(e_Gp)\hat{k}_{12}\Big);$$

$$\gamma_\sigma\hat{k}_1\frac{\hat{p}_2}{s}L(p)\hat{k}_2B^\sigma$$

$$= \frac{-\beta_1}{k_{1Q'}^2p^2}\{2\beta_1\beta_2(D-2)(e_Gp)\hat{k}_{1Q'}$$

$$- \beta_2(D-6)\hat{k}_{1Q'}\hat{p}\hat{e}_G - 2\hat{e}_G\hat{p}\hat{k}_{1Q'}\}.$$

The quark−antiquark contribution to $\Delta_s^{(3)G}$ is given by (35) with (63) instead of F_G. As has been mentioned above, in F_G^{QQ} we also have a term corresponding to a nonplanar diagram. In (63), it appears with the coefficient C_B^{2G}. Note that $C_B^{2G} = C_{G2}^{2Q'}$ [see (55)]. Moreover, comparing the first equations in (56) and the second in (65), one can see that the substitution

$$k_{1Q'} \to -k_{2Q'}, \quad k_{2G} \to -k_{1G} \qquad (66)$$

turns $\gamma_\sigma \hat{k}_1 (\hat{p}_2/s) L(k_{2G}) \hat{k}_2 B^\sigma$ into $\beta_1 L_\mu(k_{2Q'}) \gamma_{G2}^\mu$ with opposite sign. Note that, for the quark−antiquark contribution, q_2 in (35) is equal to $p_{Q'\perp} - k_{1\perp} - k_{2\perp} = \beta_2 q - k_{1Q'} - k_{2G}$. Upon the substitution (66), it turns into $\beta_2 q + k_{2Q'} + k_{1G} = k_{1\perp} + k_{2\perp} - p_{G\perp}$, which is just the t-channel quark momentum for the quark−gluon contribution. An important point is that the theta functions in (35) can be omitted for the contributions of the nonplanar diagrams due to convergence of integrals, after which the substitution (66) does not influence the integration region. Therefore, these contributions cancel each other.

Performing integration and denoting by $\Delta_{A \cdot ij}$ and $\Delta_{B \cdot ij}$ the contributions to (63) proportional to C_A^{1j} and C_B^{1j}, respectively, we obtain with account of the quark fragmentation region according to (36)

$$\Delta_{A \cdot 1G} = \frac{N_c}{8} n_f X_\Gamma \qquad (67)$$

$$\times \left\{ \frac{-2}{1+2\epsilon} \left(1 - \frac{1}{(1-\epsilon^2)(3+2\epsilon)} \right) \hat{\mathcal{Q}} \right.$$

$$\left. - \frac{4\epsilon^2}{(1-\epsilon^2)(1+2\epsilon)(3+2\epsilon)} \hat{\mathcal{E}} \right\};$$

$$\Delta_{A \cdot 2G} = \Delta_{A \cdot 1G}; \quad \Delta_{A \cdot 12} = 0;$$

$$\Delta_{B \cdot 1G} = \frac{1}{4N_c^2} \left\{ 2 \left[-\frac{3-2\epsilon}{1+2\epsilon} + \Psi_2 \right. \right.$$

$$\left. \left. + \ln \frac{s}{-t} - \frac{X_\Gamma}{\epsilon} - \frac{1}{2} I_1 \right] \hat{\mathcal{Q}} - \frac{2\epsilon}{1+2\epsilon} \hat{\mathcal{E}} \right\};$$

$$\Delta_{B \cdot 12} = \frac{1}{4} X_\Gamma$$

$$\times \left\{ -2 \left[\frac{3-2\epsilon}{1+2\epsilon} - \ln \frac{s}{-t} - \Psi - \frac{1}{\epsilon} \right] \hat{\mathcal{Q}} - \frac{2\epsilon}{1+2\epsilon} \hat{\mathcal{E}} \right\}.$$

Therefore, the quark−antiquark contribution to $\Delta_s^{(3)}$ can be written as

$$\Delta_s^{QQ} = 2\Delta_{A \cdot 1G} + \Delta_{B \cdot 1G} + \Delta_{B \cdot 12} + \Delta_{B \cdot 2G}, \qquad (68)$$

where $\Delta_{B \cdot 2G} = -\Delta_{G2 \cdot 2Q'}$, as was shown above. Because of cancellation of these contributions in

$$\Delta_s^{(3)} = \Delta_s^{GG} + \Delta_s^{GQ} + \Delta_s^{QQ}, \qquad (69)$$

$\Delta_{B \cdot 2G}$ is not present in (67), nor $\Delta_{G2 \cdot 2Q'}$ in (57).

5. TWO-LOOP CORRECTION TO THE QUARK TRAJECTORY

The total discontinuity Δ_s is given by the sum of the contributions of two- and three-particle intermediate states in the unitarity relation. The two-particle contribution $\Delta_s^{(2)}$ is given explicitly by (26). All necessary contributions to $\Delta_s^{(3)}$ (69) are calculated in the preceding section. They are given by (49) and (45) for fragmentation into two gluons, by (58) and (57) for fragmentation into a quark and gluon, and by (68), (67) for fragmentation into a quark and antiquark. Now we can compare the calculated discontinuity with the form (11) required by the quark Reggeization. First of all, we note coincidence of the terms with $\ln s$. Actually, this coincidence must be expected, since it is required by the quark Reggeization in the LLA, which was already checked on this level. Much more important is that the calculated discontinuity has the same helicity structure as Δ_R (11), with the same coefficient at the structure $\hat{\mathcal{E}}$. It is a serious argument in favor of validity of the Reggeization hypothesis in the NLA. Then, comparing coefficients at the structure $\hat{\mathcal{Q}}$, we obtain

$$\delta_T^{(2)} = C_F \left\{ -n_f \frac{X_\Gamma(1+\epsilon)}{(1+2\epsilon)(3+2\epsilon)} \qquad (70) \right.$$

$$+ N_c \left(\frac{1}{2} I_0 + I_1 - X_\Gamma[\psi(1+\epsilon) - \psi(1+2\epsilon)] \right.$$

$$\left. + \frac{7X_\Gamma}{2\epsilon} + \frac{X_\Gamma(11+7\epsilon)}{2(1+2\epsilon)(3+2\epsilon)} \right)$$

$$+ 2C_F \left(-\frac{1}{2} I_1 + \psi(1) - \psi(1-\epsilon) \right.$$

$$+ (2 - X_\Gamma)[\psi(1+\epsilon) - \psi(1+2\epsilon)]$$

$$\left. \left. - \frac{1+X_\Gamma}{\epsilon} - \frac{(1-X_\Gamma)(3-\epsilon)}{2(1+2\epsilon)} \right) \right\},$$

where X_Γ is given by (27), and I_0 and I_1 are defined in (46) and (47).

The two-loop correction to the quark Regge trajectory $j_Q = 1/2 + \delta_T(t)$ is determined by Eqs. (9), (70) at arbitrary spacetime dimension $D = 4 + 2\epsilon$. Unfortunately, at arbitrary D, the integrals I_0 and I_1

cannot be written in terms of elementary functions. In the limit $\epsilon \to 0$, we have for them (see Appendix C)

$$I_0 = \frac{1}{\epsilon} + 15\psi^{(2)}(1)\epsilon^2 + \mathcal{O}(\epsilon^3), \qquad (71)$$

$$I_1 = -\frac{4}{\epsilon} + 6\psi^{(2)}(1)\epsilon^2 + \mathcal{O}(\epsilon^3),$$

where $\psi^{(2)}$ means the second derivative of the ψ function. Using this result and the proportion $\psi^{(2)}(1) = -2\zeta_3$, where ζ_n is the Riemann zeta function, from Eq. (70), we obtain for the two-loop correction up to terms nonvanishing at $\epsilon \to 0$

$$\delta_T^{(2)} = C_F \left\{ \beta_0 \frac{2}{\epsilon} - K\frac{2}{\epsilon} + N_c \left(\frac{404}{27} - 2\zeta_3 \right) \right. \qquad (72)$$

$$\left. - n_f \frac{56}{27} + (C_F - N_c)16\zeta_3 \right\},$$

where

$$\beta_0 = \frac{11}{6}N_c - \frac{2}{3}n_f, \quad K = \left(\frac{67}{18} - \zeta_2 \right) N_c - \frac{5}{9}n_f,$$

in agreement with the result of [16].

6. SUMMARY

In this paper, we have checked compatibility of the quark Reggeization hypothesis with the s-channel unitarity by explicit two-loop calculations and have found in the case of massless quarks the two-loop correction to the quark trajectory at arbitrary space-time dimension $D = 4 + 2\epsilon$. The ϵ expansion of the correction gives the result obtained in [16]. We have calculated the two-loop s-channel discontinuity of the backward quark–gluon scattering amplitude with positive signature keeping nonlogarithmic terms and have proved that only a color triplet part of the amplitude survives at NLO as well as at LO. It was shown that the calculated discontinuity has a form required by the Reggeization hypothesis. The two-loop correction to the trajectory has been obtained from comparison of the calculated discontinuity with the Reggeized form. In the case of massive quarks, the trajectory can be found by the same method, since all necessary quantities for such calculation are known.

The cancellation of contributions of color states different from triplet in positive signature is not restricted by the two-loop approximation, but is a general property of the NLA. Therefore, in this approximation, as well as in the LLA, real parts of amplitudes with positive signature are completely determined by Reggeized quark contributions.

Note that testing of the quark Reggeization performed up to now is rather limited. Even in the LLA, self-consistency of the hypothesis was shown only in

a particular case of elastic quark–gluon scattering, although in all orders of α_s. In the NLA, it is tested in the same process only in order of α_s^2. A possible way of stricter testing and, in principle, a complete proof is examination of "bootstrap" conditions on the Reggeized quark vertices and the trajectory in QCD. These conditions appear from comparison of the Reggeized form of discontinuities of amplitudes with the discontinuities calculated by using the s-channel unitarity.

We have used dimensional regularization for both infrared and ultraviolet divergences and the bare coupling constant $g = g_s\mu^\epsilon$, so that, besides infrared poles in ϵ, our result contains the ultraviolet poles. To remove them, it is sufficient to express the bare coupling through the renormalized one. In the $\overline{MS}$ renormalization scheme,

$$g = g_\mu \mu^{-\epsilon} \left\{ 1 + \beta_0 \frac{g_\mu^2 \Gamma(1-\epsilon)}{\epsilon(4\pi)^{2+\epsilon}} \right\}, \qquad (73)$$

where g_μ is the renormalized coupling at the normalization point μ.

Appendix A

For convenience of the reader, we list here the integrals encountered in the calculation of $\Delta_s^{(2)}$ (note that, everywhere below, we use Euclidean transverse momenta and omit the transeverseness sign):

$$J_1^i = \int \frac{d^{D-2}k \, k^i}{(k^2)^{1-\epsilon}(k-q)^2} \qquad (A.1)$$

$$= q^i \frac{\pi^{(D-2)/2}}{\epsilon(q^2)^{1-2\epsilon}} \Gamma_\epsilon \cdot X_\Gamma,$$

$$J_2^i = \int \frac{d^{D-2}k \, k^i}{(k^2)^{1-\epsilon}(k-q)^2} \ln \frac{s}{k^2} \qquad (A.2)$$

[†] Deceased.

$$= J_1^i \left[\ln \frac{s}{-t} + \Psi_1 \right],$$

$$J_3^i = \int \frac{d^{D-2}k \, q^i}{(k^2)^{1-\epsilon}(k-q)^2} = \frac{3}{2} J_1^i, \qquad (A.3)$$

$$J_4^i = \int \frac{d^{D-2}k \, q^i}{(k^2)^{1-\epsilon}(k-q)^2} \ln \frac{s}{k^2} \qquad (A.4)$$

$$= \frac{3}{2} J_2^i + \frac{1}{4\epsilon} J_1^i,$$

$$J_5^\mu = \int \frac{d^{D-2}k \, k^l k^m q^i}{(k^2)^{2-\epsilon}(k-q)^2} \qquad (A.5)$$

$$= \frac{1}{\epsilon(1-\epsilon)} \left(\frac{q^k q^l}{q^2}(1-2\epsilon) + \frac{\delta^{kl}}{4} \right) J_1^i.$$

Recall that

$$\Gamma_\epsilon = \frac{\Gamma^2(1+\epsilon)\Gamma(1-\epsilon)}{\Gamma(1+2\epsilon)}, \qquad (A.6)$$

$$X_\Gamma = \frac{\Gamma(1-2\epsilon)\Gamma^2(1+2\epsilon)}{\Gamma(1+\epsilon)\Gamma(1+3\epsilon)\Gamma^2(1-\epsilon)},$$

$$\Psi_1 = \psi(1+3\epsilon) + \psi(1-2\epsilon)$$
$$- \psi(1+2\epsilon) - \psi(1-\epsilon).$$

Appendix B

Apart from I_0 (46) and I_1 (47), considered in the next appendix, integrals required for calculation of $\Delta_s^{(3)}$ can be transformed to the ones listed below. Using (A.6), (48), and

$$\Lambda = \frac{\pi^{(D-2)}}{\epsilon^2 (q^2)^{1-2\epsilon}}, \qquad (B.1)$$

we have

$$K_1 = \int \frac{dk^{(D-2)} dp^{(D-2)}}{\Lambda(\Gamma_\epsilon)^2} \qquad (B.2)$$

$$\times \frac{\hat{e}_G(kq)\hat{p}}{k^2(k-q)^2 p^2(p-q)^2} = \hat{e}_G \hat{q},$$

$$K_2 = \int \frac{dk^{(D-2)} dp^{(D-2)}}{\Lambda(\Gamma_\epsilon)^2} \qquad (B.3)$$

$$\times \frac{(e_G k)(\hat{k}-\hat{q})\hat{p}}{k^2(k-q)^2 p^2(p-q)^2}$$

$$= -\hat{e}_G \hat{q} \frac{1}{2(1+2\epsilon)} + (e_G q) \frac{\epsilon}{1+2\epsilon},$$

$$K_3 = \int \frac{dk^{(D-2)} dp^{(D-2)}}{\Lambda(\Gamma_\epsilon)^2} \qquad (B.4)$$

$$\times \frac{\hat{e}_G \hat{k}(\hat{k}-\hat{q})\hat{p}}{k^2(k-q)^2 p^2(p-q)^2} \ln \frac{s}{(k-p)^2}$$

$$= \hat{e}_G \hat{q} \left[\frac{1}{2}(I_0 + I_1) + X_\Gamma \frac{5}{2\epsilon} + \ln \frac{s}{-t} \right],$$

$$K_4 = \int \frac{dk^{(D-2)} dp^{(D-2)}}{\Lambda(\Gamma_\epsilon)^2} \qquad (B.5)$$

$$\times \frac{\hat{e}_G(\hat{k}-\hat{q})\hat{k}\hat{p}}{k^2(k-q)^2 p^2(p-q)^2} \ln \frac{s}{(k-p)^2}$$

$$= \hat{e}_G \hat{q} \left[-\frac{1}{2}I_1 - \frac{X_\Gamma}{\epsilon} + \ln \frac{s}{-t} \right],$$

$$K_5 = \int \frac{dk^{(D-2)} dp^{(D-2)}}{\Lambda(\Gamma_\epsilon)^2} \qquad (B.6)$$

$$\times \frac{(e_G k)\hat{k}\hat{p}}{k^2(k-p)^2 p^2(p-q)^2}$$

$$= -\left(\hat{e}_G \hat{q} \frac{1}{2} + (e_G q)(1+\epsilon) \right) \frac{X_\Gamma}{(1+2\epsilon)},$$

$$K_6 = \int \frac{dk^{(D-2)} dp^{(D-2)}}{\Lambda(\Gamma_\epsilon)^2} \qquad (B.7)$$

$$\times \frac{(e_G k)(\hat{k}-\hat{p})(\hat{p}-\hat{q})}{k^2(k-p)^2 p^2(p-q)^2}$$

$$= \left(\hat{e}_G \hat{q} \frac{1}{4} + (e_G q)\epsilon^2 \right) \frac{X_\Gamma}{(1-\epsilon)(1+2\epsilon)},$$

$$K_7 = \int \frac{dk^{(D-2)} dp^{(D-2)}}{\Lambda(\Gamma_\epsilon)^2} \qquad (B.8)$$

$$\times \frac{\hat{e}_G \hat{k} p^2}{k^2(k-p)^2 p^2(p-q)^2} = \hat{e}_G \hat{q} X_\Gamma,$$

$$K_8 = \int \frac{dk^{(D-2)} dp^{(D-2)}}{\Lambda(\Gamma_\epsilon)^2} \qquad (B.9)$$

$$\times \frac{\hat{e}_G \hat{k} p^2}{k^2(k-p)^2 p^2(p-q)^2} \ln \frac{s}{(k-p)^2}$$

$$= \hat{e}_G \hat{q} \left[\ln \frac{s}{-t} + \Psi - \Psi_2 + \frac{1}{\epsilon} \right] X_\Gamma,$$

$$K_9 = \int \frac{dk^{(D-2)} dp^{(D-2)}}{\Lambda(\Gamma_\epsilon)^2} \qquad (B.10)$$

$$\times \frac{\hat{e}_G(kp)(\hat{p}-\hat{q})}{k^2(k-p)^2 p^2(p-q)^2} = -\frac{1}{2}\hat{e}_G \hat{q} X_\Gamma,$$

$$K_{10} = \int \frac{dk^{(D-2)} dp^{(D-2)}}{\Lambda(\Gamma_\epsilon)^2} \qquad (B.11)$$

$$\times \frac{\hat{e}_G(kp)(\hat{p}-\hat{q})}{k^2(k-p)^2 p^2(p-q)^2} \ln \frac{s}{(k-p)^2}$$

$$= -\frac{1}{2}\hat{e}_G\hat{q}\left[\ln\frac{s}{-t} + \Psi - \Psi_2 + \frac{3}{2\epsilon}\right]X_\Gamma.$$

Appendix C

At arbitrary $D \neq 4$, the integrals I_0 (46) and I_1 (47) can be expressed only through infinite series. They belong to the class of integrals which were studied particularly in [17]. The first of them has already appeared in the calculation of the two-loop correction to the gluon Regge trajectory [18], where its limit at $\epsilon \to 0$ was found:

$$I_0 = \int \frac{d^{D-2}k_1 d^{D-2}k_2}{\Lambda(\Gamma_\epsilon)^2} \qquad \text{(C.1)}$$

$$\times \frac{q^2}{k_1^2(k_1-q)^2 k_2^2(k_2-q)^2}$$

$$\times \ln\frac{q^2}{(k_1-k_2)^2} = \frac{1}{\epsilon} + 15\psi^{(2)}(1)\epsilon^2 + \mathcal{O}(\epsilon^3).$$

Here, Γ_ϵ and Λ are given in (A.6) and (B.1); $\psi^{(2)}$ means the second derivative of ψ. We have obtained the limit of the second integral:

$$I_1 = \int \frac{d^{D-2}k_1 d^{D-2}k_2}{\Lambda(\Gamma_\epsilon)^2} \qquad \text{(C.2)}$$

$$\times \frac{(k_1-k_2)^2}{k_1^2(k_1-q)^2 k_2^2(k_2-q)^2}$$

$$\times \ln\frac{q^2}{(k_1-k_2)^2} = -\frac{4}{\epsilon} + 6\psi^{(2)}(1)\epsilon^2 + \mathcal{O}(\epsilon^3).$$

Below, some details of the calculation are given.

Representing the integral as

$$I_1 = \left.\frac{d}{d\nu}I(\nu)\right|_{\nu=0}, \qquad \text{(C.3)}$$

$$I(\nu) = \int \frac{d^{D-2}k_1 d^{D-2}k_2}{\Lambda(\Gamma_\epsilon)^2}$$

$$\times \frac{(q^2)^\nu}{k_1^2(k_1-q)^2 k_2^2(k_2-q)^2[(k_1-k_2)^2]^{\nu-1}},$$

we have from Eqs. (1), (4), (9) of [17]

$$I(\nu) = \frac{2\epsilon^2}{2\epsilon-1}\frac{\nu^{-1}(\nu-\epsilon)}{(\Gamma_\epsilon)^2} \qquad \text{(C.4)}$$

$$\times G_2(1, 1-\epsilon+\nu)G_2(1,\nu)$$

$$\times \left(\nu(\nu-1)\lim_{b\to 0}S(\epsilon-1, b, 2\epsilon-\nu, \nu-1-\epsilon)\right),$$

where

$$G_2(\alpha_1, \alpha_2) = G_1(\alpha_1)G_1(\alpha_2) \qquad \text{(C.5)}$$

$$\times G_1(2+2\epsilon-\alpha_1-\alpha_2),$$

$$G_1(\alpha) = \frac{\Gamma(1+\epsilon-\alpha)}{\Gamma(\alpha)}.$$

The function $S(a,b,c,d)$ is defined by Eqs. (17), (16), and (10) of [17]:

$$S(a,b,c,d) = \frac{\pi\cot(\pi c)}{H(a,b,c,d)} - \frac{1}{c} \qquad \text{(C.6)}$$

$$- \frac{b+c}{bc}F(a+c, -b, -c, b+d),$$

where

$$H(a,b,c,d) = \frac{\Gamma(1+a)\Gamma(1+b)\Gamma(1+c)\Gamma(1+d)\Gamma(1+a+b+c+d)}{\Gamma(1+a+c)\Gamma(1+a+d)\Gamma(1+b+c)\Gamma(1+b+d)}, \qquad \text{(C.7)}$$

and $F(a,b,c,d)$ is expressed through the generalized hypergeometric function ${}_3F_2$:

$$F(a,b,c,d) = {}_3F_2\left[\begin{matrix} -a, -b, 1 \\ 1+c, 1+d \end{matrix}; 1\right] - 1. \quad \text{(C.8)}$$

The limit $b \to 0$ in (C.4) can be easily taken. We can also use for this purpose Eq. (12) of [17] and obtain with our values of parameters

$$\nu(\nu-1)\lim_{b\to 0}S(\epsilon-1, b, 2\epsilon-\nu, \nu-1-\epsilon) \quad \text{(C.9)}$$

$$= S_1(\nu) + S_2(\nu),$$

where

$$S_1(\nu) = \pi\cot[\pi(2\epsilon-\nu)] \qquad \text{(C.10)}$$

$$\times \frac{\Gamma(3\epsilon-\nu)\Gamma(1+\nu)}{\Gamma(\epsilon)\Gamma(2\epsilon-1)} - \frac{\nu(\nu-1)}{2\epsilon-\nu},$$

$$S_2(\nu) = \nu(\nu-1)\frac{3\epsilon-1-\nu}{(\epsilon-1)(\nu-2\epsilon)} \qquad \text{(C.11)}$$

$$\times F(1-\epsilon, 2\epsilon-\nu, \nu-2\epsilon, \nu-2).$$

With this notation, we have

$$I_1 = \left.\frac{d}{d\nu}\left[S_0(\nu)(S_1(\nu) + S_2(\nu))\right]\right|_{\nu=0}, \qquad \text{(C.12)}$$

where

$$S_0(\nu) = \frac{\epsilon^2}{(\Gamma_\epsilon)^2} \qquad (C.13)$$

$$\times \frac{2}{2\epsilon - 1} \frac{\Gamma^2(\epsilon)\Gamma(2\epsilon - \nu)\Gamma(1 - 2\epsilon + \nu)\Gamma(1 - \nu + \epsilon)}{\Gamma(3\epsilon - \nu)\Gamma(1 + \nu)\Gamma(1 + 2\epsilon - \nu)}.$$

We need to know $S_i(0)$ and $S_i'(0)$, $i = 0\text{--}2$. For $i = 0, 1$, they are easily obtained from (C.13), (C.10):

$$S_0(0) = \frac{3}{2\epsilon - 1} X_\Gamma, \qquad (C.14)$$

$$S_0'(0) = S_0(0)\left(\frac{1}{6\epsilon} + \Psi - \Psi_2\right);$$

$$S_1(0) = 2\pi \cot[2\pi\epsilon]\frac{\epsilon(2\epsilon - 1)}{3}\frac{\Gamma(1 + 3\epsilon)}{\Gamma(1 + \epsilon)\Gamma(1 + 2\epsilon)};$$

$$S_1'(0) = S_1(0)$$

$$\times \left(\psi(1) - \psi(1 + 3\epsilon) + \frac{1}{3\epsilon} + \frac{2\pi}{\sin(4\pi\epsilon)}\right) + \frac{1}{2\epsilon},$$

where X_Γ is defined in (A.6), and Ψ and Ψ_2 are defined in (48). To find $S_2(0)$ and $S_2'(0)$, we use the integral representation

$$F(a, b, c, d) = -1 + \frac{\Gamma(1 + d)\Gamma(1 + c)}{\Gamma(d)\Gamma(-b)\Gamma(1 + c + b)} \qquad (C.15)$$

$$\times \int_0^1 dx(1 - x)^{d-1} \int_0^1 dz z^{-b-1}(1 - z)^{c+b}(1 - zx)^a,$$

which follows from the standard representation for hypergeometric functions. Performing integration over x by parts three times, we obtain

$$S_2(\nu) = (3\epsilon - 1 - \nu) \qquad (C.16)$$

$$\times \left(\frac{\nu}{1 - 2\epsilon + \nu} + \frac{\epsilon}{2 - 2\epsilon + \nu}\right.$$

$$\left. + \epsilon \int_0^1 \int_0^1 dx dz z^{1-2\epsilon+\nu}(1 - x)^\nu \frac{d}{dx}(1 - zx)^{-1-\epsilon}\right),$$

so that

$$S_2(0) = (1 - 2\epsilon)\frac{\Gamma(1 - \epsilon)\Gamma(1 - 2\epsilon)}{\Gamma(1 - 3\epsilon)}, \qquad (C.17)$$

$$S_2'(0) = \frac{S_2(0)}{1 - 3\epsilon} + (3\epsilon - 1)$$

$$\times \left(\frac{1}{1 - 2\epsilon} - \frac{\epsilon}{4(1 - \epsilon)^2} + \epsilon(J_1 + J_2)\right), \qquad (C.18)$$

where

$$J_1 = \int_0^1 \int_0^1 dx dz z^{1-2\epsilon} \ln z \frac{d}{dx}(1 - zx)^{-1-\epsilon}, \qquad (C.19)$$

$$J_2 = \int_0^1 \int_0^1 dz dx z^{1-2\epsilon} \ln(1 - x)\frac{d}{dx}(1 - zx)^{-1-\epsilon}. \qquad (C.20)$$

The integral J_1 can be easily found:

$$J_1 = \frac{1}{4(1 - \epsilon)^2} + \frac{\Gamma(1 - \epsilon)\Gamma(2 - 2\epsilon)}{\Gamma(2 - 3\epsilon)} \qquad (C.21)$$

$$\times \frac{(\psi(2 - 3\epsilon) - \psi(2 - 2\epsilon))}{\epsilon}.$$

For the integral J_2, replacing d/dx by $(z/x)d/dz$ in the representation (C.20) and integrating over z by parts, we obtain in the limit $\epsilon \to 0$

$$J_2 \simeq \frac{-1}{\epsilon^2} + 1 + \psi^{(1)}(1) \qquad (C.22)$$

$$+ \epsilon\left(5 - \psi^{(1)}(1) + \frac{\psi^{(2)}(1)}{2}\right).$$

Using in (C.12) the results (C.21), (C.22), (C.14) and (C.17), (C.18), we get the final result (C.2).

REFERENCES

1. L. V. Gribov, E. M. Levin, and M. G. Ryskin, Phys. Rep. **100**, 1 (1983).

2. G. Altarelli, Phys. Rep. **81**, 1 (1982).

3. M. T. Grisaru, H. J. Schnitzer, and H.-S. Tsao, Phys. Rev. Lett. **30**, 811 (1973); Phys. Rev. D **8**, 4498 (1973).

4. L. N. Lipatov, Yad. Fiz. **23**, 642 (1976) [Sov. J. Nucl. Phys. **23**, 338 (1976)].

5. V. S. Fadin, E. A. Kuraev, and L. N. Lipatov, Phys. Lett. B **60B**, 50 (1975); L. N. Lipatov, E. A. Kuraev, and V. S. Fadin, Zh. Éksp. Teor. Fiz. **71**, 840 (1976) [Sov. Phys. JETP **44**, 443 (1976)].

6. V. S. Fadin and V. E. Sherman, Pis'ma Zh. Éksp. Teor. Fiz. **23**, 599 (1976) [JETP Lett. **23**, 548 (1976)]; Zh. Éksp. Teor. Fiz. **72**, 1640 (1977) [Sov. Phys. JETP **45**, 861 (1977)].

7. M. Gell-Mann, M. L. Goldberger, F. E. Low, *et al.*, Phys. Rev. **133**, B145 (1964); B. M. McCoy and T. T. Wu, Phys. Rev. D **13**, 369 (1976).

8. S. Mandelstam, Phys. Rev. **137**, B949 (1965).

9. E. A. Kuraev, L. N. Lipatov, and V. S. Fadin, Zh. Éksp. Teor. Fiz. **72**, 377 (1977) [Sov. Phys. JETP **45**, 199 (1977)]; Ya. Ya. Balitskii and L. N. Lipatov, Sov. J. Nucl. Phys. **28**, 822 (1978).

10. V. S. Fadin, *Talk Presented at NATO Advanced Research Workshop on Diffraction 2002, Alushta, Ukraine, 2002*, p. 235.

11. Ya. Ya. Balitskii, L. N. Lipatov, and V. S. Fadin, in *Proceedings of XIV LIYAF Winter School, Leningrad, 1979*, p. 109.

12. V. S. Fadin, Yad. Fiz. **66**, 2067 (2003) [Phys. At. Nucl. **66**, 2017 (2003)].

13. L. N. Lipatov and M. I. Vyasovsky, Nucl. Phys. B **597**, 399 (2001); hep-ph/0009340.

14. V. S. Fadin and R. Fiore, Phys. Rev. D **64**, 114012 (2001); hep-ph/0107010.

15. M. I. Kotsky, L. N. Lipatov, A. Principe, and M. I. Vyazovsky, Nucl. Phys. B **648**, 277 (2003); hep-ph/0207169.

16. A. V. Bogdan, V. Del Duca, V. S. Fadin, and E. W. N. Glover, J. High Energy Phys. **0203**, 032 (2002); hep-ph/0201240.

17. D. J. Broadhurst, J. A. Gracey, and D. Kreimer, Z. Phys. C **75**, 559 (1997); hep-th/9607174.

18. V. S. Fadin, R. Fiore, and M. I. Kotsky, Phys. Lett. B **387**, 593 (1996); hep-ph/9605357.

═══ CURRENT EVENTS ═══

70th Birthday of Yuriĭ Fedorovich Smirnov

On May 26, 2005, Professor Yuriĭ Fedorovich Smirnov, leading researcher at the Institute of Nuclear Physics at Moscow State University, member of the Mexican Academy of Sciences, celebrated his 70th birthday. Yu. Smirnov is a brilliant representative of Soviet and Russian science. The main focus of his scientific interests lies in the realms of theoretical nuclear and atomic physics and mathematical (group-theory) methods in theoretical physics. He is the author of about 300 scientific publications, including ten well-known monographs. The citation index of his studies exceeds 1500. He supervised the work of 16 candidates of science in physics and mathematics and taught many different lecture courses at the Physics Department of Moscow State University. Smirnov was a recipient of the K.D. Sinelnikov Prize of the Ukrainian Academy of Sciences in 1982 and the Lomonosov Prize of Moscow State University in

2002 and is a member of the Editorial Council of the journal *Physics of Atomic Nuclei.*

The first important contribution of Smirnov to science dates back to his postgraduate years and concerns the theory of nucleon clustering in light nuclei on the basis of the multiparticle shell model. Together with two colleagues, he introduced coefficients describing the transformation of the wave function for a system of a few nucleons in the oscillator shell model from single-particle to cluster Jacobi coordinates and proposed a method for calculating these coefficients, which are presently referred to as Talmi−Moshinsky−Smirnov coefficients. By using this result, Smirnov showed (1959−1961) that by no means does the fact that reduced widths for cluster (for example, alpha-particle) emission from p-shell nuclei are close to Wigner's single-particle limit favor the alpha-particle model of nuclei; moreover, he proved that such values are quite compatible with the multiparticle shell model. This theory made it possible to describe successfully and to predict a wide variety of experimental data.

In 1966−1968, Smirnov and his colleagues proposed the method of quasielastic electron knockout by a fast electron [$(e, 2e)$ reactions] at energies of about 10 to 50 keV from atoms, molecules, and solid bodies. This was an extremely successful example of extending experience gained in nuclear physics [$(p, 2p)$ reactions at energies of about 500 MeV] to a different region. An experimental implementation of this method in several countries made it possible to "feel" (via measuring respective momentum distributions), for first time, various individual electron orbitals and to test, at this level, which is the most adequate, the Hartree−Fock method, as well as to explore, by means of $(\gamma, 2e)$ and $(e, 3e)$ experiments performed in the double- and triple-coincidence modes (such experiments were also proposed by Smirnov and his colleagues), electron−electron correlations in various multielectron systems. Many experimental and theoretical studies have been conducted in this field as well.

Finally, Smirnov and his colleagues obtained an outstanding result in the realms of group-theory methods in quantum physics. They developed a universal method of projection operators (currently

known as Asherova−Smirnov−Tolstoy projection operators) for all semisimple Lie groups. This method makes it possible to construct efficiently wave functions for quantum systems possessing preset symmetry properties. A complete and consistent mathematical theory of the $SU(3)$ spin (including respective Clebsch−Gordan and Racah coefficients) was constructed for the first time by this method. Smirnov and his colleagues also applied the method in question to quantum Lie algebras, which form a very rapidly developing field of investigations.

At seventy, Smirnov continues his studies vigorously. He writes articles (in particular, in *Physics of Atomic Nuclei*) and reviews and discusses modern scientific problems with colleagues and disciples. It is a pleasure for us to wish Smirnov good health, prosperity to him and his relatives, and many years of creative activity.

R. M. Asherova, V. V. Balashov,
L. D. Blokhintsev, G. Ya. Korenman,
V. V. Kukulin, D. E. Lanskoĭ,
V. I. Man'ko, V. G. Neudatchin,
I. T. Obukhovsky, I. M. Pavlichenkov,
V. N. Pomerantsev, V. P. Popov,
V. N. Tolstoy, A. M. Shirokov,
and Yu. M. Tchuvil'sky

===== FUTURE PUBLICATIONS =====

Production of Ω_{scb} Baryons in Photon−Photon Collisions

S. P. Baranov and V. L. Slad

Methods for calculating the total and differential cross sections for the production of Ω_{scb} baryons in photon−photon collisions and the results that these methods produce are described.

Charge Asymmetry in the Photoproduction of Charmed Mesons

A. V. Berezhnoy and A. K. Likhoded

Within the perturbative-recombination model, the charge asymmetries in the $D^{*+} - D^{*-}$, $D^{*0} - D^{*0}$, and $D_s^+ - D_s^-$ yields are estimated under the kinematical conditions of the COMPASS experiment. Corrections that arise owing to the mass of a light quark in a charmed meson are taken into account. The yield of D_s^+ mesons is predicted to be large in relation to the yield of D_s^- mesons.

Gauge-Invariant Spatial Shift in Calculating a Color Axial Anomaly

I. T. Dyatlov

A nonsinglet axial anomaly is calculated for the case where the interaction of fermions with a non-Abelian gauge field is regularized by means of a coordinate shift according to Schwinger. The methods used makes it possible to obtain a covariant expression for the anomaly directly from the effective action for the field. The anomaly in question was calculated many times by numerous different methods, but the application of the shift method to this problem (from the study of W. Bardeen in 1969) led to the result only through a number of intermediate stages and additional subtractions of specially chosen polynomials of fields.

Solving Faddeev−Merkuriev Equations within the *J*-Matrix Approach: Application to Coulomb Problems

S. A. Zaitsev, V. A. Knyr, and Yu. V. Popov

Within the J-matrix method for solving Faddeev−Merkuriev three-particle differential equations, a version is proposed that makes it possible to take into account the full spectrum of the two-particle Coulomb subsystem. Laguerre functions are used as a basis in which the total wave function for the problem being considered is expanded. In order to test the efficiency of the proposed method, the differential cross section for a single ionization of a helium atom is calculated for the case where the emerging He^+ ion remains in an excited state. The result is in satisfactory agreement with experimental data both in magnitude and in the shape of the respective curve.

Neutrino Corona of a Protoneutron Star and Analysis of Its Convective Instability

V. S. Imshennik and I. Yu. Litvinova

A numerical solution to the problem of the structure of the neutrino corona of a protoneutron star that is formed upon an star-iron-core collapse, which is peculiar to all massive stars at the end of their thermonuclear evolution, is given. The structure of a neutrino corona, which is semitransparent to neutrino radiation from the spherical envelope between the neutrinosphere and the front of the accretion shock wave, is determined by a set of ordinary nonlinear equations of spherically symmetric neutrino hydrodynamics with allowance for a full set of beta processes in a Boltzmann gas of free nucleons and an ultrarelativistic Fermi−Dirac electron−positron gas that form neutrino-corona matter. The problem of consistently taking into account nonequilibrium neutrino-absorption and neutrino-emission processes and the problem of formulating boundary conditions for a neutrino corona were the main problems in constructing the numerical solution in question, which was obtained by means of a dedicated algorithm. The problem at hand features a number of parameters: the protoneutron-star mass, M_0; the rate of accretion of the outer layers of the collapsing star being considered, $\dot{M}_0$; the

effective temperature of the neutrinosphere and the effective neutrino chemical potential there, $T_{\nu\,\text{eff}}$ and $\psi_{\nu\,\text{eff}}$, respectively; and, finally, the total neutrino emissivity of the neutrinosphere, $L_{\nu\bar{\nu}}$. Two of these parameters, M_0 and $L_{\nu\bar{\nu}}$, are varied within broad intervals in accordance with the hydrodynamic theory of a collapse. On one hand, the numerical solutions constructed in the present study give an idea of the physical conditions in the immediate vicinity of a protoneutron star in the course of its continuing gravitational collapse; on the other hand, they make it possible to obtain exhaustive information about its convective instability, which is the most important property of a so-called soundless collapse—that is, a collapse not accompanied by an explosion on the supernova scale. The increment of development of a convective instability is obtained at a linear stage, this giving sufficient grounds to introduce the hypothesis that the instability in question plays a key role in the origin of observed gamma-ray bursts. More precisely, these bursts may result from the development of the instability at the subsequent nonlinear stage, which has yet to be studied theoretically—in particular, on the basis of non-one-dimensional numerical models of neutrino hydrodynamics.

Nucleus−Nucleus Scattering in the High-Energy Approximation and Optical Potential in the Folding Model

V. K. Lukyanov, E. V. Zemlyanaya, and K. V. Lukyanov

A microscopic complex folding-model potential that reproduces the scattering amplitude of Glauber−Sitenko theory in its optical limit is obtained. The real and imaginary parts of this potential are dependent on energy and are determined by known data on nuclear-density distributions and on the nucleon−nucleon scattering amplitude. For the real part, use is also made of a folding-model potential obtained with effective nucleon−nucleon forces and with allowance for nucleon exchange. Three forms of semimicroscopic optical potentials where the contributions of the inputs—that is, the real and the imaginary folding-model potential— are controlled by adjusting two parameters are constructed on this basis. The efficiency of these microscopic and semimicroscopic potentials is tested by means of a comparison with the experimental differential cross sections for the elastic scattering of heavy ions ^{16}O on nuclei at an energy of $E \sim 100$ MeV per nucleon.

Noncompact Quantum Algebra $u_q(2,1)$: Intermediate Discrete Series of Unitary Irreducible Representations

Yu. F. Smirnov, Yu. I. Kharitonov[†], and R. M. Asherova

Unitary irreducible representations of the $u_q(2,1)$ quantum algebra that belong to an intermediate discrete series are considered. A q-analog of the Mikelson−Zhelobenko algebra is developed. Use is made of the U basis that corresponds to the $u_q(2,1) \supset u_q(2)$ reduction. Explicit expressions are obtained for the matrix elements of generators in this basis. An operator is found that projects an arbitrary vector onto the extremal vector for a representation from this series.

Nontraditional Role of Interparticle Forces in Quantum Mechanics

A. I. Steshenko

A quantum-mechanical model for systems of interacting bodies that takes into account noncommutativity of the operators of coordinates and momenta of different particles and correlation equalities for the uncertainties of these quantities is considered. Here, the noncommutativity of these operators is due to the effect of interparticle forces and arises as a natural generalization of the usual commutation relation between the coordinate and momentum operators for a single particle. The efficiency of the model is proven by calculations for systems known in atomic and nuclear physics.

[†] Deceased.

A Study of the Nuclear-Medium Influence on the Production of Neutral Strange Particles in Deep-Inelastic Neutrino Scattering

N. M. Agababyan, V. V. Ammosov, M. Atayan, N. Grigoryan, H. Gulkanyan, A. A. Ivanilov, Zh. Karamyan, and V. A. Korotkov

The influence of nuclear effects on the production of neutral strange particles (V^0) is investigated using data obtained with the SKAT propane−Freon bubble chamber irradiated in a neutrino beam (with $E_\nu = 3-30$ GeV) at the Serpukhov accelerator. The mean multiplicity of V^0 particles in nuclear interactions, $\langle n_{V^0} \rangle_A = 0.092 \pm 0.010$, is found to exceed significantly that in "quasideuteron" interactions, $\langle n_{V^0} \rangle_D = 0.063 \pm 0.013$. The ratio $\rho_{V^0} = \langle n_{V^0} \rangle_A / \langle n_{V^0} \rangle_D = 1.46 \pm 0.23$ is larger than that for π^- mesons, $\rho_{\pi^-} = 1.10 \pm 0.03$. It is shown that the multiplicity gain of V^0 particles can be explained by intranuclear interactions of product pions.

Mass and Decays of Brout−Englert−Higgs Scalar with Extra Generations

J.-M. Frère, A. N. Rozanov, and M. I. Vysotsky

The upper bound on the mass of the Brout−Englert−Higgs scalar boson arising from radiative corrections is not stable when the Standard Model is extended to include nondecoupling particles. In particular, additional generations of fermions allow for a heavier scalar. We investigate how the branching ratios for scalar-boson decays are affected by the opening of new channels.

Antineutrino Background from Spent-Fuel Storage in Sensitive Searches for θ_{13} at Reactors

V. I. Kopeikin, L. A. Mikaelyan, and V. V. Sinev

Sensitive searches for antineutrino oscillations in the atmospheric-mass-parameter region, much discussed in recent years, are based on an accurate comparison of the inverse-beta-decay positron spectra measured in two (or more) detectors, far and near, positioned, for example, at about 1000 and 100 m from the reactor(s) used. We show that antineutrinos emitted from the stored irradiated fuel can differently distort the soft part of the positron spectra measured in the far and near detectors, thereby mimicking (or hiding) an oscillation signal.

Coulomb Deexcitation and Nonresonant Charge Exchange of Muonic Hydrogen in Mixtures of Hydrogen Isotopes

A. V. Kravtsov and A. I. Mikhailov

The process of inelastic collisions of excited muonic hydrogen is considered within the asymptotic theory of nonadiabatic transitions. The Coulomb deexcitation and charge-transfer rates are calculated in the energy range 0.001−100 eV with allowance for the electron-screening effect for excited states in the range $n = 3-10$ for various isotopic configurations.

Experimental Study of Direct Photon Emission in the Decay $K^- \to \pi^- \pi^0 \gamma$ with the ISTRA+ Detector

V. A. Uvarov, S. A. Akimenko, V. N. Bolotov, G. I. Britvich, K. V. Datsko, V. A. Duk, A. P. Filin, A. V. Inyakin, V. A. Khmelnikov, A. S. Konstantinov, V. F. Konstantinov, I. Y. Korolkov, S. V. Laptev, V. M. Leontiev, V. P. Novikov, V. F. Obraztsov, V. A. Polyakov, A. Yu. Polyarush, V. I. Romanovsky, V. M. Ronjin, V. I. Shelikhov, N. E. Smirnov, O. G. Tchikilev, and O. P. Yushchenko

The branching ratio in the charged-pion kinetic energy region between 55 and 90 MeV for direct photon emission in the decay $K^- \to \pi^- \pi^0 \gamma$ was measured by using in-flight decays detected with the ISTRA+ setup operating in a 25-GeV/c negative secondary beam of the U-70 PS. The value of Br(DE) = $[0.37 \pm 0.39(\text{stat.}) \pm 0.10(\text{syst.})] \times 10^{-5}$, which was obtained from an analysis of 930 completely reconstructed events, is consistent with the average value of two stopped-kaon experiments, but it differs by 2.5 standard deviations from the average value of three in-flight-kaon experiments. The result is also compared with recent theoretical predictions.